Stefan Heinrich *Editor*

Dynamic Flowsheet Simulation of Solids Processes

Dynamic Flowsheet Simulation of Solids Processes

Stefan Heinrich
Editor

Dynamic Flowsheet Simulation of Solids Processes

Editor
Stefan Heinrich
Institute of Solids Process Engineering
and Particle Technology
Hamburg University of Technology
Hamburg, Germany

Preface

Processes of material and energy conversion often consist of multiple individual sub-processes that are interconnected by material, energy and information streams. The cross-links between the individual sub-processes have a significant impact on the dynamic behaviour and the stability of such processes. For the design and optimization, particularly in view of the conservation of energy and raw material resources, not only the individual components should be simulated, but also the dynamic behaviour of the whole process. This is the state of the art for fluid processes and different tools for dynamic flowsheet simulation are commercially available. In contrast, such program systems and process models which are generally applicable to a wide range of applications are missing for solids processes. This is due to the complex description of solids with their multivariate disperse properties and the associated processes for the conversion of solids.

The flowsheet modelling allows for an investigation of complex processes consisting of several interconnected apparatuses and sub-processes on longtime scales. For the solids process engineering, the multidimensionality of the properties of granular materials significantly complicates the solution of various problems, such as design or optimization of production processes. As most solids processing systems include unit operations that have a strong impact on the transient behaviour of the whole process, like conveyors or bunkers, the ability to simulate the behaviour of dynamic systems is crucial for applying flowsheet models for optimization or control purposes in the area of solids processing technology.

Available flowsheet simulation programs deal with the challenge of solids process simulation. However, none of the tools offer the option of dynamic process simulation of solids processes with the inherent description of the multidimensional distributed parameters of the granular material.

The German Research Foundation (Deutsche Forschungsgemeinschaft, DFG) has supported a research program in the form of the Priority Program (SPP 1679) on "Dynamic simulation of interconnected solids processes (DYNSIM-FP)" from 2013 to 2020. The goal was to study the dynamics of different processes in the area of solids process engineering and to gain a better understanding of the phenomena that arise when combining various of such sub-processes into a single interconnected

system. The central aim was to provide numerical tools for dynamic simulation of interconnected solids processes. For this, dynamic models of various equipment and machinery for solids processing are to be formulated and implemented. Furthermore, methods for the numerical treatment of such systems and new models for the description of solids properties shall be developed.

The research within SPP 1679 was classified into three research areas consisting of 27 research projects from universities and research institutes from Germany: (a), (b) models for the description of solids properties, (c) algorithms and process simulation. Additionally, a separate Central Project (Z-project) was established. Its goal was to develop a flowsheet modelling system, which should serve as a platform for combining the results of all these individual groups into a single framework. To allow for mostly independent model development and research, the flowsheet simulation framework must provide high flexibility, extensible libraries and stable interfaces. The resulting open-source modular modelling system Dyssol—an acronym for "**Dy**namic **s**imulation of **sol**ids processes"—offers these features through its high degree of modularity, open and standardized interfaces, efficient algorithms and a clear user interface.

This book summarizes the research results of this joint research project. The research program SPP 1679 DYNSIM-FP has been steered by a committee, where Prof. Stefan Heinrich, Hamburg, took over the coordination (spokesperson) and was supported by Prof. Arno Kwade, Braunschweig (vice-spokesperson); Prof. Heiko Briesen (vice-spokesperson), München; Prof. Wolfgang Peukert, Erlangen; Prof. Matthias Kind, Karlsruhe; and Prof. Achim Kienle, Magdeburg. We want to thank and greatly appreciate the DFG for financial support, and especially Dr.-Ing. Bernd Giernoth, Dr.-Ing. Georg Bechtold, Dr. Simon Jörres and Ms. Anja Kleefuß for their excellent coordination and continued support of the research activities. Of course, the great success of the SPP 1679 would not have been possible without the enthusiasm of all involved Ph.D. students and researchers and their excellent contributions. Numerous workshops, most held in Hamburg, were the clamp of the intensive cooperation within the several projects.

Hamburg, Germany   Stefan Heinrich
February 2020

Contents

Part I
New Dynamic Process Models

Chapter 1
Process Modeling for Dynamic Disperse Particle Separation and Deposition Processes

Sören Sander, Lizoel Buss, and Udo Fritsching

1 Introduction

Dynamic particulate process models are to be derived within the framework of dynamic flowsheet modeling and simulation (FSS). In the contribution FSS is developed for the separation processes of solid particles from a fluid resp. gas. Potential applications of the dynamic simulation environment of particle separation are for instance in the analysis and design of the dynamic process behavior in the purification of exhaust gases (for example to reduce emissions from combustion processes) but also in the production of particle layers with defined properties, as occur in the powder coating of surfaces.

A specific focus of the derivation is on analysis of gas cleaning of a particle-laden air stream through a plate-wire electrostatic precipitator. In this process, the intensification of the degree of separation is achieved by the application of electric field forces. The result is a coupled multiphase flow system in which interactions between the electric field, the fluid phase and the particles on several scales lead to a complex relationship between the degree of precipitation and the conditions in the process.

The properties of the particulate material, the feed stream parameters as well as the specific process control directly influence the output stream conditions as for instance the particle size distribution and dust concentration, thus the precipitation efficiency of the process. The specific spatial distribution of the particles and their charges may cause temporal changes in the deposition behavior in the apparatus. The locally varying thickness of the deposited particle layer increasingly influences the re-dispersion and re-entrainment of already deposited particles back into the flow field. This successive growing particle layer structure plays a significant role, especially during the transient startup phase of the process. For heavy load changes,

S. Sander · L. Buss · U. Fritsching (✉)
Leibniz-Institute for Materials Engineering IWT, Particles and Process Engineering,
University of Bremen, Badgasteiner Strasse 3, 28359 Bremen, Germany
e-mail: ufri@iwt.uni-bremen.de
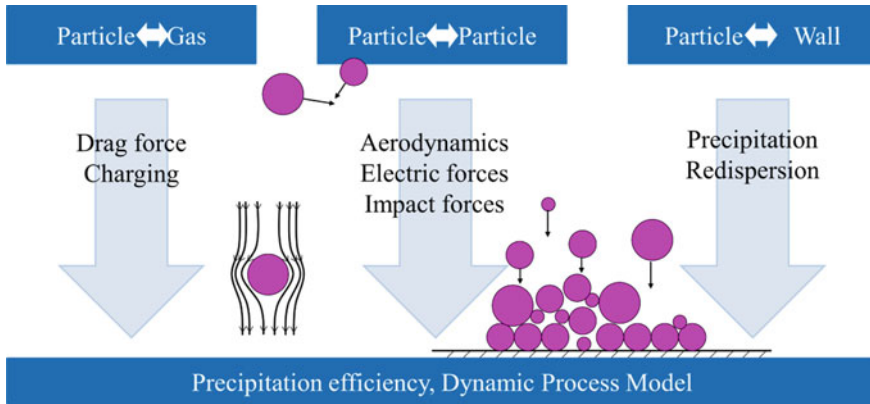
Fig. 1 Complex interaction between electric field forces, fluid, particles and walls

e.g. in the incoming particle laden gas stream, changes in the concentration, the particle size distribution and also in the composition of the disperse phase may lead to a dynamic transient behavior of the deposition process.

The separation efficiencies and performance of electrostatic precipitation processes (ESP) are analyzed by means of

1. an experimental labscale model setup of a plate-wire electrostatic precipitator and
2. simulations in a coupled Computational Fluid Dynamics (CFD) model as well as in
3. a Flow Sheet Simulation (FSS) model building block.

Here, variations in the feed material (various model dusts) as well as in the geometry of the separator are to be analyzed. The goal is to transfer the particle layer interaction with the impinging particles and the particle-layer-fluid interaction into a physically based predictive process model. These interactions result in the multiple dependencies as shown in Fig. 1.

2 Electrostatic Particle Separation: State of the Art

In order to reduce environmental pollutions with particulate matter, powders and dusts, progressively more constrictive legal obligations for fine dust separation of PM10, PM2.5 and PM1 into the environment are proposed. Electrostatic precipitators (ESP) obtain high efficiency in this particular particle size range. ESP are applied for instance to fly ash separation during exhaust gas cleaning in industrial processes such as lignite or bituminous coal fired boilers, biomass combustion or coal fired power

plants [1–4]. In addition, ESP applications to street cleaners have been investigated [5]. During the past years, new insight into dust separation from exhaust gas by electrostatic precipitators covered high gas temperatures, discharge electrode design and quenching (e.g. [6, 7]).

The dynamics in electrostatic precipitators depend on the particle charging and the field transport. Both parameters vary with local particle position, thus leading to an effective field particles traverse [4]. A frequently used and industrially applied mathematical model for the particle separation efficiency

$$\eta = 1 - EXP\left(-w_{th}A/\dot{V}\right) \tag{1}$$

has been presented by [8], where the collection area A and the flow rate $\dot{V}$ are the main process parameters. The theoretical migration velocity

$$w_{th} = q_{\max}E\frac{Cu}{3\pi\mu d_p} \tag{2}$$

depends on the electric field E of the ESP, particle size d_p and the maximum particle charge

$$q_{\max} = \left[(1 + 2Kn)^2 + \frac{2}{(1 + 2Kn)}\frac{\varepsilon_r - 1}{\varepsilon_r + 2}\right]\pi\varepsilon_0 d_p^2 E, \tag{3}$$

where ε_0 is vacuum permittivity, ε_r is the particle relative permittivity, Cu is the Cunningham correction factor and Kn is Knudsen number.

Numerical models of ESP allow tracking of particles through a channel exposed to a electrode geometry specified electric field. The effect on different electrode geometries on the overall precipitation has been shown experimentally ([1, 9]). Numerical simulation of ESP typically is limited to simple plate or wire-electrodes, as their geometry easily can be reduced to a 2D structure [10]. As these electrodes are well studied, they are a good starting point for comparison of different designs. During the last few years, some authors started analyzing more complex electrode geometry designs extending their models and meshes to 3D ([11, 12]). However, the precipitation curves e.g. presented by [8] require the input of mean field values, that are assumed to stay constant throughout the ESP, namely $n_{i,\infty}t$-product in case of nano sized particles and electric field E in case of micron particles. Numerical models allow precise tracking of this field data along the particle tracks, which exhibit the undergoing of charging and acceleration inside the field. This way, the actual particle movement and separation is connected to the mean field values and, therefore, separation efficiency inside EPS's and the assumptions necessary for derivation of integral models can be examined.

2.1 Lab Scale Electrostatic Precipitator Design

The ESP studied in this work is a 0.3 m high and 0.5 m wide rectangular channel with a length of 1.2 m. The channel walls top and bottom are made of acrylic glass. The sides consist of grounded copper plates. At the width central plane at a distance of 0.3, 0.6 and 0.9 m from the inlet, three wire spray electrodes are positioned. This design covers a section of a real size ESP, where multiple channels of the aforementioned width stringing together to allow higher throughputs of exhaust gas. These parallel channels are typically 20–60 times higher and their length is varied by a factor of 10–20 to account for nanometer to micrometer sized particle precipitation.

2.2 Numerical Methods for Flow and Electric Field

Numerical models of the electric fields, charge transport and retroactive effects on the continuous phase, so called electric wind, have been developed and improved ([10, 13, 14]). These models calculate the electrostatic field with respect to Poisson equation

$$\nabla E = -\frac{\rho_E}{\varepsilon_0} \qquad (4)$$

where ρ_E and ε_0 are the space charge density and the vacuum permittivity, respectively. The ion flux J is modelled by

$$J = \rho_E \cdot (bE + U) - D\nabla\rho_E. \qquad (5)$$

A dimensional analysis shows that the flux induced due to the electric field E is in the order of 10^{-3} while the transport with the fluid velocity U is just around 10^{-5} and the diffusional transport is of the order below 10^{-8}. It is justified to neglect the latter two. This increases the stability of the solver while only slightly lowering the accuracy. The standard iterative pressure-velocity link approach iterates between the continuity equation and the Navier-Stokes equation with an additional electric force F_{el} added to account for fluid motion due to ion acceleration induced by the electric field

$$F_{el} = \rho_E E. \qquad (6)$$

This model only includes electrophoreses and assumes isotropic permittivity inside the medium (no polarization of gas molecules). Isothermal conditions ensure the absence of electrostriction. The continuous gas phase is modeled as an Eulerian phase using the [15] 2.3.1 formulation (pimpleFoam) and an anisotropic Reynolds-Stress-Model (RSM) modeling turbulence effects ([16, 17]). It should be noted that the instable ion discharges at the electrode ([18, 19]) leads to a spatial gradient in

charge density. This corresponds to a fluctuation in fluid acceleration close to the electrode and higher velocities appear, producing turbulence. The model presented here does not properly resolve the time scales of this process and thus the additional turbulence production is neglected. The iteration limit is 200, but the solution was observed to converge after 2–3 iterations, allowing a convergence tolerance of 10^{-5}. Linear upwind and cell limited least square schemes discretize the divergences and gradients, respectively.

2.3   Numerical Grid and Mesh Setup

Three numerical mesh configurations approximate different ESP geometries. These configurations govern the principle particle transport and electric wind influence on flow structure for the ESP geometries. Regions close to the spraying electrodes are refined. The rectangular cells align with the inlet mean flow direction. The area from electrode to wall is slightly altered to fit the electric field. Reasons for adjustments in mesh cell direction are the fluid cell Courant number

$$CFL_i = u_i \frac{\Delta t}{\Delta x} \tag{7}$$

and the electric Courant number

$$CFL_{el} = b|\boldsymbol{E}| \frac{\Delta t}{\Delta x} \tag{8}$$

where u_i is continuous phase cell velocity magnitude, b is the ion mobility, $\boldsymbol{E}$ the electric field, Δx is characteristic cell length and Δt is the time step. These numbers determine the solver stability criterion. The cell limited upwind scheme is more accurate, if cells are in direction of the flow. This direction is perpendicular for the ion flux (in direction of the electric field) and the fluid flow (in direction of the channel length). The cell direction increases the accuracy of both field solutions. The two meshes for spiked wire electrode setups are developed based on the wire-electrode mesh and highly refined close to the electrode tips. For all cases, the wall distance was adjusted to fit the specific turbulence model needs. The criterion was checked after each successful run. Further cell reduction was achieved coarsening the inlet and outlet regions. For the studies of particle transport inside the spiked-wire precipitators, the volume is discretized using a maximum of about 3 Mio cells in case of asymmetric and symmetric spikes.

For the wire-electrode mesh, a simplified 2D structure is extrapolated into the third dimension using hex-cells. The near wall region is resolved while electrode regions are captured just roughly to reduce the number of cells. The mesh coarsens in intermediate regions using a cell growth function. A mesh independency study allowed reduction in the total number of cells from more than 8,000,000 to just 366,060.

Table 1 Boundary condition variations

Phys. quantity	Inlet	Walls	Anodes	Electrodes	Outlet
ρ_E	$grad = 0$	$grad = 0$	$grad = 0$	Calculated	$grad = 0$
V	$\nabla = 0$	$\nabla = 0$	0	Fixed	$\nabla = 0$
U	$(1\ 0\ 0)$	$(0\ 0\ 0)$	$(0\ 0\ 0)$	$(0\ 0\ 0)$	$\nabla = 0$
p	$grad = 0$	$grad = 0$	$grad = 0$	$grad = 0$	0

2.4 Boundary Conditions

In the area close to the spray electrodes the air is ionized, represented by a boundary value for ion space charge. In general, the electrodes create charges that hit air molecules. This way a cascade air charging follows and leads to a high increase in ions next to the electrodes [20]. The zone in which this cascade mainly occurs is about

$$r_c = r + 0.003\sqrt{r} \tag{9}$$

and depends on the electrode radius [21]. As this zone is small compared to the domain, the boundary is relocated onto the electrode surface. The values are taken from [22, 23].

Cooperman [23] described, that the parabolic dependency of the charge density on the applied voltage should be determined from experimental values. It leads to a fit of the form

$$\frac{J_b}{V} = mV + b, \tag{10}$$

where V is the applied voltage, J_b is ion flux in surface normal direction, and m and b are experimental constants. The actual value should be measured, as particles further influence the final value (compare e.g. [24]). Physical quantities of velocity, pressure, potential and ion concentration at mesh boundaries are repented in Table 1.

2.5 Particle Transport Analysis

The particle transport modeling is based on conventional Lagrangian movement formulation as implemented in [15]. In ESP's particles undergo an additional electric force based on their number of charges. Thus, a model for particle charging and acceleration due to electric forces is implemented into OpenFOAM using the approach of Lawless [25]. This unipolar charging model unites former approaches of diffusion and field charging.

The charging mechanism is based on particle size and electric field strength. Particles charge fast if they are either in a high electric field or if their surface can collect many electrons e (high surface area and, therefore, particle diameters d_p). A comparison of particles in an electric field E is done by utilizing the dimensionless charging numbers of

$$w = \frac{\frac{d_p}{2}E}{\frac{kT}{e}} \tag{11}$$

at a normal temperature $T = 21.5$ °C, where k is the Boltzmann constant. The dimensionless charge is calculated by

$$c^{'} = \frac{ne^2}{2\pi\,\varepsilon_0 d_p kT} \tag{12}$$

and the dimensionless time by

$$\tau = \frac{b\rho_E t}{\varepsilon_0}. \tag{13}$$

Both curves are in principal agreement with simulations in [25]. In the beginning, field charging is the dominant effect responsible for particle charging. At later times field charging becomes less important, as surface charges of particles reduce the electric field around the particle and electrons are more frequently transported around the particle. For a better understanding of the mechanism, upper and lower bounds of particle charging are shown in the diagram. The lower bound is obtained assuming only the dominant charging takes place. The sum of charges method assumes that diffusive and field charging as described in [25] are additive. This solution differs only slightly from the simulative results in this work. For particle charging with various permittivity the saturation charge $3w$ must be recalculated replacing it by the quantity

$$1 + 2\frac{\varepsilon_r - 1}{\varepsilon_r + 2}. \tag{14}$$

This factor is a measure for distortion of the electric field around the particle.

2.6 Experimental ESP Setup

The electrostatic precipitator studied in experiments allows the analysis of the deposition of airborne particles. Construction and operation of the laboratory plant for the investigation of electrostatic precipitators are shown in Fig. 3. The particles are fed virtually pulsation-free via a twin-screw particle feeder and dispersed into

the gas stream by means of a nozzle. The system is operated in the suction mode. The compressor at the end of the system can handle maximum volume flow rates of 1700 m^3/h. This flow rate leads to mean velocities in the flow channel (cross Sect. 30 cm × 50 cm) of max. 3 m/s. The dispersed particles are accelerated with the gas flow into the channel through a honeycomb flow straightener.

Not separated particles are detected at the outlet of the ESP by an aerosol spectrometer (GRIMM). The exiting flow from the ESP, directly connected to the channel, is cleaned of the remaining particles in the gas stream. Therefore, the gas stream first passes through a cyclone. Here the particles larger than 5 microns are deposited. The gas then passes through a cartridge filter and a filter cloth. The air is not returned but escapes through a vent to the outside (Fig. 3).

2.7 Flow Field Analysis: PIV-System

To measure the particle velocities along the channel of the electrostatic precipitator, Particle Imaging Velocimetry (PIV) is used (see also [26, 27]). A flexible shielded laser arm leads the laser beam to the inlet of the flow channel. A beam expander at the output of the arm widens the beam. The laser light section then propagates in the direction of flow perpendicular to the deposition anodes as shown in Fig. 4.

With the PIV measuring system, the flow of particles in a 2d plane is measured. The measurements are used to derive instantaneous and average velocity profiles of the particles in a section of the separator.

2.8 Particle Layer Measurement

For analyzing the deposited particle layer at the ESP wall, specific small targets (round stubs) are placed in the channel walls that easily could be removed from the walls. Three stubs with a diameter of 20 mm are mounted into the collection anode at a height of 0.15 m and lengthwise to the second electrode. The particle layers formed on these stubs are examined with a microscope to determine the thickness of the deposit. Figure 5 shows the test set-up used to determine the deposit thicknesses.

In addition to the stubs another layer sample is collected on a copper plate with the size of 20 cm × 20 cm. This sample is used for offline characterization of the layer dustiness.

2.9 Coupled CFD-Modeling

Numerical simulation studies of electrostatic precipitation (EPS's) of dust particles from exhaust gases have been carried out. In ESP's particle separation from exhaust
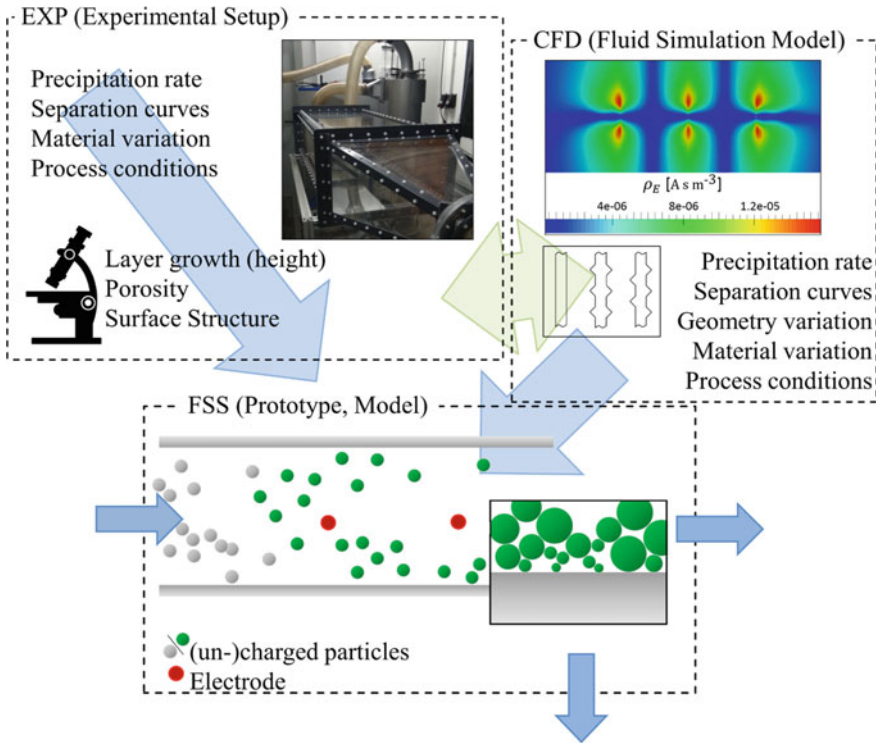
Fig. 2 Dependencies during implementation of a flow sheet model (FSS) from experimental inputs (EXP) and fluid simulation modeling (CFD)

gases is intensified by an external static electric field. Coupling effects between gas flow characteristics, electric field, induced charges and the particulate matter occur during the process [28]. Numerical modeling and simulation is increasingly used to identify the influence of these coupling effects and, therefore, particle acceleration in ESP's on precipitation efficiency (e.g. [10, 29, 30]). Particle deposition and layer formation impacts separation efficiency as the layer itself induces back corona, sparking and re-entrainment. These disturbances are strongly dependent on the local layer properties, such as particle size, packing density, chemical composition and layer thickness. The resistivity of a typical fly ash layer strongly varies with the iron and sodium content [31].

Numerical simulation is capable of tracking particle parcels throughout the domain and analyzes their deposition. Particles are treated statistically in parcels by momentum exchange with the continuous phase using well validated models available (e.g. Schiller-Naumann). Their coupling with the electric field is described using a charging model to determine their charging. Afterwards an external force field model couples their cross-section movement towards the direction of the electric field. The charge movement modeled in terms of diffusive and convective transport

alongside with the transport inside the electric field. In OpenFOAM, a test case shows the validity of the model formulation giving special attention towards an electric CFL criterion

$$CFL_{el} = \frac{\rho_E k E \Delta t}{\Delta x} < 0.5 \tag{15}$$

that specifies numerical stability for transport of a scalar in an electric field. The transport itself is bounded by Peek's formulation at the boundaries using Kapzov's assumption for cylindrical surfaces, e.g. proposed by [32]

$$E_0 = 3.1 \cdot 10^6 \left[\frac{V}{m} \right] \rho_{rel} \left(1 + \frac{0.0308}{\sqrt{\rho_{rel} r}} \right). \tag{16}$$

Inside the standard PIMPLE-loop an additional term describes the velocity change due to the ion movement based on ion density and electric field strength. This captures any influence of particulate cross section movement. The wake that occurs at the spraying electrode weakens with increasing inlet velocities wherewith particle redirection diminishes.

Results and test cases show the overall behavior of particle movement inside ESP's and the coupling between continuous phase and electric field, the so-called electric wind. The newly implemented model into OpenFOAM is validated against analytical solutions to the problem. Small microns- to nano-sized particles carry fewer charges compared to bigger ones, as their surface saturates, and the captured ions prevent impaction of more charges. This leads to a decreased velocity in radial direction. As expected, these particles in the range of 0.3–1 µm tend to impact the wall closer to the outlet. Low conductivity basically induces the same behavior. The layer develops to a coarser structure with higher porosity and less contact points along the channel while at the same the resistivity rises. Therefore, re-entrainment and back corona become more likely.

2.10   Flowsheet Simulation FSS

The FSS model for the integral predictive simulation of the deposition of particulate matter in electrostatic precipitators (flowchart simulation FSS) consists of two stages. First, the deposition of the material on the electrode wall is described, where a general theoretical deposition consideration applies. The field strength entering into the equation is supplemented by a factor, which represents the effective field of the particles. This factor is depending on the structure of the separator, in particular on the electrode geometry and is therefore an essential parameter of the system geometry. In the FSS model for ESP the separated particles distribute to the holdup and are not yet considered completely separated.

In the second stage, the possible redispersion of particles from the deposited layer back into the flow field is characterized on the basis of the particles in the holdup. A mean characteristic is determined by defining a reentry probability. Particles that do not reenter the gas stream end up as finally separated at the outlet of the model while the exhaust gas stream contains all the non-separated and redispersed particles in the first step.

The dynamic FSS simulation environment "dysSol" of Skorych et al. [33] is utilized as a simulation frame where a new dynamic model unit "ESP" calculates the evolving particle sizes and masses at the outlet of the precipitator with time. The precipitation rate defines the transformation matrix used in the framework.

While the collection area and the flow rate are easily determined and usually previously known, especially the particle migration velocity inside ESP is to be modeled [34]. A common principle is to use the terminal velocity of maximum charged particles

$$w_{th} = q_{\max,th} E_{ESP} \frac{Cu}{3\pi \mu d_p} \tag{17}$$

where E_{ESP} is the mean electric field applied to the particles inside the precipitator, Cu is the Cunningham correction factor, μ is the dynamic viscosity of the fluid, d_p is the particle size and $q_{\max,th}$ is the maximum particle charge, which again is particle size dependent as

$$
\underbrace{q_{\max,th}}_{}
$$

$$
= \underbrace{\frac{\frac{k_B T}{2Ke} d_p log \left(1 + \frac{\pi K c_{Ion} e^2 \rho_I}{2k_B T} d_p\right)}{}}_{q_{\max,diff}}
$$

$$
+ \underbrace{\frac{\left(\pi\, e\, b_{Ion}\, n_{i,\infty}\, t\, K\right)}{\left(\pi\, e\, b_{Ion}\, n_{i,\infty}\, t\, K+1\right)} \left(1 + 2\frac{\varepsilon_r-1}{\varepsilon_r+2}\right) \frac{E_{ESP}}{4K} * d_p^2}_{q_{\max,field}} \tag{18}
$$

with $K = \frac{1}{4\pi \varepsilon_0 \varepsilon_r}$, the Boltzmann constant k_B, temperature T, the mobility of ions in air b_{Ion}, the space charge density ρ_I, the charge of a single electron e and vacuum and relative permittivity ε_0 and ε_r, respectively. The particle size dependent maximum charge in diffusive and field charging has a turnover between these charging mechanisms for particles of size around 1 µm. For particles above 10 µm diffusion charging may be neglected, for particles below 100 nm field charging has a negligible influence.

2.11 Effective Electric Field

The mean electric field applied to the particles comprises of the applied voltage at the electrodes, the electrode geometry and the particle trajectories through the precipitator. Thus, a complex interplay of particle acceleration towards the walls and the charging due to the field arises, which is important as the electrodes do not generate a constant field throughout the ESP. To avoid immense computational costs, this coupling is modeled, using an electrode specific effective field parameter $CE = E_{electrode}/E_{plate}$, where E_{plate} is the electric field of a plate-to-plate capacitor with similar dimensions (see [34]).

2.12 Ion Concentration

Besides the electric field, the ion concentration inside ESP is spatially distributed. Again, the dependency of the particle tracks on charging and vice versa rises a need to model the mean field by application of an electrode geometry dependent mean ion density. The mean ion density inside a precipitator may be estimated from the critical electric field at the electrode

$$E_{crit} = 30 f_E \left(1 + \frac{0.301}{\sqrt{100 r_E}} \right) \tag{19}$$

to

$$\rho_I = \frac{d_W w j}{\pi b_{Ion} r_{Corona} E_{crit}} 10^{-5}, \tag{20}$$

where j is the current flux, which can either be measured by experiment or estimated using theoretical correlations, e.g. by Cooperman [35]. The I-V-characteristic used throughout the present approach is based on experimental measurements in a laboratory scaled ESP [34] in the rage of $V_E < 80\,\text{kV}$ and $I_E < 0.5\,\text{mA}$. The redispersion model is designed to simulate arbitrary systems. The model has been tested against the laboratory scaled ESP as it is well characterized in other research studies concerning particle migration, separation efficiencies, ion concentration as well as flow field and electric field conditions.

2.13 Re-Entrainment Model

Re-entrainment of deposited particles in ESP occurs either due to particles discharging at the collection electrode and bouncing back into the fluid due to their kinetic energy or due to shear related fluid forces, which may pull particles that already have

been attached to the separation walls back towards the free stream [36, 37]. Both effects arise mainly for low resistive particles, which keep their electric charge yield a force towards the wall, preventing detachment from the walls. In high resistive layers, electric discharges and back-corona ignite similar re-dispersive behavior of the particulate matter. The derived model is capable of mapping and calculation both phenomena, however, the analysis will focus on low resistivity particulate matter. Therefore, two oxide materials are subject to examination, a natural oxide $CaCO_3$ and a metal oxide Al_2O_3. They only slightly differ in terms of separation efficiencies and discharge quickly as they impact the layer. Yet, the metal oxide has a higher degree of hardness.

The three main mechanisms which cause redispersion for these oxides are bouncing of the unoccupied wall and the sparse layer, turbulence induced redispersion due to flow conditions and cluster removal due to particle impacts.

To simulate the probability of particle re-entrainment, a two-step calculation is performed for each particle class. The first step estimates the probability of bouncing from the walls

$$\phi_b = \sqrt{e^2 - \frac{Q_{adh}}{Q_{kin}}\left(1 - e^2\right)} \tag{21}$$

from comparison of kinetic energy in direction of the wall $Q_{kin} \sim w_{th}$ and adhesion energy Q_{adh}. The coefficient of restitution e links particle hardness to redispersion. In a second step, bouncing particles must escape the turbulent bursts near the wall [38, 39]. The streamlines in turbulent bursts are similar to those of wall impinging jets e.g. shown by Schlichting [40]

$$F''' + FF'' + 1 - F'^2 = 0 \tag{22}$$

Assuming particles moving in these bursts, their time to be transported back towards the wall is calculated by comparing their reattachment time to their residence time inside the precipitator, where Eq. 23 is solved using Runge-Kutta 4-5 integration. Afterwards, the fluid velocity is substituted into the particle movement equation of motion for low resistive particles

$$\frac{dv_p^+}{dt^+} = \frac{f_d}{\tau^+ Cu}\left(v^+ - v_p^+\right) \tag{23}$$

where the equation itself is formulated in dimensionless form presented in [41] and v is fluid velocity, v_p is the particle velocity, f_d is the drag coefficient, Cu is the Cunningham correction, τ is particle relaxation time and t is time. The amount of particle re-dispersion is then

$$\phi_r = (1 - m)^j \tag{24}$$

where $m = 1/270$ is the area ratio of a turbulent burst and j is the number of bursts particles undergo inside the precipitator. A typical mean pathway for a particle detaching from and then reattaching to the walls is shown in Fig. 8.

Concerning cluster removal by particle impact, an additional hit towards the walls increases the kinetic energy onto the particle layer and on the particle bounds inside the layer, respectively. The energy will be dissipated to some extent, e.g. into layer rearrangements, thermal and mechanical stresses, while the main part of the energy is used towards the breakage of the bounds inside the layer.

Each bound break down at a singular level. Thus, the maximal energy into the breakage of the layer is compared to the layer bonds energy. Based on layer properties, the number of bounds may be estimated, e.g. for highly porous layers. According to [42], porosity Φ is based on the force ratio between particle-particle forces and the electrostatic forces acting on the layer

$$\Phi = \Phi_0\big(1 - EXP\big(\alpha\{\chi_i\}^\beta\big)\big) \tag{25}$$

with

$$\chi_i = \sum_j \frac{\left|F_{i,j}^{VDW}\right|}{\left|F_i^e\right| + F_i^{iip}} \tag{26}$$

and

$$F_i^{iip} = KF_i^e \sqrt{\frac{\bar{H}}{d_p}}. \tag{27}$$

Thus, the porosity of the compressed layer relies on particle morphology and electric field adjustment.

During start-up of the process, the rebound constant e depends on whether the particle hits the precipitator walls or the particle layer. This probability is modelled applying a mean rebound factor and the ratio of layer height h to mean particle size d_p as well as the layer porosity Φ

$$e = e_{plate}(\Phi)^{\frac{h}{d_p}} + e_L\left[1 - (\Phi)^{\frac{h}{d_p}}\right] \tag{28}$$

The implementation of a force propagation factor f_p accounts for statistical rebound factor blending as particles impinge the highly porous particle layer, which leads to a force distribution into the layer. The layer coefficient of restitution may then be estimated by

$$e_L = e_p(f_p)^{\frac{h}{d_p}}. \tag{29}$$

As a final step the particle layer porosity is calculated, which varies with electric field strength, that compresses the layer onto the precipitation electrodes. [43] extrapolated porosities of various sized packed particles by statistically connecting settled apparent densities of sampled materials in question and their particle size distribution. The porosity of the mixture is

$$\bar{\varepsilon} = 1 - \frac{\sum_{i=1}^{m} d_{p,i}^3 f_i}{\sum_{i=1}^{m} (d_{p,i} \sim \bar{d}_p)^3 f_i + \frac{1}{n} \sum_{i=1}^{m} \left[(d_{p,i} + \bar{d}_P)^3 - (d_{p,i} \sim \bar{d}_p)^3 \right] f_i} \tag{30}$$

where $\bar{d}_p$ is the mean particle diameter of the mixture and $d_{p,i}$ the mean particle diameter of the i-th class with f_i number density of particles in this class.

The flow sheet simulation unit model (FSS-ESP unit) as shown in Fig. 9 uses a 2-stage particle separation and re-entrainment calculation method. The model tracks multidimensional properties of the particulate matter, e.g. considering particle size and material type. A predefined inflow holds information on these properties while facility properties and process conditions are defined inside the ESP unit.

Firstly, particle separation efficiency defines the number of particles that separate towards the walls. The particles then are "stored" within the holdup, which represents the (separation electrode) side walls of the precipitator. Based on the properties of this holdup, the re-entrainment probability determines the number of particles that redisperse into the gas flow, while the remaining particles are transported towards the ESP silo. The particulate streams as output for clean gas and silo may then be analyzed in terms of overall precipitation rate and particle size dependent precipitation rate.

Experimental data generated by the setup from [44] show the particle size and material dependent separation behavior in an electrostatic precipitator. Process and geometry parameters are presented in Table 2. The precipitation was measured online by a Grimm Aerosol Spectrometer 1.108 at the precipitator outlet for 30 min. Aluminium oxide Al_2O_3 ("Pural NF [®]") and limestone $CaCO_3$ ("Ulmer Weiss [®]") dried at 150 °C for 2 h are being precipitated.

3 Results and Discussion

3.1 Particle Characterization

In addition to the parameters in the exhaust gas of a separator, such as concentration, temperature and humidity, the input parameters of the electrostatic precipitator also depend on dust parameters, such as the chemical and granulometric composition and the specific electrical resistance. Therefore, input materials typically used in industrial practice as well as sample or model dust powders are used for the experimental investigations. In advance of the experiments, fly ash has been identified as one model particle for this project and has been analyzed for its composition in

Table 2 Model parameters used throughout the study sorted by geometry, process and material properties

Name	notation	Value unit
Geometry parameters		
Length	l	1.2 m
Width	w	0.5 m
Height	h	0.3 m
Coefficient of roughness f_E		0.8
Wire-to-wire distance	wwD	0.3 m
Wire radius	r_E	5e-4 m
Effective field const.	C_E	1.1
Process parameters		
Pressure	p	1 bar
Temperature	T	293 K
Applied voltage	V	70,000 V
Gas flow rate	V_g	0.12 m^3/s

Name notation		Value unit
Material parameters		
Diffusion constant D_g		1.77e-5 m^2/s
Gas viscosity M_g		1.82e-5 Pa s
Gas density ρ_g		1.19 kgm^3
Ion mobility b_{Ion}		1.6e-4 m2/V
Material parameters $CaCO_3$		
Particle size distribution q(dp)		Matrix 1/μm
Dielectric constant ε_r		3.4
Hamaker constant $A1_{32}$		2.2e-19
Coefficient of restitution e		0.3
Material parameters Al_2O_3		
Particle size distribution q(dp)		Matrix 1/μm
Dielectric constant ε_r		2.2
Hamaker constant $A1_{32}$		2.69e-20
Coefficient of restitution e		0.8

cooperation with the University of Wuppertal SPP project. Scanning Electron Microscope (ESEM) images and Energy Dispersive X-Ray (EDX) analyzes of fly ash were processed.

In a second approach of ESP analyzes also metal oxide (Al_2O_3 Pural NF) as well as natural oxide $CaCO_3$ (Ulmer Weiss) powders and particles are investigated.

The analysis of the EDX spectrum of a fly ash sample in Fig. 10 shows a significant contribution of carbon, followed by silicon, aluminum and iron. Other components occur in low concentrations of less than one percent by mass. The high percentage

of oxygen in the fly ash allows conclusions to be drawn that the elements are oxidized. The complex mixture produces a fly-ash-specific electrical resistance, which is difficult to deduce from the input variables in flowchart simulations but does affect precipitation. The same applies to the carbon content of fly ash (Fig. 10).

In addition to the dependency of deposition from composition, the deposition of fly ash depends on the particle size distribution in the input stream. The measurement of the non-agglomerated particles has been done by means of laser diffraction spectroscopy (LDS) with a wet-dispersed sample. The LDS (Malvern Mastersizer) determines the size distribution based on the light diffraction of a laser beam assuming a universal multi-modal distribution.

The fly ash consists of about 10 wt% of sub-micron particles. Below 10 μm, 30% of the mass of the particulate material is present (see Fig. 11, left). The remainder of the material consists of particles with a maximum diameter of just over 100 μm, the frequency of which is decreasing to larger particles. The LDS measured particle size distribution was compared to the distribution measured by a Malvern G3 optical microscope evaluation. Due to the lower resolution limit of the microscope no submicron components could be determined. The G3 particle size distribution corresponds to that of the LDS only for the larger particle fractions.

The LDS is able to detect particles with a minimum diameter of about 20 nm. Since the measured distribution with a minimum diameter of 100 nm is close to this limit, the particle size distribution was also qualitatively supported by electron microscope (ESEM) images (see Fig. 11, right). The images show the presence of particles below 1 μm.
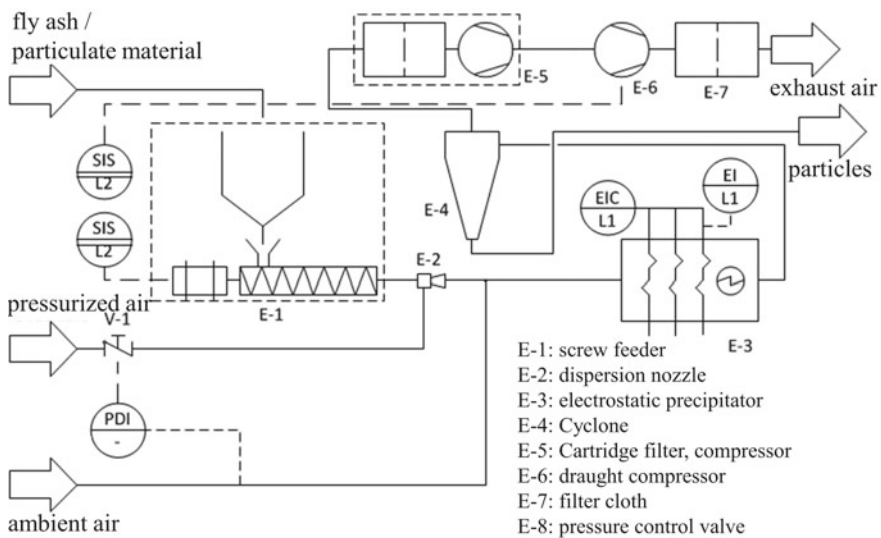
Fig. 3 P&ID of the experimental setup for electrostatic precipitation of particles from air (Reprinted from Particuology 38 (2018) 10–17, Sander et al. with permission from Elsevier)
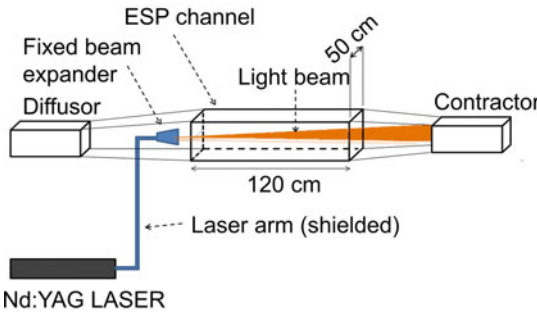
Fig. 4 PIV measurement setup

Fig. 5 Photo of the test set-up to determine the deposit thicknesses. (Reprinted from Chem. Eng. Techn. 40 (2017) 9, Fritsching et al. with permission from Wiley-VCH)
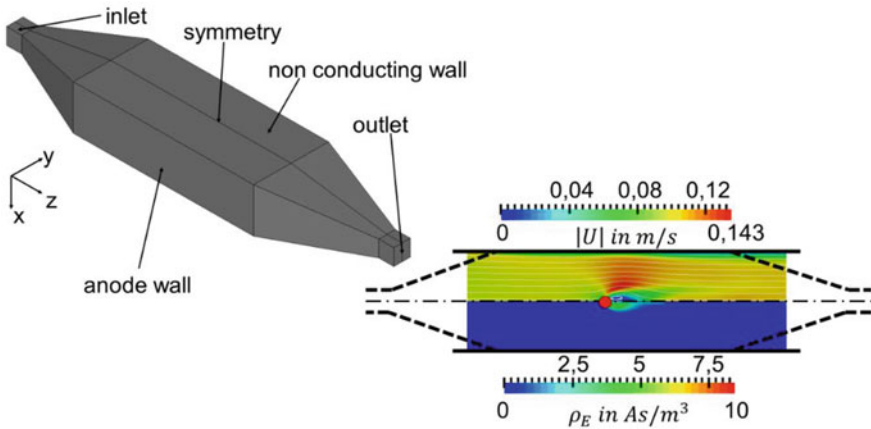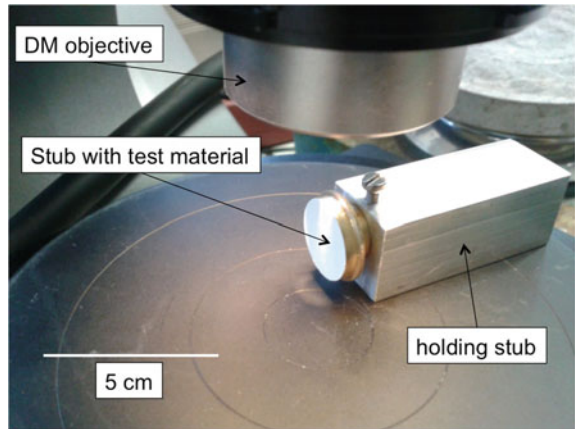
Fig. 6 Numerical simplified ESP model using a 2D axisymmetric geometry, resulting flow field at low velocities and the ion density concentration in this case

Material- and process parameters

$\dot{V}_g$ ... gas flow rate $\left[\dfrac{m^3}{s}\right]$

μ_g ... gas viscosity $\left[\dfrac{kg}{m\,s}\right]$

d_p ... particle diameter [m]
ϵ_r ... particle dielectric const.
d_m ... molekular dia. Gas [m]
p ... pressure [Pa]
T ... temperature [K]

Facility parameters

l ... ESP length [m]
w ... ESP width [m]
h ... ESP height [m]
V ... Spannung [V]
E ... mean electric
        field [V/m]
E_{eff} ... effective field [V/m]
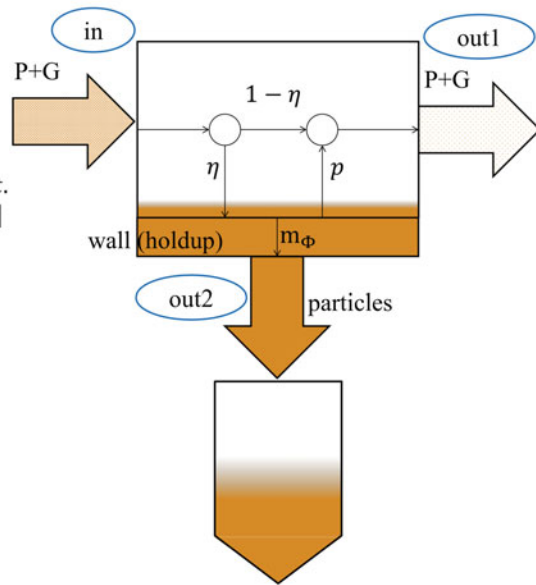
Fig. 7 Sketch of the flow sheet simulation model for dynamic disperse separation processes in electrostatic precipitators in "dyssol"

Fig. 8 Particle trajectories in a turbulent burst, assuming they will undergo only one burst before re-adhesion. Example path shown for Al_2O_3 re-entraining
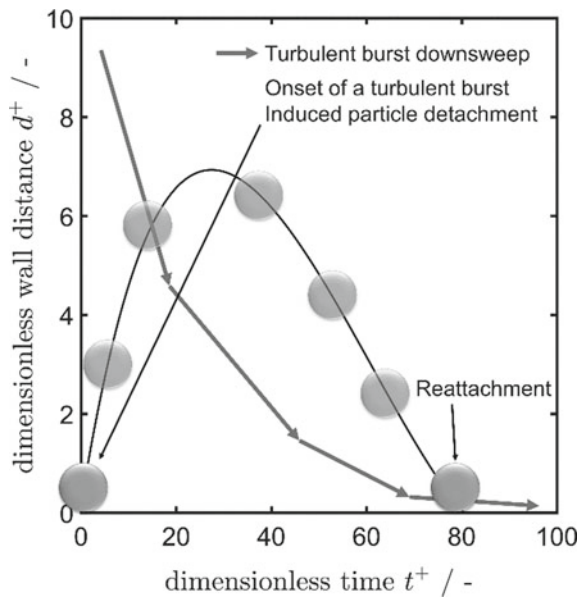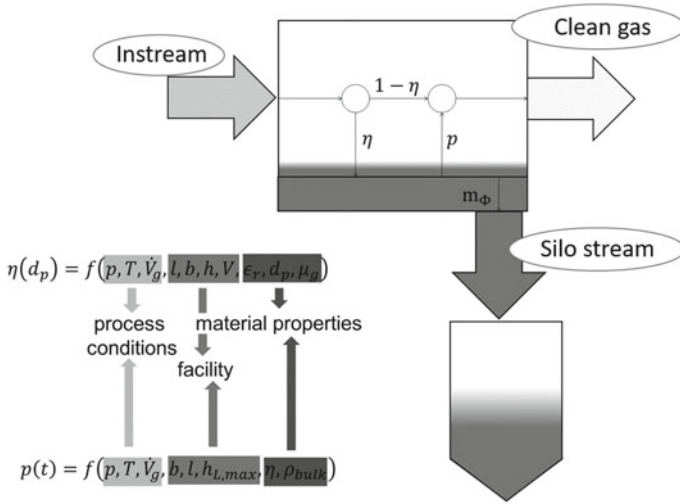
Fig. 9 Implementation of re-entrainment model to the flow sheet unit operation of a ESP including particle migration from inlet stream towards the hold-up and clean gas and bunker outstreams

Element	Wt%	At%
C	37,21	49,51
O	36,66	36,62
Si	12,54	7,13
Al	6,70	3,97
Fe	2,81	0,80
Rest	<1	<1

Muticomponent mixture

highly oxidized

inhomogenuous material properties, e.g. refractive index
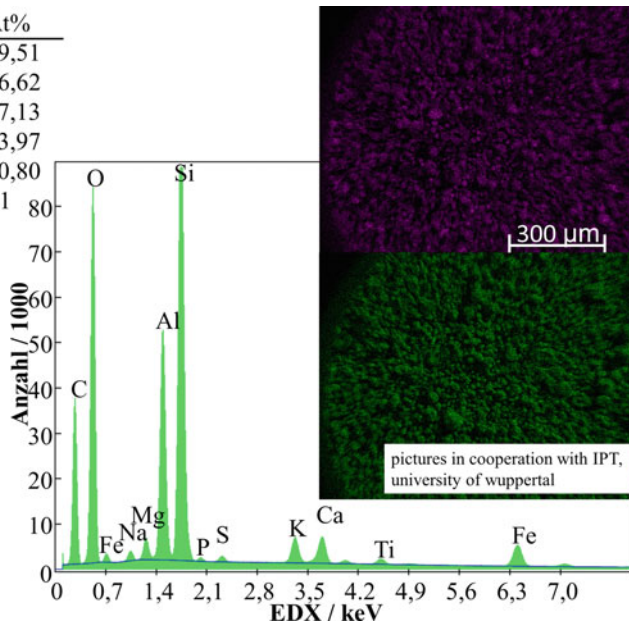
Fig. 10 Composition of fly ash from EDX-analysis in a electron microscope
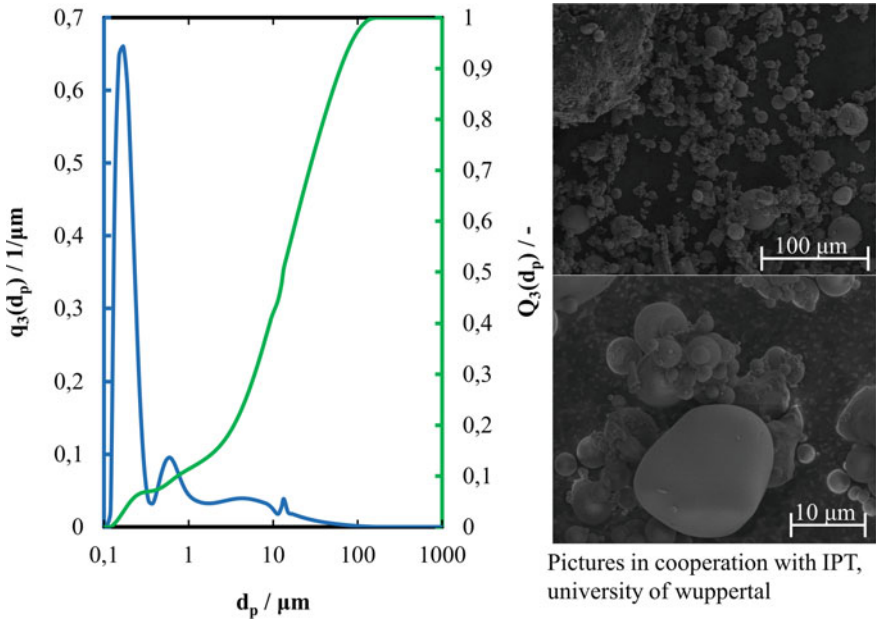
Fig. 11 Particle size distribution of fly ash. LDS analysis, wet dispersed, logarithmic scale

3.2 Particle Layer Analysis

To examine the deposited particle layers, samples are taken from the inside of the deposition anode. The samples are applied to a copper foil and are either left in the deposited state or fixed by means of adhesive for receiving the surface in the electron microscope. The samples can be viewed laterally at an angle of 90°. Figure 7, left and right, shows the surface structure of a layer formed after one hour of operation of the ESP on the side plate in the middle of the channel. The particulate structure is irregular and consists of a composite of several particle sizes. The presence of very large and small particles suggests a pre-agglomerated state of the input material. In a cross-section for the depth analysis of the layer, the same would be disrupted, in a second approach the layer was first fixed with adhesive and then cut. Figure 7, centered, is characterized by a smooth surface. The glue on the surface ensures a flattening of the structure. The depth analysis of the layer fundamentally confirms the knowledge gained from the surface analysis that the layer consists of a multimodal size distribution (Fig. 12).
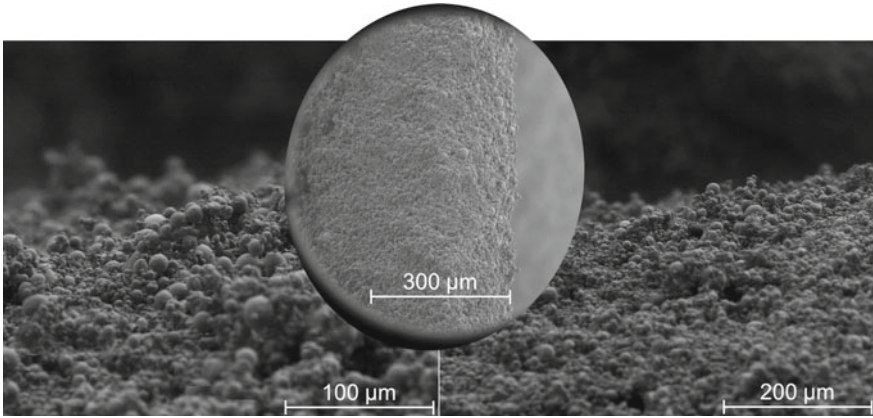
Fig. 12 Precipitated particle layer. Electron microscope picture, deep cut through the layer (left, right) and glued layer (middle)

3.3   Analysis of Particle Separation Efficiency

In the initial start phase of the precipitation system, the deposition plate electrode (duct wall) is clean and not yet filled with particles. Therefore, the particle to be separated from the gas stream directly impacts the wall. Depending on the particle size and momentum, the particle impact either leads to deposition or to the resuspension of the particles. Only a sufficiently small impact force allows the particles to be deposited on the wall (Fig. 13).
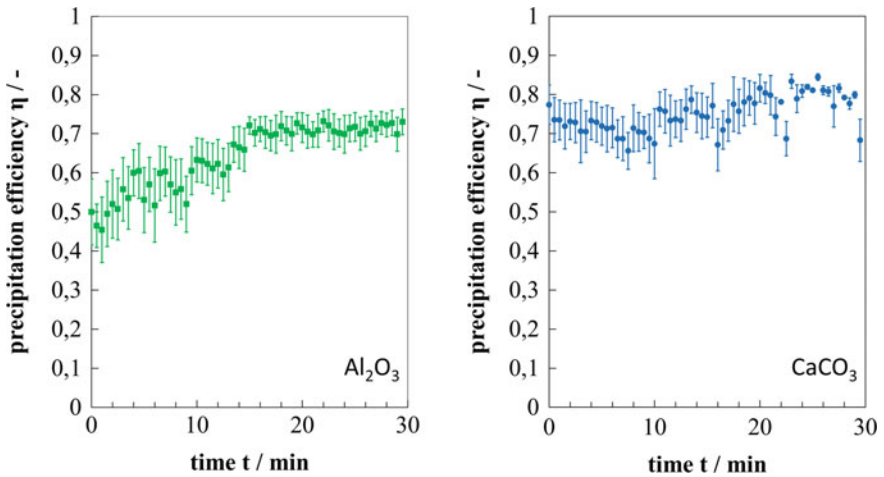
Fig. 13   Time dependent precipitation efficiency of Al_2O_3 and $CaCO_3$
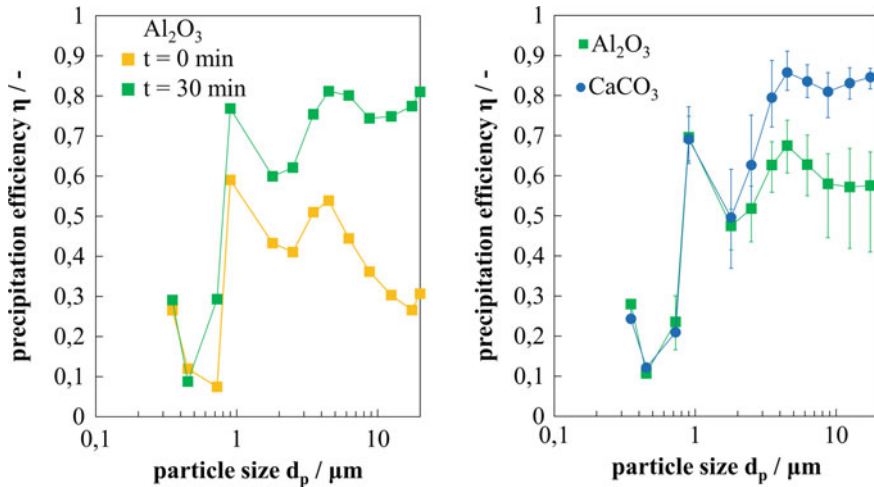
Fig. 14 Dynamic particle size dependent precipitation of Al_2O_3 and $CaCO_3$

The deposition rate of different kind of dust particles in the ESP has been analyzed with time. According to Fig. 14, the time course of the deposition rate of the metal oxide model dust (Pural NF) changes in the first 15 min, while the deposition rate for the organic oxide model dust (Ulmer Weiss) undergoes no significant changes. This behavior is attributed to the different coefficient of restituitions of the two model dusts, which is about 0.8 for Pural NF and only about 0.3 for Ulmer Weiss. The more than twice the number of impacts in Pural NF causes the more frequent rebound of the particles from the plate electrode (copper wall). In the later stages, a (porous) particle layer forms on the wall, which increases the interparticle adhesive forces and may cushion the impact of the particles. Thus, the re-suspension share of particles in the fluid decreases and the deposition rate increases (Fig. 14).

Since larger particles have more kinetic energy on impact, the redispersion rate also increases with particle size. Figure 14 (left) shows the curves for the separation curves for the start of the experiment at t = 0 min and at the end of the test at t = 30 min. The discrepancy between the separation curves increases with the particle size of 15% for 1 μm particles up to 55% for 20 μm particles. Since the larger particles also occupy a higher mass fraction in the disperse phase, they also contribute more to the overall separation efficiency, which explains the drop of about 25% in Fig. 13. Small changes in the separation curve have been detected for the model dust lime, but these are random in time, which is why they are attributed to fluctuations in the measurement signal. As expected, both curves show a similar course for electrostatic precipitators (see Fig. 14 (right)), whereas the curve for Pural NF is below that of Ulmer Weiss. If only the curves of maximum deposition are considered, the curves are closer together. Both substances achieve similarly high degrees of separation.

3.4 ESP CFD-Model and Simulation

The simulation of fluid and particle motion is with a coupled electro-hydrodynamic model shown in Fig. 6 illustrate that there is a strong response from the electric field to the movement of particles that charge and then move in the direction of the electric field to the electrode wall [Law96], which is responsible for the deposition of particles through the electric field. Charged particles, in turn, carry ions out of the continuous phase and transport them along their path. The effect is rather minor, depending on the particle concentration. Another special feature is the movement of the ionized fluid molecules. Here, the ion wind, a macroscopic movement of the fluid in the field direction, is created. In reality, charged molecules are also transported with the fluid in the main flow direction. However, convective transport is negligible compared to ion transport along the electric field. At the low particle concentrations considered here, a one-way coupling between the fluid and the particle phase is sufficient (Fig. 15).

A specific focus of the simulations has been set on the variation of geometric dimensions of the electrodes and its material properties, characterized by the relative permittivity and density. In order to cover wider boundary areas during operation, specific extreme material values have been also used in some simulations, which cannot be assigned to a real physical system (Table 3).
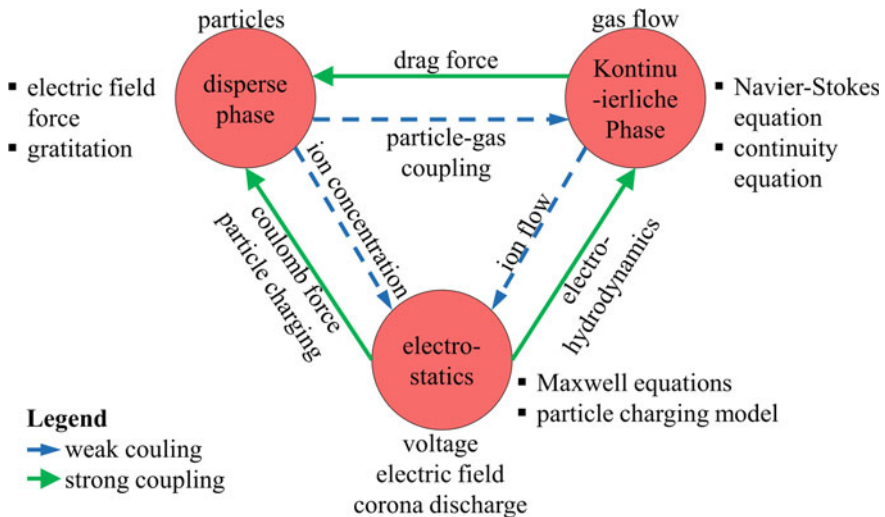
Fig. 15 Coupling between electric field, flow field and particle movement

Table 3 Variation of geometry and material in the CFD simulations

Geometry variation	Material variation			
Electrode	Name	Material	Density (kg m^{-3})	Permittivity [–]
Wire	CaC0$_3$	Calcium-carbonat	2.71	8
Asymmetric spikes	Fe$_2$O$_3$	Iron oxide	5.24	14.2
	VP1	model	2.5	100
Symmetric spikes	VP2	model	25	100
	VP3	model	2.5	1.8

3.5 Efficiency at Different Voltages

Numerous investigations on particle deposition in plate-wire electrostatic precipitators in the literature use electrodes as a 2-dimensional simple structure, which leads to simplifications in terms of generated fields and ion concentrations both in laboratory experiments and in simulations. These wire electrode form serves here as a validation case. The curves in Fig. 16 illustrate the rates of particle separation of CaCO$_3$ for voltages of 55–70 kV. The CFD results from OpenFOAM (OF) show only minor deviations from the flowchart simulation (FSS) (Fig. 16).

For particles larger than 10 µm, deviations of more than 5% occur. This is due to the gravitational separation hitherto neglected in the flowchart simulation. The deviations tend to increase at higher voltages as well since vortex formation and
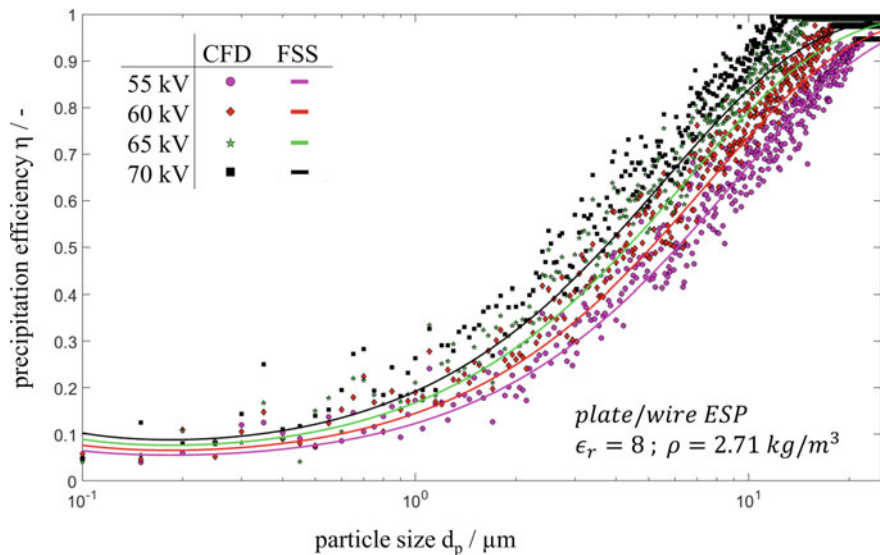
Fig. 16 Results from CFD simulations of particle separation from 55 to 70 kV (Reprinted from Particuology 38 (2018) 10–17, Sander et al. with permission from Elsevier)

multi-scale turbulence effects with increasing potentials play a greater role. These effects cannot be properly described in 2d simulations.

3.6 Electrode Geometry and Material Variation

One of the main reasons for the high degree of complexity in the design of an electro-deposition process with the help of a macro-model is the variety of electrode geometries that can be encountered in practice (Fig. 17).

The coupled fluid, particle and field simulation model in 3D for electrostatic precipitators is able to map such geometries. Figure 18 compares the degrees of precipitation of the wire electrode used in laboratory experiments with electrode types with symmetrical or asymmetrical spikes. The use of spikes locally provides higher field strengths and ion densities but cannot deliver them consistently over the entire volume. As a consequence, particles in size > 1 µm are in principle charged worse, which likewise results in a deterioration in the overall degree of separation. On the other hand, the minimum deposition rate of approximately 10% for the wire electrodes is approximately doubled. Since electric separators primarily are intended to filter out these small particle size ranges when used as end separators, the length of a separator can be significantly reduced by the use of this type of electrode. The mean field traversed by the particles is taken over into the integral model as apparatus
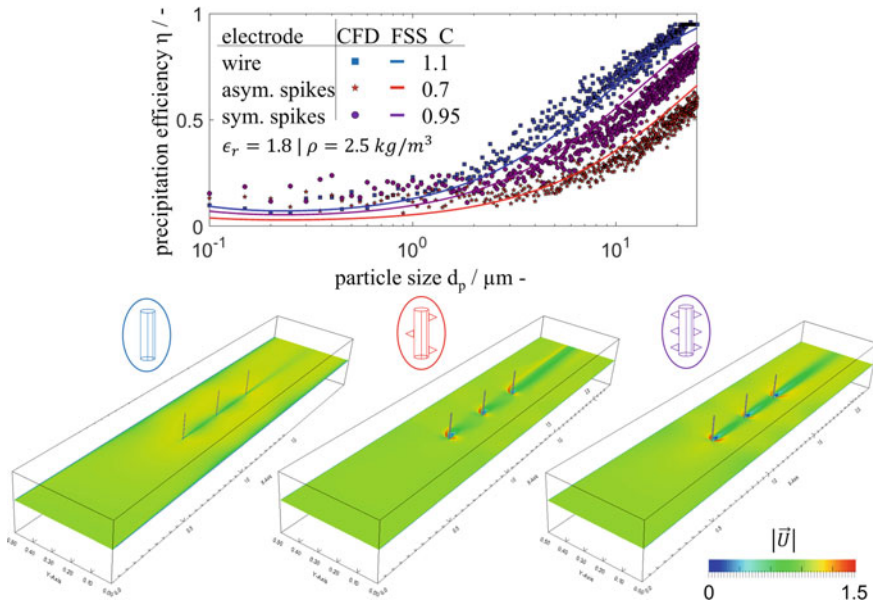
Fig. 17 Electrode design influence on particle precipitation (Reprinted from Particuology 38 (2018) 10–17, Sander et al. with permission from Elsevier)
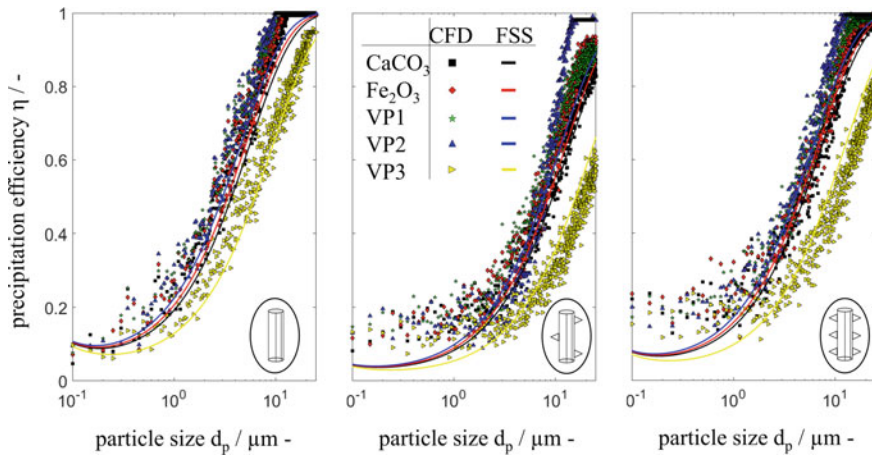
Fig. 18 Separation efficiency for experimental and model particles—comparison of fluid/field-CFD-simulation and flow sheet simulation FSS for 3 electrode designs (Reprinted from Particuology 38 (2018) 10–17, Sander et al. with permission from Elsevier)

characteristic value C. It is currently not possible to correctly model the results for the smallest particle fraction. Here further model developments are required for the representation of a diffusive transport. Overall, the FSS can also sufficiently reproduce the electrode shape by means of the geometrical parameters mentioned, and thus is applicable to the scaling of systems. The particle material can be varied and represented by the relative permittivity in the flowchart simulation. Since no module has yet been implemented for gravity separation, the curves still show deviations for particles larger than 10 μm (see Figs. 17 and 18).

3.7 Continuous Redispersion of Limestone Particles

Experiments performed with limestone show a time independent separation behavior, where neither particle size nor overall precipitation rate change over time. The model prediction is time independent in case of single stage precipitation without consideration of redispersion. The redispersion modeling predicts a time independent behavior as well, but with a slightly lower overall precipitation efficiency. However, both efficiencies are within the experimental uncertainties (Fig. 19).

Looking into the particle size resolved precipitation pattern, differences in the calculation of the single stage model and the redispersion model are observed. As no particles re-entrain from the walls i the first, the curve progresses towards a precipitation efficiency of 1 for larger particle diameters, as already predicted by multiple theoretical macroscopic and CFD models (e.g. [24, 34]). These models are limited to the assumption, that particles impinging the precipitator wall are directly separated.
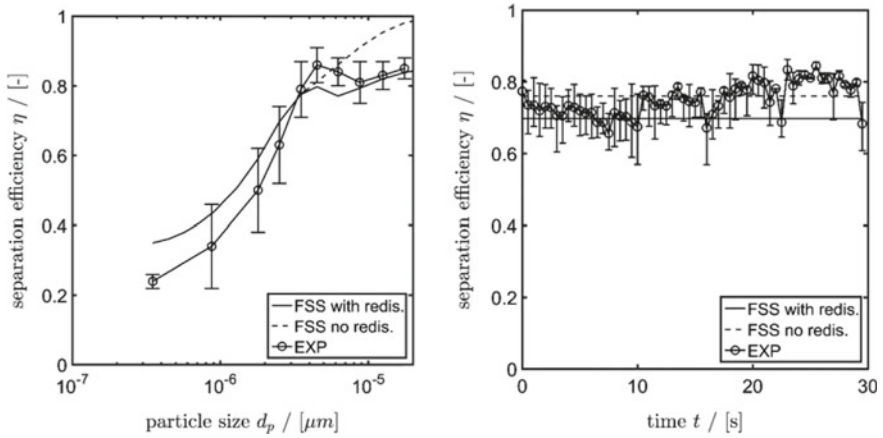
Fig. 19 Time (right) and particle size dependent (left) model validation for CaCO$_3$ with time independent precipitation rates. Modeling shown with (—) and without (- - - -) redispersion

The re-entrainment model shows a different result in the particle size range from 5 to 25 µm. Instead of increasing precipitation efficiencies with increasing particle sizes, redispersion effects become more dominant and reduce the overall precipitation efficiency to about 80%. This reduction is connected to the probability of particles detaching from the layer surface. Layer properties do not vary significantly over time, thus the increasing layer height at the walls does not alter the predicted redispersion probability, hence resulting in a time independent separation behavior. The model reflects the experimental trend and explains the particles separation limitation larger than 5 µm.

3.8 Re-Entrainment of Pural NF® Particles

Emissions from Al$_2$O$_3$ are comparable to the ones of CaCO$_3$ considering only precipitation to the walls. Including re-entrainment effects, the experimental data in Fig. 20 show a time dependent separation behavior as the initial layer at the facility startup forms. Figure 20 indicates, that the particle size dependent precipitation efficiencies are represented more accurate for particles above 5 µm utilizing the re-entrainment model. Without this model, the number of precipitated particles is overpredicted.

The proposed model covers layer formation effects, predicting time dependent precipitation efficiencies which run into a continuous precipitation rate after 15 min. There are two major effects, which add to the time dependent behavior.

Firstly, redispersion is increasing after some minutes due to rising probability of particles impinging onto other particles instead of impinging onto the wall. As the copper plate is rather soft compared to Pural NF ($e \approx 0.8$ instead of $e \approx 0.4$), less rebounding occurs. This effect is within the experimental data, thus, making it hard
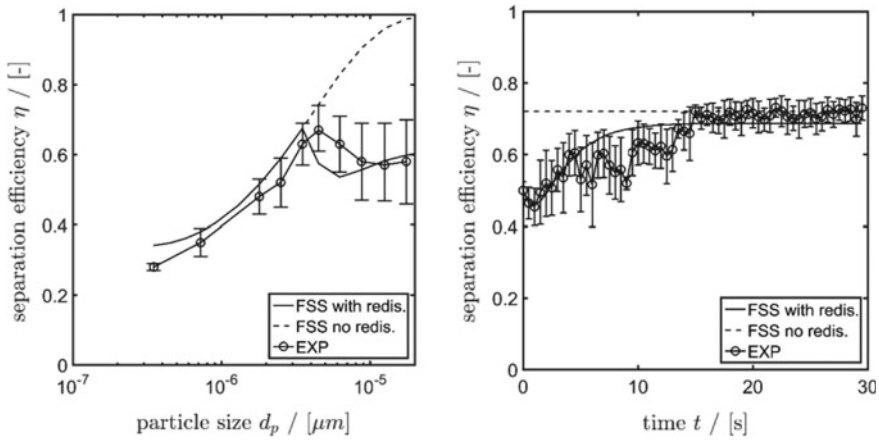
Fig. 20 Time (right) and particle size dependent (left, for t = 1 min) model validation for Al_2O_3 with time dependent precipitation efficiencies. Modeling shown with (—) and without (- - - -) redispersion

to evaluate. After a few minutes, an initial particle layer has formed on the walls. Now, mostly all particles impinge the layer and the wall effect disappears. The layer forming has a high porosity (compare [43]) and will allow force progression into it, reducing re-entrainment from the layer. After the layer reaches a certain height, the force progression into the layer is constant and, likewise, precipitation rates proceed in a steady state.

The force progression factor used in Eq. (29) is a fitting parameter which influences how fast the precipitation rate reaches a steady state. The parameter is connected to the layer porosity, as a dense particle layer (less porous) has more interparticle bounds and may withstand a higher force compared to a fluffier layer. Figure 21 shows the influence of the factor in a reasonable range of 0.9–0.98. Values above 1 are not reasonable as they would allow higher forces to act on the particles than maximum impact force theoretical available during impingement. A value of 1 neglects any layer influence. With decreasing force factors, the stable continuous process conditions are reached after about 7 min. The change in dynamics is limited to this rise. Thus, low values will only slightly alter the precipitation curves. With increasing values, the dynamics are slowing down more and more. This is expected by looking at the damping function formulation. All curves are within experimental data errors. Thus, it can be concluded, that the fitting parameter influences the results in an acceptable way. The force progression into the layer remains an uncertainty, which should be addressed in further studies.

Fig. 21 Force propagation factor influence
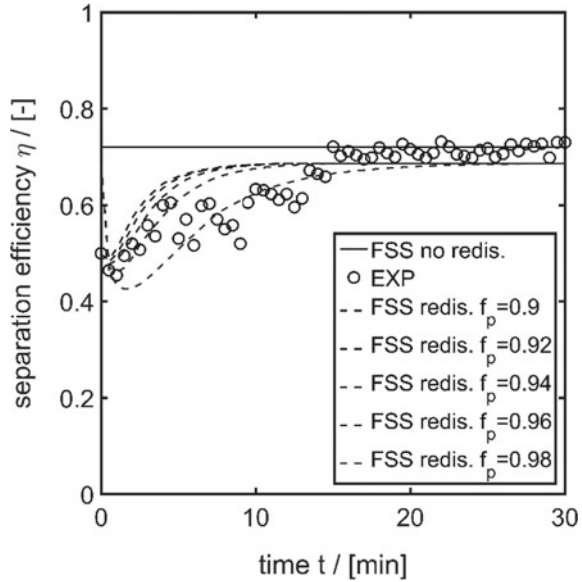
4   Summary, Conclusions and Outlook

Electric forces on gaseous and particulate phases are implemented into a numerical CFD model of the flow inside electrostatic precipitators (ESP). The gas phase gains electrons through a steady-state boundary inlet at the precipitator electrodes while particles charge according to the Lawless unipolar model. The simulation of wire, asymmetric and symmetric spiked wire electrode designs for electrostatic precipitators provide mean electric field values responsible for particle charging and acceleration. Integration of these geometries into a macroscopic precipitation model shows good agreement to the simulation. Particles start their drift towards the walls approximately after passing the first electrode, where the onset of rapid particle charging caused by high electric field strengths and ion densities is located. For the gas phase it is found that macroscopic vortices arise along the precipitator. Thus, turbulence influences the overall separation efficiency mainly of nanometer sized particles which is not captured by the macroscopic model approach. With high densities, micron sized particles accelerate vertical to the spiked electrodes and undergo higher charging and transport fields, which increases precipitation efficiency.

Particle re-entrainment mechanisms in electrostatic precipitators (ESP) are modeled for inclusion as a model unit into dynamic flowsheet simulation (FSS). Results on $CaCO_3$ and Al_2O_3 precipitation and redispersion for a laboratory scaled ESP are discussed. The new approach describes a unit operation to be incorporated in the dynamic flowsheet environment "dysSol", which allows a multidimensional analysis considering particle size and material type. Particle separation and redispersion is modeled through common theory, implementing an additional effective field constant

obtained from the CFD simulations. Re-entrainment calculations are based on force ratios and fluid flow conditions. A force progression function accounts for particle layer properties.

In case of limestone particles (Ulmer Weiss ®), a steady state redispersion is predicted by the model, showing an increased accuracy in the particle size dependent precipitation rates. The same holds true for metal oxide particles (Pural NF ®). Here, the force progression is more dominant, showing a dynamic increase in precipitation rates with time. The experimental data exhibit identical trends, however, the analysis of the force progression factor indicates remaining uncertainty. It should be addressed in further studies. A promising approach for the derivation of the factor may be by application of the Discrete-Element-Method (DEM) for studying of particle impact onto particulate layers, as DEM simulations are capable of resolving the force progression into the layer as well as the resulting force onto particles and groups of particles. In this way the particle deposition probability and possible re-entrainment of particles may be calculated directly.

References

1. Jedrusik, M., Swierczok, A., Teisseyre, R.: Experimental study of fly ash precipitation in a model electrostatic precipitator with discharge electrodes of different design. Powder Technol. **135**, 295–301 (2003)
2. Dastoori, K., Makin, B., Kolhe, M., Des-Roseaux, M., Conneely, M.: CFD modelling of flue gas particulates in a biomass fired stove with electrostatic precipitation. J. Electrostat. **71**, 351–356 (2013)
3. Prabhu, V., Kim, T., Khakpour, Y., Serre, S.D., Clack, H.L.: Evidence of powdered activated carbon preferential collection and enrichment on electrostatic precipitator discharge electrodes during sorbent injection for mercury emissions control. Fuel Process. Technol. **93**, 8–12 (2012)
4. Lübbert, C.: Zur Charakterisierung des gequenchten Zustandes im Elektroabscheider (On the characterization of the quenched regime in electrostatic precipitators). Brandenburgische Technische Universität Cottbus, Fakultät für Umweltwissenschaften und Verfahrenstechnik (2011)
5. Kaul, M., Schmidt, E.: Reduction of fine dust-emissions at inner city areas—opportunities and limitations of electrostatic precipitators. Presented at the international conference and exhibition for filtration and separation technology. Cologne, Germany (2015)
6. Xiao, G., Wang, X., Yang, G., Ni, M., Gao, X., Cen, K.: An experimental investigation of electrostatic precipitation in a wire–cylinder configuration at high temperatures. Powder Technol. **269**, 166–177 (2015)
7. Wen, T.-Y., Wang, H.-C., Krichtafovitch, I., Mamishev, A.V.: Novel electrodes of an electrostatic precipitator for air filtration. J. Electrostat. **73**, 117–124 (2015)
8. Deutsch, W.: Bewegung und Ladung der Elektrizitätsträger im Zylinderkondensator. Ann. Phys. **373**, 335–344 (1922)
9. Podliński, J., Niewulis, A., Mizeraczyk, J.: Electrohydrodynamic flow and particle collection efficiency of a spike-plate type electrostatic precipitator. J. Electrostat. **67**, 99–104 (2009)
10. Schmid, H.-J.: On the modelling of the particle dynamics in electro-hydrodynamic flow fields: II. Influences of inhomogeneities on electrostatic precipitation. Powder Technol. **135–136**, 136–149 (2003)
11. Arif, S., Branken, D.J., Everson, R.C., Neomagus, H.W.J.P., le Grange, L.A., Arif, A.: CFD modeling of particle charging and collection in electrostatic precipitators. J. Electrostat. **84**, 10–22 (2016)

12. Farnoosh, N., Adamiak, K., Castle, G.S.P.: 3-D numerical analysis of EHD turbulent flow and mono-disperse charged particle transport and collection in a wire-plate ESP. J. Electrostat. **68**, 513–522 (2010)
13. Kaiser, S.: CFD Modellierung und simulation von elektrostatischen Abscheidern nasser Bauart, Ph.D. Technische Universität Dortmund, Germany (2013)
14. Roghair, I., van den Ende, H.T.M., Mugele, F.: An OpenFOAM-based electro-hydrodynamic model. In: Presented at the 8th International Conference on Multiphase Flow Jeju. Korea (2013)
15. OpenFOAM. (14.04.2016). OpenFOAM project web pages. http://www.openfoam.org
16. Javadi, A., Nilsson, H.: Time-accurate numerical simulations of swirling flow with rotor-stator interaction. Flow Turbul. Combust. **95**, 755–774 (2015)
17. Javadi, A.: Time-accurate Turbulence Modeling of Swirling Flow for Hydropower Application, Ph.D. Department of Applied Mechanics, Chalmers university of technology, Gothenburg, Sweden (2014)
18. Aleksin, Y., Vora, A., Riebel, U.: A new understanding of electric conduction in highly resistive dusts and bulk powders. Powder Technol. **294**, 353–364 (2016)
19. Pieloth, D., Wiggers, H., Walzel, P.: Influence of thermodynamic, material, and bulk properties on electrical resistivity of particle layers. Chem. Eng. Technol. **37**, 627–634 (2014)
20. Lübbert, C.: Zur Charakterisierung des gequenchten Zustandes im Elektroabscheider. Ph.D. Thesis, Fakultät für Umweltwissenschaften und Verfahrenstechnik, BTU Cottbus (2012)
21. Flagan, R.C., Seinfeld, J.H.: Fundamentals of Air Pollution Engineering. Prentice-Hall, Inc., Englewood Cliffs (1988)
22. McDonald, J.R., Smith, W.B., Spencer III, H.W., Sparks, L.E.: A mathematical model for calculating electrical conditions in wire-duct electrostatic precipitation devices. J. Appl. Phys. **48**, 2231–2243 (1977)
23. Cooperman, G.: A new current-voltage relation for duct precipitators valid for low and high current densities. IEEE Trans. Ind. Appl. **IA-17**, 236–239 (1981)
24. Kaiser, S., Fahlenkamp, H.: CFD modelling of the electrical phenomena and the particle precipitation process of wet ESP in coaxial wire-tube configuration. Int. J. Plasma Environ. Sci. Technol. **5**, 103–109 (2011)
25. Lawless, P.A.: Particle charging bounds, symmetry relations, and an analytic charging rate model for the continuum regime. J. Aerosol Sci. **27**, 146–160 (1996)
26. Niewulis, A., Podliński, J., Mizeraczyk, J.: Electrohydrodynamic flow patterns in a narrow electrostatic precipitator with longitudinal or transverse wire electrode. J. Electrostat. **67**, 123–127 (2009)
27. Podliński, J., Dekowski, J., Mizeraczyk, J., Brocilo, D., Chang, J.-S.: Electrohydrodynamic gas flow in a positive polarity wire-plate electrostatic precipitator and the related dust particle collection efficiency. J. Electrostat. **64**, 259–262 (2006)
28. Sander, S., Fritsching, U.: "Analyse der Bewegung von Partikelkollektiven im Elektroabscheider mittels PIV (ProcessNet annual meeting), pp. 1588–1589. Aachen, Germany (2014)
29. Al-Hamouz, Z.: Numerical and experimental evaluation of fly ash collection efficiency in electrostatic precipitators. Energy Convers. Manag. **79**, 487–497 (2014)
30. Liu, Q., Zhang, S.-S., Chen, J.-P.: Numerical analysis of charged particle collection in wire-plate ESP. J. Electrostat. **74**, 56–65 (2015)
31. McLean, K.J.: Electrostatic precipitation. IEEE Rev. **135**, 347–361 (1987)
32. Adamiak, K., Atten, P.: Simulation of corona discharge in point–plane configuration. J. Electrostat. **61**, 85–98 (2004)
33. Skorych, V., Dosta, M., Hartge, E.-U., Heinrich, S.: Novel system for dynamic flowsheet simulation of solids processes. Powder Technol. **314**, 665–679 (2017)
34. Sander, S., Gawor, S., Fritsching, U.: Separating polydisperse particles using electrostatic precipitators with wire and spiked-wire discharge electrode design. Particuology (2017)
35. Cooperman, P.: A theory for space-charge-limited currents with application to electrical precipitation. Trans. Am. Inst. Electr. Eng. Part I Commun. Electron. **79**, 47–50 (1960)
36. Yamamoto, T., Mieno, M., Shibata, K., Sakai, K.: Studies of rapping reentrainment from electrostatic precipitators. In: Proceedings of 7th International Conference on Electrostatic Precipitation, pp. 163–170 (1998)

37. Londershausen, T.T.: Entwicklung von Prognosefunktionen zur Abschätzung der Staubungsneigung von trockenen und feuchten Schüttgütern. Dr.-Ing., Faculty of Mechanical Engineering and safety technology, Bergische Universität Wuppertal, Shaker Verlag, Aachen (2018)
38. Shnapp, R., Liberzon, A.: A comparative study and a mechanistic picture of resuspension of large particles from rough and smooth surfaces in vortex-like fluid flows. Chem. Eng. Sci. **131**, 129–137 (2015)
39. Henry, C., Minier, J.-P.: A stochastic approach for the simulation of particle resuspension from rough substrates: Model and numerical implementation. J. Aerosol Sci. **77**, 168–192 (2014)
40. Schlichting, H.: Boundary-Layer Theory, 8th edn. Springer Verlag, Heidelberg (2000)
41. Tsai, R., Mills, A.: A model of particle re-entrainment in electrostatic precipitators. J. Aerosol Sci. **26**, 227–239 (1995)
42. Yang, S., Dong, K., Zou, R., Yu, A., Guo, J.: Packing of fine particles in an electrical field. Granular Matter **15** (2013)
43. Ouchiyama, N., Tanaka, T.: Porosity estimation for random packings of spherical particles. Ind. Eng. Chem. Fundam. **23**, 490–493 (1984)
44. Londershausen, T., Schmidt, E., Sander, S., Fritsching, U.: Characterization of powder layer dustiness—influence of the deposit thickness. Chem. Eng. Technol. **40**, 1720–1725 (2017)

Chapter 2
Dynamic Modelling of Reactive Fluidized Bed Systems Using the Example of the Chemical Looping Combustion Process for Solid Fuels

Lennard Lindmüller, Johannes Haus, Ernst-Ulrich Hartge, and Stefan Heinrich

Abstract The novel open-source flowsheet simulation software DYSSOL was used to simulate effects inside a system of interconnected fluidized bed reactors. The development of the needed models was done exemplary for the Chemical Looping Combustion process for solid and gaseous fuels. In CLC a solid oxygen carrier material is circulated between interconnected fluidized bed reactors. In the simulation, the focus is laid on the prediction of the dynamics of the whole system, especially the process start-up, shut-down and fuel load change. A dynamic model, which can be applied for bubbling beds and circulating fluidized beds was derived. Additionally, a cyclone was introduced for gas-solid separation. Loop seals ensure gas sealing between the reactors and were included into the modeling. Fluid mechanics inside the systems are modeled with empirical and semi-empirical, one-dimensional correlations, to enable fast calculations. These considerations allow real-time simulations of long-term effects in the system. The chemical reactions for gaseous and solid fuel combustions are included in the simulation. This has an effect on the solid oxygen carrier and so the oxidation and reduction of the carrier are regarded. The simulations were validated with experiments on a 25 kWth Chemical Looping Combustion facility at TUHH. The flowsheet models are able to predict the movement of the bed material between the units after operation changes as well as the time frames in which these changes occur. Besides, the gas and solids conversions in the fluidized bed reactors were simulated accurately.

L. Lindmüller · J. Haus · E.-U. Hartge (Deceased) · S. Heinrich (✉)
Institute of Solids Process Engineering and Particle Technology,
Hamburg University of Technology, Hamburg, Germany
e-mail: stefan.heinrich@tuhh.de

L. Lindmüller
e-mail: lennard.lindmueller@tuhh.de

37

Abbreviations

AR	Air Reactor
CCS	Carbon Capture and Storage
CFB	Circulating Fluidized Bed
CFD	Computational Fluid Dynamics
CLC	Chemical Looping Combustion
CLOU	Chemical Looping with Oxygen Uncoupling
CSTR	Continuously Stirred Tank Reactor
FR	Fuel Reactor
iG-CLC	In situ Gasification-CLC
OC	Oxygen Carrier
PFR	Plug Flow Reactor
S	Siphon/loop seal
SP	Standpipe

Nomenclature

a	Decay constant in the freeboard region (–)
Ar	Archimedes number (–)
A_r	Cross-sectional area of reactor (m^2)
a_s	Share ratio of flow which is in inner cyclone vortex (–)
a_t	Ratio of interfacial area between bubble and suspension phase to the volume of a reactor element (1/m)
C	Weir coefficient (–)
$C_{b,l}$	Gas concentration of gas component l in bubble phase (mol/m^3)
$C_{d,l}$	Gas concentration of gas component l in dense suspension phase (mol/m^3)
$C_{f,l}$	Gas concentration of gas component l in the freeboard (mol/m^3)
c_v	Solids concentration (–)
$c_{v,i,\infty}$	Solids concentration above the transport disengagement height (–)
$c_{v,mf}$	Solids concentration at minimum fluidization velocity (–)
$c_{v,suspension}$	Solids concentration in the dense suspension phase (–)
D	Molar binary diffusion coefficient (m^2/s)
D_c	Cyclone design parameter (–)
d*	Cyclone cut size diameter (m)
$d_{i,p}$	Average particle size in class i (m)
d_p	Particle diameter (m)
d_v	Bubble size (m)
$d_{v,0}$	Initial bubble size (m)
E_a	Activation energy for the reaction (J)
F_g	F_d gravitational and drag force (kg m/s^2)

g	Gravitational acceleration (m/s^2)
$G_{s,i,\infty}$	Solids circulation rate ($kg/(m^2 s)$)
h	Height inside the reactor (m)
H_b	Height above the distributor where dense bottom zone ends (m)
H_w	Weir height (m)
$\dot{J}_{Q,l}$	Convective flow of gas component l (mol/m^3)
k_0	Pre-exponential factor ($mol^{1-n} L^{n-1} s^{-1}$)
$k_1 - k_7$	Reaction rate constant ($mol^{1-n} L^{n-1} s^{-1}$)
k_G	Gas diffusion resistance (mol/s)
$K_{i,\infty}$	Elutriation rate for each particle interval i ($kg/(m^2 s)$)
K_Q	Convective exchange rate of gas l (1/s)
$\dot{m}$	Mass flow rate (kg/s)
m_r	Total reactor inventory (m)
n	Reaction order (–)
p	Pressure (Pa)
$\Delta Q_{3,i}$	Particle size class fraction (–)
R	Universal gas constant (J/(K mol))
$r_{g,l}$	Reaction rate of solid with gaseous component l (mol/m^3)
$T(u_{t,i})$	Cyclone separation efficiency curve (–)
u	Superficial gas velocity (m/s)
u_b	Bubble rise velocity (m/s)
u_d	Velocity in dense suspension phase (m/s)
u_{mf}	Minimum fluidization velocity (m/s)
$u_{t,i}$	Terminal velocity of particles in size interval i (m/s)
$\dot{V}_b$	Visible bubble volumetric flow (m^3/s)
$\dot{V}_{or}$	Volumetric flow through a single orifice (m^3/s)
W	Width of the standpipe/weir (m)
$X_{j,l}$	Solids conversion of component j with gas component l (–)

Greek letters

μ	Gas viscosity (Pa·s)
ε_b	Bubble volume fraction (–)
ε_{mf}	Minimum fluidization voidage (–)
$\eta_f(d)$	Cyclone separation efficiency (–)
θ	Scale dependent geometry parameter (–)
λ	Average bubble lifetime (s)
$\rho_{m,j}$	Molar density of solid reactant j (mol/m^3)
ρ_{solid}	Solid density (kg/m^3)

Indices

0	Initial
b	Bubble
d	Dense suspension phases
f	Freeboard
i	Particle size class
j	Solid component
l	Gas component

1 Introduction

Chemical Looping Combustion (CLC) is a promising CO_2 capturing technology, which might find future use for electricity generation or in industrial processes where industrial firing systems are needed. Instead of direct air combustion, in CLC an oxygen carrying material (OC), usually a metal oxide, is circulated between a fuel reactor (FR) and an air reactor (AR). The OC is reduced by the fuel in the FR and re-oxidized in the AR by air. By avoiding contact with the fuel and air, a combustion in absence of nitrogen is realized and a flue gas stream of almost pure CO_2 and H_2O is generated in the FR. The pure CO_2 can then be used for underground storage in suitable geological formations, such as empty natural gas caverns. This process is called Carbon Capture and Storage (CCS). The basic process schematics of the investigated CLC configuration, called in-situ Gasification Chemical Looping Combustion (iG-CLC) with solid fuels, is shown in Fig. 1. There, M_xO_y stands for an oxidized OC and M_xO_{y-1} for the reduced OC. In the FR of an iG-CLC plant, the solid fuel is converted to a syngas, which then reacts with the OC. Some OCs can release a certain amount

Fig. 1 General scheme of the CLC process
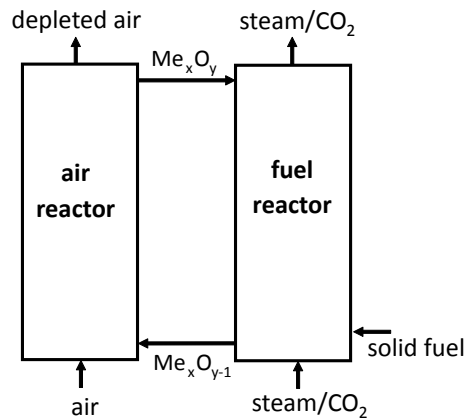
of bound oxygen directly, which then reacts with a solid fuel. This reaction route is called Chemical Looping with Oxygen Uncoupling (CLOU). This work focuses entirely on iG-CLC.

The simulation of the CLC process was conducted with a variety of methods and approaches. One typical method is Computational Fluid Dynamics (CFD). In CFD a high amount of equations is solved on a dense numerical grid which can be two or three dimensional. In contrast to this, flowsheet simulation describes macroscopic effects in the individual units with empirical models. In comparison to CFD, the operation of a whole process system can be quickly simulated regarding long term effects. Flowsheet modelling approaches for CLC were conducted by various research groups mainly with Aspen Plus [1–4] but also with MatLab/Simulink [5, 6] and IPSEpro [7]. A summary of the mentioned works can be found in Haus et al. [8]. Other mathematical modeling on macro-scale are summarized by Adanez et al. [9]. In all the mentioned research, only steady state operations were simulated. Often, the modeling of CLC concentrates on the FR since it is the most crucial part in the process. The reactions in the AR are mostly disregarded, due to a fast and complete re-oxidation of the OC. Also, the conversion of carbon, which slipped from the FR to the AR can be considered as complete. A fluid mechanical macroscale model for a fluidized bed reactor for flowsheet simulation was implemented into the SolidSim environment by Puettmann et al. [10]. The basics of this approach were used in the ASPEN Plus 8.4 package of ASPEN Tech. Prior research at TUHH has shown, that this model cannot be used directly for CLC processes.

The CLC process is characterized by the complex transient behavior between the process units due to the big holdup of the reactive units. This is disregarded in most CLC modeling approaches since most works are focused on the FR. Often artificial in- and output streams are used for every unit to mimic the effect of solid circulation. These model systems cannot predict the dynamic process behavior, since e.g. the solid circulation rate is not calculated but assumed as input value.

In the presented work, an entire CLC system, consisting of fluidized bed reactors, loops seals and a cyclone was implemented into DYSSOL. The process network is described with empirical and semi-empirical correlations. With the models, long-term behavior as well as process variations, such as start-up, shut-down and fuel load changes, can be simulated. Due to the complexity of the whole system with numerous gas solid reactions, the modeled fluidized bed reactor unit was advanced step-by-step. First, the focus was on the fluid dynamics of the interconnected system [11]. In a second step, the dynamic reactions of the OC with gaseous fuels were implemented [8]. Afterwards, the volatile gasification was added into the model. In this way, the combustion of biomass was simulated, by neglecting the char content [12]. In a last step, the focus is on the conversion of high-carbon fuels. Additionally, to the OC, char was introduced as a second reactive solid to the system. All simulations were compared to experiments on a 25 kWth CLC pilot plant with the respective fuel. The measured gas concentrations in the pilot plant's off-gas were used to fit the kinetic data to the simulations. In the following, the experimental facility and flowsheet are explained and afterwards all modeled units are described in detail.

2 Materials and Methods

2.1 Experimental Facility

A 25 kWth experimental CLC pilot plant is operated at Hamburg University of Technology. The plant is run with an oxygen carrier consisting of 9 wt% CuO on Al_2O_3 as a basis. In Fig. 2 (left) the schematics of the pilot plant with a two-stage bubbling bed FR system is shown. Solid and gaseous fuels are usually added in stage 1 of the fuel reactor (FR1). There, solid fuels are gasified by CO_2 and H_2O. The generated gases by gasification and the volatile gases are converted by the oxygen carrier. Unconverted gases enter stage 2 of the fuel reactor (FR2), where they are further converted. It was demonstrated, that the two-stage design provides very high conversions of high volatile fuels, like methane, biomass and lignite char. In the air reactor (AR), which is operated as a circulating fluidized bed (CFB) riser, the reduced oxygen is completely re-oxidized by oxygen from air. After the AR a cyclone is used for gas-solid separation. Loop seals provide gas sealing between the fluidized bed
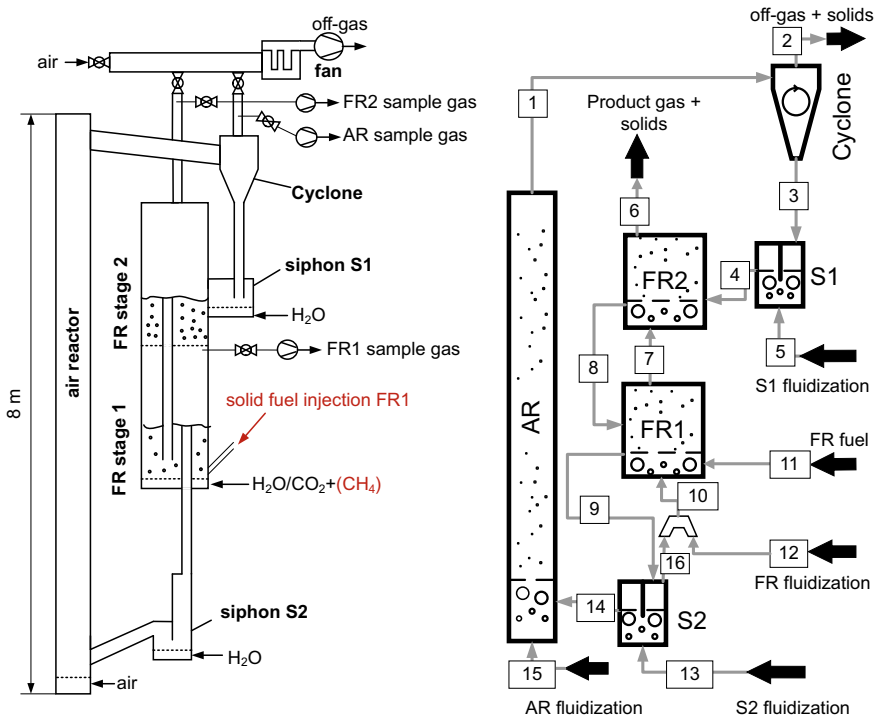
Fig. 2 Left: Schematics. Right: Flowsheet of 25 kWth CLC pilot-plant at Hamburg University of Technology. (AR: air reactor, FR: fuel reactor, S1 and S2: siphons/loop seals). From Haus et al. [8], but with extended streams

Table 1 Dimensions of the 25 kWth CLC pilot-plant at TUHH

Dimensions	Height (m)	Diameter (m)	Holdup[a] (kg)
Air reactor AR	8	0.1	~ 5
Fuel reactor FR	2 m per stage	0.25	~ 24
Bed height FR	0.6 per stage		
Cyclone	0.34	0.21	–
Dimensions	Width (m)	Length (m)	Holdup[a] (kg)
Siphon S1	0.16	0.13	~ 4
Siphon S2	0.13	0.25	~ 8

[a]Solids holdup for typical operation conditions

reactors. The dimensions of the plant are summarized in Table 1. With 32 pressure transducers the fluid mechanic situation in the system can be tracked. A more detailed analysis of the CLC facility at TUHH can be found in [13]. The data from the experimental runs on the CLC plant are used for the development and validation of the models in DYSSOL.

2.2 Flowsheet of the CLC Process

In Fig. 2 (right) the flowsheet of the pilot-scale CLC plant at TUHH is shown. The fluidized bed reactors, including the AR riser and bubbling beds (FR1 and FR2), are simulated with the same model unit, using different correlations, corresponding the to the fluidization regime. In the following, the pathway of the OC through the system is explained, starting in the AR.

The solids in the air reactor move upwards with the fluidization air (stream 15). Both gas and solids exit the reactor via stream 1. In the cyclone, air and fine particles exit the system with stream 2. The cyclones' underflow enters the syphon 1 (S1) with stream 3. The syphon is fluidized by steam (stream 5). Via stream 4 solids and steam from the syphon enter the upper stage of the fuel reactor (FR2). Fine particles and gases leave the system via stream 6. The solids enter the lower reactor stage (FR1) through a standpipe, which is submerged into the bed. The gases and fine particles leave FR1 via stream 7 to fluidize FR2. The fluidization of FR1 is done with stream 10, which contains a mixture of CO_2 (stream 12) and steam from S2 (stream 16). Solid fuel injection is done via stream 11 into the lower bed of FR1. Via the lower standpipe solids enter syphon 2 (S2) with stream 9. S2 is fluidized by steam (stream 13). Via stream 14 the solids and steam enter the air reactor. The modeled streams transfer all gas and solids parameters from one unit to another (e.g. mass flow, temperature, pressure). Two secondary particle properties are defined in the model: The particle size distribution and the oxidation state of the OC. Both parameters can change over time and are passed from one unit to another in the simulation. DYSSOL saves these attributes in matrices. A detailed description for the handling

of the secondary particle properties is presented in the previous chapter by Skorych et al. For flowsheet simulations of CLC, the oxidation state is usually described by no more than 10 intervals, for calculation speed reasons. After a reduction of the OC, the particles move from one oxidation class to the next lower one, or the next higher one for OC oxidation.

2.3 Process Units

For flowsheet simulation, the process is subdivided into individual model units. In the following section, the modeled units used for Chemical Looping Combustion are described, which are fluidized bed reactors, loop seal and a cyclone unit.

2.3.1 Fluidized Bed Reactor Unit

Fluid Mechanics

For the fluidized bed reactor, a single module was developed, which can be used for a CFB riser and a bubbling bed. The module is divided into two zones, a dense bottom zone and a freeboard zone. The bottom zone consists of a suspension phase and a solid free bubbles phase. In the freeboard zone, the solids concentration is exponentially decreasing with the rector height [14]. Figure 3 (left) shows a typical solids concentration distribution over the fluidized bed reactor height. For all process conditions, the presence of bubbles is assumed in the bottom zone. All fluid dynamic effects in the model are assumed to be one dimensional. In the following the correlations used for the description of the fluid mechanics are summarized. A more detailed description can be found in a publication by Werther and Wein [15]. The initial bubble size $d_{v,0}$ above the gas distributor is given by Davidson and Harrison [16]:

$$d_{v,0} = 1.3 \cdot \left(\frac{\dot{V}_{or}^2}{g} \right)^{0.2} \tag{1}$$

With $\dot{V}_{or}$ being the volumetric flow through a single orifice and the gravitational acceleration g. With increasing height over the distributor, the bubble diameter d_v is described with:

$$\frac{d(d_v)}{dh} = \left(\frac{2\varepsilon_b}{9\pi} \right)^{1/3} - \frac{d_v}{3\lambda u_b} \tag{2}$$

In the equation ε_b describes the bubble volume fraction and λ the average bubble lifetime. The formed bubbles rise with the velocity u_b:
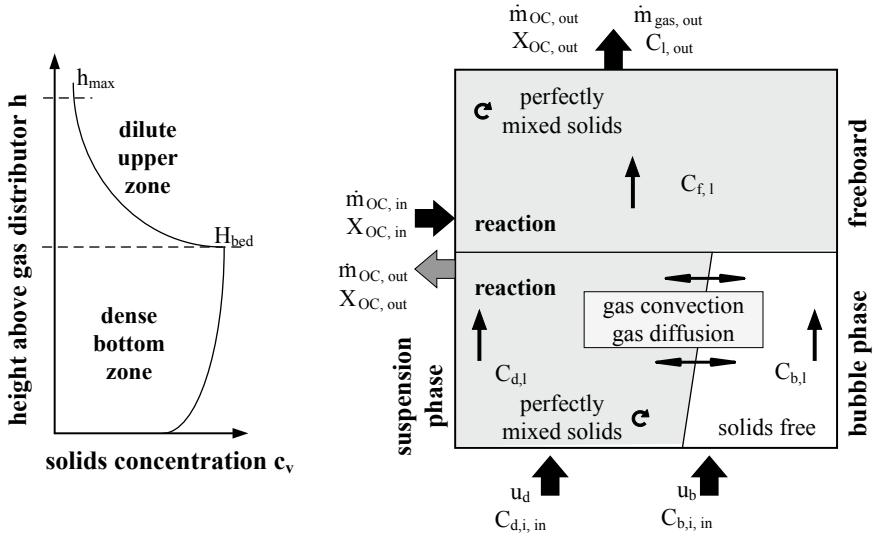
Fig. 3 Left: typical solids distribution inside a fluidized bed reactor. Right: input and output flows inside a fluidized bed reactor, as well as the flows and distributions inside (Reprinted with permission from [8])

$$u_b = \dot{V}_b + 0.71 \cdot \theta \cdot \sqrt{g \cdot d_v} \tag{3}$$

here $\dot{V}_b$ describes the visible bubble volumetric flow and θ is a scale dependent geometry parameter. From the dense bottom zone up to the border of the freeboard zone, which is at the height H_b, the solid concentration $c_v(h)$ is calculated with:

$$c_v(h) = (1 - \varepsilon_b(h)) \cdot c_{v,suspension} \quad \text{for } h < H_b \tag{4}$$

The solid concentration in the suspension phase $c_{v,suspension}$ is assumed to be similar to the solids concentration at minimum fluidization velocity $c_{v,mf}$.

Above the dense suspension phase, an exponential decay of the solids concentration towards the reactor top is assumed. This can be described with a correlation from Kunii and Levenspiel, which also considers an elutriation effect that differs for each particle size class i [17]:

$$c_{v,i}(h) = c_{v,i,\infty} + \left(c_{v,i}(H_b) - c_{v,i,\infty}\right) \cdot e^{-a(h-H_b)} \quad \text{for } h \geq H_b \tag{5}$$

The parameter a is an empirical decay constant, which represents the changing solids concentration in the freeboard region. If the decay constant a is multiplied with the superficial gas velocity u, the result has a constant value for a certain system:

$$a \cdot u = 0.5, \ldots, 3 \quad \text{for bubbling beds and } d_p \sim 300 \ \mu m \tag{6}$$

$$a \cdot u = 2, \ldots, 12 \quad \text{for turbulent beds} \tag{7}$$

In Eq. (5), $c_{v,i,\infty}$ describes the solids concentration above the transport disengagement height, which is calculated from:

$$c_{v,i,\infty} = \frac{G_{s,i,\infty}}{\rho_s \cdot u} \tag{8}$$

The solids circulation rate $G_{s,i,\infty}$ for every size fraction i is calculated from an elutriation rate $K_{i,\infty}$ for each particle class fraction i and the mass of particles in each respective class $\Delta Q_{3,i}$:

$$G_{s,i,\infty} = \Delta Q_{3,i} \cdot K_{i,\infty} \tag{9}$$

The elutriation rate $K_{i,\infty}$ can be calculated from different elutriation rate correlations. Several researchers investigated the elutriation rate at many operation regimes of fluidized bed reactors [18]. At fluidization velocities above 3 m/s, which are usually in a CFB riser and in the air reactor of the exemplary CLC system, a correlation by Choi et al. is used [19]:

$$\frac{K_{i,\infty} \cdot d_{i,p}}{\mu} = Ar^{0.5} \cdot exp\left(6.92 - 2.11 \cdot F_g^{0.303} - \frac{13.1}{F_d^{0.902}}\right) \tag{10}$$

Here $d_{i,p}$ describes the average particle size in class i, μ is the dynamic viscosity of the gas and Ar is the Archimedes number. F_g and F_d describe the gravitational and the drag force on the particles. For bubbling fluidized beds with lower gas velocities, such as the fuel reactor stages in the exemplary CLC system, the following correlation by Tasirin and Geldart is used [20]:

$$K_{i,\infty} = 14.5 \cdot \rho_g \cdot u^{2.5} \cdot exp\left(-5.4 \cdot \frac{u_{t,i}}{u}\right) \tag{11}$$

Here, the elutriation rate depends on the terminal velocity $u_{t,i}$ for each particle size class and the superficial gas velocity u. With a given mass fraction $\Delta Q_{3,i}$ and the elutriation rate of each particle size class $K_{i,\infty}$, the particle size distribution and the corresponding particle loss due to elutriation at the outlet at the reactor top can be calculated.

For the calculation of the whole fluidized bed reactor the unit is discretized in a defined number of height elements. With the correlations shown above, the solid concentrations at every height class in the dense bottom zone and the freeboard zone are calculated for each time step. The concentrations correspond to the total reactor inventory m_r, according to:

$$m_r = A_r \cdot \rho_{solid}\left(\int_0^{H_b} c_v dh + \int_{H_b}^{h_{\max}} c_v dh\right) \tag{12}$$

Here, A_r is the cross-sectional area and h_{max} the total reactor height. The fluidized bed reactor model can have two exits: A top exit and an exit over an overflow weir/standpipe. With all inlet and outlet streams, a new reactor inventory is calculated for each time step:

$$\frac{dm_r}{dt} = \dot{m}_{solids,inlet} - \dot{m}_{elutriation,freeboard} - \dot{m}_{overflow} \tag{13}$$

For a CFB riser, $\dot{m}_{overflow}$ is set to 0 because all particles are leaving the reactor together with the gas via elutriation. The number of elutriated particles depends on the solid concentration at the reactor top and the gas velocity. In a bubbling bed reactor, most particles are discharged via solid overflow and only little elutriation takes place. The particle flow over the weir is defined with a correlation by Botsio and Basu [21]:

$$\dot{m}_{overflow} = c_{v,H_b} \cdot \rho_s \cdot \frac{2}{3} \cdot C \cdot W \cdot \sqrt{2g} \cdot (H_b - H_w)^{2/3} \tag{14}$$

The parameter C is the weir coefficient, W is the width of the weir, H_w describes the height of the weir and H_b the height of the bubbling bed.

Chemical Reactions

As it is described in the fluid mechanics section, the reactor model is subdivided into a freeboard zone and a bottom zone with a solid free bubble phase and suspension phase. Figure 3 (right) illustrates the modeled phases as well as the input and output streams. Heterogenous gas-solids reactions occur only in the suspension and dilute freeboard phase. In the model, the solids are assumed to be perfectly mixed in the whole reactor. The gases rise from the distributor without any back mixing and are modeled as in a plug flow reactor.

In iG-CLC, the solid fuel is directly fed into the fuel reactor (FR), where it dries, devolatilization takes place and later the char is gasified. The generated fuel gases then react with the OC. The reaction mechanism is depicted in Fig. 4 as described previously by Adanez et al. [9] and Lyngfelt et al. [22].

The modeled devolatilization time is assumed to be immediate and thus independent from the atmosphere as well as other gas concentrations. The devolatilization of the fuel occurs in the dense bed zone of the fuel reactor. An equal distribution of the volatile gases through the whole bed height is assumed [23]. This gas mixture consists of H_2, CO, CO_2, CH_4, H_2O and N_2 including the volatiles, and the fuel moisture.

Via the same inlet stream, solid char can be added to the system. The char and the oxygen carrier are assumed to be perfectly mixed. Further, the modeled fuel is assumed to be ash and tar free. The watergas-shift reaction and other homogenous gas reactions are not regarded in the model. Furthermore, higher hydrocarbons, nitrogen

Fig. 4 Conversion route in iG-CLC for solid fuels. From Adanez et al. [9] and extended for the influence of conversion products on gasification
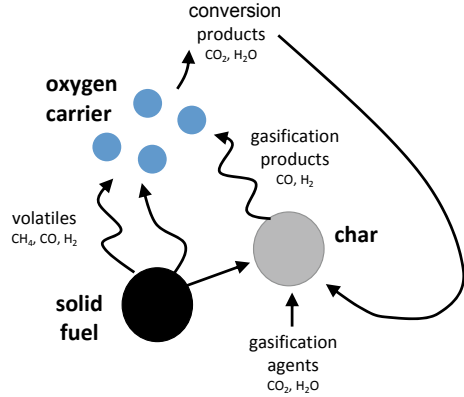
oxides and sulfur oxides are not considered. In the following, all modeled reactions are described. The gasification reactions (1) and (2) describe the conversion of char in the fuel reactor:

$$C_{char} + CO_2 \overset{k_1}{\rightarrow} 2CO \tag{R1}$$

$$C_{char} + H_2O \overset{k_2}{\rightarrow} H_2 + CO \tag{R2}$$
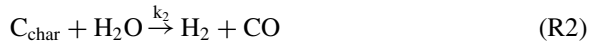
The gasification depends on the reaction rate constants k_1 and k_2 as well on the char concentration. Hence, the modeled reactions are not inhibited by the presence of CO and H_2. This is justified with the simultaneous fast reactions of the respective fuel gases with the OC, which are desribed in the following:

$$CH_4 + CuO \overset{k_3}{\rightarrow} CO + 2H_2 + Cu \tag{R3}$$

$$CO + CuO \overset{k_4}{\rightarrow} CO_2 + Cu \tag{R4}$$

$$H_2 + CuO \overset{k_5}{\rightarrow} H_2O + Cu \tag{R5}$$
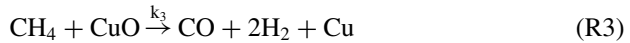
In the air reactor, the oxygen carrier oxidation is described by reaction 6. For the reaction rate constant k_6 usually high values are chosen to assure a complete OC re-oxidation in the AR:

$$0.5O_2 + Cu \overset{k_6}{\rightarrow} CuO \tag{R6}$$

Since the gasification is usually a slow process, the solid stream exiting the fuel reactor can contain unconverted char particles together with the oxygen carrier. Without further treatment, the char will then be converted in the air reactor. In an ideal

operation, this carbon slip is kept to a minimum. The combustion of char in the air reactor is described with reaction (7):

$$O_2 + C_{char} \xrightarrow{k_7} CO_2 \qquad (R7)$$

For the reaction rate constant k_7 a value that high is chosen so that all char, which has entered the air reactor via carbon slip, is converted. With reaction (7) a conventional combustion with air in the fuel reactor can be simulated as well.

The reaction of the solid (Cu, CuO or C_{char}) j with the respective gas component l is described by the reaction rate $r_{s,j,l}$:

$$r_{s,j,l} = -c_{v,j} \cdot \rho_{m,j} \cdot \frac{dX_{s,j,l}}{dt} \qquad (15)$$

Here, $c_{v,j}$ is the volumetric concentration of a solid reactant j in a reactor volume element. It is taken by multiplying the total solids concentrations c_v and the fraction of active reactant on and inside the particles. This is relevant since most oxygen carriers consist only partly of reactive material. Moreover, $\rho_{m,j}$ is the molar density of the solids reactant j and $dX_{s,j,l}/dt$ is the solids conversion rate of reactant j with respect to the fuel gas l. The solids conversion rate is usually determined experimentally. From the obtained data, Arrhenius-type reaction rates for each reaction can be obtained. Since metallic OCs differ from the structure and reaction behavior, several heterogenous reaction models were proposed for the solid conversion [9]. For the mentioned gas-solid reactions a shrinking-core model with active, spherical grains is used. Abad et al. [24] found out that this model is well suited to describe the reaction behavior of a CuO/Al_2O_3 oxygen carrier. A general form of the Arrhenius type reaction kinetics is described as follows.

$$\frac{dX_{s,j,l}}{dt} = k(C_l^n, T) \cdot f(X) \qquad (16)$$

Here, the reaction rate constant k is a function of the molar concentration of the reacting gas l, with the reaction order n and the temperature T. If the gas concentration C_l is constant over the course of the reaction in a discretized volume element $A_r \cdot dh$, the reaction rate constant can be described with the Arrhenius equation:

$$k = k_0 \cdot e^{\frac{-E_a}{RT}} \qquad (17)$$

In the Arrhenius equation, k_0 is a pre-exponential factor and E_a is the activation energy for the reaction, both are determined experimentally. The factor R is the universal gas constant. The rate of conversion also changes with the conversion X itself. For this simulation, an algebraic expression for spherical grains and a reaction limitation is used. This model assumes active round grains which shrink over time. With a declining surface area over the course of the reaction, the reaction rate declines as well [9]:
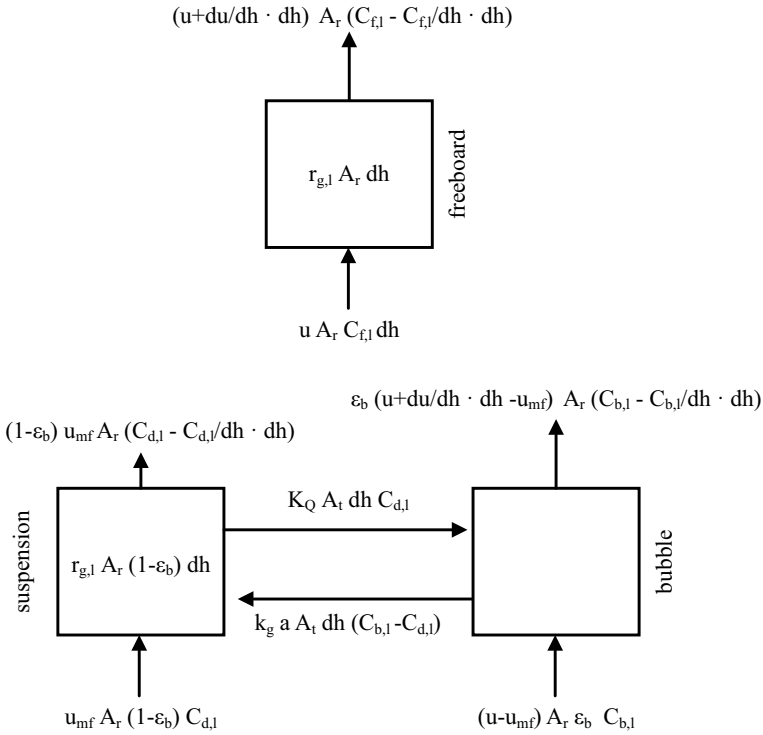
Fig. 5 Molar balances solved for each discretized height element dh. The suspension and the bubble phase are connected via diffusive and convective mass transfer (Reprinted with permission from [8])

$$f(X) = 1 - (1 - X)^{1/3} \tag{18}$$

The molar balances of the suspension, bubble and freeboard phase in the discretized volume elements $A_r \cdot dh$ for the gas species are shown in Fig. 5.

Since no homogenous gas reactions occur in the bubble phase, changes in the molar concentrations happen only due to convective and diffusive gas transfer with the suspension phase. In the following the concentration changes of all gas species l at a reactor volume element $A_r \cdot dh$, are shown for the bubble phase b, the dense suspension phase d and the freeboard f:

$$\text{bubble phase}: \frac{dC_{b,l}}{dh} = \frac{\dot{J}_{Q,l} - k_G \cdot a_t \cdot (C_{b,l} - C_{d,l}) - C_{b,l}\frac{du}{dh}}{u - u_{mf}(1 - \epsilon_b)} \tag{19}$$

$$\text{dense suspension phase}: \frac{dC_{d,l}}{dh} = \frac{\dot{J}_{Q,l} - k_G \cdot a_t \cdot (C_{b,l} - C_{d,l}) + r_{g,l}}{u_{mf}(1 - \epsilon_b)} \tag{20}$$

$$\text{freeboard}: \frac{dC_{f,l}}{dh} = \frac{r_{g,l} - C_{f,l}\frac{du}{dh}}{u} \tag{21}$$

The parameter $r_{g,l}$ describes the reaction rate of the gas l, with the oxygen carrier or char, based on the reactor volume. The chemical reactions change the molar flow of gases due to the generation or consumption of gases. Correspondingly to the generation or consumption of gases the velocity over height is changed as well. However, the velocity in the suspension phase is assumed to be constant. Therefore, all generated gases in the suspension phase are directed to the bubble phase via a convective flow $\dot{J}_{Q,l}$. If a gas is consumed in the suspension phase, a convective flow from the bubble phase is assumed:

$$\dot{J}_{Q,l} = \begin{cases} K_Q \cdot C_{d,l} \ for \ K_Q > 0 \\ K_Q \cdot C_{b,l} \ for \ K_Q < 0 \end{cases} \tag{22}$$

In these equations, the parameter C_l is the gas concentration of gas l in the dense suspension d or bubble phase b and K_Q describes the convective exchange rate. It is calculated from all heterogenous reaction rates $r_{g,l}$ of the gases in the suspension phase:

$$K_Q = \frac{R \cdot T}{p} \sum r_{g,l} \tag{23}$$

Here, p denotes the pressure inside the system, R is the universal gas constant and T the temperature. In Eqs. (19) and (21) the term $C_l \frac{du}{dh}$ describes the change of the mass flow of the gas l over the height caused by gas velocity changes. In the fuel reactor, usually the flow increases due to the solid fuel conversion to gases and due to the CH_4 reaction, in which one molecule of CH_4 creates two molecules of H_2 and one CO molecule. In the air reactor, the molar flow is decreased due to the oxidation of the OC. In the model, it is assumed that the gas passes the suspension phase close to minimum fluidization velocity u_{mf}. To maintain u_{mf} in the suspension phase, gas concentration changes due to velocity effects only occur in the bubble and freeboard phase.

Chemical reactions in suspension phase lead to different gas concentrations in bubble and suspension. This causes a diffusive mass transfer between the phases. The resulting gas diffusion resistance k_G is described with the following correlation [25]:

$$k_G = \frac{u_{mf}}{3} \sqrt{\frac{4 \cdot D \cdot \epsilon_{mf} \cdot u_b}{\pi \cdot d_v}} \tag{24}$$

Here, D describes the molar binary diffusion coefficient, ϵ_{mf} is the minimum fluidization voidage, u_b is the bubble rise velocity and d_v stands for the bubble size. To the diffusion resistance k_G in Eqs. (19) and (20) the parameter a_t is multiplied, which is the ratio of the interfacial area between bubble and suspension phase to the

volume of a reactor element. By assuming spherical bubbles, the parameter a_t can be described with the bubble size d_v and the bubble volume fraction ϵ_b:

$$a_t = \frac{6\epsilon_b}{d_v} \tag{25}$$

Calculation Procedure

The calculation procedure for the fluidized bed reactor module is shown in Fig. 6. In a first step, fixed parameters are read into the program. Since they cannot be changed during the simulation, they are only initialized once. Examples for fixed parameters are geometrical values or the particle elutriation model. In a next step, the reactor is discretized in a number of height elements over the reactor height. It is important to choose a number high enough to provide enough intermediate steps for the calculation of the fluid mechanics and chemical reactions. Afterwards, for each time step the operation conditions, like inflows from other units and fluidization velocity are read from the system.

With the actual state of the reactor (current solids holdup and its conversion state) and the operation conditions, the fluid mechanics in the system are calculated. This includes the solid concentration at each height class, the bubble size, the dense bed height and the solid elutriation. The fluid mechanics are calculated with the Sundials DAE solver, which is further described in the previous chapter by Skorych et al. Afterwards, the gas and solids conversion from chemical reactions is calculated at each height element. The gas conversion is calculated by an explicit Euler algorithm. With the Euler method, the gas concentrations, which are discretized at each height element, are calculated from the gas concentrations and kinetics from the previous height element, starting from the reactor bottom. Fluid mechanics and chemical reactions are then iterated until the gas and solid conversions match to each other. When the iteration is complete and the calculated values match to each other within a predefined tolerance, the outlet flows are calculated together with the new bed mass, the OC conversion state and the particle size distribution. The time steps for the calculations are determined by DYSSOL in a way to avoid numerical errors regarding the predefined tolerances.

2.3.2 Loop Seal Unit

The loop seals ensure gas sealing between the reactors. Furthermore, they act as holdup for solid material. The loop seals are designed with two chambers, the recycle chamber RC and the supply chamber SC, which are both fluidized. In Fig. 7 the basic geometry of the loop seal S2 between the AR and the upper stage of the FR can be seen. A standpipe above the supply chamber, which holds solid is included in the model. The model describes both chambers as fluidized beds in bubbling conditions. Thus, the solids concentration depends on the presence of bubbles. Hydrodynamic
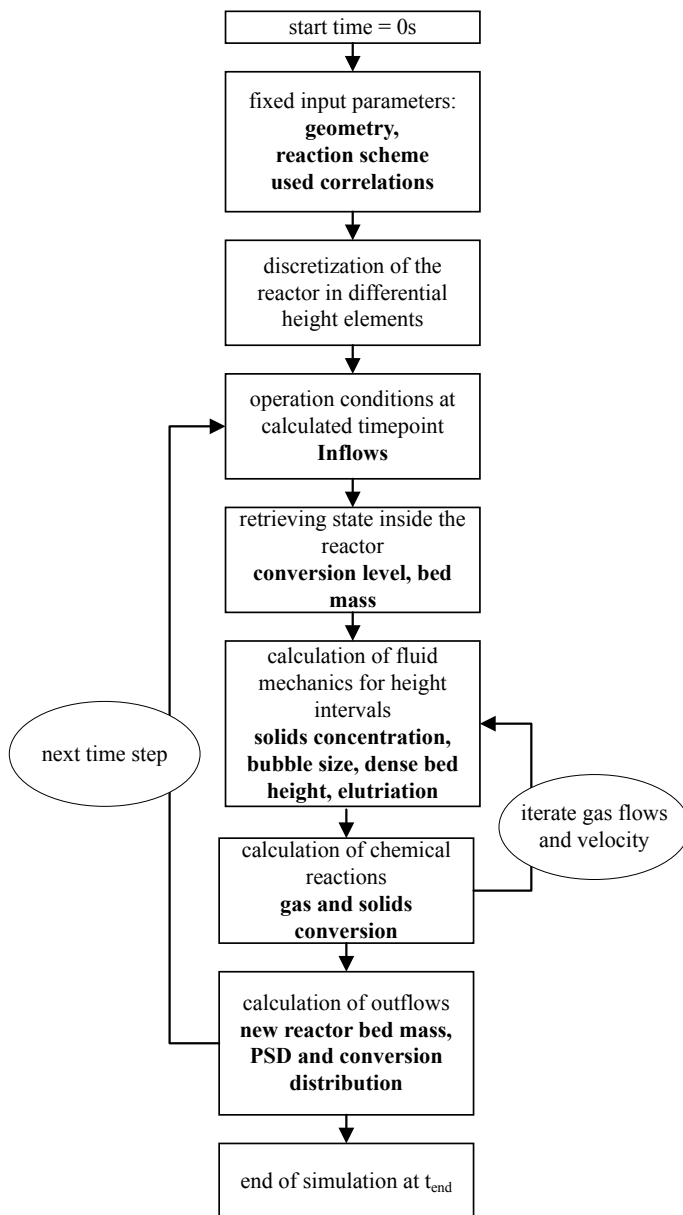
Fig. 6 Calculation procedure for the fluidized bed reactor module (Reprinted with permission from [8])

Fig. 7 Basic schematics of
the loop seal model
(Reprinted with permission
from [8])
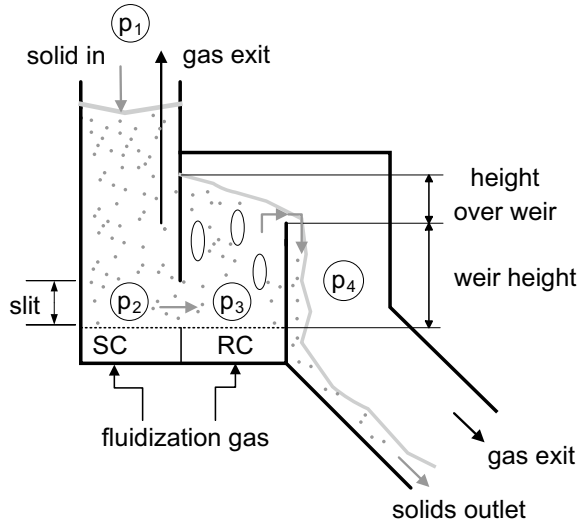
behavior is simulated the same way as in the fluidized bed reactor module. The total
mass m_{LS} inside the loop seal is the sum of the masses in the recycle chamber m_{RC}
and in the supply chamber m_{SC}. The height of the supply chamber and the weir height
H_W in the recycle chamber restrict the maximum mass of solids in the loop seal.

The solid mass distribution and the height differences in both chambers depend
strongly from the pressure difference environment around them and with it, from the
FR and AR.

Three factors influence the pressure balance between the AR and FR. Firstly, the
solids must always reach the slit height to prevent a short-circuit of the gas. Secondly,
the height from the slit to the weir defines the maximum height of solids in the recycle
chamber. Thirdly, the height of the supply chamber defines the maximum holdup of
solids in it. All described effects are implemented into the model. With Eq. (14) the
solids overflow is defined in the same way as in the fluidized bed reactor. According
to Bareschino et al. [26] the solid circulation it not influenced by the fluidization
velocity in the loop seal. Furthermore, it is shown that most of the gas leaves the loop
seal through the recycle chamber. These findings were approved by Thon [27] on a
cold flow model of the CLC pilot plant at TUHH.

The modeled loop seals allow dynamic bed mass changes, which arrange
according to the pressure drop differences of the two chambers:

$$\Delta p_{LS} = \int_{H_{C1}}^{H_{C2}} \rho_S c_V(h) g dh \qquad (26)$$

The time dependent mass in the loop seal is given by the in- and out- mass flow
rate:

$$\frac{dm_{LS}}{dt} = \dot{m}_{LS,in} - \dot{m}_{LS,out} \tag{27}$$

2.3.3 Cyclone Unit

For gas-solid separation a cyclone model is implemented into DYSSOL. A system, which is similar to the semi-empirical model by Muschelknautz [28], is implemented. This model was validated against data from several hot units and is widely used for cyclone design in Germany. In this work, the model was extended with an approach by Klett et al. [29] to avoid errors in the population balances for fine particles.

In the Muschelknautz model, the separation of particles and gas is accomplished by two different mechanisms, shown in Fig. 8. Firstly, the wall separation occurs after exceeding the saturation carrying capacity. This causes a strand, which directly leads down the wall to the solids exit. Secondly, the separation occurs inside the inner vortex. A small part of particles moves directly to the upper outlet together with the gas, the so-called overflow. After the inlet solids loading μ exceeds the threshold value μ_G, wall separation occurs. Bigger particles are preferably separated at the wall, which leads to a finer particle size distribution in the inner vortex. Generally, in circulating fluidized beds μ_G is exceeded. In the inner vortex, a cut size diameter d* defines which fraction of a particle size d leaves the cyclone with the overflow or with the underflow. The resulting separation efficiency $\eta_f(d)$ is shown in Eqs. (28)–(30). Depending from the cyclone type the parameter D_c varies from 2 to 4 and is usually set to a value of 3.

Fig. 8 Cyclone model with separation mechanisms (adapted from Muschelknautz and Trefz [28])
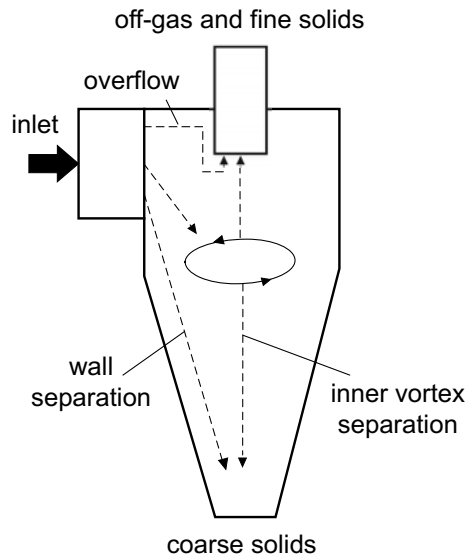
$$\eta_f(d) = 0 \quad \text{for } d < \frac{d^*}{D} \tag{28}$$

$$\eta_f(d) = 0.5 \cdot \left\{ 1 + cos \left[\pi \left(1 - \frac{log\frac{d}{d^*} + log D}{2log D} \right) \right] \right\} \quad \text{for } \frac{d^*}{D} < d < D \cdot d^* \tag{29}$$

$$\eta_f(d) = 1 \quad \text{for } D \cdot d^* < d \tag{30}$$

The described model assumes a separation, considering only a single particle diameter. This can be problematic, when a mixture of solids with different densities needs to be separated. To tackle this issue, Redemann et al. [30] proposed a separation model, which uses the terminal velocities instead of the particle diameter. In the model, a separation efficiency curve $T(u_{t,i})$, which determines the part of solids what can be separated in the inner vortex, is defined. $T^*(u_{t,i})$ depends on the terminal velocity $u_{t,i}$ for each defined terminal velocity class i:

$$T(u_{t,i}) = (1 - a) \cdot T^*(u_{t,i}) + a_s \tag{31}$$

$$T^*(u_{t,i}) = \frac{1}{1 - \frac{\sqrt{u_{t,50,e}}}{u_{t,i}} exp\left[a_s \left(1 - \sqrt{\frac{u_{t,i}}{u_{t,50,e}}}^3 \right) \right]} \tag{32}$$

Here, the parameter $u_{t,50,e}$ is the terminal velocity of a particle flow, were 50% of the particle mass has a terminal velocity below this value. The share ratio a_s describes the share of the flow which is in the inner vortex.

The presented cyclone model is a steady state model. Dynamics are not necessary, since the particle holdup is expected to be very small. It is assumed that particles, which enter the cyclone, are instantaneously separated into a gas flow with small entrained particles via overflow and a coarse particle underflow.

3   Results

In this chapter, a summary of simulation results with previously described DYSSOL models are shown. The simulation results include the effects of a dynamic operation on the fluid dynamics of the given CLC system as well as the combustion reactions, which result in a conversion of the oxygen carrier. The simulations are validated against experimental data, obtained with a 25 kWth CLC two-stage pilot plant, which is operated at Hamburg University of Technology. More detailed results of the fluid dynamics and methane conversion can be found in publications by Haus et al. [8, 11]. Results of biomass conversion simulations are presented by Lindmüller et al. [12]. In the following results, each experimental setup is briefly explained and then compared with the simulations. In all presented simulations, a desktop computer

(single core of Intel® Core™ i7-6800 K) could simulate the dynamic plant operation faster than real-time.

3.1   Movement of the Bed Mass Inside the System

When CH_4 is added as fuel to the FR, the volumetric gas flow will be increased, because one CH_4 molecule reacts with the OC to one CO and two H_2 molecules. A higher gas flow leads to an increase of the bubble volume fraction in the bed. Since the height in the bubbling bed is limited to the standpipe height, the bed holdup decreases at higher velocities. Due to the interconnected reactors, a velocity change in one unit will lead to a rearrangement of the solids distribution in the whole system. This effect is shown in Fig. 9, where the measured pressure drop of each reactor is plotted over time. At t = 4 min, CH_4 is added to FR1. This leads to a decrease of Δp in the fuel reactor stages and an increase of Δp in the AR, which means that bed material is transferred from the FR to the AR. This effect is even more notable in the AR, where the OC is re-oxidized with O_2. This leads to a reduction of the volumetric gas flow in the AR. After stopping the fuel injection, the bed material moves back again to both FR1 and FR2.

Due to strong pressure fluctuations, the exact conditions can only be estimated. The loss of bed mass in the FR is about 5–10% while the AR holdup increase is roughly 10–20%.
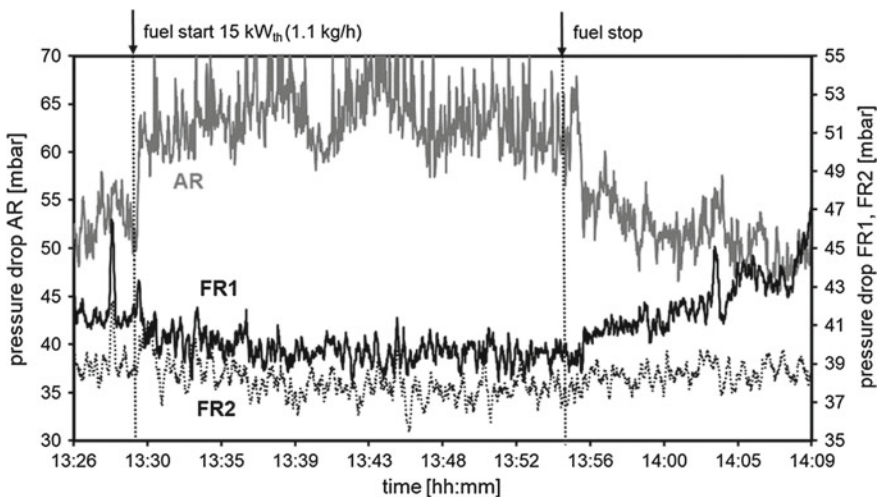
Fig. 9 Measured pressure drops over the whole reactor height of FR1, FR2 and AR at 800 °C. Methane injection started at 4 min and was stopped after 33 min (Reprinted with permission from [8])
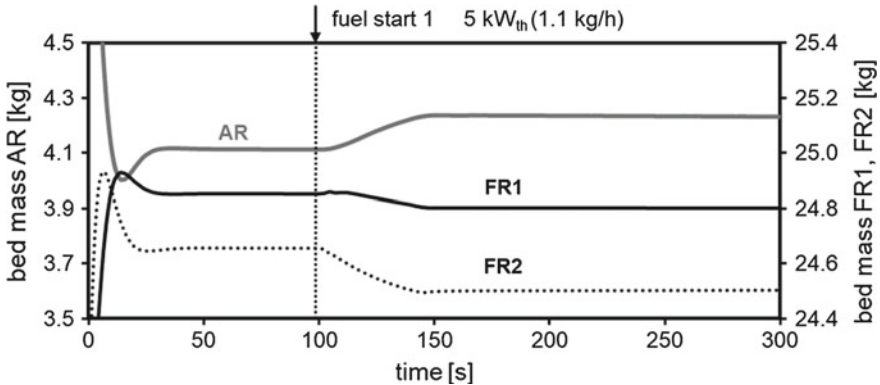
Fig. 10 Simulated bed masses inside the system over time with a response to fuel injection at t = 100 s (Reprinted with permission from [8])

For the flowsheet simulation, the same input parameters as for the experiment were used. After adding methane to the FR, the same behavior as in the experiments could be observed. The bed masses in the simulation are plotted in Fig. 10. At the start of the simulation, the bed masses arrange themselves to a stable operation point which takes about 30 s. After fuel is added at 100 s, particles move to the AR due to the aforementioned effects. Stopping the fuel injection leads to a reassembly of the bed masses in the system to the first steady state.

The simulation could predict the experimental fluid mechanical response of the reactor system. In the simulation, the fuel reactor stages lose around 5% of their bed mass while the AR bed mass increases around 20%, which is in the range of the experimental results. The simulated system took about 30–40 s to reach a new steady state.

3.2 Gas Conversion in the Fuel Reactor

During a combustion of wood biomass in the CLC pilot plant at TUHH the volumetric gas concentrations in the outlet of both fuel reactor stages FR1 and FR2 were measured. The fuel was fed into the bed of FR1. As in every experimental run, the fuel reactor is fluidized with CO_2 and steam. In the experiment with a 16 kWth power input at 850 °C, the H_2 and CO concentrations at the fuel reactor outlet (FR2) were around 0.8 vol.% and 1.2 vol.%, while the concentration of CO_2 was around 98%. CH_4 was not detected in the exhaust gas. Regarding the measurement error in the system, it can be likely assumed that H_2 and CO were completely converted. In FR1 still high amounts of fuel gases were detected. Thus, only one fuel reactor stage in this CLC facility is not enough for a complete fuel conversion.

A comparison of the measured and simulated gas concentration is shown in Fig. 11. Here it can be seen that the model is able to predict the axial gas concentrations over the whole reactor height. The composition of the simulated volatile gas is shown in Table 2. It has to be noted that in this presented work the biomass char content, which is about 5 wt%, was not regarded.

In the simulation, the concentrations in the lower dense zones (< 0.6 m) are averaged over the bubble and suspension phase. Furthermore, the fuel is evenly and instantaneously devolatilized over the total bed height H_b of FR1. This explains an increase of the fuel gas concentrations over the bed height in FR1. At the same time, the fuel gases are consumed by the OC. Therefore, the fuel gas concentrations do not increase linearly over the bed height. In the bed zone of FR2 the fuel gas is further consumed by the OC. The gases coming from FR1 react with the fully re-oxidized OC. At the border between the dense bed and the freeboard zone, changes in the gas concentrations are seen, since the solid concentration over the bed decreases quite fast.

Fig. 11 Biomass conversion at 16 kWth in fuel reactor stage 1 and 2 over height at 850 °C. Biomass inlet in bed of FR1. Comparison of simulation and experimental data at the exit of each stage
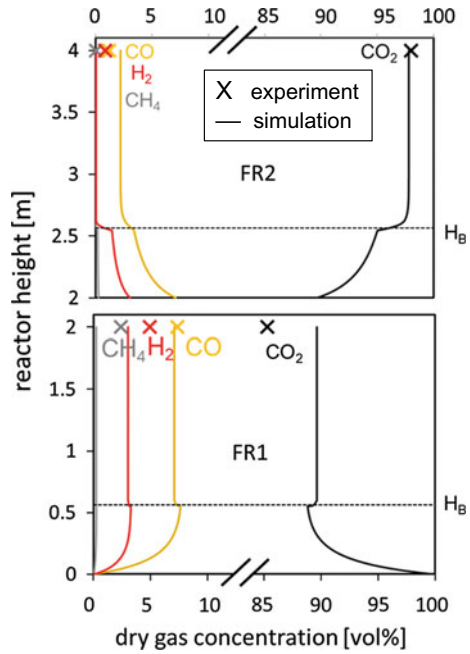
Table 2 Biomass volatile gas composition for simulation

Gas	vol.%
H_2	43.6
CO	33.2
CO_2	11.7
CH_4	11.5
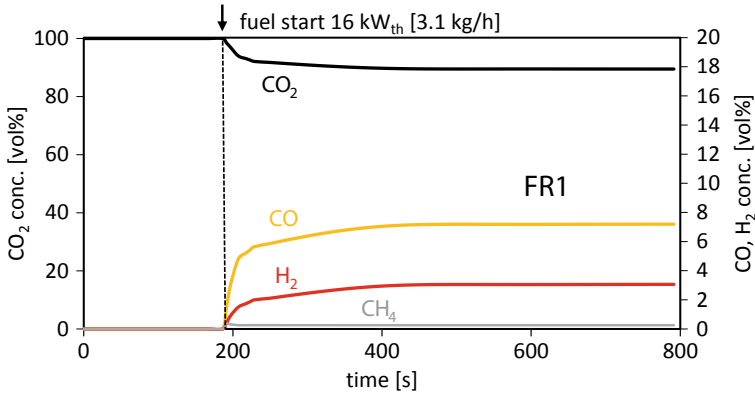
Fig. 12 Gas concentrations at exit of fuel reactor stage 1 over time during biomass conversion at 16 kWth and 850 °C

The reaction rates were fitted to resemble the experimental outlet concentrations at FR2. In this way, the target gas concentrations were accurately met in the simulation. With the same reaction rates, the reactions in FR1 were simulated. Here the gas concentrations in the simulation were still close to the experimental ones.

To analyze the reaction progression, the gas concentrations can be dynamically plotted over time. Exemplarily, Fig. 12 shows the concentrations of the gases, leaving FR1 over time, before and after a fuel start. Without any fuel, only CO_2 and steam are present in the fuel reactor. Here, the modeled steam concentration is not plotted. Adding reactive gases to the model leads to the shown concentration gradients. As it is explained in the previous paragraph, the conversion of the volatile gas mixture is not complete after only one fuel reactor stage. After around 200 s a steady state regarding the gas concentrations in the FR is reached.

3.3 Conversion of the Oxygen Carrier

In the following, the conversion state of the OC in FR1 after the start and top of a methane injection is evaluated. A detailed description of the experimental operation conditions can be found in Haus et al. [8]. The OC conversion X_s is plotted over time in Fig. 13. There $X_s = 0$ stands for a fully oxidized OC and $X_s = 1$ stands for a fully reduced OC. The experiment starts with a fully oxidized OC. At t = 100 s, a methane injection to the FR was started, leading to an increase of X_s. At t = 1400 s, the methane injection was stopped. The OC conversion decreases again, since the OC is re-oxidized in the air reactor. The OC conversion depends strongly on the solids circulation rate G_s. The higher G_s, the lower the specific OC conversion after the fuel reactors, since more solid material reacts with the same amount of fuel gas. With the same conditions in the experiment and simulation, such as fluidization velocities
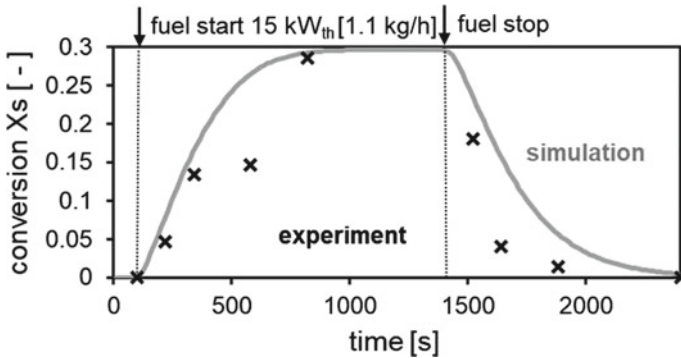
Fig. 13 Conversion of the OC, coming from FR1, during a CH_4 combustion at 800 °C. Simulation of 2400 s of operation, fuel injection starts at 100 s and stops at 1400 s. Samples were taken during hot operation at 8 points. The simulation was done with fitted kinetics (Reprinted with permission from [8])

and bed masses, the simulated solids circulation rate was 25 kg/(m·s^2). This is in the range of previous measurements, where G_s was between 15 and 45 kg/(m·s^2).

The dynamic flowsheet simulation is able to track X_s over time. These values were compared with experimental values from samples taken after 120, 240, 480 and 720 s after the fuel injection was started and 120, 240, 480 and 1000 s after the fuel was stopped.

Both, experiment and simulation needed about 800 s of fuel injection to reach a steady state at $X_s = 0.28$. The long transition time is caused by a long residence time of OC particles in FR1 and FR2, which could be accurately reproduced in the simulation. However, the decline time after a fuel stop takes considerably longer in the simulation. This discrepancy can be explained with the simulated mixing behavior in the lower loop seal between the FR exit and the AR. A perfect mixing of the holdup with the solids coming from the FR is assumed. In reality, it is possible that the solids have a shorter residence time in the loop seal because the particles can pass the loop seal like a moving bed without much mixing of solids.

Another way to observe the solid conversion is to analyze the O_2 outlet concentration of the AR. Air enters the AR with 21 vol.% O_2. The more O_2 consumed in the AR, the higher the conversion X_s of the OC after the fuel reactor. The advantage of this method is that no OC samples during the experimental operation have to be taken. However, without knowing the solid circulation rate and the OC samples, the exact conversion cannot be determined experimentally.

In the experimental run, which is further described in Sect. 3.2, the outlet O_2 concentration in the AR was measured during a dynamic combustion of wood biomass in the FR. Figure 14a shows the O_2 concentration in the AR during the experimental and simulated fuel start and stop. There, the O_2 concentration drops by 7 vol.% after starting the fuel. The more reduced OC enters the AR, the lower the O_2 concentration. By stopping the fuel supply the OC is not reduced in the FR anymore and the
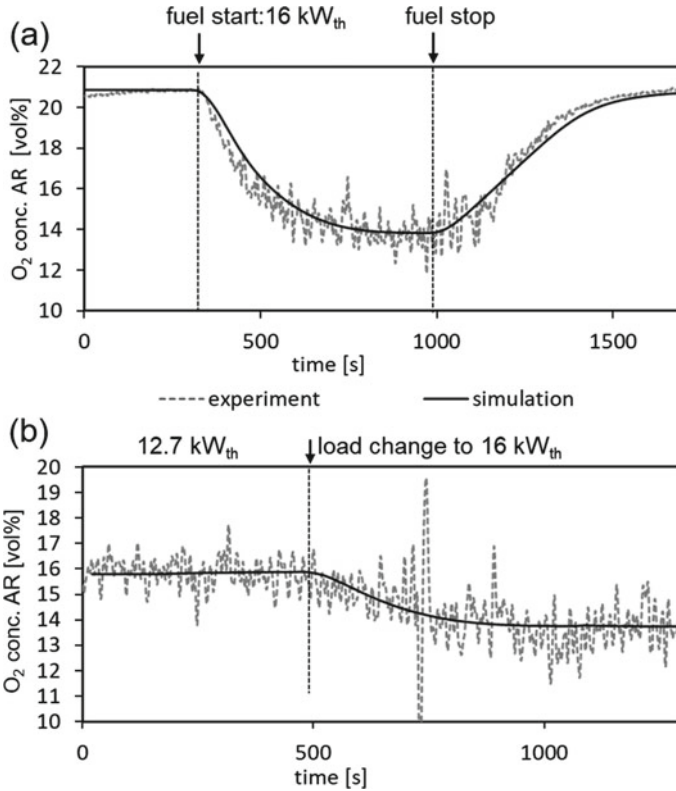
Fig. 14 Experimental and simulated O_2 concentration at AR outlet at 850 °C, **a** during start and stop of biomass injection with fitted kinetics, **b** during fuel load change with the same kinetics

remaining reduced OC from the FR is re-oxidized in the AR. Since the solid holdup in the FR needs to be transported into the AR by circulation, the oxygen in the AR is still consumed until the whole inventory from the FR was carried over. This takes around 600 s after fuel supply was stopped.

Additionally, a fuel load change from 12.7 to 16 kWth was conducted. In Fig. 14b, the measured and simulated O_2 concentration in the AR are presented. Here a new steady state was reached in about 400 s. In both cases the simulation was able to predict the dynamic course of the O_2 concentration and thus the OC conversion state. The kinetics for the simulation were fitted to match the FR gas concentrations in Fig. 11 and the AR O_2 concentration in Fig. 14a. Thus, the load change in Fig. 14b serves as validation of the simulation with the used kinetics.

4 Conclusion

Dynamic models, necessary for CLC with gaseous and solid fuels, were implemented into the flowsheet simulation environment DYSSOL. Unit models for a CFB riser reactor, a bubbling bed reactor, a cyclone and a loop seal were developed. For validation, the simulations were compared with experimental data obtained from a 25 kWth two-stage CLC pilot plant, which is operated at Hamburg University of Technology. The dynamic models were used to simulate several hot operations of the CLC plant with methane and wood biomass as fuel. In the following, the most important results of the present work are summarized:

- Solid distributions in the system could be predicted close to the experimental measurements for different operation states. The transition time from one fluid mechanical state to another was correctly predicted.
- Heterogenous chemical reactions were implemented into the fluidized bed reactor model, including the conversion of fuel gases with the OC and the gasification of solid char.
- During solid combustions, the fluidized bed reactor model is able to depict the gas conversion at the reactor exit. The simulations showed expected axial gas concentrations over height. Nevertheless, fitted kinetic parameters needed to be used for the simulation.
- Dynamic operation changes were applied to the system. In a hot plant run, fuel starts and stops as well as a load change were conducted. The resulting experimental changes of the OC conversion could be accurately predicted in the simulation. Furthermore, the response time of the OC conversion to the operation changes could be correctly determined.
- In all simulations, a desktop computer (single core of Intel® Core™ i7-6800 K) could simulate the plant operation faster than in real time. This makes model-based plant control of a complex interconnected system possible.
- DYSSOL proved to be a reliable and mighty tool to calculate units and predict long term effects in solids processes.

References

1. Porrazzo, R., White, G., Ocone, R.: Aspen Plus simulations of fluidised beds for chemical looping combustion. Fuel **136**, 46–56 (2014)
2. Mukherjee, S., Kumar, P., Yang, A., Fennell, P.: A systematic investigation of the performance of copper-, cobalt-, iron-, manganese- and nickel-based oxygen carriers for chemical looping combustion technology through simulation models. Chem. Eng. Sci. **130**, 79–91 (2015)
3. Li, F., Zeng, L., Velazquez-Vargas, L.G., Yoscovits, Z., Fan, L.-S.: Syngas chemical looping gasification process: bench-scale studies and reactor simulations. AIChE J. **56**, 2186–2199 (2010)

4. Sahir, A.H., Dansie, J.K., Cadore, A.L., Lighty, J.S.: A comparative process study of chemical-looping combustion (CLC) and chemical-looping with oxygen uncoupling (CLOU) for solid fuels. Int. J. Greenhouse Gas Control **22**, 237–243 (2014)

5. Peltola, P., Ritvanen, J., Tynjälä, T., Pröll, T., Hyppänen, T.: One-dimensional modelling of chemical looping combustion in dual fluidized bed reactor system. Int. J. Greenhouse Gas Control **16**, 72–82 (2013)

6. Peltola, P., Ritvanen, J., Tynjälä, T., Hyppänen, T.: Fuel reactor modelling in chemical looping with oxygen uncoupling process. Fuel **147**, 184–194 (2015)

7. Bolhàr-Nordenkampf, J., Pröll, T., Kolbitsch, P., Hofbauer, H.: Comprehensive modeling tool for chemical looping based processes. Chem. Eng. Technol. **32**, 410–417 (2009)

8. Haus, J., Hartge, E.-U., Heinrich, S., Werther, J.: Dynamic flowsheet simulation for chemical looping combustion of methane. Int. J. Greenhouse Gas Control **72**, 26–37 (2018)

9. Adanez, J., Abad, A., Garcia-Labiano, F., Gayan, P., de Diego, L.F.: Progress in chemical-looping combustion and reforming technologies. Progress Energy Combust. Sci. **38**, 215–282 (2012)

10. Puettmann, A., Hartge, E.-U., Werther, J.: Application of the flowsheet simulation concept to fluidized bed reactor modeling. Part I: Development of a fluidized bed reactor simulation module. Chem. Eng. Process. Process Intensification **60**, 86–95 (2012)

11. Haus, J., Hartge, E.-U., Heinrich, S., Werther, J.: Dynamic flowsheet simulation of gas and solids flows in a system of coupled fluidized bed reactors for chemical looping combustion. Powder Technol. **316**, 628–640 (2017)

12. Lindmueller, L., Haus, J., Hartge, E.-U., Heinrich, S., Werther, J.: Experimental investigation and simulation of the dynamics in a chemical looping combustion system. In: 5th International Conference on Chemical Looping, 24–27 September 2018, Park City, Utah, USA

13. Haus, J., Lyu, K., Hartge, E.-U., Heinrich, S., Werther, J.: Analysis of a two-stage fuel reactor system for the chemical-looping combustion of lignite and bituminous coal. Energy Technol. **4**, 1263–1273 (2016)

14. Werther, J., Hartge, E.-U.: A population balance model of the particle inventory in a fluidized-bed reactor/regenerator system. Powder Technol. **148**, 113–122 (2004)

15. Werther, J., Wein, J.: Expansion behaviour of gas fludized beds in the turbulent regime. AlChE Symp. **90**, 34–44 (1994)

16. Davidson, J.F., Harrison, D.: Fluidised Particles. University Press Cambridge, Cambridge (1963)

17. Kunii, D., Levenspiel, O.: Fluidization Engineering. Wiley, New York (1991)

18. Chew, J.W., Cahyadi, A., Hrenya, C.M., Karri, R., Cocco, R.A.: Review of entrainment correlations in gas–solid fluidization. Chem. Eng. J. **260**, 152–171 (2015)

19. Choi, J.-H., Suh, J.-M., Chang, I.-Y., Shun, D.-W., Yi, C.-K., Son, J.-E., Kim, S.-D.: The effect of fine particles on elutriation of coarse particles in a gas fluidized bed. Powder Technol. **121**, 190–194 (2001)

20. Tasirin, S.M., Geldart, D.: Entrainment of FCC from fluidized beds—a new correlation for the elutriation rate constants Ki∞*. Powder Technol. **95**, 240–247 (1998)

21. Botsio, E., Basu, P.: Experimental investigation into the hydrodynamics of flow of solids through a loop seal recycle chamber. Can. J. Chem. Eng. **83**, 554–558 (2005)

22. Lyngfelt, A.: Chemical-looping combustion of solid fuels—Status of development. Appl. Energy **113**, 1869–1873 (2014)

23. Gómez-Barea, A., Leckner, B.: Modeling of biomass gasification in fluidized bed. Progress Energy Combust. Sci. **36**, 444–509 (2010)

24. Abad, A., Adánez, J., García-Labiano, F., de Diego, L.F., Gayán, P.: Modeling of the chemical-looping combustion of methane using a Cu-based oxygen-carrier. Combust. Flame **157**, 602–615 (2010)

25. Sit, S.P., Grace, J.R.: Effect of bubble interaction on interphase mass transfer in gas fluidized beds. Chem. Eng. Sci. **36**, 327–335 (1981)

26. Bareschino, P., Solimene, R., Chirone, R., Salatino, P.: Gas and solid flow patterns in the loop-seal of a circulating fluidized bed. Powder Technol. **264**, 197–202 (2014)

27. Thon, A.: Operation of a System of Interconnected Fluidized Bed Reactors in the Chemical Looping Combustion Process. (Ph.D. Thesis) first ed., Cuvillier (2013)
28. Trefz, M., Muschelknautz, E.: Extended cyclone theory for gas flows with high solids concentrations. Chem. Eng. Technol. **16**, 153–160 (1993)
29. Klett, C., Hartge, E.-U., Werther, J.: Time-dependent behavior of the ash particle size distribution in a circulating fluidized bed system. Proc. Combust. Inst. **30**, 2947–2954 (2005)
30. Redemann, K., Hartge, E.-U., Werther, J.: A particle population balancing model for a circulating fluidized bed combustion system. Powder Technol. **191**, 78–90 (2009)

Chapter 3
Dynamics of Spray Granulation in Continuously Operated Horizontal Fluidized Beds

C. Neugebauer, E. Diez, L. Mielke, S. Palis, A. Bück, E. Tsotsas, A. Kienle, and S. Heinrich

Abstract This chapter presents new findings on process and product design in continuous spray layering granulation in horizontal fluidized beds. The results are achieved by a multi-scale approach, combining single-particle characterization of

C. Neugebauer · A. Kienle
Automation and Modelling, Otto von Guericke University Magdeburg, Universitätsplatz 2, 39106 Magdeburg, Germany
e-mail: neugebauer@mpi-magdeburg.mpg.de

A. Kienle
e-mail: achim.kienle@ovgu.de

E. Diez · S. Heinrich (✉)
Solids Process Engineering and Particle Technology, Hamburg University of Technology, Denickestr. 15, 21073 Hamburg, Germany
e-mail: stefan.heinrich@tuhh.de

E. Diez
e-mail: e.diez@tuhh.de

L. Mielke · E. Tsotsas
Thermal Process Engineering, Otto von Guericke University Magdeburg, Universitätsplatz 2, 39106 Magdeburg, Germany
e-mail: lisa.mielke@ovgu.de

E. Tsotsas
e-mail: evangelos.tsotsas@ovgu.de

S. Palis
Control of Distributed Parameter Systems, Otto von Guericke University Magdeburg, Universitätsplatz 2, 39106 Magdeburg, Germany
e-mail: stefan.palis@ovgu.de

A. Bück
Institute of Particle Technology, Friedrich-Alexander University Erlangen-Nürnberg, Cauerstr. 4, 91058 Erlangen, Germany
e-mail: andreas.bueck@fau.de

A. Kienle
Max Planck Institute for Dynamics of Complex Technical Systems, Sandtorstr. 1, 39106 Magdeburg, Germany

the influence of drying conditions on layer formation and properties with meso-scale information of particle flow and recirculation between process chambers separated by weirs. On the macro-scale, population balance modeling is used to describe the overall process dynamics taking into account apparatus design and process conditions. New process regime maps are presented along with control concepts to guarantee stable and safe operation as well as desired particle properties.

1   Introduction

Spray layering (granulation) is a particle formulation process in which a solid containing liquid is sprayed onto a collection of core particles. The droplets collide with the cores and wet their surface. Supplying a heated gas flow, the liquid evaporates and the solid remains on the core particle surface. By continued spraying and evaporation, full layers can be obtained. As a consequence, the particles grow in size.

Horizontal fluidized beds are a key technology in spray layering, with widespread application in the areas of food, feed, fine chemicals and pharmaceuticals. They can be used to combine more than one operation in a single apparatus, for example layering of particles with a solid-containing liquid, followed by drying and cooling. For this, the apparatus can be compartmentalized along the apparatus length, by installation of weirs, creating different process chambers (Fig. 1).

Installation of weirs generates a residence time distribution (RTD) of the particles in the apparatus, as the passing of a weir by an individual particle depends on the particle properties, for example mass density, sphericity, as well as the fluidization conditions. Residence time distributions are known to cause product property distributions, for example differences in particle size in granulation, or product moisture content in drying operation.

The knowledge of the effect of an individual weir, parameterized with respect to particle properties and fluidization conditions, would allow answering a number of important design questions, for example how many weirs are required in an apparatus to obtain a desired spread of the residence time distribution, and therefore guide the design and operation of horizontal fluidized beds.

Furthermore, thermal conditions influence the dynamics of the evaporation process and thereby the dynamics of layer formation and layer properties, for instance layer thickness and porosity. These in turn influence the evolution of the particle size distribution.

Product classification in continuous operation can be performed internally and externally, for example by a screen-mill cycle. Here, the particle size distribution in the horizontal fluidized bed determines the dynamics of the process including the classification, for example the magnitude and time-scale of recycle flows or loads on screens and mill, influencing their efficiency.

Due to the multi-scale interaction, starting with single-particle layer formation dynamics over particle flows between adjacent process chambers to large-scale pro-
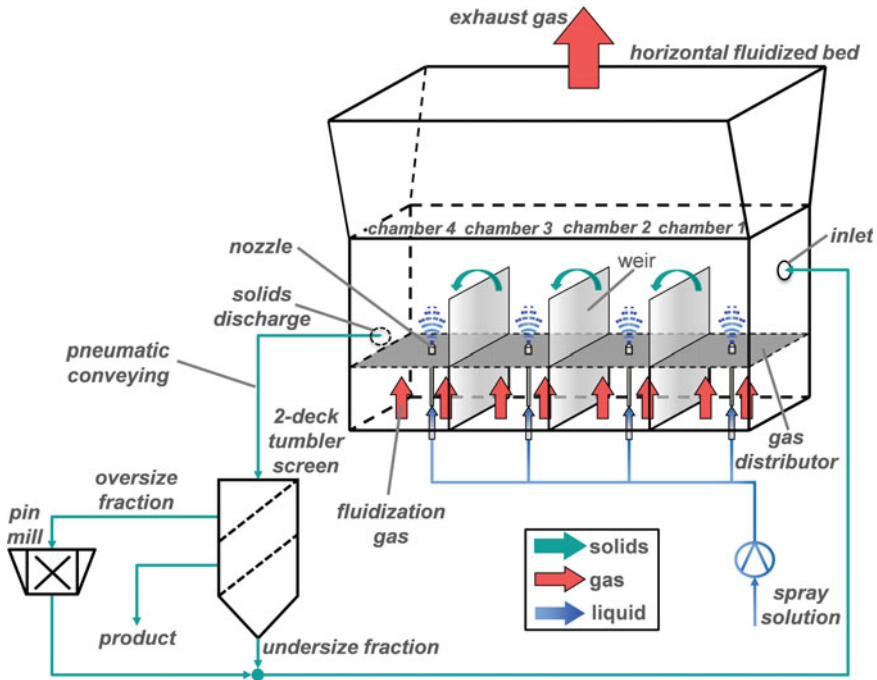
Fig. 1 Schematics of a typical spray granulation process in a horizontal fluidized bed with multiple process chambers generated by the insertion of weirs. Additionally shown is the external screen-mill cycle for product classification [1]

cess and plant behavior, spray layering granulation in horizontal fluidized beds is a prototypical interconnected solids process.

The research aims of the project were:

1. Study the influence of thermal conditions on the dynamics of layer formation and layer properties;
2. Study and characterize the influence of weir design and configuration on residence time and particle property distributions;
3. Derive and extend population balance models to describe the temporal evolution of particle properties with respect to apparatus (weir) design and operating parameters;
4. Using these models, study the dynamic and steady-state behavior of the continuous spray layering in horizontal fluidized beds;
5. Derive, design and implement control strategies to prevent unwanted process behavior and guarantee required product properties under model uncertainties and process disturbances.

This chapter is structured as follows: In Sect. 2, the basic population balance model for continuous spray layering in horizontal fluidized beds is introduced, considering

particle flows not only between adjacent process chambers but also between different functional compartments within each chamber. This is followed in Sect. 3 by experimental and simulation results on the particle exchange rates between chambers under the influence of weir design. Section 4 collects the experimental results with respect to the influence of thermal conditions on particle properties. This is followed in Sect. 5 by the presentation of a model extension, to allow predictive simulation of property development for different thermal conditions in each chamber. Using the extended model, the dynamic and steady-state behavior can be studied in detail. Section 6 presents results of the system theoretic analysis using the process model, identifying different process regimes (stable, unstable) depending on the operation and process conditions. This presentation is followed in Sect. 7 by results on control of the overall process, to stabilize operation and to guarantee desired product properties. The chapter closes with Sect. 8, a summary and outlook.

2 Basic Population Balance Model for Spray Granulation in A Multi-chamber Setup

In this section a multi-chamber and multi-compartment model of a horizontal fluidized bed apparatus for layering granulation is presented. Each chamber is designed individually and process conditions, such as spray rate, particle feed or gas temperature, can be adjusted for each chamber separately. Particle growth is described by population balance modeling. The particle exchange rates between the process chambers are determined individually to account for different weir configurations.

The growth of particles by layering is described within the population balance equation (PBE) framework as introduced for particulate processes by Ramkrishna [2].

The main idea of population balance modeling is the description of the temporal evolution of the number density function (or other density functions derived from it). For this, all relevant sub-processes that yield a change in the density have to be modelled. The density function characterizes the distribution of particle properties, for example the particle size, moisture content or temperature. Solving for the density function thereby gives information on the change of these particle properties. Population balance modeling has been used successfully to describe fluidized bed drying, agglomeration and layering granulation processes, for instance by Refs. [3–7].

To account for the fact that the sprayed solution or suspension can only reach a fraction of the particle bed it is necessary to divide the process chamber into compartments of different functionalities. For this purpose [8–10] introduced multi-compartment models for fluidized bed coating and layering granulation. Particularly, two-compartment models have been applied by Refs. [11–14] for fluidized bed layering granulation and coating processes.
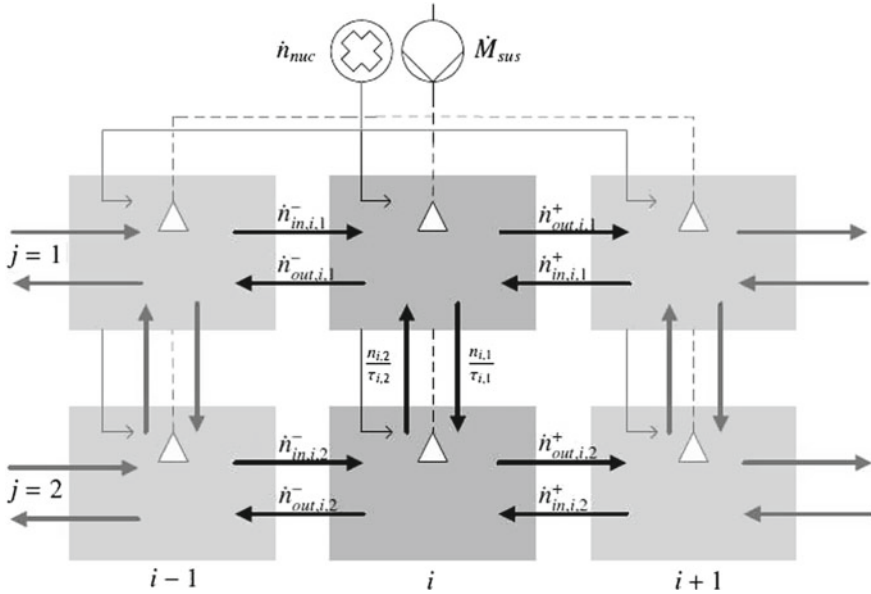
Fig. 2 Schematic representation of setup and particle flows in the multi-chamber, multi-compartment model

A two-compartment model is integrated into the multi-chamber model to describe particle growth and all relevant particle flows in each chamber. Figure 2 illustrates the developed multi-chamber and multi-compartment model. In this model the two compartments are considered to be arranged vertically in order to account for bottom or top-spray of the solid-containing spray. In case of top-spray configuration, the upper compartment (denoted by '1' in Fig. 2) is the spray compartment in which the particles are in direct contact with the sprayed liquid. In the lower zone (compartment '2') only drying and mixing of the contained particles take place. In bottom-spray configuration the lower zone '2' is assigned to be the spray zone and the upper zone '1' the drying zone, respectively.

The population balance equations for the number distribution density of particles with respect to particle size L of each compartment j in each chamber i, $n_{i,j}$, are written as follows:

$$\frac{\partial n_{i,j}}{\partial t} = -\frac{\partial \left(G_{i,j} \, n_{i,j} \right)}{\partial L} - \frac{n_{i,j}}{\tau_{i,j}} + \frac{n_{i,\bar{j}}}{\tau_{i,\bar{j}}} + \dot{n}_{i,j,in} - \dot{n}_{i,j,out}. \tag{1}$$

The total number distribution density of each chamber n_i is the sum of the number distributions of all compartments j within the chamber i,

$$n_i = \sum_{j=1}^{J} n_{i,j}. \tag{2}$$

The volume fraction of the compartment, $\omega_{i,j}$, and the particle residence time in this compartment, $\tau_{i,j}$, can be determined experimentally or taken from literature (e.g. [13] or [11]). The ratio of the mean residence times of the two zones equals the ratio of the compartment volumes:

$$\frac{\tau_{i,j}}{\tau_{i,\bar{j}}} = \frac{\omega_{i,j}}{\omega_{i,\bar{j}}}. \tag{3}$$

All particles in a chamber are contained in the two compartments, yielding the constraint:

$$\sum_{j=1}^{2} \omega_{i,j} = 1. \tag{4}$$

In the spray compartment ($j = 1$ for top-spray and $j = 2$ for bottom-spray configuration) the growth rate of particles, $G_{i,j}$, can be expressed by a relation proposed by Mörl et al. [15]:

$$G_{i,j} = \frac{2 \, y_{sus,s} \, M_{sus,i,j}}{\left(1 - \epsilon_{sh}(\eta_{dry,i})\right) \, \varrho_s \, A_{p,i,j}} \tag{5}$$

with

$$A_{p,i,j} = \pi \int L^2 n_{i,j}(t, L) \, dL = \pi \, \mu_{2,i,j}(t), \tag{6}$$

where $\mu_{2,i,j}$ is given by

$$\mu_{2,i,j}(t) = \int_{0}^{\infty} L^2 n_{i,j}(t, L) \, dL. \tag{7}$$

It contains the assumption that the sprayed liquid mass is distributed equally on the particle surface, $A_{p,i,j}$, which can be calculated from the second moment of number distribution density in the respective compartment, $n_{i,j}$. In case of spherical particles, the particle surface within the spray zone can be determined by Eq. (6).

The porosity of the formed shell, ϵ_{sh}, depends on thermal process conditions and the material of the initial core as shown experimentally by Rieck et al. [16].

The particle number flow rates between the chambers are represented by $\dot{n}_{i,j,out}$ and $\dot{n}_{i,j,in}$:

$$\dot{n}_{i,j,out} = \dot{n}_{out,i,j}^{-} + \dot{n}_{out,i,j}^{+}, \tag{8}$$

$$\dot{n}_{i,j,in} = \dot{n}_{in,i,j}^{-} + \dot{n}_{in,i,j}^{+}, \tag{9}$$

$$\dot{n}_{in,i,j}^{-} = \dot{n}_{out,i-1,j}^{+}, \tag{10}$$

$$\dot{n}_{in,i,j}^{+} = n_{out,i+1,j}^{-}. \tag{11}$$

Particle flows that enter from or leave to a previous chamber are denoted by "$-$". Those that enter from or leave to a subsequent chamber are denoted by "$+$" (see Fig. 2). In case of the first and the last chamber these equations have to be modified, since there is no previous or subsequent chamber, respectively. For the first chamber the inlet flows $\dot{n}_{in,1,j}^{-}$ and the outlet flows $\dot{n}_{out,1,j}^{-}$ are 0. The same applies for the inlet flows $\dot{n}_{in,I,j}^{+}$ of the last chamber. The product flow is the sum of forward outlet flows of the last chamber $\dot{n}_{out,I,j}^{+}$.

The particle flow at the chamber inlet and outlet depends on various factors, for example particle properties, like particle size and density distribution, the fluidization regime as well as the geometric design of the weir. Weirs, therefore, may have influence on the overall movement and recirculation of particles and mixtures in a process chamber. The characterization of the weir influence can be performed experimentally by particle tracking velocimetry (PTV) as described by Meyer et al. [17] or theoretically by combination of computational fluid dynamics (CFD) and discrete element method (DEM).

3 Determination of Inter-chamber Particle Transfer

In solids processing in horizontal fluidized beds the formation of residence time distributions and subsequently of property distributions, for instance in moisture content, particle size or chemical composition, are observed. Residence time distributions are due to partial recirculation of particles against the main transport direction. It is known that the installation of weirs, thus dividing the apparatus into multiple chambers, influences the overall residence time distribution.

Weirs are rectangular plates which are installed perpendicular to the main solid transport direction. Three common designs exist, shown in Fig. 3: Over-flow weirs which are installed directly on top of the distributor plate so that particles have to overcome the weir; under-flow weirs with a defined gap between weir and distributor plate; and side-flow weirs which are similar to under-flow weirs, however, the gap only exists over a certain portion of the apparatus width.

The effect of individual weirs on the observed dispersion has not been fully understood with respect to operation parameters, material properties or weir geometry.

Therefore, methods were developed and tested that allow investigating the particle transfer from one chamber to another and vice versa. In contrast to previous attempts to characterize the transport behavior by tracer experiments (see for instance [18–21]), particle tracking velocimetry (PTV) was utilized. The main advantage is that PTV allows the determination of exchange rates on single particle basis.
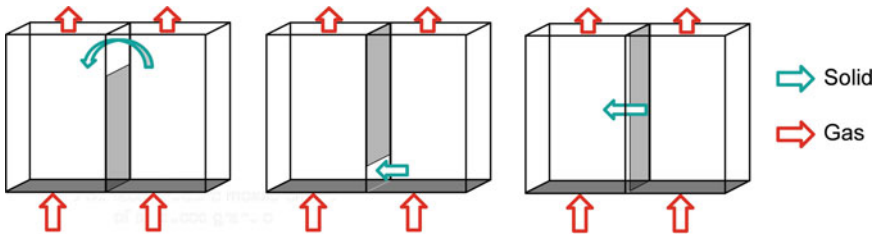
Fig. 3 Weir designs: over-flow weir (left), under-flow weir (center), side-flow weir (right)

3.1 Experimental Setup

3.1.1 Two-Dimensional Fluidized Bed

The particle tracking experiments were conducted in a batch pseudo-two-dimensional fluidized bed. It is a slightly modified version of the plant already used by Refs. [22–24] in their studies (Fig. 4a–c). The front and back plane are made of shatterproof glass that has been treated to prevent sticking of particles. Fluidization is realised by a controlled gas mass flow through a 3 mm sintered metal plate at the bottom. The plant has been modified such that one weir can be installed, either as an under-flow or as an over-flow weir. A weir plate (thickness: 4 mm) is made of PVC and can be fixed to the front and back plane, providing the required gap for the under-flow weir (here: 20 mm) and dividing the fluidized bed into two chambers of equal size and volume. The chambers are called 'left chamber' and 'right chamber' in the following.
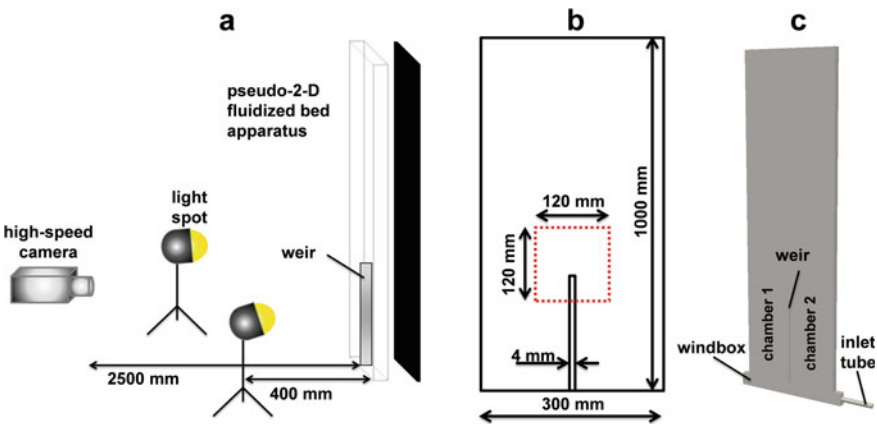
Fig. 4 Sketch, dimensions (**a,c**) and placement of the field-of-view (**b**) of the 2D-fluidized bed setup for recording of particle exchange between chambers separated by a weir (Used with permission by Elsevier)

3.1.2 Materials

All experiments were conducted with porous γ-alumina particles (Sasol Germany GmbH). The material, a model substance in drying and layering experiments, was chosen because of its thermal and mechanical robustness, i.e., there is only limited breakage and abrasion of particles even after repeated particle-particle or particle-wall collisions. This simplified the tracking of particles. Two different size distributions were used: One with a mean diameter of 1.8 mm and a standard deviation of 0.1 mm, the other with a mean diameter of 3 mm and a standard deviation of 0.1 mm. The particles belong to group D in the Geldart classification with minimum fluidization velocities of 0.5 m/s (1.8 mm) and 0.81 m/s (3 mm), respectively.

3.2 Method Development: Particle Tracking Velocimetry (PTV)

Particle tracking velocimetry (see [23–27] for details and successful applications) involves the identification of individual particles in images, constructing individual particle trajectories and determining individual (Lagrangian) particle velocities (Fig. 5). The main advantage of PTV is that particles are tracked directly and individually, allowing also the detection of small numbers of particles moving opposite to a dominating particle flow, making PTV very suitable for the investigation of exchange rates at weirs.

3.2.1 Image Acquisition

Particle movement in the two chambers was recorded with a high-speed camera system: It consists of a 1024 × 1024 pixel Photron camera with a CMOS chip, mounted on a solid frame. Two halogen bulbs with 400 W each were positioned to provide uniform lighting of the field of view (FOV). The camera was operated at full resolution at 1000 Hz, with an exposure time of 1/31000 s and a dynamic range of 10 bits. Operating the camera at these settings allows recording of 5000 images (5 s of process time), a constraint imposed by the built-in memory chip. An objective lens (60 mm, f = 4) was used to give the desired depth of field and light exposure. The field of view (95 mm × 95 mm) was placed as sketched in Fig. 4. This position was chosen in pre-trials and allows capturing the particle movement without losing spatial resolution by the observation of empty zones or of regions where particle movement is not of interest for weir passage (far left, far right of the weir). The overall setup was controlled by the DaVis image acquisition software (LaVision GmbH, Germany).
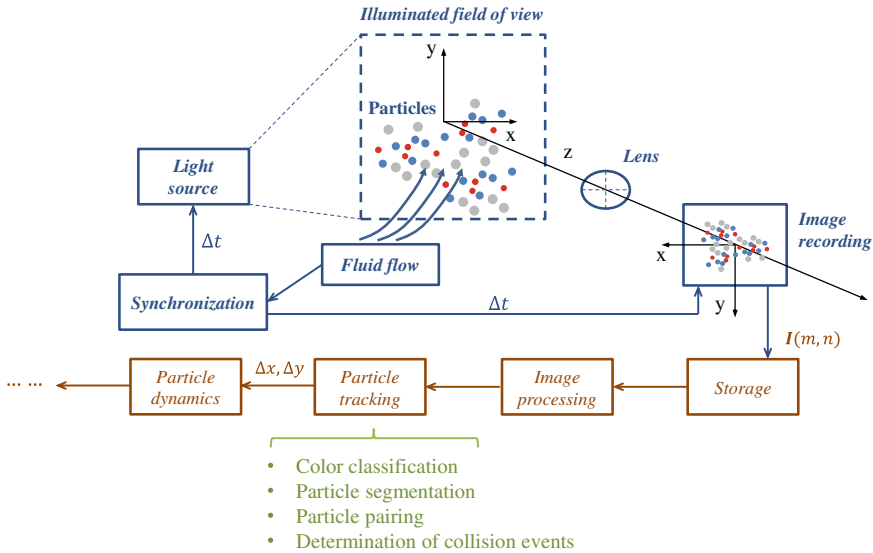
Fig. 5 General idea of and processing steps in particle tracking velocimetry

3.2.2 Image Analysis: Monodisperse Particulate Systems

Analysis of the recorded images and particle tracking were performed following the steps shown in Fig. 6: At first, individual particles were identified by choosing and cropping a sample particle in the initial image. The sample particle is cropped to the area of highest illumination; this enables the identification of particles in close packings. Using a smaller sample particle, a larger number of particles is successfully detected [17]. In each image, the centroids of detected particles were tabulated and fed to the tracking algorithm. Particle centroids were tracked between frames by Voronoi matching, as introduced by Capart et al. [26] for dilute flows and extended by Hagemeier et al. [24] for dense particle flows. Thereby, for each identified and unambiguously tracked particle, a set of positions was generated over time, forming the individual (Lagrangian) particle trajectories.

To determine the exchange rates from the left to the right chamber and vice versa, the x-position (horizontal position) of the weir in the images is defined. Then the x-component of each position of each individual particle trajectory is evaluated, checking whether it passes this threshold position, i.e., it is checked whether the x-component of a particle starting in the left chamber has increased beyond the x-value defined as the weir position, or decreased below this value if the particle was initially in the right chamber. In over-flow as well as under-flow configuration the y-component (vertical position) of the particles is arbitrary in this step. Particles cannot penetrate the weir, so in over-flow configuration they can only pass from one chamber to the other above the weir, whereas in under-flow configuration the height of the installed weir prohibits particle transfer by passing the weir in over-

Fig. 6 Flow-chart of operations involved in image processing to obtain particle exchange rates
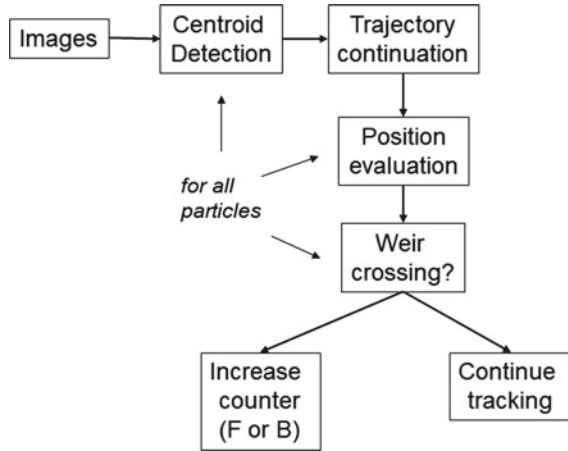
flow. Straightforward counting of passes between frames yields the number-based exchange rates.

3.2.3   Image Analysis: Polydisperse Particulate Systems

Identification of particles of different sizes is performed by an incremental approach, i.e. applying the method for monodisperse particles several times. In the first run, the sample particle used for identification is chosen such that all particle sizes are detected, yielding a total number of particles. In the second run on the same set of images as in the first, the sample size is increased such that the smallest size (1.8 mm) is no longer detected but the larger particle size (3 mm). In this step also the detection of agglomerate structures due to overlap of two or more particles is corrected. The difference in numbers of detected particles (total and 3 mm) then gives the number of 1.8 mm particles.

In each image the centroids of detected particles are tabulated and fed to the tracking algorithm. Particle centroids are tracked between frames by Voronoi matching as described in Hagemeier et al. [24] for dense particle flows. Thereby, for each identified and unambiguously tracked particle a set of positions is generated over time, forming individual particle trajectories.

3.3   Experimental Series

Particle exchange was studied for different fluidization velocities in multiples of the minimum fluidization velocity and varying mass fraction of 1.8 and 3.0 mm particles. For the mixtures, the minimum fluidization velocity is obtained using the

mean Sauter diameter of the mixture, i.e. fluidization velocities relate to multiples of the minimum fluidization velocity of the mixture. All experiments were performed at ambient temperature with non-heated fluidization gas. For under-flow experiments the weir gap height was set to 20 mm, in over-flow experiments the weir was set to height of 25 cm. In all experiments the left chamber was filled to a static bed height of 12.5 cm, the right chamber to a height of 10 cm.

In the over-flow weir scenario, both chambers were filled with particles until the static bed heights were achieved. The mass flow controller for the fluidization gas was then switched on. Following the start-up period of the mass flow controller (which can result in a small amount of particle exchange between the chambers), the high-speed recording was started and images of particle motion were taken for the next 5 s, resulting in 5000 images.

All batch experiments to study the recirculation at under-flow weirs were performed in the following way: (1) Filling both chambers of particles to a certain bed height (gap closed by a lid); (2) start of fluidization in both chambers via setting reference value for gas mass flow controller; (3) after start-up of fluidization sudden removal of lid (opening the gap) and start of image acquisition with the high-speed camera system.

An example sequence of images, showing every 500th frame, is shown in Fig. 7. These sequences form the basis for image analysis, particle tracking and the determination of the exchange rates between the chambers.

3.4 Results

The presentation and discussion of the results is structured as follows: First a measure for quantification of internal particle circulation is introduced. Then the results obtained from PTV measurements and Voronoi-tracking are presented for 1.8 mm particles at different fluidization velocities. Hereby results for under-flow weirs are compared to results obtained for over-flow weirs. Following is the presentation of results for 3 mm particles and a comparison with results for 1.8 mm particles, characterizing the influence of particle size on internal circulation. Finally, results for internal circulation for mixtures of 1.8 and 3 mm particles of different mass fractions are discussed to show the influence of bi-(poly-)disperse particles on transport at over-flow and under-flow weirs.

In order to quantify the internal recirculation R, we use the concept as introduced by Charlou et al. [28] in their study on residence time behavior in paddle dryers. They related the internal circulation as the ratio of particles moving 'backwards', B (against the dominant transport direction) to the net value of particles moving 'forwards', F:

$$R(t) = \frac{B(t)}{F(t) - B(t)} \tag{12}$$
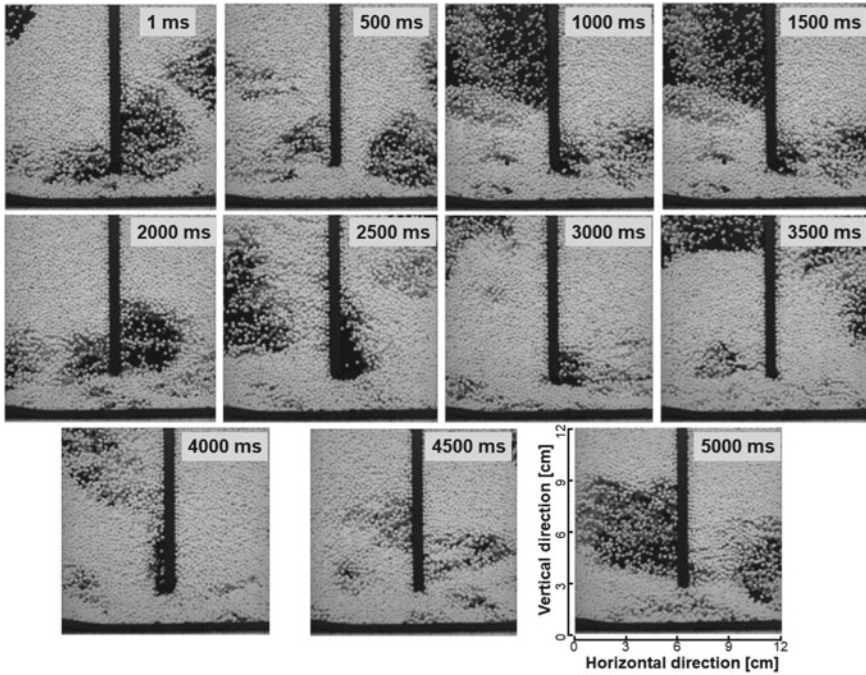
Fig. 7 Exemplary sequence of recorded high-speed images of particle transport at under-flow weir (1.8 mm particles, time resolution: 1 ms)

From the definition, R can take arbitrary values (positive and negative), signaling at each time whether more particles are moving 'forwards' or 'backwards'. For practical evaluation, however, averaging of the quantities B and F over a representative time interval provides more insight. In case of a time average of zero in the 'backwards' flow, the (averaged) value of R is zero, which in turn yields plug-flow of particles in the dominant ('forward') transport direction. Increasing values of R quantify increasing back-flow of particles, i.e. recirculation against the transport direction. If the time averages of F and B are (almost) equal, an ideally mixed system results and the absolute value of the time average of R approaches infinity.

The internal circulation R is related to the classical Bodenstein number Bo (see [29, 30]). The Bodenstein number in turn measures the axial dispersion of particles in the chamber, i.e. by determing R from particle tracking, the coefficient of axial dispersion can be obtained.

3.4.1 Internal Recirculation of 1.8 mm Particles

The time-averaged values for the internal recirculation of 1.8 mm particles at an over-flow weir are shown in Table 1. It can be observed that with increasing fluidization

Table 1 Averaged internal recirculation coefficient R_{avg} for 1.8 mm particles

u/u_{mf}	Over-flow	Under-flow
3	4.1	3.06
4	2.71	2.94
5	1.59	1.12

velocity the value of R decreases, i.e. the system tends to a plug-flow like behavior. A similar trend, although of different magnitude is also observed in the results for the under-flow configuration also presented in Table 1. Again, with increasing fluidization velocity the internal circulation decreases and the particle transport is similar to plug-flow.

In case of the over-flow configuration the result is due to the initially different bed height in the chambers, resulting in different pressure drop and the rising velocity of formed gas bubbles that propell particles over the weir. For long times an equilibration of bed heights and also transfer rates is achieved [17]. In case of the under-flow configuration, bubble formation close to the weir and rising velocity are important. If a bubble forms in one chamber close to the weir and starts to rise (as seen in Fig. 7), it creates additional drag on the particles close to the weir in both chambers, dragging significant particle numbers through the gap towards the bubble. For long process times, again, equilibration of the transport rates between the two chambers is achieved.

3.4.2 Internal Recirculation of 3 mm Particles

The obtained results of internal recirculation for beds of monodisperse 3 mm particles at over-flow and under-flow weirs are shown in Table 2. While the recirculation coefficient at the under-flow weir follows the same trend as it did for 1.8 mm particles, a reverse trend is observed in terms of the over-flow weir: With increasing fluidization velocity the internal recirculation does not decrease but increase, resulting in a system that is close to an ideally back-mixed system. This behavior can also be observed visually during the measurements with many bubbles being created on both sides of the weir, propelling large amounts of particles to the adjacent chamber, due to high momentum of the gas, and quickly driving the system to an equilibrium state of equal bed heights and transfer rates in the current set-up.

Table 2 Averaged internal recirculation coefficient R_{avg} for 3.0 mm particles

u/u_{mf}	Over-flow	Under-flow
3	2.04	66.06
4	20.72	17.32
5	30.57	5.16

Compared to 1.8 mm particles, the 3 mm particles tend to even transfer rates faster after a disturbance in the fluidization behavior, for instance due to different bed heights, for example due to feeding events in only one of the chambers, or due to bubble formation and movement inside the bed. If, however, the absolute fluidization velocities are compared, one observes that R has a similar value for both particle sizes: The ratio of the two minimum fluidization velocities $u_{mf,3.0}/u_{mf,1.8}$ is approximately 1.5. Comparing the absolute value of $u/u_{mf,3.0} = 3$ (2.43 m/s) giving an R value of 2.04 with the corresponding value of 1.8 mm (between $u/u_{mf,1.8} = 4$ and 5), the values are similar (R in [1.59, 2.71]). This means that, as long as the equilibrium has not been obtained and the fluidization conditions are equal, both particle sizes are re-circulated in the same manner. One has to note, that this does not mean that in equal times equal numbers are transported across the weir, but only that the ratio of the directed transport is equal.

3.4.3 Internal Recirculation of Bi-disperse Particle Mixtures at Over-Flow Weirs

After having studied the trends for the recirculation of mono-disperse particles at over- and under-flow weirs for different fluidization velocities, the behavior of bi-disperse particle mixtures is investigated. For this purpose, experiments with mixtures of 1.8 and 3.0 mm particles with different mass fractions were performed under otherwise the same conditions. Note that in the following u_{mf} corresponds to the minimum fluidization velocity of the mixture, calculated from the Sauter mean diameter. In most experiments, the fluidization velocity corresponds to $4 u_{mf}$; for the 50%/50%-mixture results for the overall circulation are also presented for 3 and 5 u/u_{mf}. In addition to the over-all circulation of particles at the weirs (regardless of size), also the individual recirculation of the two particle sizes is presented and discussed.

The trends of time-averaged internal recirculation R for the 50%/50%-mixture are presented in Table 3. One can observe a decrease in the value of R with increasing fluidization velocity. Comparing this trend with the two individual trends for the monodisperse material, it can be concluded that for large enough fluidization velocities the exchange behavior of the mixture is dominated by the recirculation behavior of the smaller (1.8 mm) particles.

Fixing the fluidization velocity to $4 u_{mf}$ and varying the mass fractions of 1.8 and 3.0 mm particles, the results for the over-all recirculation also shown in Table 3 are obtained: Now an increase in the value of R can be observed, i.e. the transport tends towards back-mixed flow (resp. equilibrium state). Comparing the results for the individual recirculation of the 1.8 and 3.0 mm particles, one sees that with increasing mass fraction of small particles, the recirculation of both particle sizes increases. Again, one has to note that the minimum fluidization velocity of the mixture does correspond to neither of the minimum fluidization velocities of the particles, i.e. individual particles are experiencing higher and lower velocities than four times their individual minimum fluidization velocities. This may accelerate reaching the

Table 3 Averaged internal recirculation coefficient R_{avg} of bi-disperse particle mixture at over-flow weirs

Particle sizes (mm)	Mass fractions (%)	u/u_{mf}	Over-flow
1.8 + 3.0	50:50	3	15.33
1.8 + 3.0	50:50	4	5.87
1.8 + 3.0	50:50	5	3.43
1.8 + 3.0	30:70	4	1.75
1.8 + 3.0	50:50	4	5.87
1.8 + 3.0	70:30	4	8.92
1.8[a]	30:70	4	2.68
1.8	50:50	4	6.13
1.8	70:30	4	10.19
3.0[b]	30:70	4	1.34
3.0	50:50	4	5.41
3.0	70:30	4	6.83

[a]Recirculation of 1.8 mm particles in mixture
[b]Recirculation of 3.0 mm particles in mixture

equilibrium state of the set-up with equal transfer rates, shifting the time-averaged values of R to higher values, i.e. apparently larger back-mixing.

3.4.4 Internal Recirculation of Bi-disperse Particle Mixtures at Under-Flow Weirs

Following the same approach, the particle recirculation behavior of the bi-disperse mixture was studied in the under-flow configuration. Results for the 50%/50%-mixture and different fluidization velocities are presented in Table 4, showing a decrease of the time-averaged value of R with increasing fluidization velocity, similar to the trends obtained for the monodisperse particles.

Again fixing the fluidization velocity to four times the minimum fluidization velocity (calculated with the Sauter mean diameter of the mixture) and varying the mass fractions of 1.8 mm and 3 mm particles, the results for the overall recirculation (regardless of particle size) and results for the individual particle sizes in Table 4 are obtained, respectively. Compared to the other scenarios, the trends with respect to variation of the mass ratios are not obvious. As a first approximation, the overall recirculation is almost constant with increasing mass fraction of small particles. The individual rates decrease non-uniformly with increasing mass fraction of small particles, still following the trend of the monodisperse particles. The non-uniformity has its sources in the bubble behavior (and the aforementioned force exerted on the particles, dragging them through the gap) as well as in the gap size. Compared to the over-flow case, however, the over-all values of R follow a different trend and

Table 4 Averaged internal recirculation coefficient R_{avg} of bi-disperse particle mixture at over-flow weirs

Particle sizes (mm)	Mass fractions (%)	u/u_{mf}	Under-flow
1.8 + 3.0	50:50	3	6.35
1.8 + 3.0	50:50	4	4.15
1.8 + 3.0	50:50	5	1.94
1.8 + 3.0	30:70	4	3.8
1.8 + 3.0	50:50	4	4.15
1.8 + 3.0	70:30	4	3.02
1.8[a]	30:70	4	15.17
1.8	50:50	4	4.2
1.8	70:30	4	7.75
3.0[b]	30:70	4	3.43
3.0	50:50	4	4.11
3.0	70:30	4	0.87

[a]Recirculation of 1.8 mm particles in mixture
[b]Recirculation of 3.0 mm particles in mixture

are also different in magnitude, signaling that the equilibrium state was generally not achieved in the experiment, due to the influence of the gap width on the flow behavior.

3.5 Discrete Particle Modeling

A special focus was placed on the microscopic scale of particle transport behavior between the separated chambers in horizontal fluidized beds. For this reason discrete particle modeling (DPM) was used for the characterization of the microscopic particle transport behavior. Discrete particle modeling is a very powerful tool for the investigation of flow phenomena and the particle dynamics in fluidized bed technology [31]. It can be used for the determination of the circulation frequencies and residence times in certain zones of the apparatus [32], for studying the spraying [33], mixing behavior [34–36] and for optimization of processes [37].

Coupled CFD-DEM simulations are used to characterize the particle exchange in a two-compartment system on the micro-scale. For the simulations OpenFOAM and LIGGGHTS have been used. For a detailed description of the theoretical background, the reader is referred to the work of Refs. [38, 39], while a profound review of the DPM for fluidized beds can be found in Deen et al. [31]. For the implementation of OpenFOAM, CFDEMcoupling and LIGGGHTS, Refs. [40, 41] provide comprehensive summaries.

3.5.1 Experimental Validation

Validation was performed with respect to the two-dimensional experimental fluidized bed, to adopt the setup for the numerical simulation without any assumptions or simplifications. In fact, the process conditions as well as the experimental setup and geometrical data were to be adopted for the simulation. Figure 4c shows the CAD geometry of the used setup for the numerical study. For the simulation the size of the particles was fixed to 1.8 mm.

The coupled CFD-DEM simulation was performed for 6 s for the over-flow configuration (see Fig. 4c) in order to compare the results regarding the particle transport between the individual chambers of the two-staged fluidized bed and validate the simulation by the PTV experiments. The experiments have been evaluated for 5 s of the recorded high-speed videos, while the simulations have been also evaluated for 5 s after the first second of initialization.

The snapshots in Fig. 8 show that the particle transport behavior in both, the experiment and the simulation is randomly changing from left to right and the opposite direction. The simulation and the experiment show a good agreement regarding the flow pattern of the particles within the two compartments and also the transport behavior of the particles. The quantitative exchange rate in the simulation was determined on the basis of particles crossing from one to the other chamber between two time steps (0.005 s). Similar to the PTV experiments, the horizontal trajectory of every particle that crossed the weir defined whether the particle is in the first cham-
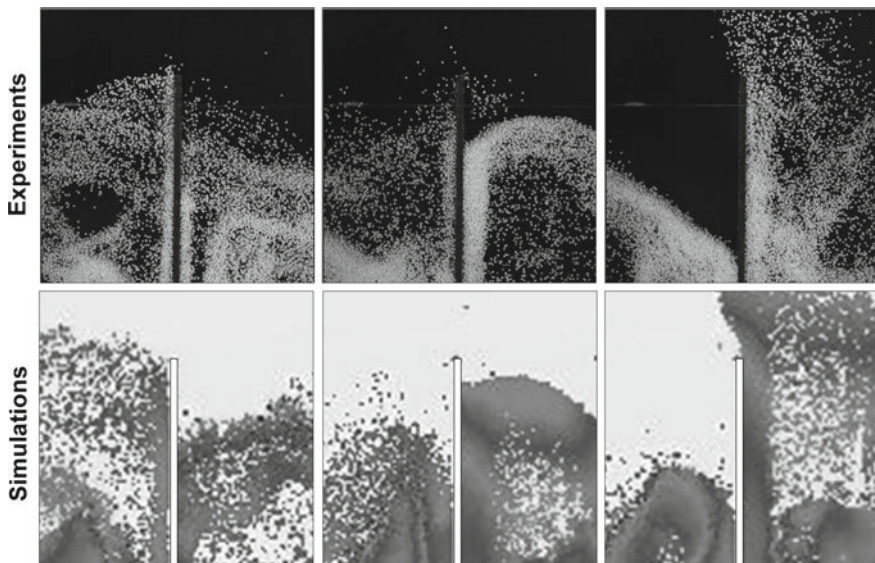

Fig. 8 Snapshots of the particle positions obtained from the experiments and the corresponding simulation at a gas inlet flow of 60 kg/h for the validation setup [42]
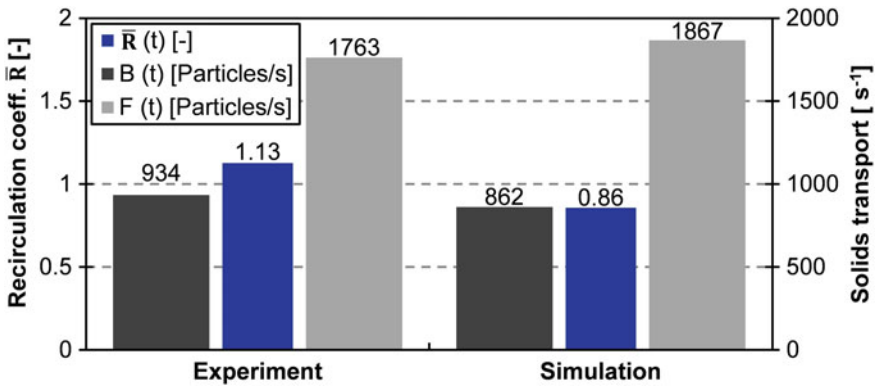
Fig. 9 Averaged particle exchange rates between the individual compartments and the average internal recirculation coefficient of the validation experiment and the simulation for a time interval of 5 s [42]

ber or the second. Consequently, the particle exchange between the two chambers was determined from one frame to the next.

The particle exchange rates and internal recirculation are evaluated using the particle identifiers provided by the simulation environment. Figure 9 shows the results of the individual averaged particle streams and the resulting average internal recirculation coefficient R (averaging over 5 s).

The results of Fig. 9 show that the amounts of exchanged particles in the experiment and the simulation are similar, while the recirculation coefficient has a slightly higher deviation, because of the sensitivity of the recirculation coefficient to small changes in both particle streams. Moreover, it cannot be guaranteed that the initial conditions of the experiment and the corresponding simulation were exactly the same. Despite these minor discrepancies, it can be concluded that the two methods show very good quantitative agreement. Thus, it could be proven that coupled CFD-DEM simulations are suitable for the evaluation of weir designs at the transition zone between two compartments.

3.5.2 Large-Scale Numerical Study of Particle Transfer

The simulation methodology was transferred to the study of the large-scale equipment at the Institute of Solids Process Engineering and Particle Technology at Hamburg University of Technology (Procell 25, Glatt Ingenieurtechnik GmbH). The geometry is shown in Fig. 10a, limited to two chambers to reduce numerical effort. The studied weir configurations and their dimensions are shown in Fig. 10b.

Continuous throughput of particles was realized within a particle generation domain, which was attached to the inlet tube of the geometry. For the continuous discharge of particles, the outlet tube was connected to a rotary valve model domain.
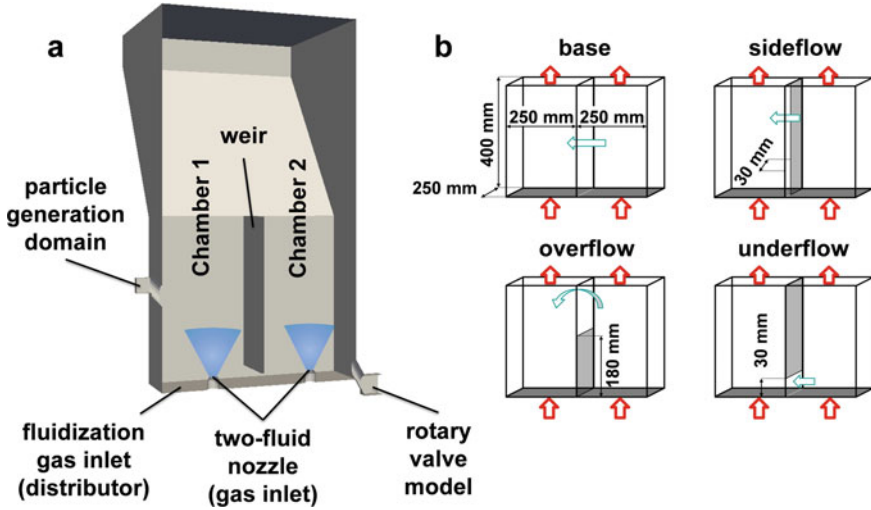
Fig. 10 **a** Scheme of the numerical setup of the two-staged horizontal fluidized bed for continuous simulations and **b** the dimensions of the two-staged systems for the different weir configurations [42] (Used with permission by Elsevier)

Table 5 Simulation conditions of the two-staged pilot plant simulations (detailed information is given by Diez et al. [42]).

CFD time step	5×10^{-5} s
DEM time step	2×10^{-6} s
Air density	1.189 kg/m^3
Air dynamic viscosity	1.82×10^{-5} Pa s
Nozzle air flow rate	21 m^3/h
Solids material	Sodium benzoate
Particle diameter	3/2 mm
Particle density	1440 kg/m^3
Initial bed mass per chamber	7.5 kg
Solids feed rate	1 kg/min
Avg. number of particles	0.74 Mio./2.6 Mio.
Fluidization rate u/u_{mf}	3.2/4.6

This model was added for keeping the hold-up mass inside the apparatus constant. The main simulation conditions and material properties are contained in Table 5. For further information on the simulation setup, see [42].

3.5.3   Large-Scale Simulation Results

Simulations were carried out for three different weir configurations and the base case for setups with 3 mm particles of mono-disperse distributions in the two-staged system. The overall goal of this study was to analyze the impact of weir designs on the microscopic transport behavior of the particles in multi-chamber systems. After an initializing time of 10 s for reaching stationary conditions regarding the supply and discharge of the solids material inside the system the evaluation procedure was started.

Results for the average internal recirculation coefficient R (averaging time interval of 60 s) for the individual setups are shown in Fig. 11.

The results in Fig. 11 show that the base (no weir) and over-flow configurations are characterized by higher particle recirculation (solids transport from the second to the first chamber), which implies more intensive axial dispersion. In contrast to this the side-flow as well as the under-flow variant show significantly lower recirculation coefficients. While in the over-flow weir design the internal recirculation decreases to about 60% of the base case, for the side-flow and under-flow a decrease to about 17% and 11%, respectively, is observed.

With regard to the weir configuration, the base (no weir) and over-flow configuration favor axial dispersion due to intense mixing between the two compartments, whereas the under-flow and side-flow weir design lead to a reduction of axial dispersion. This indicates a more directional transport for the side-flow and under-flow design. Further results are presented in Diez et al. [42], and Bachmann et al. [29] who additionally investigated the influence of gap height and particle size on particle transfer in these configurations.

Summarizing, coupled CFD-DEM simulations can be a tool for extending macroscopic particle transport approaches, like residence time experiments, by the micro-scale particle dynamics for improving solids transport models and getting
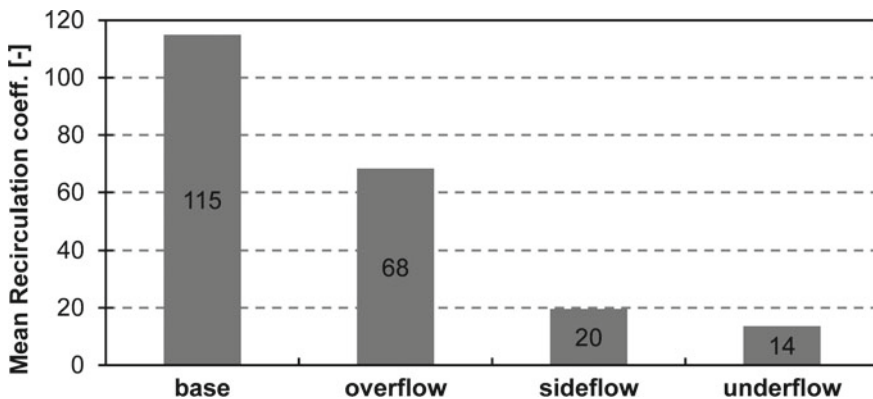

Fig. 11 Mean recirculation rates of each weir configuration with 3 mm particles (mono-disperse) and a fluidization velocity of 3 m/s for the two-compartment system [42]

comprehensive knowledge about the transport behavior of gas-solids flows, especially at high solids loading.

4 Experimental Studies on Continuous Spray Granulation in Horizontal Fluidized Beds

4.1 Experimental Setup

The experiments have been carried out in a pilot-scale horizontal fluidized bed plant (Fig. 12; ProCell 25, Glatt Ingenieurtechnik GmbH Weimar, Germany). Combined with an external pneumatic conveying and a screening-milling cycle, this process was operated continuously.

The process chamber, presented in Fig. 12a, has a length of 1 m, a width of 0.25 m and a height of about 0.40 m and can be divided into four different compartments by introducing weirs. The aim was to analyze the influence of thermal conditions on product quality. The process conditions in every stage were the same, operated with constant inlet gas velocity of 3 m/s. The solution was injected by four two-fluid nozzles in bottom-spray configuration (see Fig. 12b). Atomization was supported by compressed air. The spray solution consisted of 35 wt.-% of sodium benzoate dissolved in demineralized water. The hold-up material consisted of sodium benzoate particles in a size range of 0.5 m to 2.5 mm (undersize, product and oversize material) and an apparent density of 1440 kg/m^3.

Nuclei were exclusively produced by grinding of oversized material in a pin mill. Hence, no external feed of solid material was required in these experiments. The process was operated with a constant bed mass of 25 kg, while starting with a bed that contained 50 wt% product particles, 25 wt% oversized and 25 wt% undersized particles.

The thermal conditions of the spray granulation process can be varied, not only changing the process temperature, but also by changing the spray rate of the solution. For this reason, those two parameters, given in Table 6, have been selected as variables in the experiments.

During the experiments samples were taken from the process chamber for an offline measurement of the moisture content of the solid material and for tracking the

Table 6 Parameter variations to investigate the influence of the thermal conditions on product properties [1]

Parameter	Values		
Gas inlet temperature (°C)	100	150	200
Spray rate (kg/h)	40	80	120
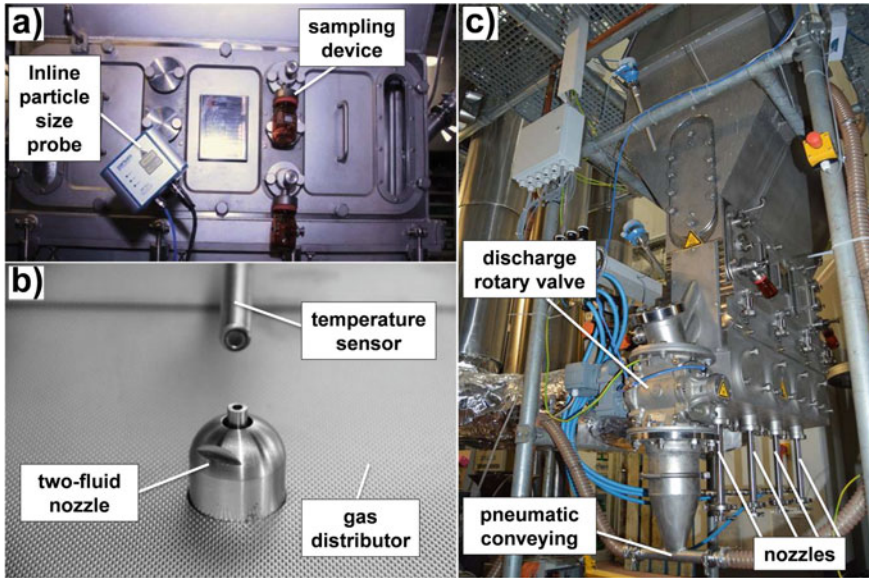
Fig. 12 Photos of **a** the sampling devices and the installed inline probe during continuous granulation, **b** an installed two-fluid-nozzle within the process chamber and **c** the used pilot plant granulator [1]

particle size distribution. Additionally, an inline probe (IPP 70-S, Parsum GmbH, Germany) for in-situ measurement of the particle size distribution was used.

The product granules were discharged by a two-deck tumbler screen in a size range of 2.00–2.24 mm. After three times the average solids residence time, steady-state was assumed. From this point onwards, samples were taken and analyzed according to the following characteristics:

- Solids moisture content
- Surface morphology and roughness
- Solids density and porosity
- Compression strength
- Wetting behavior.

4.2 Particle Characterization

4.2.1 Solids Moisture Content

The solids moisture content of the hold-up material was analyzed thermo-gravimetrically using the moisture analyzer Precisa EM-120 HR (Precisa Gravimetrics AG). For the analysis procedure a constant drying temperature of 105 °C was applied and

a switch-off criterion was used that stopped the measurement when the reduction in weight was less than 0.01 mg/s or a total measuring time of 10 min was reached. Due to the hydrophilic character of sodium benzoate the particle moisture content was determined immediately after sampling. Figure 13a shows that the particles were relatively dry in all experiments, except of two experiments. These results demonstrate that there has to be a certain boundary, at which the combination of the drying temperature and the spraying rate do not affect the moisture content of the particles anymore while reaching a certain equilibrium value which should be around 1 g/kg according to Fig. 13a. To identify this transition zone the drying potential η according to Refs. [16, 43] is used:

$$\eta = \frac{Y_{sat} - Y_{out}}{Y_{sat} - Y_{in}} \ . \tag{13}$$

The drying potential is calculated by the moisture content of the inlet gas stream Y_{in} and at the outlet Y_{out} of the process. These values were measured and recorded by installed sensors in the plant. The saturation moisture content Y_{sat} is calculated from the following equation:

$$Y_{sat} = 0.662 \cdot \frac{p_{sat}}{p - p_{sat}} \ . \tag{14}$$

The corresponding saturation vapor pressure p_{sat} is calculated according to Wagner [44]. From Fig. 13 the transition can be identified to occur at $\eta = 0.5$.
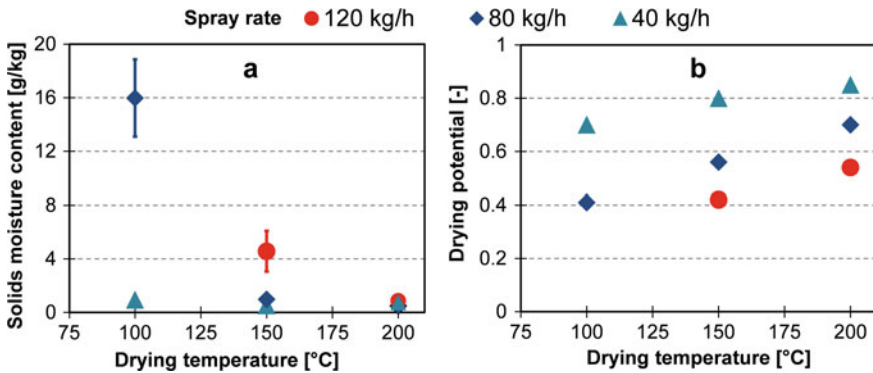
Fig. 13 **a** Solids moisture content of the material inside the process chamber and **b** calculated drying potentials of each experiment by varying the inlet temperature and the spray rate
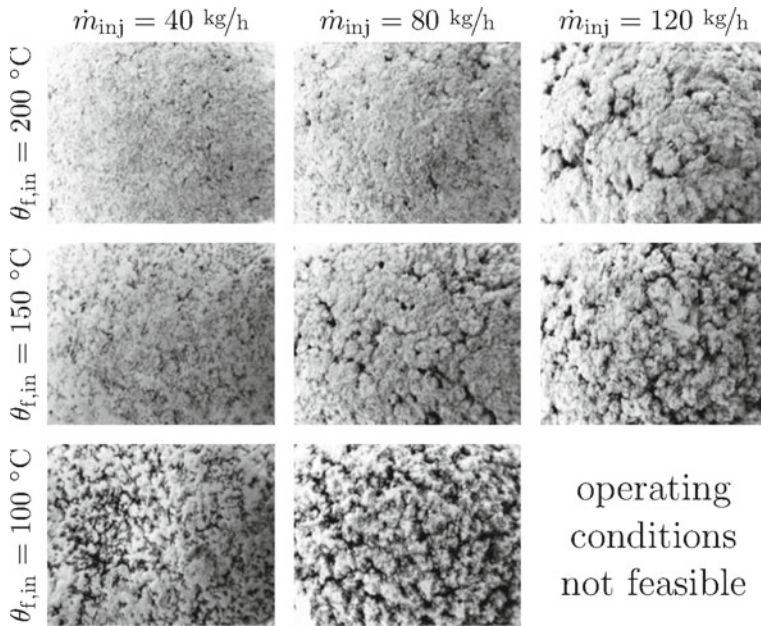
Fig. 14 SEM analysis of the product granule surfaces of each experiment [1] (with kind permission of Elsevier)

4.2.2 Surface Morphology and Roughness

For surface analysis of the product granules, a scanning electron microscope (LEO Gemini 1530, Carl Zeiss AG, Germany) was used. The results in Fig. 14 clearly show an influence of the process conditions on the morphological structure of the particles and are in line with findings of Refs. [16, 45]. The scanning electron microscope (SEM) images show that the increase in the drying temperature results in smoother surfaces, while a decrease leads to a higher surface roughness in combination with a more porous surface layer.

At the highest spray rate and lowest gas inlet temperature ($\vartheta_{drying} = 100\,°C$ and $\dot{m}_{spray} = 120\,kg/h$), the experiment could not be performed as agglomeration set in, i.e. particle clusters occured due to the formation of liquid bridges between particles.

The surface roughness was measured by focus-variation microscopy using an Alicona Infinite Focus microscope (Alicona Imaging GmbH), which provides a measurement of the 3D-surface structure, followed by an evaluation related to a surface-based roughness parameter. This surface-based evaluation included a projection area of $500 \times 500\,\mu m$ for each product granule, as shown in Fig. 15.

The roughness parameter S_{dr} belongs to the so-called hybrid topography characteristics affected by both the texture amplitude and the structural pattern [46]. It is calculated according to DIN EN ISO 25178-2 [47]:
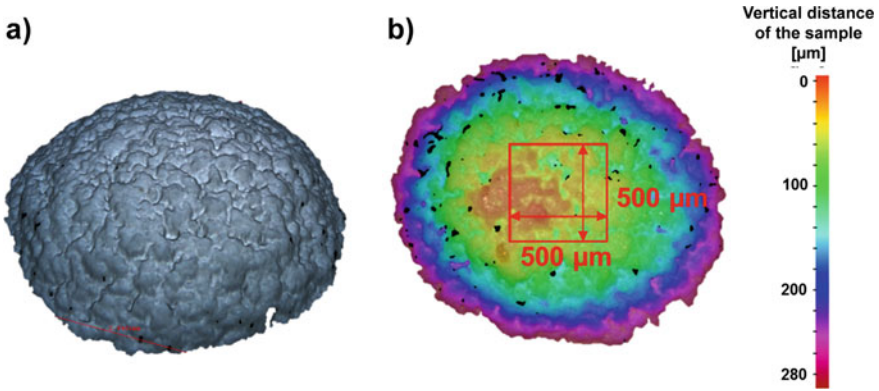
Fig. 15 Example for **a** focus-variation measurement of 3D-surface structure and **b** the height profile of the corresponding granule surface [1]

Fig. 16 Surface roughness S_{dr} of the granules according to the process conditions (drying temperature and spray rate) they are produced with
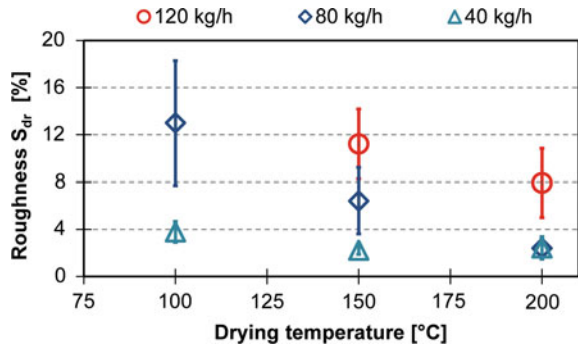
$$S_{dr} = \frac{1}{A} \left(\iint_A \left(\sqrt{(1 + \left(\frac{\partial z(x,y)}{\partial x}\right)^2 + \left(\frac{\partial z(x,y)}{\partial y}\right)^2} - 1 \right) dxdy \right) \qquad (15)$$

The results of this roughness evaluation are shown in Fig. 16. A significant increase in surface roughness is observed with increasing spray rates as well as with decreasing gas inlet temperature.

The influence of operation parameters on surface roughness was discussed in detail in Rieck et al. [16], also taking into account the crystallization behavior of the sprayed salt solution.

4.2.3 Solids Density, Porosity and Compression Strength

Thermal conditions not only influence the roughness of the granules, but also the internal structure, such as the porosity and apparent density. Moreover, these charac-

teristics are topologically related to and significantly influence other characteristics, for example the compression strength of a granule.

The apparent density of granules was measured by helium pycnometry (Multivolume Micrometrics 1305). The porosity of selected granules was measured via X-ray micro-computed tomography (CT-ALPHA, ProCon X-Ray GmbH) as described in Refs. [48, 49].

The compression strength was analyzed by single particle compression tests using a Texture Analyser TA.XT plus (Stable Micro Systems). For detailed information on the test procedure and evaluation of force-displacement curves, see [50].

Figure 17 shows results for the three characteristics. The solids density and the compression strength of the granules show an increasing trend with increasing drying potential, while the porosity reveals the opposite trend.
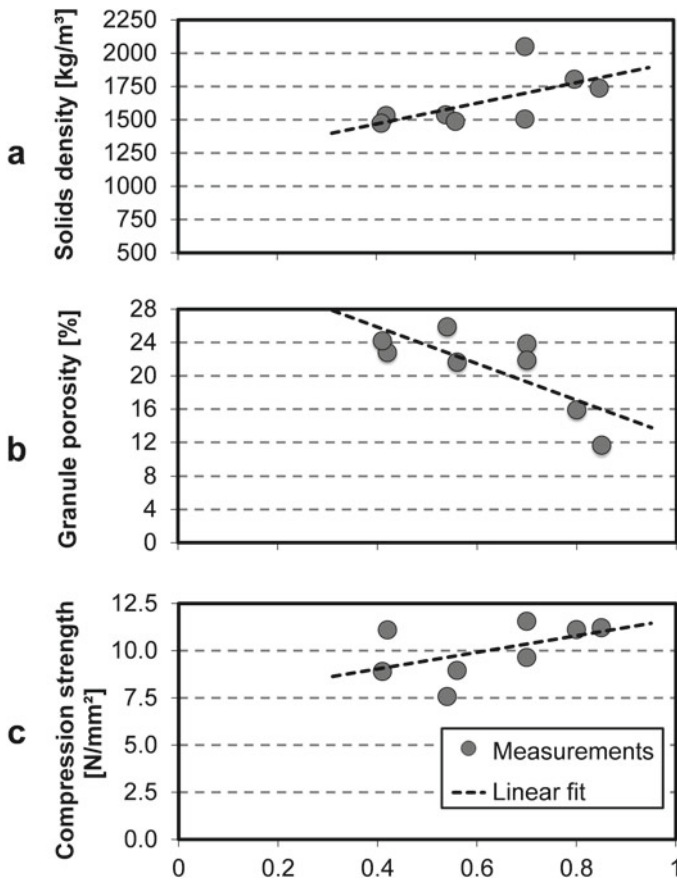
Fig. 17 **a** Average solids density, **b** granule porosity and **c** compression strength of the granules according to drying potential of the individual granulation process experiments [1] (Used with permission by Elsevier)

These trends are in line with the results from the SEM analysis and the roughness measurements. Because of the smoother and more compact surfaces of the particles with increasing drying potential, the particles are layered more compactly, resulting in higher of solids content (see Fig. 17a) due to high nucleation rates and reduced crystal growth. In consequence, the void fraction inside the granule structure decreases, resulting in a reduction of the granule porosity (see Fig. 17b). Furthermore, the reduction of voids and defects inside the granule leads to higher compression strengths (see Fig. 17c).

5 Population Balance Model Extension: Influence of Thermal Operating Conditions

Product design is one of the key disciplines in particle formulation processes, usually driven by quality-by-design principles in combination with a fundamental process understanding, focusing on key features of solids handling properties, like flowability, the dissolution behavior, the release rates or the storage stability. Furthermore granule characteristics, like the solids density, moisture content, granule surface morphology, surface roughness, compression strength and the wetting behavior play a major role for the development of tailor-made granule properties for specific uses in pharmaceutical, food and other industrial applications. The particle properties can be influenced by several process parameters, like drying temperature, liquid feed rate as well as droplet size of the atomized liquid feed. Additionally the peripheral process units and downstream processing play a distinctive role.

Figure 14 clearly shows that the morphology of the particles is changing significantly with the thermal operating conditions. In particular, the shell porosity is increasing with increasing rate of the injected liquid from the left to the right in Fig. 14. Further it is increasing with decreasing temperature of the fluidization air from the top to the bottom in Fig. 14.

Following the ideas in Refs. [1, 16], the behavior shown in Fig. 14 was modeled by correlating the shell porosity with the drying potential η.

It turns out that for the present test system the relation between shell porosity and drying potential can be described in good approximation by a linear correlation.

$$\epsilon_{shell}(\eta) = \epsilon_{shell,0} - \Delta\epsilon_{shell}\,\eta. \tag{16}$$

Other particle properties like surface roughness and compression strength can also be correlated with the drying potential as shown in the previous section. Alternatively, they can be obtained as a function of porosity and particle size distribution as suggested in Litster and Ennis [51].

Using the correlation between shell porosity and the drying potential according to Eq. (16), the population balance model presented in Sect. 2 can be extended to account for the influence of the thermal conditions on particle porosity [52]. For this,
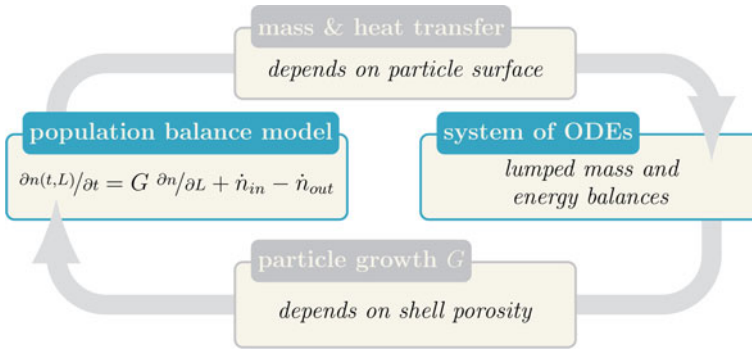
Fig. 18 Model extension to account for the influence of thermal conditions

it is assumed that all particles share the same porosity, temperature and moisture content due to the ideal mixing of the bed, but have different sizes. The particle size distribution is described by the population balance of the particle phase introduced already in Sect. 1. Therein, the growth rate has to be modified with the shell porosity as illustrated in Fig. 18 to account for the growth of porous particles. As described above the shell porosity is correlated with the drying potential which depends on the thermal conditions inside the granulation chamber. Thermal conditions are obtained from energy balances of the fluid and the particle phase, and the material balances of the solvent in the fluid, the particle phase, the dry mass of the particles and the fluidization air. Due to the assumption of ideal mixing inside the granulation chamber, these additional material and energy balances are described by ordinary differential equations. They depend on the heat and mass transfer between the particle and the fluid phase, which depends in turn on the total surface of the particle phase according to

$$A_P = \pi \int_0^\infty L^2 n(t, L) dL. \tag{17}$$

This leads to a bi-directional coupling between the population balance of the particle phase and the ordinary differential equations describing the influence of the thermal conditions as illustrated in Fig. 18. The resulting model can be used for the design and control of processes for the production of particles with tailor-made size and porosity. The latter will be discussed in Sect. 7 of this chapter.

So far, focus was on the granulation chamber. However, particle morphology affects also the milling of oversized particles in a continuous process with sieve mill cycle and has therefore also an effect on dynamic stability of this process configuration according to the experimental findings of Schmidt et al. [53], who have shown that a high inlet gas temperature leads to a stable steady state, whereas a low gas inlet temperature leads to an unstable steady state. This has been modeled qualitatively in
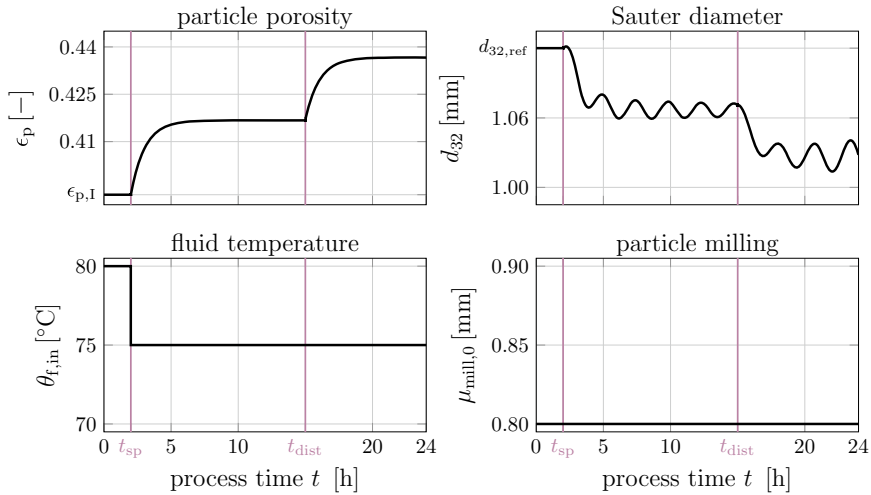
Fig. 19 Simulation scenario on the influence of thermal conditions on the stability of the fluidized bed layering granulation process with sieve-mill cycle

Neugebauer et al. [54] by correlating the mean diameter of the milled particles with shell porosity.

The resulting plant dynamics is illustrated in Fig. 19 with a simulation scenario. The simulation starts at a steady state with a constant fluidization air inlet temperature of 80 °C and a constant moisture content of the fluidization air at the inlet of 6 g/(kg dry air). The mill is operated with a constant reference value $\mu_{mill,0}$ which is only changed by some portion $\Delta\mu_{mill}(\epsilon_P)$, which depends on particle porosity ϵ_P as explained above. At time t_{sp} in Fig. 19 the inlet temperature of the fluidization air is reduced to 75 °C. This leads to an increase of particle porosity, which in turn results in finer milling. As will be discussed in the next section this affects the process stability and leads to instability in the form of self sustained oscillations of the particle size distribution, which is illustrated in Fig. 19 with the Sauter diameter d_{32}.

At time point t_{dist} in Fig. 19, the moisture content of the fluidization air at the inlet is changed from 6 to 15 g/(kg dry air). This increases the particle porosity further. As a consequence the particle size distribution is further destabilized, i.e. the amplitude of the oscillations of d_{32} is further increased.

6 Systems Theoretical Analysis

Continuously operated fluidized bed layering granulation (FBLG) processes tend to be unstable, as reported by Refs. [7, 55, 56]. A rigorous experimental investigation has been given recently by Refs. [53, 57, 58]. A model based analysis helps to further deepen the understanding of the underlying mechanisms and can be used to

predict the influence of important operational parameters on process stability using a numerical bifurcation analysis in combination with dynamic simulations. Main results are summarized in the following. For the details the reader is referred to the original publications in Refs. [11, 12, 14]. For simplicity, thermal effects are neglected in this section. The impact of thermal effects on process stability have been briefly discussed in Sect. 5 of this chapter.

In the remainder two different types of FBLG processes are considered: (i) A process with internal product classification, internal seed formation and variable bed mass, (ii) A process with external product classification, where the seeds are generated with a sieve-mill cycle and the bed mass is kept constant.

For the first type of process, focus is on top spray. Seeds are generated internally from the overspray, i.e. some small droplets which are dried before they interact with the surface of the fluidized particles. The amount of generated seeds crucially depends on the amount of the injected liquid and the bed height, Following [7], the basic model introduced in the modeling section was extended accordingly [14]. In particular, it is assumed that a part of the injected liquid is contributing to particle growth, whereas the other part leads to the formation of new seeds by overspray. The magnitude of the different fractions crucially depends on the bed height. The amount contributing to seed formation decreases linearly until the bed height reaches the nozzle height and remains constant close to zero if the bed height is larger than the nozzle height. A second important operational parameter which has large impact on process stability is the product withdrawal. The product withdrawal is characterized by the mean separation diameter L_1, which can be adjusted by means of a countercurrent air flow used for the considered internal product classification.

Main results of the theoretical analysis using the two-zone model from Neugebauer et al. [14] are summarized in Fig. 20. The right diagram shows the stability map depending on the separation diameter L_1 and the injected liquid $\dot{V}_{inj}$. Instability in the form of self-sustained oscillations of the bed height and the particle size distribution occurs in the shaded region. Along the upper limiting curve, bed height h_{bed} equals the nozzle height h_{nozzle} and is constant. Below this limiting curve a smooth onset of small amplitude oscillations is observed. Besides the upper limiting curve also a lower limit to the instability region was found. With this, the experimental findings of Schmidt et al. [57] could be explained for the first time in a consistent way. The experimental observations were reproduced qualitatively by dynamic simulation as shown in the left part of Fig. 20 with the time plots of bed hight and α, the relative size of the granulation zone which is also variable in this configuration due to the variable bed height [14]. Simulation starts at a stable steady state corresponding to point a in the stability map. After a shift of L_1 to point b the system decays to a different stable steady state. It starts oscillating after another shift of L_1 to point c within the instability region and becomes stable again after a fourth move of L_1 to point d after crossing the lower limiting curve of the instability region.

Similar patterns of behavior can be observed for the second type of process with external product classification and a sieve mill cycle. Here, bed mass is kept constant and the particles which are continuously withdrawn from the granulation chamber are classified into a product, an undersized and an oversized fraction. The oversized
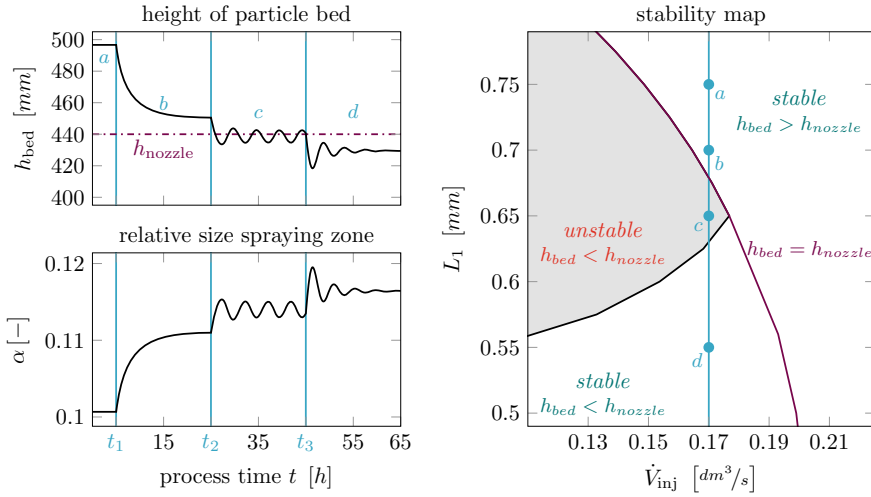
Fig. 20 Stability map and simulation scenario for FLBG with internal product classification

fraction is milled and fed back to the granulation chamber together with the under-sized fraction. On the one hand, this mode of operation is very economic due to the recycle and re-use of the off-spec particles. On the other hand it creates instability due to the positive feedback introduced by the recycle.

The influence of the most important operational parameters on process stability of this second configuration was also studied theoretically using a two-zone model [11, 12]. Results for the case, when no additional external nuclei are fed to the granulation chamber, are shown in Fig. 21. Most important parameters are now the mean diameter of the milled particles L_{mill}, the relative volume of the granulation zone α, and the time constant τ_2 characterizing the exchange rate between the granulation and the drying zone. Since the bed mass is constant, α is also constant. α and τ_2 depend on the plant design (nozzle type, size, and position and geometry of the granulation chamber) and the operating conditions [11]. It turned out that zone formation inside the granulation chamber has minor effect on process stability compared to L_{mill}. Coarse milling will result in stable steady states, whereas fine milling will lead to self sustained oscillations of the recycle flows and the particle size distribution, represented by the Sauter diameter d_{32} in Fig. 21.

The instability region shrinks, if additional nuclei are fed externally to the process chamber, which has a stabilizing effect as was already shown in Radichkov et al. [56].

The results in Fig. 21 were obtained for an ideal milling process described by a Gaussian distribution of the milled particle sizes around L_{mill}. Similar results were obtained for a more detailed model of the mill which was fitted to experimental data using a superposition of three Gaussians. However, the instability region can change its size and position in the parameter space. So that for a specific set of operating and plant parameters, oscillations are predicted by the detailed mill model
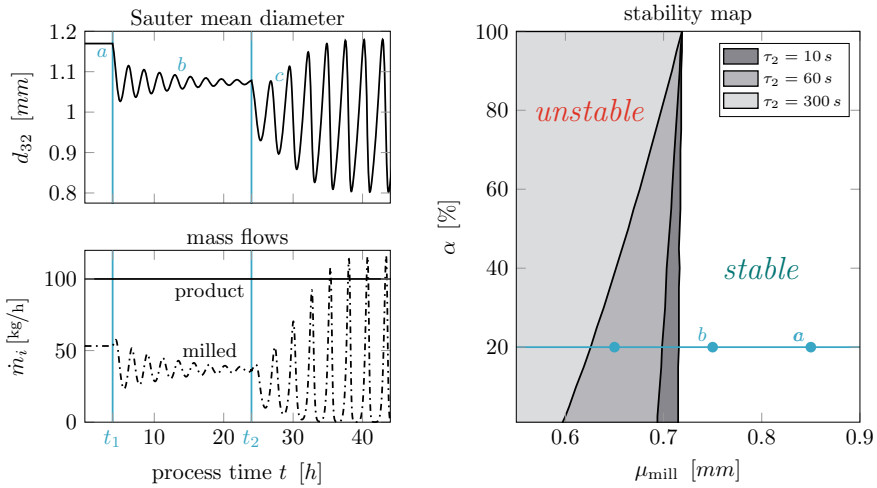
Fig. 21 Stability map and simulation scenario for $\tau_2 = 10\,s$ for FBLG with external product classification
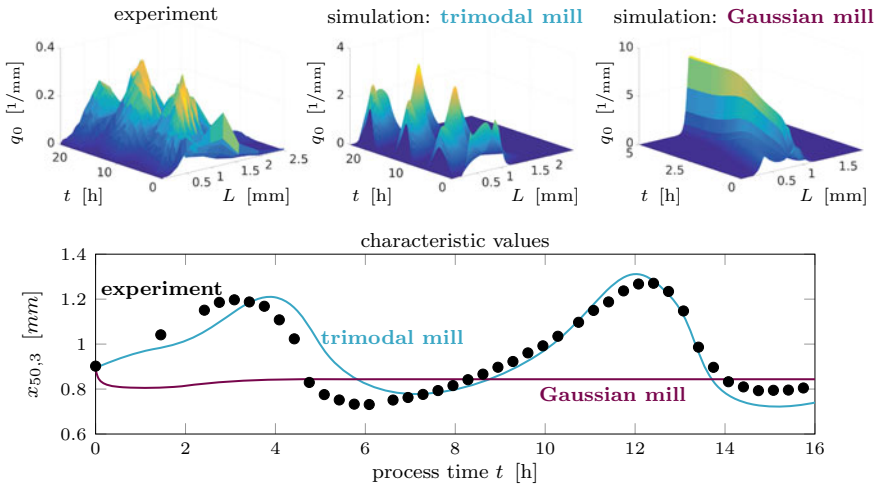
Fig. 22 Influence of mill characteristics on the stability of FBLG with external product classification

whereas the idealized mill model predicts stable steady state behavior as illustrated in Fig. 22. Hence it is concluded, that for the quantitative prediction of instability of the FBLG process with sieve-mill cycle a quantitative prediction of the milling process is essential [59].

The above results were obtained for single stage FBLG processes. An extension to multi-stage FBLG processes with sieve mill cycle is illustrated in Fig. 23. The figure gives a comparison between two different two-stage processes. In the first process half of the solution is injected in each of the two stages, whereas in the second process
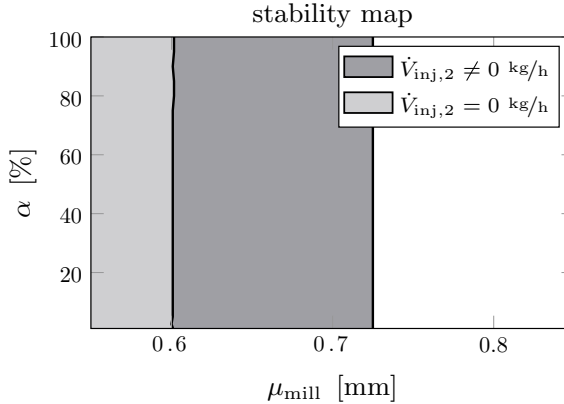
stability map

Fig. 23 Stability map for two different two stage FBLG processes with external product classification. $\dot{V}_{inj,2} = 0$—suspension injected only to the first stage, $\dot{V}_{inj,2} \neq 0$—suspension injected to the first and second stage

the whole solution is injected to the first chamber. In both cases, the injected liquid is evenly distributed on the available particle surface in the respective granulation zones contributing entirely to uniform growth. Total bed mass and total injected liquid suspension is the same in both cases and the same as in Fig. 21. In a first step, transport between the chambers is assumed to be representative. In both cases, the exchange rates between the drying and the granulation zones on each stage are assumed to be high, corresponding to a low value of τ_2. Therefore, stability in Fig. 23 does not change with α (the relative size of the granulation zones), which is consistent with the single stage process in Fig. 21 for a low value of τ_2. Further, the other operational parameters are the same as in Fig. 21. With these assumptions, the first process in Fig. 23 with injection in both stages is identical to the single stage process in Fig. 21. Instability occurs for fine milling below $L_{mill} = 0.725$ mm. In contrast to this, if the whole liquid is injected into the first chamber, instability occurs for fine milling below $L_{mill} = 0.6$ mm. Hence, the size of the shaded instability region is reduced for the second process compared to the first process. This is due to the fact, that in the second chamber of the second process no granulation is taking place but only drying. Therefore, the second chamber acts as a buffer, which dampens the oscillatory behavior and therefore has a stabilizing effect. Hence, multi-stage processes with additional drying chambers are not only useful for additional adjustment of product properties but also have a positive effect on dynamic stability when an external sieve-mill cycle is used.

7 Control of Continuous Operation

Several control concepts were developed for single and multistage FBLG processes within this project to stabilize unstable steady states, increase the reproducibility and speed up the time consuming experiments. The developed control concepts are as follows:

1. Model-free controllers using auto tuning [60]. This approach was used for direct determination of the open loop stability boundaries in closed loop operation as described in Palis et al. [61].
2. Model-based robust [62] and nonlinear control [63] of a multi-stage FBLG process.
3. Adaptive control of continuous fluidized bed spray granulation with external sieve-mill cycle [64].
4. Decentralized cascade controllers for continuous fluidized bed spray granulation with external sieve-mill cycle. Controllers were developed step by step using a detailed plant model and also validated experimentally [54, 65].

For the latter, the plant model introduced in Sect. 2 of this chapter was extended to account for the specific plant characteristics of the pilot plant in Hamburg considered in this chapter, such as

- classifying product removal from the granulation chamber,
- size dependent milling of the oversized particles,
- a variable bed mass, to test different approaches for bed mass control of the granulation chamber with the model.

For the bed mass control, the pressure difference across the fluidized bed is determined as a direct measure for the bed mass to be controlled. Manipulated variable is the rotational speed of the rotary valve at the product withdrawal from the granulation chamber. It turned out that the performance of this control loop depends crucially on the operation of the mill. The mill is used for the grinding of the oversized particles, which are fed back to the granulation chamber as new nuclei. Stable operation of the bed mass control was not possible for the standard mode of operation, where the rotational speed of the mill is kept constant. This problem could be resolved by introducing another controller to adjust the mill power instead of its rotational speed. With this, a stable bed mass control could be achieved, which is crucial for continuous operation of the plant over a prolonged period [65].

However, even for constant bed mass, oscillations of the particle size distribution and the recycle flow rate can occur as described in the previous section. Such a scenario is shown in Fig. 24 under the label open loop dynamics. Here, the particle size distribution shows a very weakly damped oscillation so that the startup of the plant takes several days, until finally a stable steady state of the particle size distribution and the Sauter diameter is obtained. For finer milling, the steady state is even unstable and will never be reached due to permanent oscillations without damping. To solve this problems and achieve not only stable bed mass but also a stable particle size distribution, a further control loop was added. Here, the Sauter diameter is determined online with a Parsum probe and the mill power is manipulated to achieve a stable given value of the Sauter diameter within short time. The model was used for the tuning and testing of this controller before it was implemented at the plant. As shown
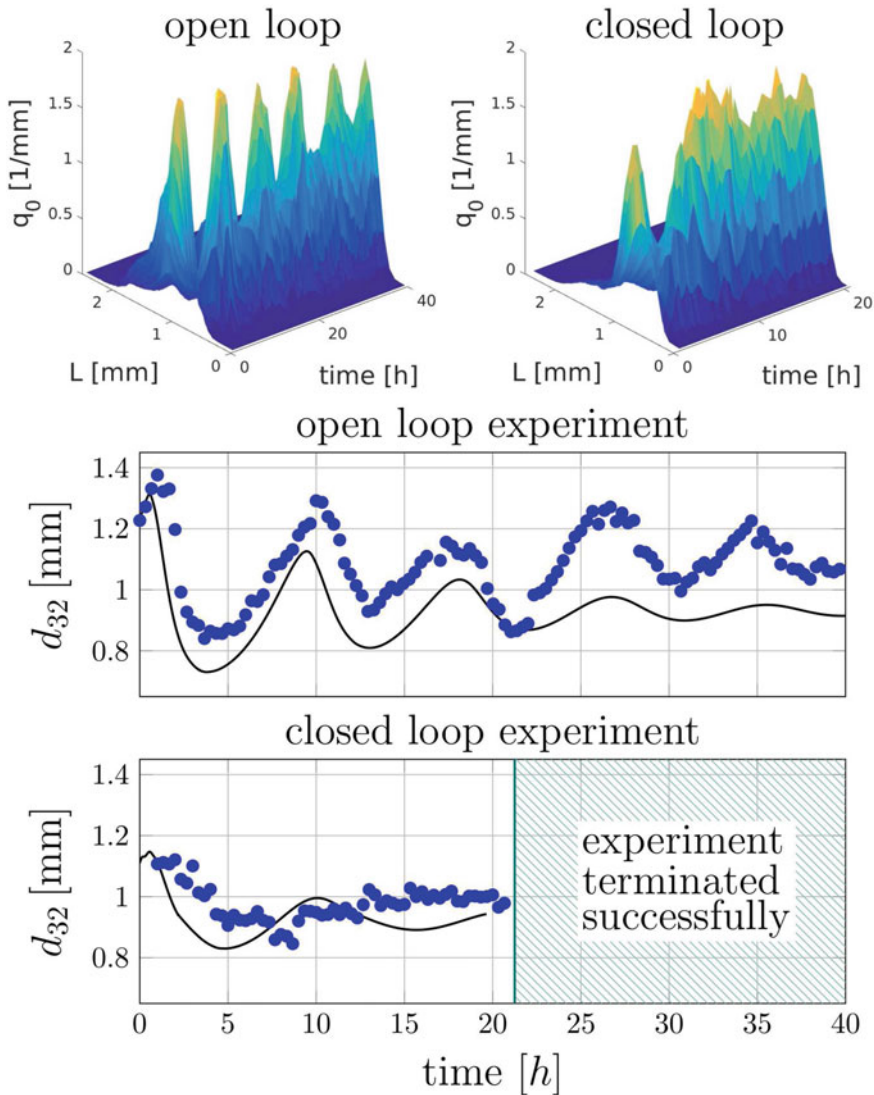
Fig. 24 Comparison of open loop and closed loop dynamics of a continuous granulation process with sieve-mill cycle during startup. Upper diagrams show the temporal evolution of the particle size distributions measured at the pilot plant in Hamburg. Lower diagrams show the corresponding time plots of the Sauter diameter d_{32}. Solid lines in the lower diagrams represent model predictions, whereas the bullets represent the experimental values. Figure taken from Ref. [54]

in Fig. 24 the controller achieved a stable steady state of the particle size distribution and the Sauter diameter within short time of less than 10 hours. Further, experimental findings agree well with the theoretical predictions.

The control algorithm for the Sauter diameter in Fig. 24 is a simple linear proportional controller. It was shown that additional integral action is destabilizing and should therefore be avoided for this process. It was shown that the simple proportional controller works very well for small disturbances. For larger disturbances, however, more advanced, model-based control concepts are required as proposed for example in Refs. [66–69].

Besides particle size, particle morphology, in particular particle porosity, is of major interest in many applications. Therefore, automatic adjustment of particle porosity by feedback control was studied in Neugebauer et al. [54]. Problem here is, that porosity cannot be controlled directly, due to a lack of available online measurement information. However, as discussed in Sect. 4, particle porosity depends directly on the drying potential which is related to the thermal conditions. The thermal conditions can be measured online easily. Therefore, the drying potential is taken as controlled variable for porosity control and the inlet temperature of the fluidization gas is taken as manipulated variable. For this control configuration a simple single loop PI controller was designed and tested using the model. For this, the plant model was extended to account for the influence of porosity on the milling of oversized particles, which is crucial for the stability of the particle size distribution.

Results taken from Neugebauer et al. [54] are shown in Fig. 25. The solid line represents a scenario where only porosity control is applied, whereas the red dashed line is for simultaneous porosity and d_{32} control. In all cases, bed mass control as described above was applied. At time t_{sp} in Fig. 25 the reference value of the particle porosity was changed from $\epsilon_{p,I}$ to $\epsilon_{p,II}$ and at time t_{dist} a step disturbance of the moisture content of the inlet gas from 6 to 15 g/kg dry air was introduced.
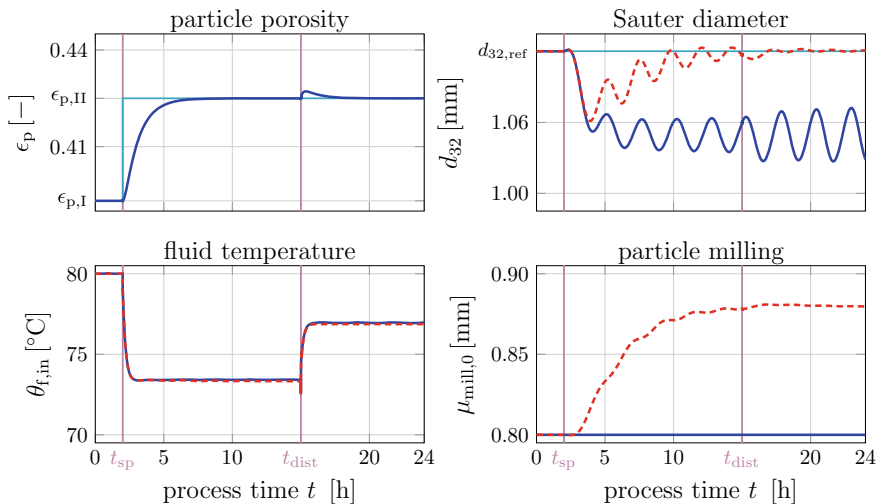
Fig. 25 Porosity control with (dashed red line) and without d_{32} control (solid line)

In both cases, the controller adjusts the porosity within a relatively short time of about 5 hours smoothly to the new reference value $\epsilon_{p,II}$ and keeps it constant. However, without the d_{32} controller, the particle size distribution represented by the Sauter diameter in the second diagram of Fig. 25 starts oscillating due to the influence of the porosity on the milling of the oversized particle. If in addition, d_{32} control was applied as described above, the Sauter diameter and the particle size distribution could also be stabilized.

8 Summary and Outlook

Within this project, new insight into the dynamics of particle formulation by spray layering in continuously operated horizontal fluidized beds has been obtained. Starting from the single-particle level, using information on the particle recirculation between functional compartments and multiple chambers by weirs, the effect of thermal conditions on layer properties, dynamic and steady-state process behavior has been illuminated. Process models were derived allowing the predictive simulation of particle properties and the dynamic and steady-state behavior. This led to the derivation of process regime maps, dividing (asymptotically) stable operating points from unstable operating points. Using this information, control concepts could be derived and tested—first in simulations and later at a full-scale industrial plant.

Combined information on micro-, meso- and macro-scale behavior, i.e. from single particles to the apparatus, and its implementation in the simulation framework "Dyssol" allows for model-driven apparatus, process and control design. This enables the inverse design of process and apparatus starting from particle property requirements, by mathematical optimization.

References

1. Diez, E., Meyer, K., Bück, A., Tsotsas, E., Heinrich, S.: Influence of process conditions on the product properties in a continuous fluidized bed spray granulation process. Chem. Eng. Res. Des. **139**, 104–115 (2018)
2. Ramkrishna, D.: Population Balances: Theory and Applications to Particulate Systems in Engineering. Academic Press, San Diego, CA (2000)
3. Bück, A., Peglow, M., Naumann, M., Tsotsas, E.: Population balance model for drying of droplets containing aggregating nanoparticles. AIChE J. **58**(11), 3318–3328 (2012)
4. Burgschweiger, J., Tsotsas, E.: Experimental investigation and modelling of continuous fluidized bed drying under steady-state and dynamic conditions. Chem. Eng. Sci. **57**(24), 5021–5038 (2002)

5. Peglow, M., Kumar, J., Heinrich, S., Warnecke, G., Tsotsas, E., Mörl, L., Wolf, B.: A generic population balance model for simultaneous agglomeration and drying in fluidized beds. Chem. Eng. Sci. **62**(1–2), 513–532 (2007)
6. Seydel, P., Blömer, J., Bertling, J.: Modeling particle formation at spray drying using population balances. Drying Technol. **24**(2), 137–146 (2006)
7. Vreman, A., van Lare, C., Hounslow, M.: A basic population balance model for fluidized bed spray granulation. Chem. Eng. Sci. **64**, 4389–4398 (2009)
8. Maronga, S.J., Wnukowski, P.: Modelling of the three-domain fluidized-bed particulate coating process. Chem. Eng. Sci. **52**(17), 2915–2925 (1997)
9. Sherony, D.F.: A model of surface renewal with application to fluid bed coating of particles. Chem. Eng. Sci. **36**(5), 845–848 (1981)
10. Wnukowski, P., Setterwall, F.: The coating of particles in a fluidized bed (residence time distribution in a system of two coupled perfect mixers). Chem. Eng. Sci. **44**(3), 493–505 (1989)
11. Bück, A., Neugebauer, C., Meyer, K., Palis, S., Diez, E., Kienle, A., Heinrich, S., Tsotsas, E.: Influence of operation parameters on process stability in continuous fluidized bed layering with external classification. Powder Technol. **300**, 37–45 (2016)
12. Dreyschultze, C., Neugebauer, C., Palis, S., Bück, A., Tsotsas, E., Heinrich, S., Kienle, A.: Influence of zone formation on stability of continuous fluidized bed spray granulation with external product classification. Particuology **23**, 1–7 (2015)
13. Hampel, N., Bück, A., Peglow, M., Tsotsas, E.: Continuous pellet coating in a Wurster fluidized bed process. Chem. Eng. Sci. **86**, 87–98 (2013)
14. Neugebauer, C., Palis, S., Bück, A., Tsotsas, E., Heinrich, S., Kienle, A.: A dynamic two zone model of continuous fluidized bed layering granulation with internal product classification. Particuology **31**, 8–14 (2017)
15. Mörl, L., Heinrich, S., Peglow, M.: Fluidized bed spray granulation. In: Granulation, Handbook of Powder Technology (Chap. 2), vol. 11, pp 21–188. Elsevier, Amsterdam (2007)
16. Rieck, C., Hoffmann, T., Bück, A., Peglow, M., Tsotsas, E.: Influence of drying conditions on layer porosity in fluidized bed spray granulation. Powder Technol. **272**, 120–131 (2015)
17. Meyer, K., Bück, A., Tsotsas, E.: Determination of particle exchange rates at over-flow weirs in horizontal fluidised beds by particle tracking velocimetry. Particuology **32**, 1–9 (2017)
18. Boucher, D., Deng, Z., Leadbeater, T., Langlois, R., Renaud, M., Waters, K.: PEPT studies of heavy particle flow within a spiral concentrator. Miner. Eng. **62**, 120–128 (2014)
19. Nilsson, L., Wimmerstedt, R.: Residence time distribution and particle dispersion in a longitudinal-flow fluidised bed. Chem. Eng. Sci. **43**, 1153–1160 (1988)
20. Satija, S., Zucker, I.: Hydrodynamics of vibro-fluidized beds. Drying Technol. **4**, 19–43 (1986)
21. de Velden, M.V., Baeyens, J., Seville, J., Fan, X.: The solids flow in the riser of a circulating fluidised bed (CFB) viewed by positron emission particle tracking (PEPT). Powder Technol. **183**, 290–296 (2008)
22. Börner, M., Peglow, M., Tsotsas, E.: Derivation of parameters for a two compartment population balance model of Wurster fluidized bed granulation. Powder Technol. **238**, 122–131 (2013)
23. Hagemeier, T., Börner, M., Bück, A., Tsotsas, E.: A comparative study on optical techniques for the estimation of granular flow velocities. Chem. Eng. Sci. **131**, 63–75 (2015a)
24. Hagemeier, T., Roloff, C., Bück, A., Tsotsas, E.: Estimation of particle dynamics in 2-D fluidized beds using particle tracking velocimetry. Particuology **22**, 39–51 (2015b)
25. Bendicks, C., Tarlet, D., Roloff, C., Bordas, R., Wunderlich, B., Michaelis, B., Thevenin, D.: Improved 3-D particle tracking velocimetry with colored particles. J. Sign. Inf. Process. **2**, 59–71 (2011)
26. Capart, H., Young, D., Zech, Y.: Voronoi imaging methods for the measurement of granular flows. Exp. Fluids **32**, 121–135 (2002)
27. You, C., Zhao, H., Cai, Y., Qi, H., Xu, X.: Experimental investigation of interparticle collision rate in particulate flow. Int. J. Multiph. Flow **30**, 1121–1138 (2004)
28. Charlou, C., Sauceau, M., Milhe, M., Arlabosse, P.: Application of Markov chains to the modeling of sludge flow in an agitated indirect continuous dryer. In: Proceedings of European Symposium on Drying (EuroDrying 2013), Paris (2013)

29. Bachmann, P., Bück, A., Tsotsas, E.: Investigation of the residence time behavior of particulate products and correlation for Bodenstein number in horizontal fluidized beds. Powder Technol. **301**, 1067–1076 (2017a)
30. Bachmann, P., Bück, A., Tsotsas, E.: Investigation of the residence time behavior of particulate products and correlation for Bodenstein number in horizontal fluidized beds with internal weirs. Powder Technol. **308**, 378–387 (2017b)
31. Deen, N., van Sint, A.M., van der Hoef, M., Kuipers, J.: Review of discrete particle modeling of fluidized beds. J. Chem. Eng. Sci. **62**, 28–44 (2007)
32. Pietsch, S., Kieckhefen, P., Heinrich, S., Müller, M., Schönherr, M., Kleine Jäger, F.: CFD-DEM modelling of circulation frequencies and residence times in a prismatic spouted bed. Chem. Eng. Res. Des. **132**, 1105–1116 (2018)
33. Kieckhefen, P., Lichtenegger, T., Pietsch, S., Pirker, S., Heinrich, S.: Simulation of spray coating in a spouted bed using recurrence CFD. Particuology **42**, 92–103 (2019)
34. Fang, M., Luo, K., Yang, S., Zhang, K., Fan, J.: Computational fluid dynamics-discrete element method investigation of solid mixing characteristics in an internally circulating fluidized bed. Ind. Eng. Chem. Res. **52**, 7556–7568 (2013)
35. Wang, S., Luo, K., Hu, C., Fan, J.: CFD-DEM study of the effect of ring baffles on system performance of a full-loop circulating fluidized bed. Chem. Eng. Sci. **196**, 130–144 (2019)
36. Yang, S., Cahyadi, A.: CFD-DEM investigation into the scaling up of spout-fluid beds via two interconnected chambers. AIChE J. **62**, 1898–1916 (2016)
37. Yang, S., Zhang, L., Sun, Y., Chew, J.: Improving the operational stability of the multi-chamber spout-fluid bed via the insertion of a submerged partition. AIChE J. **63**, 485–500 (2017)
38. Weller, H., Tabor, G., Jasak, H., Fureby, C.: A tensorial approach to computational continuum mechanics using object-oriented techniques. Comput. Phys. **12**, 620–631 (1998)
39. Zhou, Z., Kuang, S., Chu, K., Yu, A.: Discrete particle simulation of particle-fluid flow: model formulations and their applicability. J. Fluid Mech. **661**, 482–510 (2010)
40. Goniva, C., Kloss, C., Deen, N., Kuipers, J., Pirker, S.: Influence of rolling friction on single spout fluidized bed simulation. Particuology **10**, 582–591 (2012)
41. Kloss, C., Goniva, C., Hager, A., Amberger, S., Pirker, S.: Models, algorithms and validation for open source DEM and CFD-DEM. Prog. Comput. Fluid Dyn. **12**, 140–152 (2012)
42. Diez, E., Kieckhefen, P., Meyer, K., Bück, A., Tsotsas, E., Heinrich, S.: Particle dynamics in a multi-staged fluidized bed: particle transport behavior on micro-scale by discrete particle modelling. Adv. Powder Technol. **30**, 2014–2031 (2019)
43. Hoffmann, T., Rieck, C., Bück, A., Tsotsas, E.: Influence of granule porosity during fluidized bed spray granulation. Proc. Eng. **102**, 458–467 (2015)
44. Wagner, W.: New vapour pressure measurements for argon and nitrogen and a new method for establishing rational vapour pressure equations. Cryogenics **13**, 470–482 (1973)
45. Tzika, M., Alexandridou, S., Kiparissides, C.: Evaluation of the morphological and release characteristics of coated fertilizer granules produced in a Wurster fluidized bed. Powder Technol. **132**, 16–24 (2003)
46. Whitehouse, D.: Surfaces and Their Measurement, pp. 16–95. Butterworth-Heinemann, Boston (2002)
47. DIN EN ISO 25178-2 (2012) Geometrical product specifications (GPS)—Surface texture: Areal—Part 2: Terms, definitions and surface texture parameters. International Standards Organization
48. Dadkhah, M., Peglow, M., Tsotsas, E.: Characterization of the internal morphology of agglomerates produced in a spray fluidized bed by X-ray tomography. Powder Technol. **228**, 349–358 (2012)
49. Sondej, F., Bück, A., Koslowsky, K., Bachmann, P., Jacob, M., Tsotsas, E.: Investigation of coating layer morphology by micro-computed X-ray tomography. Powder Technol. **273**, 165–175 (2015)
50. Antonyuk, S., Tomas, J., Heinrich, S., Mörl, L.: Breakage behaviour of spherical granulates by compression. Chem. Eng. Sci. **60**, 4031–4044 (2005)

51. Litster, J., Ennis, B.: The Science and Engineering of Granulation Processes. Springer, New York (2004)
52. Neugebauer, C., Bück, A., Palis, S., Mielke, L., Tsotsas, E., Kienle, A.: Influence of thermal conditions on particle properties in fluidized bed layering granulation. Processes **6**(12), 235 (2018)
53. Schmidt, M., Bück, A., Tsotsas, E.: Experimental investigation of the influence of drying conditions on process stability of continuous spray fluidized bed layering granulation with external product separation. Powder Technol. **320**, 474–482 (2017)
54. Neugebauer, C., Bück, A., Kienle, A.: Control of particle size and porosity in continuous fluidized bed layering granulation processes with sieve mill cycle. Chem. Eng. Technol. **43**(5), 813–818 (2020)
55. Heinrich, S., Peglow, M., Ihlow, M., Henneberg, M., Mörl, L.: Analysis of start-up process in continuous fluidized bed spray granulation by population balance modeling. Chem. Eng. Sci. **57**, 4369–4390 (2002)
56. Radichkov, R., Müller, T., Kienle, A., Heinrich, S., Peglow, M., Mörl, L.: A numerical bifurcation analysis of fluidized bed spray granulation with external classification. Chem. Eng. Process. **45**, 826–837 (2006)
57. Schmidt, M., Bück, A., Tsotsas, E.: Experimental investigation of process stability of continuous spray fluidized bed layering granulation with internal separation. Chem. Eng. Sci. **126**, 55–66 (2015a)
58. Schmidt, M., Rieck, C., Bück, A., Tsotsas, E.: Experimental investigation of process stability of continuous spray fludized bed layering granulation with external product separation. Chem. Eng. Sci. **137**, 466–475 (2015b)
59. Neugebauer, C., Palis, S., Bück, A., Diez, E., Heinrich, S., Tsotsas, E., Kienle, A.: Influence of mill characteristics on stability of continuous layering granulation with external product classification. Comput. Aided Chem. Eng. **38**, 1275–1280 (2016)
60. Palis, S., Dreyschultze, C., Neugebauer, C., Kienle, A.: Auto-tuning control systems for improved operation of continuous fluidized bed spray granulation processes with external product classifcation. Proc. Eng. **102**, 133–141 (2015)
61. Palis, S., Dreyschultze, C., Kienle, A.: A methodology for experimental determination of stability boundaries with application to fluidized bed spray granulation. In: Computer Aided Chemical Engineering, vol. 33, pp 625–630. Elsevier, Amsterdam (2014)
62. Palis, S., Neugebauer, C., Bück, A., Heinrich, S., Tsotsas, E., Kienle, A.: Control of multi-chamber continuous fluidized bed spray granulation. In: Proceedings of PARTEC 2016: International Congress on Particle Technology: Nürnberg, Germany, April 19–21 (2016)
63. Palis, S.: Control of multi-chamber continuous fluidized bed spray granulation. In: Proceedings of the 12th IFAC Symposium on Dynamics and Control of Process Systems—DYCOPS 2019, Florianopolis/Brazil, 23-26 April, iFAC-PapersOnLine, vol. 52(1), pp. 406–411 (2019)
64. Palis, S.: Non-identifier-based adaptive control of continuous fluidized bed spray granulation with external sieve-mill cycle. J. Process Control **71**, 46–51 (2019b)
65. Neugebauer, C., Diez, E., Bück, A., Palis, S., Heinrich, S., Kienle, A.: Dynamics and control of continuous fluidized bed layering granulation with screen-mill-cycle. Powder Technol. **354**, 765–778 (2019b)
66. Bück, A., Palis, S., Tsotsas, E.: Model-based control of particle properties in fluidised bed spray granulation. Powder Technol. **270**, 575–583 (2015)
67. Palis, S., Kienle, A.: Stabilization of continuous fluidized bed spray granulation with external product classification. Chem. Eng. Sci. **70**, 200–209 (2012)
68. Palis, S., Kienle, A.: H_∞ loop shaping control for continuous fluidized bed spray granulation with internal product classification. Ind. Eng. Chem. Res. **52**, 408–420 (2013)
69. Palis, S., Kienle, A.: Discrepancy based control of particulate processes. J. Process Control **24**, 33–46 (2014)

Chapter 4
Dynamic Simulation of Technical Precipitation Processes

Hendrik Rehage and Matthias Kind

Abstract Precipitation of sparingly soluble salts is a widely applied industrial unit operation to produce color pigments or nutritional additives. Simulation of this unit operation on a flowsheet level would be a useful tool to simplify process development and optimization. However, the numerical effort of simulating the industrial standard apparatus for precipitation, the stirred-tank reactor (STR), is generally too high for process flowsheet simulation. This high computational cost is due mostly to the complex coupling of mixing and solids formation and the inhomogeneous reaction environment in STRs. Handling of this multiscale challenge in a short time scale, thus, requires the development of numerically efficient short-cut surrogate models. In this chapter, we provide an overview of the results from of our project aiming to develop a dynamic precipitation model for flowsheet simulation using the example of semi-batch precipitation of barium sulfate. This chapter covers the full development progress with step-by-step increasing complexity from steady-state to semi-batch process scale. Multiple experimental setups are used to proof the model hypotheses. The steady-state and dynamic semi-batch precipitation model are exemplarily implemented in the flowsheet framework *Dyssol*. By using these flowsheet units, the specific process dynamics of semi-batch precipitation processes is investigated. It is, furthermore, demonstrated that using dynamic process parameters (e.g. increasing impeller rotational speed) might be a suitable method to optimize the product particle size distribution (PSD) for semi-batch precipitations in the future.

Nomenclature

B	Nucleation rate [$m^{-4}s^{-1}$]
B_T	Baffles size [m]
C_T	Stirrer off-bottom clearance [m]
$\tilde{c}$	Molar concentration [$mol^1 m^{-3}$]

H. Rehage · M. Kind (✉)
Institute of Thermal Process Engineering, Karlsruhe Institute of Technology, Karlsruhe
Kaiserstraße 12, 76131, Germany
e-mail: matthias.kind@kit.edu

C	Nucleation kinetics constant [–]
$\overline{D}_{ri,sol}$	Average diffusion coefficient of reactive ions (ri) in solvent (sol) [m^{2}s^{-1}]
D_T	Impeller diameter [m]
d_{prim}	Inner feed pipe diameter [m]
E	Engulfment constant [s^{-1}]
f_{rec}	Recalculation frequency [–]
G	Growth rate [m^{1}s^{-1}]
H_T	Feed pipe off-bottom clearance [m]
J	Nucleation kinetics factor [m^{-3}s^{-1}]
K	Solubility product [mol^{2}m^{-6}]
k_B	Boltzmann constant [m^{2}kg^{1}s^{-1}K^{-1}]
L	Particle diameter [m]
$\bar{L}_{mol,ri}$	Average molecular diameter of reactive ions [m]
L_{crit}	Critical nucleation radius [m]
L_{min}	Minimal particle size of PSD grid [m]
L_{max}	Maximal particle size of PSD grid [m]
$L_{50,3}$	Median of volume-based PSD [m]
ΔL	PSD grid spacing [m]
M	Mass [kg]
$\dot{M}$	Mass flow [kg^{1}s^{-1}]
$\tilde{M}$	Molar mass [kg^{1}mol^{-1}]
m_i	Mass of particles in class i [kg]
N	Stirrer rotational speed [s^{-1}]
n	Particle number density [m^{-4}]
$n_{A/B}$	Particle number density in zone A or B [m^{-4}]
n_t	Total particle density [m^{-3}]
n_r	Refractive index [–]
Q	Volume flow [m^{3}s^{-1}]
q_0	Number-based PSD [m^{-1}]
q_3	Volume-based PSD [m^{-1}]
R	Free lattice ion ratio [–]
R_T	Radial position of feed pipe [–]
S_a	Activity-based saturation [–]
T_T	Tank diameter [m]
T	Temperature [K]
t	Process time [s]
Δt	Semi-batch model timestep [s]
$\bar{u}$	Average velocity [m^{1}s^{-1}]
$V_{mol,s}$	Molecular volume of solid [m^3]
V^L	Liquid phase volume [m^3]
V_{BF}	Bulk fluid volume [m^3]
w_i	Particle mass fraction in particle size class i [–]
x	Mass fraction [–]
x_j^L	Component mass fractions in liquid phase [–]
z	Mixer length coordinate [m]

α_{abs}	Absorption coefficient [–]
α_k	Volume fraction of zone k [–]
β	Splitting factor/recycle ratio [–]
$\gamma_{\pm}$	Activity coefficient [–]
γ_{sl}	Solid-liquid interface tension [$N^1 m^{-1}$]
δ	Dirac-delta function [m^{-1}]
$\bar{\varepsilon}$	Average energy dissipation [$m^2 s^{-3}$]
μ	Dynamic viscosity [$Pa^1 s^1$]
ν	Kinematic viscosity [$m^2 s^{-1}$]
ξ^S	Mass fraction of solid phase [–]
ξ^L	Mass fraction of liquid phase [–]
υ_s	Number of ions for solids formation [–]
$\vartheta_{m,sf}$	Stochiometric coefficients of solids formation reaction [–]
$\tilde{\rho}_s$	Molar density of solid [$kg^1 m^{-3}$]
τ_{mix}	Time scale of mixing [s]
τ_{sf}	Time scale of solids formation [s]
τ_{ct}	Computational time (real time) [s]

Indices

i	Particle size class index
j	Compound index in liquid phase (solved ions and solvent)
k	Mixing fraction index
m	Index for solved ions in liquid phase
w	Index for solvents in liquid phase
0	Index for initial value ($t = 0$)
sf	Solids formation
mix	Mixing
ri	Reactive ions
sol	Solvent
out	Outlet
mol	Molecular

Superscript Characters

L	Liquid phase
S	Solid phase
1:1	1:1 mixture of educt fluids for well-mixed condition

Abbreviations

BF	Bulk fluid
CFD	Computational fluid dynamics
CIJM	Confined impinging jet mixer
STR	Stirred-tank reactor
DLS	Dynamic light scattering
E-model	Engulfment model
MSMPR	Mixed-suspension, mixed product-removal
JICF	Jet in cross flow
PBE	Population balance equation
PFR	Plug flow reactor
PSD	Particle size distribution
SEM	Scanning electron microscopy
SLS	Static light scattering

Dimensionless Numbers

Sh	Sherwood number [–]

1 Introduction

Precipitation is an important solids formation process which is extensively applied in the chemical and pharmaceutical industry. Among the products typically produced by precipitation are active pharmaceutical ingredients, color pigments and catalyst materials. Sparingly soluble salts are a specific class of material which pose a serious challenge for industrial process development. They are often precipitated by mixing two aqueous salt solutions, each of them carrying one of the reactive ion types. Due to the low product solubility in the mixture, solid formation is triggered after mixing both educts. As the supersaturation reached for sparingly soluble salt precipitation is generally on a high level compared to other crystallization processes, the increased nucleation and growth rates cause a small time scale of solids formation τ_{sf} [s]. If $\tau_{mix}/\tau_{sf} \geq 1$ with τ_{mix} [s] designating the time scale of mixing, the latter can crucially influence the PSD of the solid product. As consecutive process steps, such as centrifugation, rely heavily on the product PSD, knowledge about the process functionality between process parameters and the PSD is required for process development.

The standard apparatus for technical precipitation is the STR in batch, semi-batch or continuous operation mode. The semi-batch operation is often the method of choice, especially for fine chemical products, as flexible production is possible here. A central drawback of the semi-batch operation, besides the process dynamics, is

the localized reaction zone. The solids formation does not take place in the full STR domain due to the low τ_{sf}. It is, instead, limited to a small volume around the feed pipe. This volume is also designated as the reaction zone. The local mixing conditions in this reaction zone have a significant impact on the final product PSD and, therefore, must be considered for simulation. It is often required to perform numerically expensive computational fluid dynamics (CFD) simulations for information about the local mixing process. This aspect is aggravated by the fact, that even while using CFD, the definition of the exact reaction volume is unclear and, thus, can often only be roughly estimated.

Flowsheet simulation simplifies process development and optimization and is widely applied in process engineering, but it requires short-cut modeling of the different unit operations involved. To date, commercial flowsheet frameworks, such as *Aspen Plus* or *gProms*, enable the steady-state and dynamic simulation of precipitation, but the underlying models are restricted to processes with only low levels of supersaturation. As they rely on the mixed-suspension, mixed-product-removal (MSMPR) concept ($\tau_{mix}/\tau_{sf} < 1$), neither different zones in the reactor nor the influence of mixing on the PSD are considered. Therefore, it has not been possible to simulate sparingly soluble salts on a process flowsheet level yet. Although numerically reduced models for semi-batch precipitation exist in literature, these models do not reach the numerical efficiency required for process flowsheet simulation. Consequently, new short-cut models must be developed to allow the process flowsheet simulation of semi-batch precipitation of sparingly soluble salts.

The aim of this project is the development of a dynamic model for precipitation which operates on time scales suitable for process flowsheet simulation. We use the knowledge gained by investigating the influence of mixing on precipitation by CFD methods [1–4] to develop a numerically efficient model for steady-state precipitation in confined impinging jet mixers (CIJMs). The latter are simple static mixing geometries in comparison to the complex dynamic STRs. The steady-state model is selectively validated by simple and complex process flowsheet simulations [5] and, furthermore, applied to investigate different mixing models from literature. The dynamic semi-batch model is developed according to the current state of the art in literature, as a considerable amount of literature exists on the modeling of mixing influenced precipitation in STRs (Fig. 1).

The models with highest computational cost fully resolve the dynamic fluid flow with CFD (a), coupled with population balance equation (PBE) approaches, to track the solids formation [6–14]. These studies, supported by experimental work [15–17], offered further insights into the complex dynamics of precipitation processes in stirred tanks. Of course, these models are numerically intense and, therefore, not suitable for process flowsheet simulation.

Zone models (b) use distinct reactor zones instead of CFD simulations to depict the fluid dynamics. Consequently, these models are much faster to calculate [8, 18–23].

Mechanistic models (c) are even further reduced. They combine a well-mixed bulk fluid (BF) with a plug flow reactor (PFR) which represents the mixing and reaction zone in the stirred tank. One of the most significant mechanistic models for semi-batch precipitation was presented by Bałdyga and Bourne [24], who used
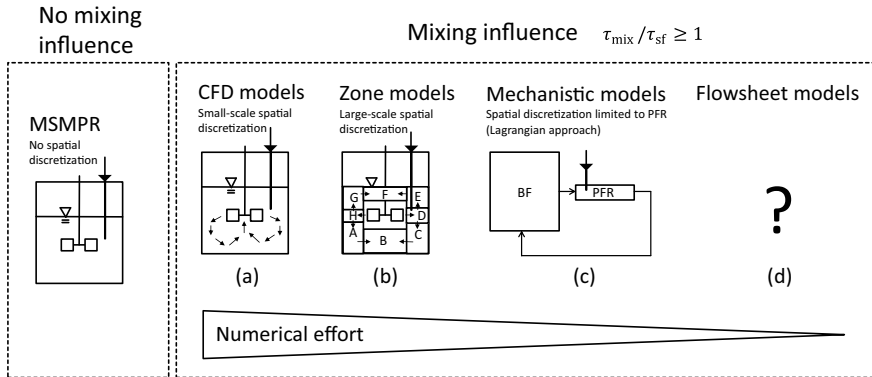
Fig. 1 Literature approaches for modeling mixing influenced precipitation in STRs. The CFD simulations resolve the full flow field **a**, zone models use discrete zones with exchange streams **b** and mechanistic models use a plug flow reactor (PFR) mixing zone **c**. To date, no models with a computational efficiency suitable for process flowsheet simulation exist **d**

the engulfment model (E-model) to simulate the influence of mixing on the product PSD. This type of model was also used by [22, 25, 26].

The mechanistic models are not as accurate as the CFD models, but they offer fast computational speed. However, as illustrated in Fig. 1, the mechanistic models in literature do not reach the time scales required for process flowsheet simulation. Nevertheless, it has been shown within this project that it is possible to further improve their numerical efficiency. We modify the mechanistic model of [24] with an additional approximation method, leading to a hybrid model design. This new approximation method increases the calculation speed by several orders of magnitude. Furthermore, we validated the equivalent concept of BF and PRF proposed by Bałdyga and Bourne [24]. Subsequently, the final semi-batch model was implemented into *Dyssol* and validated by experiments. Furthermore, we applied the model exemplarily to improve the final product PSD by using dynamic process parameters.

2 Materials and Methods

Section 2.1 introduces the model material barium sulfate, which was used for all simulations and experiments within this project. Section 2.2 deals with the different types of experiments which were conducted to validate our model assumptions. Section 2.3 presents and summarizes the most relevant model equations and the Simulation Setups investigated.

2.1 Materials

We used barium sulfate precipitation from aqueous sodium sulfate and barium chloride solution for our studies. Barium sulfate precipitation is well-investigated in literature and a typical model material for research on mixing influenced precipitation. During contact of both educt solutions, immediate reaction to solid barium sulfate according to Eq. (1) takes place.

$$BaCl_2(aq) + Na_2SO_4(aq) \rightarrow BaSO_4(s) + 2NaCl\,(aq) \tag{1}$$

The most significant process parameter for precipitation is the activity-based saturation S_a [–], as it impacts the nucleation and growth rate directly. The functionality for S_a is given in Eq. (2).

$$S_a = \gamma_\pm \sqrt{\frac{\tilde{c}_{Ba^{2+}} \cdot \tilde{c}_{SO_4^{2-}}}{K}} \tag{2}$$

K [$mol^2 m^{-6}$] designates the solubility product, $\gamma_\pm$ [–] the average activity coefficient and $\tilde{c}$ [$mol^1 m^{-3}$] the molar concentrations of the reactive ions. The real values for saturation vary greatly during the process, as the saturation buildup depends on local mixing attributes and changes due to the process dynamics. We, therefore, use the index 1:1 as a reference to a well-mixed, 1:1 volumetric mixture of both educt solutions. Therefore, $S_a^{1:1}$[–] provides a coarse estimation of the general level of saturation within the process.

In this work, we used colloidal stabilization to prevent particle aggregation, as aggregation is not part of our model yet. Colloidal stabilization was reached by an excess of barium ions using a lattice ion ratio of $R^{1:1} = \tilde{c}_{Ba^{2+}}/\tilde{c}_{SO_4^{2-}} = 5$ for all experiments and simulations. Several literature studies have confirmed that this excess of barium ions is sufficient to prevent aggregation in CIJMs [27, 28]. We, furthermore, showed in [29] that $R^{1:1} = 5$ is also a suitable value for colloidal stabilization of barium sulfate in other mixing geometries.

Our experiments and simulations were performed at a supersaturation level of $S_a^{1:1} = 1000$. By using this high level of supersaturation, the consequently low time scale of solids formation guarantees an influence of mixing on the PSD for standard process parameters for semi-batch STR and CIJM precipitation. The concentrations required to achieve $S_a^{1:1} = 1000$ and $R^{1:1} = 5$ were calculated with a Pitzer model approach. The resulting educt concentrations of $\tilde{c}_{BaCl_2,0} = 0.58$ mol/L and $\tilde{c}_{Na_2SO_4,0} = 0.144$ mol/L were used for all experiments and simulations presented in this work. The index 0 indicates $t = 0$, with t [s] as the process time. The educt solutions were prepared by solving Na_2SO_4 and $BaCl_2 \cdot 2H_2O$ (>99.99% w/w by *Carl Roth*) in deionized water.

2.2   Experiments

We conducted different types of experiments (Experimental Setups A–D) to provide a
step-by-step validation of our model. Section 2.2.1 presents the experimental setups
for validation of the steady-state model. Section 2.2.2 presents the setup for the
dynamic semi-batch experiments and the "experimental simulation" setup to allow
a specific validation of the equivalent circuit concept for semi-batch precipitation.

2.2.1   Steady State Experiments

The experimental Setup A for steady-state precipitation in CIJMs is illustrated in
Fig. 2. Two flow-controlled gear pumps P1 and P2 (*MCP-Z* by *Ismatec*) provided
the educt solution volume flows of $Q_{Na_2SO_4/BaCl_2} = 24-150$ ml/min (1:1 volumetric
mixture) for the CIJM mixer unit. The educts were prepared as described in Sect. 2.1
and filled into the educt tanks, which are temperature-controlled at $T = 20\,°C$.
Subsequently, the pumps were adjusted to the target volume flows. Samples were
taken at the CIJM outlet after several minutes and analyzed with methods described
in Sect. 2.2.3, to check for a constant PSD indicating a steady-state operation. A
technical drawing of the CIJM with indications is given in Fig. 3. More details on
this experiment are provided in [5].

The experimental Setup B extends Setup A by a recycle stream to investigate its
influence on the product PSD experimentally (Fig. 3). We used the peristaltic pump
DULCO flex by *Prominent* for P3, which was flow-controlled by a magnetic inductive
flow meter (*Optiflux* by *Krohne*). The mixer (M) and splitter (S) in Fig. 3 were realized
as three-way T ball valves (*KHTC 3/18 T* by *Landefeld*), since classifying effects were
not expected for the small particle size of the precipitate. The CIJM was constructed
according to the indications in Fig. 3. Samples were taken after the splitter to check
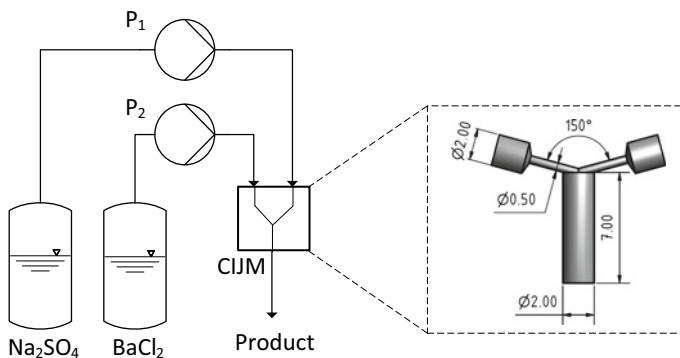

Fig. 2 Experimental Setup A with pumps (P), educt storage tanks and CIJM reactor (indications in
mm). Flow meters for P1 and P2 are neglected due to visibility reasons. Reprinted with permission
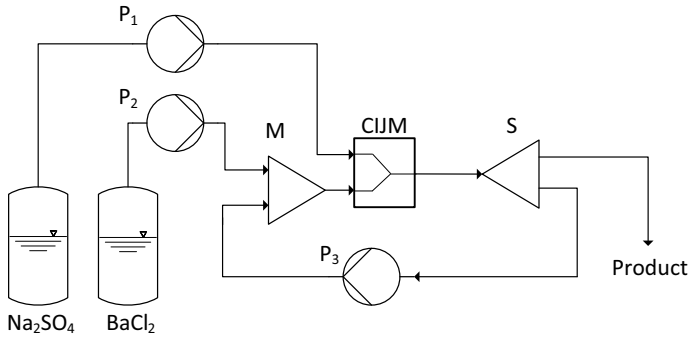from [5]

Fig. 3 Experimental Setup B to investigate the influence of recycle streams with pumps (P), mixer (M), splitter (S), and CIJM precipitation reactor. Flow meters for all pumps are neglected in the figure due to reasons of visibility. Reprinted with permission from [5]

Table 1 Educt solution composition for recycle stream simulations. Reprinted with permission from [5]

Solution	β	$\dot{M}$(g/s)	$Q\left(\text{ml}^1\,\text{min}^{-1}\right)$	$x_{H_2O}^L$	x_{Na}^L	x_{Ba}^L	x_{Cl}^L	$x_{SO_4}^L$
BaCl$_2$	0	2.62	150	0.8921	0	0.071	0.037	0
	0.1	2.24	130	0.8714	0	0.085	0.044	0
	0.2	1.68	100	0.8462	0	0.101	0.052	0
	0.3	1.28	70	0.7873	0	0.140	0.072	0
Na$_2$SO$_4$	0–0.3	2.55	150	0.9798	0.007	0	0	0.014

for a constant PSD. Setup B experiments generally reached steady-state after twelve minutes or less.

We adjusted the educt concentrations and educt volume flows according to Table 1 to investigate the impact of the recycle ratio $\beta = \dot{M}_{\text{circ}}/\dot{M}_{\text{mix},2}$ independently of changes for $S_a^{1:1}$, $R^{1:1}$ or the energy dissipation in the CIJM. $\dot{M}$ [kg^{1}s^{-1}] designates the mass flow, including liquid and solid phase, and $x_j^L = M_j^L/M^L$ are the component mass fractions in the liquid phase (L). Neither educt solution contains a solid phase. Further details on this experiment are provided in [5].

2.2.2 Dynamic Experiments

We used the plant in Fig. 4 for bulk semi-batch experiments (Type C) and two-zone experiments (Type D) to validate the equivalent circuit hypothesis for the semi-batch model. Further information on the underlying idea of this experiment is provided in Sect. 2.3.2.1. The plant consists of a 11-L tank reactor (1), a 6-L feed container (2), and an external pipe-circuit (3) with a mixing reactor (4). Only a short overview on the experimental procedure is given in this article. Further details are provided in [29].
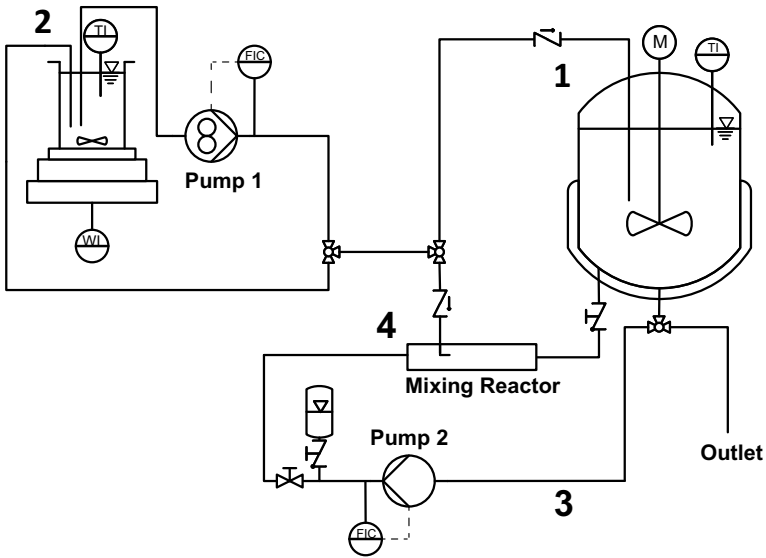
Fig. 4 Simplified process scheme of experimental Setup C and D for bulk and two-zone precipitation experiments. Reprinted with permission from [29]

A technical drawing of the tank reactor is given in Fig. 5. It was constructed according to DIN 28131 [30] with an inner tank diameter of $T_T = 240$ mm, four baffles of size $B_T = 0.1 T_T$, a six-blade Rushton Turbine of diameter $D_T = 0.35 T_T$ and an off-bottom clearance of $C_T = 0.35 T_T$. The feed pipe with inner diameter $d_{prim} = T_T/60$ was positioned at a radial distance to the stirrer axis of $R_T = 0.183 T_T$ with a feed off-bottom clearance of $H_T = 0.421 T_T$. The product sampling position is indicated by P in Fig. 5.
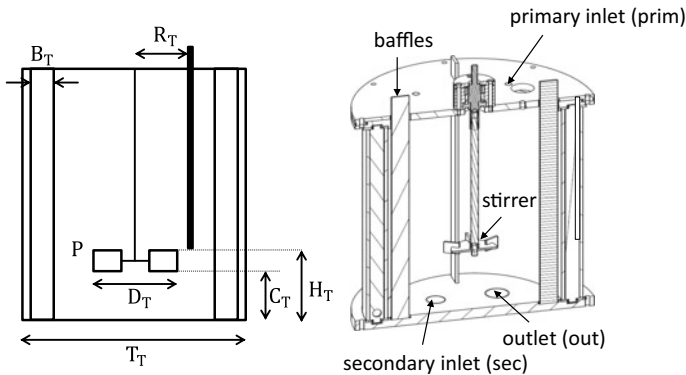
Fig. 5 Schematic (left) and technical drawing (right) of STR with four baffles and six-blade Rushton Turbine stirrer

The process plant (Figs. 4 and 5) enables two different types of experiments: Bulk and two-zone experiments.

Bulk Experiments (Experimental Setup C)

A standard semi-batch procedure is performed in bulk experiments. Therefore, the valves to the external loop (3, 4) are closed and the feed pipe is positioned in the tank reactor (1). Initially, 5.37 L $BaCl_2$ solution was poured into the tank reactor, which corresponds to 50% of final filling. The rotational velocity was adjusted to the target value. After the process started, the Na_2SO_4 solution was added through the feed pipe by using a defined feed volume flow Q_{prim} until a total addition volume of 5.37 L Na_2SO_4 solution was reached. Subsequently, probes of solid product were taken at position P in the STR.

Two-Zone Experiments (Experimental Setup D)

The feed pipe in two-zone experiments is not positioned inside the tank reactor (A). Instead, it is positioned in the external mixing reactor (C). The valves to the external loop were opened and Pump 2 was adjusted to the calculated value for the circulation flow. The stirring rotational speed was always adjusted to $N = 300$ rpm, as the stirred tank represented the well-mixed BF. At the start of the process, the Na_2SO_4 solution was added through the feed pipe into D, until a total addition volume of 5.37 L Na_2SO_4 solution was reached. Sampling was carried out at position P in the STR.

2.2.3   Analytics

The volume-based PSD $q_3(L)(m^{-1})$ for particles from steady-state experiments was measured by dynamic light scattering (DLS) using a *Zetasizer Nano ZS* by *Malvern*. Additionally, scanning electron microscopy (SEM) was used as a second measurement technique to calculate the number-based PSD $q_0(L)(m^{-1})$. Probes for SEM analysis were centrifuged three times at 11,000 rpm, including two intermediate washing steps with deionized water. Subsequently, the product was dried for 24 h at 50 °C in a drying cabinet and sputtered with 3.5 nm platin for the investigation in a *LEO 1530 SEM*. Diameters of 500 particles at different locations were determined by graphical evaluation to calculate the $q_0(L)$ distribution.

The particle sizes for dynamic semi-batch experiments exceeded the measurement range of DLS, as the mixing intensity in the STR is several orders lower than the one reached in CIJMs. Therefore, we measured the particle size for these experiments by static light scattering (SLS) using *Mastersizer 3000* or *3000E* by *Malvern*. Measurements were carried out in deionized water using a *Hydro EV* wet dispersion system by *Malvern*. Samples were measured with a laser occlusion of 10%, a refractive index of $n_r = 1.643$ and an absorption coefficient of $\alpha_{abs} = 0.1$.

2.3   Simulation

Section 2.2.1 introduces the model for steady-state precipitation. Section 2.2.2 presents the dynamic semi-batch model.

2.3.1   Steady-State Precipitation Model

The model equations are given in Sect. 2.3.1.1. The mixing model is presented in Sect. 2.3.1.2. Section 2.3.1.3 provides information about the Simulation Setups. All sections only represent the most important equations and information. Consultation of [5] is recommended for a more detailed view of the steady-state precipitation model.

Model Equations

During steady-state precipitation, both educt solution A and B with educt volume flows Q_A and Q_B are mixed along the mixer length coordinate z [m]. An exemplarily illustration for the balance volume in CIJMs and the spatial discretization is given in Fig. 6.

   The process of turbulent mixing is complex, as eddies of multiple size scales are involved in the mixing process. However, several mechanistic models have been developed to account for the mixing process in a simplified way. In our project, we used the micro mixing model proposed by Metzger and Kind [4]. Mechanistic mixing models divide the liquid phase into different zones (index k) with volume
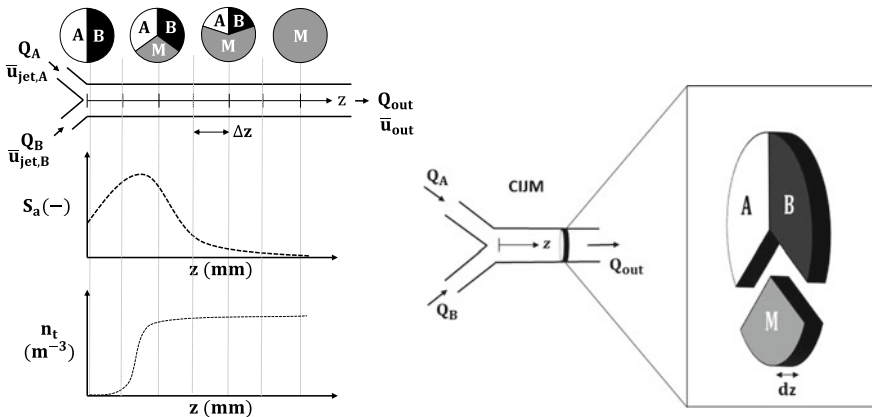

Fig. 6 Spatial discretization of the CIJM geometry with typical supersaturation S_a and total particle density n_t (left). Balance volume for steady-state precipitation, shown exemplarily with two educt environments (A, B) and one mixed environment (M) (right). Reprinted with permission from [5]

V_k^L [m^3] to track the status of mixing ($\alpha_k = V_k^L/V^L$). V^L [m^3] designates the total volume of liquid phase including all zones. Due to the mixing process, these volume fractions α_k change along the mixer length coordinate z. The balance volume is the well-mixed reaction volume fraction (M in this example), which will grow along the mixer length coordinate z by engulfing the unmixed educt fluid A and B.

The PBE is based on the particle density $n = dn_t/dL$ [m^{-4}] in the reaction zone M, with n_t [m^{-3}] as the total number of particles per volume suspension and L [m] as the particle diameter. As the rising saturation level S_a inside the reaction zone will trigger solids formation, a rising total particle number density can be observed along z (Fig. 6).

The PBE in Eq. (3) is used to calculate n along the z coordinate of the mixer. B [m^{-4}s^{-1}] designates the nucleation rate and $G = dL/dt$[m^{1}s^{-1}] the particle growth rate, $\bar{u}_{out}$[m^{1}s^{-1}] the average velocity at the mixer outlet. $n_{A/B}$[m^{-4}] are the particle densities in the educt mixing zones A and B, which are only relevant if the educt solutions already contain particles. The last two terms in Eq. (3) are exemplarily adapted to the mixing model by Metzger and Kind [4]. These terms must be changed if other mixing models are investigated.

$$\frac{dn}{dz} + n \cdot \frac{d\ln(\alpha_M)}{dz} = \frac{1}{\bar{u}_{out}}\left(B - \frac{d(Gn)}{dL}\right) - \frac{n_A}{\alpha_M}\frac{d\alpha_A}{dz} - \frac{n_B}{\alpha_M}\frac{d\alpha_B}{dz} \qquad (3)$$

The semi-empirical Eq. (4), considering homogenous and heterogenous nucleation, is used in the model to calculate the nucleation rate. $J_{max,hom/het}$ [m^{-3}s^{-1}] and $C_{hom/het}$ [–] are material specific constants. The dirac-delta function $\delta(L_{crit})$ [m^{-1}] is used to include the nuclei at the critical nucleation radius L_{crit} [m].

$$B = \delta(L_{crit}) \cdot \left(J_{max,hom} \cdot e^{-C_{hom}\cdot\ln(S_a)^{-2}} + J_{max,het} \cdot e^{-C_{het}\cdot\ln(S_a)^{-2}}\right) \qquad (4)$$

The size of the thermodynamically stable nuclei L_{crit} depends on the supersaturation and is calculated by Eq. (5) following the classical nucleation theory. The solid-liquid interface tension γ_{sl} [N^{1}m^{-1}], the molecular volume of the solid $V_{mol,s}$ [m^3], the Boltzmann constant k_B [m^{2}kg^{1}s^{-2}K^{-1}], the number of ions ν_s [–] and the system temperature T [K] are the relevant variables.

$$L_{crit} = \frac{4 \cdot \gamma_{sl} \cdot V_{mol,s}}{\nu_s \cdot k_B \cdot T \cdot \ln(S_a)} \qquad (5)$$

A size-dependent growth rate was implemented by Eq. (6), proposing a diffusion-limited growth mechanism. $\bar{D}_{ri,sol}$[m^{2}s^{-1}] designates the average diffusion coefficient of the reactive ions (ri) in the solvent (sol), $\tilde{\rho}_s$ [mol^{1}m^{-3}] designates the molar density of the solid and Sh the Sherwood number. Due to the small particle size, $Sh = 2.0$ was assumed for all simulations.

$$G = Sh \cdot \frac{2\bar{D}_{ri,sol}}{L \cdot \tilde{\rho}_s} \cdot \sqrt{K} \cdot (S_a - 1) \qquad (6)$$

$\bar{D}_{\mathrm{ri,sol}}$ is calculated by Stokes-Einstein Eq. (7). μ [kg^{1}m^{-1}s^{-1}] designates the dynamic viscosity of the solvent and $\bar{L}_{\mathrm{mol,ri}}$ [m] the average molecular diameter of the reactive ions.

$$\bar{D}_{\mathrm{ri,sol}} = \frac{k_{\mathrm{B}}T}{3\pi\mu\bar{L}_{\mathrm{mol,ri}}} \tag{7}$$

The solution composition changes along z, as ions are mixed into the reaction zone and depleted by solids formation. Consequently, the concentration balance for all ionic components in the liquid phase (index m) is given in Eq. (8). The last two terms in Eq. (8) are exemplarily adapted to the mixing model by [4]. These terms must be changed if other mixing models are investigated. Differences between the densities of the mixing environments are neglected for Eq. (8).

$$\frac{d\tilde{c}_m}{dz} + \tilde{c}_m \cdot \frac{d\ln(\alpha_{\mathrm{M}})}{dz} = \frac{d\tilde{c}_{m,\mathrm{sf}}}{dz} - \frac{\tilde{c}_{m,\mathrm{A}}}{\alpha_{\mathrm{M}}}\frac{d\alpha_{\mathrm{A}}}{dz} - \frac{\tilde{c}_{m,\mathrm{B}}}{\alpha_{\mathrm{M}}}\frac{d\alpha_{\mathrm{B}}}{dz} \tag{8}$$

The solid formation reduces the ion concentration according to Eq. (9), with $\vartheta_{m,\mathrm{sf}}$ [−] as stochiometric coefficient of ion type m in the solids formation reaction. Spherical particles are assumed with $dV_p/dL = \pi L^2/2$. V_p designates the volume of a single particle. $\vartheta_{m,\mathrm{sf}}$ obtains a negative value for educts of the solid formation reaction. If ions are not part of the solids formation reaction, $\vartheta_{m,\mathrm{sf}} = 0$.

$$\frac{dc_{m,\mathrm{sf}}}{dz} = \frac{\pi}{2}\frac{\vartheta_{m,\mathrm{sf}} \cdot \tilde{\rho}_{\mathrm{s}}}{\bar{u}_{\mathrm{out}}} \cdot \int_L n(L)G(L)L^2 dL \tag{9}$$

The saturation S_{a} is not directly calculated by the model. Instead, the model is connected to the software *PhreeqC* to calculate the activity coefficients. Further details on this software connection or additional equations for the steady-state model (e.g. for μ) can be found in [5].

We used a high-resolution finite-volume scheme with a van Leer flux limiter to solve the PBE. More information on the solver and its control is provided in [5]. The material constants for barium sulfate can be found in [5].

Mixing Model

We investigated different mixing models for CIJMs to find the most promising candidate for process flowsheet simulation. We applied the micro-mixing model by Metzger and Kind [4] for most of the steady-state simulations conducted within this project. The model consists of three mixing zones, two educt zones (A, B) and one well-mixed reaction zone (Fig. 7). The model by Metzger and Kind [4] is predictive
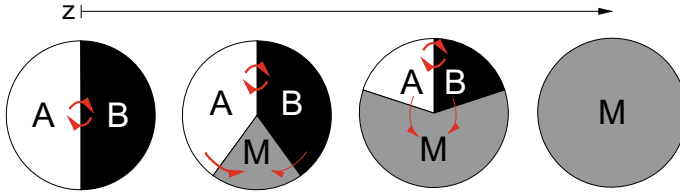
Fig. 7 Temporal mixing volume fractions evolution for the model by [4]

Fig. 8 Simulation flowsheet for steady-state model validation (Setup A). Reprinted with permission from [5]

for the given setup but does not follow the physical concept of the engulfment theory directly. Consequently, it is more an empirically based than a physically based model.

The temporal evolution of the volume fractions is given by Eqs. (10–12). $E = 0.058\,\bar{\varepsilon}^{0.5}\nu^{-0.5}$ [s^{-1}] designates the engulfment constant. $\bar{\varepsilon}$[m^{2}s^{-3}] is the average energy dissipation and ν [m^{2}s^{-1}] the kinematic viscosity.

$$\frac{d\alpha_A}{dz} = -\frac{E}{\bar{u}_{out}} \cdot \alpha_A \cdot (1 - \alpha_A) \tag{10}$$

$$\frac{d\alpha_B}{dz} = -\frac{E}{\bar{u}_{out}} \cdot \alpha_B \cdot (1 - \alpha_B) \tag{11}$$

$$\frac{d\alpha_M}{dz} = \frac{E}{\bar{u}_{out}} (\alpha_A \cdot (1 - \alpha_A) + \alpha_B \cdot (1 - \alpha_B)) \tag{12}$$

Simulation Setups

This section introduces the steady-state Simulation Setups. Flowsheet Simulation Setup A (Fig. 8) was designed according to Experimental Setup A and represents a stand-alone simulation of CIJM precipitation. The input concentrations of the educt solutions were defined according to the educt concentrations presented in Sect. 2.1 and the input volume flows were varied according to the experiments described in Sect. 2.2.1. Further details of Setup A simulations are given in [5].

The recirculation flowsheet (Simulation Setup B, Fig. 9) was constructed according to the Experimental Setup B (Fig. 3, Sect. 2.2.1). We used the units for ideal mixing/ideal splitting implemented in *Dyssol* [31] for Splitter and Mixer. Further details regarding the simulations and the *Dyssol* solver configurations can be
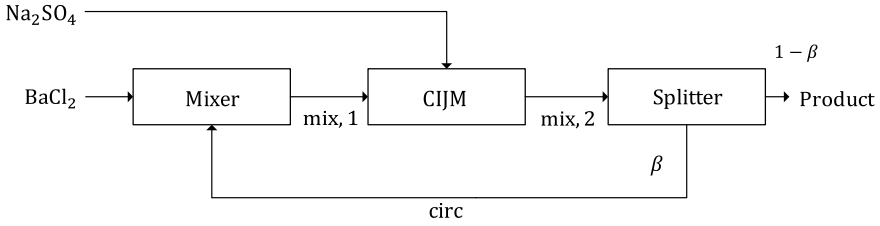
Fig. 9 Simulation flowsheet for investigating the influence of the recycle stream on the precipitation process. Reprinted with permission from [5]

found in [5]. The process conditions for the simulations with different recycle ratios $\beta = \dot{M}_{circ}/\dot{M}_{mix,2}$ were chosen according to Table 1.

2.3.2 Dynamic Semi-Batch Precipitation Model

Section 2.3.2.1 provides an overview of the model equations. The mixing model is explained in Sect. 2.3.2.2. Section 2.3.2.3 presents the newly developed approximation method, which is the reason for the outstanding numerical performance of the model. Section 2.3.2.4 provides information regarding the Simulation Setups.

Model Equations

The semi-batch model is based on the mechanistic model proposed by [24], who divided the semi-batch STR in a PFR connected to well-mixed stirred bulk fluid (BF). We could prove experimentally in [29] that this assumption can be used to model the semi-batch process. The relevant process parameters are the feed mass flow $\dot{M}_{prim}$, the outlet mass flow $\dot{M}_{out}$, the secondary inlet mass flow $\dot{M}_{sec}$ and the impeller rotational speed N. All of these process parameters can be either steady-state or dynamic. The semi-batch process itself will be dynamic in any case.

Figure 10 illustrates the main variables of the model. The BF's mass M_{BF} consists of a liquid (L) and a solid phase (S) with the mass fractions $\xi_{BF}^S = M_{BF}^S/M_{BF}$ and $\xi_{BF}^L = M_{BF}^L/M_{BF}$. Without the presence of other phases, ξ_{BF}^L can be calculated by the closure $\xi_{BF}^L = 1 - \xi_{BF}^S$. The mass fractions of the components in the liquid phase are defined by $x_{j,BF}^L = M_{j,BF}^L/M_{BF}^L$ with j as the index for all components in the liquid phase. The relative mass of the particles in each size class is defined by $w_i^S = m_i^S/M_{BF}^S$.

The system state vector of the BF is given by $\vec{B}(t) = \left(M_{BF} \; \xi_{BF}^S \; x_{j,BF}^L \; w_{i,BF}^S \right)^T$. With five components ($j = 5$) in the liquid phase (e.g. H_2O, Ba, Na, Cl, SO_4) and 150 particle size classes ($i = 150$), $\vec{B}(t)$ consists of 157 entries. No particles are considered in the feed stream $\dot{M}_{prim}$ ($\xi_{prim}^S = 0 w_{i,prim}^S = 0$). Furthermore, we assume
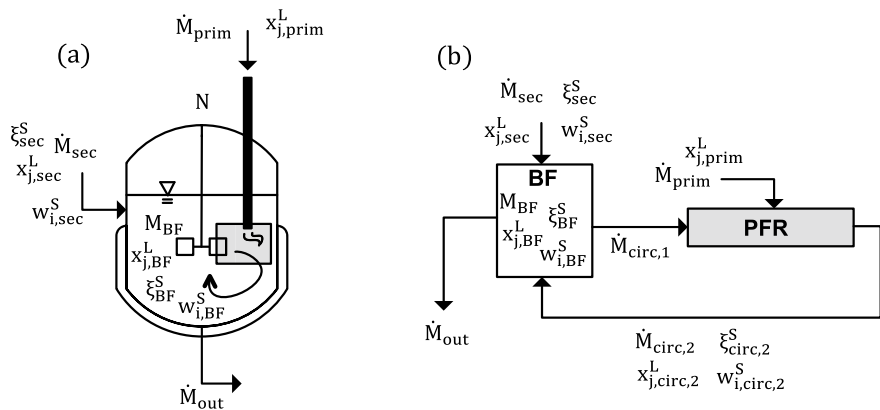
Fig. 10 Process variables for the semi-batch process **a** and the equivalent circuit of PFR and BF **b**

the presence of only one solvent. The BF volume V_{BF} is assumed to correspond to the volume of pure solvent ($V_{BF} = x_{H_2O,BF} M_{BF}^L / \rho_{H_2O}$).

The streams, which are interconnecting BF and PFR are $\vec{S}_{circ,1}$ (entering the PFR) and $\vec{S}_{circ,2}$ (leaving the PFR). The stream vector $\vec{S}$ is defined by $\vec{S} = (\dot{M}\,\xi^S\,x_j^L\,w_i^S)^T$. Corresponding to the BF, the variables for the stream vector are defined by $\xi_{circ,1}^S = \dot{M}_{circ,1}^S / \dot{M}_{circ,1}$, $\xi_{circ,1}^L = \dot{M}_{circ,1}^L / \dot{M}_{circ,1}$, $x_{j,circ,1}^L = \dot{M}_{j,circ,1}^L / \dot{M}_{circ,1}$ and $w_i^S = \dot{m}_i^S / \dot{M}_{circ,1}^S$.

The balance equations for the BF can be derived with the variables given. M_{BF} will change due to the incoming and outgoing streams, according to Eq. (13).

$$\frac{dM_{BF}}{dt} = \dot{M}_{sec} + \dot{M}_{circ,2} - \dot{M}_{out} - \dot{M}_{circ,1} \tag{13}$$

The temporal evolution of the solids phase fraction is described by Eq. (14). No source term for solids formation must be considered for the BF balance equation, as solids formation only takes place in the PFR.

$$\frac{d\xi_{BF}^S}{dt} + \xi_{BF}^S \frac{d\ln(M_{BF})}{dt}$$
$$= \frac{1}{M_{BF}} \cdot \left(\dot{M}_{sec}\,\xi_{sec}^S + \dot{M}_{circ,2}\,\xi_{circ,2}^S - \left(\dot{M}_{out} + \dot{M}_{circ,1} \right) \xi_{BF}^S \right) \tag{14}$$

The component balances are given by Eq. (15).

$$\frac{dx_{j,BF}^L}{dt} + x_{j,BF}^L \frac{d\ln\left(\xi_{BF}^L\right)}{dt} + x_{j,BF}^L \frac{d\ln(M_{BF})}{dt}$$
$$= \frac{1}{M_{BF}\,\xi_{BF}^L} \cdot \left(\dot{M}_{sec}\,\xi_{sec}^L\,x_{j,sec}^L + \dot{M}_{circ,2}\,\xi_{circ,2}^L\,x_{j,circ,2}^L \right)$$

$$-\left(\dot{M}_{\text{out}} + \dot{M}_{\text{circ},1}\right) \xi_{\text{BF}}^{\text{L}} x_{j,\text{BF}}^{\text{L}}\right) \tag{15}$$

Nucleation or growth are not relevant for the BF, as both take place only in the PFR. Consequently, the particle mass fractions for the BF can be calculated by Eq. (16).

$$\frac{dw_{i,\text{BF}}^{\text{S}}}{dt} + w_{i,\text{BF}}^{\text{S}} \cdot \frac{d\ln\left(x_{\text{BF}}^{\text{S}}\right)}{dt} + w_{i,\text{BF}}^{\text{S}} \cdot \frac{d\ln(M_{\text{BF}})}{dt}$$
$$= \frac{1}{M_{\text{BF}} \, x_{\text{BF}}^{\text{S}}} \cdot \left(\dot{M}_{\text{sec}} \, \xi_{\text{sec}}^{\text{S}} \, w_{i,\text{sec}}^{\text{S}} + \dot{M}_{\text{circ},2} \, \xi_{\text{circ},2}^{\text{S}} \, w_{i,\text{circ},2}^{\text{S}} \right.$$
$$\left. - \left(\dot{M}_{\text{out}} + \dot{M}_{\text{circ},1}\right) \xi_{\text{BF}}^{\text{S}} \, w_{i,\text{BF}}^{\text{S}}\right) \tag{16}$$

The unknown variables of this model are the circulation mass flow rate $\dot{M}_{\text{circ},1}$ and the vector $\vec{S}_{\text{circ},2}$ representing the fluid after precipitation in the PFR. A closure for $\dot{M}_{\text{circ},1}$ based on the stirrer type and size was developed by using the conceptual idea of the similarity between the local reaction zone in a stirred tank with Rushton Turbine and a JICF precipitation. Calculation of $\vec{S}_{\text{circ},2}$ is explained in Sect. 2.3.2.3. Explicit Euler's method is used to solve Eqs. (13–16) with a static time discretization $\Delta t = 0.5$. This value for Δt is appropriate for the Simulation Setups C and E.

Mixing Models

The semi-batch model uses the steady-state model presented in Sect. 2.3.1 to calculate the PFR. The mixing model for CIJMs was replaced by a mixing model for the jet in cross flow (JICF) mixing of the feed volume flow and the circulation flow. As shown in [29], a JICF mixer can be used to imitate the local flow environment around the feed pipe in STRs. The reaction zone is, therefore, defined as Q_{prim} (P), which engulfs $Q_{\text{circ},1}$ (C) over the mixer length coordinate z. A possible influence of meso mixing must be additionally considered, as the fluid must be meso mixed first to start micro mixing. Consequently, zone C_{meso} is introduced for the fluid of $Q_{\text{circ},1}$ which is already meso mixed and therefore, can act as an engulfment environment for P (Fig. 11).
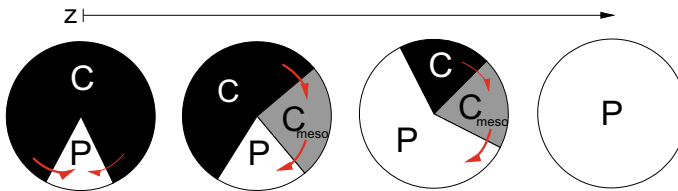

Fig. 11 Fluid prim (P) engulfing fluid circ, 1 (C) in the E-model by [24]. C_{meso} designates the fluid which is already meso mixed and, thus, provides the environment for the engulfment process of P

We used the E-model by [24] considering micro and meso mixing to depict the evolution of P over z. The timescale for meso mixing was calculated with $\tau_{\mathrm{meso}} = 1.2\, d_{\mathrm{prim}}^{2/3}\, \bar{\varepsilon}^{-1/3}$ according to [32].iterations on a flowsheet

$$\frac{d\alpha_{\mathrm{P}}}{dz} = \frac{E}{\bar{u}_{\mathrm{circ},2}}\alpha_{\mathrm{P}}\left(1 - \frac{\alpha_{\mathrm{P}}}{\alpha_{\mathrm{u}}}\right) \tag{17}$$

$$\alpha_{\mathrm{u}} = \frac{\alpha_{\mathrm{P0}}}{\alpha_{\mathrm{P0}} + (1 - \alpha_{\mathrm{P0}}) \cdot \exp(z/(\tau_{\mathrm{meso}}\bar{u}_{\mathrm{mix}}))} \tag{18}$$

The mixing model requires an average energy dissipation $\bar{\varepsilon}$, which was correlated by steady-state experiments.

Replacing the mixing model in the steady-state model also required adaptation of the PBE and the component balances. For precipitation in the PFR, P is the balance volume instead of M. Equation (3) and Eq. (8) were, therefore, replaced by Eq. (19) and Eq. (20), respectively.

$$\frac{dn}{dz} + n \cdot \frac{d\ln(\alpha_{\mathrm{P}})}{dz} = \frac{1}{\bar{u}_{\mathrm{circ},2}}\left(B - \frac{d(Gn)}{dL}\right) - \frac{1}{\alpha_{\mathrm{P}}}\frac{d\left(n_{\mathrm{C_{meso}}}\alpha_{\mathrm{C_{meso}}}\right)}{dz} - \frac{n_{\mathrm{C}}}{\alpha_{\mathrm{P}}}\frac{d\alpha_{\mathrm{C}}}{dz} \tag{19}$$

$$\frac{d\tilde{c}_m}{dz} + c_m \cdot \frac{d\ln(\alpha_{\mathrm{P}})}{dz} = \frac{d\tilde{c}_{m,\mathrm{sf}}}{dz} - \frac{1}{\alpha_{\mathrm{P}}}\frac{d\left(\tilde{c}_{m,\mathrm{C_{meso}}}\alpha_{\mathrm{C_{meso}}}\right)}{dz} - \frac{\tilde{c}_{m,\mathrm{C}}}{\alpha_{\mathrm{P}}}\frac{d\alpha_{\mathrm{C}}}{dz} \tag{20}$$

Approximation Method

The reason for the outstanding numerical performance in our semi-batch model in comparison to mechanistic models in literature is the approximation method which we developed within this project. This method takes advantage of the fact that the PFR is a steady-state system and, therefore, will only show a different output signal if its input signals, $\vec{S}_{\mathrm{circ},1}$ and $\vec{S}_{\mathrm{prim}}$, deviate significantly compared to the prior iteration. In a typical mechanistic model from literature, the PFR consumes 99.7% of computational time, whereas the BF model only requires 0.3% (measured in our example case). The BF model can be calculated much faster than the PFR, since the coupling between mixing, nucleation and growth does not have to be solved in the BF. Consequently, the PFR calculation is the bottleneck of mechanistic models. Improvements which simplify or skip the PFR calculation can, thus, increase numerical efficiency by several orders of magnitude.

The approximation method is illustrated in Fig. 12. n designates the iteration index. The vector $\vec{S}_{\mathrm{circ},2}$ can either be gained by solving the PFR (high numerical effort) or approximating its result by a component balance. We assume for this additional balance that the saturation in $\vec{S}_{\mathrm{circ},2}$ is fully depleted to thermodynamic equilibrium. For the example of barium sulfate (two reactive ions, $\vartheta_{\mathrm{Ba}} = \vartheta_{\mathrm{SO}_4} = 1$), the resulting ion concentrations in $\vec{S}_{\mathrm{circ},2}$ can be calculated by Eq. (21).
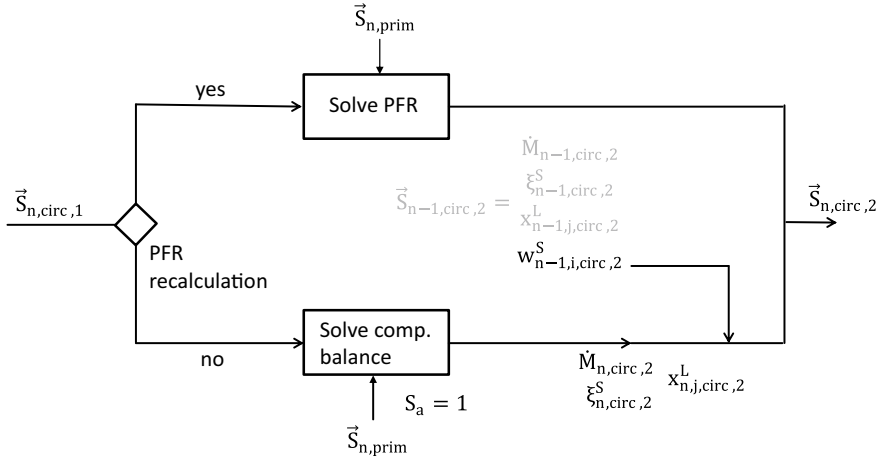
Fig. 12 Approximation method for the short-cut modeling of the semi-batch process dynamics

$$\tilde{c}_{\mathrm{Ba,circ},2} = 0.5 \cdot \left(\tilde{c}_{\mathrm{Ba,circ},1} - \tilde{c}_{\mathrm{SO_4,circ},1}\right) + \sqrt{0.25\left(\tilde{c}_{\mathrm{Ba,circ},1} - \tilde{c}_{\mathrm{SO_4,circ},1}\right)^2 + K} \quad (21)$$

$\dot{M}_{n,\mathrm{circ},2}$, $\xi^{\mathrm{S}}_{n,\mathrm{circ},2}$ $x^{\mathrm{L}}_{n,j,\mathrm{circ},2}$ can, thus, be calculated by simple balance equations without solving the PFR. Only the PSD is not calculated. It is, instead, approximated by using the PSD from the last iteration ($w^{\mathrm{S}}_{i,\mathrm{circ},2} = w^{\mathrm{S}}_{i-1,\mathrm{circ},2}$). The approximation method, thus, introduces an error on the PSD but increases computational speed by several orders of magnitude.

The recalculation frequency $f_{\mathrm{rec}} = n_{\mathrm{rec}}/n_{\mathrm{it}}$ is the number of recalculations of the PFR divided by the number of iterations. The approximation method is not active for $f_{\mathrm{rec}} = 1$ as the PFR is calculated on each iteration. The value $f_{\mathrm{rec}} = 1/10$ means that after one calculation, the approximation method is applied for the next nine iteration steps.

Simulation Setups

Two different Simulation Setups were investigated for the semi-batch precipitation model (Fig. 13). Simulation Setup C was designed according to Experimental Setup C. All simulation parameters were adapted to the experimental STR with the six-blade Rushton turbine stirrer. We conducted simulations for $N = 50 - 200$ rpm and $Q_{\mathrm{prim}} = 0.1 - 0.4\,\mathrm{L}^1\mathrm{min}^{-1}$ according to the experiments. The results from Setup C simulations, therefore, allow one to validate the semi-batch model.

Furthermore, Simulation Setup E was designed to demonstrate on the example of a dynamic stirring rate that there is currently unused potential to influence the process dynamics. We use a linearly increasing stirring rate to influence the process

Fig. 13 Simulation Setups: constant feed rate and constant stirring rate for validation (C) and dynamic increase of the stirring rate (E)
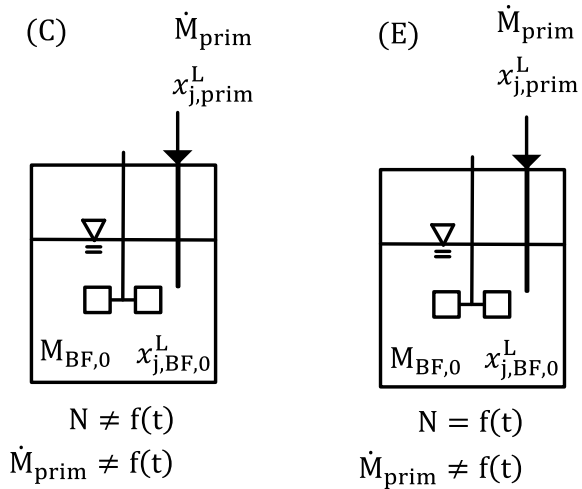
Fig. 14 Linear increase of the rotational speed versus time (Setup E)
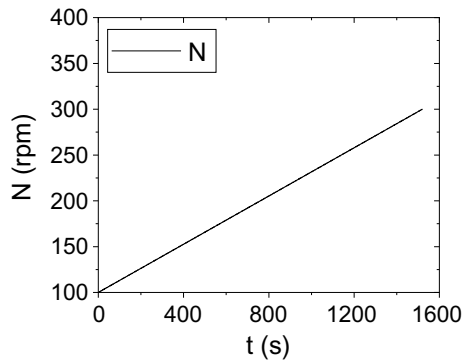
dynamics of the semi-batch process (Fig. 14). The feed volume flow is kept constant at $Q_{prim} = 0.2\,L^1 min^{-1}$.

3   Results and Discussion

This section presents selected results from steady-state and dynamic experiments and simulations. The results of the steady-state simulation are compared to the corresponding validation experiments in Sect. 3.1. Furthermore, the model is applied to investigate the influence of recycle streams on the product PSD. Section 3.2 deals with the results from "experimental simulation" to verify whether an equivalent circuit of PFR and well-mixed BF can be used to simulate a semi-batch STR. Section 3.3

compares the dynamic semi-batch simulation to experimental data and, furthermore, investigates the influence of dynamic process parameters on the product PSD.

3.1 Steady-State Precipitation

The experiments and simulations of Setup A aim at validating our steady-state model for CIJM precipitation and investigating its predictiveness towards the PSD. In addition to the micro mixing model by Metzger and Kind [4], two other models by [24, 33] are compared, which are not explicitly discussed in Sect. 2.3.1.2.

As shown in Fig. 15, the median of the volume-based PSD ($L_{50,3}$) for precipitated particles in Setup A experiments can be well-predicted with a steady-state precipitation model using the micro mixing model by Metzger and Kind [4]. Interestingly, the model by Bałdyga and Bourne [24] predicts larger particles compared to the other mixing models. We could furthermore show by mathematical analysis that the models by Metzger and Kind [4] and Schwarzer [33] do not implement the engulfment theory correctly. Both models proved to be suitable for our simulations but should be designated as empirical models.

We, furthermore, investigated the influence of recycle streams on steady-state precipitation by Setup B experiments and simulations. As observable in Fig. 16, the PSD becomes increasingly multimodal with increasing splitting factor β. This multimodality is caused mostly by recycled particles passing the CIJM more often and, therefore, growing more than particles passing the CIJM only once. Furthermore, the size of the smallest particles in the first peak, which are the particles after a single precipitation in the CIJM, is also increased for $\beta \geq 0.1$ in a nonlinear way (Fig. 16).

Fig. 15 Median of volume-based PSD ($L_{50,3}$) versus jet velocity with for simulations with different micro mixing models by [24, 33, 4] and experiments. Particle size measured by DLS
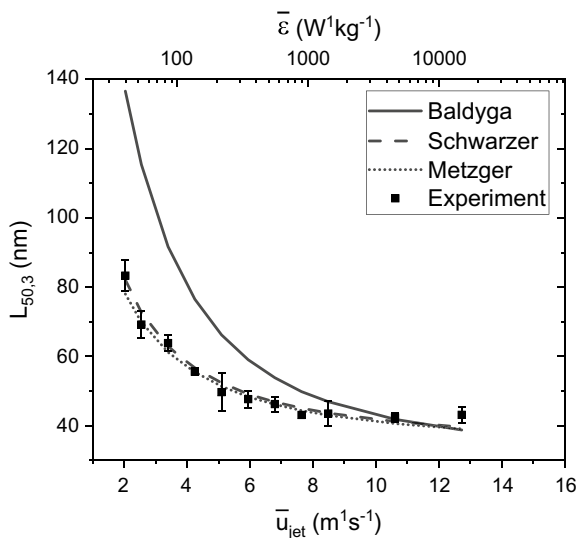
Fig. 16 Simulated influence of the splitting factor β on the number-based PSD (q_0) of the product stream for ideal mixing in the CIJM. Reprinted with permission from [5]
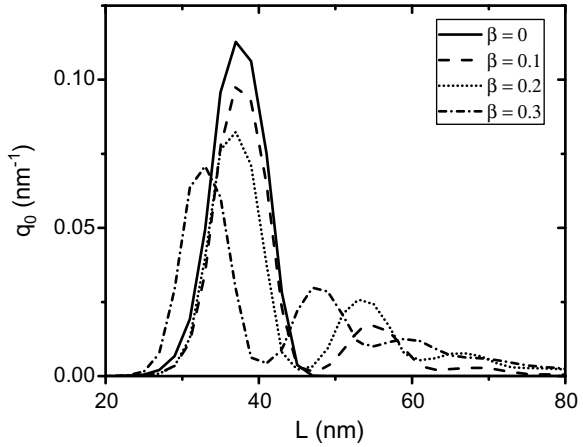
The nonlinear system behavior for increased values of the splitting factor β is also observable for the saturation curve along the z-axis (Fig. 17). Whereas the saturation does not significantly differentiate for $\beta \leq 0.2$, major changes can be observed for $\beta = 0.3$. As we could show in [5], the reason for this faster supersaturation depletion is the faster depletion of reactive ions, which becomes relevant when larger particles are present.

The particles show, independently of the value chosen for the splitting factor β, no differences in morphology, see Fig. 18.

Nevertheless, the number distribution based on the particles counted (see Sect. 2.2.3) reveals a similar size shift effect comparable to the simulation. The differences between the PSD (q_0) for a splitting factor of $\beta = 0$ and of $\beta = 0.2$ are shown exemplarily in Fig. 19.

Fig. 17 Saturation S_a over the CIJM z-axis in flowsheet B for different splitting factors β for ideal mixing in the CIJM. Reprinted with permission from [5]
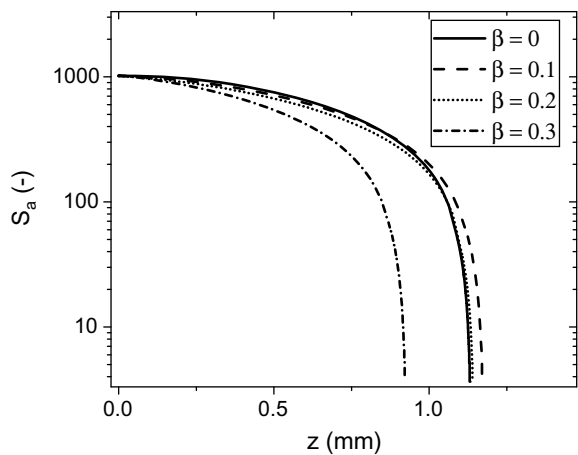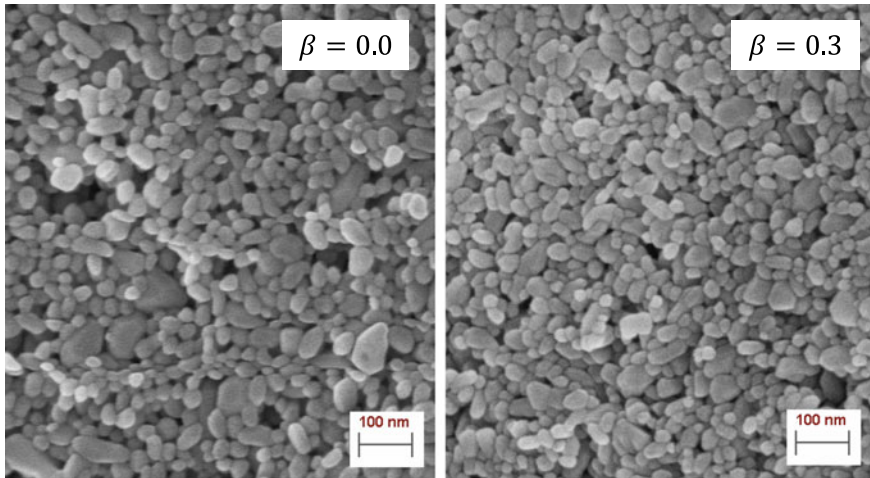
Fig. 18 REM pictures of barium sulfate precipitated for splitting factors $\beta = 0$ (left) and $\beta = 0.3$ (right). Reprinted with permission from [5]

Fig. 19 Experimental SEM results for splitting factors $\beta = 0.0$ and $\beta = 0.2$. Reprinted with permission from [5]
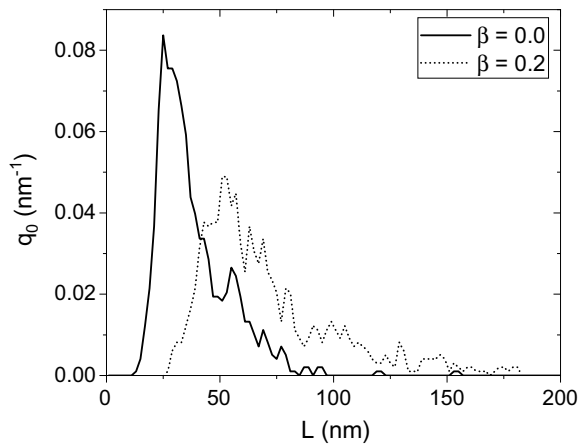
The experimental results analyzed with SLS in comparison to simulation results are given in Fig. 20. As observable, the model can predict the average particle size correctly even for a complex flowsheet including a recycle stream. The simulation with a splitting factor of $\beta = 0.3$ ($\bar{u}_{\text{jet}} = 12.7 \text{m}^1\text{s}^{-1}$) required 26 iterations on a flowsheet level with a total computational time requirement of $\tau_{\text{ct}} = 5.6$ s (ct—computational time) in *Dyssol* on one core of an *Intel Core i7-7700* 3.60 GHz processor. Consequently, even for complex flowsheets, the steady-state model combines reasonable accuracy with a high numerical efficiency.

Fig. 20 Median of volume-based PSD ($L_{50,3}$) versus the splitting factor β and two different mixing assumptions (ideal mixed and micro mixing model by [4]). Reprinted with permission from [5]
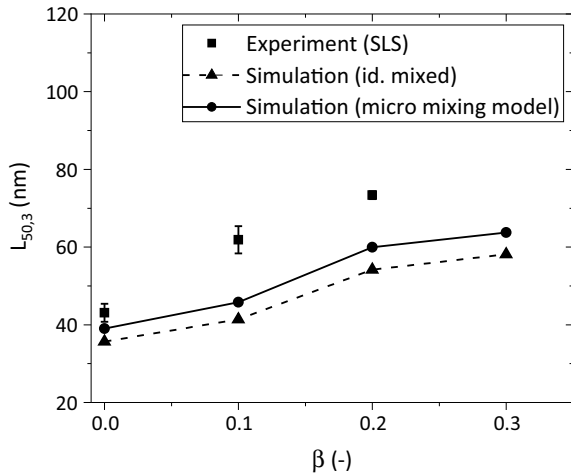
3.2 Validation of the Equivalent Circuit Model Concept

The two-zone experiments (Setup D, Sect. 2.2.2.2) were performed to verify whether the assumption of a well-mixed stirred tank connected to a PFR is, in principle, a suitable analogon for depicting the semi-batch process. As Bałdyga and Bourne [24] did not selectively investigate this aspect before using this model idea for simulation, we performed an "experimental simulation" by comparing particle sizes from the bulk semi-batch and corresponding two-zone equivalent circuit experiments. This method allows us to approximate the error which originates from this model concept. The corresponding value of $Q_{\text{circ},1}$ was calculated for a given stirring rate N of the bulk process by using the method published in [29]. The two-zone experiment was then performed according to the procedure described in Sect. 2.2.2.2 over a wide range of process conditions.

Figure 21 illustrates an exemplary result using the example of two process conditions, firstly, with 150 rpm and $u_{\text{prim}} = 0.39\,\text{m/s}$ and, secondly, with 50 rpm and $u_{\text{prim}} = 0.13\,\text{m/s}$. The resulting PSDs are quite similar with slightly larger particles generated in the two-zone process. This effect of slightly larger particles was observed over a wide range of process conditions and two different stirrer types in [29]. Therefore, it can be concluded that the equivalent circuit assumption and the correlation for $Q_{\text{circ},1}$ introduces a small error on the final PSD. However, this error is not significant in the context of process flowsheet simulations, where the simplified model assumptions only allow for a coarse estimation of the target variables. Consequently, replacing the semi-batch process by the equivalent circuit of PFR and well-mixed BF is a suitable modeling strategy for process flowsheet simulation.

Fig. 21 The volume-based PSD (q_3) of bulk (Rushton turbine stirrer) and corresponding JICF two-zone experiments for two different rotational speeds and feed velocities. Reprinted with permission from [29]
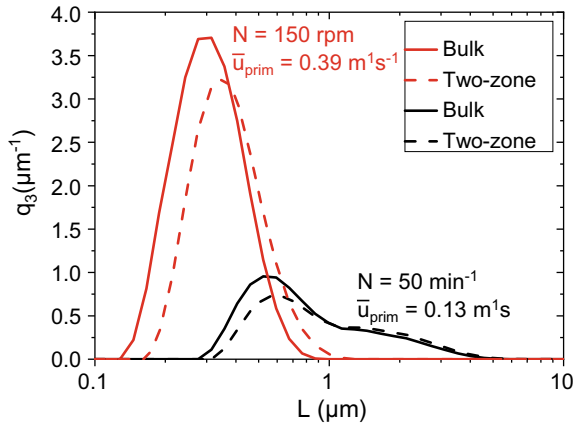
3.3 Dynamic Simulation

Results from semi-batch process simulation are compared to experimental data in Sect. 3.3.1. Furthermore, the numerical efficiency of the model of the newly developed approximation method used is demonstrated. Section 3.3.2 provides results regarding the influence of the semi-batch process dynamics for steady-state boundary conditions. Section 3.3.3 illustrates how dynamic boundary conditions might be used to optimize the product PSD for semi-batch processes in the future.

3.3.1 Validation and Numerical Efficiency

An exemplary result from validation of the semi-batch model for different stirrer rotational speeds is given in Fig. 22. As observable, the simulation predicts the experimental results well, with an error for $L_{50,3}$ below 100 nm. We also tested different feed volume flow ratios, with the result that higher deviations between model and experiments occurred for $Q_{prim} \geq 0.3$ L/min. Consequently, we did not investigate these process conditions further, as a model refinement is required to depict high feed volume flows correctly.

The computational time of the model depends mostly on f_{rec}, the PSD discretization (ΔL, $L_{max} - L_{min}$) and time discretization Δt. All influencing factors were investigated separately to ensure that none of them influences the results significantly. Reliable results can be gained with 100 equally distributed particle size classes ($\Delta L = 22$ nm) from $L_{min} = 22$ nm to $L_{max} = 2.2\,\mu m$ and $\Delta t = 0.5$. These values are, therefore, used as default values for all simulations.

The recalculation frequency f_{rec}, which is part of the approximation method described in Sect. 2.3.2.3, is the main reason for the outstanding numerical performance of our surrogate model compared to mechanistic models from literature. An exemplarily chosen case with Simulation Setup C, $Q_{prim} = 0.2$ L/min, $N = 100$ rpm

Fig. 22 Median of volume-based PSD ($L_{50,3}$) versus impeller speed for experiments and Setup C simulation
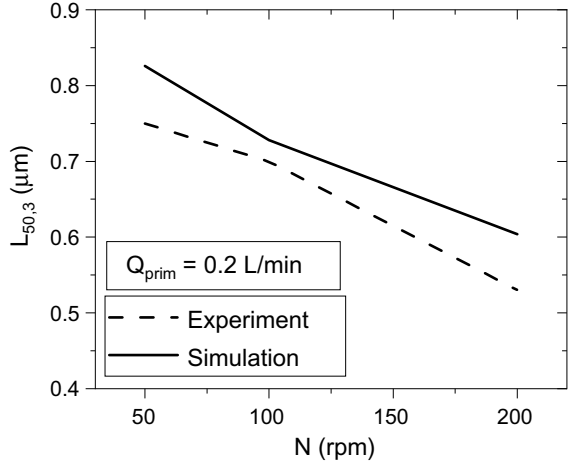
illustrates the massive improvement of numerical efficiency if the PFR is not recalculated in every timestep. Without the approximation method ($f_{rec} = 1$), this simulation case requires approximately $\tau_{ct} \approx 58$ min on a single core of an *Intel Core i-7 7700* CPU with 3.60 GHz. As shown in Fig. 23, the calculation speed can be improved by several orders of magnitude by using a lower value for f_{rec}. Interestingly, even for $f_{rec} = 1/30$, which requires $\tau_{ct} \approx 2.1$ min instead of $\tau_{ct} \approx 58$ min, the accuracy of the model is only insignificantly diminished.

Fig. 23 Median of volume-based PSD ($L_{50,3}$) for recalculation frequencies of $f_{rec} = \frac{1}{2}$ to $f_{rec} = \frac{1}{80}$. Simulations performed at $Q_{prim} = 0.2$ L/min, $N = 100$ rpm and, $\Delta t = 0.5$ s with Setup C simulation. Computational time τ_{ct} referred to a single core of an *Intel Core i-7 7700 CPU* with 3.60 GHz
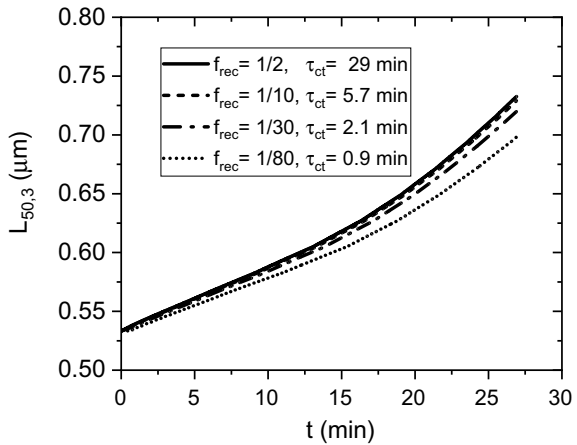
Fig. 24 Temporal evolution
of PSD for Setup C
simulation with
$Q_{\mathrm{prim}} = 0.2\,\mathrm{L/min}$ and
$N = 100\,\mathrm{rpm}$
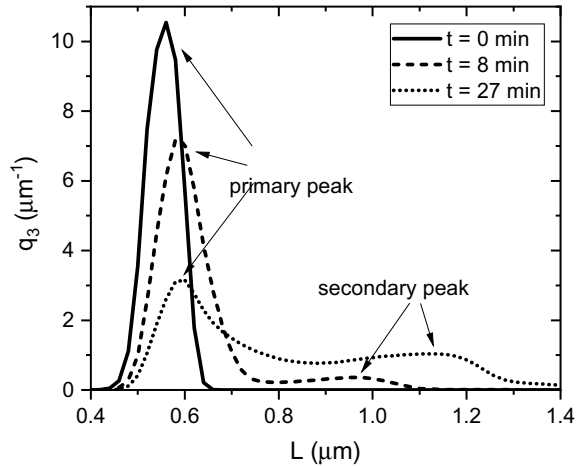
3.3.2 Process Dynamics for Steady-State Boundaries

A standard semi-batch operation with static feed rate and impeller rotational speed
shows a dynamic PSD evolution, for which several mechanisms are responsible:
Firstly, the reduction of reactive ion concentration by dilution and solids formation
reaction decreases the supersaturation level in the PFR over time. Secondly, particles
already present in the reactor can pass the PFR additional times and grow more.
At a later stage of the process, these recycled particles can massively decrease the
supersaturation in the PFR if a specific amount and size of particles is reached to
offer the particle surface for a fast depletion of reactive ions in the PFR.

Figure 24 illustrates a typical PSD evolution using the example of a Setup C
simulation with $Q_{\mathrm{prim}} = 0.2\,\mathrm{L^1 min^{-1}}$ and $N = 100\,\mathrm{rpm}$. The total process time of
this simulation is $\tau_{\mathrm{pro}} = 27\,\mathrm{min}$. A primary peak can be observed at the start of the
process. These are the first particles precipitated in the PFR. During the process, the
PSD shifts to larger particle sizes with a secondary peak observable.

3.3.3 Dynamic Optimization by Dynamic Boundary Conditions

Further analysis of $S_a(z, t)$ and of $n(z, t)$ confirm that supersaturation decreases over
the process time. As this is assumed to be the main reason for the widening of the
PSD over the process time, Setup E was used to investigate whether this specific
process dynamics can be counteracted by increasing the stirring rate over time. As
higher mixing intensities lead to the generation of smaller particles in the PFR, this
effect could be of possible use to counteract the increase of the particle size due
to lower supersaturation. We, therefore, used a dynamic stirring rate for Simulation
Setup E, which was increased from 100 to 300 rpm, as shown in Fig. 14.

Fig. 25 Variation of static stirring rate (100, 300 rpm) and linear increase (dynamic) from 100 to 300 rpm impacting the final PSD (Simulation Setup E)
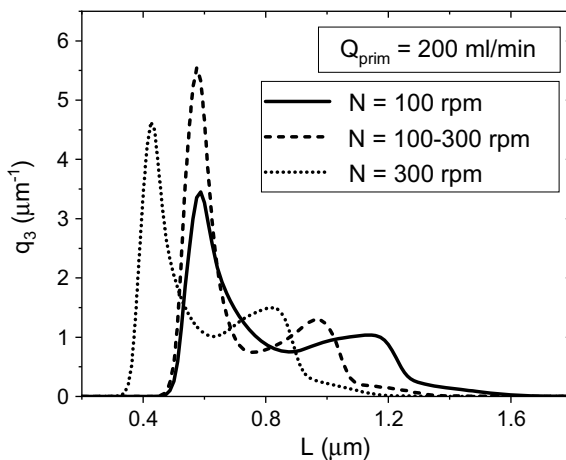
A narrower PSD can be reached by dynamically increasing the stirring rate, as observable in Fig. 25. The overall effect is not significant compared to the experimental reproducibility due to the process condition chosen. However, this simulation illustrates how dynamic optimization might be performed by using dynamic process parameters for model-based process control.

4 Conclusion

In this contribution, a steady-state and a dynamic semi-batch surrogate model for precipitation of sparingly soluble salts were presented. Both models reach the numerical efficiency required for application in flowsheet process simulations.

The steady-state model solves the coupled mixing and solids formation process along a z coordinate of the mixer (plug flow assumption). The mixing process is modeled by the interaction of different fluid environments according to the E-model by Bałdyga and Bourne [24]. The PSD is calculated by solving a PBE under consideration of nucleation and diffusion-limited particle growth. The steady-state model was implemented in *Dyssol* and validated with two Experimental Setups: A simple stand-alone precipitation experiment and a complex flowsheet with a recycle stream connecting inlet and outlet to investigate the influence of recycle streams on the PSD. Experimental validation proved that the model predicts the experimental outcomes well, also for the complex flowsheet with recycle streams involved. Furthermore, we were able to investigate the influence of the recycle stream ratio on the PSD both numerically and experimentally.

The dynamic semi-batch model is based on a semi-batch model concept by Bałdyga and Bourne [24], who divided the semi-batch stirred tank in a well-mixed BF and a PFR reactor as the mixing and reaction zone. As Bałdyga and Bourne [24] did

not experimentally proof the idea of a PFR-BF equivalent circuit, we developed the concept of an "experimental simulation," which compares experimental PSDs of the equivalent circuit to the PSD resulting from semi-batch bulk experiments. Although there is a small error introduced by the equivalent circuit concept, this concept proved to be a suitable simulation strategy for process flowsheet simulation. To implement the model, the steady-state model (with minor adaptations) was used to solve the PFR with high computational speed. It was, furthermore, possible to increase the computational speed of the model significantly by developing a hybrid modeling technique. Within this hybrid model design, which can be applied for every mechanistic model using a BF-PFR equivalent circuit in literature, the PFR is not recalculated on each iteration but, instead, most of the timesteps are approximated by simpler equations. Simulation time scales suitable for dynamic process flowsheet simulation can be reached by utilizing this new approximation method. The final dynamic semi-batch model was implemented in *Dyssol*. Except for high feed volume flows, the model predicted the experimental data well. The dynamic process simulations show that the wide PSD obtained by semi-batch precipitation originates from the semi-batch process dynamics. As an outlook to future work, it is, furthermore, demonstrated that dynamic process parameters might be used to optimize semi-batch precipitation processes.

References

1. Metzger, L., Kind, M.: Influence of mixing on particle formation of fast precipitation reactions—A new coarse graining method using CFD calculations as a "measuring" instrument. Chem. Eng. Res. Des. **10**, 176–185 (2016)
2. Metzger, L., Kind, M.: On the transient flow characteristics in confined impinging jet mixers—CFD simulation and experimental validation. Chem. Eng. Sci. **133**, 91–105 (2015)
3. Metzger, L., Kind, M.: The influence of mixing on fast precipitation processes—A coupled 3D CFD-PBE approach using the direct quadrature method of moments (DQMOM). Chem. Eng. Sci. **169**, 284–298 (2017)
4. Metzger, L., Kind, M.: On the mixing in confined impinging jet mixers—Time scale analysis and scale-up using CFD coarse-graining methods. Chem. Eng. Res. Des. **109**, 464–476 (2016)
5. Rehage, H., Scherer, S., Kind, M.: A steady-state precipitation model for flowsheet simulation and its application. Comput. Chem. Eng. **128**, 524–537 (2019)
6. Barrett, M., O'Grady, D., Casey, E., Glennon, B.: The role of meso-mixing in anti-solvent crystallization processes. Chem. Eng. Sci. **66**(12), 2523–2534 (2011)
7. Jaworski, Z., Nienow, A.W.: CFD modelling of continuous precipitation of barium sulphate in a stirred tank. Chem. Eng. J. **91**(2–3), 167–174 (2003)
8. Jones, A., Rigopoulos, S., Zauner, R.: Crystallization and precipitation engineering. Comput. Chem. Eng. **29**(6), 1159–1166 (2005)
9. Vicum, L., Ottiger, S., Mazzotti, M., Makowski, Ł., Bałdyga, J.: Multi-scale modeling of a reactive mixing process in a semibatch stirred tank. Chem. Eng. Sci. **59**(8–9), 1767–1781 (2004)
10. Vicum, L., Mazzotti, M.: Multi-scale modeling of a mixing-precipitation process in a semibatch stirred tank. Chem. Eng. Sci. **62**(13), 3513–3527 (2007)
11. Wang, Z., Mao, Z., Yang, C., Shen, X.: Computational fluid dynamics approach to the effect of mixing and draft tube on the precipitation of barium sulfate in a continuous stirred tank. Chin. J. Chem. Eng. **14**(6), 713–722 (2006)

12. Wang, Z., Zhang, Q.H., Yang, C., Mao, Z.-S., Shen, X.Q.: Simulation of barium sulfate precipitation using CFD and FM-PDF modeling in a continuous stirred tank. Chem. Eng. Technol. **30**(12), 1642–1649 (2007)
13. Zauner, R., Jones, A.G.: Mixing effects on product particle characteristics from semi-batch crystal precipitation. Chem. Eng. Res. Des. **78**(6), 894–902 (2000)
14. Zhang, Q., Mao, Z.-S., Yang, C., Zhao, C.: Numerical simulation of barium sulfate precipitation process in a continuous stirred tank with multiple-time-scale turbulent mixer model. Ind. Eng. Chem. Res. **48**(1), 424–429 (2009)
15. Matynia, A., Piotrowski, K., Koralewska, J.: Barium sulphate crystallization kinetics in the process of barium ions precipitation by means of crystalline ammonium sulphate addition. Chem. Eng. Process. **44**(4), 485–495 (2005)
16. Steyer, C., Sundmacher, K.: Impact of feeding policy and ion excess on particle shape in semi-batch precipitation of barium sulfate. J. Cryst. Growth **311**(9), 2702–2708 (2009)
17. Torbacke, M., Rasmuson, Å.C.: Mesomixing in semi-batch reaction crystallization and influence of reactor size. AIChE J. **50**(12), 3107–3119 (2004)
18. Alexopoulos, A.H., Maggioris, D., Kiparissides, C.: CFD analysis of turbulence non-homogeneity in mixing vessels. A two-compartment model. Chem. Eng. Sci. **57**(10), 1735–1752 (2002)
19. Alopaeus, V., Moilanen, P., Laakkonen, M.: Analysis of stirred tanks with two-zone models. AIChE J. **55**(10), 2545–2552 (2009)
20. Bourne, J.R., Yu, S.: Investigation of micromixing in stirred tank reactors using parallel reactions. Ind. Eng. Chem. Res. **33**(1), 41–55 (1994)
21. Judat, B., Racina, A., Kind, M.: Macro- and micromixing in a Taylor-Couette reactor with axial flow and their influence on the precipitation of barium sulfate. Chem. Eng. Technol. **27**(3), 287–292 (2004)
22. Kim, W.-S., Tarbell, J.M.: Micromixing effects on barium sulfate precipitation in an MSMPR reactor. Chem. Eng. Commun. **146**, 33–56 (1996)
23. van Leeuwen, M.L.J., Bruinsma, O.S.L., van Rosmalen, G.M.: Three-zone approach for precipitation of barium sulphate. J. Cryst. Growth **166**, 1004–1008 (1996)
24. Bałdyga, J., Bourne, J.R.: Turbulent Mixing and Chemical Reactions. Wiley. ISBN 0-471-98171-0 (1999)
25. Bałdyga, J., Podgórska, W., Pohorecki, R.: Mixing-precipitation model with application to double feed semibatch precipitation. Chem. Eng. Sci. **50**(8), 1281–1300 (1995)
26. Ståhl, M., Rasmuson, Å.C.: Towards predictive simulation of single feed semibatch reaction crystallization. Chem. Eng. Sci. **64**(7), 1559–1576 (2009)
27. Kügler, R.T., Doyle, S., Kind, M.: Fundamental insights into barium sulfate precipitation by time-resolved in situ synchrotron radiation wide-angle X-ray scattering (WAXS). Chem. Eng. Sci. **133**, 140–147 (2015)
28. Kucher, M., Babic, D., Kind, M.: Precipitation of barium sulfate. Experimental investigation about the influence of supersaturation and free lattice ion ratio on particle formation. Chem. Eng. Process **45**(10), 900–907 (2006)
29. Rehage, H., Nikq, F., Kind, M.: Experimental investigation of a two-zone model for semi-batch precipitation in stirred-tank reactors. Chem. Eng. Sci. **207**, 258–270 (2019)
30. Deutsches Institut für Normung (DIN 28131).: Agitators and Baffles for Agitator Vessels; Types, Terms and Main Dimensions. Berlin (1992)
31. Skorych, V., Dosta, M., Hartge, E.-U., Heinrich, S.: Novel system for dynamic flowsheet simulation of solids processes. Powder Technol. **314**, 665–679 (2017)
32. Bałdyga, J., Bourne, J.R., Hearn, S.J.: Interaction between chemical reactions and mixing on various scales. Chem. Eng. Sci. **52**, 457–466 (1997)
33. Schwarzer, H.-C.: Nanoparticle Precipitation: An Experimental and Numerical Investigation Including Mixing. Logos-Verlag. ISBN 978-3-8325-0916-3 (2005)

Chapter 5
Development of a Dynamic-Physical Process Model for Sieving

Check for
updates

Darius Markauskas and Harald Kruggel-Emden

Abstract For a broad range of applications sieving/screening is well suited to separate bulk materials according to particle sizes. In the treated bulk materials particles frequently prevail in broad size distributions, with non-spherical shape and sometimes even under moist conditions, complicating the separation process. Therefore, it is inevitable to gain a deeper understanding of the subprocesses of screening (size based stratification, particle passage through the screen surface and possible transport along the screen) under the aforementioned conditions. To gain this knowledge, detailed particle-based simulation approaches like the discrete element method (DEM) are available. Based on the latter method, discontinuous and continuous screening as well as its subprocesses are investigated. Therein, different screen geometries and characteristics are considered along with various mechanical excitations applying model and real particle shapes first under dry conditions and later under the influence of various liquid amounts. In order to perform reliable DEM screening simulations, the exact determination of particle properties like size, shape, material and contact parameters is essential, which is required in advance of the simulations. Besides the DEM, the integral outcome of screening can be represented by various phenomenological process models. Usually, the material-, operating-, and apparatus-specific parameters of the latter process models are empirically determined by experiments, whereas, here, the parameters for screening process models are directly obtained from DEM simulations, which allows their benchmarking under defined conditions. Additionally, suitable process models are successfully extended to represent screening processes under the presence of moisture.

1 Introduction

In mechanical process engineering, materials preparation and energy technology, it is often required to classify disperse solid systems according to their particle sizes and shapes or to separate out strongly under- or oversized material from the

D. Markauskas · H. Kruggel-Emden (✉)
Chair of Mechanical Process Engineering and Solids Processing,
Technische Universität Berlin, Berlin, Germany
e-mail: kruggel-emden@tu-berlin.de

141

desired product [1]. In typical processes, particles are often of highly non-spherical shape and of broad size distribution [2, 3]. However, in combined solids processes in industrial applications, defined narrow particle size distributions may be necessary for subsequent process steps. In this sense a technical simple, but well-suited approach for the separation of solid mixtures is sieving or screening, which can be performed discontinuously or continuously.

By definition, sieving or screening is a separation of a particle collective according to geometric features, whereby ideally, other material properties such as e.g. the particle density are not relevant [4]. Characteristic for sieving or screening is the comparison of the bulk material with approximately equal sized openings of a solid surface called apertures. Particles that are smaller than the apertures usually pass by gravity, while larger particles remain as holdup on the screen. In accordance to other classification processes, the bulk material supplied on a screen is referred to as feed material. The particles that pass through the apertures are the fines getting in the screen underflow, whereas the particles that remain on the screen consisting of coarse material form the screen overflow [1, 4]. In Fig. 1, the terms in the simple case of a discontinuous batch sieving process are summarized. Before the beginning of a batch sieving process, a particle collective, which should be separated into size classes, is fed on the classifier in individual charges. The process extends over a predetermined period and the feed remains in the apparatus throughout the process and must be discharged in a consecutive step.

The amplitude and the frequency of the vibrating sieve surface have a decisive influence on the quality of batch sieving. The movement of the sieve ensures a vertical loosening of the material, so that smaller particles can reach the sieve bottom due to the gaps formed between the larger particles (segregation). In addition, circulating and stochastic motions in the particle layer cause each particle to be compared multiple times with the aperture size. Since not every small particle passes through the sieve bottom on the first encounter due to local and time-varying conditions, it is only possible to separate the sieve material into fines and coarse material over time [1, 5]. Note that segregation in the context of sieving or screening is often referred to by the phrase stratification.

In industrial processes, predominantly continuous screening machines like the typical one shown in Fig. 2 are used [1].

In such a continuous screening process, the feed material is fed continuously on a usually slightly inclined screen surface, resulting in a thick layer of particles at the feed end of the screen apparatus. In addition to the loosening of the feed material, the vibration of the screen also causes the transport of the particle layer along the screen which is supported by the inclination. Thereby, the thickness of the bulk material

Fig. 1 Schematic of a discontinuous sieving process
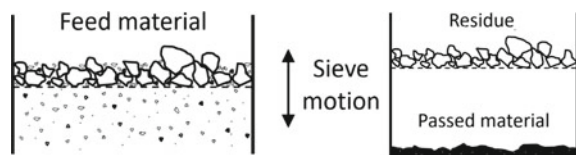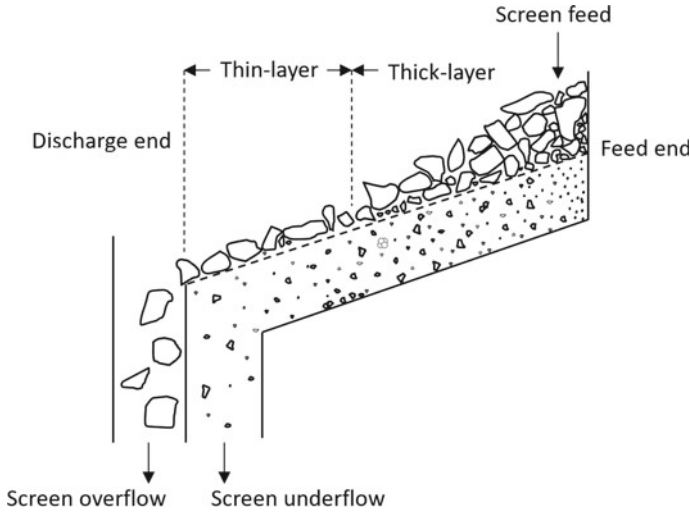
Fig. 2 Schematic of a continuous screening process

layer decreases with continuous movement of the material along the screen. At the beginning of the screening process, much more particles are near the feed end and only a few are at the discharge end. This state slightly shifts over time, whereby, it is favorable that the screening process reaches a steady state after a while. This steady state should be maintained but can be interrupted by load changes or by a shutdown of the screening apparatus. From the screening process, the separated fractions are discharged as overflow and underflow [1, 6].

Screening is rarely operated as a stand-alone process but mostly integrated in a process chain with other combined solids processes in the industrial context. In order to prevent disturbances in such connected industrial processes, the knowledge of the influence from upstream process steps on the actual process and its impacts on subsequent downstream processes is significant and therefore, the single processes must be at best fully understood. Despite its wide usage in industry and recent promising developments concerning the dynamics of screening and its subprocesses influenced by different mechanical agitations or by a fluid, a satisfactory understanding of screening processes is still not fully given for mixtures of real solids, leaving the design, optimization and scaling of this process operation a challenging task. The underlying different processes (stratification, particle passage and particle transport), their interaction and dynamic behavior still lack detailed understanding [7]. Furthermore, flexible, simple and physically based process models for a quantitative representation of screening on the background of a transient description are not available.

At least the two subprocesses stratification and passage are closely interlinked during screening. Due to the mechanical excitation of the screen, smaller particles move through the interstices of the larger particles in the direction of the screen

surface (stratification), whereby particles smaller than the aperture size pass through the screen openings depending on their shapes [8]. In addition, the transport of the bulk material during the continuous screening process and various mechanical excitations also influence the particle passage [9, 10].

For the design and optimization of apparatus-specific parameters as well as operational ones of a screening process under stationary conditions, various phenomenological process models are available. Some simple models, which are commonly used in stationary process simulation packages, only consider the integral outcome of the separation operation, while others represent the particle size separation temporally or spatially resolved. In addition, some of the models take the interacting processes of stratification and the actual particle passage through the screen into account. All phenomenological models have in common that they require a set of empirical parameters, which are material, operation and apparatus-specific and are usually determined from experimental investigations. In contrast, particle-based simulation methods such as the discrete element method (DEM), based on the work by Cundall und Strack [11], provide detailed insights into the process of screening and allow, after appropriate validations, the design and optimization of equipment as well as of operating parameters. Up to now, only a few screening investigations addressed systems of realistic particles of complex shape or under the influence of liquid. Applications of the DEM with the aim to directly derive parameters for dynamic phenomenological models for the process step screening were rarely carried out and are yet not adequately accomplished.

That the DEM is capable after appropriate calibration to perform a benchmarking of screening process models and can even address moist particles is shown in the following. The data obtained from the DEM can thereafter be utilized to derive and optimize novel process models which can then be utilized in solids process simulation frameworks.

2 Discrete Element Method (DEM)

The discrete element method (DEM) first proposed by Cundall and Strack [11] as well as Walton and Braun [12] is a particle-based simulation approach that provides detailed insights into various processes and has become a common tool for modeling particulate systems (see [13–16]). After validation, it offers the possibility to optimize equipment and operating parameters without carrying out extensive experiments before each study. By applying this method, the movement and interaction of each individual particle within a considered computational domain can be represented and tracked. Contact forces between the particles and the system environment as well as possible additional forces resulting from the presence of liquid are used to determine velocities, positions and spatial orientations of all particles contained in the system using the Newton's and Euler's equations of motion.

2.1 Particle Geometries in the DEM

Due to its simplicity, in particular with respect to the determination of the contacts, the majority of studies in the field of DEM were using spherical particles [17]. In contrast, non-spherical particles require a higher complexity for the contact determination [18]. In most industrial processes, where bulk solids occur, including sieving, the actual particle geometries, however, differ significantly from the spherical shape. Therefore, methods for describing complex particle geometries within the DEM have to be applied.

A common method for approximation of non-spherical particles in DEM simulations is the use of superquadrics or ellipsoids (see Fig. 3a). Several studies have demonstrated the ability to represent a wider variety of particle geometries and significantly increase the shear strength of loose packings compared to spherical particles [19–21]. Superellipsoids or-quadrics, however, are limited to symmetrical body shapes and cannot reproduce sharp-edged particles.

Another common type of representation of non-spherical particles within the DEM are polyhedra, which are arbitrary convex bodies defined by surface triangulation (see Fig. 3b). Since polyhedra can have a variety of structures, the contact geometry that occurs can be very complex. Although polyhedra have the advantage of being versatile in use, the challenging determination of the overlaps and the resulting forces lead to a high computational effort. This limits their applicability to large-scale screening simulations where, in addition to many particle contacts, a large number of particle wall contacts is unavoidable.

In addition, non-spherical particles in the DEM can be represented by the multi-sphere method developed by Jensen et al. [22], Favier et al. [23, 24] and Vu-Quoc et al. [25] (see Fig. 3c). Following this flexible approach, a series of spheres of any size are bundled to determine the desired shape of the non-spherical particle as accurately as possible [26]. As a result, the spheres can overlap while the geometry of such a particle remains unchanged during the simulation. In addition to the flexibility to represent a variety of shapes, the contact detection inherits its simplicity from the spheres [17]. Although sharp-edged shapes can only be represented to a certain
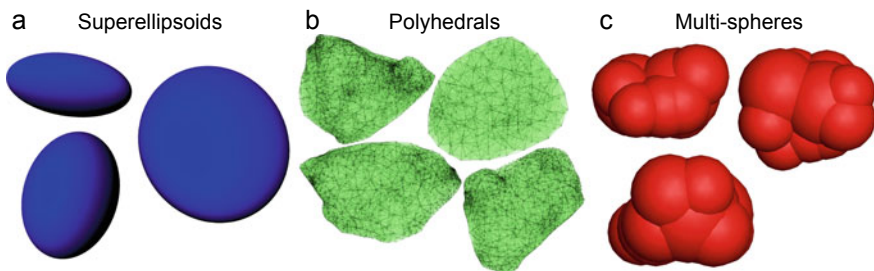
Fig. 3 Comparison of different approximations of non-spherical particles, comprising of **a** superellipsoids, **b** polyhedral and **c** multi-sphere method

degree with the multi-sphere method, it is well suited for modeling of screening of non-spherical particles. Due to the relatively low computational effort the multi-sphere approach is the most popular method for representing non-spherical particles. However, the number of spheres required to properly approximate the real particle must be estimated on a case by case basis [27] which is further addressed in Sect. 2.5.

2.2 Equations of Motion Governing the DEM

The DEM is routinely used to model systems with spherical particles [13, 14]. To obtain the translational and rotational motion in such a system, the Newton's and Euler's equations are integrated

$$m_i \frac{d^2 \vec{x}_i}{dt^2} = \vec{F}_i^c + m_i \vec{g} + \vec{F}_i^l, \tag{1}$$

$$I_i \frac{d\vec{\omega}_i}{dt} = \vec{M}_i, \tag{2}$$

with particle mass m_i, particle acceleration $d^2 \vec{x}_i / dt^2$, contact force $\vec{F}_i^c$, forces arising from a possible liquid amount $\vec{F}_i^l$, gravitational force $m_i \vec{g}$, moment of inertia I_i, angular acceleration $d\vec{\omega}_i / dt$, angular velocity $\vec{\omega}_i$ and external moments resulting out of contact and other sources $\vec{M}_i$.

When non-spherical particles are used in the DEM, the integration of the Euler's equation reads

$$\hat{I}_i \frac{d\vec{W}_i}{dt} + \vec{W}_i \times \left(\hat{I}_i \vec{W}_i \right) = \Lambda_i^{-1} \vec{M}_i, \tag{3}$$

where $d\vec{W}_i / dt$ is the angular acceleration, $\vec{W}_i$ is the angular velocity in the body fixed frame, $\vec{M}_i$ is the external moment resulting out of contact and other sources, $\hat{I}_i$ is the inertia tensor along the principal axis and Λ_i^{-1} is the rotation matrix converting a vector from the inertial into the body fixed frame. Explicit integration schemes are used to solve the equations for translational and rotational motion (see [28]). The relevant forces required in Eqs. (1)–(3) are described in Sects. 2.3 and 2.4. Contributions due to rolling friction are neglected.

2.3 Contact Forces

After determining a pair of colliding particles or a contact between a particle and a boundary object, the resulting forces are evaluated by applying a suitable contact force model. In this sense Fig. 4a shows a collision of two spherical particles i and
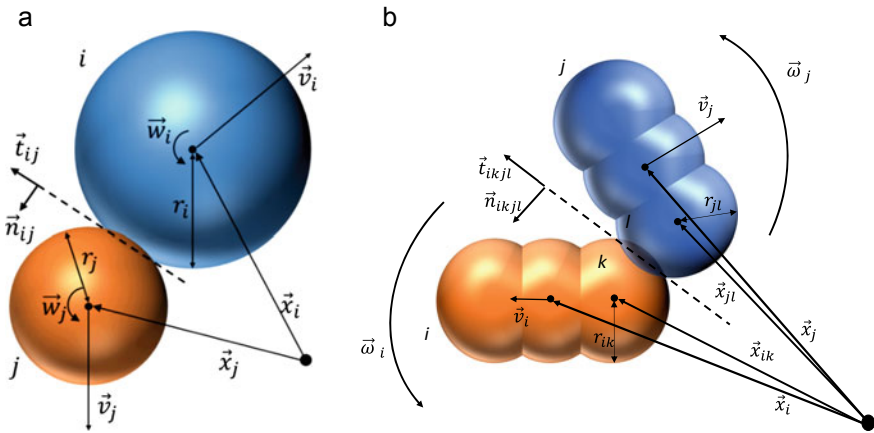
Fig. 4 A collision of two **a** spherical particles and **b** multi-sphere particles. Reprint with permission from [29, 30]

j, whereas in Fig. 4b the two spheres l and k of two non-spherical (multi-sphere) particles i and j collide.

2.3.1 Normal Force Model

For the calculation of the normal force, different models are available. The most common is the linear viscoelastic spring damper model [31, 32], which is also used here for the determination of the normal component of the contact forces. The normal force is given as the sum of an elastic and a dissipative component

$$\vec{F}_{ij}^n = \vec{F}_{el}^n + \vec{F}_{diss}^n = k^n \delta_{ij} \vec{n}_{ij} + \gamma^n \vec{v}_{ij}^n, \tag{4}$$

where k^n is the spring stiffness, δ_{ij} is the virtual overlap, $\vec{n}_{ij}$. is a normal vector, γ^n. is a damping coefficient and $\vec{v}_{ij}^n = \left((\vec{v}_i - \vec{v}_j) \cdot \vec{n}_{ij} \right) \vec{n}_{ij}$ is the relative normal velocity at the contact point with the velocities $\vec{v}_i$ and $\vec{v}_j$ [31]. Note that in case of the multi-sphere particles in Fig. 4b the force is calculated analogously between the contacting spheres k and l of particles i and j. The damping coefficient γ^n is obtained by

$$\gamma^n = -\left(2\ln\left(e^n\right) m_{eff}\right)/t^n, \tag{5}$$

with the coefficient of restitution e^n, which has to be experimentally determined or obtained from literature, the duration of a collision

$$t^n = \pi / \left(\sqrt{ \left(k_n / m_{eff} - \left(\gamma_n / \left(2 m_{eff} \right) \right)^2 \right) } \right) \tag{6}$$

and the effective mass $m_{eff} = m_i m_j / (m_i + m_j)$.

2.3.2 Tangential Force Model

In addition to the normal force, a force component in the tangential direction for modeling of occurring friction effects is taken into account in order to prevent particles from sliding apart in a particle bed. Also for the tangential force, different models are applicable [33]. Similar to the normal force, the most common tangential models are linear (see e.g. [34–36]). Here, the tangential forces are calculated by applying a linear spring limited by the Coulomb condition and calculated as

$$\vec{F}_{ij}^t = -\min\left(\vec{F}_{spring}^t, \vec{F}_{coul}^t\right) = -\min\left(k^t \left|\vec{\xi}_{ij}\right|, \mu_C \left|\vec{F}_{ij}^n\right|\right)\vec{t}_{ij}, \qquad (7)$$

where k^t is the tangential stiffness of a linear spring, μ_C is the friction coefficient, $\vec{\xi}_{ij}$ is the relative tangential displacement and $\vec{t}_{ij}$ is the tangential unit vector [33]. For the contact of two spheres k and l of two multi-sphere particles i and j (comp. Fig. 4b), only the indices are changed in Eq. (7). The tangential spring stiffness k^t is obtained as

$$k^t = \kappa m_{eff} \left(\pi / t^n\right)^2, \qquad (8)$$

where κ is given through the mechanical properties as

$$\kappa = \left((1 - v_i)/G_i + \left(1 - v_j\right)/G_j\right)/\left((1 - 0.5v_i)/G_i + \left(1 - 0.5v_j\right)/G_j\right), \quad (9)$$

where v is the Poisson's ratio and $G = E/(2 + 2v)$ is the shear modulus of the two interacting materials of particles i and j depending on Young's modulus E and again Poisson's ratio v [37].

2.4 Liquid Bridge Forces

For slightly wet or moist particles liquid bridge forces have to be considered [38]. Several researchers have proposed expressions for the determination of capillary forces (see e.g. [39–41]), viscous forces (see e.g. [42–45]), as well as for the formation, the shape, the liquid volume and the redistribution of liquid due to the rapture of a liquid bridge [46, 47]. In addition, some expressions in closed form have been proposed for the accurate calculation of liquid bridges [48, 49] and the derived models have to some extend been used in DEM simulations (see e.g. [50–54]). However, all these models are limited to the calculation of forces in pendular states, while only a few researchers also investigated the condition of the funicular state [55–57].

Considering the pendular state with small amounts of liquid, individual liquid bridges exist between pairs of particles, which leads to certain resulting adhesive forces. In the DEM model used here, only the capillary force $\vec{F}_{ij}^{cap}$ as well as the viscous forces in normal $\vec{F}_{ij}^{nvis}$ and tangential direction $\vec{F}_{ij}^{tvis}$ are applied, resulting in the total liquid bridge force

$$\vec{F}_{ij}^{l} = \vec{F}_{ij}^{cap} + \vec{F}_{ij}^{nvis} + \vec{F}_{ij}^{tvis}, \tag{10}$$

which is calculated in addition to the contact force in Eq. (1). The external moment $\vec{M}_i$ in Eq. (2) is also extended and is now the sum of the moments due to a contact $\vec{M}_{C,i}$ and a liquid bridge $\vec{M}_{L,i} = \vec{r} \times \vec{F}_i^{tvis}$.

When two particles i and j such as in Fig. 4a or a particle and a wall get into contact in a moist surrounding, a liquid bridge forms out between them. Both contact partners contribute to the liquid bridge, which is assumed to be constant in volume (V_{lb}) until it breaks, which occurs according to Willett et al. [40] when the distance S between two contact partners with $r_i \geq r_j$ is larger than

$$S_{rup} = 2r_{reff} \left(1 + (0.25\theta_{ij}) \left(1 + \frac{r_j}{r_i} \right) \right)$$
$$\left(\left(\frac{V_{lb}}{8r_{reff}^3} \right)^{1/3} + \left(\frac{r_j}{2r_i} - \frac{2}{5} \right) \left(\frac{V_{lb}}{8r_{reff}^3} \right)^{2/3} \right). \tag{11}$$

During the liquid bridge contact, the capillary forces between two particles as well as between a particle and a wall are obtained according to Rabinovich et al. [39] and Pitois et al. [44] as

$$\vec{F}_{ijpp}^{cap} = \left(-\frac{2\pi\sigma r_{reff}(\cos\theta_i + \cos\theta_j)}{1 + 1/\left(\sqrt{1 + \frac{V_{lb}}{(\pi r_{reff}S^2)}} - 1 \right)} - 4\pi\sigma r_{reff}\sin(\theta_{ij})\sin(\theta_{ij} + \varphi_{ij}) \right) \vec{n}_{ij}, \tag{12}$$

$$\vec{F}_{ipw}^{cap} = \left(-\frac{2\pi\sigma r_i(\cos\theta_i + \cos\theta_w)}{1 + S\sqrt{\pi r_i/V_{lb}}} - 2\pi\sigma r_i\sin(\theta_{iw})\sin(\theta_{iw} + \varphi_{iw}) \right) \vec{n}_{iw}, \tag{13}$$

with the surface tension coefficient σ, the static contact angles θ_i, θ_j and θ_w of the particles i, j and a wall, respectively as well as their mean values θ_{ij} and θ_{iw} (comp. [58]), the separation distance S, the reduced effective radius r_{reff} and the half filling angles

$$\varphi_{ij} = \sqrt{S/2r_{reff} \left(-1 + \sqrt{1 + V_{lb}/(\pi r_{reff}S^2)} \right)} \tag{14}$$

and

$$\varphi_{iw} = \sqrt{2S/r_i\sqrt{1 + V_{lb}/\left(\pi r_i S^2\right)}}. \tag{15}$$

Furthermore, viscous forces are considered, calculated in normal direction according to Pitois et al. [44] as

$$\vec{F}_{ij}^{nvis} = -\frac{6\pi \eta r_{reff}^2 \vec{v}_{ij}^n}{S}\left(1 - 1/\sqrt{\left(1 + V_{lb}/\left(\pi r_{reff} S^2\right)\right)}\right)^2, \tag{16}$$

with the liquid dynamic viscosity η. In tangential direction, Goldman et al. [43] introduced the following correlations

$$\vec{F}_{ij}^{tvis} = -6\pi \eta r_{reff}\left(\frac{8}{15}\ln\frac{r_{reff}}{S} + 0.9588\right)\vec{v}_{ij}^t$$
$$- 6\pi \eta r_{reff}\left(\frac{2}{15}\ln\frac{r_{reff}}{S} - 0.2526\right)\vec{\omega}_{ij} \times \vec{n}_{ij}, \tag{17}$$

$$\vec{F}_{ij}^{tvis} = -6\pi \eta r_{reff}\left(\frac{8}{15}\ln\frac{r_{reff}}{S} + 0.9588\right)\vec{v}_{ij}^t$$
$$- \frac{6\pi \eta r_{reff}}{8}\left(\frac{r_{reff}}{S + r_{reff}}\right)^4\left(1 - \frac{3r_{reff}}{8\left(S + r_{reff}\right)}\right)\vec{\omega}_{ij} \times \vec{n}_{ij}, \tag{18}$$

valid for $S < 0.1r_{reff}$ and $S \geq 0.1r_{reff}$, respectively, with $\vec{v}_{ij}^t = \vec{v}_i - \vec{v}_j - \vec{v}_{ij}^n$ as the tangential relative velocity and $\vec{\omega}_{ij} = r_i\vec{\omega}_i + r_j\vec{\omega}_j$ as relative rotational velocity of the spheres. When a liquid bridge ruptures its liquid amount is spread among particles and particles and walls—for details see [29].

2.5 Determination of DEM Parameters

In order to be able to carry out DEM simulations reliably, various parameters such as particle size, shape and density, as well as stiffness, friction and restitution coefficients are required. Various procedures and methods for the experimental determination of the latter DEM parameters have been introduced and applied in recent studies [59]. According to [59], it is possible to choose between two general methods or a combination of both to determine DEM parameters. In the first, bulk experiments and simulations are performed with the same setup, iteratively adapting the simulation parameters to exactly match the experimentally obtained outcome, regardless of the accurate representation of each individual property. Disadvantages of this method are the possible limitation to the examined application and the used DEM submodels as well as the partial loss of the physical meaning of the DEM parameters [60]. In contrast, these disadvantages are not present when the second method is used, in which the individual particle properties are measured directly. Difficult in this approach

is the parameter determination for small and arbitrarily shaped non-spherical particles [59, 60]. Even if the values are measured with high accuracy, the results in bulk experiments and simulations may differ, due to computational limitations with which the particle size and shape is resolved in the simulations [61–63]. Another possibility is to combine both methods by first determining the parameters with the second method, followed by an parameter adaptation with small scale experiments according to the first method as proposed by Elskamp et al. in [30].

2.5.1 Determination of DEM Parameters at the Single Particle Scale

Two of the most important parameters for DEM simulations are the particle size and shape, which must be determined in advance to other parameters. While the particle size usually can be measured easily, the representation of particle shape is more challenging although it can be relied on the approaches as outlined in Sect. 2.1. In the past some researchers represented simple model shapes by manually assembling spheres when relying on the multi-sphere method. Among others, Markauskas et al. [64] used 3 to 50 spheres of different sizes to represent ellipsoid particles. Particles with a slightly more complex shape were reported by Pasha et al. [65], which represented maize grains with a clump of several spherical particles generated by an automated optimization process based on 3D X-ray tomography data. In contrast, Williams et al. [66] evaluated descriptions of the irregular particle shapes of iron ore using a digital image segmentation technique and generated corresponding non-spherical DEM particles. Mollon and Zhao [67] presented a method for producing 3D non-spherical particles based on three 2D contours of the cross sections of random realistic grains of sand. A similar method was derived in [30] using an automated shape adaption algorithm.

Other important parameters for DEM simulations, which can be determined by direct measurement at the individual particle level, are the particle density, stiffness, Young's and shear modulus, sliding and rolling friction, damping and the coefficient of restitution.

If, as here, a linear contact model is used, particle stiffness is specified based on an appropriate calibration with various small scale experiments (e.g. shear tests) or by sensitivity analyzes. In contrast, when using Hertz-Mindlin models it is required to calculate contact stiffness based on Young's modulus, shear modulus, and Poisson's ratio. The modulus of elasticity is obtained by uniaxial compression tests in which individual particles are compressed [68–70].

Several researchers have reported the particle-wall sliding friction obtained with different approaches. One method for determining slip friction between two particles was described by Senetakis et al. [71], who designed a device to perform shear tests for small displacements, loads and non-spherical particles. Barrios et al. [63] determined the contact coefficient of sliding friction with a rotating pin-on-disk tribometer. In addition, the coefficient of sliding friction can be obtained using a direct shear box (e.g. Jenike shear cell) in which a wall is replaced by the desired wall material and the particles are sheared over it (see e.g. [72–75]).

For the investigations presented here, the sliding friction between two contact partners is taken from literature data or determined with the experimental set-up shown in Fig. 5 (see [36, 76]). In a similar experiment without a spindle, the coefficient of static friction is determined at the moment when the plate with the particles begins to move [36, 76].

The coefficient of restitution between two particles is determined by the method shown in Fig. 6a according to Wong et al. [77], González-Montellano et al. [70] and Alonso-Marroquín et al. [78]. In this case, a particle connected to the end of a pendulum is released from a vacuum tweezer to fall off, resulting in a particle motion on a circular path until it collides with another motionless particle consisting of the
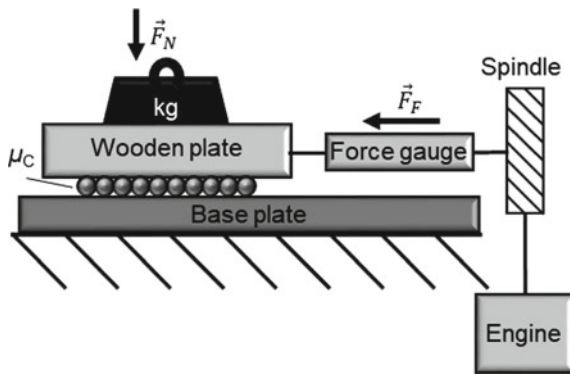

Fig. 5 Determination of the sliding friction by dragging one contact partner over another. Reprint with permission from [30]
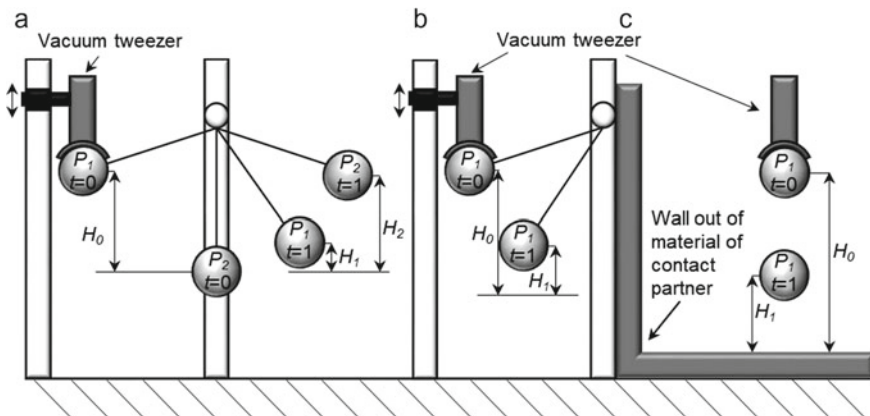

Fig. 6 Determination of the restitution coefficient for **a** particle-particle contacts with the double pendulum method [70, 77, 78] and particle-wall contacts with **b** the pendulum method and **c** the drop test [70, 78–80]

material of the second contact partner. Then the coefficient of restitution for this particle-particle contact is determined based on H_0, H_1 and H_2.

The construction of Fig. 6a may be modified to study particle wall collisions according to the construction shown in Fig. 6b, in which the second particle is replaced by a wall of the desired material. Another method for obtaining the coefficient of restitution between a particle and a wall is the common drop test shown in Fig. 6c (see e.g. [68, 70, 78–81]). The latter approach can be used for spherical and non-spherical particles, considering the angle of motion and angular velocity [82–84]. Note that the drop test can also be used to measure the coefficient of restitution for particle-particle contacts (see e.g. [68, 70, 78–81]).

2.5.2 Determination of DEM Parameters at the Bulk Particle Scale

For the determination of DEM parameters at bulk level, various tests are carried out at small scale, whereby one or more parameters of the respective DEM simulations are iteratively adapted to the obtained experimental results. To adjust the bulk density, simple experiments can be carried out to fill a container of known volume, and the same particle bed height should be obtained in experiments and simulations (see e.g. [85–88]).

A very common method for taking into account sliding friction, in particular between particles, but also between particles and walls, is the measurement of the static angle of repose in a pile formation test (see e.g. [27, 60, 62, 63, 72, 74, 89]). In this case, a container, which is filled with the particles used in the real application, is lifted from a plate or opened at the bottom, which leads to the release of the particles. This results in the formation of a pile from which the angle to the horizontal can be measured. The material of the container and especially the bottom plate should be made of the same material as the wall elements in the simulations. As an example, see Fig. 7, where this approach is applied to spherical particles of polyoxymethylene (Fig. 7b) and gravel (Fig. 7c).

Another approach to adjust the coefficients of sliding friction is based on the measurement of the dynamic angle of repose formed by bulk materials in a rotating drum. The measured experimental angle can be compared with the results of the
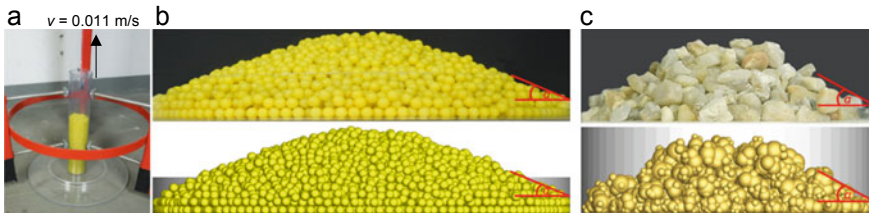
Fig. 7 **a** Experimental set-up to measure the static angle of repose and **b** resulting piles of 5 mm POM spheres as well as **c** piles of gravel in the experiments (top) and the simulations (bottom). Reprint with permission from [30]
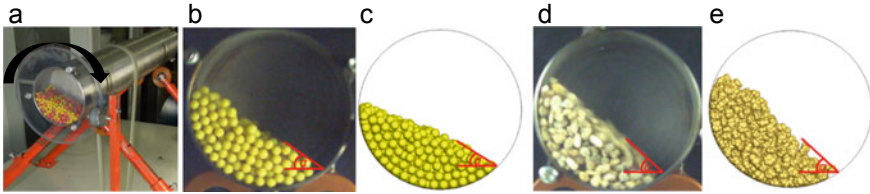
Fig. 8 **a** Experimental set-up to measure the dynamic angle of repose as well as resulting piles of **b**, **c** 5 mm POM spheres and **d**, **e** gravel in **b**, **d** the experiments and **c**, **e** the simulations. Reprint with permission from [30]

respective simulations, in which the same particle and wall properties are used as in the experiment (see e.g. [63, 68, 90–93]). For example, see Fig. 8, where this calibration is again performed for polyoxymethylene spheres (Fig. 8b and 8c) and gravel (Fig. 8d and 8e).

The restitution coefficient or the damping coefficient can also be adjusted by experimental and numerical comparison of particle behavior and average particle height in vibrating beds (e.g. [94]) and by backward calibration using the drop test [63]. Further details on the approximation algorithm for non-spherical particles and on the determination and adaptation of DEM parameters can be found in [30].

3 Process Models

Flowsheet simulations of solids processes allow the modelling of larger process chains with reasonable resources. They allow to look at process feasibility, sensitivity with regard to process parameters as well as process optimization of individual process steps, but also of the overall process chain. In contrast to DEM modelling as described in Sect. 2 they require much less computational resources and therefore are much quicker to perform. On the other hand, however, as a prerequisite, they require phenomenological process models which for screening are introduced and briefly discussed in the following.

3.1 Flowsheet Simulations of Solids Processes

A large amount of parameters has to be considered when solids production processes should be developed or optimized. These processes are often very complex and comprise of a multitude of interconnected subprocesses. A good way to look at the overall process is given in terms of the underlying flow sheet [95], which also offers a good way of modelling. Thereby a distinction can be made between stationary and dynamic modeling [96]. In the first case, all processes are calculated under steady-state operating conditions, including time-constant process variables and a fulfilled

mass and energy balance without accumulations. In contrast, dynamic modeling can take into account accumulations and unbalanced states to cover a variety of additional issues such as oscillations, batch or semi-batch processes, load changes, and startup and shutdown procedures [95]. In addition to the direct dynamic behavior in a process unit, dynamic effects can also be attributed to changes in upstream process steps and, in addition, influence subsequent downstream processes. To avoid interruptions or mechanical failures in industrial processes, the understanding of transient processes and the development of transient process models is essential [97]. To study the dynamic behavior of entire solids process chains without extensive experimental investigations, these models need to be linked by a robust and efficient framework for dynamic process simulation [98]. It should be noted that due to the complexity and disparity of the solid phase with sets of distributed parameters that may even be interdependent [99], such a framework for solids processes needs to meet very different requirements than a similar framework for fluid processes [100]. Therefore, most of the current dynamic simulation tools are designed for liquid processes with some limited extensions for the solid phase. In this context, a new framework for dynamic simulations of solid processes (Dyssol) was developed as part of the DFG priority program SPP 1679. Further information on the Dyssol framework can be found in the work by Skorych et al. [95], in which this novel tool for dynamic flowsheet simulations of solids processes is introduced, and of course throughout this book.

3.2 Phenomenological Process Models for Screening

In order to analyze entire process chains of interconnected solids processes, the understanding of the individual processes and their modeling as process models is unavoidable. Usually, these models are often partially empirical, their parameters have to be adjusted to measured data to obtain reliable results, and therefore they depend on material properties and device geometries [101, 102]. In particular, a predictive process model for screening that includes consideration of its inherent transient nature as well as directly induced or resulting dynamic effects would be important for industrial process design, monitoring, and optimization [97]. To represent the particle size separation during a screening process without extensive experiments, several phenomenological screening process models are available which are discussed in the following.

3.2.1 Steady State Separation Curve Screening Models

One way of obtaining a process model for screening is the utilization of a separation curve that is limited to the steady state. For known fractional mass flow rates in the feed and in the overflow, which are obtained from experiments or simulations, overflow separation curves can be derived as

$$T_i = T(d) = \frac{\dot{m}_{i,overflow}}{\dot{m}_{i,feed}}. \tag{19}$$

In the literature, several authors proposed equations to estimate the aforementioned separation curves. Most of these model equations are based on the parameter a_S, which is the fine material that does not come into contact with the screen surface and leaves as an overflow, the cut size d_{cut}, which is the particle size where $T_i = 0.5$, and the separation sharpness α_S which is an adjustable parameter. In this context, Dehghani et al. [103] suggested the following two parameter equation based on the model of Hatch and Mular [104], which is referred to as model No. I

$$T(d)_{Dehghani} = 1/\left(1 + exp\left(\theta\left(d_{cut}^3 - \left(d_l\sqrt{2}d\cos\theta\sqrt{2}d\sin\theta\right)\right)/\alpha_S\right)\right), \tag{20}$$

where $\theta = \tan^{-1}(d_t/d_w)$ and d_t, d_w and d_l are the thickness, width and length of the particle, respectively. The particle diameter d in Eq. (20) is obtained as $d = \sqrt{(d_t^2 + d_w^2)/2}$.

Plitt [105] described the classification with the following three parameter separation function

$$T(d)_{Plitt} = (1 - a_S) \cdot \left(1 - exp\left(-\ln 2 \cdot \left(\frac{d}{d_{cut}}\right)^{\alpha_S}\right)\right) + a_S, \tag{21}$$

referred to as model No. II. Based on the model by Hatch and Mular [104], Rogers [106] proposed a refined three parameter separation curve equation referred to as model No. III

$$T(d)_{Rogers} = \frac{(1 - a_S)}{1 + \left(\frac{d_{cut}}{d}\right) \cdot exp\left(\alpha_S \cdot \left(1 - \left(\frac{d}{d_{cut}}\right)^3\right)\right)} + a_S. \tag{22}$$

Another model equation normally utilized in the context of air classifiers, but also applicable for screening processes was derived by Molerus and Hoffmann [107]. It is referred to as model No. IV in the following, including the possible bypassing of fines (comp. [106])

$$T(d)_{Molerus} = \frac{(1 - a_S)}{1 + \left(\frac{d_{cut}}{d}\right)^2 \cdot exp\left(\alpha_S \cdot \left(1 - \left(\frac{d}{d_{cut}}\right)^2\right)\right)} + a_S. \tag{23}$$

In order to provide a better adaptability, based on the model structure by Trawinski [108], three other four parameter separation functions are considered here

$$T(d)_{Trawinski\_1} = \left(1 - \left(1 + \left(\sqrt[\alpha_S]{2} - 1\right)\left(\frac{d}{d_{cut}}\right)^{\alpha_S \cdot \beta_S}\right)^{-\alpha_S}\right) \cdot (1 - a_S) + a_S,$$

(24)

$$T(d)_{Trawinski\_2} = \left(1 - \left(1 + 3 \cdot \left(\frac{d}{d_{cut}}\right)^{\left(\left(\frac{d}{d_{cut}} + \alpha_S\right) \cdot \beta_S\right)}\right)^{-0.5}\right) \cdot (1 - a_S) + a_S,$$

(25)

$$T(d)_{Trawinski\_3} = \frac{\left(\frac{d}{d_{cut}}\right)^{\alpha_S \cdot \left(\frac{d}{d_{cut}} + \beta_S\right)}}{1 + \left(\frac{d}{d_{cut}}\right)^{\alpha_S \cdot \left(\frac{d}{d_{cut}} + \beta_S\right)}} \cdot (1 - a_S) + a_S.$$

(26)

Their additional fourth adjustable parameter β_S conduces to represent the asymmetry of the separation curve. Further they are referred to as models Nos. V–VII. For more details on the models I-VII see [109].

3.2.2 Steady State Spatially Resolved Screening Models

The available phenomenological continuous screening models are divided into kinetic [3, 110–114] and probabilistic theoretical models [3, 103, 115–118]. Both model groups allow a spatially resolved representation of a screening process in the steady state and thereby provide more information than the separation curve screening models provided in Sect. 3.2.1. The presented phenomenological screening models are also applicable to discontinuous [110] screening processes [111] by replacing the length l by the time t in the model equations (see Sect. 3.2.3). It should be noted that a discontinuous screening process is by definition transient, whereas a continuous screening process may be transient (e.g. during startup and for load or operational changes), but normally assumes a steady state after some time. This allows the use of the in Table 1 summarized screening process models that provide spatially resolved information on passage along the screen at the obtained steady state. At the moment there are no transient, spatially resolved screening process models available.

First-order kinetics provides the basis for kinetic models that can be augmented by a particle passage probability [112] which require low computational effort to solve the underlying equations. The resulting models are limited to shallow particle beds on continuously operated screens [119]. In contrast, probabilistic approaches require a greater number of parameters [112], which typically include the probability that small size particles will pass through an aperture, such as derived e.g. by Gaudin [120]. Operating parameters of screening processes such as mechanical agitation, screen size and properties (e.g. aperture shape) and particle composition (e.g. particle elongation) can be taken into account when using probabilistic models [3, 103, 115]. However, probabilistic models usually only consider the particle passage itself during

Table 1 Governing equations of the studied continuous screening process models. Reprint with permission from [109]

Model number and origin	Major equations	Adjustable parameters	Features
1. Standish and others [110, 112, 117]	$E = 1 - \exp(-kl)$	k	Kinetic
2. Andreev et al. [113]	$E = 1 - \exp(-kl^n)$	k, n	Kinetic
3. Trumic/Magdalinovic [112]	$E = 1 - 1/(1 + kl)$	k	Kinetic
4. Standish [110]	$E = \sum_{i=1}^n \left((1 - \exp(-Ak_il))\dot{m}_{i,0}/\dot{m}_0\right)$ A: screen area; n: number of undersized fractions	$k_1, \ldots, k_n$	Kinetic, fractioned
5. Grozubinsky et al.; deterministic [3]	$E = 1 - \exp(-(a - d)(1 - \exp(-\beta l))lq/\beta)$	q, β	Kinetic
6. Subasinghe et al.; deterministic [114]	$E = 1 - [k_s\exp(-k_pl) - k_p\exp(-k_sl)]/(k_s - k_p)$ k_s: rate constant of stratification and k_p: rate constant of passage	k_s, k_d	Kinetic, stratification
7. Grozubinsky et al.; probabilistic [3]	$E = 1 - \exp(-q(a - d)(1 - \exp(-\beta l))l/\beta) \cdot (1 + 0.5(ql/\beta)^2(a_D - d_{d0})(1 - \exp(-\beta l))^2)$ $a_D = \frac{1}{h-1}\sum_{i=1}^h (a_i - \bar{a})^2; \; d_{d0} = \frac{1}{n-1}\sum_{i=1}^n (d_i - \bar{d})^2$ a_D, d_{d0}: dispersion index of a (aperture size) and d (particle diameter) n: number of undersized particles; h: number of apertures $\bar{d}$: average undersized particle diameter; $\bar{a}$: average aperture size	q, β	Probabilistic
8. Subasinghe et al.; probabilistic [115]	$E = 1 - (1 - P)^N$; $P = (((a + w)\cos\varphi - w - d)(a - d))/((a + w)^2\cos\varphi)$ w: wire diameter; φ: screen inclination angle $N = \begin{cases} c_1 \cdot l^{\tau_1} \cdot (d/a) & for\,(d/a) < c_2 \cdot l^{\tau_2}/(c_1 \cdot l^{\tau_1} + c_2 \cdot l^{\tau_2}) \\ c_2 \cdot l^{\tau_2} \cdot (1 - d/a) & for\,(d/a) > c_2 \cdot l^{\tau_2}/(c_1 \cdot l^{\tau_1} + c_2 \cdot l^{\tau_2}) \end{cases}$	c_1, c_2, τ_1, τ_2	Probabilistic, fractioned, inclination angle

Table 1 (continued)

Model number and origin	Major equations	Adjustable parameters	Features
9. Nakajima/Whiten [116]	$E = 1 - \exp(-NP)$; $N = kl$ $P = \cos^4(\theta - \pi/8)\alpha\left(1 - \left(\frac{d}{a_0}\right) \times \left(\left(\frac{a_1}{a_2}\right)^2 \sin^2\theta + \cos^2\theta\right)^{0.5}\right)^2$ or $P = 0$ for $d > a_0/((a_1/a_2)^2 \sin^2 d_t + \cos^2 d_t)^{0.5}$ $\theta = \tan^{-1}(d_t/d_w)$; $d = \sqrt{d_t^2 + d_w^2}/2$; $a_0 = \sqrt{a_1^2 + a_2^2}$ with $a_1 > a_2$ d_t, d_w: particle thickness, width	k	Probabilistic, fractioned, complex shape
10. Dehghani et al. [103]	$E = 1 - \exp(-NP)$; $N = kl$ $P = \alpha\left(\left(a_1 - \sqrt{2}d\cos\theta\right)\left(a_2 - \sqrt{2}d\sin\theta\right)/(a_1 a_2)\right)$ $\theta = \tan^{-1}(d_t/d_w)$; d_t, d_w: particle thickness/width; α: fraction open area	k	Probabilistic, fractioned, complex shape
11. Ferrara et al. [117]	Crowded $1 \leq l_c$: $m_0\left(\sum_{j=1}^n y_{j,0}\left(\frac{1}{X_{ji}}\right)\left(E_i(l)^{X_{ji}} - 1\right) + \ln E_i(l)\sum_{j=n+1}^r y_{j,0}\right) = -k2^\sigma\left(1 - \frac{d_i}{a}\right)^\sigma l$ Separated $1 > l_c$: $E_i(l) = \exp(-(k/m(l))2^\sigma(1 - d_i/a)^\sigma l$ $y_{j,0}$: initial weight fraction of particle fraction j; $X_{ji} = ((a - d_j)/(a - d_i))^\sigma$ d_i, d_j: studied/other present particle diameters n, r: number of undersized/undersized + oversized particle classes	k, l_c (length related to the mode of operation) σ (screen mesh dependent)	Probabilistic, fractioned, iterative, bed depth, stratification

Table 1 (continued)

Model number and origin	Major equations	Adjustable parameters	Features
12. Soldinger; not resolving undersized fractions [9]	$E_{j+1} = k_j B_j(t_{j+1} - t_j) + E_j$ $t_j = 1_j/v$ $B_{j+1} = B_j + (c_j(1 - S_j) - k_j B_j)(t_{j+1} - t_j)$ j: time index $k_j = b(1 - E_j); c_j = f(w_q, w_d)$ B: fractional mass of undersized particles in bottom layer S: fractional mass of undersized particles stratified into bottom layer E: fractional mass of undersized particles passed through apertures	v (transport velocity) w_q (dependent on proportion of undersized material) w_d (dependent on width of particle size distribution) b (dependent on particle size)	history dependent, bed depth, stratification
13. Soldinger; resolving undersized fractions [10]	$E_{i,j+1} = k_{i,j} B_{i,j}(t_{j+1} - t_j) + E_{i,j}; t_j = 1_j/v$; i: particle class; j: time index $E_j = \sum_{i=1}^n E_{i,j}; B_j = \sum_{i=1}^n B_{i,j}; n$: number of undersized particle classes $B_{i,j+1} = B_{i,j} + (c_{i,j}(S_{i,\infty} - S_{i,j}) - k_{i,j} B_{i,j})(t_{j+1} - t_j)$; $k_{i,j} = b_i(1 - E_{i,j}); c_{i,j} = f(w_q, c_{d,i})$ B_i: fractional mass of undersized particles in bottom layer S_i: fractional mass of undersized particles stratified into bottom layer E_i: fractional mass of undersized particles passed through apertures	v (transport velocity) w_q (dependent on proportion of undersized material) $b_1, ..., b_n$ (dependent on particle diameter and aperture size)	History dependent, fractioned, bed depth, stratification

the screening process and thus do not provide any further insight into other related subprocesses [119].

In contrast, some phenomenological screening models account for concurrent subprocesses by providing additional input parameters, e.g. the opposing processes of stratification and particle passage through the screen apertures [7, 9, 10]. In this sense the original model of Soldinger [9] was extended by the influence of the particle layer thickness and the consideration of the bulk material composition [10]. The prediction of the conveyance speed of the bulk material on the screen as a further extension of this model was dealt with in another paper by the same author [121].

Table 1 gives an overview of all investigated screening process models including the name of the author and a model number (Arabic numerals), including the main equations and the adjustable model parameters used. A more detailed description of all investigated models can be found in [109].

All models outlined in Table 1 have in common that they rely on the overall screening efficiency E as a screen length dependent variable for continuous screening. It is given as

$$E = E(l) = (\dot{m}_0 - \dot{m})/\dot{m}_0, \tag{27}$$

where $\dot{m}_0$ is the initial undersized mass flow at $l = 0$ and $\dot{m}$ is the remaining mass flow of the undersized material at the screen position l. In the case when the undersized particles are considered as different fractions, the screening efficiency is stated per particle size class i

$$E_i = E_i(l) = \left(\dot{m}_{i,0} - \dot{m}_i\right)/\dot{m}_{i,0}, \tag{28}$$

where $\dot{m}_{i,0}$ is the initial fractional and $\dot{m}_i$ is the actual fractional undersized mass flow. This is related to the overall screening efficiency by $E = \sum_{i=1}^{n}\left(E_i \cdot \dot{m}_{i,0}/\dot{m}_0\right)$, where n is the number of undersized particle classes.

3.2.3 Transient Screening Models

In Table 1 presented steady state spatially resolved screening models can also be applied to transient discontinuous screening by replacing length l by time t. In addition to the thirteen models listed in Table 1 two other models by Shimosaka et al. [118] and Yoshida et al. [7] become applicable. The complete list of models is presented in Table 2 (for details see [122]). The models allow the calculation of the overall screening efficiency E which is a time dependent variable during batch screening given as $E = E(t) = (m_0 - m)/m_0$, where m_0 is the initial undersize mass at $t = t_0$ and m is the actual mass of the undersize material on the screen at time t. Often the screening efficiency is stated per particle size class i as $E_i = E_i(t) = \left(m_{i,0} - m_i\right)/m_{i,0}$, which is related to the overall screening efficiency by $E = \sum_{i=1}^{n}\left(E_i \cdot m_{i,0}/m_0\right)$, where n is the number of undersize particle classes. The screening efficiency for each particle

Table 2 Governing equations of the studied discontinuous screening process models. Reprint with permission from [122]

Model number and origin	Major equations	Adjustable parameters
α. Standish and others [110, 112, 117]	$E = 1 - \exp(-kt)$	k
β. Andreev et al. [113]	$E = 1 - \exp(-kt^n)$	$k,\ n$
γ. Trumic/Magdalinovic [112]	$E = 1 - 1/(1 + kt)$	k
δ. Standish [110]	$E = \sum_{i=1}^{n}\big((1 - \exp(-Ak_i t)) \cdot m_{i,0}/m_0\big)$ A: screen area; n: number of undersize fractions	$k_1,\ldots,\ k_n$
ε. Grozubinsky et al.; deterministic [3]	$E = 1 - \exp(-(a - d)(1 - \exp(-\beta t))tq/\beta)$	$q,\ \beta$
ζ. Subasinghe et al. [114]	$E_i = 1 - [k_{si}\exp(-k_{pi}t) - k_{pi}\exp(-k_{si}t)]/(k_{si} - k_{pi})$; $E = \sum_{i=1}^{n}\big(E_i \cdot m_{i,0}/m_0\big)$ k_{si}: rate constant of segregation and k_{pi}: rate constant of passage	$k_{s1},\ldots,\ k_{sn}$ $k_{d1},\ldots,\ k_{dn}$
η. Grozubinsky et al.; probabilistic [3]	$E = 1 - \exp(-q(a - d)(1 - \exp(-\beta t))t/\beta)$ $\quad \cdot \big(1 + 0.5(qt/\beta)^2(a_D - d_{d0})(1 - \exp(-\beta t))^2\big)$ $a_D = \frac{1}{h-1}\sum_{i=1}^{h}(a_i - \bar{a})^2$; $d_{d0} = \frac{1}{n-1}\sum_{i=1}^{n}(d_i - \bar{d})^2$ a_D, d_{d0}: dispersion index of a (aperture size) and d (particle diameter) n: number of undersized particles; h: number of apertures $\bar{d}$: average undersized particle diameter, $\bar{a}$: average aperture size	$q,\ \beta$
θ. Subasinghe et al. [115]	$E = 1 - (1 - P)^N$; $P = (a - d)^2/(a + w)^2$ for screen incl. $\varphi = 0°$ $N =$ $\begin{cases} c_1 \cdot t^{\tau_1} \cdot (d/a) & for\,(d/a) < c_2 \cdot t^{\tau_2}/(c_1 \cdot t^{\tau_1} + c_2 \cdot t^{\tau_2}) \\ c_2 \cdot t^{\tau_2} \cdot (1 - d/a) & for\,(d/a) > c_2 \cdot t^{\tau_2}/(c_1 \cdot t^{\tau_1} + c_2 \cdot t^{\tau_2}) \end{cases}$	c_1, c_2, τ_1, τ_2
κ. Shimosaka et al. [118]	$E = 1 - exp(-Pt)$; $P = k P_g P_e P_f C_p$; P_e: initial undersized particle ratio $P_f = H/H_{50}$; $C_p = 0.1463 \cdot v_{frq} \cdot v_{amp}$; P_g: passage probability [120] v_{frq}: vibration frequency; v_{amp}: vibration amplitude H: max. height of initial position of particles; H_{50}: height of 50% of particles	k

<div align="right">(continued)</div>

Table 2 (continued)

Model number and origin	Major equations	Adjustable parameters
λ. Nakajima/Whiten [116]	$E = 1 - \exp(-NP); N = kt$ $P =$ $\cos^4(\theta - \pi/8)\alpha\left(1 - \left(\frac{d}{a_0}\right) \times \left(\left(\frac{a_1}{a_2}\right)^2 \sin^2\theta + \cos^2\theta\right)^{0.5}\right)^2$ $\theta = \tan^{-1}(d_t/d_w); d_t, d_w$: particle thickness/width; $a_0 = \sqrt{(a_1^2 + a_2^2)}$	k
μ. Dehghani et al. [103]	$E = 1 - \exp(-NP); N = kt$ $P = \alpha\left(\left(a_1 - \sqrt{2}d\cos\theta\right)\left(a_2 - \sqrt{2}d\sin\theta\right)/(a_1 a_2)\right)$ $\theta = \tan^{-1}(d_t/d_w); d_t, d_w$: particle thickness/width; α: fraction open area	k
ν. Ferrara et al. [117]	$m_0\left(\sum_{j=1}^{n} y_{j,0}\left(\frac{1}{X_{ji}}\right)\left(E_i(t)^{X_{ji}} - 1\right) + \ln E_i(t)\sum_{j=n+1}^{r} y_{j,0}\right) =$ $-k2^\sigma\left(1 - \frac{d_i}{a}\right)^\sigma t$ $y_{j,0}$: initial weight fraction of particle fraction j $X_{ji} = \left((a - d_j)/(a - d_i)\right)^\sigma$ d_i, d_j: studied/other present particle diameters n, r: number of undersized/undersized + oversized particle classes	k σ (screen mesh dependent)
ξ. Soldinger; without undersized fractions [9]	$E_{j+1} = k_j B_j\left(t_{j+1} - t_j\right) + E_j$ $B_{j+1} = B_j + \left(c_j\left(1 - S_j\right) - k_j B_j\right)\left(t_{j+1} - t_j\right)$ j: time index $k_j = b\left(1 - E_j\right); c_j = f\left(w_q, w_d\right)$ B: fractional mass of undersized particles in bottom layer S: fractional mass of undersized particles stratified into bottom layer E: fractional mass of undersized particles passed through apertures	w_q (dependent on proportion of undersize material) w_d (dependent on width of particle size distribution) b (dependent on particle size)

(continued)

size class $E_i(t)$ is calculated on the basis of the fractional initial undersize mass $m_{i,0}$ and fractional actual undersize mass m_i.

Table 2 (continued)

Model number and origin	Major equations	Adjustable parameters
π. Soldinger; with undersized fractions [10]	$E_{i,j+1} = k_{i,j} B_{i,j} (t_{j+1} - t_j) + E_{i,j}$; i: particle class; j: time index $E_j = \sum_{i=1}^{n} E_{i,j}$; $B_j = \sum_{i=1}^{n} B_{i,j}$; n: number of undersized particle classes $B_{i,j+1} = B_{i,j} + (c_{i,j} (S_{i,\infty} - S_{i,j}) - k_{i,j} B_{i,j})(t_{j+1} - t_j)$; $k_{i,j} = b_i (1 - E_{i,j})$; $c_{i,j} = f(w_q, c_{d,i})$ B_i: fractional mass of undersized particles in bottom layer S_i: fractional mass of undersized particles stratified into bottom layer E_i: fractional mass of undersized particles passed through apertures	w_q (dependent on proportion of undersize material) $c_{d,1}, \ldots, c_{d,n}$ (dependent on particle size distribution) $b_1, \ldots, b_n$ (dependent on particle diameter and aperture size)
ρ. Yoshida et al. [7]	$E_j = 1 - 1/m_0 (1 - P_j) \cdot m_{j-1}$ $P_j = P_r P_{p,j-1,n_L}$; j: trial index with $j = f \cdot t$; $P_r = P_b B + P_s (1 - B)$ P_b, P_s: probability of particles passing screen boundary/screen openings B: area ratio of the boundary on the screen surface P_p: probability of particles existing at a certain vertical position in the bed $P_{p,j,n_L} = P_{pe,n_L} P_{p,j-1,n_L-1} + (1 - P_r)(1 - P_{pe,n_L}) P_{p,j-1,n_L}$; n_L: bottom layer $P_{pe} = f(c)$: probability of undersized particles passing through a particle layer	$c = \{0, \ldots, 1\}$

3.2.4 Extended Transient Screening Models to Cope for Moisture

In [123], selected phenomenological models for discontinuous screening as outlined in Sect. 3.2.3 have been extended to include the presence of moisture within the treated granular material. The special feature of the models is that, after adjusting the model parameters, they also have predictive capabilities for changes in amplitude, frequency, particle diameter, and moisture content. Table 3 gives an overview of the advanced screening process models which are titled with the name of the author and an alphabetic character. Table 3 also contains the most important equations as well as the model parameters used. All models calculate the fraction retained over time by particle size class i:

$$Y_i = Y_i(t) = m_{p,l,i}/m_{p,l,i,0}, \tag{29}$$

where $m_{p,l,i,0}$ is the initial fractional mass of the particles at $t = 0$ s and $m_{p,l,i}$ is the remaining fractional mass of the particles at time t. Note that both masses include

Table 3 Governing equations of the extended and applied phenomenological screening process models. Reprint with permission from [123]

Model number and origin	Major equations	Adjustable parameters
a. Dong et al. [124] (based on Subasinghe et al. [115])	$Y_i = (1 - P_i)^{N_i}$ $P_i = (a - d_i)^2 / (a + w)^2$ a: aperture size w: wire diameter; d_i: particle diameter $N_i = k \left(\frac{Af(1-M)^\gamma}{\sqrt{d_i}g} \right)^\alpha \frac{t}{t_{end}}$	k, α, γ
b. Subasinghe et al. [114]	$Y_i = \left(k_{s,i} exp(-k_{p,i}t) - k_{p,i} exp(-k_{s,i}t) \right) / \left(k_{s,i} - k_{p,i} \right)$ $k_{s,i} = k_s \left(\frac{Af(1-M)^\gamma}{\sqrt{d_i}g \frac{d_i}{d_{av}}} \right)^\alpha$ $k_{p,i} = k_p \left(\frac{Af(1-M)^\delta}{\sqrt{d_i}g \frac{d_i}{a}} \right)^\beta$	$k_s, k_p, \alpha, \beta, \gamma, \delta$
c. Soldinger [10]	$Y_{i,j+1} = Y_{i,j} - k_{i,j}B_{i,j}(t_{j+1} - t_j)$; i: particle class; j: time index $B_{i,j+1} = B_{i,j} + \left(c_{i,j}(S_{i,\infty} - S_{i,j}) - k_{i,j}B_{i,j} \right)(t_{j+1} - t_j)$ $Y_j = \sum_{i=1}^n Y_{i,j}$; $B_j = \sum_{i=1}^n B_{i,j}$; n: number of undersized particle classes $k_{i,j} = b_i Y_{i,j}$; $c_{i,j} = f\left(w_{q,i}, c_{d,i,j} \right)$ $w_{q,i} = k_s \left(\frac{Af(1-M)^\gamma}{\sqrt{d_i}g \frac{d_i}{d_{av}}} \right)^\alpha$ $b_i = k_p \left(\frac{Af(1-M)^\delta}{\sqrt{d_i}g \frac{d_i}{a}} \right)^\beta$ B_i: fractional mass of undersized particles in bottom layer S_i: fractional mass of undersized particles stratified into bottom layer	$k_s, k_p, \alpha, \beta, \gamma, \delta$

the particle mass and additionally the mass of liquid assigned to the particles. The fraction retained Y is related to the screening efficiency by $Y = 1 - E$.

4 Benchmarking and Extension of Process Models Based on Discrete Element Simulations

In the following, DEM investigations basing on the modelling framework as introduced in Sect. 2 of dry particle systems are performed in Sect. 4.1 for continuous [109] and in Sect. 4.2 for discontinuous [122] screening, respectively. Main features

of the relevant screening subprocesses are derived and available process models as introduced in Sects. 3.2.1–3.2.3 are benchmarked for both continuous and discontinuous processes. In Sect. 4.3 results for discontinuous screening under the influence of moisture are validated against experiments. Thereafter process models as derived in [123] and stated in Sect. 3.2.4 are benchmarked against the obtained DEM results.

4.1 Continuous Screening

As a first case screening of a polydisperse feed material is investigated by the DEM in a continuously operated screen apparatus as shown in Fig. 9a. In Sect. 4.1.1 the numerical setup is described and the required simulation parameters are outlined. In Sect. 4.1.2 the results are presented as obtained from the DEM (section "Numerical Investigations") and the process models (Section "Benchmarking of Steady State Separation Curve Screening Models").

4.1.1 Numerical Setup and Simulation Parameters

The considered apparatus is equipped with a wire screen of 0.35 m x 0.1 m size. The square aperture size is 4.9 mm while the wire diameter is 1 mm. In the initial configuration, the apparatus is vibrated with 27.6 Hz with a stroke angle of 45° to the horizontal at an amplitude of 1.76 mm (Fig. 9a). The mass flow of the polydisperse feed material amounts to 0.1 kg/s in the initial setup. The material comprises of particles with a density of 2700 kg/m^3 subdivided equally into 100 size classes ranging from 2.4 mm to 7.35 mm. Besides spheres, cylinder-like and double cone-like particles are studied in this investigation (see Fig. 9b). The non-spherical particles (shapes (2) and (3)) have an aspect ratio of 1.55. The cylindrical particles (shape (2)) are volume equivalent to the spherical particles and have a hemispherical termination at both ends. The double cones (shape (3)) have the same minor dimension as the spheres. If needed for analysis or as a parameter for a screening model, the
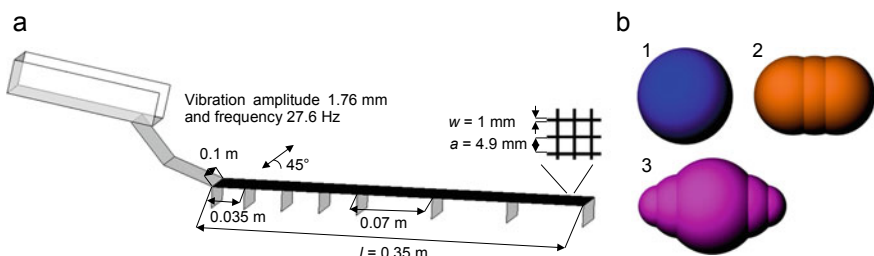

Fig. 9 a Continuous screening apparatus with wire structure; **b** Considered particle shapes. Reprint with permission from [109]

equivalent diameter of a complex shaped particle is calculated from its volume as $d_{vol} = \sqrt[3]{6 \cdot V / \pi}$, where V is the volume of the particle.

DEM parameters were used for the simulations in accordance with Delaney et al. [125] and Cleary [15] applicable for standard industrial quarry rock, with the stiffness of the normal spring $k^n = 1000$ N/m, the stiffness of the tangential spring $k^t = 500$ N/m, the particle-particle restitution coefficient $e_{PW}^n = 0.4$, the particle-wall restitution coefficient $e_{PW}^n = 0.5$, and the particle-particle and particle-wall friction coefficients $\mu_{c,PP} = \mu_{c,PW} = 0.5$.

4.1.2 Results and Discussions

For each particle shape, the influence of the parameter modifications outlined in Table 4 is examined. Starting from the initial setup (base case), variations of the vibration amplitude and frequency, stroke angle and particle mass flow are performed. Only one parameter is varied at a time. The simulation results are subsequently compared to results attained by separation curve and phenomenological screening process models (comp. Sects. 3.2.1 and 3.2.2) whose adjustable parameters are fitted by genetic algorithms [126] for the separation curves or to the fraction/fractions retained on the screen obtained from the DEM, respectively.

Numerical Investigations

In the DEM simulations, particles are continuously fed onto the vibrated screen well mixed until a steady state is reached. The steady state is reached, when the inlet flow rate is equal to the sum of overflow and underflow. The simulations are then maintained for at least $\Delta t = 10$ s, thereafter. All analysis presented are based on this time period of $\Delta t = 10$ s in the steady state. Due to the inclined vibration of the screen, particles are transported along it. The finest particles nearly instantly pass the apertures after getting in contact with the screen surface. Larger undersized particles need more attempts, and hence time, to pass and therefore travel along the screen for some distance before they pass through the screen. A bottom layer of particles larger than the aperture size forms out on the screen which hinders the subsequent passage of the undersized particles. The bottom layer is whether dilute or dense and covered with further layers of coarse material, whereby this depends on the

Table 4 Initial setup and performed variations of the continuous screening investigations

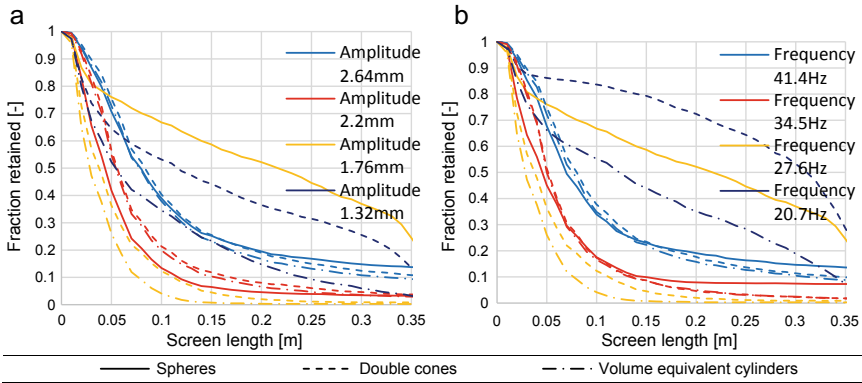| Parameter	Initial	Var. 1	Var. 2	Var. 3
Amplitude [mm]	1.76	1.32	2.2	2.64
Frequency [Hz]	27.6	20.7	34.5	41.4
Stroke angle [°]	45	30	60	–
Particle mass flow [kg/s]	0.1	0.05	0.15	0.2

Fig. 10 **a**, **b** Particle passage through the screen openings for the three considered particle shapes over screen length for varying amplitudes (**a**) and frequencies (**b**). Reprint with permission from [109]

screen configuration, the operational parameters and the shape of the particles. As a consequence, fine and near mesh sized particles have to stratify downwards through the gaps between the oversized particles to approach the screen surface. Only then the fine particles regain the possibility to pass through the screen apertures.

In order to achieve comparability for the particle passage between the different cases examined, the mass flow rate passed through is summed up for all particle classes with smaller diameters than the apertures and normalized by the feed throughput. For all shapes the threshold diameter $d = d_{vol}$ is aligned with the aperture size. Thereby, the fraction retained Y over the screen length is obtained which is related to the screening efficiency by $Y = 1 - E$. The fraction retained is outlined in Figs. 10 and 11. Among the particle shapes considered, the highest passage ability in most studies is achieved by volume equivalent cylinders, followed by double cones and then spheres, which is mostly caused by pegging of apertures by the latter.

In the base case configuration using spheres (shown in Figs. 10 and 11 in yellow), the steady state is reached at about $t = 65$ s. In the start-up phase, particles pass through the apertures at the beginning of the screen, but over time, particles accumulate due to pegged apertures. As a result, the passage of the particles shifts towards the end of the screen over time, which is associated with long residence times, especially for particles close to the mesh size. Parts of the screen surface are completely blocked by particles of near mesh size, and therefore the fraction retained curves in Figs. 10 and 11 for the base case show a flat, near-linear decline, rather than an initial rapid decline, followed by a flattening as observed mostly for non-spherical particles. Because of the thick particle layer, very small particles in particular require more time to stratify and thereby move along the screen, resulting in a delayed/shifted transition into the underflow, or they even remain on the screen and get discharged into the overflow. In the base case, some of the undersized particles pass the apertures near the end of the screen, as larger particles previously pegging the apertures get aerated when being discharged into the overflow.
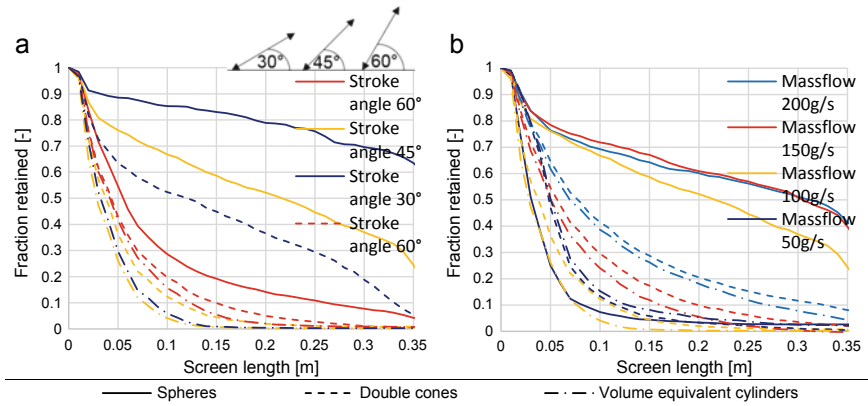
Fig. 11 **a**, **b** Particle passage through the screen openings for the three considered particle shapes over screen length for **a** varying stroke angles and **b** mass flows. Reprint with permission from [109]

In the first variation performed (Fig. 10a), the initial amplitude of 1.76 mm is varied according to Table 4. A reduction of the amplitude is not feasible for spheres due to too excessive accumulation of particles on the screen, whereas an amplitude of 1.32 mm is applicable for complex shaped particles. However, this leads to an intensive accumulation of particles and thus to a shifted/delayed particle passage, especially for double cones. Here, the steady state is reached after $t = 50$ s. Increasing the amplitude to 2.2 mm eliminates the problems for spheres, improves their particle passage by enhancing their transport along the screen. If a larger amplitude is applied beyond a threshold (amplitude >2.2 mm) undersized near mesh particles reside longer on the screen because of an extended free flight period resulting in less particle screen contacts and thus less available attempts to pass (not shown in Fig. 10) which results in a reduced particle passage (Fig. 10a).

The second parameter variation (Fig. 10b) deals with the change of the frequency in accordance with Table 4. The results are qualitatively consistent with those from the first investigation. In case of a reduced frequency for non-spherical particles, the steady state is not reached before $t = 70$ s. Accordingly, a lower frequency results in an intensively retarded particle passage and reduced transport for all particle classes. A frequency of 34.5 Hz in case of spheres results in an improved particle passage and a stronger transport for all size classes (not shown in Fig. 10b). A further increase above a threshold frequency reduces the passage rates.

In the simulations, a stroke angle of 45° to the horizontal is first used, which is changed according to Table 4 in the third investigation (Fig. 11a). For spheres, a lower vertical stroke component (vibration plane tilted by 30°) leads to a pronounced piling of particles already on the first parts of the screen because it is less probable for pegged spheres to leave blocked sieve openings. Thus, the undersized material passes the apertures delayed/shifted along the screen towards its end or it is discharged from the screen as part of the overflow. In this way, 60% of the undersized material

is released. Although the support for horizontal transport is lower, a stronger vertical motion component (vibration plane tilted by 60°) speeds up the transport of spheres and thereby also improves the particle passage due to a faster removal of pegged particles. For double cones, the change in the stroke angle in both directions leads to delayed particle passage. A stroke angle of 30° leads to particle accumulation and therefore slower particle transport and longer residence times. In contrast, a stroke angle of 60° leads to delayed/shifted passage. For volume equivalent cylinders, a decreased stroke angle has only minor effects on the passage of particles, although particle accumulation is observed. An increased stroke angle leads to a reduced transport, delayed particle passage and less near mesh particles in the overflow.

The fourth variation takes into account the particle mass flow rate (Fig. 11b). The probability of pegging for spheres is increased for larger particle mass flows with more near orifice sized particles being present. Due to a larger bed height and therefore a greater necessity for stratification, the use of higher mass flow results in delayed/shifted particle passage and flat fraction retained curves (Fig. 11b). In comparison, spheres in a shallower bed caused by a lower particle mass flow require less time for stratification and hence passage, especially with so few near mesh sized particles present that pegging is a rare event. If the mass flow is further increased from $\dot{m} = 150$ g/s to $\dot{m} = 200$ g/s, the percentage of undersized particles remaining on the screen does not appear to change for spheres (Fig. 11b). Due to the higher mass flow $\dot{m} \geq 100$ g/s, the undersized particles, but also the oversized particles entrained in the bed layer remain longer on the screen with slightly increased transport. An increase in the mass flow in the case of complex shaped particles also leads to a delayed/shifted particle passage (comp. Fig. 11b). However, the fraction retained curves remain steep compared to spheres as there is no pegging of particles or blocking on the screen.

Benchmarking of Steady State Separation Curve Screening Models

In a first step, the steady state separation curve screening models are fitted and then benchmarked against the data obtained in section "Numerical Investigations" by the DEM. For the benchmarking over a larger number of investigations in case of separation curve models an average deviation of the simulated and model predicted separation curves is calculated with $\left(\sum_{i_S=1}^{r_S} |T_{sim}(i_S) - T_{mod}(i_S)|\right)/r_S$ where r_S is the total number of considered particle classes i_S. Figure 12 shows the summed up deviations between steady state separation curve screening models according to Sect. 3.2.1 and simulations using the DEM with spheres (Fig. 12a), double cones (Fig. 12b) and volume equivalent cylinders (Fig. 12c) according to Table 4.

With exception of model No. I by Dehghani et al., the investigated steady state separation curve screening models do not consider the particle shape. Nevertheless, the differences between the adjusted models and the DEM results remain small because the separation curve models are adjusted separately for each simulation since they do not have any predictive capabilities. Separation curve screening models can easily represent partition numbers forming an ideal separation curve (unit step function) or a symmetrical S-shaped curve. For spheres (Fig. 12a), the closest result to an ideal
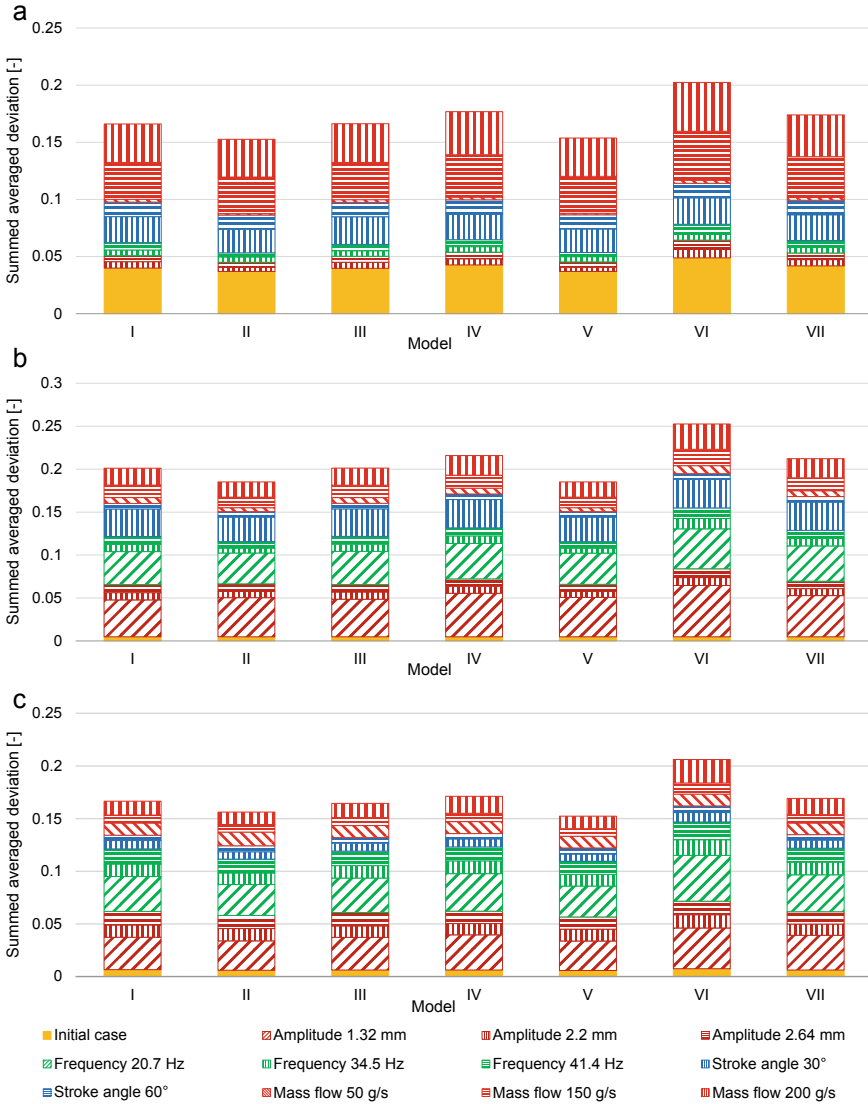
Fig. 12 Deviations between steady state separation curve screening models (Sect. 3.2.1) and discrete element simulations summed up for all investigated variations (Table 4) for **a** spheres, **b** double cones and **c** volume equivalent cylinders. Reprint with permission from [109]

separation curve can be achieved when either an amplitude, a frequency, a stroke angle or an inclination angle slightly larger than in the base case configuration is used. Therefore, pegging is prevented, but the particle transport is still slow enough to ensure a good passage. The very low deviations are caused by undersized near

mesh particles which do not pass through the apertures and thus lead to symmetric separation curves. Geometric scaling (size reduction) or a lower mass flow rate also leads to nearly ideal separation curves, resulting in small differences between DEM results and separation curve models. The amount of small particles in the overflow increases in cases with a greater transport velocity induced by larger amplitudes, frequencies or inclination angles. The simulation results do not lead to symmetrical S-shaped curves, because undersized near mesh particles not passing the screen. This leads to larger deviations between the separation curve screening models and the simulation results. For the base case configuration or when a higher mass flow or a stroke angle with a larger horizontal motion component is employed, the near mesh sized particles are intensively pegging the apertures. Because of it, many small and even very small particles are discharged into the overflow. As a result, separation curve screening models show larger deviations when adjusted to these simulation results.

Non-spherical particles (Fig. 12b, c) having an equivalent diameter larger than the orifice size can pass the sieve apertures into the underflow if their minor-diameter is smaller than the aperture size. In turn, undersized near mesh particles are discharged into the overflow. As a result, the simulation results form symmetric S-shaped curves that are readily represented by separation curve screening models. However, the passing rates of near mesh sized non-spherical particles are more sensitive than with spherical particles, especially when a higher mass flow is applied or when particles accumulate on the screen when the screen is operated at a small amplitude or frequency. In these cases, the separation curves increase unevenly and therefore, much larger deviations occur. A faster particle transport, which is achieved by applying a larger amplitude or frequency, also results in a few more small and oversized near mesh particles in the overflow amounting to larger deviations.

Smaller deviations for separation curve models result in some cases when double cones are screened instead of spheres (Fig. 12b) due to a lower pegging probability. The largest deviations result from applying of lower amplitudes and frequencies followed by stroke angles with small vertical motion components. The smallest deviations for double cones arise for the base case configuration.

The summed up deviations for volume equivalent cylinders (Fig. 12c) show the lowest deviations of the investigated shapes due to the lowest pegging probability. The largest deviations with volume equivalent cylinders occur for low amplitudes and frequencies due to the formation of unsymmetrical separation curves. On the other hand, good results are achieved for the base case configuration independent of stroke angle, and for cases with a slightly enlarged mass flow.

The lowest overall deviations, summed up over all investigations, can be obtained using the model No. II by Plitt and the first revised model by Trawinski (No. V). In both models, the term (d/d_{cut}), which increases with particle diameter, is influenced by one or even two adjustable parameters in the exponent independent of additional parameters [see Eqs. (21) and (24)] which gives a good adaptability for both models. The largest deviations are found in the case of the second revised model of Trawinski (No. VI). Here, both adjustable parameters are present in the exponent of the term (d/d_{cut}), but both depend on the particle size d [comp. Eq. (25)].

Benchmarking of Steady State Spatially Resolved Screening Models

In a second step, the simulation results presented in section "Numerical Investigations" are used to benchmark the steady state spatially resolved screening process models described in Sect. 3.2.2. Thereby the fraction retained on the continuous screening apparatus in dependence on screen length obtained from the DEM simulations is compared with data from spatially resolved phenomenological models which are fitted to the DEM results by adjusting their respective model parameters. For the benchmarking of a larger number of investigations, an average deviation of the simulated and process model predicted fraction retained is calculated for models, where the whole fine material is considered as one lumped undersized fraction by using $\left(\sum_{k=1}^{j}|E_{mod}(k) - E_{sim}(k)|\right)/j$, where j is the total number of considered positions along the screen k. For models in which the different undersized particle classes i are considered as fractions (Nos. 4, 8, 9, 10, 11, 13), the average of the obtained fractional deviations is calculated by using $\left(\sum_{i=1}^{l}\left(\sum_{k=1}^{j}|E_{mod}(i, k) - E_{sim}(i, k)|\right)\right)/(j \cdot r)$, where r is the total number of undersized fractions. The screen of length 0.35 m in this process is divided into intervals of 0.01 m.

In Fig. 13 the summed up particle passage deviations between steady state spatially resolved screening models according to Sect. 3.2.2 and discrete element simulations for spheres (Fig. 13a), double cones (Fig. 13b) and volume equivalent cylinders (Fig. 13c) for all investigated variations (see Table 4) are shown.

Regardless of shape, the models that do not account for the division of undersized particle fractions (Nos. 1, 2, 3, 5, 6, 7 and 12) are the fastest to adjust and get low deviations as only the lumped fraction retained curve is to be fitted to the simulation results instead of the fraction retained curves of all undersized particle classes. Among these models, the model by Soldinger (No. 12) followed by Andreev et al. (No. 2), Subasinghe et al. (No. 6) and Grozubinsky et al. (Nos. 5, 7) show the lowest overall deviations when spheres as shape are considered (Fig. 13a). All of these models use more than one adjustable parameter. The models Nos. 5 and 7 can be easily reduced to the rate law (model No. 1); for the screening intensity $\beta \gg 1$ the term $exp(-\beta t)$ becomes zero (see [122]). In both models the additionally introduced coefficient of proportionality q provides an improvement in accuracy for screening if many different size classes are under consideration. The model by Trumic and Magdalinovic (No. 3) shows the largest deviations of the models, which does not take into account the division of undersized particle fractions due to the use of only one adjustable parameter.

For a model that accounts for the division of undersized particle fractions, relatively low deviations are obtained by the model of Standish (No. 4). This is achieved by using one adjustable parameter per size class. Although the model by Ferrara et al. (No. 11) exhibits overall minor deviance and accounts for different particle size classes as well as uses only a few adjustable parameters, it has the disadvantage of a long adjustment time because it has to be fitted iteratively. Slightly larger deviations are visible for the fractioned model by Soldinger (No. 13) with the benefit of a shorter fitting time. The probabilistic model by Subasinghe et al. (No. 8) is adjusted
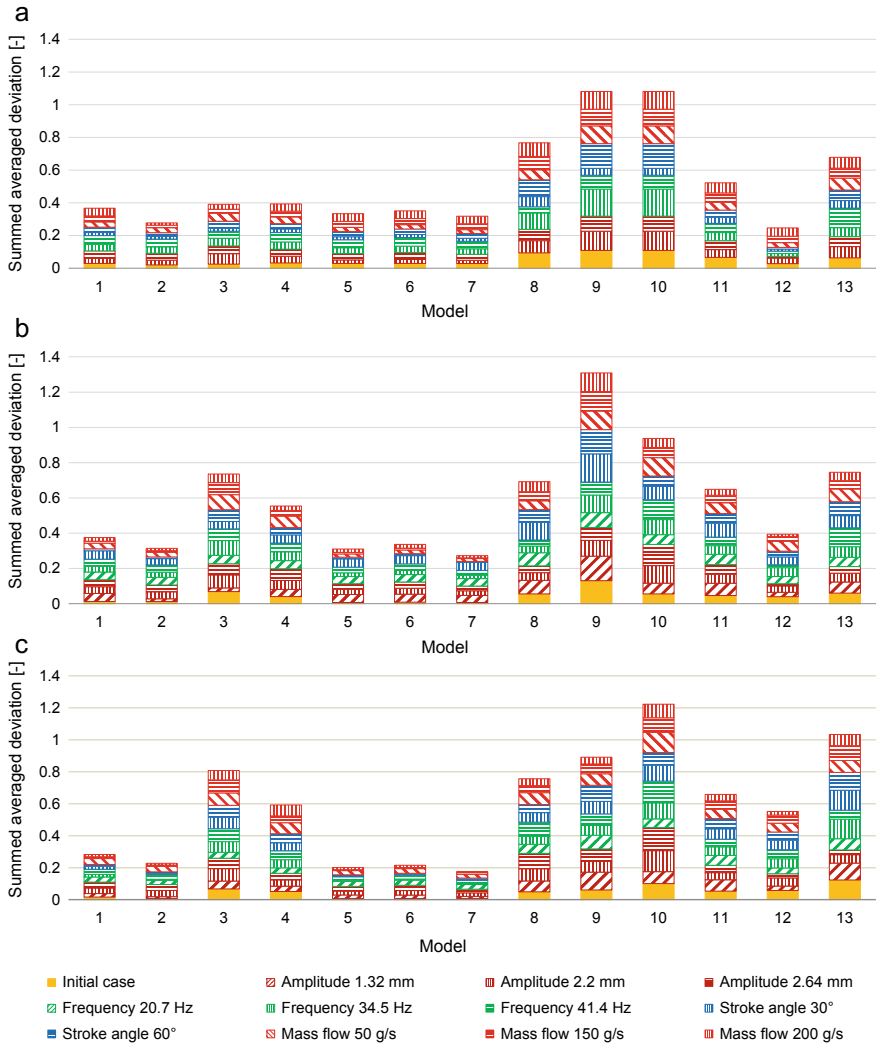
Fig. 13 Particle passage deviations between steady state spatial resolved screening models sorted according to Table 1 and discrete element simulations summed up for all investigated variations according to Table 4 for **a** spheres, **b** double cones and **c** volume equivalent cylinders. Reprint with permission from [109]

and applied also fast, however exhibits larger deviations. The models by Nakajima et al. (No. 9) and Deghani et al. (No. 10) demonstrate the largest overall deviations when considering spheres. This is due to the fact that they represent particle size class resolved results of a screening process using only one adjustable parameter. Note, that these models (No. 9 and No. 10) are identical in the case that spherical particles are addressed.

The initial (base) case with delayed/shifted particle passage and a resulting flat fraction retained curve is comparatively easy to model. This results in minor deviations for most of the investigated models. Also simulation cases with immediate particle passage and strongly decreasing fraction retained curves show no major discrepancies between models and DEM results, likewise. Greater differences occur when the fraction retained curves stagnate over a certain length of the screen or when they are decreasing unevenly. The models that account for the division of undersized particle fractions, in particular models Nos. 8–10, have greater difficulties when the differences between the passage rates of undersized particles are erratic. This could be the case, if the particles are transported with higher velocity on the screen when e.g. a large amplitude, frequency or inclination angle is used.

In the considered cases using double cones (Fig. 13b) the models by Grozubinsky et al. (Nos. 5, 7) and Andreev et al. (No. 2) followed by the model by Subasinghe et al. (No. 6) are adjusted to the simulation results with the smallest deviations. Although model No. 4 needs many adjustable parameters, it demonstrates comparatively large deviations because it does not consider the shape of the particles. Again, model No. 11 is the model with lowest deviations which accounts for the division of undersized particles in fractions without adjusting parameters for each size class. For the case of double cones, however, it leads to larger deviations and model No. 8 by Subasinghe et al. achieves nearly the same results with less computations. With the models by Nakajima et al. (No. 9) and Deghani et al. (No. 10), the largest deviations are obtained again.

The models by Grozubinsky et al. (Nos. 5, 7) demonstrate the smallest deviations for volume equivalent cylinders (Fig. 13c). Here, the probabilistic model No. 7 achieves slightly better results than the deterministic model, since the dispersion of the particles is taken into account. Unlike the two former investigated shapes (spheres and double cones), model No. 12 by Soldinger does not get the lowest deviations caused by randomly passing particles with an equivalent diameter larger than the aperture size. For the same reason, model No. 13 by Soldinger shows more deviations in comparison to the other shapes. Again, model No. 3 by Trumic and Magdalinovic reveals comparatively large deviations because of its simplicity and not considering the particle shape. For the volume equivalent cylinders, model No. 11 by Ferrara et al. shows only slightly larger deviations in the comparison to model No. 4 by Standish, which requires much more adjustable parameters. In addition, model No. 11 has much lower deviations than model No. 3, in which only the undersized fraction as a lumped entity is considered. For volume equivalent cylinders, model No. 10 by Deghani et al. shows the largest deviations due to its condition for the probability function and because the use of only one parameter for all particle size classes. The revised model No. 9 with a similar model structure and the same number of model parameters gives comparatively lower deviations.

4.2 Discontinuous Screening Without Moisture

As a second case screening of a polydisperse feed material is investigated by the DEM in a batch screen apparatus as shown in Fig. 14. In Sect. 4.2.1 the numerical setup is described and simulation parameters are outlined as required for the DEM. In 4.2.2 the numerical results are presented as obtained from the DEM in section "Numerical Investigations" and as derived by process models in section "Comparison of Phenomenological Screening Process Models".

4.2.1 Numerical Setup and Simulation Parameters

The considered batch screening apparatus is equipped with a wire screen comprising 34×34 apertures on a floor area of 0.2 m × 0.2 m with the aperture size 4.9 mm and the wire width 1 mm. In initial configuration, the apparatus is vibrated with 27.6 Hz with a stroke angle of 90° to the horizontal at an amplitude of 3.52 mm (Fig. 14).

The polydisperse feed consists from particles with a density of 2700 kg/m^3. The particles are subdivided into three relevant size classes consisting of coarse, near mesh and fine material represented, in case of spheres, by particles with average diameters of 7.35 mm, 4.2875 mm and 2.45 mm, respectively. In the base case, the mass of feed amounts to 4 kg, divided equally into the examined particle classes. The applied DEM parameters are the same as used in Sect. 4.1.1. Besides spheres, differently sized cylinders and double cones are studied in this investigation (see Fig. 9b). Starting from the base case, variations of the stroke angle, vibration frequency and amplitude, and total particle mass are performed for all three particle shapes varying one of the parameters at a time (Table 5).

Fig. 14 Batch screening apparatus with wire structure. Reprint with permission from [122]
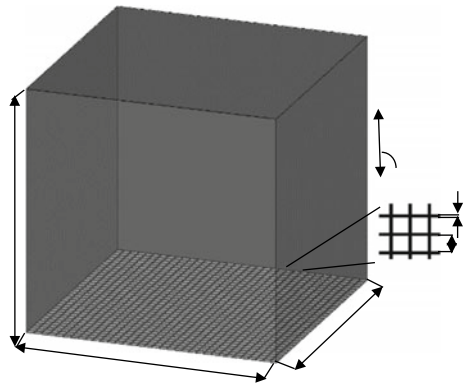
Table 5 Initial setup and performed variations of the batch screening investigations

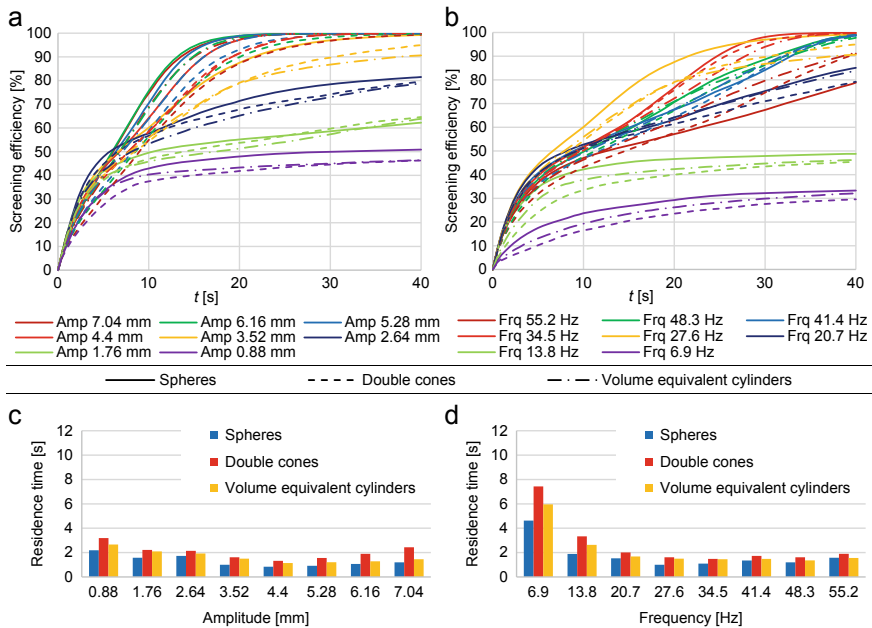| Parameter	Initial	Var. 1	Var. 2	Var. 3	Var. 4	Var. 5	Var. 6	Var. 7	Var. 8
Amplitude [mm]	3.52	0.88	1.76	2.64	4.4	5.28	6.16	7.04	10.56
Frequency [Hz]	27.6	6.9	13.8	20.7	34.5	41.4	48.3	55.2	–
Stroke angle [°]	90	60/120	45/135	30/150	–	–	–	–	–
Particle mass [kg]	4	1	2	3	5	6	–	–	–

Fig. 15 **a**, **b** Particle passage through the screen openings for the three considered particle shapes for **a** varying amplitudes and **b** frequencies and **c**, **d** corresponding average residence times in the bottom layer for **c** varying amplitudes and **d** frequencies. Reprint with permission from [109]

4.2.2   Results and Discussions

DEM simulations are performed. The obtained outcomes from the simulations are later compared to results attained by phenomenological screening process models (Table 2, Sect. 3.2.3) whose adjustable parameters are fitted by genetic algorithms to the retained mass on the screen obtained from the DEM [126].

Numerical Investigations

Well mixed particles are fed into the screen apparatus and then vibrated for $t = 40$ s. Due to the movement of the screening surface, fine particles and near mesh size particles stratify downwards through the gaps between the bigger particles. By reaching the bottom in particular the fine particles get the possibility to pass through the apertures in the screening surface. Due to the smallest ratio between the fine particle's minor axis and the oversized particles or else the screen apertures, the possibility of passing through interstices between particles and screen openings is highest for them. Among the particle shapes considered, the highest passage ability is achieved by spheres followed by the non-spherical shapes in all investigations (see Figs. 15, 16 and 17).
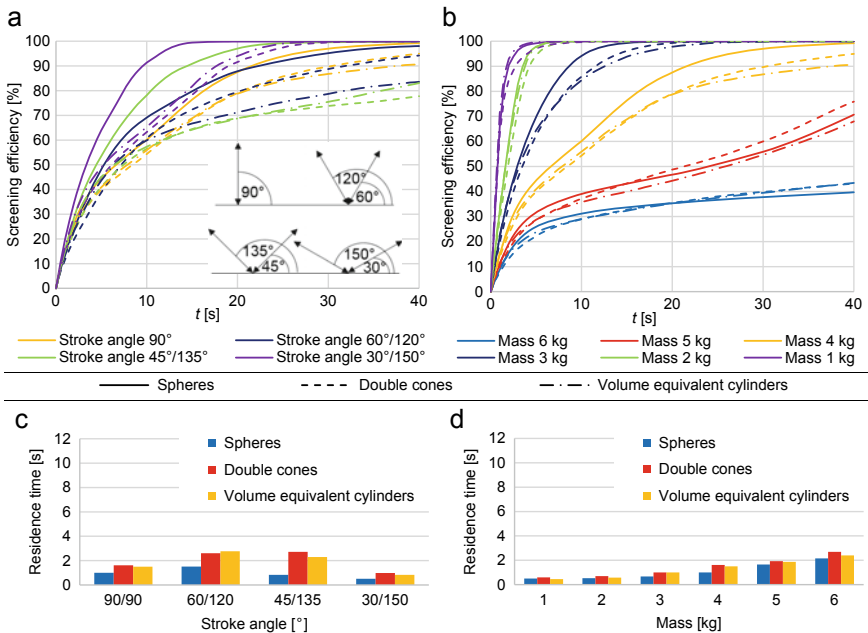
Fig. 16 **a**, **b** Particle passage through the screen openings for the three considered particle shapes for **a** varying stroke angles and **b** bulk masses and **c**, **d** corresponding average residence times in the bottom layer for **c** varying stroke angles and **d** bulk masses. Reprint with permission from [109]

In the first study (Fig. 15a) the amplitude of 3.52 mm in the base case is varied according to Table 5. Considering the results for the smallest amplitude of 0.88 mm, with approximately 50% residuals remaining on the screen, the particle passage for larger amplitudes significantly increases regardless of the particle shape. The passage increases up to a critical amplitude of 6.16 mm (5.28 mm for double cones) and then stagnates or decreases slightly. Larger amplitudes increase the porosity in the particle bed which leads to larger gaps between the oversized particles resulting in an improved stratification of smaller particles. In contrast, larger amplitudes beyond a critical amplitude result in an elevation of the particle bed and therefore to larger distances between particles and the screen surface reducing overall passage. In addition, at higher amplitudes, impacts are of higher velocity and therefore characterized by a stronger rebound which also affects the passage through the apertures.

This behavior can be confirmed by Fig. 15c, in which the simulations with an amplitude of 4.4 mm show the shortest residence time in the bottom layer, which is the layer directly on top of the screen surface, for undersized particles regardless of shape. At this amplitude, the possibility to pass through the apertures is greatest. However, larger amplitudes provide a better overall passage rate, because overall passage is affected by both stratification and the ability to pass through the apertures. It can explain why highest overall passage is shifted to amplitudes larger than 4.4 mm where stratification is increased and residence time in the bottom layer is yet not

strongly lengthened. For double cones, it can be seen exemplarily that residence times are increased in the bottom layer for larger amplitudes (Fig. 15c) which reduces overall particle passage (Fig. 15a).

The second study (Fig. 15b) deals with the variation of the frequency (Table 5). Here, also the two lowest frequencies result in the least particle passage with under 50% after $t = 40$ s, due to a low stratification. In addition, the particles are in an immobile state, leaving them few opportunities to come in direct contact with apertures, forcing them to reside an extended period of time in the bottom layer independent of particle shape (Fig. 15d). All the other settings show similar results for the overall passage throughout the first 10 s of the investigation, but with final residual mass on the screen varying between 0 and 20% at the end of the screening time. The frequency value of 27.6 Hz shows the best passage ability over more than half of the simulation time, before being surpassed by the frequency of 34.5 Hz.

Initially, the simulations use a stroke angle of 90° to the horizontal (Table 5) which in the third investigation is changed to an oscillating movement consisting of two stroke angles with varying horizontal and vertical components (Fig. 16a). An alternating stroke angle of 45°/135° significantly improves the particle passage for spheres, however reduces the passage of complex shaped particles. In contrast, a stroke angle of 30°/150° increases the screening efficiency of all particle shapes because particles have enhanced chances to enter an aperture and pass it. Using an angle of 60°/120° significantly reduces the passage only for cylindrical particles. The above mentioned observations can also be confirmed by the enhanced residence times of non-spherical particles in the case of 60°/120° and 45°/135° stroke angles as well as by the reduced residence times in the bottom layer for spheres for stroke angles of 45°/135° and for all particle shapes for stroke angles of 30°/150° (Fig. 16c). In general, a combination of a stronger horizontal with a less intense vertical motion component as e.g. for 30°/150° facilitates more possibilities to pass the screen openings for all undersized particle shapes, while a combination of a stronger vertical with a weaker horizontal motion forces the oversized elongated non-spherical particles to align vertically with the screening surface, which leads to pronounced pegging of the apertures.

The fourth investigation deals with a variation of total particle mass (Fig. 16b). Due to a lower bed height and thus a faster stratification, the application of a lower mass leads to a faster particle passage. In comparison, particles in a thicker bed layer, which is caused by a larger particle mass, take extra time to stratify and then to pass. The probability of pegging is larger for particle masses with more oversized particles being present. As a result, the undersized particles remain longer in the bottom layer when more mass is applied to the screen (Fig. 16d).

Comparison of Phenomenological Screening Process Models

The simulation results described in section "Numerical Investigations" are used to benchmark the phenomenological screening models as outlined in Table 2. An average deviation of the simulated and model predicted mass is calculated for

models, which consider the whole fine material as one lumped undersized fraction, by $\left(\sum_{k=1}^{j}|m_{sim}(k) - m_{mod}(k)|\right)/j$, where j is the total number of considered time steps k. For models, which consider the different undersized particle classes i as fractions, the average of the obtained fractional deviations is considered by $\left(\sum_{i=1}^{l}\left(\sum_{k=1}^{j}|m_{sim}(i,k) - m_{mod}(i,k)|\right)\right)/(j \cdot l)$, where l is the number of undersized fractions.

In Fig. 17 the summed up deviations of all performed simulations using spherical particles (Fig. 17a, b), double cones (Fig. 17c, d) and volume equivalent cylinders (Fig. 17e, f) for varying amplitudes (Fig. 17a, c, e) and frequencies (Fig. 17b, d, f) for all considered process models are presented. Almost all models have problems for representing flat residual mass curves, which are caused by small amplitudes or low and high vibration frequencies. The kinetic models by Andreev et al. (model β), Standish (model δ) and Subasinghe et al. (model ζ) as well as the probabilistic models by Subasinghe et al. (model θ) and Ferrara et al. (model ν) as well as the fractional complex model by Soldinger (model π) demonstrate the best overall results. However, they rely on empirical model parameters (model β) or, because of their non-explicit functional form, require long adjustment times during fitting (model ν).

At different amplitudes, the models β and γ show particularly suitable results. The functional forms with an additional adjustable parameter as exponent of the time t can compensate well for the variations in residual mass on the screen caused by different amplitudes. Due to optimization for continuous screening and due to a simple parameter structure, deviations from the model by Trumic and Magdalinovic (model γ) are largest, although acceptable results for some small amplitudes and frequencies of e.g. 6.9, 20.7 and 55.2 Hz are obtained. However, model γ has difficulties to represent simulations with strong residual mass decrease and complete depletion of material caused by large amplitudes and passage optimized frequencies, respectively. In all investigated cases (Fig. 17) the models α, ε, η, θ, κ, λ and μ indicate deviations of the same order of magnitude. Models κ, λ and μ rely directly on the screening efficiency of the rate law (model α), where only the ranges of the model parameters are changed. These altered ranges may affect the setting of the model parameters (easier guess of initial values and quicker convergence) or improve their physical meaning as e.g. in model κ, where passage probabilities are introduced, but overall model accuracy is unaffected.

In addition to quantitatively better results, nearly all models represent the simulations with complex shaped particles qualitatively similar to those with spheres. Total deviations are smaller for double cones in comparison with volume equivalent cylinders. Model ρ by Yoshida et al. shows despite its complexity comparatively large deviations, because it is derived for a batch simulation setup differing from the setup used here. From the comparison of the two models by Soldinger (models ξ and π), it can be concluded that a representation of different fractions in a lumped way can reduce model accuracy, especially in complex models where stratification is considered in detail.
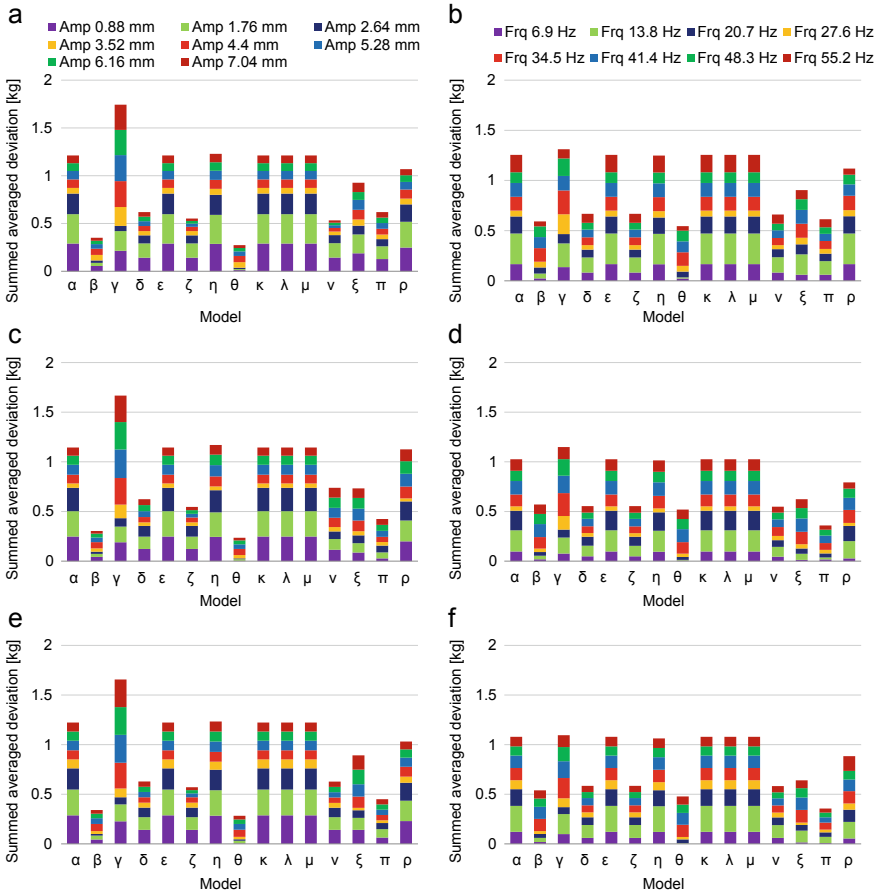
Fig. 17 Particle passage deviation between phenomenological models sorted according to Table 2 and discrete element simulations summed up for various **a**, **c**, **e** amplitudes (spheres, double cones, volume equivalent cylinders); **b**, **d**, **f** frequencies (spheres, double cones, volume equivalent cylinders). Reprint with permission from [109]

In Fig. 18 particle passage deviation between phenomenological models and DEM simulations performed with spheres (Fig. 18a, b), double cones (Fig. 18c, d) and volume equivalent cylinders (Fig. 18e, f) for varying stroke angles (Fig. 18a, c, e) and masses (Fig. 18b, d, f) are shown.

The results for various vibrations differ from the previously discussed results by obtaining much better results for spheres in comparison to non-spherical particles, except when model γ is used. The model γ shows a better accuracy for complex shaped particles, because in the simulated cases a final screening efficiency of 100% is not reached, which is relatively easy to represent with this model. Some models have problems to represent complex shaped particles agitated by an oscillating movement
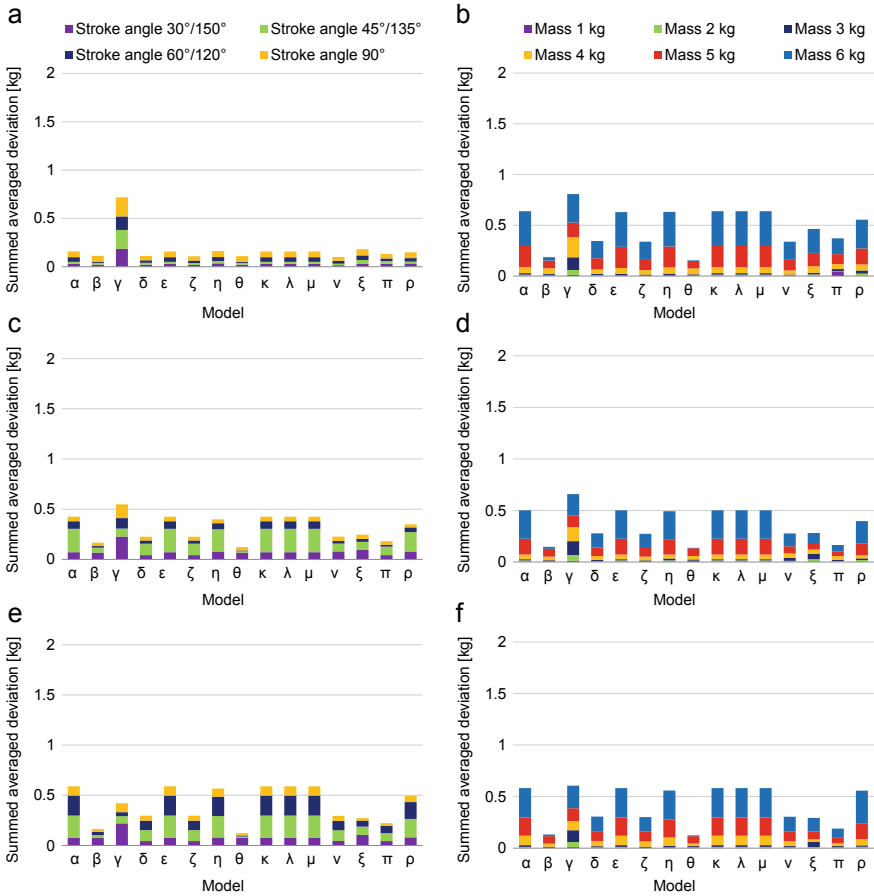
Fig. 18 Particle passage deviation between phenomenological models sorted according to Table 2 and discrete element simulations summed up for various **a**, **c**, **e** stroke angles (spheres, double cones, volume equivalent cylinders); **b**, **d**, **f** masses (spheres, double cones, volume equivalent cylinders). Reprint with permission from [109]

especially for combinations of 45°/135° and to some extend also for 60°/120° (see Fig. 18c, e). Strong pegging of apertures is reported for these agitation modes in case that non-spherical particles are used. As is expected, screening process models are not able of representing these phenomena, which are observed in the DEM, where orientations of every particle are tracked.

Variation of the mass has a similar effect on all three investigated particle types as the variation of amplitudes (see Fig. 17a, c, e)—deviations increase when a larger initial particle mass is applied to the screen. Although model β shows good time averaged behavior, larger maximum deviations are evident for simulations with very low mass (not shown in Fig. 18), especially at the beginning of the screening. Under-sized particles are less disturbed by oversized particles during screening, when a

lower bulk mass is used. This results in a more steadily decreasing retained mass on the screen allowing for more accurate modeling by the screening process models as a consequence. For both cases, a varying stroke angle and a mass variation, models β and θ show particularly suitable results due to their functional forms, which can take varying mass depletions into account.

4.3 Discontinuous Screening with Moisture

To reliably go the step from DEM modelling of dry screening to screening under moist conditions requires the validation of the model extensions described in Sect. 2.4 under real screening conditions. Therefore, a validation of the used DEM model under these conditions has been performed shading light on the related subprocesses and their linkage to liquid bridge formation, stressing and rupture (see [29]). Results on this are presented in Sect. 4.3.2 by comparing insights obtained from batch screening experiments and simulations. The investigated setup is outlined in Sect. 4.3.1. The successful validation allows the application of the extended screening models from Sect. 3.2.4 (see [123]) in the final Sect. 4.3.3.

4.3.1 Experimental and Numerical Setup

A batch screening apparatus, which can be applied for dry and wet screening (see Fig. 19), is used for the experiments and the modelling in this study. The screen apparatus is a modified "Haver and Boecker EML digital plus" batch screen tower with a circular screen surface, which is on top additionally equipped with a feed bin to ensure that the particles in experiments and simulations reach the screen surface at the same time and to ensure that the screen excitation is already in a continuous motion when particles get into the contact with the screening surface. In addition, there is an outlet below the screen to measure the particle passage through the apertures when they reach the collecting bin placed on a balance. Above the outlet various screens with different aperture sizes can be places. In the study performed here, one screen surface is applied in each case with the aperture sizes adjusted to the particle sizes as presented in Table 6. The screen is operated with a fixed frequency of 50.6 Hz; two amplitudes of A = 1 mm and A = 0.8 mm are considered. For details on the elliptical stroke motion of the screen surface see [29].

In the investigation, POM and glass spheres are applied in three different size classes. They are assumed to be ideal spheres of $d_1 = 5$ mm, $d_2 = 7$ mm, $d_3 = 10$ mm in a first and $d_1 = 3$ mm, $d_2 = 5$ mm and $d_3 = 7$ mm in a second configuration. In both configurations, the particles and the aperture size are related as $d_1 < d_2 < a < d_3$, where a is the size of an aperture. To perform the experiments POM spheres are filled into the feed bin with a mass of $m_p = 3m_{pi} = 3 \times 250$ g $= 750$ g. The amount of glass spheres is chosen to be volume equivalent with the POM spheres giving a mass of $m_p \approx 1410$ g (see Table 6). For both materials, three different liquid
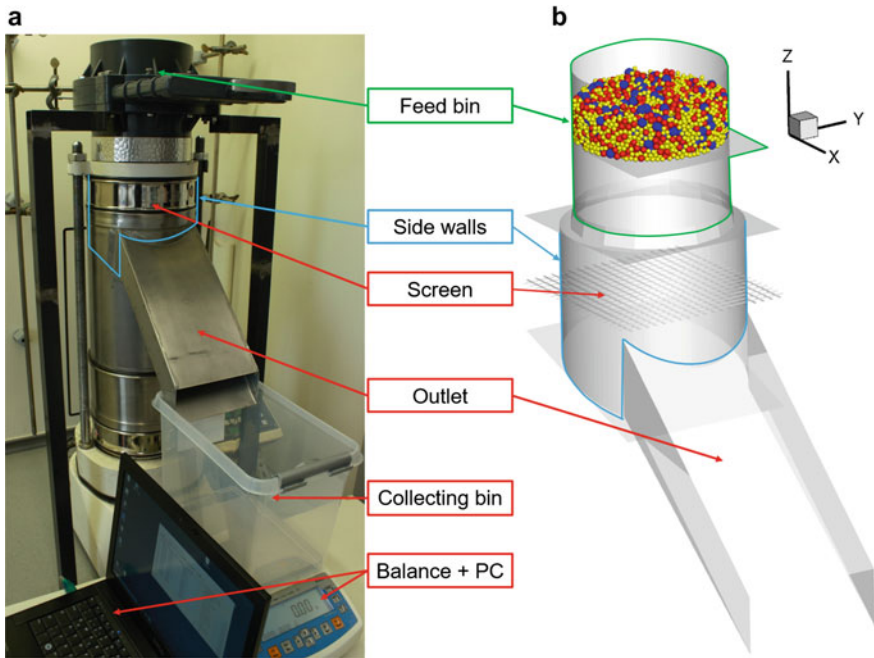
Fig. 19 **a** Experimental setup and **b** corresponding approximation in the DEM simulations of the batch screening apparatus. Reprint with permission from [29]

Table 6 Experimental properties for batch screening experiments. Reprint with permission from [29]

Properties	POM	Glass
Particle mass [kg]	0.75	~1.41
Liquid amount [%]	0/5/10	0/2.5/5
Surface tension [N/m]	0.07275	
Aperture size [mm]	8.00 ± 0.02/5.60 ± 0.01	
Wire diameter [mm]	2.00 ± 0.01/1.60 ± 0.01	
Scree wire profile [−]	Circular (woven)	
Set amplitude [mm]	1/0.8	
Frequency [Hz]	~50.6	
Stroke behavior	Elliptical, mainly vertical	

amounts in the range of $0\% \leq M \leq 10\%$ are applied. In the case of glass spheres, the percentage amount is lower in order to maintain a pendular regime. Mechanical and physical particle and wall properties are presented in Table 7. Distilled water is use as a liquid.

In Table 8 the DEM parameters coulomb friction μ_c, rolling friction μ_{roll} and the coefficient of restitution e^n for POM and glass spheres with their respective contact partners are listed. Details according their determination can be found in [30].

Table 7 Particle and wall properties. Reprint with permission from [29]

Mechanical particle property	Particle		Wall	
	POM	Glass	Steel	PVC
Diameter d [mm]	3/5/7/10 ± 0.1	3/5/7/10 ± 0.1	–	–
Mass m [g]	0.0192/0.0935/0.2459/0.7210 ± 0.02	0.0353/0.1636/0.4490/1.3090 ± 0.02	–	–
Density ρ [kg/m³]	1.3570E+03/1.3580E+03/1.3356E+03/1.3425E+03 ±1.50	2.5240E+03/2.5351E+03/2.5373E+03/2.5300E+03 ±1.50	7.85E+03	1.30E+03
Young's modulus E [N/m²]	2.84E+09	5.00E+10	2.08E+11	2.20E+09
Poisson's ratio ν [–]	0.35	0.2	0.30	0.4
Stiffness k_{PP}^n / k_{PW}^n [N/m]	1.00E+05	1.00E+05	–	–
Contact angle θ [°]	40	15	45	50

Table 8 DEM parameters for POM and glass spheres and various contact partners. Reprint with permission from [29]

Contact partner 1	Contact partner 2	μ_c [−]	μ_{roll} [m]	e^n_{dry} [−]
POM sphere	Steel (side walls, screen wires, bottom, outlet walls)	0.3484	5.97E−05	0.8473
POM sphere	POM sphere	0.3725	4.63E−05	0.8038
Glass sphere	Steel (side walls, screen wires, bottom, outlet walls)	0.2866	1.09E−04	0.4351
Glass sphere	Glass sphere	0.1966	8.95E−05	0.7808

4.3.2 Numerical and Experimental Results Obtained

In the following, fractions retained Y obtained by experiments and by DEM simulations are presented and compared against each other. In Figs. 20 and 22, the results are presented as fraction retained over time $Y = Y(t) = m_{p,l}/m_{p,l,0}$, where $m_{p,l,0}$ is the initial mass at $t = 0$ s and $m_{p,l}$ is the remaining mass of the particles together with the liquid which is not in the collecting bin at time t.

In the first investigations, dry material with different sizes of the particles is screened and the experimental results for the fraction retained on the screen over time are compared to the results obtained by DEM simulations in Fig. 20.

The simulation results of the POM spheres agree very well with the experimental ones except for slight deviations (see Fig. 20a). With an aperture size of $a = 8$ mm ($d_{1/2/3} = 5/7/10$ mm), an amplitude of $A = 1$ mm results in a rapid reduction of the fraction retained value until all particles are screened at $t \approx 15$ s. In contrast, an amplitude of $A = 0.8$ mm reduces the passing of particles after $t = 5$ s. With an
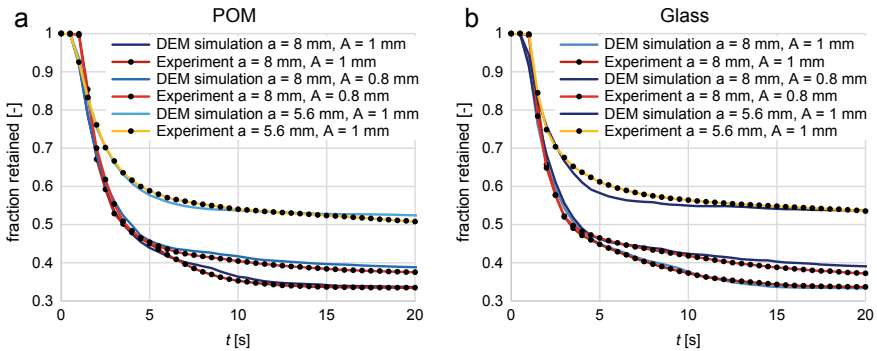

Fig. 20 Fraction retained on the screen over time applying **a** dry POM spheres with $a = 8$ mm ($d_{1/2/3} = 5/7/10$ mm) with $A = 0.8$ mm and $A = 1$ mm as well as $a = 5.6$ mm ($d_{1/2/3} = 3/5/7$ mm) with $A = 1$ mm and **b** dry glass spheres with $a = 8$ mm ($d_{1/2/3} = 5/7/10$ mm) with $A = 0.8$ mm and $A = 1$ mm as well as $a = 5.6$ mm ($d_{1/2/3} = 3/5/7$ mm) with $A = 1$ mm. All results are obtained by experimental investigations (results are averaged over 15 experiments) and DEM simulations, respectively. Reprint with permission from [29]

aperture size of $a = 5.6$ mm ($d_{1/2/3} = 3/5/7$ mm), the particles pass the apertures rapidly in the first seconds, but after $t = 2$ s the passage is hindered and lasts longer than in the first investigation, both in DEM simulation and experiment. After a part of undersized particles have passed the apertures, the larger particles peg the apertures more intensively than in the initial investigation. Therefore, the stratification through the large particles to the screen surface is hindered slowing passage down. The results for dry glass spheres are very similar to those obtained for POM, but some deviations occur when a smaller aperture size is used (see Fig. 20b).

In the next investigations, small amounts of liquid are added to the particles. Figure 21 shows the distribution of the liquid on the particles and walls in varying blue tones at $t = 3$ s. At this instance in time, a part of the undersized particles has already passed the screening surface and the remaining ones reveal thinner liquid films than the larger particles. Most of the wall elements reveal only thin liquid films. The liquid bridges between the particles are presented as cuboids in Fig. 21b whose volume visible outside the spheres corresponds to the volume of the liquid bridge.

The experimental results together with the ones obtained by DEM simulations are presented in Fig. 22, where the fraction retained on the screen over time for dry particles and particles under the influence of different liquid amounts can be compared.

As can be seen in Fig. 22a, a small liquid amount ($M = 5\%$) reduces the particle passage in the initial configuration, whereas a larger amount ($M = 10\%$) does not affect it further, both in experiment and simulation. The influence of the water is relatively low due to the large contact angles and particle sizes. In the DEM simulations,
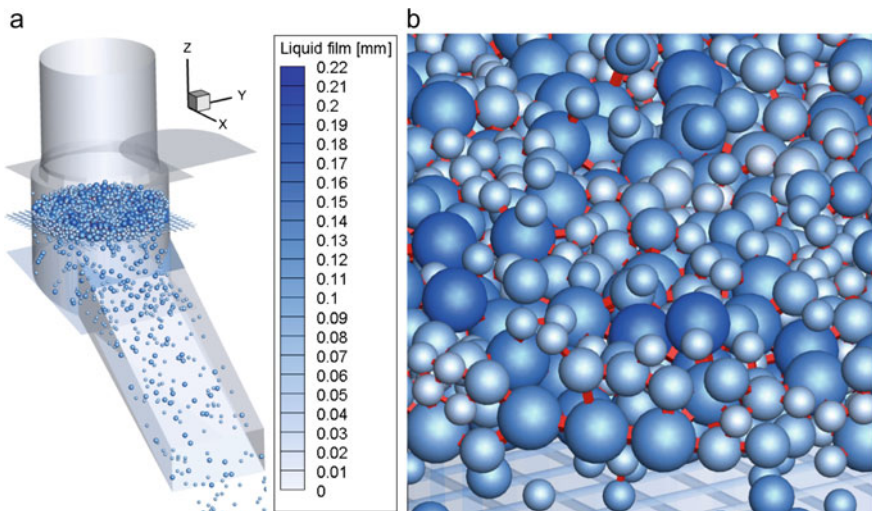

Fig. 21 Visualization of the liquid distribution on the particles and walls presented as liquid film thickness at $t = 3$ s for POM spheres ($a = 8$ mm, $d_{1/2/3} = 5/7/10$ mm) and a liquid amount of $M = 10\%$ for **a** the whole screen apparatus and **b** zoomed into reveal the liquid bridge volume between particles presented as cuboids. Reprint with permission from [29]
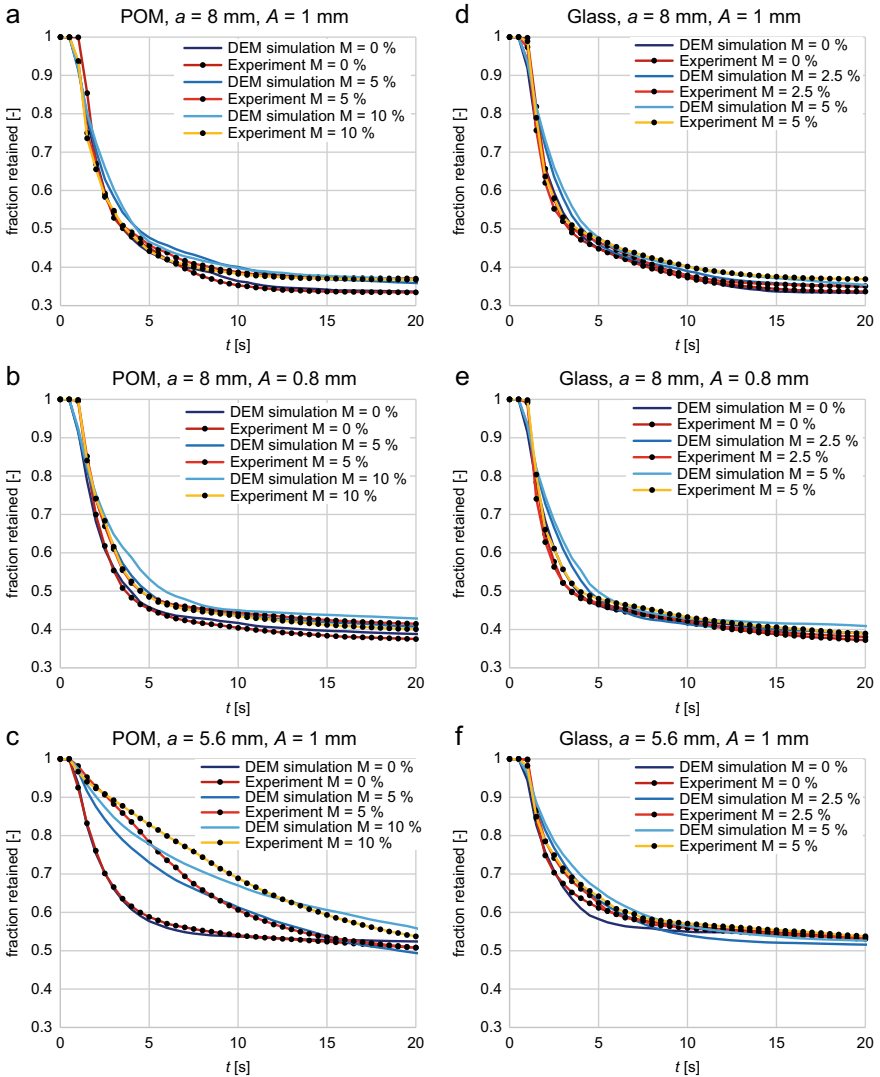
Fig. 22 Fraction retained on the screen over time applying (**a–c**) dry and wet ($M = 0/5/10\%$) POM spheres with $a = 8$ mm ($d_{1/2/3} = 5/7/10$ mm) with **a** $A = 1$ mm and **b** $A = 0.8$ mm as well as **c** $a = 5.6$ mm ($d_{1/2/3} = 3/5/7$ mm) with $A = 1$ mm as well as (**d–f**) dry and wet ($M = 0/2.5/5\%$) glass spheres with $a = 8$ mm ($d_{1/2/3} = 5/7/10$ mm) with **d** $A = 1$ mm and **e** $A = 0.8$ mm as well as **f** $a = 5.6$ mm ($d_{1/2/3} = 3/5/7$ mm) with $A = 1$ mm. All results are obtained by experimental investigations (results are averaged over 15 experiments) and DEM simulations, respectively. Reprint with permission from [29]

slightly more particles remain on the screening surface between $t = 2.5$–10 s, but afterwards the results fit very well. At an amplitude of $A = 0.8$ mm (see Fig. 22b), the obtained fraction retained values are higher when water is added. The numerical and experimental results for a smaller amount of water ($M = 5\%$) fit together very well. In the DEM simulations, however, the fraction retained for a larger amount of water ($M = 10\%$) is slightly overpredicted. In the configuration with smaller particle diameters $d_{1/2/3} = 3/5/7$ mm, the influence of liquid is more pronounced (see Fig. 22c). For smaller particle sizes used in this investigation, the capillary forces become larger relative to the weight force, which is relatively small because of the low density of POM. The fraction retained is similar after $t = 20$ s for $M = 0\%$ and $M = 5\%$ and only slightly larger for $M = 10\%$ due to the pegging of particles in the dry case. The DEM simulations reveal the same trends but show some deviations between $t = 1$–10 s.

When analyzing the initial configuration with glass spheres (see Fig. 22d), a larger amount of water increases the fraction retained obtained experimentally and numerically. However, the influence of the liquid is relatively low due to the large particle masses. The simulation results show some deviations between $t = 2$–5 s under the influence of water. After that, the results fit very well. The same trends can be seen with an amplitude of $A = 0.8$ mm (see Fig. 22e). However, here all results obtained are closer to each other. The results derived using glass spheres with smaller particle diameters of $d_{1/2/3} = 3/5/7$ mm (comp. Fig. 22f) differ greatly from those obtained using POM spheres. In particular, the experimental results are close to each other with slightly larger values when more water is added. Because of the larger density of glass particles, the influence of the capillary force is smaller than for POM. The simulation results show a bit more differences and slightly overpredict the fraction retained until $t \approx 7$ s and underpredict it afterwards. Due to the pegging of the dry particles, less particles remain on the screening surface at $t = 20$ s if liquid is added. Overall, the simulation results agree well with the experimental ones.

4.3.3 Benchmarking of Extended Screening Models

Based on the successful validation of moist DEM screening simulations in Sect. 4.3.2, in this section, results on the three in [123] introduced and in Sect. 3.2.4 outlined modified process models for batch screening under the influence of moisture are shown when adjusting their parameters to fit the results obtained by DEM simulations such as outlined in Sect. 4.3.2 which are further extended. To compare the introduced models over a larger number of investigations, an average deviation of the fraction retained per particle size class obtained by DEM simulations and process models is calculated. For the different undersized particle classes i, the average of the obtained fractional deviations is given by $\left(\sum_{i=1}^{l} \left(\sum_{k=1}^{j} |Y_{mod}(i, k) - Y_{sim}(i, k)| \right) \right) / (j \cdot r)$, where j is the total number of considered time steps k and r is the total number of undersized fractions (here $r = 2$). The total time of the screening process $t = 20$ s is divided into intervals of $\Delta t = 0.5$ s here.

The process models are first adjusted to the simulation results applying one set of parameters for all simulations which is presented in Fig. 23 (bars on the left side of each model). The average deviations for the models are 0.0593 (model a), 0.0387 (model b) and 0.0417 (model c). The parameter sets for the three models are as follows:

- No. 1: $k = 1142.6444$, $\alpha = -0.0193$, $\gamma = -161.2886$
- No. 2: $k_s = 1.3883$, $\alpha = 0.8288$, $\gamma = 2.2026$, $k_p = 0.0542$, $\beta = -5.5913$, $\delta = 0.4581$
- No. 3: $k_s = 5.3935$, $\alpha = -9.3318$, $\gamma = 9.6818$, $k_p = 5.0896$, $\beta = 0.7160$, $\delta = 2.4247$

In addition, these results are compared to the best possible fit when one set of parameters is used for each simulation (Fig. 23, bars on the right side of each model; parameter sets not shown here). The best possible average deviations for the models obtained are 0.0392 (model a/model b) and 0.0403 (model c). The achieved accuracy is very similar for all three models, because the quality of the adjustment is independent of the values of the operational parameters or the liquid amount (see Fig. 23, right bars).
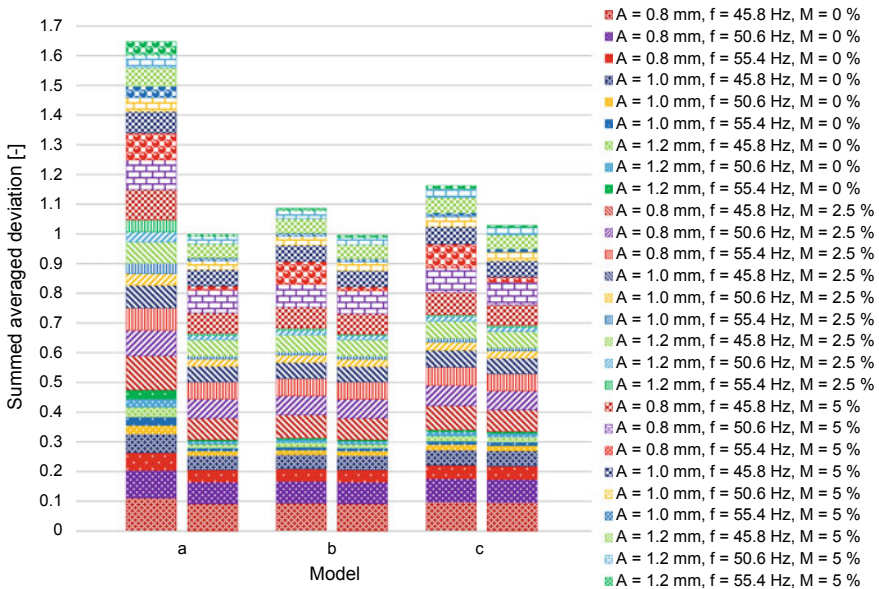

Fig. 23 Deviations between the fraction retained per size class obtained by phenomenological screening models as stated in Table 3 and discrete element simulations summed up for all investigated simulations. The process models are adjusted to the simulation results by applying one set of parameters for all simulations (bars on the left side of each model) and by applying one set of parameters for each simulation, showing the best possible adjustment (bars on the right side of each model). Reprint with permission from [123]

Overall, all three models can better represent simulations with an instant decline of the fraction retained, whereas the deviations increase for a less instant decline of the fraction retained due to larger liquid amounts, frequencies and lower amplitudes. If the models are adjusted with one set of parameters to all simulation results (see Fig. 23, left bars), the ranking of the models from the lowest to the largest deviation is model b, model c and model a, for each configuration. The results for the models b and c are similar whether one set of parameters is used for all simulations (Fig. 23, left bars) or one for each simulation (Fig. 23, right bars). In contrast, the deviations for model a are much larger when only one set of parameters is used for all simulations. It can be concluded, that the functional forms of all three process models can represent the progression of the fraction retained per size class for one individual configuration well. However, in batch screening with several particle layers on the screen, it is essential to consider the subprocesses stratification and passage like is done in model b and model c to represent the results for a wider range of configurations.

5 Conclusions

To conclude, the findings made provide insights in the relevant subprocesses stratification, passage and transport as well as particularities of screening like operational parameters and particle characteristics including their influence on time or spatial dependent outcomes like the fraction retained. To obtain the aforementioned findings the modeling of screening processes with the discrete element method was improved and extended by the possibility to address sieving/screening under the influence of a certain amount of liquid. In addition, a general straightforward procedure to determine DEM simulation parameters reliably was developed. Furthermore, appropriate validations against experiments have been carried out in order to underline the correctness of the DEM simulations and to apply the respective DEM submodels for further investigations even beyond sieving/screening. With the information and data obtained from steady state and dynamic DEM simulations, process models were benchmarked and successfully extended for sieving/screening under moist conditions. Consequently, the derived process models can be applied as prototypes in dynamic process simulation frameworks of combined solids processes.

References

1. Stieß, M. Mechanische Verfahrenstechnik - Partikeltechnologie 1, Springer, Berlin (2009)
2. Liu, K.: Some factors affecting sieving performance and efficiency. Powder Technol. **193**(2), 208–213 (2009)

3. Grozubinsky, V., Sultanovitch, E., Lin, I.J.: Efficiency of solid particle screening as a function of screen slot size, particle size, and duration of screening—the theoretical approach. Int. J. Miner. Process. **52**(4), 261–272 (1998)

4. Bunge, R.: Mechanische Aufbereitung - Primär- und Sekundärrohstoffe, 1st edn. Wiley-VCH Verlag, Weinheim (2012)

5. Kruse, R.: Mechanische Verfahrenstechnik - Grundlagen der Flüssigkeitsförderung und der Partikeltechnologie. Wiley-VCH Verlag, Weinheim (1999)

6. Schmidt, P., Körber, R., Coppers, M.: Sieben und Siebmaschinen - Grundlagen und Anwendungen. Wiley-VCH Verlag, Weinheim (2003)

7. Yoshida, Y., Ishikawa, S., Shimosaka, A., Shirakawa, Y., Hidaka, J.: Estimation equation for sieving rate based on the model for undersized particles passing through vibrated particle bed. J. Chem. Eng. Jpn. **46**(2), 116–126 (2013)

8. Cleary, P.W., Sinnott, M.D., Morrison, R.D.: Separation performance of double deck banana screens—Part 1: flow and separation for different accelerations. Miner. Eng. **22**(14), 1218–1229 (2009)

9. Soldinger, M.: Interrelation of stratification and passage in the screening process. Miner. Eng. **12**(5), 497–516 (1999)

10. Soldinger, M.: Influence of particle size and bed thickness on the screening process. Miner. Eng. **13**(3), 297–312 (2000)

11. Cundall, P.A., Strack, O.D.L.: A discrete numerical model for granular assemblies. Géotechnique **29**(1), 47–65 (1979)

12. Walton, O.R., Braun, R.L.: Viscosity, granular-temperature, and stress calculations for shearing assemblies of inelastic, frictional disks. J. Rheol. **30**, 949–980 (1986)

13. Zhu, H.P., Zhou, Z.Y., Yang, R.Y., Yu, A.B.: Discrete particle simulation of particulate systems: theoretical developments. Chem. Eng. Sci. **62**(13), 3378–3396 (2007)

14. Zhu, H.P., Zhou, Z.Y., Yang, R.Y., Yu, A.B.: Discrete particle simulation of particulate systems: a review of major applications and findings. Chem. Eng. Sci. **63**(23), 5728–5770 (2008)

15. Cleary, P.W. Large scale industrial DEM modelling. Eng. Computations **21**(2/3/4), 169–204 (2004)

16. Lu, G., Third, J.R., Müller, C.R.: Discrete element models for non-spherical particle systems: from theoretical developments to applications. Chem. Eng. Sci. **127**, 425–465 (2015)

17. Höhner, D., Wirtz, S., Kruggel-Emden, H., Scherer, V.: Comparison of the multi-sphere and polyhedral approach to simulate non-spherical particles within the discrete element method: influence on temporal force evolution for multiple contacts. Powder Technol. **208**(3), 643–656 (2011)

18. Mio, H., Shimosaka, A., Shirakawa, Y., Hidaka, J.: Optimum cell size for contact detection in the algorithm of the discrete element method. J. Chem. Eng. Jpn. **38**(12), 969–975 (2005)

19. Cleary, P.W.: The effect of particle shape on simple shear flows. Powder Technol. **179**(3), 144–163 (2008)

20. Mead, S.R., Cleary, P.W., Robinson, G.K. Characterising the failure and repose angles of irregularly shaped three-dimensional particles using DEM. In: Ninth International Conference on CFD in the Minerals and Process Industries, Melbourne, Australia, pp. 1–6 (2012)

21. Delaney, G.W., Cleary, P.W. The packing properties of superellipsoids. Europhys. Lett. **89**(3), (2010)

22. Jensen, R.P., Bosscher, P.J., Plesha, M.E., Edil, T.B.: DEM simulation of granular media-structure interface: effects of surface roughness and particle shape. Int. J. Numer. Anal. Meth. Geomech. **23**(6), 531–547 (1999)

23. Favier, J.F., Abbaspour-Fard, M.H., Kremmer, M., Raji, A.O.: Shape representation of axisymmetrical, non-spherical particles in discrete element simulation using multielement model particles. Eng. Comput. **16**(4), 467–480 (1999)

24. Favier, J.F., Abbaspour-Fard, M.H., Kremmer, M.: Modeling nonspherical particles using multisphere discrete elements. J. Eng. Mech. **127**(10), 971–977 (2001)

25. Vu-Quoc, L., Zhang, X., Walton, O.R.: A 3-D discrete emelent method for dry granular flows of ellipsoidal particles. Comput. Methods Appl. Mech. Eng. **187**, 483–528 (2000)

26. Kruggel-Emden, H., Rickelt, S., Wirtz, S., Scherer, V.: A study on the validity of the multi-sphere Discrete Element Method. Powder Technol. **188**(2), 153–165 (2008)
27. Markauskas, D., Kačianauskas, R.: Investigation of rice grain flow by multi-sphere particle model with rolling resistance. Granular Matter **13**(2), 143–148 (2011)
28. Munjiza, A., Latham, J.P., John, N.W.M.: 3D dynamics of discrete element systems comprising irregular discrete elements—integration solution for finite rotations in 3D. Int. J. Numer. Meth. Eng. **56**(1), 35–55 (2003)
29. Elskamp, F., Kruggel-Emden, H.: DEM simulations of screening processes under the influence of moisture. Chem. Eng. Res. Des. **136**, 593–609 (2018)
30. Elskamp, F., Kruggel-Emden, H., Hennig, M., Teipel, U.: A strategy to determine DEM parameters for spherical and non-spherical particles. Granular Matter **19**(3), 46 (2017)
31. Kruggel-Emden, H., Simsek, E., Rickelt, S., Wirtz, S., Scherer, V.: Review and extension of normal force models for the Discrete Element Method. Powder Technol. **171**(3), 157–173 (2007)
32. Di Renzo, A., Di Maio, F.P.: Comparison of contact-force models for the simulation of collisions in DEM-based granular flow codes. Chem. Eng. Sci. **59**(3), 525–541 (2004)
33. Kruggel-Emden, H., Wirtz, S., Scherer, V.: A study on tangential force laws applicable to the discrete element method (DEM) for materials with viscoelastic or plastic behavior. Chem. Eng. Sci. **63**(6), 1523–1541 (2008)
34. Kruggel-Emden, H., Rickelt, S., Wirtz, S., Scherer, V.: A numerical study on the sensitivity of the discrete element method for hopper discharge. J. Pressure Vessel Technol. **131**(3), 031211 (2009)
35. Cleary, P.W., Sawley, M.L.: DEM modelling of industrial granular flows: 3D case studies and the effect of particle shape on hopper discharge. Appl. Math. Model. **26**(2), 89–111 (2002)
36. Höhner, D., Wirtz, S., Scherer, V.: Experimental and numerical investigation on the influence of particle shape and shape approximation on hopper discharge using the discrete element method. Powder Technol. **235**, 614–627 (2013)
37. Di Renzo, A., Di Maio, F.P.: An improved integral non-linear model for the contact of particles in distinct element simulations. Chem. Eng. Sci. **60**, 1303–1312 (2005)
38. Ge, W., Wang, L., Xu, J., Chen, F., Zhou, G., Lu, L., Chang, Q., Li, J.: Discrete simulation of granular and particle-fluid flows: from fundamental study to engineering application. Rev. Chem. Eng. **33**(6), 551–623 (2017)
39. Rabinovich, Y.I., Esayanur, M.S., Moudgil, B.M.: Capillary forces between two spheres with a fixed volume liquid bridge: theory and experiment. Langmuir **21**(24), 10992–10997 (2005)
40. Willett, C.D., Adams, M.J., Johnson, S.A., Seville, J.P.K.: Capillary bridges between two spherical bodies. Langmuir **16**(10), 9396–9405 (2000)
41. Weigert, T., Ripperger, S.: Calculation of the Liquid bridge volume and bulk saturation from the half-filling angle. Part. Part. Syst. Charact. **16**(5), 238–242 (1999)
42. Adams, M.J., Perchard, V.: The cohesive forces between particles with interstitial liquid. Int. Chem. Eng. Symp. Ser. **91**, 147–160 (1985)
43. Goldman, A.J., Cox, R.G., Brenner, H.: Slow viscous motion of a sphere parall to a plane wall—I Motion through a quiescent fluid. Chem. Eng. Sci. **22**(4), 653–660 (1967)
44. Pitois, O., Moucheront, P., Chateau, X.: Liquid bridge between two moving spheres: an experimental study of viscosity effects. J. Colloid Interface Sci. **231**, 26–31 (2000)
45. Pitois, O., Moucheront, P., Chateau, X.: Rupture energy of a pendular liquid bridge. Eur. Phys. J. B **23**, 79–86 (2001)
46. Pepin, X., Rossetti, D., Iveson, S.M., Simons, S.J.R.: Modeling the evolution and rupture of pendular liquid bridges in the presence of large wetting hysteresis. J. Colloid Interface Sci. **232**, 289–297 (2000)
47. Shi, D., McCarthy, J.J.: Numerical simulation of liquid transfer between particles. Powder Technol. **184**, 64–75 (2008)
48. Lian, G., Thornton, C., Adams, M.J.: A theoretical study of the liquid bridge forces between two rigid spherical bodies. J. Colloid Interface Sci. **161**, 138–147 (1993)

49. Lian, G., Seville, J.: The capillary bridge between two spheres: new closed-form equations in a two century old problem. Adv. Coll. Interface. Sci. **227**, 53–62 (2016)
50. Gladkyy, A., Schwarze, R.: Comparison of different capillary bridge models for application in the discrete element method. Granular Matter **16**(6), 911–920 (2014)
51. Mikami, T., Kamiya, H., Horio, M.: Numerical simulation of cohesive powder behavior in a fluidized bed. Chem. Eng. Sci. **53**(10), 1927–1940 (1998)
52. Washino, K., Chan, E.L., Miyazaki, K., Tsuji, T., Tanaka, T.: Time step criteria in DEM simulation of wet particles in viscosity dominant systems. Powder Technol. **302**, 100–107 (2016)
53. Schmelzle, S., Nirschl, H.: DEM simulations: mixing of dry and wet granular material with different contact angles. Granular Matter **20**, 19 (2018)
54. Radl, S., Kalvoda, E., Glasser, B.J., Khinast, J.G.: Mixing characteristics of wet granular matter in a bladed mixer. Powder Technol. **200**(3), 171–189 (2010)
55. Scholtès, L., Chareyre, B., Nicot, F., Darve, F.: Discrete modelling of capillary mechanisms in multi-phase granular media. Comput. Model. Eng. Sci. **52**(3), 297–318 (2009)
56. Melnikov, K., Mani, R., Wittel, F.K., Thielmann, M., Herrmann, H.J.: Grain scale modeling of arbitrary fluid saturation in random packings. Phys. Rev. E **92**(2), 022206 (2015)
57. Wang, J., Gallo, E., François, B., Gabrieli, F., Lambert, P.: Capillary force and rupture of funicular liquid bridges between three spherical bodies. Powder Technol. **305**, 89–98 (2017)
58. Butt, H.-J., Kappl, M.: Surface and Interfacial Forces. Wiley-VCH Verlag, Weinheim (2010)
59. Coetzee, C.J.: Review: calibration of the discrete element method. Powder Technol. **310**, 104–142 (2017)
60. Marigo, M., Stitt, E.H.: Discrete element method (DEM) for industrial applications: comments on calibration and validation for the modelling of cylindrical pellets. KONA Powder Part. J. **32**(32), 236–252 (2015)
61. Simons, T.A.H., Weiler, R., Strege, S., Bensmann, S., Schilling, M., Kwade, A.: A ring shear tester as calibration experiment for DEM simulations in agitated mixers—a sensitivity study. Procedia Eng. **102**, 741–748 (2015)
62. Grima, A.P., Wypych, P.W.: Investigation into calibration of discrete element model parameters for scale-up and validation of particle-structure interactions under impact conditions. Powder Technol. **212**(1), 198–209 (2011)
63. Barrios, G.K.P., de Carvalho, R.M., Kwade, A., Tavares, L.M.: Contact parameter estimation for DEM simulation of iron ore pellet handling. Powder Technol. **248**, 84–93 (2013)
64. Markauskas, D., Kačianauskas, R., Džiugys, A., Navakas, R.: Investigation of adequacy of multi-sphere approximation of elliptical particles for DEM simulations. Granular Matter **12**(1), 107–123 (2010)
65. Pasha, M., Hare, C., Ghadiri, M., Gunadi, A., Piccione, P.M.: Effect of particle shape on flow in discrete element method simulation of a rotary batch seed coater. Powder Technol. **296**, 29–36 (2016)
66. Williams, K.C., Chen, W., Weeger, S., Donohue, T.J.: Particle shape characterisation and its application to discrete element modelling. Particuology **12**(1), 80–89 (2014)
67. Mollon, G., Zhao, J.: Generating realistic 3D sand particles using Fourier descriptors. Granular Matter **15**(1), 95–108 (2013)
68. Just, S., Toschkoff, G., Funke, A., Djuric, D., Scharrer, G., Khinast, J., Knop, K., Kleinebudde, P.: Experimental analysis of tablet properties for discrete element modeling of an active coating process. AAPS PharmSciTech **14**(1), 402–411 (2013)
69. Chung, Y.-C., Ooi, J.Y.: A study of influence of gravity on bulk behaviour of particulate solid. Particuology **6**(6), 467–474 (2008)
70. González-Montellano, C., Fuentes, J.M., Ayuga-Téllez, E., Ayuga, F.: Determination of the mechanical properties of maize grains and olives required for use in DEM simulations. J. Food Eng. **111**(4), 553–562 (2012)
71. Senetakis, K., Coop, M.R., Todisco, M.C.: The inter-particle coefficient of friction at the contacts of Leighton Buzzard sand quartz minerals. Soils Found. **53**(5), 746–755 (2013)

72. Ucgul, M., Fielke, J.M., Saunders, C.: Defining the effect of sweep tillage tool cutting edge geometry on tillage forces using 3D discrete element modelling. Inf. Process. Agric. **2**(2), 130–141 (2015)
73. Chung, Y.C., Lin, C.K., Ai, J.: Mechanical behaviour of a granular solid and its contacting deformable structure under uni-axial compression—Part II: multi-scale exploration of internal physical properties. Chem. Eng. Sci. **144**, 421–443 (2016)
74. Kretz, D., Callau-Monje, S., Hitschler, M., Hien, A., Raedle, M., Hesser, J.: Discrete element method (DEM) simulation and validation of a screw feeder system. Powder Technol. **287**, 131–138 (2016)
75. Ucgul, M., Fielke, J.M., Saunders, C.: Three-dimensional discrete element modelling of tillage: determination of a suitable contact model and parameters for a cohesionless soil. Biosys. Eng. **121**, 105–117 (2014)
76. Li, Y., Xu, Y., Thornton, C.: A comparison of discrete element simulations and experiments for 'sandpiles' composed of spherical particles. Powder Technol. **160**(3), 219–228 (2005)
77. Wong, C.X., Daniel, M.C., Rongong, J.A.: Energy dissipation prediction of particle dampers. J. Sound Vib. **319**(1–2), 91–118 (2009)
78. Alonso-Marroquín, F., Ramírez-Gómez, Á., González-Montellano, C., Balaam, N., Hanaor, D.A.H., Flores-Johnson, E.A., Gan, Y., Chen, S., Shen, L.: Experimental and numerical determination of mechanical properties of polygonal wood particles and their flow analysis in silos. Granular Matter **15**(6), 811–826 (2013)
79. Dong, H., Moys, M.H.: Measurement of impact behaviour between balls and walls in grinding mills. Miner. Eng. **16**(6), 543–550 (2003)
80. Gorham, D.A., Kharaz, A.H.: The measurement of particle rebound characteristics. Powder Technol. **112**(3), 193–202 (2000)
81. Höhner, D., Wirtz, S., Scherer, V.: A study on the influence of particle shape and shape approximation on particle mechanics in a rotating drum using the discrete element method. Powder Technol. **253**, 256–265 (2014)
82. Hastie, D.B.: Experimental measurement of the coefficient of restitution of irregular shaped particles impacting on horizontal surfaces. Chem. Eng. Sci. **101**, 828–836 (2013)
83. Wang, L., Zhou, W., Ding, Z., Li, X., Zhang, C.: Experimental determination of parameter effects on the coefficient of restitution of differently shaped maize in three-dimensions. Powder Technol. **284**, 187–194 (2015)
84. Chou, H.T., Lee, C.F., Chung, Y.C., Hsiau, S.S.: Discrete element modelling and experimental validation for the falling process of dry granular steps. Powder Technol. **231**, 122–134 (2012)
85. Coetzee, C.J., Els, D.N.J.: Calibration of discrete element parameters and the modelling of silo discharge and bucket filling. Comput. Electron. Agric. **65**(2), 198–212 (2009)
86. Coetzee, C.J., Els, D.N.: Calibration of granular material parameters for DEM modelling and numerical verification by blade-granular material interaction. J. Terrramech. **46**, 15–26 (2009)
87. Coetzee, C.J., Els, D.N.J., Dymond, G.F.: Discrete element parameter calibration and the modelling of dragline bucket filling. J. Terrramech. **47**(1), 33–44 (2010)
88. Coetzee, C.J.: Calibration of the discrete element method and the effect of particle shape. Powder Technol. **297**, 50–70 (2016)
89. Wensrich, C.M., Katterfeld, A.: Rolling friction as a technique for modelling particle shape in DEM. Powder Technol. **217**, 409–417 (2012)
90. Frankowski, P., Morgeneyer, M.: Calibration and validation of DEM rolling and sliding friction coefficients in angle of repose and shear measurements. AIP Conf. Proc. **1542**, 851–854 (2013)
91. Combarros, M., Feise, H.J., Zetzener, H., Kwade, A.: Segregation of particulate solids: experiments and DEM simulations. Particuology **12**(1), 25–32 (2014)
92. Santos, D.A., Barrozo, M.A.S., Duarte, C.R., Weigler, F., Mellmann, J.: Investigation of particle dynamics in a rotary drum by means of experiments and numerical simulations using DEM. Adv. Powder Technol. **27**(2), 692–703 (2016)
93. Cabiscol, R., Finke, J.H., Kwade, A.: Calibration and interpretation of DEM parameters for simulations of cylindrical tablets with multi-sphere approach. Powder Technol. **327**, 232–245 (2018)

94. Chung, Y.C., Liao, H.H., Hsiau, S.S.: Convection behavior of non-spherical particles in a vibrating bed: discrete element modeling and experimental validation. Powder Technol. **237**, 53–66 (2013)
95. Skorych, V., Dosta, M., Hartge, E.-U., Heinrich, S.: Novel system for dynamic flowsheet simulation of solids processes. Powder Technol. **314**, 665–679 (2017)
96. Dimian, A., Bildea, C., Kiss, A.: Integrated design and simulation of chemical processes. Elsevier **13**, 73–156 (2014)
97. Dosta, M., Heinrich, S., Werther, J.: Fluidized bed spray granulation: analysis of the system behaviour by means of dynamic flowsheet simulation. Powder Technol. **204**(1), 71–82 (2010)
98. Marquardt, W. Dynamic process simulation—recent progress and future challenges. In: Chemical Process Control CPC-IV, CACHE Publications, pp. 131–180 (1991)
99. Schwier, D., Hartge, E.U., Werther, J., Gruhn, G.: Global sensitivity analysis in the flowsheet simulation of solids processes. Chem. Eng. Process. **49**(1), 9–21 (2010)
100. Hartge, E.U., Pogodda, M., Reimers, C., Schwier, D., Gruhn, G., Werther, J.: Flowsheet simulation of solids processes. KONA **24**, 146–158 (2006)
101. Reimers, C., Werther, J., Gruhn, G.: Flowsheet simulation of solids processes. Data reconciliation and adjustment of model parameters. Chem. Eng. Process.: Process Intensification **47**(1), 138–158 (2008)
102. Dosta, M., Antonyuk, S., Hartge, E.-U., Heinrich, S.: Parameter estimation for the flowsheet simulation of solids processes. Chem. Ing. Tec. **86**(7), 1073–1079 (2014)
103. Dehghani, A., Monhemius, A.J., Gochin, R.J. Evaluating the Nakajima et al. model for rectangular-aperture screens. Minerals Eng. **15**, 1089–1094 (2002)
104. Hatch, C.C., Mular, A.L. Simulation of the Brenda Mines Ltd. secondary crusher. In: SME-AIME Annual Meeting, pp. 54–79 (1979)
105. Plitt, L.R.: The analysis of solid—solid separations in classifiers. CIM Bull. **64**, 42–47 (1971)
106. Rogers, R.S.C.: A classification function for vibrating screens. Powder Technol. **31**, 135–137 (1982)
107. Molerus, O., Hoffmann, H. Darstellung von Windsichtertrennkurven durch ein stochastisches Modell, Chemie Ingenieur Technik **41** (5+6), 340–344 (1969)
108. Trawinski, H.: Die mathematische Formulierung der Tromp-Kurve. Aufbereitungstechnik **17**(248–254), 449–459 (1976)
109. Elskamp, F., Kruggel-Emden, H., Hennig, M., Teipel, U.: Benchmarking of process models for continuous screening based on discrete element simulations. Miner. Eng. **83**, 78–96 (2015)
110. Standish, N.: The kinetics of batch sieving. Powder Technol. **41**, 57–67 (1985)
111. Standish, N., Meta, I.A.: Some kinetic aspects of continuous screening. Powder Technol. **41**, 165–171 (1985)
112. Trumic, M., Magdalinovic, N.: New model of screening kinetics. Miner. Eng. **24**, 42–49 (2011)
113. Andreev, S.E., Perov, V.A., Zverevic, V.V.: Droblenie izmelcenie i grohocenie poleznyh iskopaemyh. Nedra, Moscow (1980)
114. Subasinghe, G.K.N.S., Schaap, W., Kelly, E.G.: Modelling screening as a conjugate rate process. Int. J. Miner. Process. **28**, 289–300 (1990)
115. Subasinghe, G.K.N.S., Schaap, W., Kelly, E.G.: Modelling the screening process: a probabilistic approach. Powder Technol. **59**, 37–44 (1989)
116. Nakajima, Y., Whiten, W.J.: Behaviour of non-spherical particles in screening. Trans. Inst. Min. Metall. **88**, C88–C92 (1979)
117. Ferrara, G., Preti, U., Schena, G.D. Computer-aided use of a screening process model. In: Twentieth International Symposium on the Application of Computers and Mathematics in the Mineral Industries, pp. 153–166 (1987)
118. Shimosaka, A., Higashihara, S., Hidaka, J.: Estimation of the sieving rate of powders using computer simulation. Adv. Powder Technol. **11**(4), 487–502 (2000)
119. Li, J., Webb, C., Pandiella, S.S., Campbell, G.M.: Discrete particle motion on sieves—a numerical study using the DEM simulation. Powder Technol. **133**, 190–202 (2003)
120. Gaudin, A.M.: Principles of mineral dressing. McGraw-Hill, New York, USA (1939)

121. Soldinger, M.: Transport velocity of a crushed rock material bed on a screen. Miner. Eng. **15**, 7–17 (2002)
122. Elskamp, F., Kruggel-Emden, H.: Review and benchmarking of process models for batch screening based on discrete element simulations. Adv. Powder Technol. **26**, 679–697 (2015)
123. Elskamp, F., Kruggel-Emden, H.: Extension of process models to predict batch screening results under the influence of moisture based on DEM simulations. Powder Technol. **342**, 698–713 (2019)
124. Dong, K.J., Wang, B., Yu, A.B.: Modeling of particle flow and sieving behavior on a vibrating screen: from discrete particle simulation to process performance prediction. Ind. Eng. Chem. Res. **52**(33), 11333–11343 (2013)
125. Delaney, G.W., Cleary, P.W., Hilden, M., Morrison, R.D.: Testing the validity of the spherical DEM model in simulating real granular screening processes. Chem. Eng. Sci. **68**(1), 215–226 (2012)
126. Goldberg, D.E.: Genetic Algorithms in Search, Optimization and Machine Learning. Addison-Wesley, Longman, Boston, Massachusetts (1989)

Chapter 6
Dynamic Process Models for Fine Grinding and Dispersing

Greta Fragnière, Ann-Christin Böttcher, Christoph Thon, Carsten Schilde, and Arno Kwade

Abstract Fine grinding and dispersing, such as grinding in stirred media mills, gains importance in several industrial processes. Solid materials processing is frequently subjected to dynamic changes, effecting the performance of milling. To accurately model milling processes, dynamic flowsheet simulation turns out as a promising approach to gain quick and reliable solutions, describing the milling process over time. The connection of different process units is even closer to the industrial setup. Therefore, the focus of the study is the introduction of a dynamic model for stirred media mills that can be implemented into flowsheet simulation. The modelling approach aims at separating grinding and transport phenomena in the mill. Starting with an investigation of a batch grinding process in a "calibration mill", the dependency of the breakage rate on machine and material parameters is shown. The stressing conditions in this calibration mill are determined theoretically and via simulations using coupled CFD-DEM simulations. In the study, the prediction of influences such as varying grinding media, stirrer speed and solids concentration on the breakage rate worked out well. In continuous processes, the particle transport and axial grinding media distribution, effecting the dynamics, are simulated as a series of instantly mixed cells, connected by mixing streams. With the dynamic flowsheet simulator Dyssol, the dynamic response of the product to changes in the feed was compared to experimental investigations with limestone in a laboratory stirred media mill. Material parameters for the model were tested in a newly designed breakage tester.

G. Fragnière · A.-C. Böttcher · C. Thon · C. Schilde (✉) · A. Kwade (✉)
Institute of Particle Technology, Technische Universität Braunschweig,
Brunswick, Germany
e-mail: c.schilde@tu-braunschweig.de

A. Kwade
e-mail: a.kwade@tu-braunschweig.de

1 Introduction

The importance of ultrafine grinding and dispersing has increased in various industries like chemical, pharmaceutical, ceramic, electronic and ore industry. For these operations, stirred media mills are often used in which the particles are ground in a suspension by relative velocities of grinding media down to the micrometer or nanometer size. Especially expensive products and large installations require the enhancement of models describing fine grinding in stirred media mills, for example to decrease product quality fluctuations and to decrease the amount of wasted material. Grinding and dispersing in stirred media mills is often modeled by looking on the mill operation parameters but neglecting the suspension properties. However, both influence the kinetic energy of grinding media, the product transport of particles, and the uneven axial distribution of grinding media. Next to grinding, these parameters also influence the power consumption of the mill and the wear of mill and grinding media. Through optimal adjustment of operation parameters, it is possible to reduce the power consumption significantly, so that grinding processes are more economic and work more environmental friendly.

Even though fine grinding in stirred media mills has been investigated for several years now, a model describing the effect of uneven grinding media distribution was not considered so far. Furthermore, fluctuations of feed material and the effect of start-up and shut-down processes are unknown contributions on product quality. Using mill control might stabilize sensitive processes. Especially in circulation mode, often used in pharmaceutical, chemical and paint industry, particle size distribution and viscosity of the supplied suspension change dynamically during the grinding process due to increasing particle interactions with decreasing particle size. Supplementary, in passage mode, coarse material can influence the grinding process if an internal deflector wheel, which retains the grinding media in the grinding chamber, is installed.

Incorporating stirred media mills in longer process chains, there is an increasing demand for the prediction of material's particle size distribution as function of operation time. In literature, most flow sheet models work with characteristic particle size values and do not consider particle size distributions or the influence of operating parameters. Therefore, the description of entire particle size distributions in dependency of geometry, operating parameters and processing mode is practically impossible. However, there are models for dry comminution in ball mills, which describe the breakage rate as a function of the size-dependent strength distribution of the material and the distribution of stress energy [1, 2]. Additionally, it is possible to calculate the evolution of particle size distribution during comminution by population balance modelling.

This contribution presents a process model for fine grinding in horizontally orientated stirred media mills for application in a dynamic flow sheet simulation. The modelling approach is based on separating machine and material function, as well as on considering grinding and transport phenomena (Fig. 1). In order to achieve this, on the one hand the stress conditions in a "calibration mill" were investigated
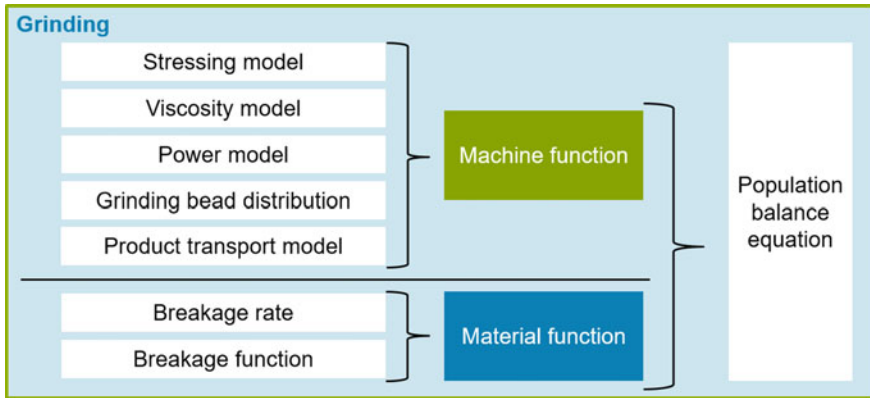
Fig. 1   Model approach for stirred media mills

experimentally (grinding tests and radiometric densitometer) and via simulations (coupled CFD-DEM) for several operation and process parameters. On the other hand, a method has to be developed to efficiently measure the material properties of particles in the lower micrometer range.

For a continuous grinding process within a stirred media mill a dynamic model needs to account for the particle transport and the axial grinding media distribution due to the suspension flow. To do so, the horizontally orientated stirred media mill can be simulated as a series of instantly mixed cells that are connected by mixing streams. The cell volumes and positions are defined according to the stirrer discs (compare Fig. 2). The magnitude of the suspension mixing streams is calibrated based on residence time experiments. The grinding media transport is investigated with radiometric densitometry. For both transport phenomena (suspension and grinding media), the dependency of the mixing coefficients on various operational parameters is presented.

Fig. 2   Schematic representation of cells for a transport model in stirred media mills
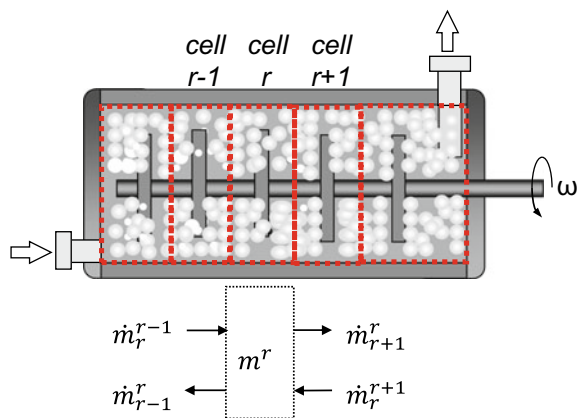
In order to account for the full particle size distribution, the change of the particle size due to grinding is calculated via population balance equations. Thus, the mass balance for size class i in cell r is given by

$$\frac{dm_{i,r}}{dt} = \dot{m}_{i,r}^{i,r-1} + \dot{m}_{i,r}^{i,r+1} - \dot{m}_{i,r+1}^{i,r} - \dot{m}_{i,r-1}^{i,r} - S_{i,r}m_{i,r} + \sum_{j=i}^{i_{max}} S_{j,r}m_{j,r}b_{ij} \qquad (1)$$

with the mass flow over cell boundaries $\dot{m}$, the specific breakage rate S of particles with size x_i in size class i, and the breakage distribution function b, where b_{ij} describes the mass fraction of material that breaks from size class j into size class i. The breakage rate is considered to be dependent on the local stress conditions in each cell, while the breakage distribution function is here assumed to be constant irrespective of the stress conditions.

Furthermore, this study presents a new approach to determine the breakage function experimentally and relate those data to energy states. Since the dominating stress mechanism was found to be compression between two surfaces, a two-roll mill was adjusted to measure breakage characteristics in dependency of different energy levels down to 5 µm.

2 Stressing Conditions in Stirred Media Mills

In the past century, many research studies have investigated the stressing conditions in stirred media mills. Researchers developed a broader and better understanding of breakage mechanisms and breakage energy used in stirred media mills [3–6]. Since the process optimization is a time-consuming process due to several experiments that have to be executed for each material, new approaches focus on models describing the material dependent effects, thus reducing the number of experiments. Therefore, the following chapter deals with stress mechanisms and conditions in stirred media mills. First, through Discrete Element Method, stress energies and contact frequencies could be calculated. Second, the micro scale simulations of two single grinding beads give detailed information about particle capture probability. These two aspects can be taken into account for improving the stress model of stirred media mills.

2.1 Stress Energy and Contact Frequency

Coupled CFD-DEM simulations were carried out to investigate the fluid and grinding media motion and the grinding media collisions. The set-up is shown by Beinert et al. [7]. The stress energy distributions in a representative mill section were determined for various operating conditions (grinding bead size, density and stirrer speeds) and two rotor types. Moreover, they are also calculated for a planetary ball mill. The

kinetic energy at the beginning of the grinding media contact was evaluated. This represents the maximum available energy for particle stressing. The relative grinding media movement at the beginning of the contact with respect to normal, shear and roll motion in translational and rotational direction was described in detail. The results and especially the model are described in depth by Beinert et al. [7]. The detailed contact analysis enables a quantification of the dominating contact type over the whole range of stress energy. For an example of a stirred media mill with glass grinding beads of 0.8 mm in diameter and with a disc stirrer operated with a circumferential speed of 9 m/s the stress energy distribution is shown in Fig. 3. Additionally, the ratio of the six investigated stressing energies is shown over the whole range of stress energy. Three different ranges can be identified: At low stressing energies shearing, rolling and impact are prevalent. In the middle of the spectrum, translational normal and translational shear energy rise while the other energies vanish. At high stressing energies translatoric shear energy is dominant that originates in media-wall and media-stirrer contacts.

For the stress energy resulting from the grinding bead collisions in translational normal direction Kwade formulated the following dependency on the operational parameters circumferential speed v_t grinding bead diameter d_{gm} and their density ρ_{gm} as a characteristic measure of the maximum expectable stress energy [9]:

$$SE_{model,} \propto v_t^2 d_{gm}^3 \rho_{gm} \tag{2}$$

This characteristic model parameter is compared to the simulation results in Fig. 4 in which the correlation of the mean value of the stress energy resulting from the
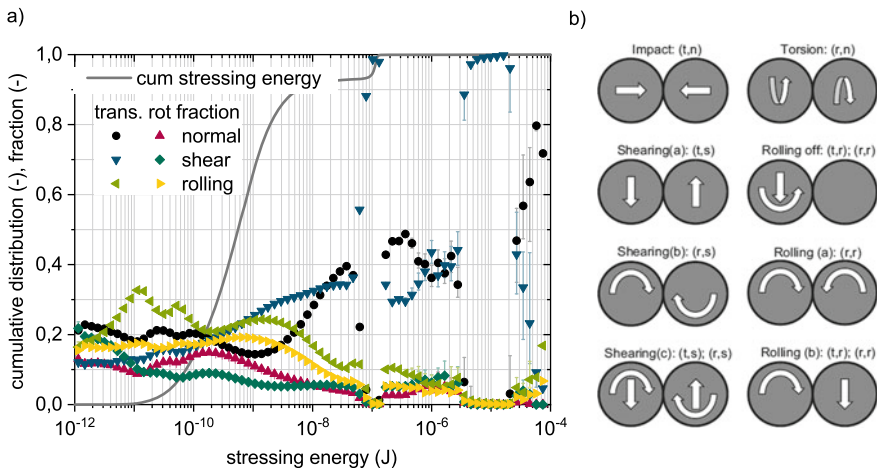

Fig. 3 a Cumulative distribution of the stressing energy and the energy fractions resulting from six different contact types, **b** schematic overview on the possible different ideal contact types with the directions of velocities. Indices are as follows: t: translational, n: normal, r: rotational, s: shear [Reprinted with permission from [8] (**a**) and [7] (**b**)]
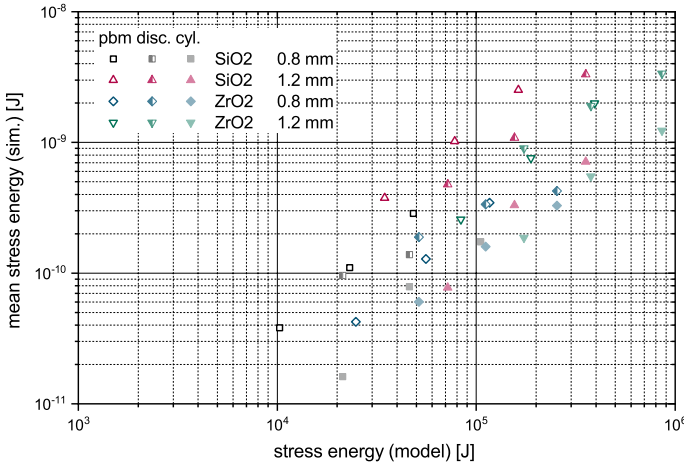
Fig. 4 Simulated mean stress energy SE_{sim} plotted over the stress energy SE_{model} from Eq. (3) for varied grinding media material and sizes, mills (stirred media mills with disc and cylinder rotor and planetary ball mill) and rotation velocities (Reprinted with permission from [7])

simulated translational motion in normal direction, SE_{sim}, and the analytical results of the model parameter, SE_{model}, is shown.

The difference in the absolute value of the stress energy is due to the different assumptions and calculation bases, especially in determining a mean value in case of the simulations and in calculating a characteristic value for the maximum stress energy in case of the mechanistic model of Kwade. However, it can be seen that the trend is identical for both results, i.e. the slope of the resulting correlation is about 1. For the simulation results, an approximate function for the mean stress energy was sought on the basis of the varied operating parameters circumferential speed v_t, grinding bead diameter d_{gm} and their density ρ_{gm}. This results for the stirred media mill in the following relationship:

$$SE_{t,n,} = c_{ma} v_t^{1.12} d_{gm}^{3.98} \rho_{gm}^{0.71} \tag{3}$$

The approximate function found shows a slightly increased dependence regarding the circumferential speed, a significantly increased dependence of the grinding bead diameter as well as a decreasing significance of the grinding bead density in comparison to the mechanistic model.

In addition to the average stress energy, the number of contacts per time must be known in order to evaluate different mills. Kwade describes the following dependency of the collision frequency $N_{c,model}/t$ on the operational parameters rotational speed n and number of grinding media N_{gm} [9]:
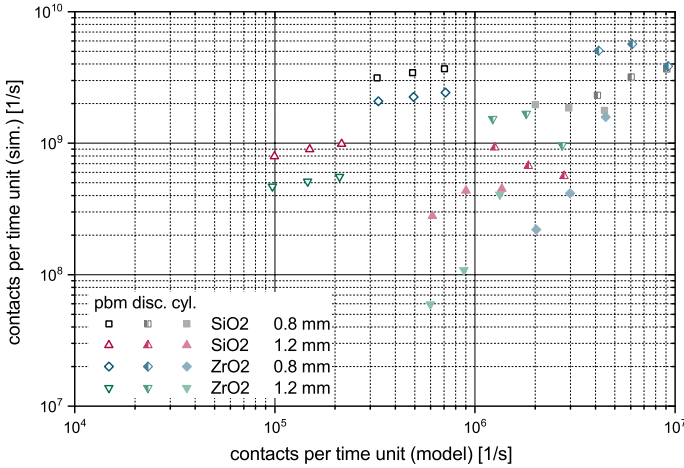
$$\frac{N_{c,model}}{t} \propto n N_{gm} \tag{4}$$

Fig. 5 Number of simulated grinding bead contacts plotted over the number of contacts predicted with the analytical model at 12 operating conditions for the three different mills (Reprinted with permission from [7])

Figure 5 shows the number of contacts per time for the simulative $N_{c,sim}/t$ and analytical $N_{c,model}/t$ results. For the stirred media mill, the following dependency can be observed: In general, the number of contacts increases with decreasing diameter and increasing speed. For the grinding media material, there is a different correlation for stirred media mills and planetary ball mills. The influence of the grinding media material decreases with increasing speed. For the approximation function of the contact frequency on the base of the operating parameters this yields:

$$\frac{N_{c,sim}}{t} = c_{ma} n^{0.55} N_{gm}^{1.18} \tag{5}$$

The influence of the speed is significantly reduced; the influence of the grinding media is almost identical to the analytical model. However, the coefficient of determination is slightly increased. The reason for the low agreement regarding the stirrer speed is that the material values of the grinding media are not taken into account in the calculation for the analytical model. The simulative results partly show clear differences for different grinding media materials.

2.2 Particle Capture Probability

In this chapter the probability of product particles to be captured between approaching grinding beads or between beads and mill walls is discussed. The different contact types of grinding beads resulting out of variating translational and rotational motion

patterns and their impact on the product particle capturing probability are investigated. In the previous chapter only the grinding media contacts were studied, the simulations described in this chapter describe the number of product particles being stressed during these contacts.

The first simulation environment is set on the mesoscale, meaning only two grinding beads and their local environment around or in the gap between them are being considered to determine the effect on fluid displacement. Data on the relative grinding bead motion is derived from stirred media mill simulations performed on the macroscale [10]. The CFD domain around the beads is fully resolved, the simulation of the grinding beads motion is possible due to mesh deformation. Since the mesh deformation at the contact point would be too large it is not possible to simulate the actual contact. The immersed boundary method is used for the coupling of CFD and DEM. The grinding bead impact is set to be elastic, meaning below a critical distance from the symmetry plane a complete reversal of grinding media motion occurs. The grinding beads and product particles are assumed to be spherical. For comparison an analytical method is applied to allow the direct comparison of the normalized velocity of a collision of two grinding beads (normalized to the starting velocity). The analytical model is the sum of the fluid displacement force and the fluid resistance force. The fluid displacement for ball-ball and ball-wall contacts is calculated according to Beinert et al. [10].

$$F_{dis,bb} = -\frac{3}{2}\pi\eta v \frac{r}{h_0} \tag{6}$$

$$F_{dis,bw} = -6\pi\eta v \frac{r}{h_0} \tag{7}$$

The fluid resistance force is calculated based on Kürten et al. [11] and depends on the Reynolds number present in the system:

$$c_w = \begin{cases} 24/Re, \text{ if } Re \leq 0.25 \\ 21/Re + 6/\sqrt{Re} + 0.28, \text{ if } 0.25 \leq Re \leq 4000 \\ 0.45, \text{ if } Re \geq 4000 \end{cases} \tag{8}$$

For the following comparison of the numerical and analytical determination the diameter of the grinding media is $d_{GM} = 375\,\mu m$, the grinding media density (ZrO_2) $\rho_{GM} = 6067$ kg/m^3 and the surrounding fluid is water. The distance between the grinding beads and the symmetry plane (0.25 * d_{GM}; 0.50 * d_{GM}; 1.00 * d_{GM}; 2.00 * d_{GM}) as well as the starting velocity (0.2; 1.0; 5 m/s) are varied. These three starting velocities result in different Re numbers (8.4; 42.0; 210.0). The numerical and analytical results for the normalized velocity in dependence of the normalized distance between the grinding beads can be seen in Fig. 6 for the time before and after the collision, with the lower values around 0.6 describing the velocity after the collision:
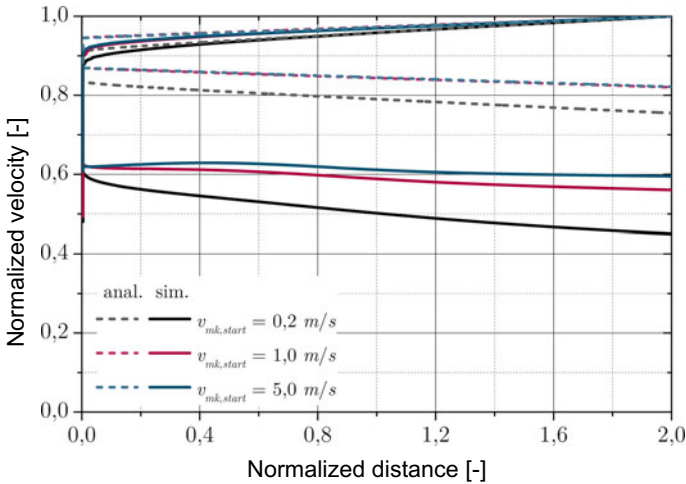
Fig. 6 Grinding media velocity normalized to starting velocity depending on normalized distance before and after a bead-bead collision [12]

Comparing the numerical and analytical solutions for the normalized velocities and distances, in both cases the smaller the distance to the symmetry plane is, the greater is the fluid displacement force. While the two grinding beads are approaching, there is good agreement for the normalized velocities. The reduction of the grinding bead velocity is higher for lower starting velocities, due to the lower Reynolds number and therefore, the greater impact of frictional fluid forces. The velocity loss is the highest shortly before the reversal of the motion direction occurs. The force acting by the displacement of the fluid is proportional to the velocity and inversely proportional to the distance. When, after the collision, the grinding beads are moving away from each other, the velocity decreases linearly. However, the difference between the simulation and the analytical model is greater than on the initial path (till collision) since the flow is influenced by the sudden alteration of the grinding bead motion. For the simulation there is no uniform pattern regarding the influence of the starting distance. The comparison of the fluid displacement in the numerical and the analytical solution shows, that the influence of the fluid displacement is underestimated in the analytical solution [12].

In the following the capture probability is investigated in two additional simulation set ups using resolved simulations performed as described above. In the first case a completely resolved flow around the grinding beads and their interaction with the product particles is simulated. Secondly the flow is investigated in the gap between two grinding beads. In the first case (the simulation of the local environment of the grinding beads) the two grinding beads have a diameter of $d_{GM} = 500$ μm each. They are approaching each other. In the centre between the grinding beads nine spherical particles with a diameter of $d_p = 50$ μm ($d_p/d_{GM} = 0.1$) are evenly

arranged. The distance of the grinding beads to the centre at the starting point is $l =$ 750 μm. In Table 1 the resulting angle to the middle as well as the respective velocity and Reynolds numbers are shown for given starting velocities. In Fig. 7 exemplary resulting flow patterns with the product particles are shown.

While approaching each other, the grinding bead velocities decrease due to fluid displacement. As a result of the approach the product particles in between are moved out. Still, the particle concentration in the shrinking capturing volume increases, due to the higher mass inertia of the particles compared to the fluid. During the collision of the grinding beads the kinetic energy is transferred to the elastic-plastic stress state. As a result, the grinding media is slowed down and then accelerated in the opposite direction due to the elastically stored energy. Hereby velocity and acceleration are dependent on the damping of the fluid. On the "return-way" of the grinding beads the product particles are accelerated towards their initial position by the pull of the grinding beads. Hence, the decrease in velocity is greater for the lower velocity since the influence of friction of the fluid is more pronounced for lower Reynolds numbers. The complete projections of the trajectories of the centres of the grinding beads (black, thick lines) and of the particles (coloured, thin lines) are exemplarily shown in Fig. 8 for the starting velocity of 0.050 m/s in a–c and of 0.100 m/s in d–f.

Table 1 Parameters in dependence of starting velocity [12]

Starting velocity [m/s]	Angled velocity [m/s]	Resulting angle [°]	Reynolds number [−]
±0.050	±0.000	0	25
±0.050	±0.001	1.15	25
±0.050	±0.002	2.29	25
±0.050	±0.003	3.43	25
±0.100	±0.000	0	50
±0.100	±0.001	1.15	50
±0.100	±0.002	2.29	50
±0.100	±0.003	3.43	50

Fig. 7 Velocity fluid fields and particle position for different start velocities (Reprinted with permission from [8])

v_{start}=0.100 m/s v_{start}=0.050 m/s
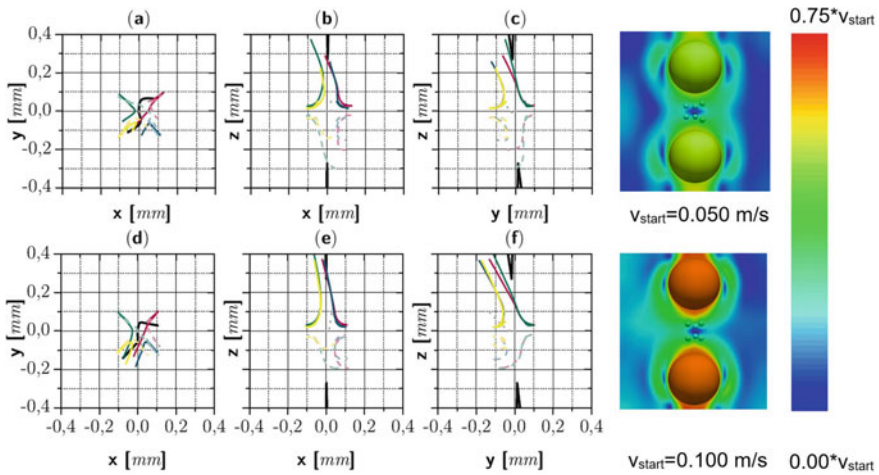
v_{angle}=0.06 m/s v_{angle}=0.000 m/s
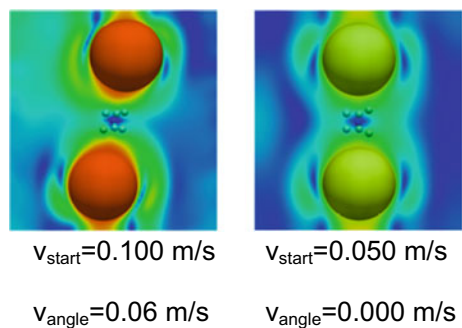
Fig. 8 Projections and trajectories of grinding bead center points and of particles (Reprinted with permission from [12])

For approaches with greater angles between the two grinding beads motions, the product particle velocity reduction caused by the impact itself increases. This influence increases in the further course as the particles are accelerated and moved due to the pull induced by the grinding beads [12]. It can be seen that the particles are accelerated following a contact in the pull of the fluid moving into the gap between the grinding beads, which are moving away from each other. As a consequence, the product particles are carried away from their initial position. The paths of the product particles before and after the grinding media collision are different due to the flow field around the grinding beads being different as result of the angle of motion during collision.

The difference for various Reynolds numbers is notable. In general, the decrease in product particle velocity is lower for higher velocities due to the reduced influence of friction caused by a more turbulent flow at higher Reynolds numbers. In case of angled impact, no clear influence on the overall reduction of velocity can be observed, the influence on the velocity during the contact at different contact angles is however noticeable. The velocity reduction caused by the impact is greater with increasing angle between the grinding bead velocity vectors. Thus, in macro scale simulations the coefficient of restitution should contain the deceleration caused by the fluid displacement to gain more realistic results [8]. In Table 2 the influence of grinding bead velocities on product particle motion is displayed. The grinding media velocity is described by the start velocity in normal direction and a low transversal velocity. The resulting mean product particle velocity is shown as well as the mean position change as a function of the product particle diameter d_p of eight particles [12].

Table 2 Average velocity and position change for contact cases [12]

Contact case Start velocity—crosswise velocity	Average velocity [m/s]	Average change in position [m]
0.050–0.000	$0.257 \cdot v_{start}$	$0.420 \cdot d_p$
0.050–0.001	$0.250 \cdot v_{start}$	$0.546 \cdot d_p$
0.050–0.002	$0.229 \cdot v_{start}$	$0.439 \cdot d_p$
0.050–0.003	$0.210 \cdot v_{start}$	$0.683 \cdot d_p$
0.100–0.000	$0.276 \cdot v_{start}$	$0.520 \cdot d_p$
0.100–0.002	$0.280 \cdot v_{start}$	$0.446 \cdot d_p$
0.100–0.004	$0.270 \cdot v_{start}$	$0.470 \cdot d_p$
0.100–0.006	$0.239 \cdot v_{start}$	$0.301 \cdot d_p$

The absolute product particle velocity increases with rising grinding media starting velocity. The more angled the impact of the grinding beads is, the smaller is the average acceleration of the product particles. No clear dependency can be detected for the mean position change. Here significantly more variations need to be examined and for the analysis of the flow in the gap another method is required, observing this area with higher resolution.

In the second simulation shown in Fig. 9 a highly resolved CFD-mesh in the gap between the grinding beads, in particular in regard for the boundary layer, is used. In the simulation bidirectional interaction (two way coupling) between fluid phase and product particles is enabled. However, the motion of the grinding beads is not affected by the fluid, i.e. their velocity remains constant. In addition to the relative velocity in normal direction, the rotation of the grinding beads is taken into account in order to determine its effect on the capture probability of product particles in between the grinding beads. The diameter of the grinding beads and the product particles was set to $d_{GM} = 1000\ \mu m$ and $d_p = 50\ \mu m$ ($d_p/d_{GM} = 0.05$). As normal velocity of the grinding beads $v_n = \pm 5$ mm/s and accordingly as relative velocity $v_{rel} = 10$ mm/s are chosen. The resultant Reynolds number is Re = 5. The initial distance from the centre of the grinding beads to the plane of symmetry is $l = 600\ \mu m$, the time span required to cover the distance is $\Delta t = 200$ ms, the time period being considered in
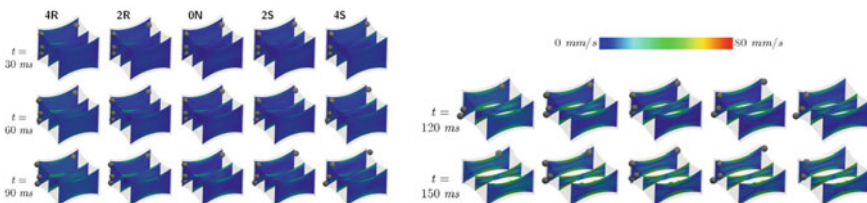
Fig. 9 Cutting slides through flow fields and product particles (Reprinted with permission from [8])

the simulation is $\Delta t = 150$ ms. Due to reasons of the mesh refinement the contact of the grinding beads was not examined.

Through varying the angular velocities of the grinding beads the rotation based effects of shearing and rolling on the capture probability of product particles were considered. Due to the approach of the grinding beads the fluid is accelerated out of the gap between the grinding media resulting in a transport of the product particles with the fluid out of the resulting gap. Depending on the local flow field, the acceleration of the product particles is less pronounced with increasing angular velocity of the approaching grinding beads, leading to an increased capture probability. Five speed combinations are examined, shear and rolling motion are calculated using an extended contact analysis [7]. The parameters of the different contact cases, grinding bead velocity v_n, angle velocity w_x, the normal shear and the rolling stresses $\xi_{rot,r}$ are shown in Table 3, and the resulting gaps and particles and Fig. 9 [12].

It can be seen, that the fluid velocity increases significantly with a smaller gap size. For the normal impact (0N), the velocity distribution (without product particles) is completely symmetrical with respect to the contact plane. The product particles are forced out of the contact point and out of the remaining gap, respectively. As the angular velocity increases, the symmetry is reduced to the contact plane for rolling (4R and 2R) and to the contact point symmetry for shearing (2S und 4S). In these cases, the rotation of the grinding media counteracts the displacement flow. The rotational movement of the grinding beads in the gap is aligned in the same direction during rolling and aligned in the opposite direction during shearing. By imprinting the rotation in the opposite direction (rolling, case 4R and 2R), product particles are forced in the direction of the gap or further away from the contact point on the opposite side. The same effect occurs with rotation of particles with identical motion alignment (shearing) on the opposite side to the displacement.

For a quantitative evaluation, the number of collisions, the number of contacts and the number of product particles involved are considered. Multiple collisions (each numerical contact between grinding bead and product particles), which occur in short succession, are summarized into a contact. In Table 4 they are shown for the different contact types [12].

Table 3 Parameters for different contact cases [12]

4R, Normal collision with rolling	$v_n = \pm 5$ and mm/s and $w_x = \pm 4\pi$ 1/s with $\xi_{tra,n} = 0.613$ and $\xi_{rot,r} = 0.387$
2R, Normal collision with rolling	$v_n = \pm 5$ and mm/s and $w_x = \pm 2\pi$ 1/s with $\xi_{tra,n} = 0.864$ and $\xi_{rot,r} = 0.136$
0R, Normal collision	$v_n = \pm 5$ and mm/s and $w_x = \pm 0\pi$ 1/s with $\xi_{tra,n} = 1.000$ and $\xi_{rot,r} = 0.000$
2S, Normal collision with shearing	$v_n = \pm 5$ and mm/s and $w_x = \pm 2\pi$ 1/s with $\xi_{tra,n} = 0.864$ and $\xi_{rot,r} = 0.136$
4S, Normal collision with shearing	$v_n = \pm 5$ and mm/s and $w_x = \pm 4\pi$ 1/s with $\xi_{tra,n} = 0.613$ and $\xi_{rot,r} = 0.387$

Table 4 Contact and collision parameters for different contact cases [12]

Contact case	Particle number at start	Particle number at end	Average velocity	Average position change	Stressed particles/contacts	Collision Nr
4R—normal impact and rolling	5	2	1.165 * v_{GM}	0.955 * d_p	3	65
2R—normal impact and rolling	5	5	0.807 * v_{GM}	0.665 * d_p	3	64
0N—normal impact	5	5	0.614 * v_{GM}	0.465 * d_p	3	61
2S—normal impact and shearing	5	5	0.654 * v_{GM}	0.569 * d_p	3	62
4S—normal impact and shearing	5	3	0.797 * v_{GM}	0.767 * d_p	3	64
4R—normal impact and rolling	10	6	1.408 * v_{GM}	1.015 * d_p	5	84
2R—normal impact and rolling	10	9	1.007 * v_{GM}	0.733 * d_p	4	64
0N—normal impact	10	9	0.866 * v_{GM}	0.561 * d_p	4	88
2S—normal impact and shearing	10	10	0.901 * v_{GM}	0.588 * d_p	5	62
4S—normal impact and shearing	10	10	0.939 * v_{GM}	1.107 * d_p	5	60

For the five contact cases with five product particles there is no apparent difference in the number of contacts, for the calculations with ten product particles there is an increase in the number of contacts with increasing rotational velocity. In addition to direct strain by grinding beads, strain by the fluid is also possible. More hydrodynamic stress is presumably caused by higher acceleration through the fluid due to the higher product particle velocity with a similar effect on the position change. The mean product particle velocity increases with increasing angular velocity which is more pronounced in rolling motion than in shearing motion. A higher angular velocity leads to a greater change in position with rolling motion having a larger effect on product particles. In summary, the rotation of the grinding beads has a considerable influence on the capture probability [12].

To sum up, the conveying into the gap for both shearing and rolling motion is evident, leading to increased capturing probabilities. A complete statement about the type of contact is not yet possible due to limited computing capacity, an evaluation of the capture probability is however possible [12].

3 Measuring Material Function of Fine Particles

For the calibration of a flow sheet simulation, quantitative knowledge about the breakage function of product particles and aggregates as well as about the specific breakage energy is required. Although there are ways to determine the breakage energy distribution of single product particles via microcompression, this method is very time-consuming due to sufficient statistics necessary for a representative database. Moreover, a breakage function can only hardly or not be determined. Therefore, this method is not suitable for industrial application due to high investment costs and extreme high measurement time. In addition, it delivers limited information about the resulting fragment size distribution. Another method stated in literature is the back-calculation of model parameters from the results of mill experiments. However, the use of literature model equations for the breakage function is limited for ultra-fine comminution and the results achieved by back-calculation are often restricted to the test mill. Furthermore, this method is unsuitable for industries like pharmaceutics where often only very small product samples are available for testing.

In order to connect these, a breakage tester was constructed, based on the working principle of an EXAKT-three-roll-mill (E-line) with a precise roller to bearing clamping unit. It allows the investigation of a small but still reasonable amount of particle breakage to guarantee the required statistical significance. In addition, the fraction size distribution of an initial narrow particle size distribution can be measured after the stressing between the rolls. For this purpose, only two of the three rolls are used for particle breakage. The gears are modified to set counter-rotating motion of identical velocity, and only the normal pressure is applied and shearing between the rolls is prohibited. The breakage tester can be seen as a scheme in Fig. 10 and as the real device in Fig. 11.

The gap between the rolls can be adjusted in the range of 5–180 μm with an accuracy of one micrometre depending on the bearing clearance, the parallelism of the rolls, the fine-adjustment of the gap as well as the simultaneous measurement of the low compression forces and torques. In addition to the original construction of the three roller-mill, a torque meter is added to the third roll, which is not directly involved in the crushing of the particles.

The particle deposition is carried out via a vibration conveyer on top of the devise which allows for a defined velocity and the deposition of a specified particle mass of a limited number of particles. The tailor-made feed platforms allow the deposition along the entire width of the rolls according to the required distribution patterns. Under the rolls, a removal unit enables the particle uptake. For torque measurements, the direct contact of the removal unit to the rolls was prohibited.
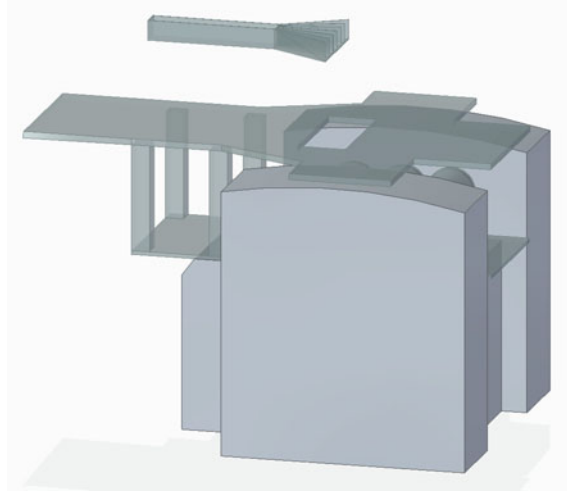
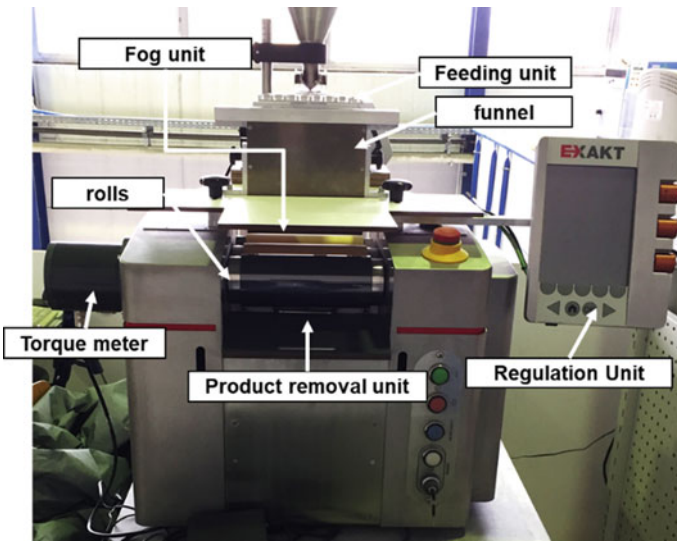**Fig. 10** Schematic of breakage tester

Fig. 11 Photo of breakage tester in laboratory

The breakage tester enables to adjust various parameters such as roller speed, product mass flow, distance of the particles falling on the rolls, the gap sizes between the rolls, and the feed particle size. The effect of the gap size on the applied breakage force and resulting breakage function was investigated systematically in order to guarantee the breakage of each particle within the feed particle fraction but excluding multiple particle breakage. The aim is the identification of an optimal gap size to

feed size ratio. Therefore, the gap size was varied between 40 and 80 µm and the feed particles have been sieved into four different fractions from 50 up to 110 µm (Table 5).

The systematic variation of feed particle size and gap size has shown that the gap size has to be significantly lower than the $x_{50,3}$ for breakage, even though there are particles with greater particle size in the feed (Fig. 12). Therefore, a sufficient energy input and, thus, gap size to particle size ratio is necessary to observe their effects in the particle size distribution. When this breakage energy is reached, the number of particles breaking depends on the ratio of gap size to particle size. In Fig. 12b, the resulting breakage function of the particle size fraction from 80 to 90 µm is unchanged for gap sizes smaller than 50 µm. This effect can be attributed to two effects: First, coarser particles might be collected above the rolls until they are small enough passing the roll so that they are ground in two steps, effecting the final particle size. Second, dust formation is increasing significantly, increasing the loss of fines. Therefore, there are two limits of the gap size. An upper limit where most particles are too small and just fall through the gap, and a lower limit, where the detection of fines is limited due to increasing loss at decreasing gap sizes.

These findings result in the aim to identify the optimal ratio between the feed particle and gap size of the two roller tester. After determining these two limiting ratios for all particle size fractions, it is observed that between 45 and 94% the applied energy increases and the breakage behavior of the particles changes. At ratios of gap to particle size being smaller than 45%, further specific energy input increases the

Table 5 Matrix of experiments with variation of feed particle size and gap size

Feed size [µm]	Gap sizes [µm]
50–71	40, 50, 60, 70, 80
71–80	40, 50, 60, 70, 80
80–90	40, 50, 60, 70, 80
90–100	40, 50, 60, 70, 80

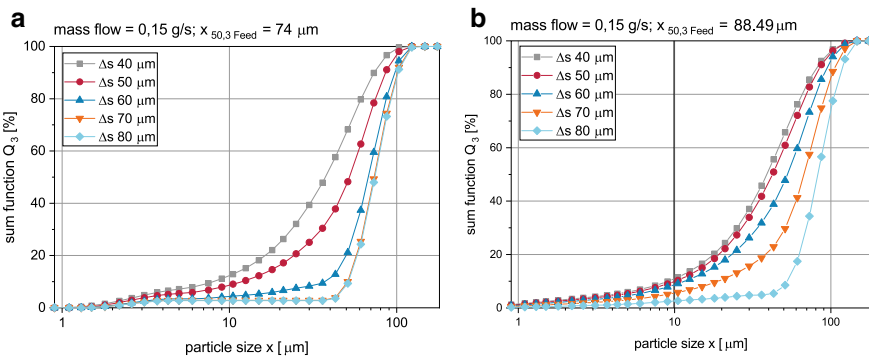**Fig. 12** Effect of the gap size on the particle size distribution—**a** Feed particle size of $x_{50,3} = 74$ µm and **b** $x_{50,3} = 88.49$ µm

loss of fines, complicating the detection of further breakage to smaller fractions. It can be concluded that there is a limit of detection in size reduction for a defined particle size. At ratios above 94%, most particles simply fall through the gap, resulting also in smaller energy values.

Summarizing this results, the breakage behavior of materials and especially the breakage function can be predicted through the tailor-made breakage tester. Further aim is to calculate the breakage function dependent on feed particle size and breakage energy for the given material. Further investigations will deliver more information about the usage of the two-roller tester and will be published soon. One focus will be to evaluate to what extent the breakage function can be used to predict breakage in stirred media mills.

4 Grinding

4.1 Effects of Operating Condition Variations on the Breakage Rate

The evolution of the particle size distribution in grinding processes can be described by population balance modelling. In order to model the transition of particles to smaller particle sizes, the parameters specific breakage rate and breakage (distribution) function are required. These can be determined by experiments. However, the specific breakage rate determined experimentally for one operating condition is not easily transferable to other operating conditions as it depends strongly on particle size, material properties and the stressing conditions in the mill.

The stress conditions in stirred mills can be determined with semi-empirical models (e.g. [13–16]). The shear-based power model represents the stirred mill as a viscometer and shows the effect of stirrer speed, geometry and viscosity on the power consumption of the mill [15]. The stress energy model shows with the parameters stress energy and stress frequency, which are calculated from simple proportionalities, the influence of process parameters on the grinding result [14]. Eskin et al. [13] estimate the mean velocity and frequency of grinding media oscillations using approximate values of turbulent energy dissipations on a micro scale. Based on this micro hydrodynamic view of the particle stressing, Afolabi et al. [16] define a process parameter depending milling intensity factor that correlates with the breakage kinetics of drug nanoparticles. As an alternative to the semi-empirical models, the stress conditions can be obtained by simulating the grinding media motion in wet operated stirred media mills via coupling of discrete element method (DEM) with computational fluid dynamics (CFD) (e.g. [7, 17]) or smoothed particle hydrodynamics (SPH) (e.g. [18]). Gers et al. [19] characterize collision characteristics by determining collisional Stokes and Reynolds numbers from direct numerical simulations. Distribution of stress energy from DEM simulations in combination with

material breakage behavior have already been applied to ball mills for estimating the effect of operating parameters on the breakage rate [20–23].

In the following the influence of different operating and machine parameters on the specific breakage rate in wet stirred media milling is discussed. On the one hand, the stress conditions in a stirred media mill are determined by the semi-empirical, mechanistic model of Kwade and on the other hand with two approaches based on coupled CFD-DEM simulations. The results of the three procedures are compared with experimentally measured specific breakage rates of limestone, a material frequently used to study the grinding process in stirred mills [24–26].

Stress energy approach: It can be shown that the breakage rate directly depends on the product of stress energy and stress frequency (determined according to Kwade's stress model). The product of both, stress energy and frequency, can be seen as a measure for the product volume specific power input acting on the product particles during the grinding or dispersing process. This makes it possible to describe the influence of grinding media density and size as well as stirrer speed on the breakage rate [27]. Furthermore, the influence of additional parameters, namely stirrer geometry (Fig. 13a) and product concentration of the suspension (Fig. 13b) on the breakage rate of limestone particles was investigated. The stress energy coefficient SE is calculated using the mass of a grinding media m_{gm} and the peripheral stirrer speed v:

$$SE = \frac{1}{2} m_{gm} v^2 \tag{9}$$

The coefficient stress frequency, SF, is proportional to the grinding media collision frequency per volume (i.e. the volume specific collision frequency) n_c/t, the number of particles per volume n_P^* and the capture probability P_c.

$$SF \propto \frac{n_c}{t n_P^*} P_c = \frac{n_K}{t n_P \left(1 - \varphi_{gm}(1 - \epsilon)\right)} P_c \tag{10}$$
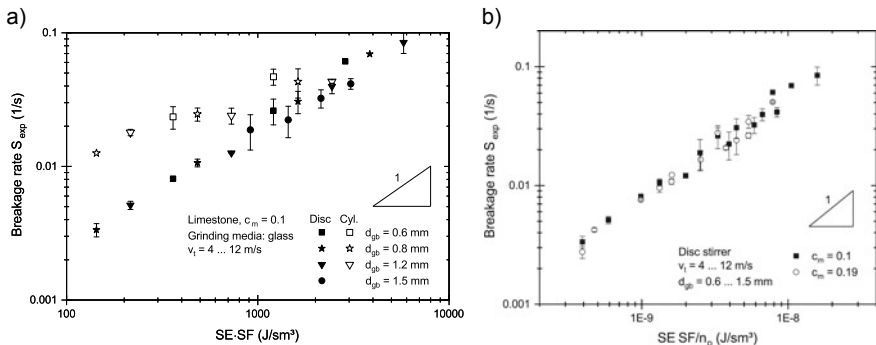

Fig. 13 Experimentally determined breakage rate of limestone for two different stirrer geometries (left) and two solid concentrations (right) applied via the product of stress energy and stress frequency or SE * SF normalized to the number of particles (Reprinted with permission from [27])

Here n_P is the number of particles per suspension volume, φ_{gm} the grinding bead filling degree and $\in$ the grinding bead porosity. The collision frequency and, thus, the load frequency are proportional to the stirrer speed and number of grinding media. The capture probability is calculated using an "active volume" between two grinding media during a contact. A further assumption is that in the actual size and concentration range only one particle is trapped between two grinding media and significantly stressed.

Using this approach, the breakage rate was determined for different grinding media sizes and stirrer speeds as well as two different stirrer geometries and solids concentrations. Figure 13 shows very clearly that the stress model well describes the influence of changes in operating parameters on the breakage rate in batch operation per stirrer geometry. However, a simple transfer to another stirrer geometry is not possible, which is usually unproblematic since the stirrer geometry is normally not a variable quantity in the process. Furthermore, the model approach for the breakage rate according to the stress model does not allow predicting the absolute value of the breakage rate from scratch. Few experiments with the used material in the respective mill are necessary to determine the location parameters of the linear function of the breakage rate.

Approach via mean values from CFD-DEM simulations: The collision energy distribution and the collision number were calculated for various operating parameters using CFD-DEM simulations and the result was compared with the characteristic values of the stress model [7]. It was shown that simulated grinding media contacts and collision energies do not show exactly the same dependencies on the operating parameters as defined for the stress model. For the product of the two parameters SE and SF, however, the dependency is approximately the same. This is an indication of why the combination of stress energy and stress frequency shows good correlations with experimentally measured breakage rates. It should be noted that the capture probability was not determined from the DEM-CFD simulations. A strong correlation between the simulation results and the experimental breakage rates could be shown (Fig. 14). The breakage rate of a product particle size class can be described by a linear function. The smaller particles exhibit higher strength; therefore, their breakage rate is lower. No material parameter is included in the index in Fig. 14, so two curves can be seen. The integration of material values into the model is shown in the next section.

Approach via CFD-DEM simulation and material function: The CFD-DEM simulations provide complete stress energy distributions that are characteristic for different mills and operating parameters. Tavares and Carvalho [22] consider in their approach for dry ball mills the stress energy distribution of the mill as well as the particle breakage energy distribution through the convolution of the two distributions. In combination with the collision frequency and the capture probability, this results in the breakage rate. For validation of this model for stirred media mills, yeast cells were used as test material [27]. The yeast cells have the advantage that the burst or breakage energy can be adjusted by the osmotic conditions and that they are almost monodisperse with a particle size of ~5 μm. In addition, yeast cells show no breakage function after digestion and the burst or breakage rate can be clearly determined
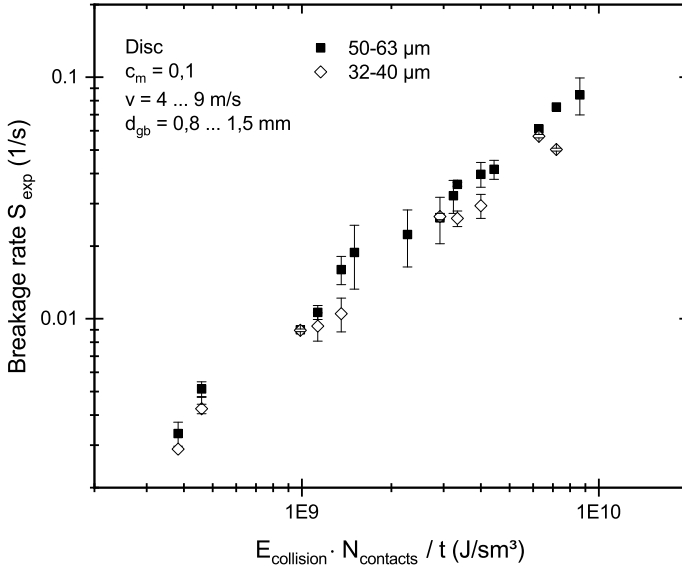
Fig. 14 Experimental breakage rate plotted against specific energy input determined from CFD-DEM simulations for two limestone size classes (Reprinted with permission from [27])

by measuring the released protein concentration. The breakage energy distribution of the yeast cells was measured by microcompression and is shown in Fig. 15. "Yeast #1" and "Yeast #2" indicate two different osmotic conditions which influence the breakage energy distribution. Furthermore, Fig. 15 shows the effective collision frequency $\mathbf{n_{c,eff}(E)}$. The effective collision frequency represents the summation of the frequency of collisions with energy E and higher and is determined from the CFD-DEM simulations:

$$\frac{n_{c,eff}(E)}{t} = \int\limits_{E}^{E_{max}} \frac{n_c(E)}{t} dE \tag{11}$$

The breakage rate is then calculated taking into account the material breakage energy distribution $g_{mat}(E)$:

$$S_{sim} = \frac{P_c}{n_P(1 - \varphi(1 - \epsilon))} \int\limits_{E_{min}}^{E_{max}} g_{mat}(E) \frac{n_{c,eff}(E)}{t} dE \tag{12}$$

Figure 16 shows the comparison between the experimentally determined breakage rate S_{exp} and the simulatively determined breakage rate S_{sim} on a double logarithmic scale. It should be emphasized that S_{sim} is based solely on the microcompression data,
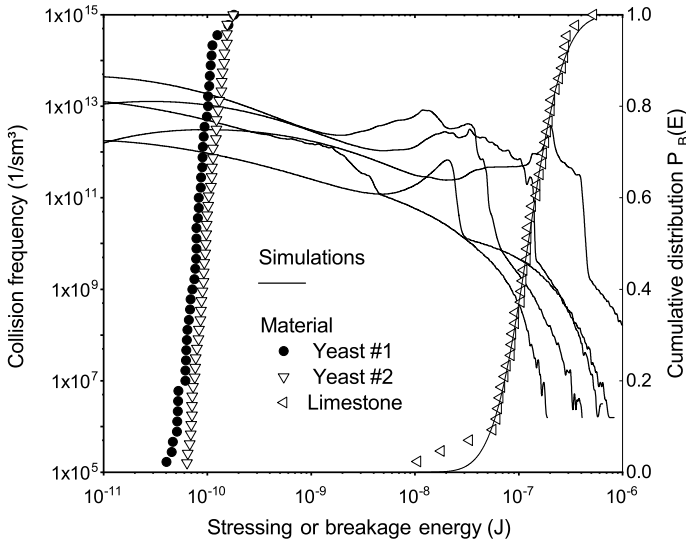
Fig. 15 Effective collision frequency determined from CFD-DEM simulations and breakage energy distribution of yeast and limestone. The breakage energy distributions can be described by lognormal distributions (Reprinted with permission from [27])
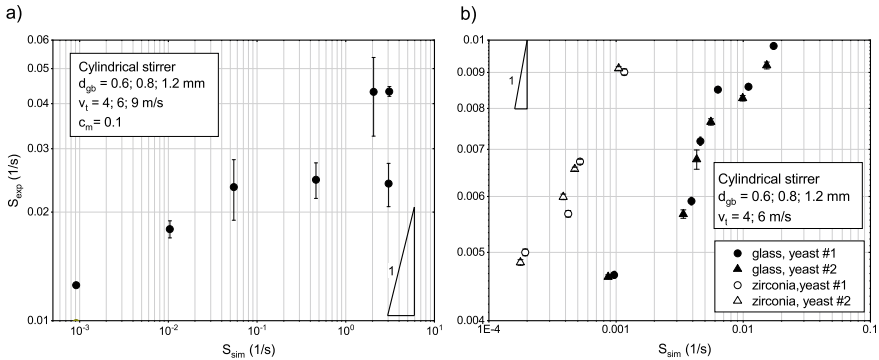

Fig. 16 Experimentally determined breakage rate compared to the simulative determined breakage rate for limestone (**a**) and yeast cells (**b**) (Reprinted with permission from [27])

simulation results and model assumptions and does not contain any fitted parameters. Figure 16b shows that for yeast the influence of stirrer speed, material strength and grinding bead size on the breakage rate can be well mapped. In the case of glass grinding media, the simulated breakage rate corresponds to 0.2–1.7 times the experimentally determined breakage rate. However, the influence of the change of grinding media from glass grinding media to zirconium oxide grinding media cannot be reproduced correctly and S_{sim} for zirconium oxide grinding media is clearly

below the experimental values. For limestone (Fig. 16a) there are two clear outliers and no linear correlation could be found between S_{sim} and S_{exp}. The poorer agreement of the results for limestone may be due to the fact that the collision energy distribution shows strong fluctuations in the range of the breakage energy distribution values for limestone (see Fig. 15). In addition, the energy actually transferred to the particles does not exactly correspond to the collision energy, which is a maximum value. Therefore, it should be checked whether the simulated collision energies are in principle too low, or whether multiple stressing is also an important factor in the grinding of limestone.

4.2 Circulation Mode

Materials can be ground in four different modes. Therein, continuous passage mode is most often used in industry. Circulation mode is an approach often used in laboratory scale to understand grinding processes, avoiding the usage of large amounts of material. In 1996, Kwade developed a stress energy model that calculated the stress energy based on the kinetic energy of the grinding beads [28]. After correlation with the specific energy and the information of the final product size, it is possible to obtain an optimum curve for specific energy input.

Circulation mode is often the favored method in laboratory scale to determine the operation parameters for a certain final product size, but also in industry if very fine particles have to be produced. Therefore, it is of great interest to identify the important influencing parameters in circulation mode and correlate it towards one or multiple passage mode, i.e. different continuous modes that are often applied in industry for medium fine and coarse products like minerals, agrochemicals and ores. Kwade introduced several parameters that influence the kinetic energy and one of those parameters affecting the energy transfer coefficient is the viscosity of the product suspension [29]. Thereby, the viscosity is dependent on the mass concentration, particle size and fluid viscosity. If the fluid viscosity is not varied, but the mass concentration, then beside viscosity also the capture probability is influenced.

Generally grinding in circulation mode results in broader particle size distributions compared to running in multiple passage mode. Especially the first circulations result in broader distributions, but longer grinding times and with that higher number of cycles reduce the poly dispersity index PDI. However, operation in circulation mode with a sufficient number of cycles delivers distinctly narrower residence time distributions and, thus, particle size distribution than operating the mill in one passage mode (Fig. 17) [30].

The grinding experiments were executed in two different types and sizes of mills to consider mill specific effects: One was the LM4 IsaMill^{TM} from Netzsch, the other one the PM-1 from Drais. The LM4 has an internal deflector wheel and its volume is around 4.5 L. Six perforated discs have been used with a distance of 35 mm. The PM-1 is smaller and its volume is around 700 mL. There are five perforated discs installed. In the LM4 IsaMill^{TM}, the mass concentration was kept constant to
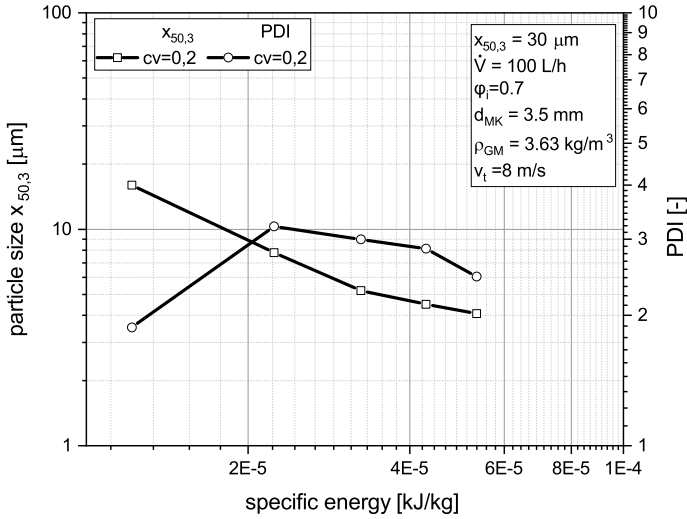
Fig. 17 Development of particle size $x_{50,3}$ and PDI in circulation mode for limestone

30 wt%, but the fluid viscosity was varied through the addition of polyethylene glycol to observe the effect of pure viscosity changes on grindability. The volume flow was set to 100 L/h and the tip speed was 8 m/s. For the PM-1, the mass concentration was varied to additionally look at the effect of capture probability on grinding events. The volume flow was set to 50 L/h and the tip speed was constant at 10 m/s.

In Fig. 18a, the viscosity increases because of the increase in mass concentration and the decrease in particle size. Higher solid concentrations lead to longer circulation times. This effect can be normalized by the throughput capacity. The effect is
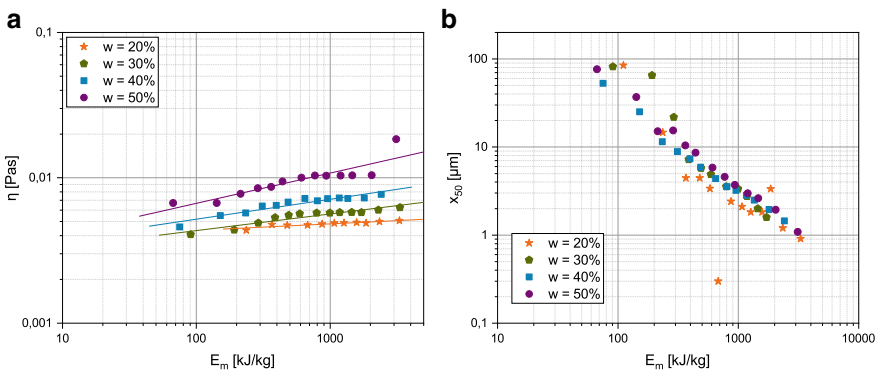

Fig. 18 Grinding of soda-lime-glass in circulation mode in PM-1—**a** viscosity development and **b** corresponding $x_{50,3}$ in dependency of specific energy consumption

interesting during the first 20 min of operation when it was possible to reach significantly smaller particle sizes if the solid concentration is reduced. This effect can be accounted to two phenomena: On one hand, 20 wt% should be enough material to capture particles during each stress event. Increasing the amount of particles in the system would lead to further energy distribution among the particles, resulting in less events per particles and an increase in grinding time. On the other hand, the viscosity increases with a higher solids concentration leading to a decrease in energy transfer coefficients and in kinetic energy transferred from the grinding bead onto the captured particles. This effect also increases grinding time until the same final particle size is reached.

Since the industry often uses passage mode for comminution if medium or coarse product size are required, negative side effects due to increased solids concentration can be reduced through the stabilization of the product particles. In the majority of instances, reduction of solids concentration is avoided since the throughput is decreased. For economic reasons, engineers often increase the specific energy to obtain the same result in shorter time. Still, the grinding efficiency dependent on solids concentration might be increased for larger mills. In this study, the laboratory mill (Drais PM-1) has no internal classifier that would influence the product or grinding media transport.

The effect of fluid viscosity on the grinding efficiency was also investigated. In this study, the viscosity does not only influence the grinding itself but also the product and the grinding media transport through the internal deflector wheel of the mill. For comparison, the temperature was recorded during grinding and the viscosity was measured at the same temperature measured within the grinding chamber. Figure 19a represents the development of viscosity with increasing specific energy under various fluid viscosities. It is observed that the viscosity remains constant over the grinding time and that it is mainly dependent on the fluid viscosity (continuous phase). This leads to the conclusion that particle size (disperse phase) which is changing over grinding time does not affect the suspension viscosity in this case. Reasons are that
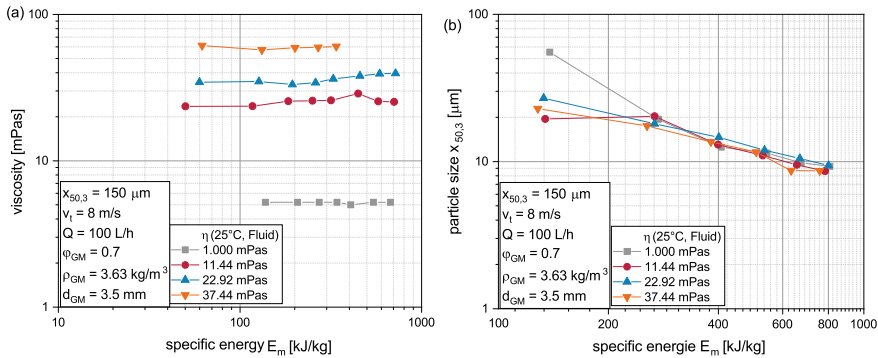

Fig. 19 Grinding of quartz in circulation mode in LM4 IsaMill[TM]—**a** viscosity development and **b** corresponding $x_{50,3}$ in dependency of specific energy consumption

the particle size for the given solids concentration is still above or in the range of a critical value (Knieke et al.) under which the viscosity starts to significantly rise and, that the effect of the reduction in particle size is compensated by the increase of the temperature inside the grinding chamber (Fig. 19a). Comparing these results with the particle size (x_{50}) change in Fig. 19b, only slightly difference in the measurement values could be found. Even though the increase in viscosity probably improves the grinding bead distribution along the length of the LM4, the dissipation of kinetic energy through increased damping of bead collisions decreases grinding efficiency. Therefore, no effect of viscosity on grinding result could be ascertained here. However, at the beginning of the grinding process, i.e. at low residence times, an increase in viscosity improves the grinding efficiency in the LM4 (Fig. 19b).

In general, the viscosity is an important aspect for grinding at low grinding times. With increasing number of cycles, the effect of viscosity is decreasing. One aspect might be that the product residence time is increasing with higher viscosities, which is important in the beginning of the process. Another aspect might be that particles greater than 20 μm can be captured more efficiently at higher viscosities, since the drag force acting on the grinding beads and particles distributes them equally in all cells in the mill, so that the effective velocities of grinding beads in the cells is increased.

In conclusion, viscosity is only changing the grinding process, if the viscosity is high enough to reduce the kinetic energy of the beads and the bead distribution along the length of the mill. If the viscosity is only influenced by the particle diameter, the change in viscosity is marginal as long as the particles sizes are clearly above 1 μm. The influence of increased solids concentrations is reduced through longer grinding times, since the energy is distributed among more particles. A longer grinding time results in a narrower particle size distribution when circulation mode is used at constant mill throughputs. In case of one passage mode longer grinding times and, consequently, lower mill throughputs result in wider residence time distributions and, thus, wider particle size distributions.

5   Product Transport

For stirred media mills it was already shown that the residence time distribution can be simulated by a series of ideal stirring vessels with recirculating flow [31, 32]. The volumes of the ideal stirring vessels are positioned around the stirring discs, as shown schematically in Fig. 20. Thereby, the geometry of the stirred mill is considered. Keeping the series of well mixed cells in mind, in the simulation the product particle concentration should change stepwise in axial direction after a change in the product inlet. This also corresponds to the experimentally observed behavior of the fluid transport [32]. Back mixing is described by the return flow coefficient R, which indicates the ratio of mixing flow to volume flow: $R = \dot{R}/\dot{V}$

Fig. 20 Schematic representation of the cell model with return flow for stirred media mills
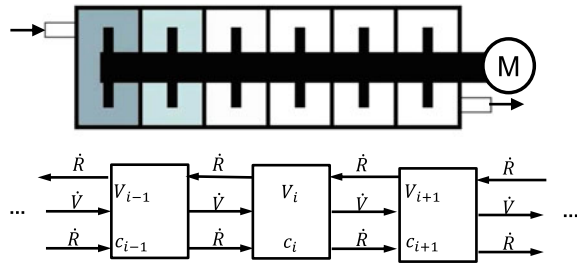
In this model, the return flow coefficient is assumed to be constant over the entire mill. The return flow coefficient must be determined experimentally and can be modelled to a limited extent depending on the operating parameters [32]. Additionally, it is assumed that in fine grinding the product particles move together with the fluid [33]. This allows the product transport to be determined experimentally by tracer experiments for the fluid phase, as described in the following (see also Fig. 21).

In order to measure the residence time distribution in stirred media mills, a pulse of saturated sodium chloride solution was injected at the grinding chamber inlet. At the grinding chamber outlet, the electrical conductivity was measured. This gives directly the residence time density function, which was normalized and corrected for outliers. The dead time of the flow between injection point and grinding chamber inlet as well as between grinding chamber outlet and conductivity probe was approximated by assuming an ideal plug flow [34]. For the cell model with back-mixing, a state space model was created in Matlab. By minimizing the sum of the error squares using the Matlab function fminsearch, the simulated residence time distribution was adapted to the experimentally measured distribution and the return flow coefficient R was determined.

The examination of the product transport took place in the same two stirred media mills that were mentioned earlier: first, a laboratory sized mill (PM-1, Drais) with in this case 4 grinding discs and a working volume of 613 mL and second, a mill with deflector wheel (M4 IsaMill, Netzsch) and a volume of 4.6 L. The effect of the viscosity on the residence time distribution was investigated using a polyethylene glycol-water mixture in different proportions as Newtonian model fluid. The temperature at the grinding chamber inlet and outlet was recorded and its influence on the viscosity was taken into account. In addition to the viscosity, the operating parameters stirrer speed, volume flow, grinding bead size and grinding media filling were varied.

It was shown that the cell model with back-mixing is capable of mapping the residence time distribution in the two stirred media mills investigated. With increasing circumferential speed, a steady increase of the mixing flow was observed (see example parameters in Fig. 22a). Figure 22b shows the influence of the medium viscosity on the mixing flow. With increasing viscosity, the mixing flow decreases, whereby the values for the low viscosity of water partly do not fit into the overall
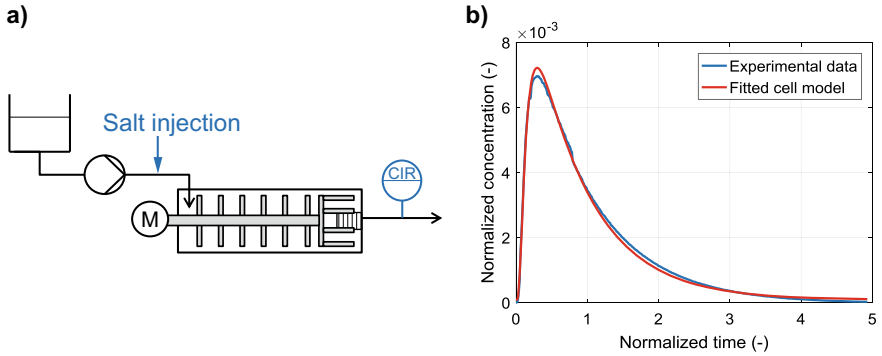
a)

Salt injection

b)

Fig. 21 **a** Experimental procedure to measure the residence time distribution of the fluid phase by a trace method. **b** Fitted cell model with mixing flow to experimentally measured residence time density function
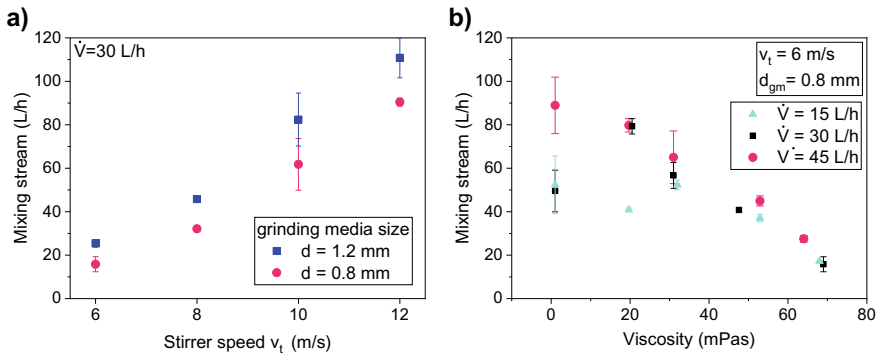
a)

b)

Fig. 22 Back-calculated mixing streams in the cell model in dependency of the parameters **a** stirrer speed and **b** viscosity of the medium

trend, probably due to a more even axial distribution of grinding media. The variation of the volume flow has a small influence on the mixed flow. A constant mixed flow at higher volume flows means that the return flow coefficient R is reduced and, therefore, a narrower residence time distribution is achieved.

Figure 23 shows the mixing stream that was fitted to residence time experiments in the M4 IsaMill. The overall media filling degree has a clear influence on the mixing stream. A higher filling degree leads to a lower mixing stream between cells and, thus, a narrower residence time distribution. The effect of the pump capacity of the deflector wheel (classifier) was investigated by reducing the number of pins. It can be seen in Fig. 23 that the deflector wheel increases the mixing stream.
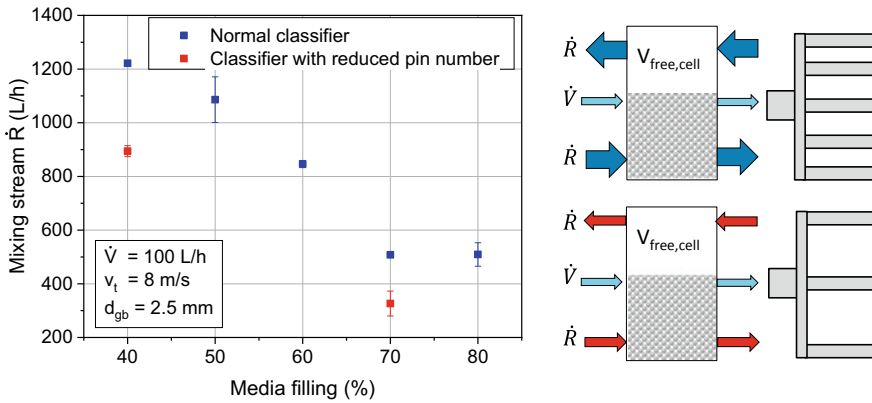
Fig. 23 Back-calculated mixing streams for the M4 IsaMill

6 Axial Grinding Media Distribution

Depending on the type of mill, it is observed that the grinding media is distributed along the x-axis due to drag forces, which lead to a grinding media transport. This effect can reduce the performance of a mill drastically, up to a point where the grinding beads are packed at the outlet of the mill. Therefore, some mill types include an internal deflector wheel which is counteracting towards the volume flow. This mill design leads to a change in grinding bead distribution along the x-axis, which is not understood completely up to this point. In this study, the effect of single parameters such as tip speed, volume flow, bead size and density, grinding media filling degree and viscosity changed the grinding media distribution along the x-axis.

Since the grinding media filling ratio changes the stress conditions in the mill and therefore affects the grinding conditions, it is of interest to combine the single effects on the grinding media transport and model the effect of the grinding media filling degree on the grinding process.

In order to determine the local grinding media filling ratio, radiometric densitometry was used, dealing with the weakening of a gamma source through the grinding beads. Depending on the strength of the signal, it was possible to back-calculate the grinding media concentration in each cell for different positions before and after the discs. The exponential loss of radiation intensity follows the Lambert-Beer's law [35].

The radiometric densitometer was set above the mill design to closely investigate the grinding media transport during running of the mill (see Fig. 24). The mill consists of six perforated discs with a diameter of 100 mm. The distance of the discs is 35 mm. An internal deflector wheel was used as a classifier and was installed directly in front of the outlet to avoid bead packing.
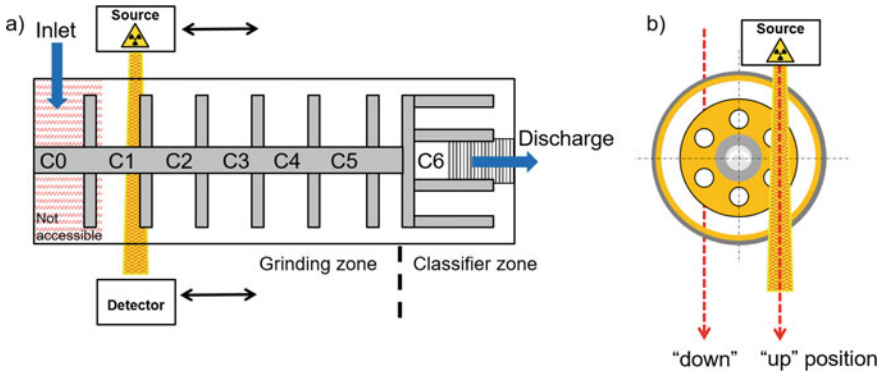
Fig. 24 Scheme of axial (**a**) and radial (**b**) setup for the measurements with radiometric densitometer [35]

The gamma radiation source consists of Cs^{137} (661 keV) nuclide. The detector is a thallium activated NaI crystal. For the detection two positions were chosen, one on the right mill side, the other one on the left side to avoid measurements closely to the shaft. 17 positions were measured along the x-axis. To avoid overlaying effects of the grinding media with the grinding beads, all tests were performed using model fluids with different viscosities. The grinding beads were varied in density and size. Furthermore, the total grinding media concentration were varied between 40 and 80% of the grinding chamber volume.

It was observed that all parameters change the measured filling degree in the separate cells. In Fig. 25a), the grinding media concentration was varied between 40 and 80%. First of all, the cells seem to be filled gradually. The cells at the inlet are filled with grinding beads before the cells closer to the outlet, in conclusion the backwards transport by the classifier has to be stronger than the forward transport by the volume flow. The classifier itself never sees any grinding beads. The disc before the classifier acts as transition zone between the grinding and classifying zone, showing some grinding beads before and some behind disc 5. This partitioning and the way the cells are filled with grinding beads leads to a characteristic repeating pattern of the development of the local filling degree over the length of the mill: The highest local filling degree is most often measured in cell 1 (C1) at the mill inlet. The filling ratio value of this cell influences the filling of all following cells. Depending on the density and size of the grinding beads, it is possible to vary this maximum filling degree.

Figure 25a–b show the grinding bead distribution for a bead density of 3.7 g/cm^3 and a bead size of 2.5 mm for different filling ratios and viscosities. In both cases, the maximum concentration seems to be close to 80%. Comparing this to a decreased density of 3.63 or 1.5 g/cm^3 (Fig. 25c), the maximum reached concentration in cell 1 is increased. For greater grinding bead sizes on the other hand the maximum local concentration is decreasing. Depending on this first cell, all other cell will be filled with grinding beads. The solids concentration of the product particles influences
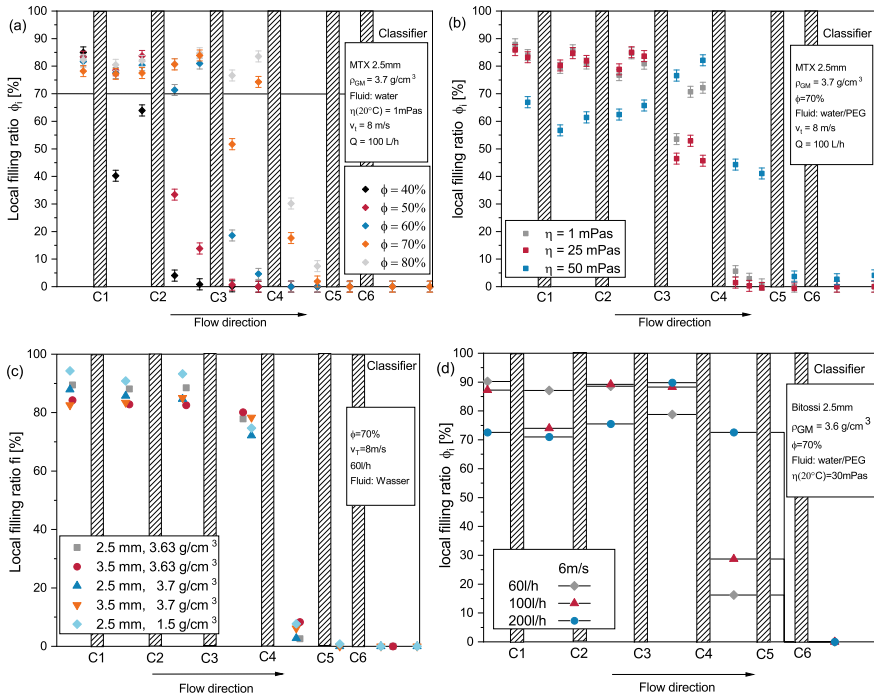
Fig. 25 Local filling degree in dependency of **a** grinding bead concentration [35], **b** viscosity, **c** grinding bead density and **d** volume flow

the effect of the drag and centrifugal forces on the grinding beads. If the beads are denser and, thus, heavier, then the centrifugal forces increase more than the drag forces applied by the classifier and, therefore, the drag has less effect on the axial grinding media distribution.

Exactly the same phenomena can be seen when the viscosity is increased up to 50 mPas (see Fig. 25b) The classifying effect is reduced, because more kinetic energy is lost by the transport of the beads through the medium. Although, it can be seen that an increase in viscosity effectively distributes the particles more along the x-axis in direction of the mill outlet and as a result the grinding beads can move more freely in the single cells.

On the one hand, Fig. 25d shows the influence of a reduced rotor tip speed on the local filling degree. Compared to (c), the maximum local filling degree in cell 1 does not change at low volume flow. It might be that the influence of the tip speed is increasing with greater volume flows. On the other hand, Fig. 25d shows the great influence of the volume flow on the maximum tip speed at least for low rotor tip speed.

It is obvious that there is a close interaction of the parameters affecting the axial grinding media distribution. Especially the tip speed and the volume flow rate influence the grinding media transport along the x-axis and can easily be adjusted during the operation of the mill.

7 Flowsheet Model

In the following the application of the dynamic grinding model for a horizontal stirred media mill is shown. The model is implemented in the dynamic flowsheet simulation software Dyssol [36]. The change of the particle size distribution is calculated via population balance equations. The milling chamber is simulated as a series of instantly mixed cells that are connected by mixing streams. The cells allow for a simplified simulation of the grinding bead filling level and the product transport through the stirred media mill. Exemplarily, the effect of the solids concentration and the volume flow on grinding and residence time distribution is investigated. The dynamic response of the product particle size distribution at the mill outlet after stepwise change of these process parameters is shown. The simulations are compared to experimental investigations with limestone in a laboratory stirred media mill.

The simulated flowsheet is shown in Fig. 26. The reason for the delay unit is to account for not ideal plug flow in tubes of the experimental setup. The answer on a step function of salt concentration was measured for the tubes in the experimental set-up via a conductivity sensor. The result cannot be described with ideal plug flow (see Fig. 27). Therefore, the change in concentration is described with Eq. 13, that was fitted to meet the experimental step function response of the tubes:
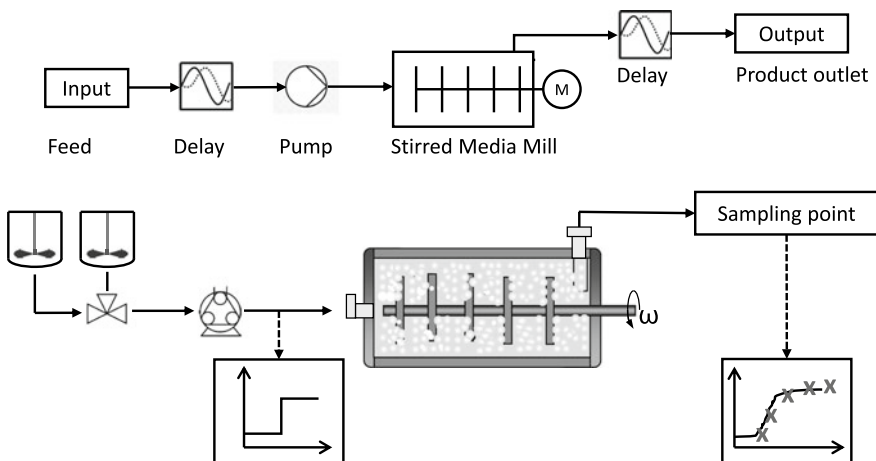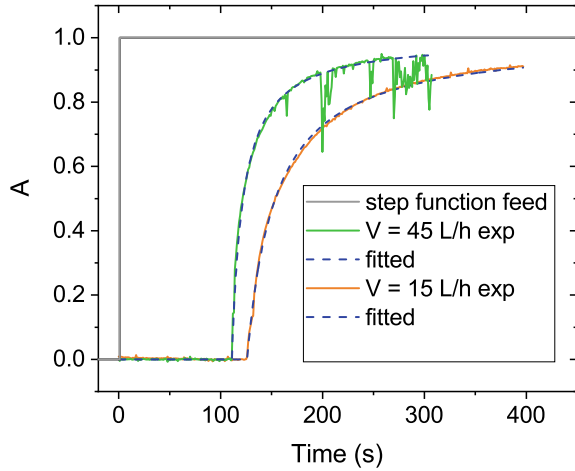

Fig. 26 Flowsheet for continuous grinding operation

Fig. 27 Measured and fitted
answer of tubes on a step
function for two different
flow rates

$$\dot{x} = k\left(x(t) - x\left(t - t_{delay}\right)\right)^2 \tag{13}$$

The pump unit's only purpose is to set the volume flow, which is a time dependent user parameter. The dynamic stirred media mill unit performs grinding of particles in a suspension. The axial grinding media distribution was not considered at this point in the simulations and is assumed to be constant.

The set-up of the continuous experiments is shown in Fig. 26. It is comparable to the simulated set-up. After a steady state is reached in the grinding process the feed is switched from one stirred tank to another to mimic a step function in input parameters. At the product outlet samples are taken at 0.5, 1, 2, 3, 4, and 6 times the ideal filling times after the switch plus the ideal dead time in the tubing considering ideal plug flow. The samples are analyzed for the mass concentration and the particle size was measured via laser diffraction (Helos, Sympatec).

First, the mass concentration in the feed was varied in a step function from 0 to 0.1 to 0.3 to 0.5 to 0. In Fig. 28a the experimental and simulated response of the suspension's solids concentration at the product outlet is shown. In general, the simulations show the adaption of the product outlet to the step function in the feed. However, the scatter of the experimental values is relatively high. In Fig. 28b and Fig. 29 the particle sizes at the product outlet can be seen. As a response to the rise in mass concentration in the mill, the characteristic particle sizes in the product outlet increase. Both, experiments and simulations show this effect.

As another example, the step change in the flow rate was simulated. The volume flow was changed from 30 to 15 L/h. Figure 30 shows at the top the volume flow over time and at the bottom characteristic values of the product particle size over time. It can be seen that it takes about three ideal filling times until a new steady state is reached. A lower volume flow leads to longer residence times of the suspension in the mill and, therefore, smaller particle sizes at the product outlet. At the same time, with the smaller volume flow there is a higher back-mixing in relation to the volume
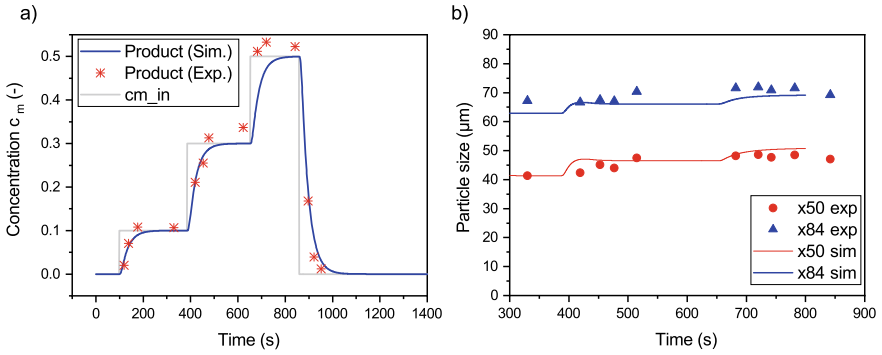
Fig. 28 a Mass concentration of the feed and at the product outlet for the experiments and simulations; **b** median and x_{84} value for the particle size at the product outlet starting from the first reached steady state
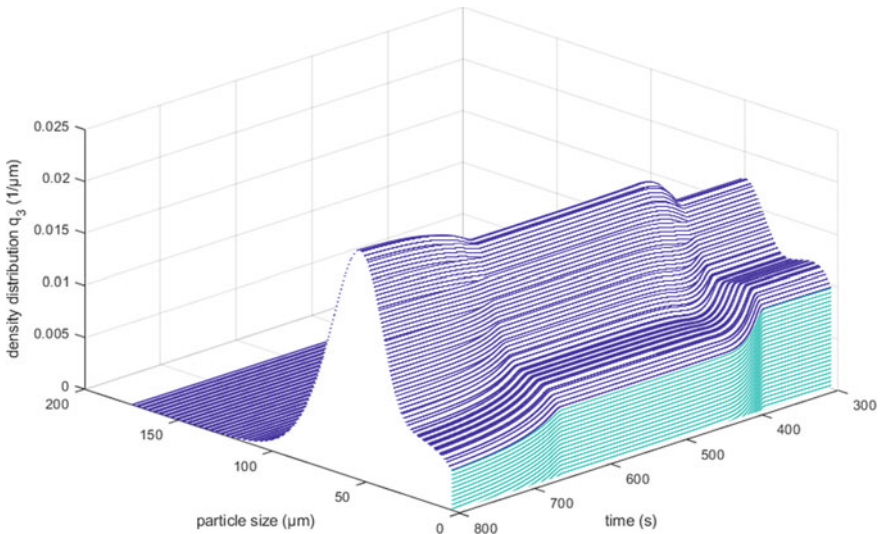

Fig. 29 Simulated particle size distribution at the product outlet after step wise increased solids concentration of the feed suspension

flow, hence a higher mixing coefficient R. At the product outlet, a broader particle size distribution can be detected, which can be explained by the broader residence time distribution.
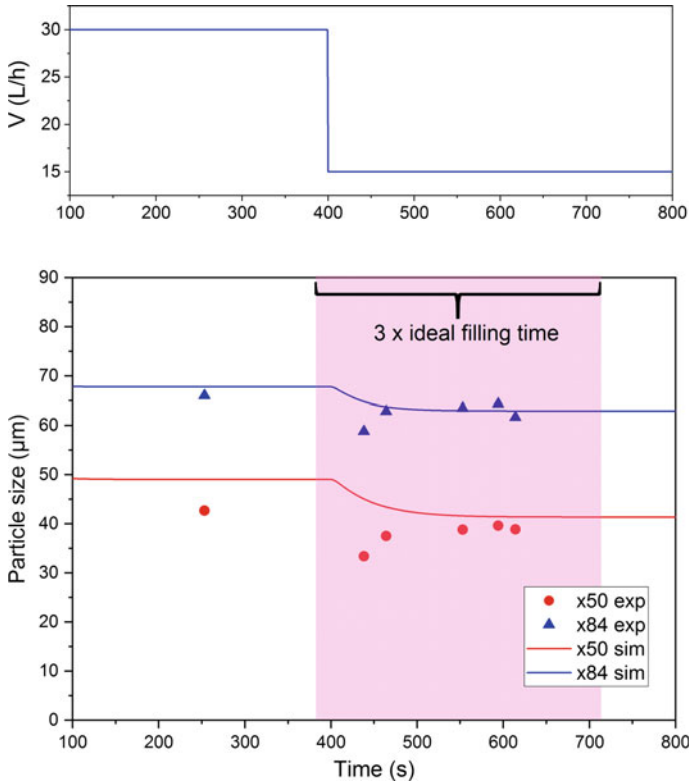
Fig. 30 Median and x_{84} value for the particle size at the product outlet (below) responding to a step function of the flow rate (above)

8 Conclusion

In this contribution two types of horizontal stirred media mills (with and without deflecting wheel) were investigated experimentally and with simulation in order to describe relevant machine parameters for a dynamic process model for stirred media mills. Coupled CFD-DEM simulations were performed to determine the contact frequency and stress energy of the grinding bead collisions. The unresolved simulations showed good agreement to existing models for describing stress energy. The distribution of different collision types such as normal collisions, shearing and rolling could be derived to be used as input parameter for resolved simulations. In these the capturing probability of product particles between approaching grinding beads were investigated, depending on the proportion of the above mentioned collision types. Principle insights could be gained such as increased capturing probabilities for shearing and rolling motion. The capturing probability in combination with the collision frequency and stress energy delivers the relevant machine parameters for flow sheet simulations.

In case of the unresolved CFD-DEM simulations, the product of stressing frequency and energy showed good correlation with experimental grinding results. For the validation different particles were investigated using microcompression, including yeast cells, to experimentally determine the respective breakage probability. Correlating these breakage probabilities with the collision frequencies gained from the simulations allowed for a direct comparison with experimentally gained breakage rates from performing grinding experiments.

For the systematic analysis of fine particle breakage via compression between grinding beads a breakage tester was constructed. Material specific fracturing properties were investigated in dependence of the original particle size and the gap size between the rolls. Force and torque were captured for an energetic evaluation. The device enabled the prediction of material specific breakage behavior which, in a normalized form, should enable the prediction within flow sheet simulations.

The temporal development of particle size distribution was modeled with population balance equations. On this basis the impact of various operating and machine parameters on the breakage rate was examined. It could be verified that collision frequency and thereby load frequency has a linear dependence of the stirrer speed and the number of grinding beads. The so determined breakage rates showed a good correlation with experimental results. The product transport through the mill was simulated via a cell model with mixing flow.

Additionally, circular mode grinding experiments were performed to investigate the impact of operation parameters. For instance, it was shown, that only viscosities high enough to impact the kinetic energy have an impact on the grinding process. Additionally, radiometric densitometry was used to investigate grinding media transport. A high correlation between tip speed and volume flow on the grinding media transport along the horizontal axis could be detected.

The results from these experiments and simulations were included in Dyssol as a flow sheet simulation. The implemented model was then examined by performing simulations and comparing them with experimental results for the particle size at the outlet of a stirred media mill.

References

1. Tavares, L.M., de Carvalho, R.M.: Modeling breakage rates of coarse particles in ball mills. Miner. Eng. **22**(7–8), 650–659 (2009)
2. Capece, M., Bilgili, E., Davé, R.: Insight into first-order breakage kinetics using a particle-scale breakage rate constant. Chem. Eng. Sci. **117**, 318–330 (2014)
3. Theuerkauf, J.: Numerische und experimentelle Untersuchungen von Fluid- und Mahlkörperbewegungen in Rührwerkskugelmühlen, Zugl.: Braunschweig, Techn. Univ., Diss., 2000, 1. Aufl., Cuvillier Göttingen, 2000, ISBN 3897128039
4. Conway-Baker, J., Barley, R.W., Williams, R.A., et al.: Measurement of the motion of grinding media in a vertically stirred mill using positron emission particle tracking (PEPT). Miner. Eng. **15**(1), 53–59 (2002)
5. Jankovic, A.: Variables affecting the fine grinding of minerals using stirred mills. Min. Eng. **16**(4), 337–345 (2003)

6. Hennart, S.L.A., Wildeboer, W.J., van Hee, P., Meesters, G.M.H.: Identification of the grinding mechanisms and their origin in a stirred ball mill using population balances. Chem. Eng. Sci. **64**(19), 4123–4130 (2009)
7. Beinert, S., Fragnière, G., Schilde, C., et al.: Analysis and modelling of bead contacts in wet-operating stirred media and planetary ball mills with CFD–DEM simulations. Chem. Eng. Sci. **134**, 648–662 (2015)
8. Beinert, S., Fragnière, G., Schilde, C., et al.: Multiscale simulation of fine grinding and dispersing processes: stressing probability, stressing energy and resultant breakage rate. Adv. Powder Technol. **29**(3), 573–583 (2018)
9. Kwade, A., Schwedes, J.: Wet grinding in stirred media mills. In: Handbook of Powder Technology, vol. 12, pp. 251–382. Elsevier Science B.V. (2007)
10. Beinert, S., Schilde, C., Kwade, A.: Simulation of stress energy and grinding media movement within a wet-operated annular-gap mill using the discrete-element method. Chem. Eng. Technol. **35**(11), 1911–1921 (2012)
11. Kürten, H., Raasch, J., Rumpf, H.: Beschleunigung eines kugelförmigen Feststoffteilchens im Strömungsfeld konstanter Geschwindigkeit. Chem. Ing. Tec. **38**(9), 941–948 (1966)
12. Beinert, S.: Mehrskalige Simulationen zur Partikelbeanspruchung bei der Zerkleinerung und Dispergierung, Zugl.: Braunschweig, Techn. Univ., Diss., 2015, 1. Aufl. IPAT-Schriftenreihe, Sierke Göttingen, ISBN 9783868447231 (2015)
13. Eskin, D., Zhupanska, O., Hamey, R., et al.: Microhydrodynamics of stirred media milling. Powder Technol. **156**(2), 95–102 (2005)
14. Kwade, A.: Determination of the most important grinding mechanism in stirred media mills by calculating stress intensity and stress number. Powder Technol. **105**(1–3), 382–388 (1999)
15. Radziszewski, P.: Shear based stirred mill power model—An adimensional analysis. Miner. Eng. **73**, 16–20 (2015)
16. Afolabi, A., Akinlabi, O., Bilgili, E.: Impact of process parameters on the breakage kinetics of poorly water-soluble drugs during wet stirred media milling: a microhydrodynamic view. Eur. J. Pharm. Sci. Official J. Eur. Fed. Pharm. Sci. **51**, 75–86 (2014)
17. Jayasundara, C.T., Yang, R.Y., Yu, A.B., et al.: Prediction of the disc wear in a model IsaMill and its effect on the flow of grinding media. Miner. Eng. **24**(14), 1586–1594 (2011)
18. Cleary, P.W., Sinnott, M.D.: Computational prediction of performance for a full scale Isamill: Part—Wet models of charge and slurry transport. Miner. Eng. **79**, 239–260 (2015)
19. Gers, R., Climent, E., Legendre, D., et al.: Numerical modelling of grinding in a stirred media mill: Hydrodynamics and collision characteristics. Chem. Eng. Sci. **65**(6), 2052–2064 (2010)
20. Concas, A., Lai, N., Pisu, M., et al.: Modelling of comminution processes in Spex mixer/mill. Chem. Eng. Sci. **61**(11), 3746–3760 (2006)
21. Tuzcu, E.T., Rajamani, R.K.: Modeling breakage rates in mills with impact energy spectra and ultra fast load cell data. Miner. Eng. **24**(3–4), 252–260 (2011)
22. de Carvalho, R.M., Tavares, L.M.: Predicting the effect of operating and design variables on breakage rates using the mechanistic ball mill model. Miner. Eng. **43–44**, 91–101 (2013)
23. Capece, M., Bilgili, E., Davé, R.N.: Formulation of a physically motivated specific breakage rate parameter for ball milling via the discrete element method. AIChE J. **60**(7), 2404–2415 (2014)
24. Kwade, A., Schwedes, J.: Breaking charakteristics of different materials and their effect on stress intensity and stress number in stirred media mills. Powder Technol. **122**, 109–121 (2002)
25. He, M., Wang, Y., Forssberg, E.: Parameter effects on wet ultrafine grinding of limestone through slurry rheology in a stirred media mill. Powder Technol. **161**(1), 10–21 (2006)
26. Rácz, Á.: Reduction of surface roughness and rounding of limestone particles in a stirred media mill. Chem. Eng. Technol. **37**(5), 865–872 (2014)
27. Fragnière, G., Beinert, S., Overbeck, A., et al.: Predicting effects of operating condition variations on breakage rates in stirred media mills. Chem. Eng. Res. Des. **138**, 433–443 (2018)
28. Kwade, A.: Autogenzerkleinerung von Kalkstein in Rührwerkmühlen, Zugl.: Braunschweig, Techn. Univ., Diss., 1996. Berichte aus der Verfahrenstechnik, Shaker Aachen, ISBN 3-8265-2082-3 (1997)

29. Kwade, A.: A stressing model for the description and optimization of grinding processes. Chem. Eng. Technol. **26**(2), 199–205 (2003)
30. Stadler, R., Polke, R., Schwedes, J., et al.: Naßmahlung in Rührwerksmühlen. Chem. Ing. Tec. **62**(11), 907–915 (1990)
31. Berthiaux, H., Heitzmann, D., Dodds, J.A.: Validation of a model of a stirred bead mill by comparing results obtained in batch and continuous mode grinding. Int. J. Miner. Process. **44–45**, 653–661 (1996)
32. Kwade, A.: Axialer Transport der Produktsuspension in Rührwerkskugelmühlen. Schüttgut **4**(1), 13–18 (1998)
33. Stehr, N.: Zerkleinerung und Materialtransport in einer Rührwerkskugelmühle, Dissertation (1982)
34. Kwade, A., Schwedes, J.: Autogenzerkleinerung in Rührwerkmühlen. Chem. Ing. Tec. **68**(7), 809–812 (1996)
35. Schons, D., Kwade, A.: Determination of the axial grinding media distribution in the IsaMill using radiometric densitometry. Miner. Eng. **130**, 110–116 (2019)
36. Skorych, Vasyl, Dosta, Maksym, Hartge, Ernst-Ulrich, et al.: Novel system for dynamic flowsheet simulation of solids processes. Powder Technol **314**, 665–679 (2017)

Chapter 7
Dynamic Simulation of Mechanical Fluid Separation in Solid Bowl Centrifuges

Marco Gleiss and Hermann Nirschl

Abstract Solid bowl centrifuges are used in a wide range of applications in the process industry. The aim is to separate the individual phases of a liquid/liquid, liquid/solid or liquid/liquid/solid system. The design of solid bowl centrifuges is based on the Σ-theory, which does not describe the separation process with a sufficiently high accuracy. This process results in numbers of experiments with high time and cost expenditure. In addition, Σ-theory only describes the stationary state and therefore do not allow the calculation of start-up processes and load changes. This chapter shows a new real-time capable numerical algorithm, which ensures a high computational efficiency and is therefore suitable for dynamic simulations of the process behavior of solid bowl centrifuges. The introduction deals with the state of the art and the existing problems concerning of the design of solid bowl centrifuges. Subsequently, material functions representing the separation properties in solid bowl centrifuges are expounded. The developed material functions are the basis for the dynamic simulation of the process behavior in solid bowl centrifuges described below. The residence time and flow conditions of the apparatus significantly influence the process behavior for semi-batch and continuous processes. The last two sections present the dynamic modeling of continuously operating decanter and semi-batch tubular centrifuges. Example simulations and comparisons to experiments validate the developed dynamic models and demonstrate the applicability for dynamic simulations.

Nomenclature

A_s	Cross section of the sediment [m]
B_{sc}	Screw pitch [m]
C	G-force [$-$]
D	Flow number [$-$]

M. Gleiss (✉) · H. Nirschl
Institute of Mechanical Process Engineering and Mechanics, Karlsruhe Institute of Technology (KIT), Karlsruhe, Strasse am Forum 8, 76131 Karlsruhe, Germany
e-mail: marco.gleiss@kit.edu

$E(D)$ Residence time distribution function [−]

E Separation efficiency [−]

$F(D)$ Residence time distribution [−]

G Grade efficiency [−]

h Hindered settling factor [−]

L_{cyl} Length of the cylindrical drum [m]

L_{hel} Length of the unrolled screw channel [m]

$\dot{m}_{s,i-1}$ Incoming mass flow of solids [kg s^{-1}]

$\dot{m}_{s,i}$ Outgoing mass flow of solids [kg s^{-1}]

$\dot{m}_{s,sep}$ Mass flow of separated solids [kg s^{-1}]

N Total number of compartments [−]

n_{RZ} Exponent Richardson and Zaki [−]

p_1 Empirical parameter for solids pressure function [Pa]

p_2 Empirical parameter for solids pressure function [−]

p_s Solids pressure [Pa]

P Product loss [−]

$q_{3,i}$ Mass density distribution [m^{-1}]

Q Volumetric flow rate [m^3 s^{-1}]

r_1, r_2 Empirical parameters for hindered settling function [−]

R_d Radius of the bowl [m]

R_m Mean radius of the bowl [m]

R_{max} Maximum radius of the sediment [m]

R_s Radius of sediment surface [m]

R_w Radius of the weir [m]

Re_p Particle Reynolds number [−]

S_{dyn} Normalized dynamic change [−]

t Time [s]

T Transport efficiency [−]

x Particle diameter [m]

$x_{50,3}$ Mean particle diameter dependent on mass [m]

U Volumetric Filling level [−]

U_{max} Maximum volumetric filling level [−]

V_{hel} Volume of the screw channel in the cylindrical part of the decanter centrifuge [m^3]

V Volume of a compartment in the sedimentation zone [m^3]

V_{sed} Sediment volume [m^3]

β Screw angle [rad]

Δl Length of a compartment [m]

Δn Differential speed between screw and drum [rpm]

η Dynamic viscosity [Pa s]

ϕ Solids volume fraction [−]

$\overline{\phi_c}$ Mean solids volume fraction of the sediment [−]

ρ Density [kg m^{-3}]

τ Mean residence time [s]

ω Angular velocity [s^{-1}]

Indices

0	Initial position of the particle
i	Compartment
l	Liquid
N	Total number of compartments
S	Solid
sol	Solution
tr	Transport

Abbreviations

CFD	Computational fluid dynamics
CSTR	Continuous stirred tank reactor
MPC	Model predictive control
ODE	Ordinary differential equation
PFR	Plug flow reactor
PVC	Polyvinylchloride
RTD	Residence time distribution
SRF	Single rotating frame

1   Introduction

Processes dealing with particle formation such as crystallization or precipitation, syntheses but also the fermentation of biological components usually take place in an aqueous medium [1, 2]. For better handling and transport as well as further processing of the mostly particulate valuable material, mechanical fluid separation is essential as a subsequent separation step after particle generation. Since centrifuges apply large centrifugal forces, there is a decrease of particle settling time compared to the settling in the gravity field, which reduces the process time significantly. In the field of centrifugation, a distinction is made between solid bowl and filter centrifuges. Solid bowl centrifuges have an impermeable bowl. In filter centrifuges, in contrast, the bowl is permeable for the filtrate. The particles usually remain on the filter cloth. At this point, it should be noted that this contribution is limited to the modeling of solid bowl centrifuges.

The design of solid bowl centrifuges is based on highly simplified models such as the Σ-theory [3, 4]. The Σ-theory regards the physical behavior of the material in solid bowl centrifuges as a "black box" and neglects transient phenomena, which occur due to the spin-up process or as a reaction to load changes. Additionally, Σ-theory does not consider flow conditions, settling behavior, cake formation and

sediment transport [5]. For the scale-up of solid bowl centrifuges the manufacturers use numbers of experiments on a pilot scale. This procedure is time-consuming and cost-intensive and does not allow any prediction about the dynamic process behavior [6]. For a theoretical description of the transient response of solid bowl centrifuges, it is necessary to consider flow conditions and separation behavior. A major challenge in depicting the separation process in solid bowl centrifuges arises from the fact, that particle separation depends on the residence time in the apparatus. In contrast to thickeners, the flow direction in solid bowl centrifuges results in a classification of particles along the rotor [7].

In the field of flowsheet simulation, it is important to predict the steady-state or dynamic behavior of a process plant using time-efficient mathematical models. For other applications such as Model Predictive Control (MPC) it is essential to calculate faster than real time to enable a coupling of dynamic modeling with the process control level. Mesh-based methods such as Computational Fluid Dynamics (CFD) are not suitable for flowsheet simulations [8, 9]. CFD simulations rather serve to derive parameters, that are not achievable experimentally from numerical experiments [10, 11].

The following section begins with an overview of the experimental setup to investigate material functions for the settling behavior and the cake formation process. The dynamic model for solid bowl centrifuges uses material functions for process-orientated dynamic simulations. Subsequently, different experimental methods to characterize the system and residence time behavior for decanter centrifuges are presented. Based on the investigations of material and process behavior the following section deals with the mathematical modeling of the dynamic behavior of continuously working decanter centrifuges. The comparison of dynamic simulations with pilot-scale experiments for decanter centrifuges shows the applicability of the developed numerical approach. The following section shows the development of a dynamic model for semi-continuously operating tubular centrifuges. Simulations of a tubular centrifuge on a pilot scale reveal a different process behavior of tubular centrifuges compared to decanter centrifuges. Finally, the conclusion summarizes the main results and gives a short outlook on further work.

2 Material Functions and Separation Properties

The properties of the disperse and the fluid phase such as particle size, particle shape, solid volume fraction, physicochemical properties, density of solid and liquid as well as dynamic viscosity have a significant influence on the material behavior during mechanical fluid separation [12]. Due to the large number of influencing quantities, there are no generally applicable models for the arbitrary product. Rather, it is preferable to investigate the material properties in a laboratory apparatus and to develop material functions for the theoretical description of the separation process [13]. The use of well-established laboratory equipment, such as beaker centrifuges or filters is one way to achieve this goal [14, 15]. In the case of solid bowl centrifuges,

the process behavior depends on various influencing factors for instance, the settling behavior, sediment build-up, sediment transport and mechanical dewatering [16, 17]. In the following subsection the experimental investigation of material functions for finely dispersed materials is presented in more detail.

2.1 Settling Behavior of Finely Dispersed Particles in the Centrifugal Field

The settling behavior of finely dispersed particles has a decisive influence on the separation efficiency of solid bowl centrifuges. Especially in the case of a high solid content, the particles affect each other due to an increasing hydrodynamic interaction between solid and liquid. As a result, Stokes law for particle settling is no longer valid and a correction function for hindered settling is necessary. A measuring system for determining the settling behavior of slurries is the LUMiSizer, which is an analytical centrifuge for the investigation of small product quantities of a few milliliters [15].

Figure 1a shows schematically the measuring setup within the analytical centrifuge which consists of a light source, a cuvette and a CCD sensor. The CCD sensor records the transmission versus time along the radial position of the cuvette. The integrated software calculates the settling velocity of the samples from the raw data of the transmission profiles, see right-hand side in Fig. 1. The LUMiSizer allows the simultaneous analysis of up to twelve samples. The maximum speed is $n = 1000$ rpm, which corresponds to a g-force of $C = 2320$. The hindered settling function serving to describe the settling behavior of the investigated slurry, results from the analysis of different solid volume fractions.
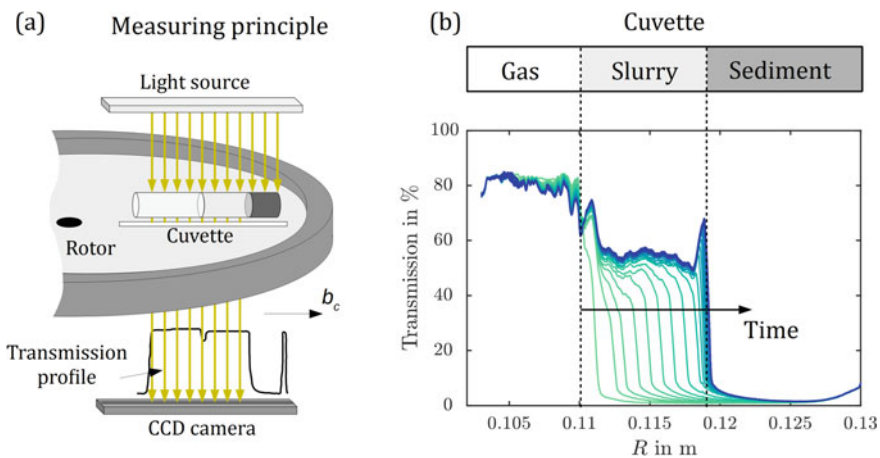

Fig. 1 Schematic representation of the measuring principle for the analytical centrifuge LUMiSizer (**a**). Temporal change of transmission along the radius of a cuvette for the product limestone (**b**)

Richardson and Zaki [18] postulate a power law based on experimental investigation for the hindered settling

$$h = (1 - \phi)^{n_{RZ}}, \tag{1}$$

for slurries consisting of monodisperse particles. For creeping flows ($Re_p < 0.1$), the exponent n_{RZ} is 4.65. The approach of Richardson and Zaki, however, is only valid for monodisperse particles and therefore represents a simplification of the real behavior of a polydisperse particle system. To investigate these, it is appropriate to measure the material function for settling behavior by means of analytical centrifugation. Often the hindered settling approach

$$h = \left(1 - \frac{\phi}{r_1}\right)^{r_2}, \tag{2}$$

of Michaels and Bolger is applied in this case to adapt to the experimental data [19]. Here, r_1 and r_2 be adapted to fit the experimental data. Figure 1 Schematic representation of the measuring principle for the analytical centrifuge LUMiSizer (a). Temporal change of transmission along the radius of a cuvette for the product limestone (b).

Figure 2 shows the normalized settling velocity related to the g-force as a function of the solids volume fraction for limestone-water suspensions with different mean particle sizes. With higher solid content the influence of hydrodynamic interactions on the particle settling increases significantly. The impact of particle size on the investigated limestone-water suspensions is also evident. There is a shift of the settling velocity towards higher values with the increase of the particle size.

Fig. 2 Normalized settling velocity for limestone-water suspensions with for differing particle size distributions [20]
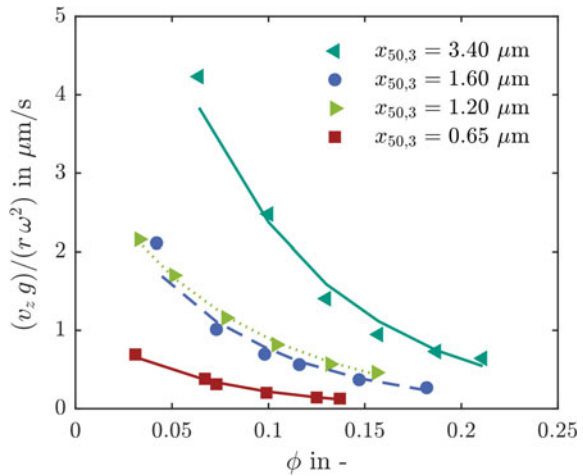
2.2 Sediment Build-up in the Centrifugal Field

Additionally to the settling behavior, sediment build-up in solid bowl centrifuges effects the separation performance. Here, the properties of the disperse phase have a huge impact on the physical behavior during the sediment formation process. Coarsely dispersed particles form an incompressible cake. In contrast, finely dispersed particles form a compressible cake. The reason for this varying behavior results from the increasing strength of interparticle forces on finely dispersed particles ($x < 10\,\mu$m).

The difficulty in describing the sediment structure of finely dispersed particles lies in the fact that the material behavior changes suddenly at the transition between suspension and sediment. Particles in a slurry move freely and hydrodynamic effects primarily influence the settling behavior. The sediment transmits normal and shear stresses inside the cake. In literature [21, 22], the gel point is defined to mark the transition between particle settling and cake compression. It is the solids volume fraction of the top sediment layer for which the solids pressure is $p_s = 0$ Pa.

Table 1 shows the comparison of the gel point for six different particulate systems, which differ in particle size. For polyvinylchloride (PVC) and limestone 1, the gel point corresponds approximately to the solids volume fraction of the formed sediment. For both products, the impact of inertial forces is significantly great compared to particle-particle interactions. For finer particles, it is clearly visible, that the behavior is entirely different. By reducing the particle size, the influence of mass forces is neglectable and thus, as a result, the particle-particle interactions increasing remarkably. For these particulate systems, the gel point is below the maximum achievable solids volume fraction in the sediment.

Laboratory centrifuges are also suitable for characterizing the sediment structure. For the experimental investigation of the cake heights for low pressures in the range of up to $p_s = 10^5$ Pa the analytical centrifuge LUMiSizer is used. Here, Usher et al. [23] show a measuring procedure for the investigation of compressible saturated sediments. The solids pressure can be derived as a function of the solids volume fraction for the equilibrium state. The analytical centrifuge starts at low rotational speed and centrifuges the sample to the equilibrium state. If there is no change in the transmission profile, the next step is to increase the rotational speed. Afterwards, the

Table 1 Comparison of the gel point for different particulate systems

Product	$x_{50,3}$ in μm	ϕ_{gel} in −
PVC	30	0.48
Limestone 1	80	0.48
Limestone 2	3.4	0.23
Limestone 3	1.6	0.16
Limestone 4	1.2	0.09
Limestone 5	0.7	0.07

sediment is centrifuged to the equilibrium for the next speed. Each measuring point represents a solids volume fraction and a solids pressure.

At this point, it should be mentioned that the filling level of the cuvette and the maximum speed are limiting factors measuring the compression behavior of the sediment in the LUMiSizer. However, solid bowl centrifuges achieve significantly higher solids pressures of up to $p_s = 10^6$ Pa. Experimental investigation for higher rotational speeds is therefore necessary. Hermle cooling centrifuge type ZK630 achieves larger centrifugal accelerations of up to $C = 6000$ and therefore serve to investigate of higher solids pressures. Special bucket systems allow the analysis of the cake formation based on investigations of the equilibrium state by gravimetric measurements.

Figure 3 illustrates the solids pressure as a function of the normalized solids content which is the ratio of solids volume fraction and gel point, for four limestone fractions with mean particle sizes of $x_{50,3} = 0.65\,\mu m$, $x_{50,3} = 1.2\,\mu m$, $x_{50,3} = 1.6\,\mu m$ and $x_{50,3} = 3.4\,\mu m$. Comparing the individual limestone fractions, it is noticeable that there is a shift in the curves with a reduction of particle size. The finer the particles, the more compressible is the formed sediment. For an average particle size of $x_{50,3} = 3.4\,\mu m$ the sediment at $p_s = 10^5$ Pa compresses up to a maximum of 2.3 times compared to gel point. For the limestone with a mean size of $x_{50,3} = 0.65\,\mu m$, the sediment has a higher compressibility. For a solids pressure of $p_s = 10^6$ Pa cake compresses up to a maximum of six times compared to the gel point.

To transfer the experimental data to the dynamic model for solid bowl centrifuges, a power law by Green et al. [24] serves to adapt the experimental data. Solids pressure

$$p_s = p_1 \left[\left(\frac{\phi}{\phi_{gel}} \right)^{p_2} - 1 \right],$$

(3)

is a function of the solids volume fraction. p_1 and p_2 represent empirical parameters. Furthermore, sediment flow and sediment transport have a significant influence on the process behavior of solid bowl centrifuges. The pores of finely dispersed sediments have a very high capillary pressure. Therefore, the undersaturation of the sediment is not possible. Rather, a pasty, liquid-saturated sediment formed by finely dispersed particles has a non-Newtonian rheology [25, 26]. Due to the dependency of

Fig. 3 Comparison of solids pressure as a function of normalized solids volume fraction for four finely dispersed limestone-water suspensions [20]
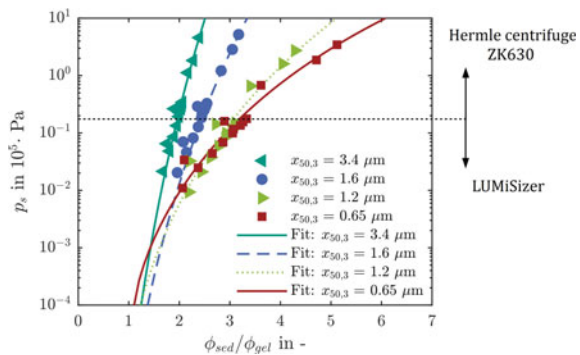
the existing yield point on the solids pressure, the experimental determination of the rheological material properties is very challenging. Here, the yield point increases with the reduction of porosity. Moreover, the material is either dilatant or shear thinning. Since no measurement methods are currently available to determine the rheological material properties, an adjusting parameter is defined to describe the sediment transport. The influence of this parameter is shown in more detail in Sect. 4.2.

3 System and Residence Time Behavior

In addition to the material behavior of the suspension, the flow conditions have a considerable influence on the operation of solid bowl centrifuges. For tubular and decanter centrifuges, for example, the residence time limits particle separation. Knowledge about the residence time behavior is therefore essential for the design of these centrifuge types. One possibility for the description of the flow conditions is the determination of the residence time and system behavior by means of experimental or numerical investigations. This approach considers the integral output response after a sudden change at the inlet. Dead zones and vortices create a dispersion in the system. This means that a step response at the outlet does not follow from a step change at the inlet.

The left-hand side in Fig. 4 shows exemplarily the residence time behavior of a density distribution and a sum distribution as a function of the flow number D. The ratio of measuring time and mean residence time τ yields the flow number. The sum distribution $F(D)$ is integral value of the density distribution $E(D)$:
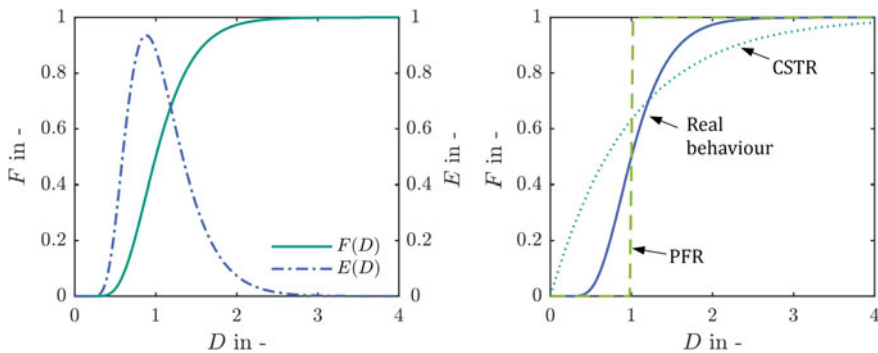

Fig. 4 Left: exemplary residence-time distribution function $E(D)$ and cumulative distribution curve $F(D)$ as a function of flow number. Right: cumulative distribution function for three different flow types [20]

$$F(D) = \int\limits_0^D E(D)dD. \tag{4}$$

For the mean residence time $D = 1$, the residence time spectrum reaches its maximum and the residence time distribution reaches the mean value.

The right side in Fig. 4 illustrates the comparison of the real residence time behavior with an ideal plug flow reactor (PFR) and a continuous stirred tank reactor (CSTR). PFR modeling assumes, that the flow is uniform and there is no exchange of forces along the cross-section. This results in a sudden change of the residence time behavior after reaching the mean residence time. CSTR modeling supposes no gradients in the apparatus and the change occurring immediately at the output. This leads to a broad sum distribution with high axial dispersion. Real processes generally differ significantly from the performance of a PFR and CSTR, see Figs. 1 and 4, because the axial dispersion depends on the flow conditions. Dead zones and back-mixing are present inside centrifuges. Consequently, the real residence time behavior of a process differs considerable from ideal behavior.

Several methods are suitable for determining the real residence time behavior, see Fig. 5. The characterization of the residence time behavior for decanter centrifuges has been examined applying three methods: experimental residence time measurement, investigation of the system behavior and CFD simulations of a tracer transport. Experimental residence time measurements are based on the transport of a tracer material through the apparatus. In this work, saturated sodium-chloride solution is in use with a mass fraction of 2 wt%. This corresponds to a density of the saturated solution of $\rho_{sol} = 1012$ kg m^{-3}. For the determination of the real residence time behavior of the centrifuge it plays an important role, that there is only a neglectable difference in density between the liquid and the tracer. Otherwise segregation of the two fluids occur due to the acting g-force. At this point it should be

Fig. 5 Comparison of the investigated three different methods to determine the residence time distribution for solid-bowl decanter centrifuges [20]
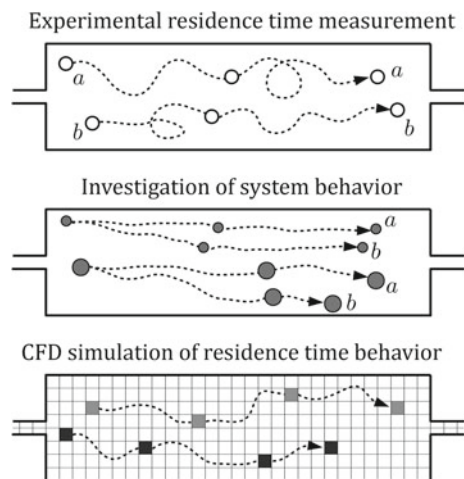
noted, that experimental residence time measurement only considers a machine filled with liquid.

The second method is the determination of the system behavior for the same lab-scale decanter centrifuge. Here, the particle size or the solids volume fraction is changed at the inlet to investigate the response of the machine to the load change applied. The third method applies CFD simulations in combination with a passive tracer transport.

The left-hand side of Fig. 6 shows the response to an abrupt change of the solids volume fraction at the inlet. After reaching the steady state, the solids volume fraction was determined at time $t = 0$ s switching the installed three-way valve from tank 1 with $\phi_{in} = 0.02$ to tank 2 with $\phi_{in} = 0.03$. A time-delayed system behavior can be derived from the experiments, which results from the present flow conditions and the existing hold-up in the decanter centrifuge. As a consequence of the growing solids volume fraction at the inlet the momentum exchange between solid and liquid increases significantly.

For a better comparison of the temporal behavior during the abrupt change of the solids volume fraction, the right-hand side of Fig. 6 exhibits the normalized dynamic change as a function of the flow rate. The normalized dynamic change

$$S_{dyn} = \left| \frac{\phi_{start} - \phi(t)}{\phi_{end} - \phi_{start}} \right|. \tag{5}$$

describes the temporal change between the initial and final state of the sudden change at the inlet. Thus, the values range between $S_{dyn} = 0$ and $S_{dyn} = 1$. This enables the comparison between individual measurements as well as the experimental and numerical residence time investigation. The comparison of the normalized dynamic change shows an approximately identical behavior for the three investigated methods, which is represented by the s-shaped curve on the right-hand side in Fig. 6.
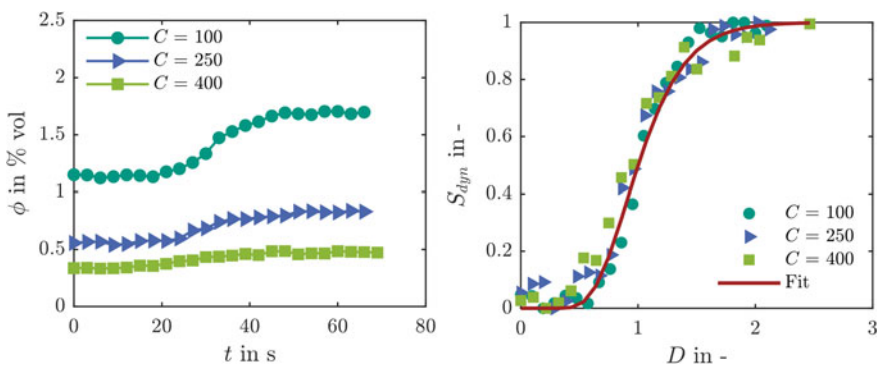

Fig. 6 Left: temporal change of solids volume fraction at the overflow dependent on g-force (C = 100, C = 250, C = 400) for a decanter centrifuge type MD80 from Lemitec GmbH. Right: normalized dynamic change as a function of flow number for the investigated change of solids volume fraction [6]

The third method to determine the residence time behavior is based on CFD simulations in combination with a transport equation taking into account the dispersion of a tracer by a passive scalar [27]. Modeling a passive scalar using a transport equation requires that the tracer has the same physical properties as the fluid. Thus, there is no cross-exchange due to a density difference.

The CFD simulations assume, that the screw rotates at the same speed as the bowl. Thus, a SRF describes the influence of centrifugal and Coriolis force. Additionally, a stationary flow is expected for the CFD simulations. Moreover, at the beginning there is no tracer in the centrifuge ($F = 0$). The step change to $F = 1$ simulates the injection of the tracer into the lab-scale decanter centrifuge. By specifying $F = 1$ at the inlet, the residence time behavior results directly from the tracer concentration at the overflow.

Figure 7 shows schematically the procedure for determining the residence time behavior using CFD simulations. The investigation of the residence time behavior based on CFD simulations is currently only applicable for a decanter centrifuge filled with liquid. The inclusion of the real behavior during operation requires the consideration of the sediment build-up and sediment transport. Currently, however, no meaningful models are available that allow CFD simulations in combination with sediment transport in decanter centrifuges. Hammerich et al. [11] show a first approach for the description of the rheological behavior for finely dispersed sediment using the example of tubular centrifuge.

The left side in Fig. 8 compares the three methods investigated for the step change of solids volume fraction, the tracer experiment and the CFD simulation. Here, it can be summarized that there is good agreement between the three methods and the residence time behavior also influences the dynamic behavior of the lab-scale decanter centrifuge. The reason for this is that the temporal change of the solids volume fraction at the overflow after a sudden change at the inlet depends on the
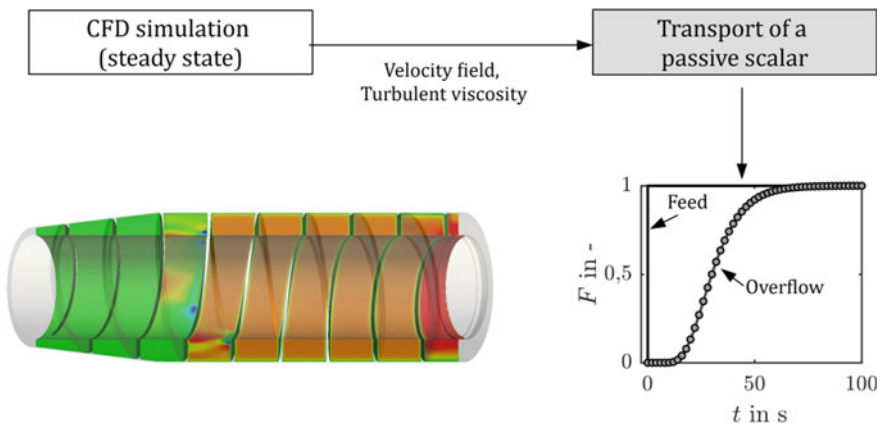

Fig. 7 Schematic representation of the CFD simulations to determine the residence time behavior of a lab-scale decanter centrifuge type MD80. Reprinted with permission from [20]
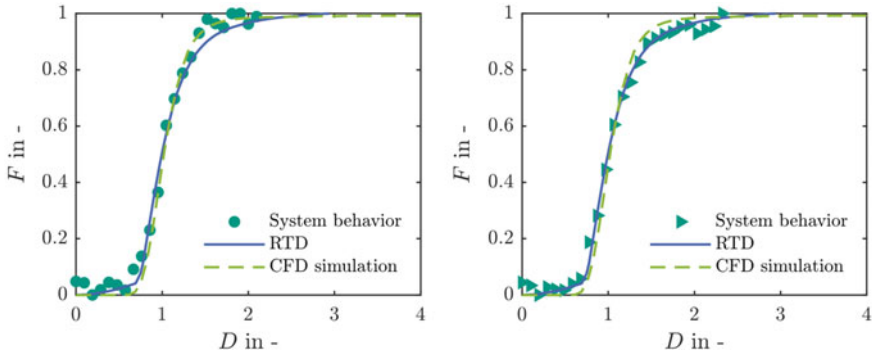
Fig. 8 Left: comparison between tracer experiment, tracer simulation and system behavior for a stepwise change of solids volume fraction at the inlet. Right: comparison between the tracer experiment, tracer simulation and stepwise change of particle size distribution at the feed [20]

flow conditions inside the machine. The rotor and the screw body limit the flow domain. No slip conditions apply to all walls. This results in the formation of a flow profile. In addition, the turbulent flow generates vortices leading to an increased momentum exchange. The left-hand side in Fig. 8 compares the residence time and the system behavior for the abrupt change of the particle size distribution at the inlet. It is apparent that three methods show a good agreement. In the next step, the system behavior is used for the dynamic modeling of decanter centrifuges.

4   Dynamic Modeling of Decanter Centrifuges

Decanter centrifuges are used in many sectors of the process industry for the separation of solids and liquids. They consist of a cylindrical-conical bowl, a screw conveyor and the feed pipe. A schematic representation of a decanter centrifuge is shown in Fig. 9. The suspension flows axially into the centrifuge where it is pre-accelerated at the transition between the cylindrical and conical part. The slurry flows along the formed channel in the screw body towards the overflow. The solid material, which usually has a higher density, settles in towards the inner wall of the bowl and is deposited there as liquid-saturated sediment. For a countercurrent decanter centrifuge, the screw body transports the sediment within the conical part of the machine.

So far, the known theoretical models for decanter centrifuges neglect the dynamic behavior. However, this occurs in decanter centrifuges during the spin-up process or as a reaction to load changes at the inlet. In the following, the dynamic modeling of countercurrent decanter centrifuges by means of the interconnection of individual compartments (index i) is presented. Figure 9 illustrates schematically the compartment model for the cylindrical part of a decanter centrifuge. The sedimentation zone and the sediment zone define two areas with differing physical behavior for the
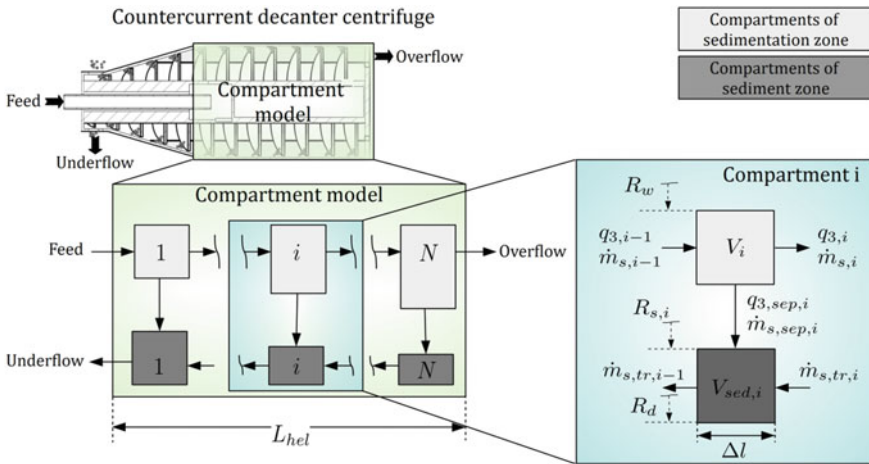
Fig. 9 Schematic representation of the compartment model for countercurrent decanter centrifuges [6]

mathematical modeling of settling behavior and sediment build-up. The linking of the individual compartments characterizes the dynamic behavior of the apparatus. This approach is also well known from chemical reaction engineering as tank-in-series model. The serial connection of ideally back-mixed compartments maps the residence time behavior of the apparatus.

The right-hand side in Fig. 9 depicts the incoming $(\dot{m}_{s,i-1})$ and outgoing $(\dot{m}_{s,i})$ mass flow of solids. Additionally, the incoming $(q_{3,i-1})$ and outgoing $(q_{3,i})$ mass density distribution are shown, which consider the change of particle size for each compartment (index i). In contrast to the well-known Σ-theory, the solid mass flow, and the particle size distribution change locally within the machine. This enables a process-related description of the classification process for decanter centrifuges.

Due to the centrifugal separation of the particles within the apparatus, the approach considers the partial removal of particle fractions for each compartment. The sediment zone then takes the separated solid mass flow $(\dot{m}_{s,sep,i})$ into account for the calculation of the sediment formation.

Furthermore, sediment transport occurs in decanter centrifuges, which influences significantly the filling process. The numerical approach considers the physical behavior during the sediment transport by an incoming $(\dot{m}_{tr,i})$ and outgoing $(\dot{m}_{tr,i-1})$ sediment mass flow in the mass balance of the sediment in each compartment. In the case of decanter centrifuges, the screw conveyor inside the rotating bowl prevents the flow of the slurry in axial direction. In fact, the material flows along the formed screw channel towards the overflow. Thus, the mathematical modeling of the spatial and temporal change requires unwinding the screw channel and its discretization along the settling paths. Figure 10 shows the unwinding of the screw channel, the discretization of the sedimentation and sediment zone as well as the sediment distribution along the screw channel exemplarily for two different time steps $t_0 = 0$ s
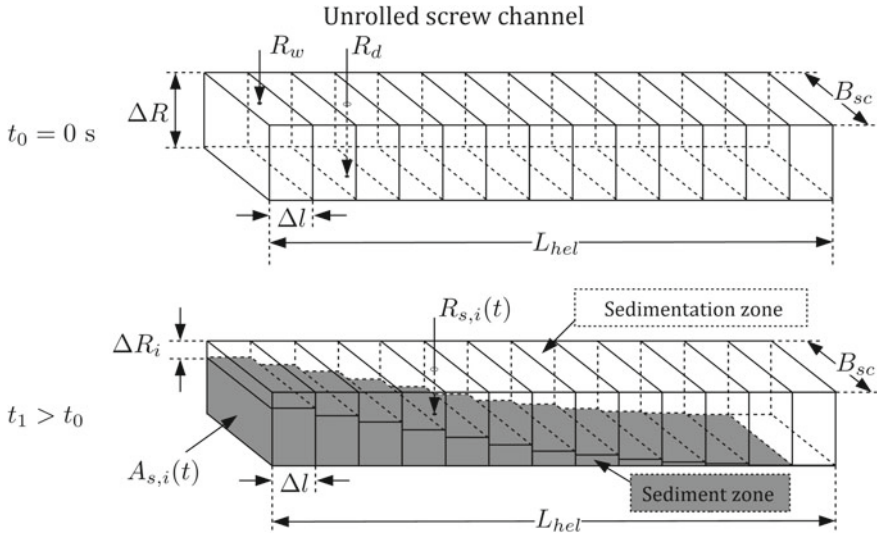
Fig. 10 Schematic representation of the unrolled screw channel, its discretization, and the sediment distribution for a countercurrent decanter centrifuge at two different time steps $t_0 = 0$ s and $t_1 > t_0$ [20]

and $t_1 > t_0$. The dynamic model considers the influence of the sediment build-up on the residence time behavior. In addition, the algorithm calculates the radial position of the sediment surface $R_{s,i}(t)$ from the volume of the sediment $V_{sed,i}$ for each compartment (index i). At the start time, different parameters such as the radius of the weir R_w, the radius of the drum R_d, the screw pitch B_{sc} and the length of the unrolled screw L_{hel} define the calculation domain.

4.1 Mathematical Modeling of the Sedimentation Zone

The sedimentation zone comprises the transport of the slurry in direction of the overflow and for the particle settling towards the inner bowl wall. For the mathematical description of the physical behavior mentioned, a series of equations are mandatory. The solids mass balance

$$\frac{dm_{s,i}}{dt} = \dot{m}_{s,i-1} - \dot{m}_{s,i} - \dot{m}_{s,sep,i,}$$ (6)

is applied to calculate the accumulation of solids $\frac{dm_{s,i}}{dt}$ for each time step and compartment i. Here, $\dot{m}_{s,i-1}$ is the incoming mass flow of solids, $\dot{m}_{s,i}$ is the outgoing mass flow of solids and $\dot{m}_{s,sep,i,}$ is the mass flow of separated solids. The mass flow of separated solids is calculated as the product of incoming solids mass flow and separation efficiency $E_i(t)$:

$$\dot{m}_{s,sep,i} = E_i(t) \cdot \dot{m}_{s,i-1}. \tag{7}$$

The separation efficiency is an integral measure to describe the separation performance of a process and can be calculated by integrating the product of the mass density distribution function $q_{3,i-1}(x, t)$ entering a compartment and grade efficiency $G_i(x, t)$ over the entire particle size range $x_{min} \leq x \leq x_{max}$:

$$E_i(t) = \int_{x_{min}}^{x_{max}} G_i(x, t) q_{3,i-1}(x, t) dx. \tag{8}$$

Inserting Eq. (7) in (6) yields the equation for the solids mass in compartment with in the sedimentation zone:

$$\frac{dm_{s,i}}{dt} = \dot{m}_{s,i-1} \left(1 - E_i(t) - \frac{\dot{m}_{s,i}}{\dot{m}_{s,i-1}} \right). \tag{9}$$

To convert the mass balance into a volume balance, the solid mass and the solid mass flow are converted into the volume and the volume flow rate. The volume balance for the compartment (index i) of the sedimentation zone

$$\frac{d\phi_i}{dt} = Q_{i-1}\phi_{i-1} \left(1 - \int_{x_{min}}^{x_{max}} G_i(x, t) q_{3,i-1}(x, t) dx - \frac{Q_i \phi_i}{Q_{i-1}\phi_{i-1}} \right), \tag{10}$$

follows by inserting the solid mass $\left(m_{s,i} = \rho_s \phi_i V_i \right)$, the solid mass flow $\dot{m}_{s,i} = \rho_s \phi_i Q_i$ and Eq. (8) in (10). A constant volume (V_i) and ideal backmixing in the compartment is assumed to solve the ordinary differential equation (ODE) in Eq. (10). In addition, the separation process depends on the change in the particle size distribution along the screw channel. The change in the particle size distribution for the compartment with index i is as follows:

$$\frac{d\left[m_{s,i} q_{3,i}(x) \right]}{dt} = \dot{m}_{s,i-1} q_{3,i-1}(x) - \dot{m}_{s,i} q_{3,i}(x) - \dot{m}_{s,sep,i} q_{3,sep,i}(x). \tag{11}$$

Here, $\dot{m}_{s,i-1} q_{3,i-1}(x)$ is the incoming mass flow of particles with size x, $\dot{m}_{s,i} q_{3,i}(x)$ is the mass flow of outgoing particles with size x and $\dot{m}_{s,sep,i} q_{3,sep,i}(x)$ is the mass flow of separated particles with size x. For further consideration, the accumulation term in Eq. (11) is neglected. The assumption is made to calculate the mass density distribution of the separated solids

$$q_{3,sep,i}(x, t) = q_{3,i-1}(x, t) \frac{G_i(x, t)}{E_i(t)}, \tag{12}$$

and the mass density distribution of the outgoing stream

$$q_{3,\mathrm{i}}(x, t) = q_{3,\mathrm{i}-1}(x, t)\frac{(1 - G_\mathrm{i}(x, t))}{(1 - E_\mathrm{i}(t))}. \tag{13}$$

The unknown variables of the presented equations are the grade efficiency and the volume of a compartment (index i). For decanter centrifuges, the grade efficiency depends on the material properties, the centrifuge geometry and the process conditions. Gleiss et al. [6] show a shortcut model based on a grade efficiency function

$$G_\mathrm{i}(x, t) = \frac{R_{\mathrm{s},\mathrm{i}}(t)}{R_{\mathrm{s},\mathrm{i}}(t) - R_\mathrm{w}}\left\{1 - exp\left[-\frac{(\rho_\mathrm{s} - \rho_\mathrm{l})h(\phi)x^2\omega^2}{18\eta_\mathrm{l}}\frac{B_{\mathrm{sc}}(R_{\mathrm{s},\mathrm{i}}(t) - R_\mathrm{w})\Delta l}{Q_{\mathrm{i}-1}}\right]\right\} \tag{14}$$

to predict temporal and spatial changes along the screw channel of a decanter centrifuge as a function of the parameters described previously. Here, ρ_s is solids density, ρ_l is liquid density, η_l is the dynamic viscosity of the liquid, x is the particle size, ω is the angular velocity, B_{sc} is the screw pitch and Δl is the length of a compartment for the unrolled screw channel. The volume of the sedimentation zone (in a compartment i) is calculated as follows:

$$V_\mathrm{i} = (R_{\mathrm{s},\mathrm{i}}(t) - R_\mathrm{w})\Delta l\, B_{\mathrm{sc}}. \tag{15}$$

4.2 Mathematical Modeling of the Sediment Zone

After particle separation, the material accumulates on the inner wall of the bowl as liquid-saturated sediment. The sediment structure depends on the separated solids and on the sediment transport. Therefore, it is essential to consider the physical behavior for the modeling of the process behavior. For this reason, this subsection deals with the mathematical modeling of the temporal and spatial changes in sediment formation. In this case, it is assumed that the maximum compaction of the sediment formed by finely disperses particles is present at the transition between the cylindrical and conical part. As a result, the conical part in the dynamic model is neglected. The description of the accumulation of solids in the centrifuge requires a mass balance of solids for each compartment (i = 1, …, N):

$$\frac{dm_{\mathrm{s},\mathrm{sed},\mathrm{i}}}{dt} = \dot{m}_{\mathrm{s},\mathrm{tr},\mathrm{i}} + \dot{m}_{\mathrm{s},\mathrm{sep},\mathrm{i}} - \dot{m}_{\mathrm{s},\mathrm{tr},\mathrm{i}-1}. \tag{16}$$

Here, $m_{\mathrm{s},\mathrm{sed},\mathrm{i}}$ is the accumulated solid mass, $\dot{m}_{\mathrm{s},\mathrm{tr},\mathrm{i}}$ is the solid mass flow transported into the compartment, $\dot{m}_{\mathrm{s},\mathrm{tr},\mathrm{i}-1}$ is the solid mass flow transported out of the compartment. Both mass flows occur because of the relative motion between bowl and screw conveyor. For the direct calculation of the sediment volume, the solids mass balance is converted into a volume balance.

$$\frac{dV_{s,sed,i}}{dt} = Q_{s,tr,i} + Q_{s,sed,i} - Q_{s,tr,i-1}. \tag{17}$$

$Q_{s,tr,i}$ is the flow rate of solids which is transported into the compartment, $Q_{s,tr,i-1}$ is the volume flow rate of solids which is transported out of the compartment and

$$Q_{s,sed,i} = \phi_{i-1} Q_{i-1} E_i(t), \tag{18}$$

is the volume flow rate of separated solids. The volume flow rate of solids transported by the screw conveyer system is described as follows:

$$Q_{s,tr,i} = \overline{\phi}_{c,i} A_{s,i} \cdot \frac{T B_{sc} \Delta n}{\sin(\beta)}. \tag{19}$$

Here, $\overline{\phi}_{c,i}$ designates the mean solids volume fraction of the cake, $A_{s,i}$ is the cross-section of the cake, T is the transport efficiency, β is the screw angle and Δn is the differential speed between screw conveyer and drum. The transport efficiency ($0 \leq T \leq 1$) is unknown and must be derived from experiments on a laboratory decanter centrifuge. $T < 1$ applies to the transport efficiency as friction and sliding occur during sediment transport. The cross-sectional area of the sediment

$$A_{s,i}(t) = B_{sc}(R_d - R_{s,i}(t)), \tag{20}$$

is calculated from the area of a rectangle with the width of the screw pitch and the difference between drum radius and the radius of the sediment surface. The latter results from the volume of the sediment in the compartment with index i:

$$R_{s,i}(t) = R_d - \frac{V_{sed,i}(t)}{B_{sc} \Delta l}. \tag{21}$$

Furthermore, the length of the unrolled screw is required for the calculation of the sedimentation zone:

$$L_{hel} = \frac{L_{cyl}}{B_{sc}} \cdot \left[(2\pi R_m)^2 + B_{sc}^2 \right]^{0.5}. \tag{22}$$

The length of the unrolled screw is necessary to calculate the total volume of the cylindrical drum:

$$V_{hel} = L_{hel} B_{sc} (R_d - R_w). \tag{23}$$

The total volume of the cylindrical drum is used here to predict the temporal change of volumetric filling level during the separation process. Furthermore, the dynamic model is based on the assumption that no sediment can grow out of the calculation area. The maximum radial position of the sediment is calculated and compared with the actual radial position of the sediment surface for each time step:

$$R_{\max} = R_d - U_{\max}(R_d - R_w). \tag{24}$$

It is assumed that a maximum filling degree of $U_{\max} = 0.95$ occurs in decanter centrifuges [28]. The reason for this behavior is that a fast-flowing layer forms on the sediment surface which results in equilibrium between settling and lift of particles. For a detailed description of the dynamic modeling of the cake compression behavior of finely disperse particles, please refer to Gleiss [20].

4.3 Validation of the Dynamic Model for Decanter Centrifuges

This subsection shows selected results for the experimental validation of the dynamic model for a pilot-scale decanter centrifuge. The basis of dynamic simulations is the mathematical modeling presented in Sects. 4.1 and 4.2. Limestone-water and PVC-water slurries were used for the validation trials of the presented approach for decanter centrifuges on a lab and pilot scale. Table 2 shows the geometric parameters of the lab-scale and pilot scale decanter centrifuges investigated here.

Figure 11 shows the influence of the total number of compartments N on the transient behavior of the solids volume fraction at the overflow. An exemplary case with the simulation setup $Q = 30\,\text{l·h}^{-1}$, $C = 500$ and $\Delta n = 5\,\text{rpm}$ illustrates the temporal change of the solids volume fraction on the left-hand side. After the spin-up process which ends after $t = 150\,\text{s}$, the simulation results reveal a steady behavior. At $t = 250\,\text{s}$, the solids volume fraction changes abruptly from $\phi_{in} = 2\,\%$ vol to $\phi_{in} = 3\,\%$ vol at the inlet. The results indicate that the reaction of the machine to this load change occurs time-delayed at the overflow, which has already been described in Sect. 3. The total number of compartments N has an influence on both the start-up process and the simulated load change. The reason is the reduction of the axial dispersion with the increase of N. The influence of the total number of compartments on the normalized dynamic change is depicted the right-hand side of Fig. 11.

An important parameter for the dynamic modeling of decanter centrifuges is the transport efficiency T, which describes the transport behavior of the formed sediment. Since the sediment build-up has a decisive influence on the process behavior of

Parameter	Lab-scale decanter (m)	Pilot scale decanter (m)
Length cylindrical bowl	0.18	0.98
Weir radius	0.034	0.104
Bowl radius	0.04	0.14
Screw pitch	0.025	0.125

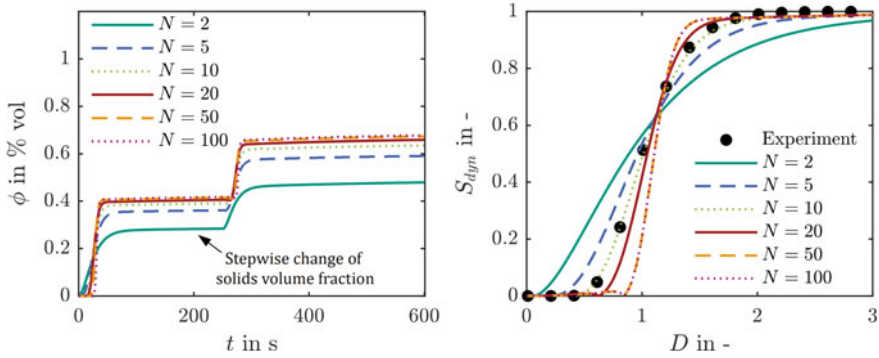**Table 2** Geometric parameters of the decanter centrifuges investigated

Fig. 11 Left: transient behavior of solids volume fraction at the overflow. Right: simulation for the normalized dynamic change as a function of flow number. Both diagrams show the influence of the total number of compartments N on the dynamic and residence time behavior. Simulations performed for a lab scale decanter centrifuge type MD80 at $Q = 30$ lh^{-1}, $C = 500$ and $\Delta n = 5$ rpm [20]

decanter centrifuges, it is important to know the effect of this parameter to predict separation with a good accuracy. Therefore,

Figure 12 demonstrates the influence of transport efficiency on the solids volume fraction in the overflow (left) and underflow (right). The simulation setup is based on pilot scale experiments with $Q = 500$ m^3 h^{-1}, $\phi_{in} = 0.15$ and $\Delta n = 15$ rpm to verify the influence of the transport efficiency on the dynamic simulation.

According to definition, the transport efficiency is between $0 < T < 1$. For small values of T, the transport is inefficient. Conversely, $T = 1$ represents an ideal transport without friction losses. The screw conveyor moves the cake during one rotation by the screw pitch. The influence of transport efficiency on the solids
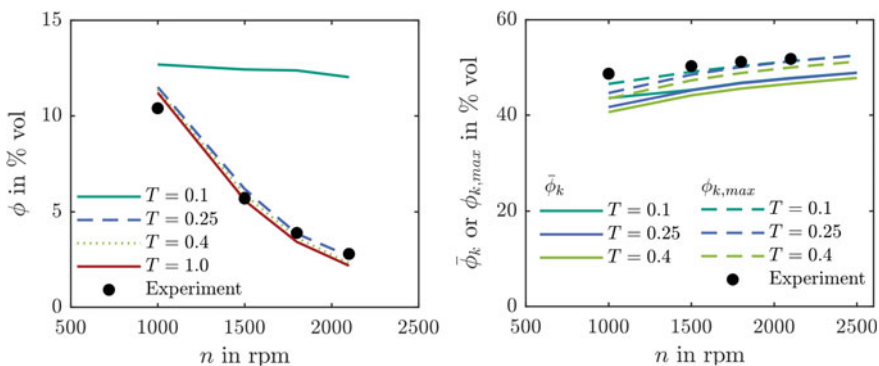

Fig. 12 Left: influence of the transport efficiency on the solids volume fraction at the overflow. Right: mean solids volume fraction at the underflow as a function of rotational speed and transport efficiency. The simulation setup is $Q = 0.5$ m^3 h^{-1}, $\phi_{in} = 0.15$ and $\Delta n = 5$ rpm. Simulations performed for a pilot scale decanter centrifuge. Reprinted with permission from [20]

volume fraction in the overflow is negligible in a wide range of $0.25 \leq T \leq 1$. A clear deviation from simulation and experiment is only detectable for $T = 0.1$. For this setting, the sediment transport is inefficient and the machine fills almost completely. As a result, only a small volume is available for the separation and the solids volume fraction at the overflow increases due to the short residence time in the apparatus.

The right-hand side in Fig. 12 exhibits the impact of transport efficiency on the mean solids volume fraction $\overline{\phi}_c$ and the maximum solids volume fraction at the inner wall of the drum $\phi_{c,max}$ as a function of rotational speed. The comparison of the results points out that there is only a small influence of the transport efficiency on the solids volume fraction in the underflow. This results in only a slight shift of the curves towards a larger solids volume fraction due to the rising sediment volume.

Another field of application for decanter centrifuges is the classification of finely dispersed particles. The aim here is to adjust selectively the particle size of the valuable product. For testing the applicability of dynamic modeling, finely dispersed limestone is classified in a pilot decanter centrifuge. The following parameters serve as simulation setup: $Q = 0.5 \, \text{m}^3 \, \text{h}^{-1}$, $\phi_{in} = 0.15$ and $\Delta n = 15$ rpm.

Figure 13 presents the mass sum distribution at the overflow for experiments and simulations for the investigated pilot decanter centrifuge as a function of rotational speed. The results indicate that there is a shift in the mass sum distribution with the increase of rotational speed. In addition, the dynamic simulations reproduce the results of the classification accurately. Thus, the dynamic model also considers the change in particle size distribution.

The sediment build-up in solid bowl centrifuges depends not only on the process conditions, but also on the material properties of the disperse phase. Additionally, the sediment build-up in decanter centrifuges is influenced by the differential speed between screw and bowl. The left side in Fig. 14 illustrates the influence of the inlet solids volume fraction on the mean solids volume fraction of the underflow. The

Fig. 13 Particle size distribution at the overflow for simulation and experiment dependent on rotational speed for the classification of limestone-water slurries with a pilot-scale decanter centrifuge. The simulation setup is $Q = 0.5 \, \text{m}^3 \, \text{h}^{-1}$, $\phi_{in} = 0.15$ and $\Delta n = 5$ rpm [20]
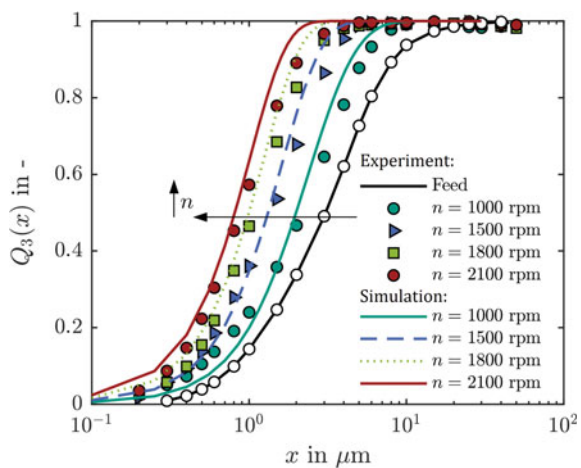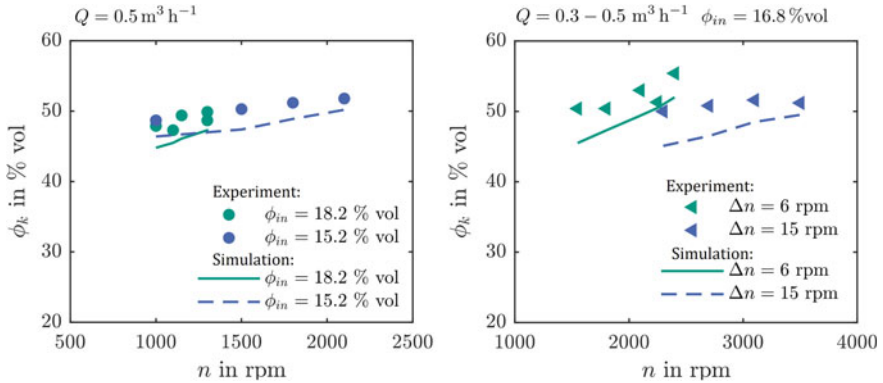
Fig. 14 Comparison of the mean solids volume fraction of the underflow dependent on rotational speed. Left: influence of feed volume fraction for finely dispersed limestone with a mean particle size of $x_{50,3} = 3.4\,\mu m$. Right: impact of differential speed between screw conveyor and drum for a limestone-water slurry with a mean particle size of $x_{50,3} = 1.6\,\mu m$ [20]

measuring ranges overlap, which indicates that there is only a small influence of the solids volume fraction. Furthermore, the solids volume fraction of the underflow increases for higher speeds. Comparing simulation and experiment, it is easy to see that the calculation underestimates the solids volume fraction of the sediment. At this point, shear compression can lead to a denser packing of the formed saturated cakes.

The right-hand side in Fig. 14 shows the influence of differential speed (Δn) on the mean solids volume fraction at the underflow for $\Delta n = 6$ rpm and $\Delta n = 15$ rpm. The influence of the differential speed on the solids volume fraction is significantly higher for the investigated process compared to the variation of the feed solids volume fraction. This results in a denser sediment for $\Delta n = 6$ rpm at a lower speed compared to the simulation setup with $\Delta n = 15$ rpm. In addition, the simulation underestimates the experimental values for both differential speeds.

5 Dynamic Modeling of Tubular Centrifuges

Another machine type in the class of solid bowl centrifuges are fast-rotating tubular centrifuges. Due to the slim design, this centrifuge type achieves g-forces up to $C = 100000$. This makes the apparatus suitable for the separation of nanoparticles and proteins from fermentation processes. Another field of application is the defined classification of nanoparticles. Figure 15 depicts the schematic design of a tubular centrifuge. A pump delivers the mostly diluted suspension at the bottom axially into the apparatus. The geometry of the machine forms a liquid pond and a gas core. The suspension flows in axial direction and leaves the apparatus on the top. The
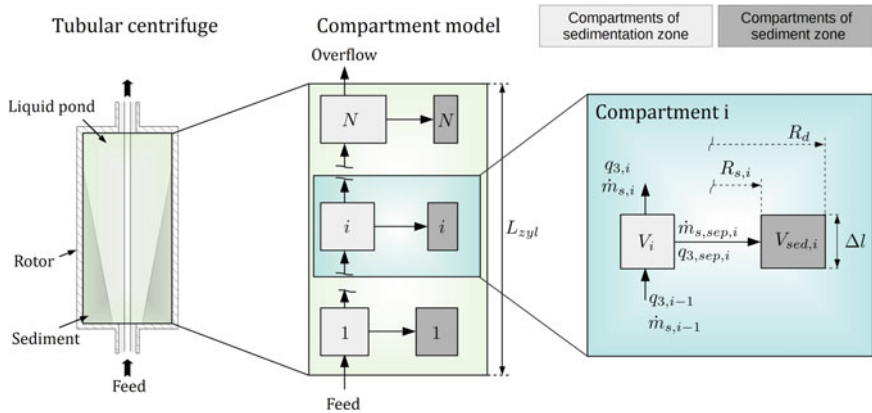
Fig. 15 Schematic representation of a tubular centrifuge, developed compartment approach and balancing of an individual compartment. Reprinted with permission from [20]

centrifugal field created by the rotation leads to particle settling in the direction of the inner rotor wall.

The basis for the mathematical modeling is the dynamic model for decanter centrifuges presented in Sect. 4.1. Sedimentation and sediment zone describe the separation of the dispersed phase and the sediment formation in the investigated tubular centrifuge. In contrast to decanter centrifuges, no sediment transport takes place. The starting point is a cohesive particle cluster that does not move because of the rheological properties of the sediment. Once the particles have been separated, the sediment remains at this axial position in the rotor. Only sediment compression in the radial direction takes place. As for decanter centrifuges, a total number of compartments (N) subdivides the inner space of the rotor. The right-hand side in Fig. 15 shows the variables modeled exemplarily for the compartment (index i). Sections 5.1 and 5.2 discuss the mathematical modeling of tubular centrifuges in more detail.

Figure 16 depicts the temporal change of sediment build-up exemplarily for three-time steps $t_0 < t_1 < t_2$. At the beginning of the dynamic simulation $t_0 = 0\,\text{s}$, only liquid is present in the centrifuge. Discretization of the rotor length L_{ax} allows calculating of the sediment distribution for each time step t. After a certain time (t_2), the regions close to the inlet are almost completely filled due to the classification of the product along the rotor length. Here, simulation results from Hammerich et al. [11] show that a fast-flowing layer forms in these regions. Due to the short residence time of the slurry, no further separation occurs. Instead, the flow collects particles from the sediment surface. However, this physical behavior is not taken into account in the presented approach. If the radius of the sediment is equal or smaller than the maximum radial position of the sediment surface R_{max}, no further separation is considered in this section of the tubular centrifuge.
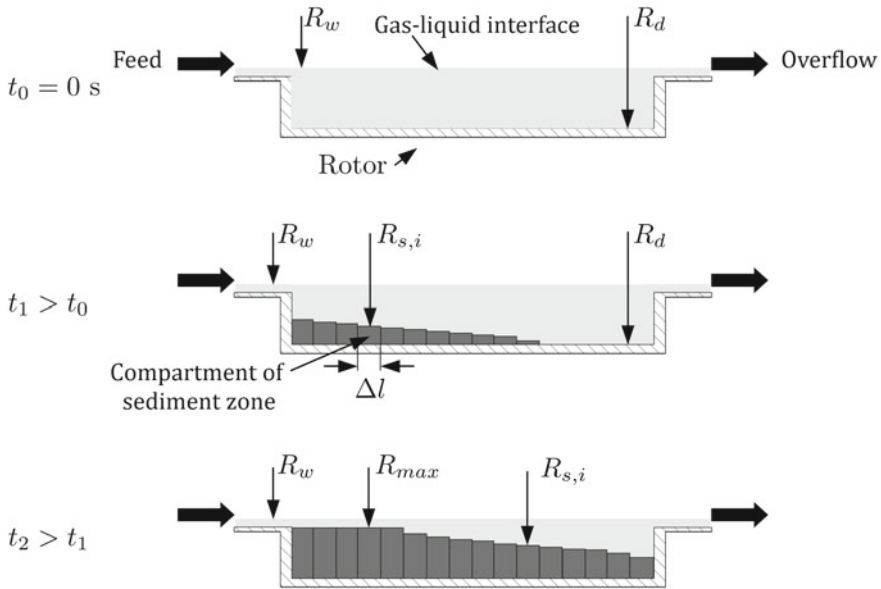
Fig. 16 Schematic representation of the temporal filling process exemplary for three-process steps $t_0 < t_1 < t_2$. Reprinted with permission from [20]

5.1 Modeling of the Sedimentation Zone

The dynamic modeling of the sedimentation zone in tubular centrifuges is based on almost the same assumptions as for decanter centrifuges. However, in contrast to decanter centrifuges, the main flow direction is axial towards the overflow. The modified residence time behavior requires to adapt the grade efficiency calculation:

$$G_i(x,t) = \frac{R_{s,i}(t)^2}{R_{s,i}(t)^2 - R_w^2} \left\{ 1 - \left(exp\left\{ -\frac{(\rho_s - \rho_l)h(\phi)x^2\omega^2}{18\eta_l} \frac{V_i(t)}{Q_{i-1}} \right\} \right)^2 \right\}. \quad (25)$$

The main difference to the grade efficiency model for decanter centrifuges results from the differing geometry of tubular centrifuges. Neglecting the pre-acceleration zone and the overflow region, it can be described as a hollow cylinder. The volume of a compartment (index i) is calculated using the geometric dimensions of a hollow cylinder:

$$V_i(t) = \pi \left(R_{s,i}(t)^2 - R_w^2 \right) \Delta l. \quad (26)$$

The length of a compartment Δl is unknown. The ratio of the length of the cylindrical rotor L_{cyl} to the total number of compartments N describes Δl. Furthermore, the total volume of the cylindrical rotor

$$V_{\text{cyl}} = \pi\left(R_{\text{d}}^2 - R_{\text{w}}^2\right)L_{\text{cyl}}, \tag{27}$$

is decisive for the calculation of the volumetric filling level. The mass balance for solid, liquid and particle size distribution is the same for the dynamic modeling of decanter and tubular centrifuges. At this point, it should be noted that the rotating gas core and thus the gas liquid-interphase are not considered in the dynamic model presented. Additionally, no particle breakage occurs in the feed zone of the tubular centrifuge. Moreover, the slurry rotates as a rigid body. This means that an insufficient pre-acceleration is not taken into account by the presented approach.

5.2 Modeling of the Sediment Zone

Since a tubular centrifuge is a semi-continuous apparatus, the process behavior for sediment build-up differs from that of a decanter centrifuge. Here, the solid accumulates continuously on the inner rotor wall until the apparatus is completely filled. As a result, the solids mass balance in a compartment of the sediment zone simplifies as follows:

$$\frac{dm_{\text{s,sed,i}}}{dt} = \dot{m}_{\text{s,sed,i}}. \tag{28}$$

The continuous supply of solids during the entire process leads to a complete filling of the rotor up to the maximum volumetric filling level theoretically. For the prediction of the radial position of the sediment surface for the compartments $i = 1$, …, N the solids mass balance is transformed into a volume balance of solids:

$$\frac{dV_{\text{s,sed,i}}}{dt} = Q_{\text{s,sed,i}}. \tag{29}$$

The dynamic simulation of the sediment build-up along the axial position of the rotor allows the temporal prediction of the sediment distribution. The accumulated volume of the sediment is used to determine the radial position of the sediment surface

$$R_{\text{s,i}}(t) = \left[R_{\text{d}}^2 - \frac{V_{\text{sed,i}}(t)}{\pi\,\Delta l}\right]^{0.5}, \tag{30}$$

for each compartment (index i). The radial position of the sediment surface is then used to calculate the volume of the sedimentation zone in Eq. (26) and thus to map the residence time behavior which deviates with process time. Stahl et al. [29] show that the sediment in tubular centrifuges only increases up to a critical volumetric filling level of $U_{\text{max}} = 0.95$. This means that the sediment does not emerge from

the liquid pool. Rather, separated and dragged solids are in equilibrium in the fast-flowing layers of the centrifuge. The dynamic model considers the described process behavior by estimating the maximum possible radius of the sediment:

$$R_{\max} = \left[(1 - U_{\max}) \cdot \left(R_{\mathrm{d}}^2 - R_{\mathrm{w}}^2\right) + R_w^2\right]^{0.5}. \tag{31}$$

For each time step, the radial position of the sediment surface for each compartment (index i) is compared to the maximum sediment radius. For $R_{\mathrm{s,i}}(t) \geq R_{\max}$, no further particles are separated in this compartment and $G_{\mathrm{i}}(x, t) = 0$ apply for the grade efficiency. The evaluation of the temporal behavior of the separation process is based on two parameters: the product loss $P(t)$ and volumetric filling level $U(t)$. The temporal change of the volumetric filling level results from the ratio of the overall accumulated sediment volume for all compartments i = 1, …, N to the volume of the rotor:

$$U(t) = \frac{\sum_{\mathrm{i}=1}^{\mathrm{N}} V_{\mathrm{sed,i}}(t)}{V_{\mathrm{cyl}}}. \tag{32}$$

The product loss

$$P(t) = \frac{\dot{m}_{\mathrm{s,of}}}{\dot{m}_{s,\mathrm{feed}}}, \tag{33}$$

is the ratio of the solid mass flow at the overflow $\dot{m}_{\mathrm{s,of}}$ to the solid mass flow at the feed $\dot{m}_{\mathrm{s,feed}}$. The algorithm developed for the sediment formation process distinguishes between an incompressible and a compressible cake. For an incompressible cake, the porosity is not a function of the solids pressure. This results in a practically constant porosity over the sediment height. Such materials are also analyzed in beaker centrifuges to determine the porosity of the sediment for dynamic simulation. For compressible cakes, the behavior differs significantly. Here, as described in Sect. 2.2, porosity is a function of the solids pressure. For the mathematical description of the sediment build-up for compressible materials please refer to Gleiss [20].

5.3 Validation of the Dynamic Model for Tubular Centrifuges

This subsection deals with the verification of the dynamic model to predict the process behavior of tubular centrifuges. The parameters to validate the dynamic model are the product loss and the volumetric filling level. The tubular centrifuge investigated is a pilot machine of the company CEPA GmbH type GLE. Table 3 summarizes the geometric dimensions and discretization of the centrifuge.

Additionally, Fig. 17 depicts the mass distribution functions of silica with the commercial name Aerosil 200 which is applied as an initial parameter for the dynamic modeling. The mass related mean particle size is $x_{50,3} = 76$ nm.

Table 3 Summary of the key data of the investigated tubular centrifuge

Parameter	Value (m)
Rotor length	0.18
Drum radius	0.0215
Weir radius	0.0152
Number of compartments	50
Number of sediment slices	100
Number of particle classes	100

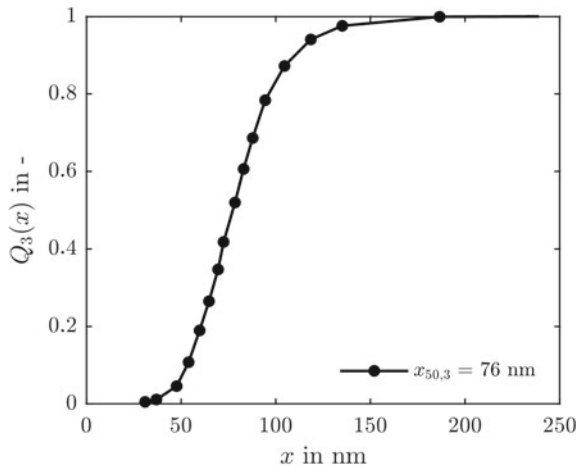**Fig. 17** Mass distribution function of silica nanoparticles with the commercial name Aerosil 200

Figure 18 shows the temporal change of product loss for the separation of silica nanoparticles, dependent on the empirical parameters of the material function for the solids pressure. The simulation setup is $Q = 0.1 \ 1 \cdot \text{min}^{-1}$, $C = 19200$ and $\phi_{\text{in}} = 0.005$. The product loss changes linearly with time in the range of 1 min $< t < 90$ min.

One of the three parameters p_1, p_2 and ϕ_{gel} was changed exemplarily for each simulation. As can be seen from Fig. 17 Mass distribution function of silica nanoparticles with the commercial name Aerosil 200.

Figure 18, the parameter variation shows a small influence on the temporal change of the product loss, but also a good agreement with the experiment.

A significant influence results for the volumetric filling level and thus for the sediment build-up in the tubular centrifuge, see Fig. 19. The variation of parameters p_1 and p_2 shifts the curve for the volumetric fill level up by about 10%. This clearly shows the influence of the compression behavior on the sediment structure and thus the importance of the meaningful prediction of the material behavior based on the methodology shown in Sect. 2.2 on a laboratory scale. Here, measurement uncertainties lead to deviations in the dynamic simulation of process behavior for tubular centrifuges and thus to deviations in the separation efficiency.

Fig. 18 Comparison of simulation und experiment for the temporal change of product loss dependent on the material properties to describe solids pressure. The simulation setup is $Q = 0.11 \cdot min^{-1}$, $C = 19.200$ and $\phi_{in} = 0.005$ [20]

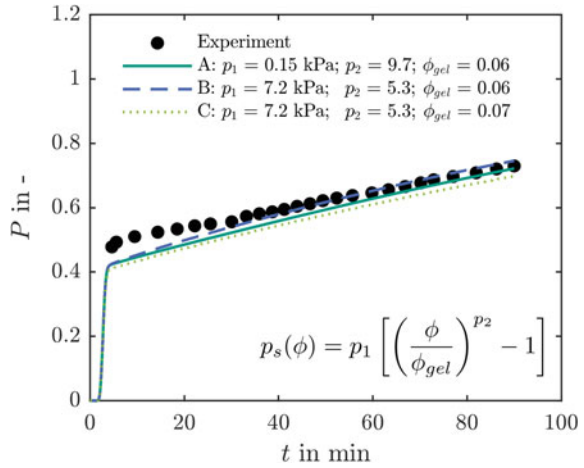$$p_s(\phi) = p_1 \left[\left(\frac{\phi}{\phi_{gel}} \right)^{p_2} - 1 \right]$$

Fig. 19 Comparison of simulation and experiment for the temporal change of the filling level for the tubular centrifuge investigated dependent on the material function for the compression behavior. The simulation setup is $Q = 0.1l \cdot min^{-1}$, $C = 19200$ and $\phi_{in} = 0.005$ [20]
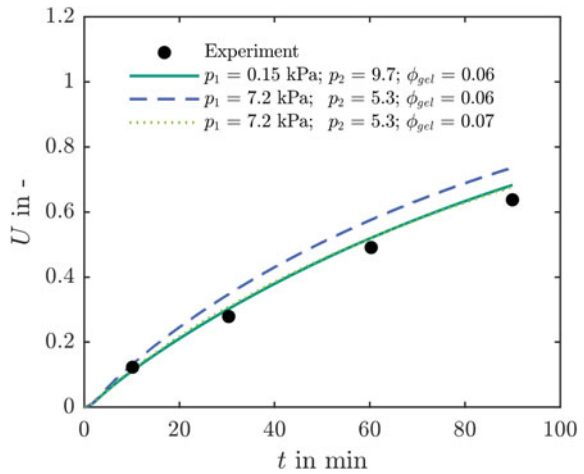
Figure 20 illustrates the simulated temporal change of the grade efficiency under variation of the volumetric flow rate for two different time steps $t = 10$ min and $t = 30$ min. In this case, the simulation setup is based on $C = 19200$ and $\phi_{in} = 0.005$. The results show a shift in the degree of separation with respect to the process time towards larger particle fractions, which worsens the classification.

Furthermore, the influence of the volume flow can be clearly seen. At this point there is a shift of the curves towards larger particles with the increase of the volume flow rate. The process behavior can be explained by the reduction of the residence time in the tubular centrifuge. Furthermore, the results indicate a broader grade efficiency for higher volume flow rate.

Another advantage of the dynamic model is the description of the temporal evolution of the sediment height and the sediment distribution along the rotor. As a

Fig. 20 Dynamic simulation of grade efficiency dependent on time and volumetric flow rate. Simulation setup is $C = 19200$ and $\phi_{in} = 0.005$ [20]
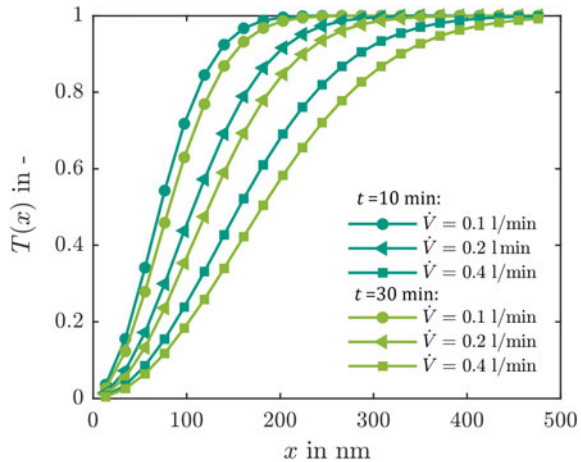

result the sediment volume can be derived for each time step. Figure 21 presents the sediment height as a function of the rotor length for $C = 9600$, $C = 28900$ and $C = 38500$. Here, the g-force refers to the bowl radius. Each iso-line corresponds to a constant time. The interval between two lines is $\Delta t = 10$ min. The results indicate deviating process behavior for the sediment build-up as a function of the volume flow. A thin sediment layer is formed in the rotor for $C = 9600$ at time $t = 90$ min. For $C = 38,500$ the rotor is almost completely filled. This process behavior results from the increasing amount of the separated solid for a higher g-force.

6 Conclusion

This work presents the development of two dynamic models for continuous working decanter centrifuges and semi-batch tubular centrifuges. Both models are computationally efficient and therefore suitable for dynamic flowsheet simulation and Model Predictive Control. Dynamic simulation requires material functions and the residence time behavior to predict the real process behavior with sufficient accuracy. In contrast to the Σ-theory, which carries out experiments on a pilot scale, the settling behavior and the sediment build-up were investigated sing well-established laboratory equipment. This allows a detailed numerical investigation of the process level for solid-bowl centrifuges.

Another important parameter for the description of continuous and semi-batch machines are the flow conditions, which influence the residence time of the particles. For this reason, three methods have been applied to investigate the flow conditions: the experimental residence time measurement, CFD simulations and characterization of the system behavior. The experimental data for the system behavior results from a stepwise change of particle size distribution and solids volume fraction at the feed

Fig. 21 Temporal change of sediment height as a function of rotor length for three g-forces $C = 9600$, $C = 28900$ and $C = 38500$. Each line represents an iso-curve for a point in time. Reprinted with permission from [20]
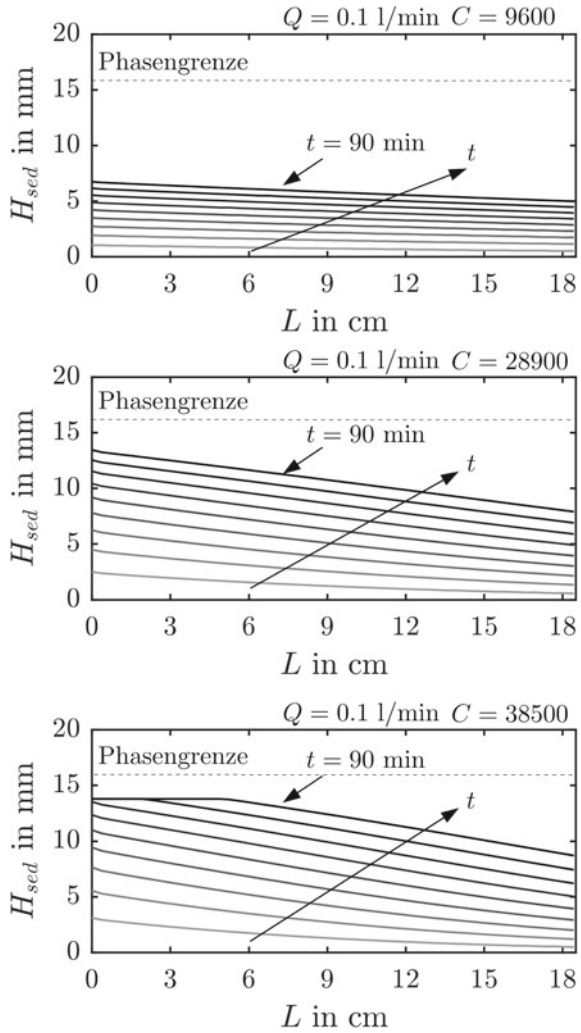
of a lab-scale decanter centrifuge. The results show the correlation between the residence time and the dynamic behavior. The dynamic model for decanter centrifuges is based on the interconnection of individual compartments. The numerical algorithm solves the mass balance of solids and liquid as well as for the particle size class for each compartment. Since the material behavior at the transition between suspension and sediment changes abruptly, the mathematical model divides the centrifuge into a sedimentation zone and a sediment zone. The sedimentation zone describes the dynamic behavior during the separation of the particles. Whereas the sediment zone,

considers the calculation of sediment build-up and sediment transport. The comparison of dynamic simulations with experiments for finely dispersed particle systems shows a good conformity.

Finally, the broad applicability of the developed compartment model was demonstrated by transferring the dynamic model of a continuous working decanter to semi-batch tubular centrifuges. It can be shown that the deviating process behavior of tube centrifuges is due to the sediment build-up in the rotor. In contrast to decanter centrifuges, the accumulated solids remain in the apparatus and thus reduce the flow cross-section. As a result, the residence time decreases permanently until the sediment occupies the entire rotor. The comparison with experiments for nanoscale silica also shows a good agreement between simulation and experiment for the temporal change of product loss and grade efficiency. The developed models are not only suitable for dynamic flowsheet simulation, but also for other applications. For example, it is conceivable to use dynamic models for MPC or to carry out an optimization regarding raw material or resource efficiency.

References

1. Kowalczyk, B., Lagzi, I., Grzybowski, B.A.: Nanoseparations: strategies for size and/or shape-selective purification of nanoparticles. Curr. Opin. Colloid Interf. Sci. **16**, 135–148 (2011). https://doi.org/10.1016/j.cocis.2011.01.004
2. Kanarska, Y., Lomov, I., Antoun, T.: Mesoscale simulations of particulate flows with parallel distributed Lagrange multiplier technique. Comput. Fluids **48**, 16–29 (2011). https://doi.org/10.1016/j.compfluid.2011.03.010
3. Ambler, C.M.: The evaluation of centrifuge performance. Chem. Eng. Prog. **48**, 150–158 (1952)
4. Ambler, C.M.: The theory of scaling up laboratory data for the sedimentation type centrifuge. J. Microb. Biochem. Technol. **1**, 185–205 (1959)
5. Leung, W.W.-F.: Industrial Centrifugation Technology. McGraw-Hill, New York (1998)
6. Gleiss, M., Hammerich, S., Kespe, M., Nirschl, H.: Application of the dynamic flow sheet simulation concept to the solid-liquid separation: separation of stabilized slurries in continuous centrifuges. Chem. Eng. Sci. **163**, 167–178 (2017)
7. Konrath, M., Brenner, A., Dillner, E., Nirschl, H.: Centrifugal classification of ultrafine particles: Influence of suspension properties and operating parameters on classification sharpness. Sep. Purif. Technol. **156**, 61–70 (2015)
8. Romanni Fernández, X., Nirschl, H.: A numerical study of the impact of radial baffles in solid bowl centrifuges using computational fluid dynamics. Phys. Sep. Sci. Eng. (2010)
9. Romaní Fernández, X., Nirschl, H., Fernández, X.R., Nirschl, H.: Simulation of particles and sediment behaviour in centrifugal field by coupling CFD and DEM. Chem. Eng. Sci. **94**, 7–19 (2013). https://doi.org/10.1016/j.ces.2013.02.039
10. Hammerich, S., Gleiß, M., Nirschl, H.: Modeling and simulation of solid-bowl centrifuges as an aspect of the advancing digitization in solid-liquid separation. Chemie Ing. Tech. **91**, 215–227 (2019)
11. Hammerich, S., Gleiß, M., Kespe, M., Nirschl, H.: An efficient numerical approach for transient simulation of multiphase flow behavior in centrifuges. Chem. Eng. Technol. **41**, 44–50 (2018)
12. Stahl, W.: Fest-Flüssig-Trennung Band II: Industrie-Zentrifugen, Maschinen-und Verfahenstechnik. DRM Press, CH-Männedorf (2004)
13. Skinner, S.J., Studer, L.J., Dixon, D.R., Hillis, P., Rees, C.A., Wall, R.C., et al.: Quantification of wastewater sludge dewatering. Water Res. **82**, 2–13 (2015). https://doi.org/10.1016/j.watres.2015.04.045

14. Lerche, D.: Dispersion stability and particle characterization by sedimentation kinetics in a centrifugal Field. J. Dispers. Sci. Technol. **23**, 37–41 (2007)
15. Detloff, T., Sobisch, T., Lerche, D.: Particle size distribution by space or time dependent extinction profiles obtained by analytical centrifugation. Powder Technol. **174**, 50–55 (2007)
16. Anlauf, H.: Recent developments in centrifuge technology. Sep. Purif. Technol. **58**, 242–246 (2007). https://doi.org/10.1016/j.seppur.2007.05.012
17. Beiser, M., Bickert, G., Scharfer, P.: Comparison of sedimentation behavior and structure analysis with regard to destabilization processes in suspensions. Chem. Eng. Technol. **27**, 1084–1088 (2004). https://doi.org/10.1002/ceat.200403252
18. Richardson, J.F., Zaki, W.N.: Sedimentation and fluidisation: Part I. Chem. Eng. Res. Des. **75**, 82–100 (1997)
19. Michaels, A., Bolger, J.: Settling rates and sediment volumes of flocculated kaolin suspensions. Ind. Eng. Chem. Fundam. **1**, 24–33 (1962)
20. Gleiß, M.: Dynamische Simulation der Mechanischen Flüssigkeitsabtrennung in Vollmantelzentrifugen, KIT Scientific Publishing (2018)
21. Stickland, A.D.: Solid-liquid separation in the water and wastewater industries. University of Melbourne (2005)
22. Spelter, L.E., Nirschl, H., Stickland, A.D., Scales, P.J.: Pseudo two-dimensional modeling of sediment build-up in centrifuges: a compartment approach using compressional rheology. AIChE J. **59**, 3843–3855 (2013)
23. Usher, S.P., Studer, L.J., Wall, R.C., Scales, P.J.: Characterisation of dewaterability from equilibrium and transient centrifugation test data. Chem. Eng. Sci. **93**, 277–291 (2013)
24. Green, M.D., Eberl, M., Landman, K.A.: Compressive yield stress of flocculated suspensions: determination via experiment. AIChE J. **42**, 2308–2318 (1996)
25. Mladenchev, T., Tomas, J.: Modellierung der Filtrations- und Konsoldierungsdynamik von geflockten und nicht geflockten feindispersen Kalksteinsuspensionen. Chemie Ing. Tech. **76**, 1814–1818 (2004)
26. Erk, B., Luda, A.: Beeinflussung der Schlammkompression in Vollmantelzentrifugen. Chemie Ing. Tech. **75**, 1250–1254 (2003). https://doi.org/10.1002/cite.200303260
27. Le Moullec, Y., Potier, O., Gentric, C., Leclerc, J.: Flow field and residence time distribution simulation of a cross-flow gas-liquid wastewater treatment reactor using CFD. Chem. Eng. Sci. **63**, 2436–2449 (2008)
28. Gleiss, M., Nirschl, H.: Modeling separation processes in decanter centrifuges by considering the sediment build-up. Chem. Eng. Technol. **38**, 1873–1882 (2015)
29. Stahl, S., Spelter, L.E., Nirschl, H.: Investigations on the separation efficiency of tubular bowl centrifuges. Chem. Eng. Technol. **31**, 1577–1583 (2008)

Chapter 8
Flowsheet Simulation of Integrated Precipitation Processes

Mark Michaud, Michael Haderlein, Doris Segets, and Wolfgang Peukert

Abstract This work presents the fundamentals and exemplary applications of a generalized model for precipitation, aggregation and ripening processes including the formation of solid phases with two dimensions. The particle formation is governed by a widely applicable population balance approach. Solid formation processes are described via the numerically efficient Direct Quadrature Method of Moments (DQMOM), which can calculate the evolution of multiple solid phases simultaneously. The particle size distribution (PSD) is approximated by a summation of delta functions while the moment source term is approximated by a two-point quadrature. The moments to calculate the multivariate distributions are chosen carefully to represent the second order moments. Solid formation is based on the model of Haderlein et al. (2017) and is extended by a multidimensional aggregation model. Now, the influences of mixing, complex hydrochemistry and particle formation dynamics including nucleation, growth and aggregation on multiphase precipitation processes are modelled and simulated along independent dimensions with high efficiency.

Nomenclature

A	Fraction of zone in mixing model [–]
A'	Fraction of zone in mixing model [–]
B	Fraction of zone in mixing model [–]
B'	Fraction of zone in mixing model [–]
B_{Hom}	Homogeneous nucleation rate [$1/(m^3*s)$]

M. Michaud · M. Haderlein · W. Peukert (✉)
Institute of Particle Technology, Friedrich-Alexander-Universität
Erlangen-Nürnberg, Erlangen, Germany
e-mail: wolfgang.peukert@fau.de

D. Segets
Process Technology for Electrochemical Functional Materials, Institute for Combustion and Gas Dynamics - Reactive Fluids (IVG-RF), and Center for Nanointegration Duisburg-Essen (CENIDE), Essen, Germany
e-mail: doris.segets@uni-due.de

269

B_{Sec}	Secondary nucleation rate [$1/(m^3*s)$]
B_{Het}	Heterogeneous nucleation rate [$1/(m^3*s)$]
c_i	Concentration of species i [mol/l]
c_L^∞	Bulk concentration [mol/l]
D_p	Diffusion coefficient of phase p [m^2/s]
E	Engulfment factor [1/s]
f	Particle size distribution density [1/m]
$f_{A,i}$	Shape factor of phase i [–]
g	Residual describing the complex equilibria [–]
G_i	Diffusion limited growth rate in direction i [m/s]
H_A	Hamaker constant [J]
He	Adsorption constant [–]
$h_{i,m}$	Net particle formation rate of solid phase i in zone m [$1/(m*s)$]
J	Jacobian of the residual describing the complex equilibra [–]
I	Ion activity product of all solid phases [mol^x/l^x]
k	Order of moment [–]
k_B	Boltzmann constant [J/K]
l	Oder of mixed moment [–]
k_i	Equilibrium constant of reaction i [mol^x/l^x]
$K_{SP,P}$	Solubility product of phase p [mol^x/l^x]
M	Mixing matrix [–]
M_i	Molar mass of species i [kg/mol]
N	Total number of nodes for DQMOM [–]
N_s	Size of the property vector for node positions [–]
$n_{i,m}$	Particle number density of phase i in zone m [$1/(m*s)$]
n_0	Particle number at the beginning of the simulation [–]
o_j	Logarithmic concentration of species j [–]
R	Ripening rate [m/s]
R_s	Reaction stoichiometry matrix [–]
R_i	Radius of interacting particle [m]
S_p	Supersaturation of solid phase p [–]
S_ξ	Source term for moment transformation [$1/(m*s)$]
Sh	Sherwood number [–]
T	Temperature [K]
U	Molar balance stoichiometry matrix [–]
u_i	Mean velocity of internal variable [m/s]
V_M	Molecular volume [m^3/mol]
ΔV_{Growth}	Volume growth during time step Δt [m^3]
w_i	Weighting factor for the Nelder-Mead optimization [–]
W_{ij}	Fuchs stability ratio [–]
W_{tot}	Total interaction potential [J]
x	Particle diameter [m]
x_{crit}	Critical particle diameter [m]
Y	Normalized center-to-center distance of interacting particles [–]
z_i	Ion charge of species i [–]

β	Sum of all sources S_i [$(m/s)^{k+1}$]	
β_{Brown}	Brownian aggregation kernel [m^3/s]	
β_{Turb}	Turbulent aggregation kernel [m^3/s]	
γ	Interfacial energy [N/m]	
γ_i	Activity coefficient of species i [–]	
ε	Specific power input [W/kg]	
ε_0	Vacuum permittivity [A*s/(V*m)]	
ε_r	Relative permittivity [–]	
ζ	Target functional of the Nelder-Mead optimization [–]	
η	Dynamic viscosity [Pa*s]	
θ	Contact angle for heterogeneous nucleation [–]	
Θ	Heaviside function [–]	
κ	Debye length [1/m]	
μ_{ij}	Stoichiometric coefficient of component i in species j [–]	
ν	Kinematic viscosity [m^2/s]	
ν_{ij}	Stoichiometric coefficient of species j in reaction i [–]	
$\xi_{N,\alpha}$	Node position of property N of node α [m]	
π	Archimedes constant [–]	
ρ	Solid density [kg/m^3]	
σ	Standard deviation of particle size distribution [m]	
$\sigma_{i,p}$	Stoichiometric coefficient of species i in solid phase p [–]	
Φ	Solution of implicit equation [–]	
Ψ_i	Surface potential of face i [C/m^2]	
$\omega_{N,\alpha}$	Node weight of property N of node α [–]	

1 Introduction

Precipitation from solution leads to a wide range of solid particles of vastly varying sizes ranging from a few nanometers to hundreds of microns, different shapes such as spheres, platelets or cylinders and different composition of inorganic or organic compounds.

Typical examples considered in this report are the binary compounds ZnO quantum dots (QDs) for opto-electronic applications [1, 2]. $BaSO_4$ used as white pigment, and the more complex systems Goethite ($FeOOH$ [3, 4]) as yellow pigment and Gerhardtite ($Cu_2(NO_3)(OH)_3$) as a side product for methanol catalyst preparation (Cu/ZnO [4, 5]). The design of precipitation processes is a highly complex field of intense research due to the various and complex underlying phenomena. In general, the sequence of mixing, reaction, nucleation, growth, ripening and agglomeration must be considered. Any predictive tool for precipitation must be able to describe the dynamics of the transient solid formation processes. This includes a sufficient resolution of fluid dynamics in the reactor coupled to population balance equations (PBE) for the evolution of solid phases. Today, the full resolution of fluid flow by

direct numerical simulation is possible up to Re < 4000 in simple reaction geometries (T-mixers [6, 7]). Driving force for solid formation is the chemical potential of the key component, i.e. the supersaturation given as the ratio of the actual concentration and the equilibrium concentration. Particle formation can be either reaction- or mixing-controlled. The former leads to a rather uniform distribution of components in the reactor, whereas the latter leads even in simple geometries such as T- or Y-mixers to more widely distributed component distributions. For flowsheet simulation, however, simple approaches are implemented while sufficient accuracy of predictions must be guaranteed. In most industrial applications, a well-defined, often narrow property distribution is targeted.

The topic of the current chapter is the development of such a dynamic flowsheet simulation module using a well-known moment method for predicting the mean size and shape of precipitated particles. The model covers mixing, activity-based supersaturation build-up even in systems of complex hydrochemistry, and solid formation processes. Briesen et al. provided fundamentals to simulate independent particle properties simultaneously [8]. To expand on this work, a generalized modelling tool is developed, which is capable of describing the evolution of multi-component and multiphase particle systems [1, 3, 5], which will then be implemented into a simulation framework. Additionally, our model is used to determine unknown or difficult-to-measure material parameters such as surface energy or intermediate products. The bivariate model formulation allows the prediction of multiple particle properties. In particular, we apply the model to core-shell QDs and to the formation of needle-shaped crystals. Both systems are examples of particles with two dimensions influencing the final product property. The model architecture represents a modular micro-reaction plant consisting of a T-mixer for nucleation and a subsequent vessel for defined particle growth. The setup was characterized with respect to mixing efficiency and residence time distribution.

The model allows transient predictions of a large number of different multivariate precipitation processes in dependence of the underlying mixing and hydrochemistry [9]. Precipitation processes are categorized into mixing- or reaction-controlled systems enabling efficient and problem-specific calculations. The computational effort for these calculations is kept low by using appropriate numerical simplifications, such as the DQMOM, which allows the calculation of multiple disperse properties while keeping the relative error within reasonable bounds. Finally, the individual sub-models are combined into one single module and coupled with a solver, which can be integrated into the Dyssol framework [10].

2   Model Architecture

The developed model is best described as a generalized population balance approach for the subsequent or parallel formation of multiple solid phases with up to two dimensions including agglomeration and ripening. Solid formation is described via the
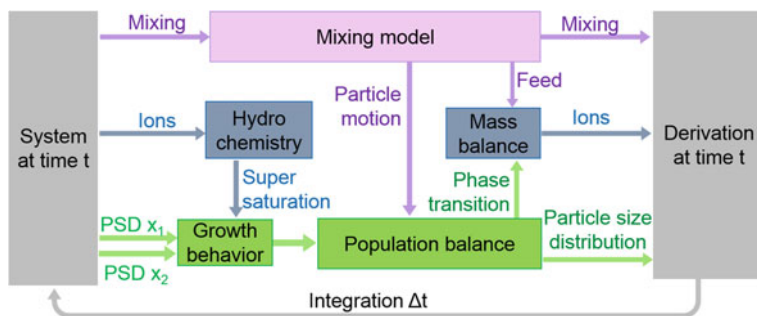
Fig. 1 Architecture of the generalized models for precipitation processes. A system state at time step t is used as the starting point to generate moment transport equations. The information flow follows the creation of population balances and their reintegration into the system. (Adapted from [4] with kind permission from Elsevier)

DQMOM, in which the population balances are represented by a set of moment transport equations, to enable multiphase and multicomponent precipitation simulation with integrated hydrochemistry. We encompass the influences of mixing, chemical reaction networks and particle formation dynamics along independent dimensions. The model architecture is detailed in Fig. 1.

The system state at a time step t summarizes all relevant pieces of information such as concentration, mixing state, supersaturation and particle size. This information is arranged by the submodels to describe the system behavior at this time step. The system behavior is represented by a set of partial differential equations, which are solved by an explicit Runge-Kutta algorithm [11]. The state of the system at time t comprises three major information classes, namely (i) the state of mixing, (ii) the chemical composition of the mixing zones, and (iii) the properties of the disperse phase. The model uses several sub-models, namely

- a mixing module which describes volume segregation,
- a hydrochemistry module which models the thermodynamic driving force for particle formation and growth and finally,
- a general population balance module to calculate the dynamic behavior of disperse phases during the precipitation process.

The state of mixing is used by a sub-model to compute the current engulfment behavior. The hydrochemistry module determines the supersaturation and the resulting nucleation and particle growth. The temporal change of the chemical composition is determined via mass balances and depends on the feed rate and the consumption of chemical components by solid formation. PBEs describe the evolution of disperse properties and are mainly influenced by the supersaturation, the transfer of particles between zones and their aggregation behavior [1]. The PBEs are solved by a multivariate DQMOM approach to calculate the moments of the size distribution developed in [12], which was generalized in our previous work [5, 9]. Finally, the separate datasets are merged to describe the overall system behavior. The forward

integration of the underlying system of ordinary differential equations delivers the system state at the next time step in an explicit Eulerian approach. Particle formation is sub-divided into reaction-limited and transport-limited systems, i.e. for the former the influence of the mixing module can be neglected. In both cases, the thermodynamic driving force, i.e. the local distribution of supersaturation controls space- and time-dependent nucleation and growth.

3 Mixing Model

Precipitation processes can be classified into being either reaction-controlled or mixing-controlled. The former process can be easily modelled by assuming driving forces at each point of the reactor. The latter is strongly influenced by the preceding mixing of the reactants and will yield results depending on the mixing history [13, 14]. CFD simulations including direct numerical simulation would allow for a precise calculation of the mixing behavior, however this kind approach is numerically too expensive for flowsheet simulation [6, 15]. Therefore, we use the Engulfment-Deformation-Diffusion model (EDD model) which was originally developed for stirred tank reactors and later extended to various other types of mixers [16, 17]. In particular, the asymmetric Baldyga model was adapted and improved by the development of the symmetric engulfment model (SEM) to closer represent the symmetric Y- and T-mixers by Haderlein et al. [4], based on an earlier model of [14, 18].

The SEM divides the mixer into four compartments of individual composition, namely the two compartments with pure A and B whose compositions equal the composition of the feed, and two compartments A' and B' in the contact area. Each compartment is considered to be ideally mixed. The SEM assumes bidirectional fluxes between A' and B' allowing for reactive mixtures in both compartments. The compartments interact with each other, the mass transport from one compartment to another is assumed to be proportional to the Engulfment factor E [17]:

$$E = 0.058\sqrt{\frac{\varepsilon}{\nu}} \tag{1}$$

E depends on the specific power input ε and the kinematic viscosity of the liquid. The interaction between the compartments of the SEM is written as a set of differential equations each detailing the volume flow rate of the four individual zones per time step Δt [1]:

$$\frac{dA}{dt} = -E\left(A(A' + B) + AB\frac{A}{A + B}\right) \tag{2}$$

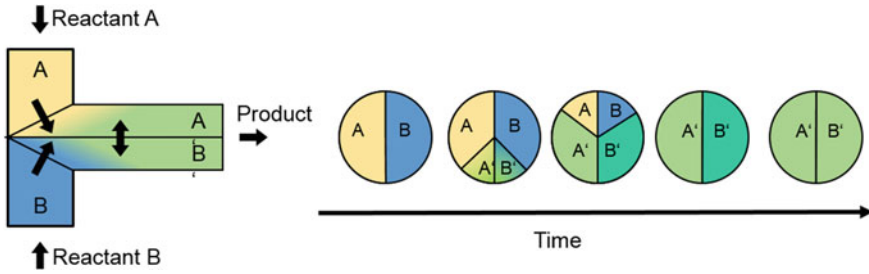$$\frac{dB}{dt} = -E\left(B(A' + B) + AB\frac{B}{A + B}\right) \tag{3}$$

Fig. 2 Graphical description of the symmetrical engulfment model (SEM). The sketch on the left shows the direction of the flows in the contact zone. The temporal evolution on the right shows the mixing behavior (Adapted from [4] with kind permission from Elsevier)

$$\frac{dA'}{dt} = -E\left(A(A'+B) + AB\frac{A}{A+B} + \frac{A'^2B'}{A'+B'} - \frac{A'B'^2}{A'+B'} \right) \tag{4}$$

$$\frac{dB'}{dt} = -E\left(B(A'+B') + AB\frac{A}{A+B} - \frac{A'^2B'}{A'+B'} + \frac{A'B'^2}{A'+B'} \right) \tag{5}$$

These volume changes over time can be arranged into a mixing matrix detailing the flow from one compartment into another. The evolution of the compartment volume fractions can be seen in Fig. 2.

It is important to note that the compositions of the fractions A' and B' do not necessarily need to be equalized even when both volume fractions have reached quasi-equilibrium. This corresponds to concentration gradients inside the mixer at a time at which no pure feed is present anymore.

Mathematically, the mixing model is implemented into the precipitation module via the mixing matrix X in which the volume flow rate from each zone into each other zone is summarized. In this matrix, entries are comprised of two indices. Each line describes the flow from the zone of the first index, while each column describes the flow into the zone of the second index. Each entry of the mixing matrix thus indicates the flow from the zone referenced by the first index into the zone referenced by the second index, allowing for easy summation of total volume flow from each individual zone:

$$M = \begin{pmatrix} AA & AB & AA' & AB' \\ BA & BB & BA' & BB' \\ A'A & A'B & A'A' & A'B' \\ B'A & B'B & B'A' & B'B' \end{pmatrix} \tag{6}$$

While the diagonal elements of the matrix are zero, the non-zero elements are equal to the volume change of the individual zones listed above. The aforementioned total volume change of each zone Z_i can be written as the sum over column j and line j of M associated with the zone:

Fig. 3 Comparison of characteristic mixing time of MEM (black) and SEM (grey) with experimental data (red dots). (Adapted from [4] with kind permission from Elsevier)
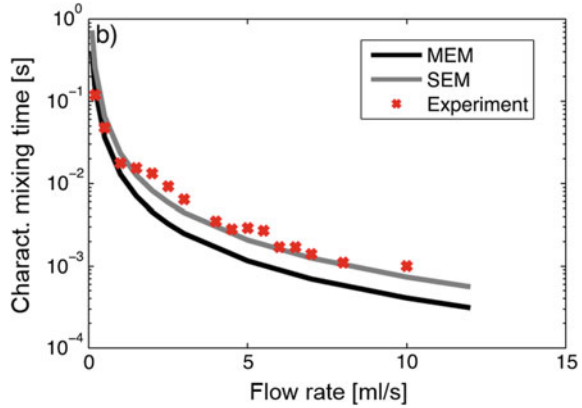
$$\frac{dZ_i}{dt} = \sum_j M_{ji} - \sum_j M_{ij} \qquad (7)$$

M_{ij} denotes the entry of the mixing matrix M at line i and column j. The mixing model was validated by characterization of a T-mixer via the Villermaux-Dushmann protocol [19] using the empirical approach developed by Commenge and Falk [20]. The excellent agreement is an improvement to the earlier MEM model (see Fig. 3).

4 Hydrochemistry

The concentration of species is of major importance for modelling solid formation as it has direct impact on the determination of supersaturation and thus nucleation and growth kinetics. To predict the behavior of precipitating solids, the supersaturation as driving force needs to be calculated with high precision. This is done by setting up mass action laws to calculate the relevant concentrations and then predict the supersaturation using only the solubility product as additional data. However, at already moderate concentrations, activity models such as the Davies equation (Eq. 8) must be taken into account [21]. Due to its simplicity and good agreement with experimental data, it is frequently used for the description of the underlying ionic species:

$$\log_{10} \gamma_i = -0.5079 z_i^2 \left(\frac{\sqrt{\frac{\sum_i c_i z_i^2}{2}}}{1 + \sqrt{\frac{\sum_i c_i z_i^2}{2}}} - 0.3 \frac{\sum_i c_i z_i^2}{2} \right) \qquad (8)$$

The variable c and z refer to the concentration and charge of the involved species. Description of equilibrium concentrations are dynamically solved with mass actions laws and mass balance equations:

$$k_i = \prod_j \left(\gamma_j c_j \right)^{v_{ij}} \tag{9}$$

$$c_i = \sum_j \mu_{ij} c_j \tag{10}$$

with k_i being the equilibrium constant and v_{ij} being the stoichiometric species coefficient accounting for the influence of the j-th species on the i-th equilibrium reaction and μ_{ij} the stoichiometric component coefficient accounting for the stoichiometric coefficient of component i within the species j. These equations are compiled into a hydrochemistry model, which under the given activities and equilibrium concentrations, calculates the supersaturation of each individual solid phase, which is needed in the next step:

$$S_P = \left(\frac{\prod_i \left(\gamma_i c_i \right)^{\sigma_{i,p}}}{K_{SP,p}} \right)^{\frac{1}{\sum \sigma_{i,p}}} \tag{11}$$

with K_{sp} being the solubility product of phase p. Due to numerical reasons, the equations are transferred to a logarithmic scale:

$$o_j = \ln c_j \tag{12}$$

$$\ln k_i = \sum_j v_{ij} \left(\ln \left(\gamma_j + o_j \right) \right) \tag{13}$$

$$c_i = \sum_j \left(\mu_{ij} \exp \left(o_j \right) \right) \tag{14}$$

The model can now be written conveniently in matrix notation as:

$$g(p) = \begin{bmatrix} g_R \\ g_M \end{bmatrix} = \begin{bmatrix} R \cdot (\ln(\gamma + o) - \ln k \\ M \cdot \exp o - c \end{bmatrix} \tag{15}$$

g denotes the residual and g_R and g_M denoting the reaction, respectively mass balance, related part of the residual. In a system of p components and q species, the number of reactions is $r = q - p$. The size of R describing this system is $(r \times q)$ and the element R_{ij} represents the stoichiometric coefficient of species j in reaction i. In contrast, the size of M is $(p \times q)$ and its elements M_{ij} represent the stoichiometric coefficients of the component j in species i. Now, the determination of the species equilibrium can be achieved by finding the root of g. The corresponding algorithms make use of the Jacobian of the system:

$$J = \begin{bmatrix} \frac{\partial g_1}{\partial o_1} & \cdots & \frac{\partial g_1}{\partial o_m} \\ \vdots & \ddots & \vdots \\ \frac{\partial g_n}{\partial o_1} & \cdots & \frac{\partial g_n}{\partial o_m} \end{bmatrix} = \begin{bmatrix} J_R \\ J_M \end{bmatrix} \tag{16}$$

with:

$$J_M = \frac{\partial g_M}{\partial o} = M \cdot \exp o$$

$$J_R = \frac{\ln(10)}{2} \cdot A \cdot \left(\frac{1}{2\sqrt{I}\left(1 + \sqrt{I}\right)^2} - b \right) \cdot R \cdot z^2 \otimes \left(\exp(o) \circ z^2 \right) + R \tag{17}$$

For brevity, the following operators are used:

Matrix product: $\bullet$

Hadamard product: $\circ$

Dyadic product: $\otimes$

The ion activity product can now be written in short matrix notation by working in logarithmic scales to reduce calculation time and easy readability:

$$\ln I = \sigma^T \cdot (\ln \gamma + o) \tag{18}$$

with σ^T as transposed solid phase stoichiometry matrix whose element $\sigma_{i,p}$ is the stoichiometric coefficient of the species i in the solid phase p [4].

5 Moment Methods/DQMOM

The direct quadrature method of moments (DQMOM) was first published by Marchisio et al. in 2005 [12]. It offers an approximate solution of PBEs via the moment transport equation. DQMOM is less computationally demanding than finite volume methods or Monte Carlo methods. DQMOM has two major advantages over other moment methods. Firstly, it is highly efficient, flexible but sufficiently simple when applied to multivariate distributions. Secondly, it allows for coupling the internal coordinates and phase velocities in polydisperse systems. DQMOM tracks the evolution of variables in the quadrature approximation (QMOM) directly rather than the moments, however yields the same result if compared to QMOM. DQMOM allows the implementation of multivariate PBEs by exchanging the variable with a weighted property vector for which the solver of the model has to be adjusted. Tracking the absolute value of the mixed order moments during the simulation is directly possible and does not require any additional computational steps. The growth laws in the code can directly dictate the growth behavior of the tracked phases. A detailed derivation of the DQMOM can be found in the original publication [12]. In brief, the particle

mass balance inside the mixing zones described above can be expressed by:

$$\frac{\partial n_{i,m(x,t)}}{\partial t} - \frac{\partial G(x, t, S_i, n_{i,m})}{\partial x} = h_{i,m}(x, t, S_{i,m}, n, X) \qquad (19)$$

h_i is the internal particle net formation rate in which all particle formation processes except of growth are summarized. The model substitutes the PSD by a sum of multi-dimensional Dirac functions:

$$f(\xi; x, t) = \sum_{\alpha=i}^{N} \omega_\alpha(x, t)\delta[\xi - \langle\xi\rangle_\alpha(x, t)] \qquad (20)$$

where N is the number of delta functions, ω is the weight of the node α. And each dirac function can be written as:

$$\delta[\xi - \langle\xi\rangle_\alpha(x, t)] = \prod_{j=1}^{N_S} \delta\big(\xi_j - \langle\xi_j\rangle_\alpha(x,t)\big) \qquad (21)$$

and $\langle\xi\rangle_\alpha$ is the property vector of node α with dimensionality j. Introducing this approximation into a general PBE with the internal coordinate ξ:

$$\frac{\partial f(\xi_j)}{\partial t} + \frac{\partial}{\partial x_i}\left[\langle u_i|\xi_j\rangle f(\xi_j)\right] - \frac{\partial}{\partial x_i}\left(\frac{D_x \partial f(\xi_j)}{\partial x_i}\right) = S_\xi(\xi_j) \qquad (22)$$

where $\langle u_i|\xi\rangle$ is the mean velocity conditioned on the property value ξ and $S_\xi(\xi)$ is the source term. By rearranging, the following moment transport equation for two-dimensional calculations can be derived:

$$\sum_{\alpha=1}^{N}\left[(1 - k - 1)\langle\xi_1\rangle_\alpha^k\langle\xi_2\rangle_\alpha^l a_\alpha + k\langle\xi_1\rangle_\alpha^{k-1}\langle\xi_2\rangle_\alpha^l b_{1\alpha} + l\langle\xi_1\rangle_\alpha^k\langle\xi_2\rangle_\alpha^{l-1} b_{2\alpha}\right]$$

$$= \sum_{\alpha=1}^{N}\Big[k(k - 1)\langle\xi_1\rangle_\alpha^{k-2}\langle\xi_2\rangle_\alpha^l C_{11\alpha} + 2kl\langle\xi_1\rangle_\alpha^{k-1}\langle\xi_2\rangle_\alpha^{l-1} C_{12\alpha}$$

$$+ l(l - 1)\langle\xi_1\rangle_\alpha^k\langle\xi_2\rangle_\alpha^{l-2} C_{11\alpha}\Big] + \overline{S}_{kl}^{(N)} \qquad (23)$$

with a and b and C_k $\overline{S}_k^{(N)}$ abbreviating:

$$a_\alpha = \frac{\partial\omega_\alpha}{\partial t} + \frac{\partial}{x_i}(\langle u_i\rangle\omega_\alpha) - \frac{\partial}{\partial x_i}\left(D_x\frac{\partial\omega_\alpha}{\partial x_i}\right) \qquad (24)$$

$$b_{1\alpha} = \frac{\partial(\langle\xi_1\rangle_\alpha\omega_\alpha)}{\partial t} + \frac{\partial}{x_i}(\langle u_i\rangle\langle\xi_1\rangle_\alpha\omega_\alpha) - \frac{\partial}{\partial x_i}\left(D_x\frac{\partial\langle\xi_1\rangle_\alpha\omega_\alpha}{\partial x_i}\right) \qquad (25)$$

$$b_{2\alpha} = \frac{\partial(\langle\xi_2\rangle_\alpha\omega_\alpha)}{\partial t} + \frac{\partial}{x_i}(\langle u_i\rangle\langle\xi_2\rangle_\alpha\omega_\alpha) - \frac{\partial}{\partial x_i}\left(D_x\frac{\partial\langle\xi_2\rangle_\alpha\omega_\alpha}{\partial x_i}\right) \qquad (26)$$

$$C_{\beta\gamma\alpha} = \omega_\alpha D_x \frac{\partial(\langle\xi_\beta\rangle_\alpha)}{\partial x_i}\frac{\partial(\langle\xi_\gamma\rangle_\alpha)}{\partial x_i} \qquad (27)$$

$$\overline{S}_{kl}^{(N)} = \int\limits_{-\infty}^{+\infty}\int\limits_{-\infty}^{+\infty}\xi_1^k\xi_2^l S_\xi(\xi)d\xi_1 d\xi_2 \qquad (28)$$

and S_ξ is the moment transport source for the mixed moment including terms for growth, nucleation and aggregation. The left hand side of Eq. 23 represents an arbitrary choice of lower order moments needed to calculate the wanted PSD properties, such as diameter and total surface area. The choice for integer moments can be represented by a set containing the moment order k = {(0,0); (1,0); (0,1); (2,0); (0,2); (2,2)}. DQMOM is implemented into the code as a set of linear ordinary differential equations and solved using the ODE23 solver for nonstiff equations, which satisfies the general DQMOM equation:

$$A\alpha = \beta \qquad (29)$$

In our case, the individual terms need only to represent six mixed moments for two bi-dimensional nodes to cover all included processes:

$$A = \begin{bmatrix} 1 & 1 & 0 & 0 & 0 & 0 \\ 0 & 0 & 1 & 1 & 0 & 0 \\ 0 & 0 & 0 & 0 & 1 & 1 \\ -\langle\xi\rangle_{11}^2 & -\langle\xi\rangle_{12}^2 & 2\langle\xi\rangle_{11} & 2\langle\xi\rangle_{12} & 0 & 0 \\ -\langle\xi\rangle_{21}^2 & -\langle\xi\rangle_{22}^2 & 0 & 0 & 2\langle\xi\rangle_{21} & 2\langle\xi\rangle_{22} \\ -3\langle\xi\rangle_{11}^2\langle\xi\rangle_{21}^2 & -3\langle\xi\rangle_{21}^2\langle\xi\rangle_{22}^2 & 2\langle\xi\rangle_{11}\langle\xi\rangle_{21}^2 & 2\langle\xi\rangle_{21}\langle\xi\rangle_{22}^2 & 2\langle\xi\rangle_{11_{11}^2}\langle\xi\rangle_{11_{21}} & 2\langle\xi\rangle_{11_{12}^2}\langle\xi\rangle_{11_{22}} \end{bmatrix} \qquad (30)$$

$$\alpha^T = \begin{bmatrix} a_1 & a_2 & b_{11} & b_{12} & b_{21} & b_{22} \end{bmatrix} \qquad (31)$$

The mixed moments were chosen by keeping the maximum number of empty cell spaces in the solution arrays while ensuring that the matrix A is of full rank:

$$R_{cond}(A) > 0 \qquad (32)$$

The implementation of a second abscissa in these equations allows the continuous description of two length parameters, e.g. core and shell of QDs or length and diameter of nanorods, respectively, by tracking a set of kl-mixed moments. The advantage of this approach is threefold. Firstly the combination of the growth rate and the particle net formation rate into one moment source term locates all data on both chemical properties of the solid and liquid phases and process data like supersaturation in one part of the equation. Therefore, the general equation of the system can

be applied to many different systems. Secondly, the integration of different mixing models in separate equations allows the application in different mixing regimes or reactor geometries. Lastly, the establishment of individual sets of equations for each mixing zone and each solid phase allows the parallelization of the solution and thus reduces the computational effort.

The solid formation process is condensed into a source term within the moment transport equations by a sum of the N-point quadrature moment sources, which govern physical phenomena such as nucleation, growth and aggregation. The central equation can be reduced to a set of four independent differential equations, whose solution allows tracking the first four moments of the solid phases inside each mixing zone in the aforementioned mixing model.

6 Solid Formation

Nucleation, growth and aggregation are addressed in the model and briefly summarized in the following. Homogeneous nucleation is typically used to describe the precipitation of particles from a supersaturated solution. According to classical nucleation theory (CNT), homogeneous nucleation follows from repeated reversible addition of monomers until a stable cluster is formed. The driving force for the phase transition is the supersaturation. In this work, we consider nucleation and diffusion-limited growth. Nevertheless, the overall framework can easily be extended by other models for nucleation and growth ensuring the wide applicability of our approach. In our model, we assume a stepwise solid formation process, which assumes primary nucleation of particles with critical size and subsequent growth. Three different nucleation rates are available as sources for the model:

$$B_{Hom} = 1.5D \frac{(K_{SP}SN_A)^{\frac{7}{3}}}{V_M} \sqrt{\frac{\gamma}{k_BT}} \exp\left(-\frac{16\pi}{3}\left(\frac{\gamma}{k_BT}\right)^3 V_M^2 \frac{1}{(\nu\ln(S))^2}\right) \quad (33)$$

$$B_{Sec} = \frac{D}{x^2} \cdot \exp\left(-\frac{4(k_c^A)^3 V_m^2 \gamma_{sek}^3}{27(k_c^V)^2 k_B^2 T^2 (\ln(S))^2}\right) \quad (34)$$

$$B_{Het} = \frac{A_{tot}}{2\pi} \sqrt[3]{6V_M/\pi} He(a_i^* N_A S)^{\frac{7}{3}} V_M \sqrt{f\gamma/k_BT}$$

$$\left[\sin\theta \frac{D}{r_{crit}} He\sqrt{6V_M/\pi}(a_i^* N_A S)^{\frac{1}{6}} + 3\pi D(1-\cos\theta)\right] \exp\left(-\frac{f4\pi\gamma x_{crit}^2}{6k_BT}\right) \quad (35)$$

D is the diffusion coefficient, K_{SP} is the solubility product, x is the particle diameter, V_M is the molecular volume, γ is the interfacial energy, He is the adsorption constant of a building block on the surface of the nucleus, f is a geometric correction factor, S is the supersaturation which is introduced by the hydrochemistry model, and ν is the stoichiometric coefficient. The model assumes nucleation of particles

with a critical size x_c, which is calculated by the Gibbs-Thomson equation which is derived from the assumption of energy equilibrium between free Gibbs enthalpy of volume versus free Gibbs enthalpy of surface:

$$x_c = \frac{4V_M\gamma}{k_B T \ln(S)} \tag{36}$$

For a detailed derivation of these equations the reader is directed to [22]. The second step in solid formation is growth of nucleated particles. Growth is calculated in each time step depending on the system state. The growth rates used for fast precipitation processes are assumed to be diffusion-limited:

$$G_i = 4D \sqrt{K_{SP}} \frac{M_i}{\rho} \frac{S-1}{x} \tag{37}$$

M refers to the molar mass, ρ is the density of the solid phase and x is the current diameter of the growing particle. This source term can mathematically be described as adding a layer of solid material to an existing particle during each time step Δt during the simulation. The term is closed by the mass balance which removes the corresponding amount of mass from the solution that is needed to grow the particle of size ξ:

$$\Delta V_{Growth} = \sum_i^{N_S} f_{A,i} \xi_i^2 G_i \Delta t \tag{38}$$

with $f_{A,i}$ being a shape factor. Conversion of the growth rate for the use in DQMOM requires a mixed-point transformation for each moment that is calculated, while the extension to a bivariate model requires additional information about the second spatial direction. In this case, the information for net particle formation and growth rate for each node and dimension is provided to the source term for the moment transport equation by a combined arbitrary source term of G_1 and G_2. Each line in term for the moment transport equation thus has to encompass the net growth rate for each node and dimension:

$$\beta = \begin{bmatrix} 0 \\ \omega_1 G_1 + \omega_2 G_1 \\ \omega_1 G_2 + \omega_2 G_2 \\ 2\omega_1 G_1 \xi_{11} + 2\omega_2 G_1 \xi_{12} \\ 2\omega_1 G_2 \xi_{21} + 2\omega_2 G_2 \xi_{22} \\ 2\omega_1 G_1 \xi_{11} \xi_{21}^2 + 2\omega_1 G_2 \xi_{11}^2 \xi_{21} + 2\omega_2 G_1 \xi_{12} \xi_{22}^2 + 2\omega_2 G_2 \xi_{12}^2 \xi_{22} \end{bmatrix} \tag{39}$$

This results in the possibility to model different geometrical particle shapes. The flexibility of our code allows for source terms with independent variables to be

implemented, which are schematically displayed in Fig. 4. These source terms can be adjusted to account for different geometries or sequential growth.

The example of sequential growth is a good starting point to test the numerical stability of the code for bivariate systems. Sequential growth of core-shell particles represents two independent growth rates. Here, initial nucleation and growth of the core has no influence on the subsequent growth of the shell, the former only delivers the boundary condition for the node positions at the beginning of the shell growth. The two independent parameters are the core diameter and the shell thickness with a boundary condition restricting the values of the sizes to a positive domain. This is necessary, as DQMOM is solvable for negative node positions and in consequence negative particle sizes. The mean diameter of each phase can be derived from a lower order mixed moment:
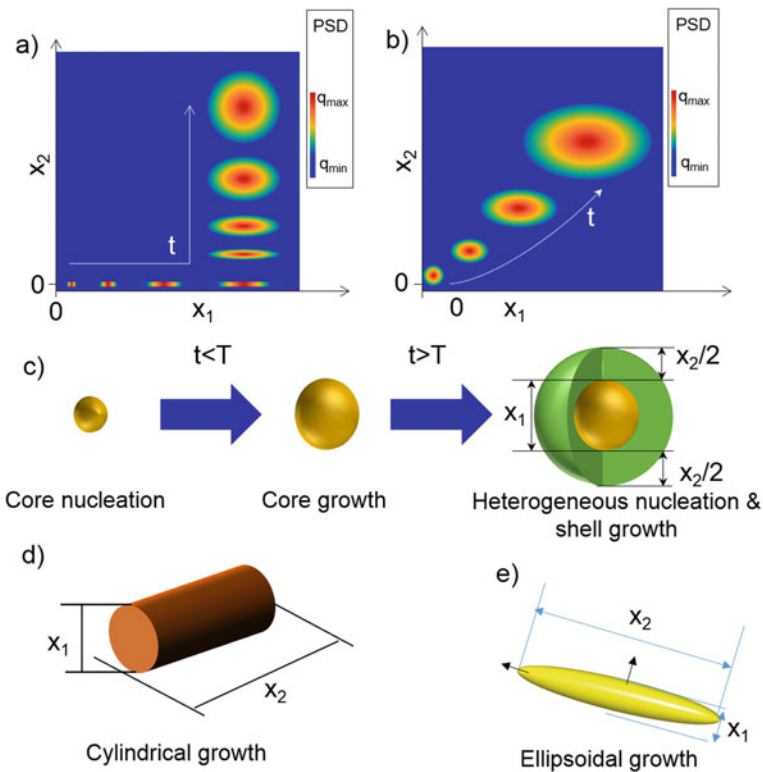
Fig. 4 Schematic display of the different ways to model bivariate PSD. **a** Uncoupled growth allows growth of one dimension independent of the other. **b** Coupled growth always changes each entry of the property vector simultaneously. **c** Production of core-shell particles as an example of sequential growth. **d–e** Cylinders and ellipsoids as examples of structure resulting from growth rates pointing in different spatial dimensions

$$x_i = \frac{\sum_\alpha^N \xi_{\alpha i} \omega_\alpha}{\sum_\alpha^N \omega_\alpha} \tag{40}$$

in which ω is the node weight and ξ is the position of node α for phase i. In the case of sequential processes, temporal separation of growth is achieved by Heaviside step functions Θ multiplied to the solid growth model:

$$G_1 = (1 - \Theta(t - T)) \frac{2 \, \text{Sh} \, D_p \, M_p}{\rho \, S \, x_1} \left(\frac{K_{SP}}{\beta_{i,p}} \right)^{\upsilon_{i,p}} \tag{41}$$

$$G_2 = (\Theta(t - T)) \frac{2 \, \text{Sh} \, D_p \, M_p}{\rho \, S \, (x_1 + x_2)} \left(\frac{K_{SP}}{\beta_{i,p}} \right)^{\upsilon_{i,p}} \tag{42}$$

in which T is the process time for the first step. These equations describe a sequential process with temporal separation of core and shell growth. For the simulation, this means only 3 of the 6 lines in Eq. 39 are nonzero for each calculated time step. This avoids badly scaled matrices as long as the starting point of the node positions are unique.

For simultaneous growth in each spatial dimension, matrix β in Eq. 39 is nonzero in at least 5 lines. A good example of this would be the growth of non-spherical particles such as rods, spindles and ellipsoids. For the nanorods, a simple cylindrical geometry was assumed by multiplying the growth rate with a constant factor in order to modulate the final particle. When calculating the growth of anisotropic particles the mass balance has to be revised in comparison to spheres, since the volume of added solid is now dependent on all other dimensions. This coupling is done by separately calculating the mean volume, here given for a cylinder and the respective surface from diameter D and length L:

$$V_{\text{cylinder}} = \frac{\pi}{4} D^2 L \tag{43}$$

$$A_{\text{cylinder}} = \pi D \left(\frac{D}{2} + L \right) \tag{44}$$

and added into the mass balance:

$$m_{\text{zone}}(t_i + 1) = m_{\text{zone}}(t_i) - \rho_{\text{solid}} G(t_i) * A(t_i) \tag{45}$$

Here m_{Zone} is the total mass of the solid in the current mixing zone and ρ is the density of the solid.

Additionally to growth and nucleation, the code includes an aggregation model for anisotropic particles. Aggregation is the result of successful particle collisions due to either Brownian motion, laminar or turbulent fluid flow. The aggregation rate is estimated by the product of the particle number density in the dispersion and the aggregation kernel given by the product of collision frequency and aggregation

efficiency. The general aggregation kernels for Brownian motion and turbulent flow are given by:

$$\beta_{Brown} = \frac{1}{W_{ij}} \frac{2}{3} \frac{k_B T}{\mu} \left(\langle \xi_1 \rangle_\gamma^k + \langle \xi_2 \rangle_\gamma^k \right) \left(\frac{1}{\langle \xi_1 \rangle_\gamma^k} + \frac{1}{\langle \xi_2 \rangle_\gamma^k} \right) \tag{46}$$

$$\beta_{Turb} = \frac{1}{W_{ij}} \sqrt{\frac{8}{15} \frac{\varepsilon}{\nu}} \left(\langle \xi_1 \rangle_\gamma^k + \langle \xi_{2)_\gamma}^k \right)^3 \tag{47}$$

in which ε is the turbulent energy dissipation rate and ν the viscosity of the fluid. With the exception of the aggregation efficiency all other terms can be directly extracted from the system state. Since aggregation is no purely isotropic process [3], a second information modulating the oriented aggregation process is necessary. The model assumes collisions between two crystals by letting any two faces interact with each other. The energy barrier W_{ij} of this interaction and the frequency of successful collisions are calculated. This is accomplished by extending the Fuchs stability ratio for spherical particles where the inverse aggregation efficiency is given by [23]:

$$W_{ij} = 2 \int_2^\infty \frac{\left(\exp\left(\frac{W_{tot}(Y)}{kT} \right) \right)}{Y^2} dY \tag{48}$$

with Y being the dimensionless center-to-center distance normalized by the arithmetic mean of the radii of the interacting particles. This equation uses the total interaction potential between two particles and can be adapted to include a wide range of different geometries. For example, the total interaction potential between spherical particles is calculated with:

$$W_{tot} = -\frac{H_A R_1 R_2}{6(R_1 + R_2) Y} + \varepsilon_0 \varepsilon R_1 R_2 \left(\Psi_1^2 + \Psi_2^2 \right)$$
$$\times \left(\frac{2 \Psi_1 \Psi_2}{\Psi_1^2 + \Psi_2^2} \ln \left(\frac{1 + \exp(-\kappa Y)}{1 - \exp(-\kappa Y)} \right) + \ln(1 - \exp(2\kappa Y)) \right) \tag{49}$$

with Y being the dimensionless center-to-center distance normalized by the arithmetic mean of the radii of the interacting particles, H_A being the Hamaker constant, Ψ being the respective charges of the paired faces and κ being the Debye length. This notation gives the possibility of introducing surface potentials of different crystal faces to model the aggregation probability of different possible combinations of interacting faces during collisions of anisotropic particles.

Since the model already incorporates modular sources in the moment transport equation, aggregation can be modelled by a simple extension of the moment transport equation by an N-point quadrature aggregation term for the kl-mixed moment:

$$\overline{S}_{kl}^{(N)} = \frac{1}{2} \sum_{\alpha=1}^{N} \sum_{\gamma=1}^{N} \omega_\alpha \omega_\gamma \Big[\big(\xi_{1\alpha} + \xi_{1\gamma}\big)^k \big(\xi_{2\alpha} + \xi_{2\gamma}\big)^l - \xi_{1\alpha}^k \xi_{2\alpha}^l$$
$$- \xi_{1\gamma}^k \xi_{2\gamma}^l \Big] \beta_{\alpha\gamma} \tag{50}$$

Closure of this term is achieved within the framework of DQMOM. Tracking the absolute value of the mixed order moments for aggregation processes during the simulation is directly possible via these extended source terms in the central set of equations, and thus does not require any additional computational steps.

7 Application Examples

The applicability of the simulation tool was validated for a set of different systems shown in Table 1. Each of those systems provides unique challenges such as mixing controlled precipitation of $BaSO_4$, the multiphase precipitation of copper-zinc salts (multiphase process with complex hydrochemistry) [15] and iron hydroxide and oxyhydroxide nanoparticles (system with difficult to access properties) [3]. The properties of the solids are taken from literature depending on their stoichiometry and the reactants available (displayed in Table 1). The literature values for the solubility product of $Fe(OH)_2$ vary over a wide range and to encompass a large range of values an upper and lower bound were selected for investigation.

7.1 Mixing-Controlled Systems: Barium Sulfate (BaSO₄) and Iron Hydroxide (Fe(OH)₂)

Barium sulfate is a widely studied material system. Mixing, nucleation and diffusion-limited growth are considered as sub-processes. While only one phase can evolve, the mean particle size strongly depends on the mixing efficiency as reported in literature

Table 1 Solubility products and densities

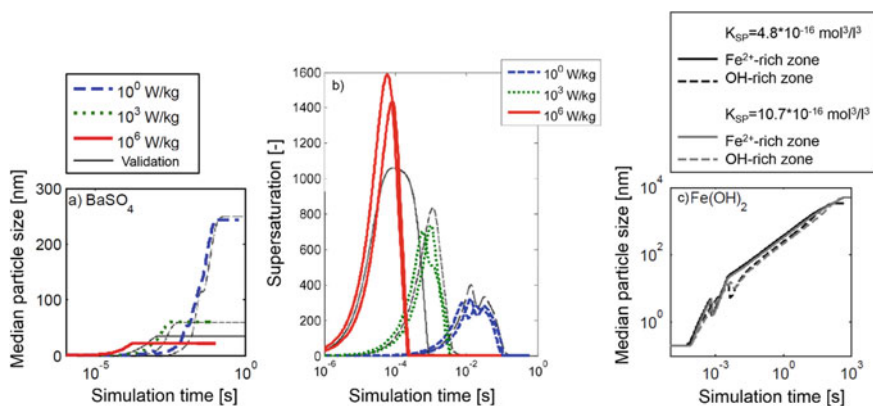| Solid name	Composition	Density (kg/m^3)	Solubility product (mol/l)^n
Barium sulfate	$BaSO_4$	4500	9.8×10^{-11} [24]
Copper hydroxide	$Cu(OH)_2$	3370	4.7×10^{-20} [25]
Zinc hydroxide	$Zn(OH)_2$	3050	1.7×10^{-17} [26]
Malachite	$Cu_2CO_3(OH)_2$	4050	6.9×10^{-34} [25]
Gerhardtite	$Cu_2NO_3(OH)_2$	3389	5.3×10^{-33} [27]
Rosasite	$Cu_{1.4}Zn_{0.6}CO_3(OH)_2$	4150	4.0×10^{-37} [28]
Ferrous hydroxide	$Fe(OH)_2$	3400	4.8×10^{-16} and 10.7×10^{-16} [29]

Fig. 5 Validation of the precipitation model by comparison of simulated data (solid lines) with literature data (dashed lines). **a** Median particle size formed in the T-mixer for energy inputs of $10°$ W/kg (blue dashed line), 10^3 W/kg (green dotted line) and 10^6 W/kg (red solid line) in comparison to literature data (black lines). **b** Supersaturation during $BaSO_4$ precipitation compared to literature [14]. **c** Mean particle size of ferrous hydroxide $Fe(OH)_2$ particles (initial concentration 0.14 M $FeSO_4$, 0.56 M NaOH). Specific energy dissipation 10^3 W/kg, simulation for the literature range of solubility values of 4.8×10^{-16} mol^3/l^3 (red and purple lines) and 10.7×10^{-16} mol^3/l^3(green and blue lines) (Adapted from [4] with kind permission from Elsevier)

[15]. This finding is reproduced with the presented tool showing the applicability of the mixing model. For the case of mixing-controlled systems, the precipitation module is applied to the case of a T-mixer using the sub-models detailed in the above sections. The specific energies have a strong influence on the mixing rate (see chapter on mixing model) and thus the resulting particle size. The mean particle size (Fig. 5a) is given as an integral mean value over all reaction zones. As shown in (Fig. 5b) each of the two mixing zones A′ and B′ has an individual supersaturation leading to different solid formation kinetics. Both reaction zones are displayed in the same color, they converge over time. The difference to the literature data (displayed in black) is mainly attributed to the use of different mixing models [3].

The next case is the precipitation of iron hydroxide (Fig. 5c). Iron hydroxide forms as an intermediate precursor for goethite FeOOH pigments [3] under the exclusion of oxygen. Therefore, it reflects a case where experimental access is difficult and the numerical investigation can yield important insights to the understanding of this distinct synthesis and to the transient particle formation process. $Fe(OH)_2$ is highly unstable due to oxidation. However, using our tool, the precipitation behavior can be evaluated in detail. The code was applied to two sets of literature data for the solubility product using the symmetrical engulfment model. The standard deviation of the values given (2.97×10^{-16} mol^3/l^3) is subtracted, respectively added, to the mean value (7.7×10^{-16} mol^3/l^3) giving a lower (4.8×10^{-16} mol^3/l^3) and a higher (10.7×10^{-16} mol^3/l^3) estimation. Although more work needs to be done to gain deeper insight to material data (e.g. with respect to solubility, surface energy, particle shape, which are main challenges in particle technology in general), this example

already gives a reasonable estimate on the precipitation kinetics. As expected for a mixing-controlled system, in the beginning of the formation process, the mean particle size differs in the two mixing zones. Growth in the iron-rich zone is faster than in the alkaline zone. In both zones, a rapid increase in nucleation after a short time causes an intermediate decrease of the mean particle sizes. However, the final sizes in both zones are equal for each solubility product as both zones exchange particles and therefore converge after a sufficiently long enough mixing time. The calculated mean final particle size is situated in the low μm range and lies in a similar regime as reported in literature [3].

In both of the discussed cases, mixing strongly influences the transient particle formation dynamics and thus the final particle properties. Accordingly, mixing must be carefully considered in particular with respect to up-scaling. Recently, we found self-similar profiles of supersaturation and of the resulting PSDs for the case of precipitation of drug molecules in a T-mixer [7]. These promising results provide strong hints that unifying scale-up principles can be derived, at least during flow synthesis of nanoparticles.

7.2 Systems with Complex Phase Composition: gerhardtite $(Cu_2NO_3(OH)_3)$

As the next example, we consider the simulation of a multicomponent system. Literature data for solubility products are available and are in very good agreement to the simulated values [25–28]. The alkaline precipitation of copper salts leads to multiple solids of different chemical composition. The addition of zinc sources leads to copper-zinc salts, which are important precursors for Cu/ZnO catalysts for methanol synthesis [5]. The solids that form during this precipitation include copper hydroxide ($Cu(OH)_2$), zinc hydroxide ($Zn(OH)_2$), malachite ($Cu_2CO_3(OH)_2$), gerhardtite ($Cu_2NO_3(OH)_3$) and the mixed phase rosasite ($Cu_{1.4}Zn_{0.6}CO_3(OH)_2$). The complex chemical network for precipitating the desired compound rosasite (see Table 2) is implemented into the hydrochemistry model as a stoichiometric matrix α (Eq. 61) listing all of the reactive species of the system.

The resulting stoichiometry matrix implemented into the hydrochemistry model can be written as:

Table 2 Reactions considered for the aqueous preparation of precursors for Cu/ZnO methanol catalysts

Reaction	K	Log$_{10}$ K	References
$Cu(OH)_2 \rightleftharpoons Cu^{2+} + 2OH^-$	$K_{SP,1}$	-19.33	[25]
$Cu_2(NO_3)(OH)_3 \rightleftharpoons 2Cu^{2+} + NO_3^- + 3OH^-$	$K_{SP,2}$	-32.274	[27]
$Cu_2(CO_3)(OH)_2 \rightleftharpoons 2Cu^{2+} + CO_3^- + 2OH^-$	$K_{SP,3}$	-33.16	[25]
$Cu_{1.4}Zn_{0.6}(CO_3)(OH)_2 \rightleftharpoons 1.4Cu^{2+} + 0.6Zn + CO_3^- + 2OH^-$	$K_{SP,4}$	-36.4	[28]
$Zn^{2+} + 2OH^- \rightleftharpoons Zn(OH)_2$	$K_{SP,5}$	-16.77	[26]
$H^+ + OH^- \rightleftharpoons H_2O$	K_W	14	[25]
$Cu^{2+} + 2OH^- \rightleftharpoons Cu(OH)_2$	K_1	11.8	[25]
$Cu^{2+} + 3OH^- \rightleftharpoons Cu(OH)_3^-$	K_2	15.34	[25]
$2Cu^{2+} + 2OH^- \rightleftharpoons Cu_2(OH)_2^{2+}$	K_3	17.57	[25]
$3Cu^{2+} + 4OH^- \rightleftharpoons Cu_3(OH)_4^{2+}$	K_4	34.9	[25]
$Cu^{2+} + CO_3^{2-} \rightleftharpoons CuCO_3$	K_5	6.75	[25]
$Cu^{2+} + H^+ + CO_3^{2-} \rightleftharpoons CuHCO_3^+$	K_6	12.169	[27]
$Cu^{2+} + 2CO_3^{2-} \rightleftharpoons Cu(CO_3)_2^{2-}$	K_7	10.3	[27]
$Cu^{2+} + No_3^- \rightleftharpoons Cu(NO_3)^+$	K_8	0.5	[27]
$H^+ + CO_3^{2-} \rightleftharpoons HCO_3^-$	K_9	10.329	[27]
$2H^+ + CO_3^{2-} \rightleftharpoons H_2CO_3$	K_{10}	16.681	[27]

$$
\alpha = \begin{pmatrix}
1 & 0 & 0 & 0 & 0 & 0 \\
0 & 1 & 0 & 0 & 0 & 0 \\
0 & 0 & 1 & 0 & 0 & 0 \\
0 & 0 & 0 & 1 & 0 & 0 \\
0 & 0 & 0 & 0 & 1 & 0 \\
0 & 0 & 0 & 0 & 0 & 1 \\
0 & 0 & 0 & 0 & -1 & 1 \\
1 & 0 & 0 & 0 & -2 & 2 \\
1 & 0 & 0 & 0 & -3 & 3 \\
2 & 0 & 0 & 0 & -2 & 2 \\
3 & 0 & 0 & 0 & -4 & 4 \\
1 & 0 & 0 & 1 & 0 & 0 \\
1 & 0 & 0 & 1 & 1 & 0 \\
1 & 0 & 0 & 2 & 0 & 0 \\
1 & 1 & 0 & 0 & 0 & 0 \\
0 & 0 & 0 & 1 & 1 & 0 \\
0 & 0 & 0 & 1 & 2 & 0
\end{pmatrix}
\begin{matrix}
Cu^{2+} \\
NO_3^- \\
Na^+ \\
CO_3^{2-} \\
H^+ \\
H_2O \\
OH^- \\
Cu(OH)_2 \\
Cu(OH)_3^- \\
Cu_2(OH)_2^{2+} \\
Cu_3(OH)_4^{2+} \\
Cu(CO_3) \\
CuHCO_3^+ \\
Cu(CO_3)_2^{2-} \\
Cu(NO_3)^+ \\
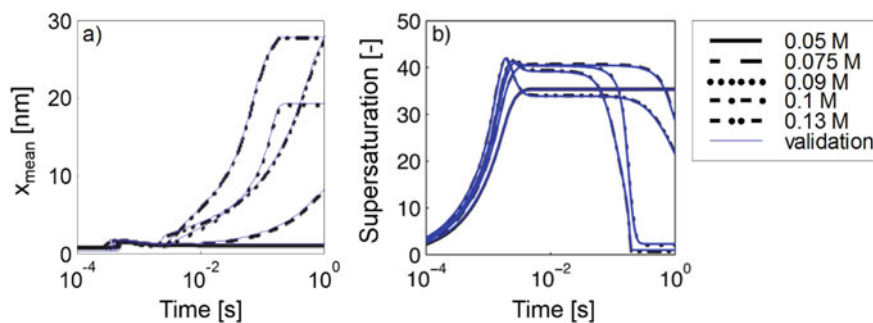HCO_3^- \\
H_2CO_3
\end{matrix}
\qquad (51)
$$

Fig. 6 Comparison of predicted data by the model (solid blue lines) with literature data [5] (black lines). Evolution of mean particle size of rosasite after multiphase precipitation at different concentrations of $Cu(NO_3)_2$ ranging from 0.05 to 0.13 M, Na_2CO_3 concentration constant at 0.13 M; Comparison to copper carbonate precipitation at different concentrations from literature [5]. **a** Evolution of mean rosasite particle size. **b** Evolution of supersaturation. (Adapted from [4] with kind permission from Elsevier)

in which the columns represent the components and the rows represent the species. All these species were then considered in mass action laws as detailed into section above. The considered reactions and their constants are shown in Table 2.

In this study, all five solids were considered simultaneously and the impact of a changing Na_2CO_3 compound on the product concentration was investigated. The code predicts in agreement with experiments that for all initial concentrations the only solid phase precipitating is rosasite with a phase purity of close to 100% as this is the phase with the lowest solubility [4].

Thus, in case of rosasite precipitation, the process is reliable with respect to the formation of side products. The results of the study are depicted in Fig. 6. The mean diameter of rosasite and the corresponding supersaturation are shown for varying concentrations of Na_2CO_3.

So far, it has been shown that the precipitation model is capable of handling multiple solid phases without restriction to the number of components and species. Additionally, if the synthesis targets solid phases other than rosasite, process conditions favoring distinct phases can be identified by numerical investigation.

7.3 Systems with Anisotropic Aggregation: goethite (FeOOH)

The bivariate DQMOM-approach was applied to the complex synthesis of goethite nanorods. Goethite forms not only by crystalline growth but also by oriented attachment [3]. This oriented attachment process has previously been investigated at our institute. Simulations with a low number of particles have shown good agreement

to experimental data [30]. The DQMOM model, however, offers the chance of scaling this simulation to a much larger particle number without the limitation of high computing time, which is often a limitation for the simulation of discrete particles.

Experimentally, the goethite particles were synthesized by aeration of an alkalized 0.9 M iron sulfate solution at 45 °C. While the mechanism of goethite synthesis is complex, the present study uses a simplified model developed at our institute to model the generation of goethite at constant pH [30]:

$$4Fe^{2+} + O_2 + 8OH^- \rightarrow 4FeOOH + 2H_2O \tag{52}$$

The oxygen was supplied via bubbling synthetic air through a porous plate with a constant volume flow rate of 100 ml/min. Samples were taken from the solution at intervals of 5 min. The samples were investigated using SEM imaging and evidenced that first clearly visible needles formed around 30 min and continued to grow from this point on. After 55 min, the iron of the solution was depleted and the reaction ended (Fig. 7).

The tool was then used to explore the formation of goethite by oxidizing iron hydroxide platelets (see Sect. 7.2). These platelets act as nuclei for the formation of
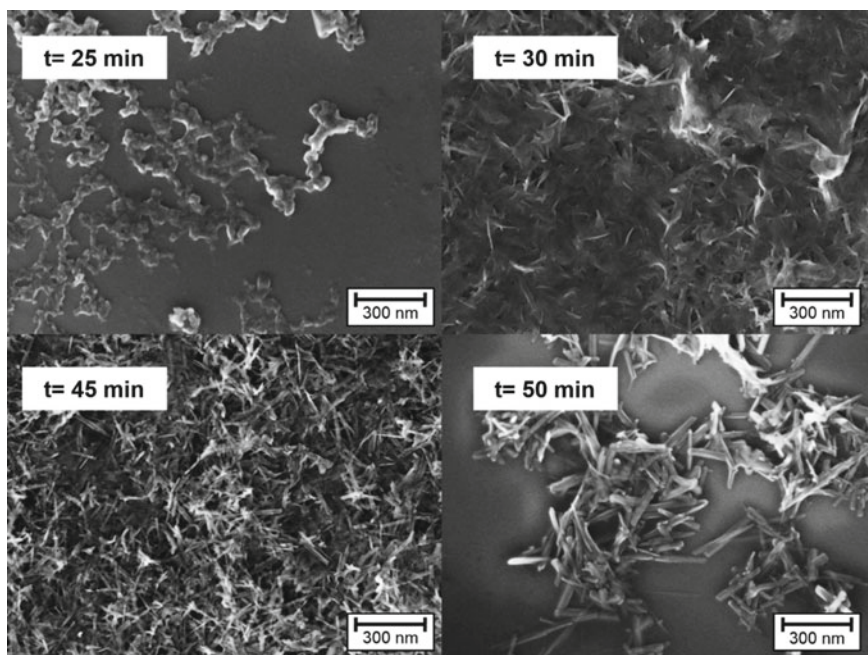
Fig. 7 SEM images of the samples taken during goethite synthesis after 25, 30, 45 and 50 min. At 25 min the hexagonal precursor phase can be seen, however no goethite needles are visible. At 30 min, first goethite needles are visible, as well as the precursor. At 45 and 50 min, goethite needles have grown when compared with the previous samples

goethite from solution under consumption of dissolved oxygen [3]. Goethite crystals are orthorhombic and typically elongated along the crystallographic 001 direction and terminated by the {021} faces at the end and {110} faces on the sides. Since the surface energies of these faces are similar, the final particle shape is determined by aggregation kinetics rather than by thermodynamics [31]. For modeling, the orthorhombic goethite crystals were considered as cylinders terminated by {021} faces with the mantle surface considered as a {110} face. The multivariate aggregation model was then applied to the case of Brownian aggregation at 293 K in aqueous solution. The source term was adapted for the case of cylindrical geometry. Since the aggregation of cylindrical particles depends on both dimensions of the particles, it provides additional challenges in contrast to monovariate aggregation processes such as the aggregation of spheres. The resulting aggregation term provides data on the two interacting particle dimensions and the particle geometry. Furthermore, aggregation was modelled including van der Waals attraction between cylinders of different sizes and electrostatic repulsion between the two crystal facets. For the latter, data for the surface charge density of the two different crystal faces of goethite were used, which were obtained from a multisite complexation model [32]: 46 mC/m^2 for the {110} face and 57 mC/m^2 for the {021} face. The Hamaker constants were calculated by [33]:

$$A = 24\pi \gamma D_0^2 \tag{53}$$

where γ is the interfacial energy and D is the contact distance of two particles. The comparison of experimental and modelling data is displayed in Fig. 8 in which the mean diameter and mean length gathered from the SEM images is compared to the mean diameter of the two particle dimensions from the simulation. The simulated values coincide with the experimental values determined by statistical SEM measurements and follow the mean values very nicely for both dimensions. The deviations in

Fig. 8 Results of the complete behavioral study on the formation of Goethite nanorod aggregation
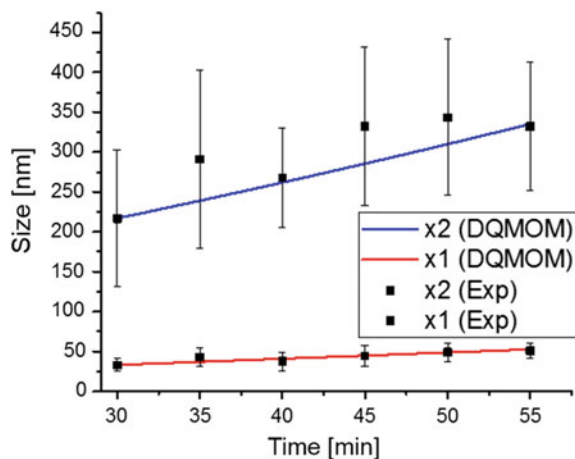
the experimental results can be attributed to effects from breakage and aggregation processes in cases that the attached particles are not properly aligned [30]. This effect was neglected for the simulation study.

Noteworthy, the extension to non-spherical particles is seen as one of the largest limitations for solving by PBEs. Here it is shown that the fully bivariate model can be applied to complex source terms in the case of bivariate aggregation. The extension to bivariate systems is capable to simulate a large range of particle shapes with varying source terms in the moment transport equation. This is possible for manifold different geometries and thus allows addressing increasingly complex structures to be simulated with the model.

7.4 Reaction-Controlled Systems: zinc oxide (ZnO) Quantum Dots

An example for a reaction-limited system is the formation and temporal evolution of ZnO QDs [1]. Modelling of particle formation processes incorporates two distinct challenges. On the one hand, a high accuracy is desired to ensure outstanding product quality with respect to narrow PSDs and optical properties, whereas on the other hand the numerical efficiency limits the feasibility of simulation studies. As described in the above section the present tool requires repetitive solution of PBEs, which for long time processes such as ripening, requires small step sizes due to the mathematical stiffness of the governing Gibbs-Thomson equation, which might lead to prohibitive long calculation times:

$$R(x, t, c) = \frac{4D\,M\,c_L^\infty}{\rho x}\left[\frac{c(t)}{c_L^\infty} - \exp\left(\frac{4\gamma V_m}{vx\,k_B T}\right)\right] \tag{54}$$

This equation, which describes the size-dependent solubility of small particles, often leads to extreme gradients, when solved for moderate experimental conditions. This equation can be introduced into a general PBE:

$$\frac{\partial}{\partial t}q(x, t) + \frac{\partial}{\partial x}(R(x, t, c)q(x, t)) = 0 \tag{55}$$

Usually the exponential term of the Gibbs-Thomson equation is abbreviated by a Taylor series expansion:

$$R(x, t, c) \approx \frac{4D\,M\,c_L^\infty}{\rho x}\left[\frac{c(t)}{c_L^\infty} - \left(1 + \frac{4\gamma V_m}{vx\,k_B T}\right)\right] \tag{56}$$

This description, leads to an increasing error for decreasing particle size as seen in Fig. 9. The ripening rates of larger particles deduced from the linear approximation are in good agreement with the full solution of the exponential function independent
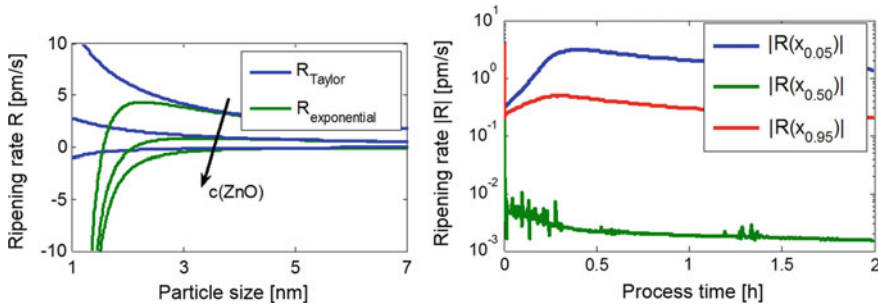
Fig. 9 (Left) Nonlinearity of the ripening rates calculated by the full exponential term (green lines) and by using the Taylor series approximation (blue lines) at a ZnO concentration of 10^{-8} kg*m^{-3} to 10^{-12} kg*m^{-3}. (Right) Magnitudes of the ripening rates R at $x_{5,0}$ (blue line), $x_{50,0}$ (green line), and $x_{95,0}$ (red line) of the number density distribution $q_0(x,t)$ between 1 and 5 nm simulated in PARSIVAL for T $= 40$ °C (Adapted from [9] with kind permission from Elsevier)

of the solid concentration. In contrast, at typical QD sizes clearly below 10 nm and especially for smallest particles below 3 nm large deviations are observed. The solution of the governing stiff equation leads to fluctuating ripening rates for small particle sizes. Thus, an efficient numerical solution (FIMOR) was developed by our colleagues in Applied Mathematics [9].

The Gibbs-Thomson equation can better be solved with a fully implicit iterative solution:

$$y_{(k+1)}^{n+1} = y_{(k)}^{n+1} - \left(D\Phi\big(y_{(k)}n + 1\big)\right)^{-1}\Phi\left(y_{(k)}^{n+1}\right) \tag{57}$$

with k being the iteration counter, y the condensed variable and Φ is the solution of the implicit equation:

$$\Phi\big(y^{n+1}\big) := y^{n+1} - y^n - \frac{1}{2}\big(\Delta y^n + \Delta y^{n+1}\big) \tag{58}$$

The surface energy was calculated according to Mersmann:

$$\gamma = \frac{0.414 k_B T}{\sqrt[3]{V_M^2}} \ln\left(\frac{\rho}{c_L^\infty M}\right) \tag{59}$$

The surface tension was calculated with an Arrhenius-like expression to predict the temperature-dependent ripening behavior:

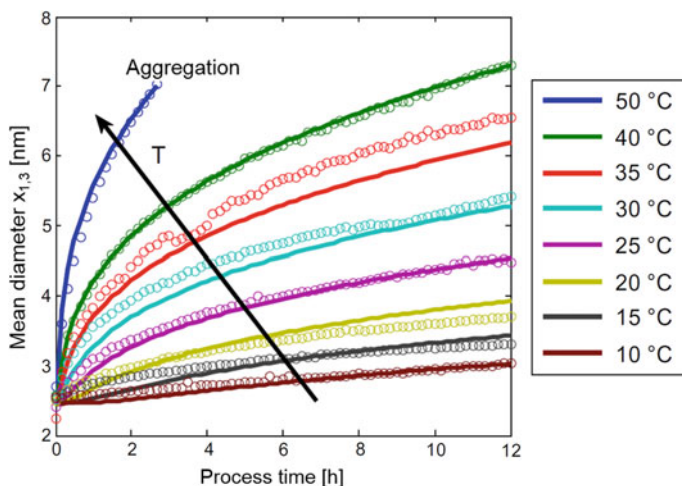$$c_L^\infty(T) = C\exp\left(-\frac{E_{A,r}}{RT}\right) \tag{60}$$

Fig. 10 Comparison of the mean volume-weighted particle sizes $x_{1,3}$ that evolve during 12 h of the ripening process for temperatures of 10 °C (brown), 15 °C (black), 20 °C (yellow), 25 °C (purple), 30 °C (cyan), 35 °C (red), 40 °C (green) and 50 °C (blue) calculated by FIMOR (solid lines) and the full exponential solution with the experimental results obtained from absorbance measurements (symbols). (Adapted from [9] with kind permission from Elsevier)

The data generated by this approach was compared to ZnO QDs on ZnO QDs synthesized from mixing a 0.1 M zinc acetate solution with a 0.1 M LiOH solution. Particles produced by this method were stored below $-10°$ C to prevent ageing.

The excellent agreement between the mean particle sizes predicted by FIMOR and the experimentally derived particle diameters measured for temperatures between 20 and 50 °C underlines the validity of the implicit model widely outperforming the Taylor approximation (Fig. 10). A maximum relative deviation of 8% in the mean volume weighted particle sizes between simulation and experiment is found for a temperature of 20 °C after a total ageing time as long as 12 h. The maximum absolute deviation in $x_{1,3}$, which is found for a temperature of 35 °C is even below 0.4 nm. Based on the successful description of simple temperature constant batch ripening, a study on time–temperature profiles and their validation against experimental data recorded in the batch mode will be discussed. Therefore, an initial suspension with mean size $x_{1,3}$ of 2.4 nm has been exposed to two different temperature profiles. As shown in Fig. 11, the first temperature profile consisted of an initial high temperature phase at 35 °C kept for 2 h followed by a low temperature phase at 10 °C persisting for additional 4 h (blue circles). The second temperature profile followed the same timing but the first section was at a low temperature of 10 °C while in the second section a moderate temperature of 25 °C was applied (red circles). The simulation results coincide again very well with the experimental data. The maximum deviation of 5% in $x_{1,3}$ observed between experiment and simulation after 6 h of ripening is in the same order of magnitude as already discussed in the context of Fig. 10.
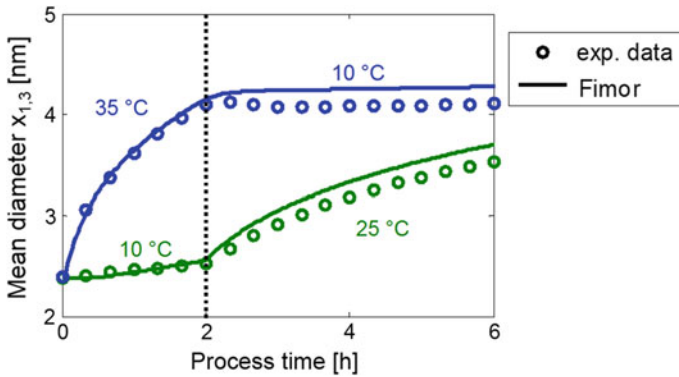
Fig. 11 Evolution of the mean volume weighted particle size $x_{1,3}$ for two different temperature profiles (blue) (red) calculated from the measured absorbance data (circles) and simulated by FIMOR (solid line) (Adapted from [9] with kind permission from Elsevier)

The a priori estimation of process parameters, which result in a product with desired properties, reduces the experimental effort for process design considerably. The predictive character and the high numerical efficiency of FIMOR allow the mapping of product properties on the process parameter space. The use of a map allows the precise tailoring of process parameters according to future product properties. For the present study on the ripening of ZnO QDs, the process parameter space spans over the ripening temperature and the ripening time. With respect to the experimental boundary conditions, we consider times up to 30 h and temperatures between 0 and 50 °C. Long experimental times are usually avoided, the upper temperature limit is determined by the fact that agglomeration occurs when the temperature exceeds 50 °C. The result of the FIMOR-derived time–temperature (t–T) map is presented in Fig. 12. A sufficiently dense set of evaluated temperatures results in a smooth map showing the evolution of the mean particle size x1,3 and the width of the PSD.
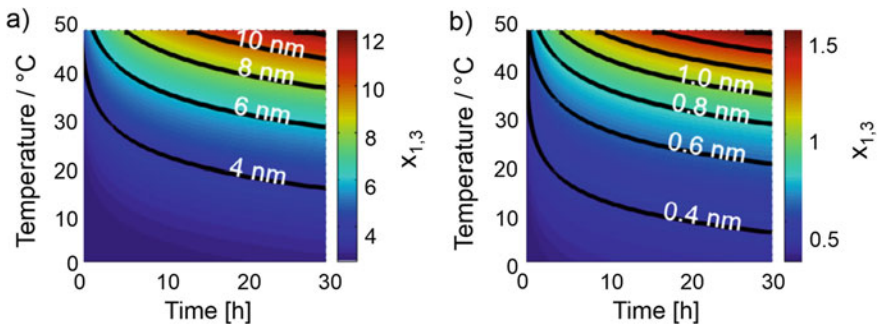

Fig. 12 Time and temperature (t–T) maps for the mean particle size (**a**) and the width of the PSDs (**b**) derived for the ripening of ZnO quantum dots by FIMOR (Adapted from [9] with kind permission from Elsevier)

Such t–T maps do not only allow a prediction of the dispersity of a sample for different process conditions but also provide insights and improve the general understanding of the Ostwald ripening process. The evolution of the width of the PSDs along the black isolines illustrated in Fig. 12 raises the question whether there is a specific time/temperature combination to achieve a particularly narrow distribution. Therefore, the data is processed further with the results being summarized in Fig. 13. The analysis of the standard deviations plotted vs ripening time shown in Fig. 13a reveals that each mean particle size is connected to a specific width of the distribution. This width is independent of the time needed to achieve a certain particle size. Thus, all PSDs along one iso-line are self-similar and independent of the chosen time/temperature combination, since time is dependent on temperature as long as a single particle size is considered.

The slight decrease of the width with time is attributed to numerical effects rather than on a real focusing of the PSD. Going one step further, when the width of a PSD is fixed for a particular mean particle size, the data can be re-evaluated to find the respective correlation. In Fig. 13b the average width of the PSD as a function of the mean particle size is shown. Noteworthy, the apparently simple straight line consists of the evaluation of 92 mean particle sizes and the respective PSDs. From the various conditions extracted from the t–T map, a linear correlation with a slope of 0.13 is found. This behavior—although astonishing at first sight—has been described in literature long time ago when Lifshitz and Slyozow theoretically predicted the self-similarity of PSDs during Ostwald ripening [22]. The self-similarity is based on the existence of a stable shape of PSDs exposed to Ostwald ripening. The shape of such a PSD will be conserved by FIMOR and is shown in Fig. 13c. Due to the high numerical efficiency of FIMOR, this effect can be used in the framework of optimization studies and represents a promising way towards tailor-made colloids. The good agreement with experimental data and the confirmation of general observations like self-similarity found in the literature is an excellent validation for batch processes in small volumes where no pronounced concentration and temperature gradients are observed. However, industrial applications more and more demand for continuous processes.
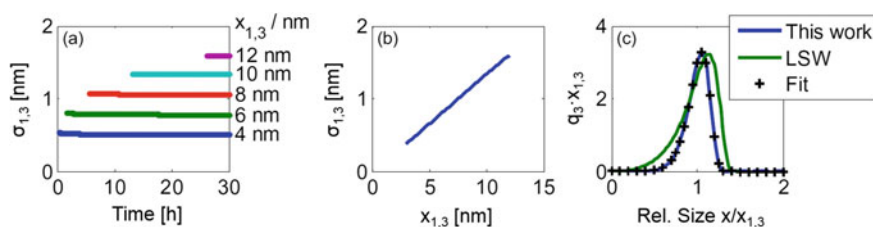

Fig. 13 a Width of PSD along the isolines of uniform mean particle size drawn in Fig. 9. **b** Mean width evaluated for 92 particles with mean particle sizes between 3 and 12 nm. **c** Normalized stable shape of the PSD (blue), the predicted shape from Lifshitz and Slyozow (green) [22] and fitted values according to a lognormal distribution (black crosses) (Adapted from [9] with kind permission from Elsevier)

This new procedure is numerically stable and uses the unaltered equations with high accuracy. The typical calculation time for several hour long ripening processes decreases to a few minutes. Furthermore, processes with dynamically changing temperatures can be modeled with high precision and excellent agreement with experimental data. Due to its predictive nature it saves experimental time and considerably improves the understanding of continuous colloidal processing [9].

7.5 Systems with Sequential Growth: CdSe@ZnS Quantum Dots

The bivariate extension of the model was applied to the precipitation and growth of cadmium selenide—zinc sulfide (CdSe@ZnS) quantum dots. Mathematically these particles can be represented as a structure growing sequentially from the inner core to the outer shell in a 2-step process. In order to simplify the complex nucleation behavior any influence of heterogeneous nucleation of shell material on the core surface is neglected.

The synthesis of core-shell CdS/ZnS quantum dots is usually done by injecting shelling agents to seeded core particles by heterogeneous nucleation and growth of the shell on the core. The so called hot injection technique for the synthesis of quantum dots is a well-established and widely used method in the lab and was performed using an automated Chemspeed Technologies Swing XL autoplant synthesis platform. Typically, a Cd-containing stock solution is prepared by introducing CdO and oleic acid. The hot cadmium oleate solution is injected into a selenium solution in trioctylphosphene. The high supersaturation induces fast nucleation of CdSe followed by rapid particle growth on a timescale of a few s. The shelling agent, e.g. a diethylzinc solution, is then injected in a second step to produce the desired core-shell nanoparticles.

This sequential experimental procedure is a good starting point to introduce bivariate particle simulation, since the temporal separation of the different growth steps allow for simplification of Eq. 39. The two-step synthesis can be modeled by the introduction of two Heaviside functions to save calculation time as shown in preceding chapters. Neglecting nucleation and aggregation, the growth terms G_1 and G_2 can be expressed by distinct growth laws multiplied with a Heaviside function, ensuring sequential growth (see Eqs. 41 and 42) with T being the injection time of the shelling agent and $\log(K_{SP}) = -33$ being to solubility product [38]. This proves the bivariate code retains the flexibility of the monovariate model, which is important to ensure applicability to a wide range of different particulate systems. The code was tested on experimental data from Mahmoud et al. and showed excellent agreement as seen in Fig. 14. The shell thickness can be modulated with simulation time and provides a good basis for future optimization studies.

Fig. 14 Comparison between the numerical results and experimentally determined particle sizes for CdSe and CdSe@ZnS quantum dots. Experimental data was obtained from [39]
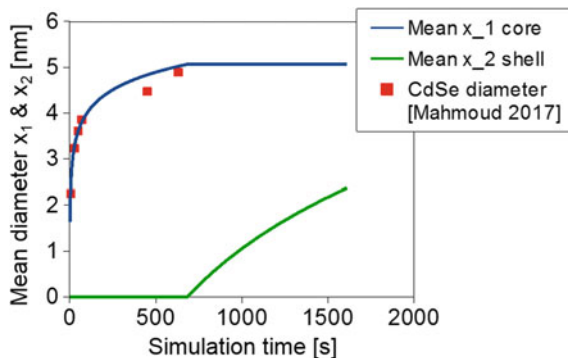
7.6 Property Optimization: ZnO Quantum Dots

In cooperation with our colleague Lukas Pflug from the institute of applied mathematics a numerical scheme for modelling ZnO QD ripening was established and employed to optimize the ZnO QD formation in a batch and in a continuous microreactor [9]. In general, optimization in particle technology can be applied to various aspects of precipitation:

- Model-based determination of otherwise difficult-to-measure particle variables, e.g. surface energy, intermediate phases or highly transient phenomena.
- Optimization of process variables to ensure preferred product properties.
- Optimization of particle property distributions.

The optimization of material composition has previously been done at our institute during a study on the estimation of material parameters for multiphase, multicomponent precipitation modeling [34]. In this study, the simultaneous precipitation of multiple phases inside a T-mixer was investigated with the present model. An optimization study allowed predicting the phase composition of the solid product of a simultaneous precipitation of $BaSO_4$ and $BaCO_3$ inside a T-mixer. In the present study, the preferred precipitation of one solid product was achieved by adjusting the pH by a free parameter optimization [2]. The model is capable of predicting experimental results proving the effectiveness of this method.

In Chap. 7.2, we demonstrated the generation of self-similar PSDs, which makes classical optimization rather difficult [9]. Therefore, a three-step process to control the PSD was developed (see Fig. 15a). Using the colloidal dispersion A with a monomodal distribution, the monomodal distribution B is grown. An additional part of dispersion A is then mixed with dispersion B to yield a bimodal distribution C. Afterwards, additional growth and ripening of solution C leads to the final monomodal distribution D.

In total 5 process parameters are available for optimization: temperature, ripening time in steps 1 and 3 and mixing ratio in step 2. In the first step, time and temperature are dependent and can be reduced to one variable to accelerate optimization. Setting

the process temperature to 30 °C the simulated values for the median size and standard deviation of a bimodal PSD are displayed in Fig. 15b. The point marked with C corresponds to the colloidal solution with bimodal distribution at point C in Fig. 15a. During ripening, the width of the distribution, expressed as the standard deviation, initially increases until it drops significantly and finally reaches a minimum. X marks the condition with a minimum standard deviation σ and median size. The chosen optimization parameter is the ripening time, which of course is dependent of the temperature. This concludes three parameters for optimization purposes: the ripening time of the first process (t_1), the mixing ratio (r of A and B), and the second step temperature (T_2).

Next, the effect of the parameters on the final PSD was investigated. The target size defines the mixing ratio, which is required to meet a specific particle size. The process time follows from the choice of mixing ratio, since for each ratio an optimal time was found. This yields a 2D optimization problem. The optimization was done by defining a cost functional and using a Nelder-Mead algorithm to calculate a residence time and temperature, which correspond to a particle size distribution. The cost functional can be written as:

$$\zeta = \left(x_{current,mean} - x_{target}\right)^2 w_x + \sigma^2 w_\sigma + t w_t \tag{61}$$

with x being the size, σ being the standard deviation of the PSD and t being the residence time. A weighting factor w orders the optimization parameters in a preferred order.

The results shown in Fig. 16 display three trials with target sizes of 3.0, 4.5 and 5.5 nm. Each trial uses three points to determine a starting position needed to initialize the Nelder-Mead algorithm. The dots indicate simulation results during optimization. The resulting PSDs for each size follow the principle of self-similarity reported for ripening processes as seen in Fig. 15b [9].

The present model allows for easy implementation of optimization studies which can be extended to new material systems in the monovariate case. Thus, the present studies offer unique opportunities for the optimization of shape-dependent particle properties in multivariate systems.
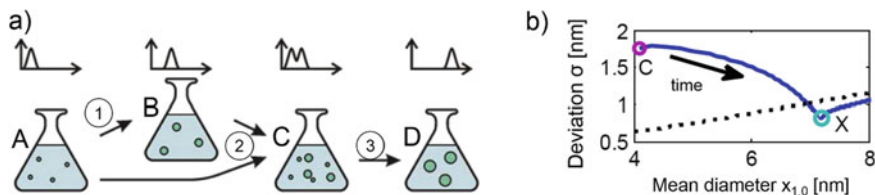

Fig. 15 **a** Schematic of the three-step process to optimize the PSD for a reaction controlled growth. **b** Exemplary course of the median particle size versus deviation for the bimodal case (blue), in comparison to the self-similar growth of a monomodal PSD (black)

7.7 Coupling to a Separation Process

Typically, particle formation is coupled to other unit operations, most importantly with separation or even classification. Today, methods of nanoparticle classification are rare. We have shown that semiconducting nanoparticles such as ZnS can be size-classified by antisolvent precipitation [35]. More recently, we introduced nanoparticle chromatography as another possible scalable solution for size-classification. In particular, results exist for fullerenes [36], ZnS and Au [37] nanoparticles.

Here, we couple the described ripening module with nanoparticle classification. The coarse fraction m_c is considered as product while the fine fraction m_f is recycled back to particle formation. This way, particles of larger sizes can be produced by recirculating particles back to the reactor several times. The flowsheet of this setup is displayed in Fig. 17a.

The developed ripening module was used to model a dynamic screening process with a recirculation in a modular plant. For the separation we assume a separation efficiency of $\kappa = 0.8$ and a cut size of 6.75 nm, which corresponds to the maximum size of a particle traveling once through the reactor. The flowsheet displayed in
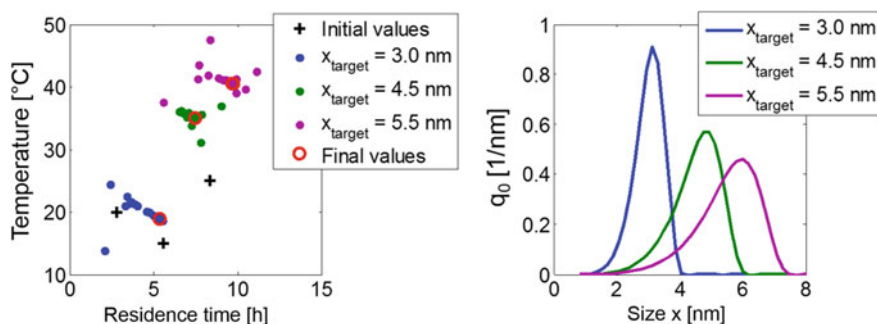

Fig. 16 Results of the optimization process. **a** Reduction of the optimization parameters to a 2D problem. Starting values are marked in black for the target size of 3.0 nm (blue), 4.5 nm (green) and 5.5 nm (purple). **b** Corresponding PSDs to the calculations on the left
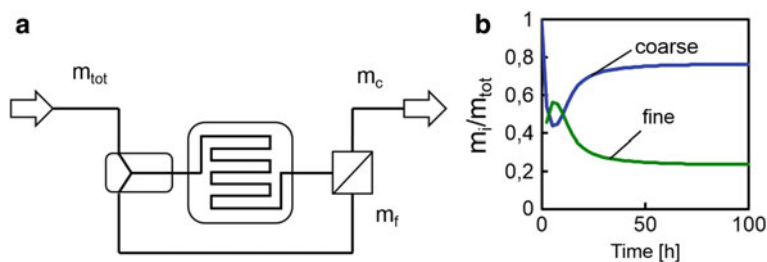

Fig. 17 **a** Sketch of the ripening process coupling to nanoparticle classification. **b** Mass fraction of the coarse (blue) and fine (green) material leaving the classifier

Fig. 17a leads to exemplary behavior shown in Fig. 17b for the course and the fine fraction at the end of the separator. The data are based on an exemplary process temperature of 40 °C and a ripening time of 2.5 h. The influence of the chosen separation size can be seen in the temporal evolution of fines and coarse fractions, which drop initially and afterwards rise again until a stationary state is reached.

8 Conclusion

A widely applicable tool for modeling precipitation processes in aqueous phase is presented. The tool encompasses several individual modules, such as, mixing, hydrochemistry, and solid formation. All modules are designed to ensure minimum numerical effort and maximum flexibility in terms of material systems, complexity of material, additional hydrochemical species and solid formation processes. To account for multiple solid phases, the present equations have been extended to cover multi-phase aggregation. The two-dimensional model is capable of simulating multi-phase and multi-component precipitation with bivariate properties. The model was applied to various particle systems such as mixing-controlled $BaSO_4$ and reaction-controlled ZnO formation. Complex applications include methanol catalyst precursor formation on the basis of Cu and Zn where up to 30 chemical reactions were included in the hydrochemistry model. As well as the formation of iron oxide pigments such as FeOOH nanorods, an anisotropic particle system with a non-classical growth mechanism.

The variety of the given examples illustrates the flexibility of the tool, which allows it to be applied to a wide range of particle formation processes. The modified bivariate code retains its flexibility, which is important to ensure applicability to anisotropic particulate systems. Simulation of bivariate systems is possible for manifold different geometries and thus allows addressing increasingly complex structures. This integrated model is the framework to simulate and to optimize reaction- and mixing-controlled precipitation processes with up to two independent parameters and will thus pave the way for advanced particle properties tailored to the needs of the later application. This will become important for various pressing issues in the field of particle technology such as process design, scale-up and process optimization for particles of complex composition or non-spherical shape. The truly two-dimensional model is capable of calculating a multi-phase precipitation process with bivariate properties.

References

1. Segets, D., Hartig, M.A.J., Gradl, J., Peukert, W.: A population balance model of quantum dot formation: oriented growth and ripening of ZnO. Chem. Eng. Sci. **70**, 4–13 (2012)
2. Voigt, M., Klaumünzer, M., Thiem, H., Peukert, W.: Detailed analysis of the growth kinetics of ZnO nanorods in methanol. J. Phys. Chem. C **114**, 6243–6249 (2010)
3. Encina, E.R., Distaso, M., Klupp Taylor, R.N., Peukert, W.: Synthesis of goethite α-FeOOH particles by air oxidation of ferrous hydroxide Fe(OH) 2 suspensions: insight on the formation mechanism. Crystal Growth Des. **15**, 194–203 (2015)
4. Haderlein, M., Güldenpfennig, A., Segets, D., Peukert, W.: A widely applicable tool for modeling precipitation processes. Comput. Chem. Eng. **98**, 197–208 (2017)
5. Hartig, M.A.J., Jacobsen, N., Peukert, W.: Multi-component and multi-phase population balance model: the case of georgeite formation as methanol catalyst precursor phase. Chem. Eng. Sci. **109**, 158–170 (2014)
6. Gradl, J., Peukert, W.: Simultaneous 3D observation of different kinetic subprocesses for precipitation in a T-mixer. Chem. Eng. Sci. **64**, 709–720 (2009)
7. Schikarski, T., Trzenschiok, H., Avila, M., Peukert, W.: Influence of mixing on the precipitation of organic nanoparticles: a lagrangian perspective on scale-up based on self-similar distributions. Chem. Eng. Technol. **23**, 1635–1642 (2019)
8. Rollié, S., Briesen, H., Sundmacher, K.: Discrete bivariate population balance modelling of heteroaggregation processes. J. Colloid Interface Sci. **336**, 551–564 (2009)
9. Haderlein, M., Segets, D., Gröschel, M., Pflug, L., Leugering, G., Peukert, W.: FIMOR: an efficient simulation for ZnO quantum dot ripening applied to the optimization of nanoparticle synthesis. Chem. Eng. J. **260**, 706–715 (2015)
10. Skorych, V., Dosta, M., Hartge, E.-U., Heinrich, S.: Novel system for dynamic flowsheet simulation of solids processes. Powder Technol. **314**, 665–679 (2017)
11. Bogacki, P., Shampine, L.F.: A 3(2) pair of Runge—Kutta formulas. Appl. Math. Lett. **2**, 321–325 (1989)
12. Marchisio, D.L., Fox, R.O.: Solution of population balance equations using the direct quadrature method of moments. J. Aerosol Sci. **36**, 43–73 (2005)
13. Bourne, J.R.: Mixing and the selectivity of chemical reactions. Org. Process Res. Dev. **7**, 471–508 (2003)
14. Schwarzer, H.-C., Peukert, W.: Combined experimental/numerical study on the precipitation of nanoparticles. AIChE J. **50**, 3234–3247 (2004)
15. Gradl, J., Schwarzer, H.-C., Schwertfirm, F., Manhart, M., Peukert, W.: Precipitation of nanoparticles in a T-mixer: coupling the particle population dynamics with hydrodynamics through direct numerical simulation. Chem. Eng. Process. **45**, 908–916 (2006)
16. Baldyga, J., Bourne, J.R.: Simplification of micromixing calculations. I. Derivation and application of new model. Chem. Eng. J. **42**, 83–92 (1989)
17. Bałdyga, J., Bourne, J.R.: Turbulent Mixing and Chemical Reactions. Wiley, Chichester (1999)
18. Schwarzer, H.-C.: Nanoparticle Precipitation: An Experimental and Numerical Investigation Including Mixing. Logos-Verl, Berlin (2005)
19. Guichardon, P., Falk, L., Villermaux, J.: Characterisation of micromixing efficiency by the iodide–iodate reaction system. Part II: kinetic study. Chem. Eng. Sci. **55**, 4245–4253 (2000)
20. Commenge, J.-M., Falk, L.: Villermaux-Dushman protocol for experimental characterization of micromixers. Chem. Eng. Process. **50**, 979–990 (2011)
21. Davies, C.W.: 397. The extent of dissociation of salts in water. Part VIII. An equation for the mean ionic activity coefficient of an electrolyte in water, and a revision of the dissociation constants of some sulphates. J. Chem. Soc. 2093–2098 (1938)
22. Lifshitz, I.M., Slyozov, V.V.: The kinetics of precipitation from supersaturated solid solutions. J. Phys. Chem. Solids **19**, 35–50 (1961)
23. Zur, Fuchs N., der Koagulation, Theorie: Z. Phys. Chem. **171A**, 199–208 (1934)
24. Monnin, C.: A thermodynamic model for the solubility of barite and celestite in electrolyte solutions and seawater to 200 °C and to 1 kbar. Chem. Geol. **153**, 187–209 (1999)

25. Powell, K.J., Brown, P.L., Byrne, R.H., Gajda, T., Hefter, G., Sjöberg, S., Wanner, H.: Chemical speciation of environmentally significant metals with inorganic ligands Part 2: The Cu^{2+}, OH^-Cl^-, $CO_3{}^{2-}$, $SO_4{}^{2-}$, and $PO_4{}^{3-}$ systems (IUPAC Technical Report). Pure Appl. Chem. **79**, 95–950 (2007)
26. Reichle, R.A., McCurdy, K.G., Hepler, L.G.: Zinc hydroxide: solubility product and hydroxy-complex stability constants from 12.5–75 °C. Can. J. Chem. **53**, 841–3845 (1975)
27. Martell, E., Smith, R.M.: NIST Standard Reference Database 46. NIST Critically Selected Stability Constants of Metal Complexes: Version 8.0 (2016)
28. Alwan, A.K., Thomas, J.H., Williams, P.A.: Mineral formation from aqueous solution. Part III. The stability of aurichalcite, (Zn, Cu)5(CO3)2(OH)6, and rosasite (Cu, Zn)2(CO3)(OH)2. Transition Met. Chem. **5**, 3–5 (1980)
29. Leussing, D.L., Kolthoff, I.M.: The solubility product of ferrous hydroxide and the ionization of the aquo-ferrous ion. J. Am. Chem. Soc. **75**, 2476–2479 (1953)
30. Güldenpfennig, A., Distaso, M., Klupp Taylor, R.N., Peukert, W.: Modelling the two-dimensional growth and oriented attachment of goethite nanorods synthesized via oxidation of aqueous ferrous hydroxide slurries. Chem. Eng. J. **347**, 798–807 (2018)
31. Russell, B., Payne, M., Ciacchi, L.C.: Density functional theory study of Fe(II) adsorption and oxidation on goethite surfaces. Phys. Rev. B **79**, 165101–165114 (2009)
32. Rustad, J.R., Felmy, A.R., Hay, B.P.: Molecular statics calculations of proton binding to goethite surfaces: a new approach to estimation of stability constants for multisite surface complexation models. Geochim. Cosmochim. Acta **60**, 1563–1576 (1996)
33. Israelachvili, J.N.: Intermolecular and surface forces. Academic Press, MA, Burlington (2011)
34. Güldenpfennig, A., Pflug, L., Peukert, W.: How to estimate material parameters for multiphase, multicomponent precipitation modeling. Cryst. Growth Des. **19**, 2785–2793 (2019)
35. Akdas, T., Distaso, M., Kuhri, S., Winter, B., Birajdar, B., Spiecker, E., Guldi, D.M., Peukert, W.: The effects of post-processing on the surface and the optical properties of copper indium sulfide quantum dots. J. Colloid Interface Sci. **445**, 337–347 (2015)
36. Süß, S., Michaud, V., Amsharov, K., Akhmetov, V., Kaspereit, M., Damm, C., Peukert, W.: Quantitative evaluation of fullerene separation by liquid chromatography. J. Phys. Chem. C **123**, 16747–16756 (2019)
37. Süß, S., Metzger, C., Damm, C., Segets, D., Peukert, W.: Quantitative evaluation of nanoparticle classification by size-exclusion chromatography. Powder Technol. **339**, 264–272 (2018)
38. Khomane, A.S., Hankare, P.P.: Structural, optical and electrical characterization of chemically deposited CdSe thin films. J. Alloys Compd. **489**, 605–608 (2010)
39. Salaheldin, A.M., Walter, J., Herre, P., Levchuk, I., Jabbari, Y., Kolle, J.M., Brabec, C.J., Peukert, W., Segets, D.: Automated synthesis of quantum dot nanocrystals by hot injection: mixing induced self-focusing. Chem. Eng. J. **320**, 232–243 (2017)

Chapter 9
Impact Comminution in Jet Mills

Alexander Strobel, Benedikt Köninger, Stefan Romeis, Karl-Ernst Wirth, and Wolfgang Peukert

Abstract Modelling the comminution in jet mills with respect to the complex two-phase flow and the dynamic process behaviour is still a challenging task. The processed solids pass through several stages in the mill: The comminution process in the lower part, the pneumatic transport towards the classifier in the middle section, and the classification step at the top. In this contribution, the grinding kinetics and process behaviour during quasi-batch and fed-batch operational mode for different holdups, classifier speeds, and particle sizes are examined in detail. A previously developed method using well-characterized aluminium particle probes to access the stressing conditions is adapted for application in the investigated jet mill: The relative particle impact velocity is linked to the geometric changes of the particles upon impact. A high number of impact events happen in the mill, while at the same time, the average particle velocity is comparatively low. Besides the stressing conditions, breakage probabilities for the used glass beads are determined by single particle impact experiments and described by the model of Vogel and Peukert. Solids concentration measurements and high-speed imaging reveal the formation of particle clusters at the classifier and its periphery. These clusters have a massive impact on the classification step itself: Fine particles are trapped inside the clusters and are not discharged. Based on an adaption of the breakage model, and using the mean relative particle impact velocity determined by the particle probes, a model for the product mass flow is introduced.

Nomenclature

$(1 - \varepsilon)$	Solid volume fraction [–]
$(1 - \varepsilon)_r$	Solid volume fraction at radius r [–]
$(1 - \varepsilon)_{jet}$	Solid volume fraction in the jet [–]
a	Particle acceleration [m s^{-2}]

A. Strobel · B. Köninger · S. Romeis · K.-E. Wirth · W. Peukert (✉)
Institute of Particle Technology, Friedrich-Alexander-Universität
Erlangen-Nürnberg, Erlangen, Germany
e-mail: wolfgang.peukert@fau.de

A_r	Annulus area of the mill chamber with radius r [m^2]
A	Cross-sectional area of the mill [m^2]
c_w	Drag coefficient [–]
d_0	Nozzle diameter [mm]
E	Young's modulus [Pa]
f_{mat}	Particles' resistance against breakage [$kg\ J^{-1}\ m^{-1}$]
F_W	Drag force [N]
k	Number of impacts [–]
$K^{(1)}(x)$	First Kapur function [s^{-1}]
M	Mass [g]
m_i	Mass of size class i [g]
$m_{i,0}$	Initial mass of size class i [g]
$m_{particle}$	Particle mass [g]
$\dot{m}_i$	Mass flow transported to the classifier [$g\ min^{-1}$]
$\dot{m}_{jet}$	Mass flow through a single jet [$g\ min^{-1}$]
$\dot{m}_p$	Product mass flow [$g\ min^{-1}$]
n	Number of nozzles in the mill [–]
N	Total number of evaluated particles [–]
N_i	Number of particles with I contacts [–]
p	Grinding pressure [bar]
P_B	Breakage probability [–]
P_i	Relative number of particles with i contacts [–]
q_3	Volume-weighted density distribution [m^{-1}]
Q_0	Number-weighted cumulative sum distribution [–]
Q_3	Volume-weighted cumulative sum distribution [–]
r	Radial distance in the milling chamber [m]
R	Outer radius of the milling chamber [m]
R_{cl}	Radius at the outer classifier blade [m]
Re_p	Particle Reynolds number [–]
S	Breakage rate [$g\ min^{-1}$]
$SN_\%$	Percentage of stressed particles [–]
SN_{stress}	Average contact number per stressed particle [–]
t	Process time [s]
T(x)	Separation efficiency curve [–]
$u_{p,jet}$	Particle velocity in the jet [$m\ s^{-1}$]
v	Particle velocity [$m\ s^{-1}$]
v_{cl}	Circumferential velocity classifier wheel [$m\ s^{-1}$]
v_r	Gas velocity in radial direction [$m\ s^{-1}$]
Δv	Relative particle impact velocity [$m\ s^{-1}$]
V	Overall volume of all particles [m^3]
V_i	Volume of individual particle [m^3]
$W_{m,min}$	Minimum mass-specific energy input [$J\ kg^{-1}$]
$W_{m,kin}$	Mass-specific kinetic energy input [$J\ kg^{-1}$]
x	Particle diameter [μm]
$x_{1,2}$	Sauter diameter [μm]

$x_{50,3}$	Mean volume-weighted particle diameter [µm]
x_c	Contact diameter on the particle surface after impact [µm]
x_{cut}	Particle cut size for breakage probability [µm]
x_T	Cut size classifier [µm]
z	Nozzle distance in jet mill [mm]
η	Dynamic viscosity [Pa s]
ν	Poisson ratio [–]
ξ	Product residue [–]
ρ_p	Particle density [kg m^{-3}]
ψ_i	Sphericity of individual particle [–]
ψ	Volume-based mean sphericity [–]

Indices

m	Milling chamber
p	Product
t	Process time
gas	Gas

1 Introduction

Dynamic processes are becoming increasingly important in the field of solid process engineering. The on-demand production, faster product cycles and fluctuating energy supply of renewable (wind or solar) energy are the driving forces of this development. First and foremost, before addressing the modelling of interconnected solids processes, a well-founded understanding of the dynamics of individual unit operations and overall processes is essential [1]. To date, in-depth information on the dynamic behaviour of comminution processes is rare. Modelling of comminution processes is a challenging task [2]: Within the mill, very complex transport phenomena prevail, resulting in mostly unknown stressing conditions. In particular, classifier mills are highly interesting because they involve three coupled unit operations: The comminution in the jet area, the transport to the classification zone, and the classification itself [3]. Although advanced CFD [4–6] or coupled CFD-DEM [2, 7] approaches are available today, the highly turbulent two-phase flows in the mills are far from being understood sufficiently. Other approaches use dynamic model systems for the calculating of closed loop systems [8–10] or population balance methods [11, 12]. The high Reynolds numbers and the steep velocity gradients in combination with the high solids concentrations limit the application of numerical methods [2].

One particular type of classifier mills is the fluidized bed opposed jet mill, which is the method of choice for size reduction of hard, abrasive, and thermosensitive

materials [13]. Through the autogenous comminution by particle-particle impacts induced by the gas jets, a high degree of fragmentation can be achieved for the production of fine powders <10 μm. Since no moving parts for impaction are needed, the comminution proceeds without any wear of the machinery, avoiding also the contamination of the product. The processing of different materials in fluidized bed opposed jet mills is addressed in several different publications [14–18]. These approaches propose empirical models to describe the two-phase flow or just illustrate experimental effects. Other authors describe batch processing in fluidized bed opposed jet mills while global grinding kinetics are employed to model size reduction [19–21]. The complex two-phase flow, the high gas velocities, and the difficulties to directly assess the stressing conditions comprise major challenges. The classification process is studied both experimentally and numerically in stand-alone classifiers, including the fluid mechanics inside the vanes of the rotating classifier wheel [6, 22–28].

The following chapter is dedicated to the study of particle-particle interactions, revealing the overall stressing conditions, and the dynamics of the two-phase flow during non-stationary fine grinding. For this purpose a lab-scale fluidized bed opposed jet mill is investigated in detail: Besides the grinding behaviour during different operational modes, a novel approach for the direct determination of relative particle velocities will be presented. Any comprehensive description of the comminution process requires the knowledge about the materials properties and the materials response to the determined stresses. For this reason the single particle breakage behaviour is studied and analysed by single particle compression and impact tests. The presented observations are then finally used for a model of the product mass flow.

2 Materials and Methods

2.1 Fluidized Bed Opposed Jet Mill

The experiments were performed in a lab-scale fluidized bed opposed jet mill (AFG 100, Hosokawa Alpine AG, Germany). A scheme of the setup is depicted in Fig. 1 [29]. The mill consists of a cylindrical milling chamber (inner diameter of 100 mm). Three Laval nozzles [exit diameters of 1.9 mm (1)] are arranged in a 3D configuration at the bottom of the mill chamber and are directed towards the central focal point. The nozzles are supplied with pressurized air, which leads to a gas flow directed upward towards the classifier wheel (2), whose outer diameter is 50 mm. The mill was operated at a pressure level of 10–20 mbar below ambient conditions. An online laser diffraction system (3) (Insitec, Malvern Panalytical, UK) is installed in the product stream to continuously record the product particle size distributions (PSDs) (sample rate of 1 Hz). Before the online particle size measurement, the product particles are dispersed by a ring nozzle (4). Particle separation after the measurement was ensured by a cyclone and a filter. For the characterization of the material inside
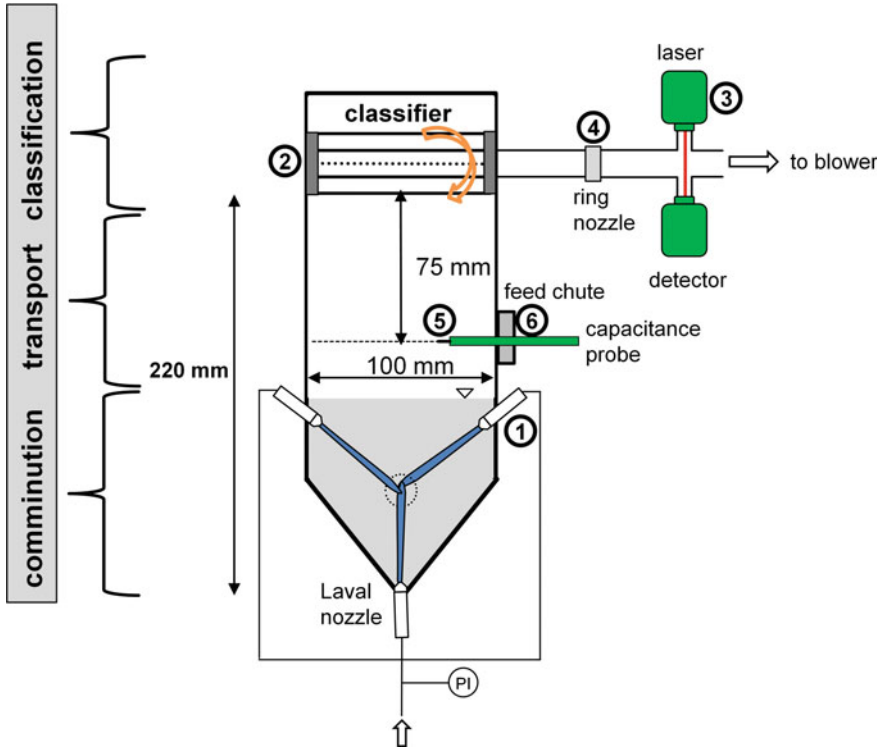
Fig. 1 Scheme of the lab-scale mill AFG 100. (1) Laval nozzles, (2) classifier wheel, (3) online laser diffraction setup, (4) ring nozzle, (5) needle shaped capacitance probes inserted into the custom-made adapter fitted into the original feed chute (6). Adapted from Köninger et al. [29], with kind permission of Elsevier

the mill, the grinding process was interrupted, and the PSD was determined by offline laser diffraction (Mastersizer 2000, Malvern Panalytical, UK). The holdup was determined by weighing.

To measure the solid volume fraction $(1 - \varepsilon)$ in the zone between the upper Laval nozzles and the classifier, capacitance probes (5) were inserted into the milling chamber through a customized measurement adapter which was fitted into the original feed chute (6) (75 mm below the classifier). The capacitance probes are sensitive to changes in the surrounding electromagnetic field caused by the solids: These changes in the capacitance, which are converted to a voltage signal and are further processed by a two-channel amplifier, can be related to the solids concentration surrounding the probes. A calibration procedure is applied [30] to convert the measurement signal to the corresponding solid volume fraction $(1 - \varepsilon)$. The local solid volume fraction $(1 - \varepsilon)_r$ was measured at six different radial positions r, and the data was converted to an overall solid volume fraction as shown by Eq. 1.

$$(1 - \varepsilon) = \frac{\sum_{r=0}^{R}(1 - \varepsilon)_r \cdot A_r}{A} \tag{1}$$

With A_r being the annulus area of the mill chamber for each position r and A the cross-sectional area of the mill. Measurements close to the walls (r = R) were not possible. The formation of a slight crust on the walls was observed (for the processing of the later introduced limestone). A solids fraction of $1 - \varepsilon = 0.55$ (similar to conditions of a fixed bed) was assumed.

Absolute pressures of up to 6 bar were applied to the gas before entering the grinding chamber via the nozzles, which corresponds to a maximum volumetric gas flow rate of 11.7 $m^3 h^{-1}$ through each of the nozzles. The classifier speed was varied between 6000 (circumferential wheel velocity $v_{cl} = 15.7$ m s^{-1}) and 15,000 rpm ($v_{cl} = 39.3$ m s^{-1}). The solids holdup was varied between 100 and 700 g. Within the presented experiments the mill was operated in quasi-batch and fed-batch mode.

To optically access the classifying process, an identical AFG 100 with a customized shaft was used [26, 31]: The original drive shaft of the classifier wheel was replaced by a hollow shaft to visualize the flow through the classifier (customization was done by the Weber group). For further details on the collaboration, please refer to the joint publication [31]. The hollow shaft and the original feed chute are placed on opposing sites in the milling chamber, allowing optical access to the fluid and particle flow through the classifier wheel and the surrounding area, while the original geometries are maintained. Imaging was performed by placing a high-speed camera (Keyence VW-600M, 640 × 240 or 320 × 240 pixels resolution, 8000 or 12,000 fps) in front of a window located in the original feed chute. Illumination is realized with a tripod lamp across the ceiling window to prevent any light reflections. For further details, we refer to Stender et al. [26] and Spötter et al. [32].

2.1.1 Quasi-Batch Experiments

For quasi-batch grinding experiments, the mill was only operated with the initially given amount of solids. Besides product-sized material being discharged during the process, the holdup did not change by more than 15% (for the processing of soda-lime glass beads). The process was interrupted at predefined time intervals to measure the powder mass in the milling chamber and its PSD. Thus, by simple mass balancing, the product mass flow rate was calculated. For this purpose, the complete holdup was removed from the mill and thoroughly mixed. Three individual samples were taken for size analysis (Mastersizer 2000, Malvern Panalytical, UK). All experiments were repeated three times, and mean values and standard deviations were calculated accordingly. Changes in the sampling intervals did not show a significant influence on the obtained results.

2.1.2 Fed-Batch Experiments

During quasi-batch experiments, the holdup and the PSD in the milling chamber are changing simultaneously. Therefore, the influences of individual parameters on the process cannot be differentiated. To minimize the influence of the changing holdup, fed-batch experiments were performed: The process is interrupted in fixed intervals to stock up the holdup with the feed material. Within the first 5 min of operation, an interval of 1 min was chosen, followed by a 5 min interval for the remaining process time. Sampling was performed according to the protocol given above.

2.2 Fluidized Bed with Secondary Gas Injection

For some case studies, a lab-scale fluidized bed [33, 34] (inner diameter of 94 mm, circulation zone height of 570 mm) with secondary gas injection was used. Fluidization gas velocity was set to $2.4 \, \text{cm s}^{-1}$. A sintered metal plate at the bottom of the bed was used to ensure a homogeneously distribution of the gas. For particle separation, a cyclone and a filter are installed at the top. The diameter d_0 of the used nozzles was 2 mm. A single nozzle setup and a two-opposing nozzle setup were investigated. The distance to the focal point of the opposing nozzles was 42 mm. The jet velocity was set to $200 \, \text{m s}^{-1}$ (velocity at the nozzle threat). Sampling was performed after intervals of 10 min by dismantling the lower segment of the fluidized bed: The solid was manually mixed and samples were taken at three different spots and merged.

2.3 Material

2.3.1 Soda-Lime Glass Beads

Spherical soda-lime glass beads (Silibeads®, Type S) by Sigmund Lindner (Germany) were used as model particles. In comparison to other investigated materials like talc [35], hydrargillite [9, 19] or ethenzamide [20, 36] the glass beads have distinct advantages for the chosen application: They show superior mechanical properties (Mohs hardness ≥ 6, Young's modulus E = 63 GPa, [37]) and thus show rather slow breakage. By purposely slowing down the comminution process, the dynamic changes of the process can be observed in greater detail. The density of the beads was $2500 \, \text{kg m}^{-3}$.

For the investigation of the grinding dynamics and kinetics, as-received feed fractions with Sauter diameters $x_{1,2}$ of 61, 93, and 127 μm and corresponding spans $((x_{90,3} - x_{10,3})/x_{50,3})$ of 0.71, 0.68 and 0.64, respectively, were used. The corresponding PSDs are given in Fig. 2a together with an SEM image of one of the feed fractions (Fig. 2b). From the SEM images, the sphericity ψ_i of the individual particles is calculated according to Eq. 2:
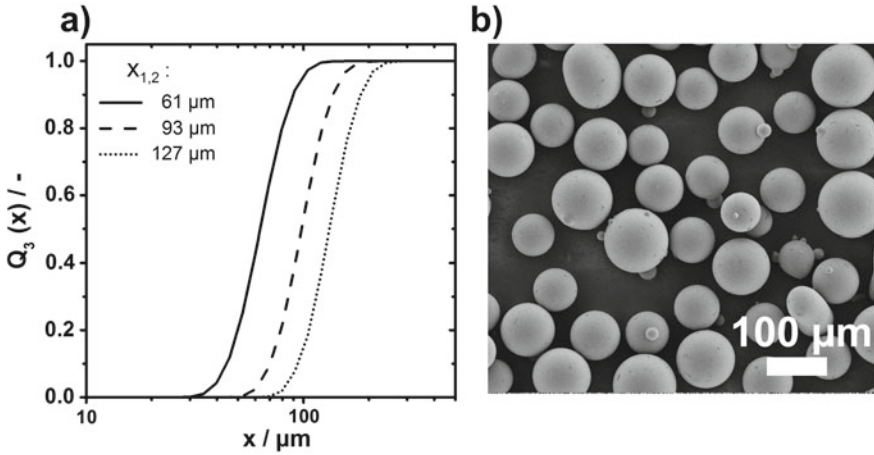
Fig. 2 PSDs of the as-received soda-lime glass beads. Sauter diameters of the fractions are 61, 93, and 127 μm (**a**). **b** SEM-image of the $x_{1,2} = 93$ μm feed material. Adapted from Köninger et al. [29], with kind permission of Elsevier

$$\psi_i = \frac{2\sqrt{\pi \cdot area}}{perimeter} \qquad (2)$$

From the perimeter of each analysed particle, an equivalent diameter was determined, which was further used for calculating the volume V_i of the corresponding equivalent sphere. Subsequently, the volume-based mean sphericity is calculated according to Eq. 3:

$$\psi = \sum \psi_i \frac{V_i}{V} \qquad (3)$$

For the evaluation of the relative particle impact velocities, the feed material from Sigmund Lindner was narrowed by sieving, resulting in a particle fraction with an $x_{50,3}$ and a span of 55.1 μm and 0.71, respectively (Mastersizer 2000, Malvern Panalytical, UK). The distribution is displayed in Fig. 3a.

2.3.2 Aluminium Probe Particles

To assess the relative particle impact velocities, spherical aluminium particles (TLS Technik & Spezialpulver, Germany) were used together with glass beads as feed material; the size distribution was likewise adjusted by sieving. The resulting PSD is displayed in Fig. 3a. The $x_{50,3}$ value for the aluminium spheres was 53.8 μm (span 0.87). An SEM image of the particles is given in Fig. 3b. The density was 2.70 g/cm^3
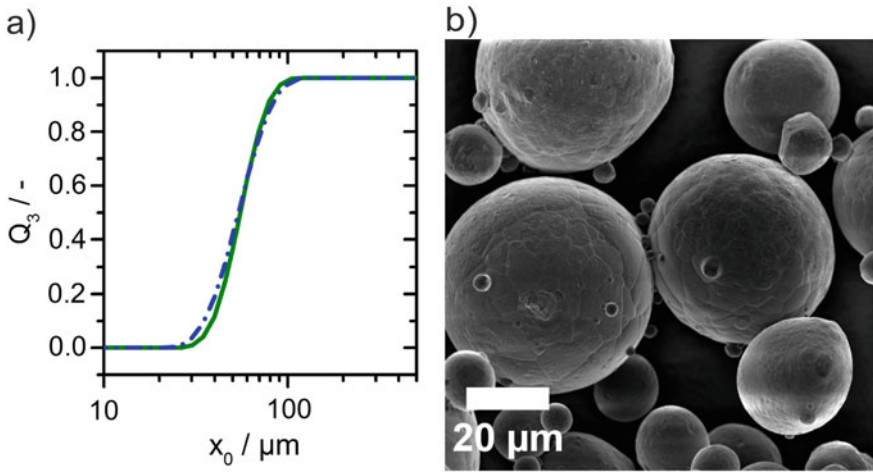
Fig. 3 **a** PSDs of the narrowed glass (blue, dashed-dotted) and aluminium (green, solid) fraction. **b** SEM image of aluminium spheres. Adapted from Strobel et al. [33], with kind permission of Elsevier

as measured by helium pycnometry (Accupyc, Micromeritics, USA). The aluminium particles were later mixed with the glass beads (1:19 m/m) for the experiments.

2.3.3 Limestone

For the presented experiments targeting the particle transport and the separation at the classifier, irregular limestone particles (Saxolith, SH-Minerals GmbH, Germany) were used. Compared to the glass beads, the PSD is rather broad, i.e. $x_{50,3}$ and $x_{1,2}$ of 67 μm and 15 μm, respectively, have been measured. The density of the particles is 2700 kg m^{-3}. By pressure drop measurements, a minimum fluidization velocity of 0.007 m s^{-1} was determined.

2.4 Characterization Methods

2.4.1 Scanning Electron Microscopy (SEM)

Scanning electron microscopy was performed with a GeminiSEM 500 (Carl Zeiss Jena, Germany). Both, a secondary electron detector and a through-the-lens detector (Inlens) were used for imaging. The acceleration voltage was set to 2 kV.

2.4.2 Offline Laser Diffraction

A Mastersizer 2000 equipped with the wet dispersing unit hydro 2000S (Malvern Panalytical, UK) with water as dispersant was used for offline particle size measurements. Loose agglomerates were broken by ultrasound. All samples were measured 5 times with an accumulation time of 10 s, the average values are reported.

2.4.3 Single Particle Impact Testing

Single particle breakage and deformation behaviour was characterized by impacting individual particles using the Schönert breakage device and a custom-build low-pressure impact device. A detailed description of the Schönert device can be found in the work of Meier et al. [38]. In brief, the particles are fed by a vibrational channel onto the centre of a horizontal rotor disc. The rotating disc accelerates the particles towards an outer tooth-shaped ring. The shape of the outer ring ensures an angle of 90° upon impact. To minimize friction, the whole device can be operated at reduced pressure. From the rotational speed of the disc, the impact velocity is then calculated.

A scheme of a second low-pressure impact device is depicted in Fig. 4. The attached vacuum pump reaches pressures down to 20 mbar. For speed regulation, the pressure inside the impact chamber is varied. Impact distance and angle can be changed. Particle velocity was measured by particle image velocimetry (PIV). The PIV system (ILA GmbH, Jülich, Germany) consisted of two pulsed Nd–YAG lasers, a fast high resolution recording CCD camera (PCO2000, 2048 × 2048 pixels) and a synchronizer. The time step between two consecutive images was 4 µs. From the know time step and the travelled particle distance, the velocity prior to the impact is calculated.

From the PSDs prior and after impacting the breakage probability P_B can be calculated. On basis of the well-known Vogel and Peukert model [39], the breakage probabilities P_B and changes in mass for individual size classes (index i) were determined. A simplified calculation according to Eq. 4 was used for the evaluation. Similar to sieve analysis, a nominal cut size x_{cut} is used. The evaluation is based on the assumption that the breakage probability for a given impact velocity is the same for all particles belonging to the identical size class. After impacting the material, the change in mass of the fraction above the cut size is then related to the initial mass before any impact took place (k = 0).

$$P_B = \frac{\Delta m_i}{m_{i,0}} = \frac{Q_3(x_{cut}) - Q_{3,k=0}(x_{cut})}{1 - Q_3(x_{cut})} \tag{4}$$

Impact experiments in a third custom-build impact device were performed to identify the yield strength and the tangent modulus for the material's model needed in
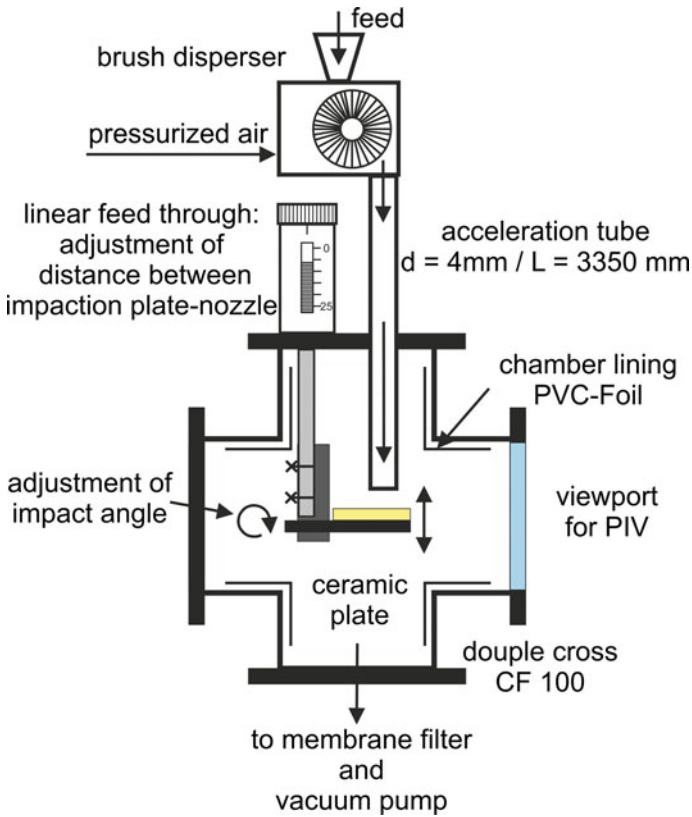
Fig. 4 Low-pressure particle impact device

the finite element calculations. Therefore, aluminium spheres with an initial diameter of 6 mm (Umarex, Germany) were accelerated towards a rectangular steel plate (150 mm × 150 mm × 20 mm, length × width × height) using pressurized air. Before impact, the velocity of the particles was measured by two light barriers installed in close distance to the impact plate. The size of the formed spherical contact area (minimum Feret diameter) on the surface of the particles was related to the particle size ratio x_c/x. By using a scale paper placed in the plain of the contact, the minimum Feret diameter of the contact area was determined from photographic images. Therefore, the waist diameter equals the initial particle diameter. No changes in the waist diameter were detected within the evaluated impact velocity range.

2.4.4 Finite Element Modelling (FEM)

Simulations of the particle-particle as well as the particle-wall impacts were performed using the software package Ansys V.17.2 (Ansys Inc., USA). A 3D model was used for all simulations. To access the mechanical properties of the used aluminium spheres for simulating the particle-particle impacts in the jet mill, a first set of simulations for the impact of an aluminium sphere (6 mm) on a steel plate (90° angle) were performed. Yield strength and tangent modulus of the aluminium sphere were fitted until a sufficient match of the simulated and experimentally observed geometries was found. Young's moduli and Poisson ratios are listed in Table 1.

Dimensions of the sphere and the impact plate were chosen according to the experimental setup. The number of nodes and eight-node quadratic quadrilateral elements used in the simulation is given in Table 2. The coefficient of static friction was determined to be 0.44 by using the impact plate and the contact surface of an impacted 6 mm sphere (impact velocity of 60 m s^{-1}) in an inclined plane experiment (average of 20 repetitions).

In the second step, the particle-particle impact between a glass and an aluminium sphere along the line connecting their gravity centres was simulated. Dimensions were set according to the used feed materials. The inclined plane experiment of a glass bead layer on aluminium gave a static friction coefficient of 0.28.

Table 1 Mechanical properties used for the simulation

	E/GPa	ν/–
Aluminium sphere [40]	68	0.34
Steel plate	200	0.30
Glass sphere	63	0.20 [41]

Table 2 Number of nodes and eight-node quadratic quadrilateral elements of the simulated geometries

	Nodes	Elements
Impact sphere-plate		
Aluminium sphere	720,000	530,000
Impact plate	145,000	105,000
Impact sphere-sphere		
Glass sphere	143,000	103,000
Aluminium sphere	700,000	517,000

3 Results and Discussion

3.1 Dynamics of Quasi-Batch Comminution

3.1.1 Size Evolution and Morphology

The generation of a fine product of a few µm in size requires a sufficiently high classifier speed. The classifier speed was set to 12,500 rpm, which corresponds to a circumferential classifier velocity v_{cl} of 32.7 m s^{-1} and a nominal cut size $x_T = 4.3$ µm at the vanes of the classifier wheel [30].

In Fig. 5 changes in the particle size and sphericity during quasi-batch grinding are depicted. The particle sizes $x_{1,2}$ and $x_{50,3}$ decrease with time (Fig. 5a); within the first 80 s an almost linear trend is observed. However, after the first 80 s, the Sauter diameter $x_{1,2}$ decreases significantly faster than x_{50}. This observation is attributed to a slow initial breakage of the feed particles, while the breakage of the fragments is accelerated. The fragments show a higher specific surface area and, in consequence, cause the observed change of $x_{1,2}$. A similar trend is observed for the volume-based mean sphericity ψ: Up to a processing time of 80 s, the sphericity decreases strongly. After this period, the overall morphology and with it, the sphericity of the broken fraction stays almost constant. The SEM images in Fig. 5b confirm that for short
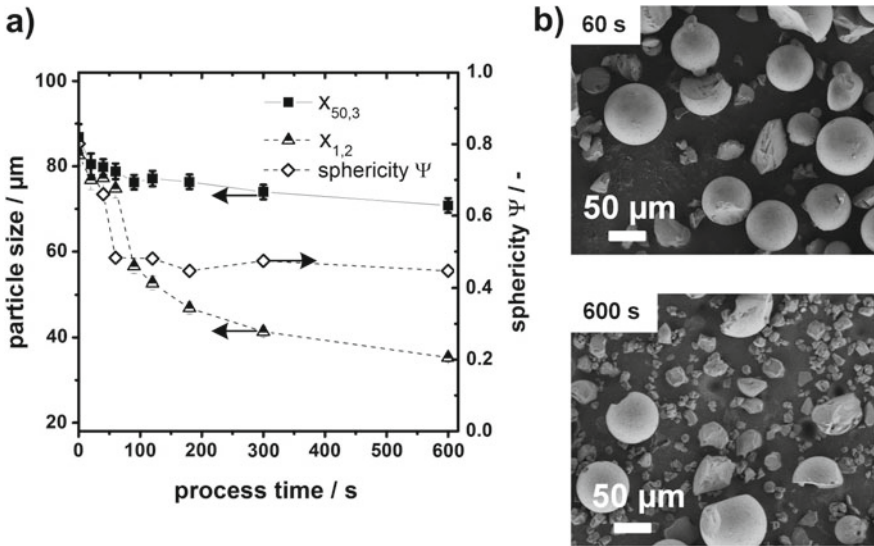
Fig. 5 a Change of particle sizes $x_{1,2}$, $x_{50,3}$ and sphericity during batch grinding. **b** SEM images for a feed particle size of $x_{1,2} = 93$ µm and a holdup of 400 g after 60 and 600 s. Adapted from Köninger et al. [29], with kind permission of Elsevier

processing times (1 min, top image), the number of unbroken feed particles is still high. After 10 min of processing (lower image) mainly fragments dominate.

The few remaining, almost intact particles exhibit dents on the surface. As such, the dent formation is seen as an alternate process to chipping, which causes rather fine fragments. These observations indicate that the feed material is not likely to be broken by one high energy impact but rather by a higher number of impacts producing small fragments. The impacts leading to these small fragments are associated with a high number of impact events at rather low impact velocities. Moderate particle velocities in high-speed gas jets that were injected into fluidized beds were also found by Köninger et al. [34] by particle image velocimetry.

Schönert [42] and later Salman et al. [43] quantitatively characterized the morphological changes of glass spheres after impaction on a target: Different fracture and deformation modes have been assigned to the appearing morphologies whereby each category corresponds to a specific range of the applied mass-specific kinetic energy $W_{m,kin}$. To get a first impression of the grinding conditions in the milling chamber, the method introduced by Salman et al. [43] was applied to the samples in the first 60 s of the quasi-batch grinding experiment. For this purpose the morphology of the particles and fragments is divided into four different types: unstressed immaculate particles (no fracture, smooth surface), particles with low energy impact marks (chipping, dents), fragments showing Hertzian cone cracking, and high impact velocity fragments (appearing as hemispheres, high velocity form). In Fig. 6a examples of the different stressing modes are depicted. In case a particle or fragment could be
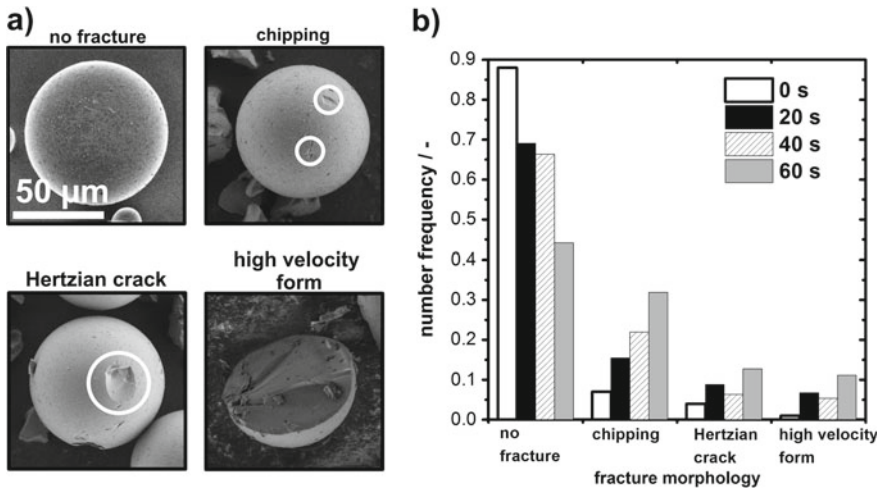
Fig. 6 **a** Four different fracture (respectively impact velocity) categories. **b** Number frequency of the different failure modes after 20, 40 and 60 s of processing. Starting conditions: $x_{1,2} = 93\ \mu m$ and a holdup of 400 g. Adapted from Köninger et al. [29], with kind permission of Elsevier

assigned to different classes, the particle was assigned to the class with higher associated impact energy. A minimum of 200 particles was evaluated per sample. The number frequency of the four categories was determined according to Eq. 5:

$$number\ frequency = \frac{number\ of\ particles\ with\ specific\ morphology\ type}{number\ of\ all\ evaluated\ particles} \quad (5)$$

Figure 6b shows the fracture modes for the quasi-batch grinding experiment after processing for 20, 40, and 60 s: Within the first 40 s over 85% of the particles remained unstressed or only traces of a low energy impact (chipping) are visible. Only 5–7% of the spheres could be assigned to the highest impact class. After 60 s the number of particles without visible damage drops significantly, whereas the proportion of particles with several low energy marks on the surface, and particles which have experienced a high-energy stress event (Hertzian cracks and high velocity form), increases. All these observations are in good agreement with the observed trend in Fig. 5. These results already suggest that lower grinding energies are dominant (e.g., in the jet perimeter) and, therefore rather surprisingly, the impact frequency is an essential driving force in fine grinding, if not the most important one. After 60 s a reasonable evaluation of the morphology is impossible due to the high amount of created fines (represented by $x_{1,2}$ in Fig. 5).

However, this method gives no explicit values for the number of impacts and the impact velocity. To target these values more precisely, a technique initially introduced by Peukert and co-workers to characterize the stressing conditions in wet operated stirred media mills [44–46] was adapted: The morphological changes of spherical, well-characterized ductile metal particles are related to the relative particle impact velocities prior to impact. Additionally, the exact number of dents on the particle surface gives information about the stressing frequency. This method will be presented in detail in Sect. 3.3.

3.1.2 Modelling Grinding Kinetics

An excellent approach to modelling grinding kinetics—as proposed by Berthiaux and Dodds [19]—is Kapur's model for batch grinding [47], which is a simple measure for the overall comminution process. Equation 6 gives the particle size-dependent Kapur function $K^{(1)}(x)$, which describes the change of mass within a specific particle size range:

$$\ln\left(\frac{1 - Q_3(x, t)}{1 - Q_3(x, t = 0)}\right) = K^{(1)}(x) \cdot t \quad (6)$$

Equation 6 can be used to directly estimate size-dependent breakage rates from the measured PSDs for short comminution times (approximately 80 s): Only small amounts of solid are discharged from the milling chamber during this time interval,

while the process behaves like a batch experiment. These assumptions are only valid for a time-independent breakage rate $K^{(1)}(x)$ and when no nonlinear effects occur [48]. The discharged mass $m_{p,t}$ can be taken into account by adapting the PSD $(1 - Q_3(x, t))$:

$$1 - Q_3(x, t) = \frac{m_{m,t}}{m_{m,t=0}}(1 - Q_3(x, t))_m + \frac{m_{p,t}}{m_{m,t=0}}(1 - Q_3(x, t))_p \qquad (7)$$

In Eq. 7 $m_{m,t}$ denotes to the mass inside the milling chamber and $m_{p,t}$ to the total discharged mass at the process time t. Additionally, the mass load at t = 0, which is indicated by the same index, is taken as a reference. By using Eq. 7, the Kapur function $K^{(1)}(x)$ from Eq. 6 can be calculated. As already stated, within the first 80 s a linear decrease of the particle size (see Fig. 5a) is observed. The Kapur function was calculated accordingly. The Kapur functions for different holdups of 100, 300, 400, and 700 g (same feed material, $x_{1,2} = 93\ \mu$m) and different initial particle sizes ($x_{1,2} = 61, 93$, and 127 μm, holdup of 400 g) are shown in Fig. 7. The grinding constant $K^{(1)}(x)$ is plotted against the particle size class: The faster the comminution process within a particle size class, the more negative the values become. For holdups of 100 and 700 g no local extremum is observed, i.e. grinding kinetics increase with the particle size. For medium holdups (300 and 400 g) the fastest grinding kinetics are found in the range of a Sauter diameter of 60–90 μm. Targeting the breakage of particles in the size range between 50 and 90 μm, the corresponding optimum holdup is found between 300 and 500 g: Here, the lowest value of $K^{(1)}(x)$ is observed.

For a load of 100 g, the probability of particle impacts is considered rather low due to the low solid concentration. These low impact probabilities lead to longer path lengths for acceleration before the particles impact with each other. The low holdup corresponds to high kinetic energies per unit mass. A holdup of 700 g is the
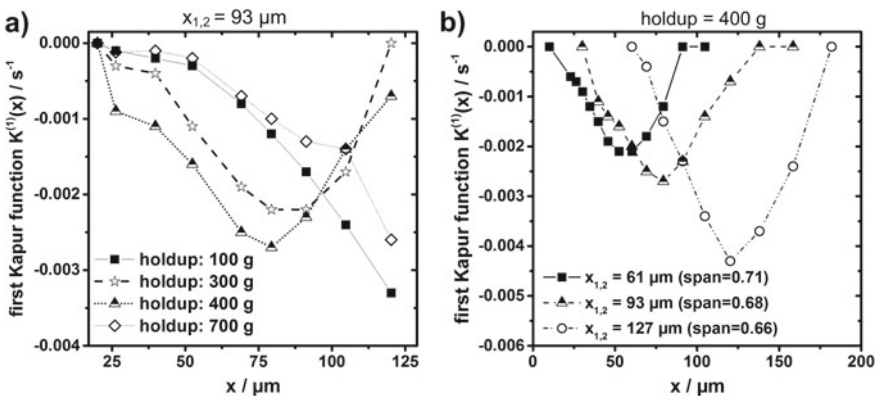

Fig. 7 **a** Kapur function $K^{(1)}(x)$ after 80 s for different holdups with feed particle size $x_{1,2} = 93\ \mu$m and for different feed particle sizes with an initial holdup of 400 g (**b**). Adapted from Köninger et al. [29], with kind permission of Elsevier

other extreme case: the bed height is above the nozzles and back mixing of small particles might be decreased. Due to the high mass concentration, impacts are more likely to happen after shorter acceleration times, whereas the impact probability is comparatively high. For an intermediate holdup of 300 g, the nozzles are covered and the best trade-off between acceleration path lengths and stressing probability is found.

Figure 7b shows the influence of the feed particle size on the Kapur function for an initial holdup of 400 g: For all tested feed materials, a maximum in the grinding kinetics is observed for sizes close to the Sauter mean diameter of the individual fraction. The determined maximum comminution efficiency increases with the particle size. For smaller particles, the entrainment into the jet and the pneumatic transport from the grinding zone is promoted, whereas large particles experience less acceleration inside the jets. Therefore, a higher number of larger particles around the jets is expected which result in an increased impact probability. As will be shown later in Sect. 3.6, the breakage probability is increased for larger particles.

3.2 Fed-Batch Comminution

A changing holdup has a significant influence on the grinding performance of the mill for larger process times. Therefore, the holdup is now kept constant to eliminate this influencing variable. Thus, fed-batch experiments were performed to simulate a constant holdup: During sampling, feed material was added to replace the discharged product. In Fig. 8a $x_{50,3}$ in the milling chamber is shown for different holdups. Similar to the results from the quasi-batch experiments, during the whole process (40 min) no constant particle size is reached. When looking at $x_{50,3}$ for the discharged product, no difference between the holdups was observed. In general, the trend for the discharged fines was found to be similar for the quasi-batch experiment with different holdups shown in Fig. 5a. An increased holdup leads to a faster size reduction of the largest particles in the mill: For more particles being stressed in the active grinding zone, a larger amount of smaller sized fragments is produced. As stated by Fukanaka, comminution is faster at lower holdups due to an increased grinding energy per unit mass [36]. When increasing the pressure and thus the jet speed, an excess of available energy may exist: By increasing the holdup again, the number of impacts inside the jets increases and a faster comminution results. For an increased amount of fines inside the milling chamber, the overall flowability of the solid is decreasing due to agglomeration and adhesion. In consequence, the fluidization behaviour and with it the two-phase flow inside the jets changes. However, this affects the stressing conditions of the particles. Figure 8c gives the discharged product mass flow. The observations are in agreement with Fukanaka: Initially, the mass flow rate is rapidly increasing until reaching a maximum value followed by a steady-state phase. For higher holdups, the time until a steady product mass flow is reached increases. The
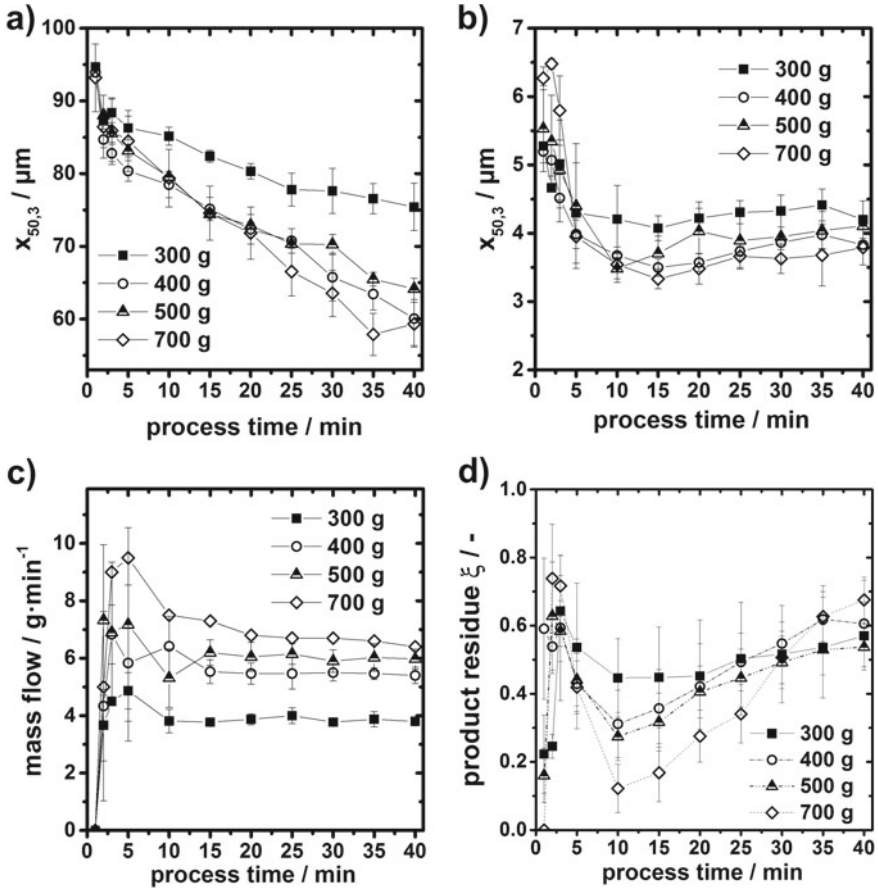
Fig. 8 **a** Particle size $x_{50,3}$ in the milling chamber, **b** $x_{50,3}$ of the discharged product, **c** product mass flow rate, **d** fines residue inside the milling chamber. Data for fed-batch experiments with varying initial holdups. Adapted from Köninger et al. [29], with kind permission of Elsevier

residence time was calculated by dividing the product mass flow rate by the initial holdup. From the product mass leaving the mill during 40 min of processing, residence times between ~75 min (100 g) and ~110 min (700 g) can be calculated for holdups of 100 g and 700 g, respectively. Since the number of impacts strongly correlates with the holdup, the number of impacts increases with increasing residence time.

Within the first 10 min, coarser product particles leave the mill until the steady-state is reached (Fig. 8b). This time was found for all different holdups. A similar observation was made for the corresponding mass flow rates. Independent of the continuously changing fluid mechanical behaviour, which is caused by the decreasing

mean particle size, a stationary product flow rate is reached. Typically, the product fineness and output is sensitive to decreasing particle sizes. However, size-dependent particle pre-separation in the transport zone could minimize that effect on the classifier [49]. Since the various holdups result in different product mass flow rates, a crucial role must be attributed to the load at the classifier and, thus, to the whole process.

Since there is no perfect separation in technical applications, always a certain amount of product-sized particles remains in the coarse fraction. According to Altun and Benzer [50], the effect of fine particles by-passing the classifier and re-entering the circulation system is influenced by the solid concentration. In comparison to stand-alone classifiers, where the rejected material is entering the coarse fraction, the fines are recirculated until they leave the classifier mill. Thus, the product particles re-enter the transport and classification section, before approaching the classifier again. The classifier is therefore exposed to a continuous stream consisting of fresh, crushed and rejected material. Hence, product-sized particles are accumulated inside the milling chamber. The relative amount of product-sized particles which remain inside the milling chamber can be expressed by the product residue ξ (Eq. 8).

$$\xi = 1 - \frac{m_p}{m_m \cdot Q_{3,m}(x = x_{90,p}) + m_p} \tag{8}$$

The $x_{90,3}$-value of the discharged product is used as threshold diameter for the product particles inside the milling chamber. This approach allows comparing the product discharge process for different holdups—even if the particle size distributions inside the mill differ and the separation curves are unknown. For no accumulation of product-size particles happening inside the milling chamber, ξ should be zero, i.e., all product particles are discharged immediately. Figure 8d gives the product residue ξ as a function of the process time for different holdups. Within the first minutes, most of the product remains inside the mill, despite relatively coarse material being discharged (Fig. 8b). Once the products' target-fineness is reached at approximately 10 min, a minimum in ξ is observed. Despite the now reached stationary product discharge, further grinding again increases the accumulation of the product particles inside the mill.

Regarding the minimum ξ, a higher holdup is beneficial. However, with the ongoing grinding process accompanied by the faster production of fines, the product residue ξ becomes worse for higher holdups. Please note that the product residue is not in a steady state after 40 min of processing since the particle size and with it, the amount of fines inside the milling chamber keeps changing.

3.3 Characterization of Stressing Conditions

3.3.1 Method Development

In general, grinding must be understood by the mill function and the material function. The mill function describes the type of stressing, the transferred stress energy, and the stress number. The material function accounts for the particles' reaction to the applied stress in form of breakage probability and breakage function, i.e. the size distribution of the fragments. For modelling of comminution processes and its grinding kinetics, knowledge about the stressing conditions applied to the particles is essential. To target the impact velocity, i.e. the applied stress energy, and the stressing frequency in the jet mill, a method developed to characterize the stressing conditions in wet operated stirred media mills [45, 46] was adapted: The morphological changes of spherical, well-characterized ductile metal probe particles are related to the relative particle impact velocities prior to impact [33]. Briefly, single particles can be compressed by a flat punch micromanipulator installed in a SEM. Stress-strain curves of several 100 particles can be measured and material properties such as Young's modulus, hardness, yields stress, and absorbed energy can be extracted [51]. The manipulation device in the SEM, also allows to access pictures of the stressed and partly broken particles. Surprisingly, images of compressed silica particles below their brittle-ductile transition (<1 μm) in the SEM and those stressed in a stirred media mill looked very similar, indicating that compression in the SEM mimics compression between two grinding beads. On this basis, the method was initially developed for the case of two-sided stressing in stirred media mills. As probe particles, ductile metal particles are used which do not break but plastically deform. The deformation is a measure of the absorbed energy and thus can be used to extract the kinetic energy of the milling beads. This approach provides the stress energy distribution acting in the mill. Fundamental background information and details of the methodical procedure are reported in two publications of Peukert et al. [45, 46].

In comparison to the method for stirred media mills, a mixture of soda-lime glass beads and aluminium beads was used with a radio of 19:1 m/m. As can be seen in Fig. 3a the two PSDs match perfectly. Since the two materials have a similar density, separation during the comminution process is prevented. As shown earlier, almost no fracture of the glass beads occurs during the first 20 s of the comminution process. The absence of small fragments is essential for the method since they might penetrate into the surface of the softer aluminium particles. Thus, the evaluation of the formed dents would not be possible.

To determine the material parameters for the FEM material's model for the aluminium spheres, single particle impact experiments with 6 mm aluminium spheres against a steel plate were performed. In total, 108 particles were impacted in the velocity range between 10 and 60 m s^{-1}. The obtained correlation (orange dotted line in Fig. 9a) between the velocity v prior to the impact and the resulting contact ratio x$_c$/x was fitted in a FEM model: Results are depicted in Fig. 9a by the blue
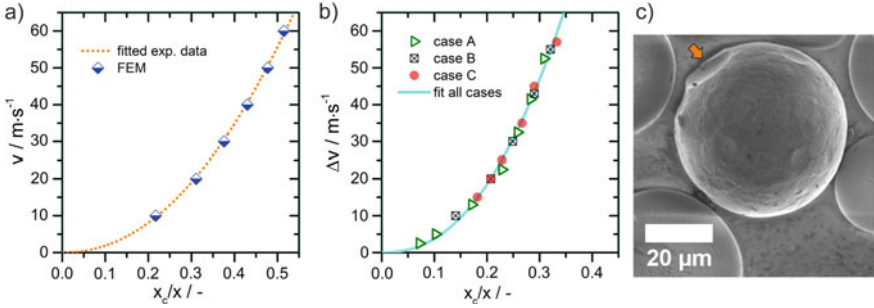
Fig. 9 a Fitted experimental data for 6 mm aluminium spheres impacted on a steel plate, impact velocities against normalized contact size x_c/x. **b** Adjusted FEM for different impact cases, relative impact velocities against normalized contact size x_c/x. Case A: "Only one sphere is moving"; case B: "Unidirectional moving of both spheres"; case C: "Head-on collision of both spheres". **c** SEM image of stressed particle (400 g hold-up, 3 bar, $v_{cl} = 32.7$ m s^{-1}). Adapted from Strobel et al. [33], with kind permission of Elsevier

squares (semi-filled, rotated). The fitting procedure resulted in a yield strength and tangent modulus of 95 MPa and 50 MPa, respectively. To ensure similar deformation behaviour of both, the 6 mm and 53.8 µm aluminium spheres, experiments in the impact device of Schönert have been conducted. Almost identical deformation behaviour could be confirmed. The material data of the impacted 6 mm aluminium spheres can thus be used in the next step to simulate particle-particle impact behaviour in the mill.

Figure 9b shows the results from FEM modelling of the particle-particle impact scenario: Since both particles are moving prior to the impact, the relative particle impact velocity Δv is considered. The data for the different impact scenarios "only one sphere is moving" (green triangle, hollow, case A), "unidirectional moving of both spheres" (black square, hollow, crossed-out, case B) and "head-on collision of both spheres" (red circle, full, case C) does not deviate. An exemplary SEM image of an aluminium particle stressed in the fluidized bed opposed jet mill (Fig. 9c) shows the formation of spherical dents on the surface. The glass beads are only elastically deformed; no visible breakage occurred throughout the experiment. FEM simulations indicate that the normalized contact area diameter x_c/x scales with the relative velocity prior to the impact (normal to the particles' surfaces). To account for foreshortening (distortion due to tilted surfaces) Feret diameters of the contact areas were used to determine the contact area diameter x_c.

The stress frequency was addressed by counting the number of dents on the probe particles. The proportion of particles with i contacts $P_i = N_i/N$ (N_i: number of particles with i contacts, N: total number of evaluated particles) is used for calculating the stress numbers $SN_\%$ (Eq. 9) and SN_{stress} (Eq. 10).

$$SN_\% = 1 - P_0 \tag{9}$$

$$SN_{stress} = \frac{\sum_{i=1}^{n} P_i \cdot i}{1 - P_0}$$ (10)

$SN_\%$ provides the overall percentage of stressed particles, while SN_{stress} gives the average contact number per stressed particle. For each sample, the contact areas on the visible hemispheres of 100 aluminium particles were evaluated.

3.3.2 Particle Impact Velocity and Contact Numbers

Temporal Evolution

Experiments were performed in the described lab-scaled fluidized bed jet mill for process times of up to 40 min. Figure 10a shows the obtained temporal evolution of the stress number distributions. The overall profile of the curve is maintained while it shifts constantly throughout the process. No fracture of the glass particles was observed during the whole process.

$SN_\%$ and SN_{stress} are given in Fig. 10c. After 20 min $SN_\%$ approaches 1, i.e. all probe particles have been stressed at least once. Throughout the process, SN_{stress} increases almost linearly. After 40 min an average of eleven contacts per particle was found. The average contact number increases linearly with time, multiple stressing of an existing contact on the probe particles' surface can be excluded. The characteristic shapes of dents on the surface is depicted in Fig. 10d. Further, the distributions of the impact velocity normal to the surface (Fig. 10b) are of similar shape for all investigated processing times. A large number (~90%) of all impacts happens at relative velocities between 6.8 and 9.1 m s^{-1}, respectively. For some impact events, impact velocities of up to 25 m s^{-1} could be found. Remarkably, particle stressing in a single jet occurs at impact velocities significantly lower than the pre-set jet velocity. These surprising and important results imply that the current understanding of grinding in fluidized bed opposed jet mills must be revised. High impact energy events are rare, the stress number seems to be much more important than high stress energy. Consequently, attrition and weakening effects may play a more important role than previously anticipated.

The stressing in stirred media mills, in contrast to the here shown results for the comminution in jet mills, shows fewer, but much larger flat contact pairs (the formation of pairs is attributed to the bilateral stressing by compression). After a process time of 10 min in a stirred media mill, we found an average of 2.5 flat contact pairs on the surface [45, 46]. However, the impact velocity of the approaching grinding beads, and, therefore, the introduced energy, was closer to the values expected by common models.
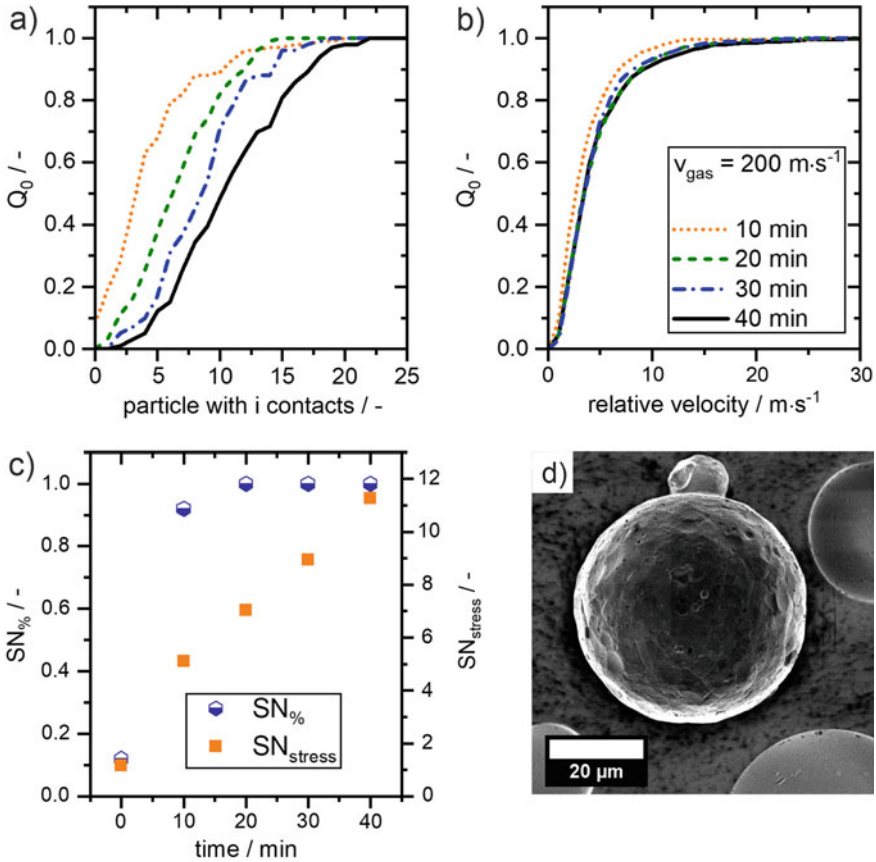
Fig. 10 Number-weighted contact number (**a**) and relative impact velocity distributions (**b**) for different process times in a fluidized bed jet mill (one nozzle). **c** Stress numbers $SN_\%$ and SN_{stress} for the respective distributions. **d** SEM image of one probe particle after 40 min. 200 m s^{-1} gas velocity at the nozzle threat. Adapted from Strobel et al. [33], with kind permission of Elsevier

Nozzle Arrangement

The next set of experiments targeted the change in the stressing behavior for two opposing nozzles. Additionally to the increase in number, the distance of the nozzle was systematically varied. Figure 11 again shows the cumulative number-weighted sum distributions for the contacts (a) and the relative velocity (b) for normalized nozzle distances $(z \cdot d_0^{-1})$ of 10 and 21, respectively. As a reference, the corresponding distributions for the single nozzle setup from the previous section are given.

The opposing jet setup shows higher contact numbers (a) and higher relative impact velocities (b) after a processing time of 10 min. The configuration with the
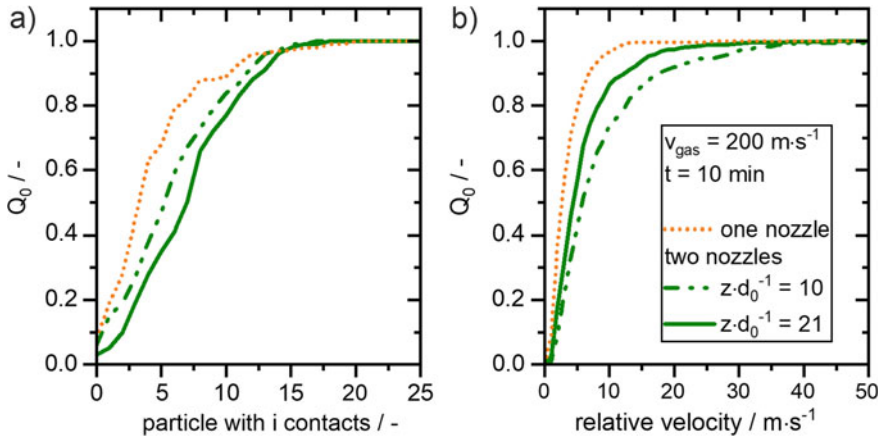
Fig. 11 Cumulative number-weighted sum distributions of the stressing events (**a**) and the relative particle impact velocity (**b**) for different nozzle setups in a fluidized bed reactor with secondary gas injection. Gas velocity of 200 m s^{-1} at the nozzle threat. Adapted from Strobel et al. [33], with kind permission of Elsevier

larger distance between the nozzles ($z \cdot d_0^{-1} = 21$) exhibits the highest number of contacts ($SN_\% = 0.97$, $SN_{stress} = 7.6$) as compared to the closer configuration ($z \cdot d_0^{-1} = 10$, $SN_\% = 0.94$, $SN_{stress} = 6.6$) and the single jet configuration. Surprisingly, the impact velocities are higher for the smaller nozzle distance. In comparison to the single nozzle setup, the mean velocity of the two nozzle setup is increased by a factor of 1.73 ($z \cdot d_0^{-1} = 21$) and 2.52 ($z \cdot d_0^{-1} = 10$), respectively. We attribute the stress numbers to the differences in the total available jet surface area, i.e. the surface area between the developed jets and the surrounding solid bed. Of course, the surface area is larger for the configuration with the larger nozzle-nozzle distance. However, decreasing the nozzle distance results in a reduced jet boundary area. The single nozzle setup yields the smallest area for particle entrainment, resulting in the lowest overall stress number. We attribute the differences of the relative impact velocities to two factors: Firstly, to the movement of particles in opposite directions, which makes impacts with higher velocities more likely compared to the single nozzle setup, and secondly, to the reduction in the gas velocity due to widening of the jets. The latter effect is more prominent for larger nozzle distances.

Influence of the Holdup

In the following, the above-described method was used to determine the relative particle impact velocity for different holdups [33]: the mills' loading was varied between 100 and 700 g. Grinding pressure was set to 1 bar. Figure 12 shows the results after a processing time of 20 s. This limited process time was chosen due to
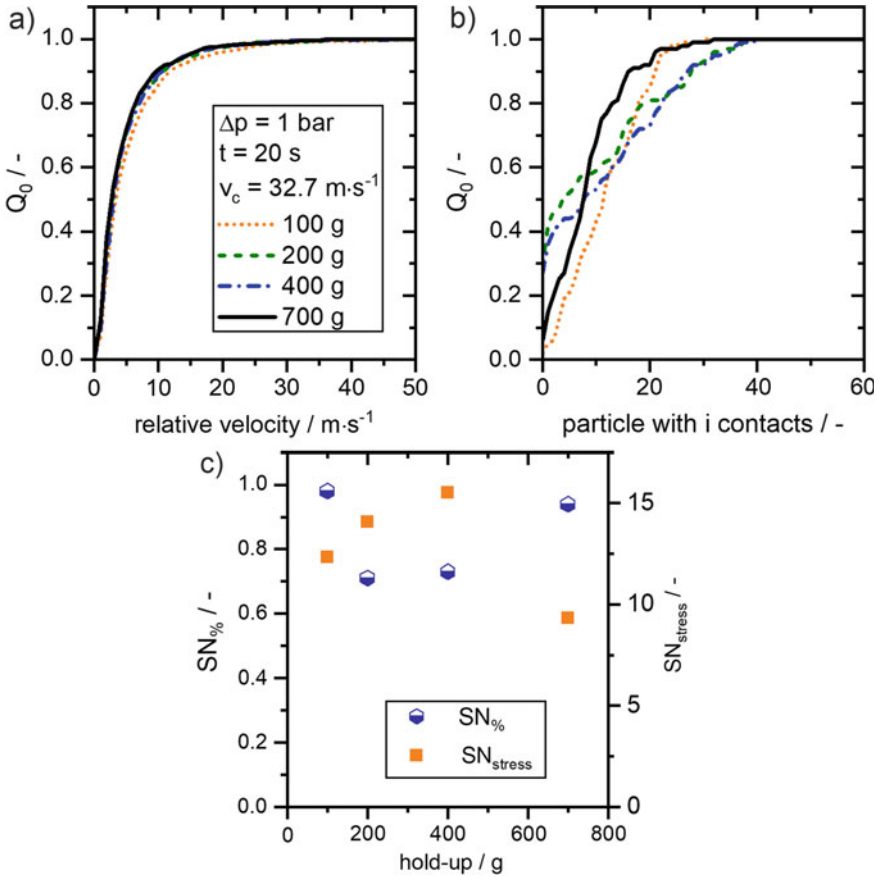
Fig. 12 **a** Relative impact velocity distribution for different holdups in the AFG 100. **b** Number-weighted sum distributions of the contacts on the aluminium probe particles. **c** $SN_\%$ and SN_{stress} for the respective distributions. Adapted from Strobel et al. [33], with kind permission of Elsevier

the high number of formed contacts for higher process times. No fracture of the glass beads occurred during this time [52].

Obviously, the relative impact velocity does not depend on the holdup (Fig. 12a): A median impact velocity of approximately 4.8 m s^{-1} was found. Comparing the obtained distributions to the maximum speed in the expanding gas jets, the relative particle impact velocity is significantly lower. However, as Fig. 12b shows, the contact number distributions clearly depend on the hold-up: Looking at the holdups of 100 and 700 g, almost all particles are stressed and show contacts on their surfaces. Further, the number of contacts is higher for the lower holdup. For the holdups of 200 and 400 g, only ~70% of the probe particles show dents. Nonetheless, the stressed probes (200 and 400 g) show the highest number of contacts (see Fig. 12b, c). To gain further insight into the underlying mechanism, the solid distribution inside the mill

Fig. 13 Solid distribution as function of distance to the classifier for different hold-ups in the AFG 100 accessed by capacitive probes (positive values for the direction of the focal point). Adapted from Strobel et al. [33], with kind permission of Elsevier
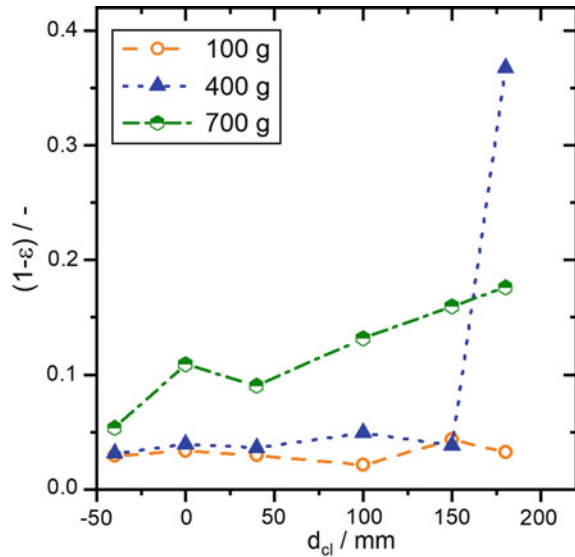
was measured by capacitance probes as a function of the distances to the classifier wheel (Fig. 13). The axis of the classifier wheel is used as zero point (positive values for the direction of the focal point). Due to the highly abrasive conditions within the jets, the focal point of the jets is not accessible.

For the lowest holdup, the solid is equally distributed over the whole transport zone. In contrast, for the holdup of 700 g, a linear increase of solids loading towards the grinding zone is visible. For the intermediate holdup of 400 g, the solid concentration measurement indicates a separation inside of the mill: Towards the focal point (high distance) a strongly increased solid concentration was measured (exceeding 35 vol%), while a low solids content (2–5 vol%) was measured for a distance of 150 mm and lower. However, the lower values are comparable to the measured data for a hold-up of 100 g. Thus, the hold-up influences the distribution of the solid content in the grinding chamber during the comminution process: Two compartments with different solid content and a yet unknown mass exchange seem to exist. Therefore, the recirculation inside the mill is crucial for the process. The indications from Fig. 13 are in agreement with previous observations from Sect. 3.1.2: A holdup between 300 and 500 g was found to be most efficient for the comminution of glass beads (yielded the lowest value of $K^{(1)}(x)$ [29]).

Pressure Variation

In the next step, we consider the stress frequency distribution and the stress numbers for a fixed hold-up of 400 g and a grinding pressure of 1, 2 and 3 bar (the rotating speed of the classifier wheel remains constant $v_{cl} = 32.7$ m/s). The results are given
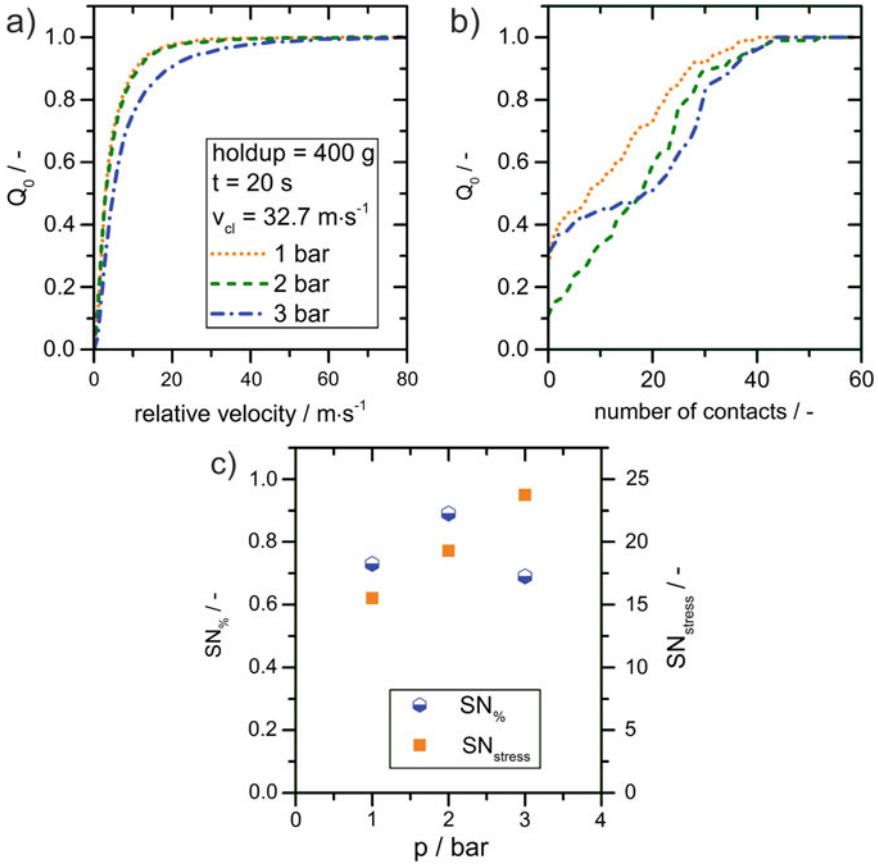
Fig. 14 **a** Relative impact velocity normal to the particle surface. **b** Number-weighted sum distributions of the impact events. **c** Stress numbers $SN_\%$ and SN_{stress} (see Eq. **9** and **10**)

in Fig. 14. Obviously, in all cases, the stress numbers are consistently high (Fig. 14c), SN_{stress} lies between 15 and 25). When increasing the pressure to 2 bar, the number of non-stressed probe particles is reduced (Fig. 14b). Increasing the pressure further to 3 bar, a higher number of unstressed particles is observed. Simultaneously, particles with a higher number of contacts appear in the sample. Köninger et al. recently showed for fluidized beds with secondary gas injection, that the solid concentration within the jets decreases upon increasing the gas pressure [34]. Figure 14a shows the influence of the grinding pressure on the relative impact velocity distribution calculated from the measured contact diameters. Between a pressure of 1 and 2 bar only slight differences are visible. At the investigated maximum pressure of 3 bar, the distribution shifts to higher impact velocities. Nonetheless, even at 3 bar maximum impact velocities of 50 m s^{-1} were found only in few cases. However, all median impact velocities ($Q_0 = 0.5$) were smaller than 10 m s^{-1}, a surprising result.

In conclusion, higher grinding pressures lead to higher impact numbers. Accordingly, we attribute the widely observed higher grinding efficiency at higher pressures to a significant increase in the impact numbers rather than to the impact velocity. Considering the approximated residence times from Sect. 3.2 (40 min of processing, feed-batch mode, $x_{1,2} = 93$ µm, between 75 min at 100 g holdup, and 110 min for the 700 g holdup), the influence of the impact number becomes apparent. The number of impacts would add up to several thousand per particle. Considering the high impact numbers and the unexpectedly low relative impact velocities, a fatigue-like behaviour of the stressed particles must be considered as the main driving force of this dry comminution process.

3.4 Transport Zone

For the discharge of the fine solids produced in the grinding zone at the bottom of the grinding chamber, transport to the classifier at the top of the machine is required. Therefore, to participate in the transport, the diameter of the particles must be below the single grain settling diameter in the up-flow: For the used limestone particles the settling diameter was calculated to be ~120 µm [31]. Since already 90% of the initial feed particles are smaller than the single grain settling diameter, the transport of the solids material in the chamber towards the classifier should be promoted. The knowledge of the solid concentration and, therefore, the mass flow towards the classifier is of essential knowledge for the modelling of the apparatus. (Note: For the results discussed in Sects. 3.4 and 3.5, limestone was processed at a grinding pressure of 3 bar in quasi-batch mode. Holdup and classifier speed were changed according to the notifications).

The solid concentration $(1 - \varepsilon)$ in the transport zone (the section between the grinding chamber and the classifier) for different holdups was measured during the comminution process by capacitance probes. Results are shown in Fig. 15a. A linear increase from 0.01 to 0.03 with progressing time is detected for the lowest investigated holdup of 100 g. For the other cases, a maximum in solid concentration is observed right after the start. Besides, the maximum value scales with the initial holdup. With proceeding time, the solid concentration decreases, passes a minimum and rises again, while the differences between the holdups vanish. The rising values following the start indicate an increased production and subsequent transport of fine and intermediate particles towards the classifier. Thus, the load in the transport zone is decreased. Passing the minimum, a significantly higher amount of intermediate particles, which are not discharged but only recirculated in the milling chamber, has to be present. Towards the end of the depicted experiments, the solid concentrations approach a steady-state value. From the processing of glass beads and for the here shown data for limestone, the same overall trend is found: Higher holdups lead to higher solid concentrations in the transport region [29].
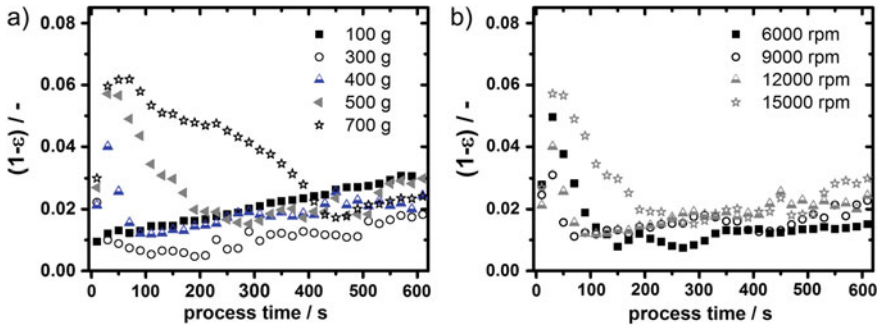
Fig. 15 **a** Solid concentration for different holdups (classifier speed of 12,000 rpm). **b** Solid concentration for different classifier speeds (initial holdup of 400 g). Adapted from Köninger et al. [31], with kind permission of Elsevier

All variations of the classifier speed for a constant initial holdup of 400 g (Fig. 15b) show a similar start-up behaviour with an initial maximum. The time until a steady state is reached increases with the classifier speed. The only exception was found for the lowest classifier speed. Since bigger particles can pass the classifier at smaller circumferential speeds, the range of intermediate-sized particles, that recirculate in the milling chamber and are further stressed, decreases. Accordingly, at 6000 rpm more particles are transported towards the classifier and are discharged.

3.5 Classification

Classification takes place at the upper part of the mill. Fine product particles approach the classifier and are rejected if their diameter is larger than the cut size x_T. Using Eq. 11, which follows from the force equilibrium for a single spherical particle from Stokes law [53], the cut sizes x_T can be estimated. A cut size x_T of 4.4 μm results at a classifier speed of 12,000 rpm.

$$x_T = \sqrt{\frac{18 \cdot v_r \cdot R_{cl} \cdot \eta}{\rho_p \cdot v_{cl}^2}} \tag{11}$$

ρ_p is the particle density, η the dynamic viscosity of the fluid and R_{cl} the radius at the outer classifier blade. As discussed earlier in Sect. 3.2, the discharge of fines during the process changes: Fine product particles are accumulated after a minimum in the product residue ξ is reached for fed-batch experiments. However, for quasi-batch processing of limestone a similar trend was observed, i.e. the product residue changes throughout the whole observation time (see Fig. 16, the cut size is marked by a dotted line).
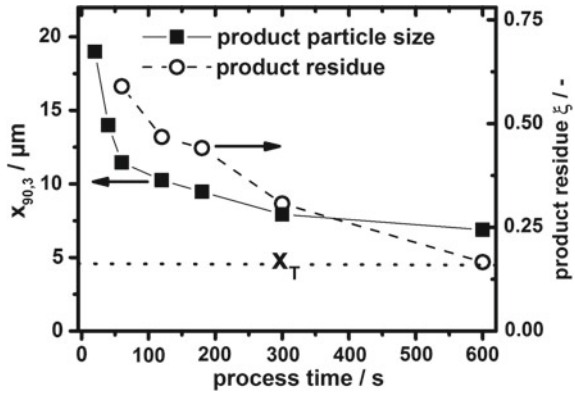
Through the continuously changing size distribution and holdup, the two-phase flow around the classifier changes, too. Further, the rejected particles recirculate in contrast to stand-alone classifiers. Therefore, the determination of separation efficiency curves T(x) is challenging.

Classically, separation efficiency curves relate the mass of particles with the size x which are rejected from a separator to the total mass of particles with the size x fed to the separator. Taking the respective mass flow rates into account, the separation efficiency curve describes the mass flow ratio of particles with the diameter x rejected from the classifier and the particle mass flow with the same diameter x transported to the classifier (Eq. 12). The PSD fed to the classifier is assumed to be equal to the one inside the milling chamber ($q_{3,m}$).

$$T(x, t) = \frac{\dot{m}_{p,t} \cdot q_{3,p}(x, t)}{\dot{m}_{i,t} \cdot q_{3,m}(x, t)} \tag{12}$$

The product mass flow rate $\dot{m}_{p,t}$ and the PSD of the discharged product $q_{3,p}(x, t)$ are directly accessible. The internal mass flow rate transported to the classifier $\dot{m}_{i,t}$ is, however, unknown. An exact calculation of the separation efficiency curve T(x) is thus not possible.

Nonetheless, values for internal mass flow rates have been estimated. Based on the assumption of solely positive values of separation efficiency curves for all particle sizes, the calculated curves after 60 s of processing are plotted in Fig. 17a for values of $\dot{m}_{i,t}$ between 300 and 800 g min^{-1}. Figure 17b displays the estimated efficiency curves after 600 s. $\dot{m}_{i,t}$ was varied between 400 and 1200 g min^{-1}. All separation curves reveal a prominent minimum at approximately 2 µm. This shape of the separation curves is known as "fish-hook". The effect is commonly attributed to the formation of agglomerates and their subsequent rejection at the separator. Thus, fine particles are transferred to the coarse fraction or in our case, are accumulated inside the milling chamber. Relating to the high speed particle tracking results presented later in this section, the observed fish-hooks are attributed to the retaining effect of particle clusters at the periphery of the classifier wheel.
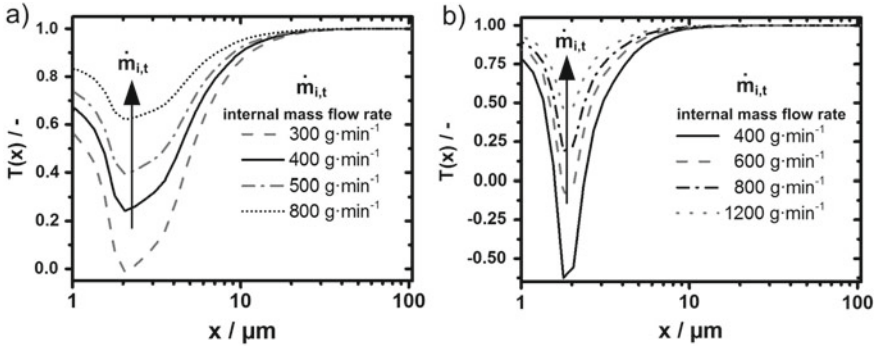
Fig. 17 Separation efficiency curves T(x) after 60 s (**a**) and 600 s (**b**) of processing limestone (3 bar, 400 g initial holdup, 12,000 rpm classifier speed). Different internal mass flow rates were assumed. Adapted from Köninger et al. [31], with kind permission of Elsevier

For a processing time of 60 s a minimum internal mass flow rate of 300 g min^{-1} must be assumed to obtain positive values of the separation efficiency curves, while for 600 s a minimum internal mass flow of at least 400 g min^{-1} needs to be achieved. For internal mass flow rates exceeding the minimum internal mass flow rate, the classification process turns out to be even more ineffective: Due to the ongoing comminution and the associated decrease in particle size, the amount of re-circulating solid increases. Particles impacting on the classifier wheel and thus being broken have been considered as the cause of the partially negative separation efficiency curves. However, from single particle experiments, minimum impact velocities of about 10–20 m s^{-1} to initiate breakage of limestone have been reported [29]. This relative impact velocity of particles at the classifier's blades might only be reached occasionally [32]. Therefore, breakage at the classifier wheel is not likely to happen and can be neglected.

Based on the assumed internal mass flow rates in Fig. 17b, mass loadings at the classifier between 0.265 g g^{-1} (300 g min^{-1}) and 1.05 g g^{-1} (1200 g min^{-1}) result. The differences in operating conditions between classifier mills and stand-alone classifiers are striking: For stand-alone classifiers, mass loadings in the range of 0.1–0.2 are common for fine cut sizes below 10 μm [32, 53, 54].

As explained in the previous sections, the holdup inside the mill influences the internal flow conditions. Obviously, the second influencing variable is the rotational speed of the classifier. When the rotational speed increases, the centrifugal force is rising. Therefore, the discharge of a finer product should be promoted. Further, a broadening of the PSD and an increased residence time should emerge. As displayed in Fig. 18a, the product mass flow increases with decreasing classifier speed during the start-up period of the milling process. Additionally, the ratio of $m_{t=600\,s}$ and $m_{t=0}$, giving the relative amount of solid remaining in the milling chamber after 600 s, is given in Fig. 18a. Only for the highest rotational speeds (12,000 and 15,000 rpm), steady-state conditions are established, whereas the holdup sinks fast for 6000 and
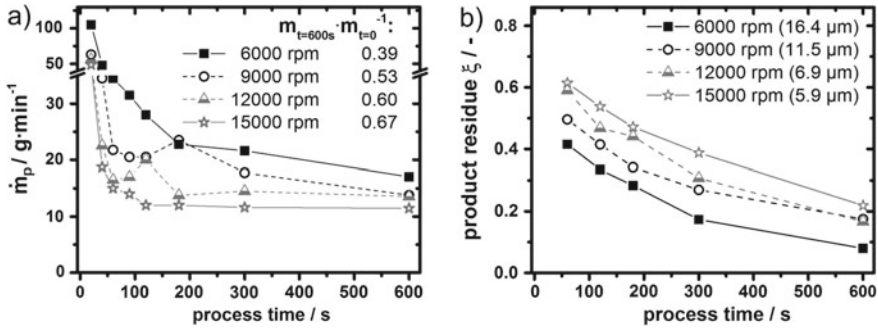
Fig. 18 Product mass flow rates, together with the ratio of $m_{t=600s}$ and $m_{t=0}$, giving the relative amount of solid remaining in the milling chamber after 600 s (**a**) and product residues (**b**) during quasi-batch grinding of limestone for different classifier speeds (initial holdup of 400 g). Adapted from Köninger et al. [31], with kind permission of Elsevier

9000 rpm, respectively. However, the accumulation of fine product is more pronounced for higher centrifugal forces (Fig. 18b). Next to the rotational speed in Fig. 18b, the $x_{90,3}$ values of the discharged product after reaching steady-state conditions are listed: These values indicate that the product accumulation inside the milling chamber is, besides the holdup (explained in Sect. 3.2), a function of the top cut size set by the classifier speed.

Concluding the findings presented so far, a major role can be attributed to the transport and classification process at the classifier and, therefore, has to be considered in greater detail. For that reason, the solid concentration close to the classifier wheel and in its periphery are analysed in the following.

The high-speed images, which have been taken for the visualization of the particle movement, revealed high solid concentrations at the classifier wheel. In the periphery of the classifier wheel, clusters of particles are formed (see Figs. 19 and 20). Particle cluster formation not only takes place at the classifier: As a result of the high solid load inside the mill, clusters can form in the transport zone as well. Even for the lowest investigated holdup of 100 g, the formation of clusters was observed. After a specific time, when solid material is accumulated in the clusters, strands of clusters move tangentially from the outer edge of the classifier wheel to the periphery (see Fig. 19a–c). In Fig. 19d, the cluster frequency, i.e. the number of clusters moving away from the classifying wheel per unit time, is depicted as a function of the classifiers' rotational speed. The observed dependence is in agreement with observations of Spötter et al. [32].

We attribute the previously shown fish-hook effect to the formation of these clusters: Product-sized particles might not be able to penetrate the observed clusters, will be trapped within the clusters, and be thrown back into the periphery. Thus, the discharge of fines from the mill decreases.

With increasing rotational speed and solids holdup, additional clusters are formed in the periphery of the classifier at an outer distance: Two clusters, one at the blade and one in the periphery, are visible in Fig. 20a. The second type of clusters—with
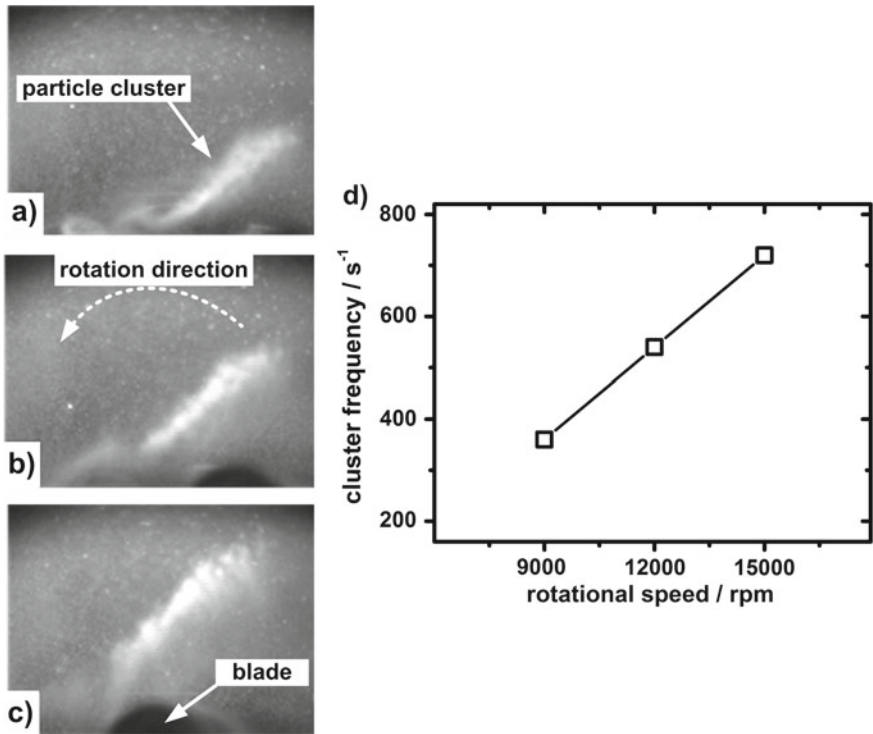
Fig. 19 a–c Three consecutive images extracted from high-speed videos [time difference of 3 ms from (**a–c**)]. Movement of a particle cluster away from the outer edge of a classifier blade (100 g initial holdup, 12,000 rpm classifier speed). **d** Cluster formation frequency as a function of the classifier speed (400 g initial holdup). Adapted from Köninger et al. [31], with kind permission of Elsevier

its accumulated particles—rotates in a certain distance to the classifier wheel for some time. Figure 20b–c show three consecutive images of this cluster type. The formed clusters will thus interfere with the solid transport towards the classifier and the following classification process, i.e. they can be seen as scavengers for the fine particles.

Besides the detained fine particles, the clusters mostly consist of intermediate particles, which are too big to pass the classifier, yet are too small to settle and re-enter the grinding zone. The overall amount of clusters increases with increasing holdups [32].
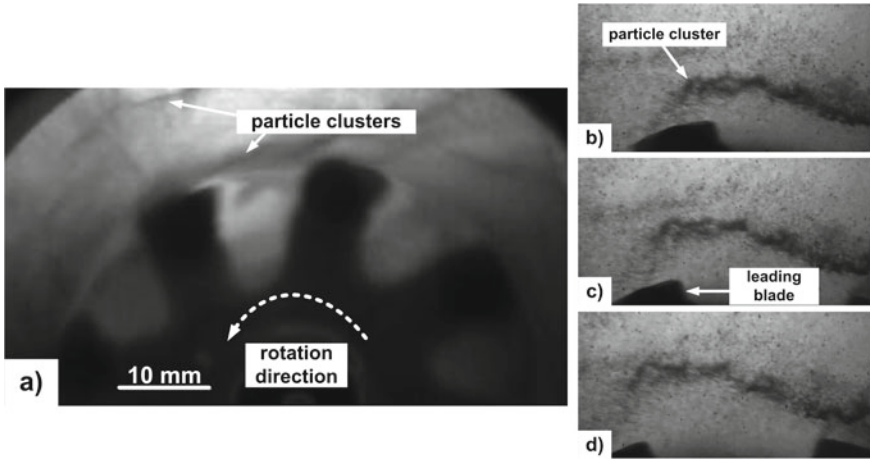
Fig. 20 a Particle clusters in the periphery of the classifier wheel (100 g holdup, 12,000 rpm rotational speed). **b–d** Three consecutive images at the outer edge of the classifier [time difference of 3 ms from (**b–d**)], 400 g of holdup, 12,000 rpm rotational speed. Adapted from Köninger et al. [31], with kind permission of Elsevier

3.6 Modelling the Breakage Behaviour

The response of the material to the experienced stress conditions in the mill is the essential part of any grinding model. The stressing conditions are defined in terms of the experienced energy upon impact—in case of jet mills by the impact velocity—and the impact frequency. However, the breakage events in jet mills are not directly accessible due to the highly complex fluid mechanics. In particular, the impact velocities, the impact frequency, and the residence times in the jets are widely distributed. The impact conditions will therefore differ widely: Straight and oblique particle-particle impacts can occur and the impacting particles can be of different size and shape. To model the breakage behaviour of materials, the described Schönert device was used to determine the breakage probability P_B according to the procedure of Vogel and Peukert [39].

Figure 21a shows the measured breakage probability P_B of the previously used glass bead fraction ($x_{1,2} = 93\ \mu$m) given as a function of the number of successive stressing events k, the particle size x, the particles' resistance against breakage f_{mat}, $W_{m,kin}$ and $W_{m,min}$. $W_{m,kin}$ is the mass-specific kinetic energy of the particles prior to the impact, while $W_{m,min}$ is the minimum mass-specific kinetic energy, which resembles a threshold that needs to be exceeded to induce breakage. Therefore, to induce breakage $W_{m,kin}$ needs to exceed $W_{m,min}$. Equation 13 describes the exact relation:

$$P_B = 1 - e^{\left\{-f_{mat}\cdot x\cdot k\cdot\left(W_{m,kin}-W_{m,min}\right)\right\}} \tag{13}$$

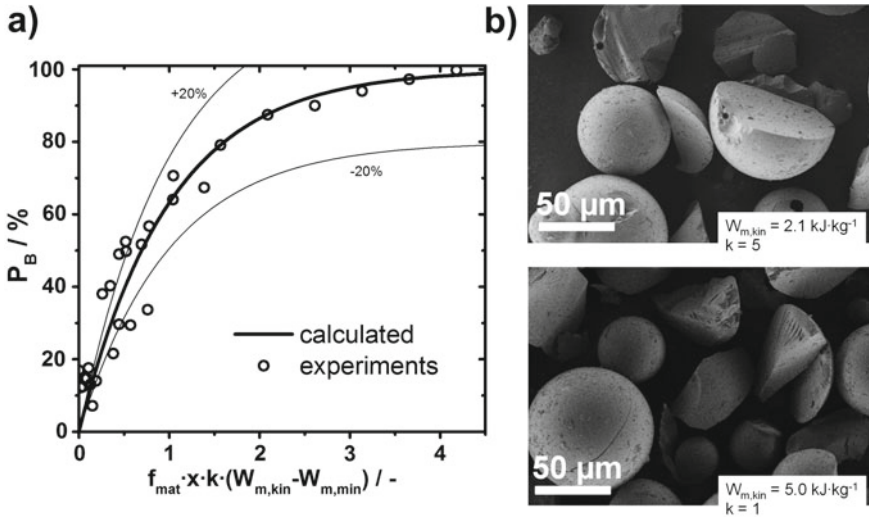**Fig. 21** **a** Breakage probabilities and fitted master curve for the used glass beads ($x_{1,2} = 93\ \mu$m). Material parameters $f_{mat} = 0.944$ kg J m^{-1} and x · $W_{m,min} = 0.1225$ J m kg^{-1} [37]. **b** SEM images of broken particles for different stressing conditions. Adapted from Köninger et al. [29], with kind permission of Elsevier

Impact velocities were in the range of 40–110 m s^{-1} and the number of successive events per particle k was varied between 1 and 8. The shown data points are in good agreement with the master curve. Values for x · $W_{m,min}$ (0.1225 J m kg^{-1}) and f_{mat} (0.944 kg J m^{-1}) are taken from literature [39]. For $W_{m,kin}$ and k being too low, no fragmentation of the particles was observed. Only the formation of rather small dents or cracks on the particles' surfaces was observed. The appearing surface structures are quite similar to the ones from comminution experiments. An insignificant amount of fines is produced. Full fragmentation and a high amount of fines result with increased impact velocity and at a higher number of impacts k. Figure 21b shows the SEM images of two experiments with similar dimensionless stressing parameters f_{mat} · x · k · ($W_{m,kin} - W_{m,min}$) (~0.35) and their degree of fragmentation. The resulting breakage probabilities are quite similar. The particles were stressed one to five times with an energy $W_{m,kin}$ of 2.1 kJ kg^{-1} and 5.0 kJ kg^{-1}, respectively. The breakage function inherently depends on the material properties of the glass beads and on the absorbed energy. Two strategies to increase the breakage probability P_B arise from Eq. 10: Either by increasing the impact velocity and, therefore, the solids kinetic energy $W_{m,kin}$ or by increasing the number of impacts k. The solid concentration influences both cases in the mill.

Low solid concentrations result in longer acceleration distances for the particles in the gas jets before impacting with each other. For higher solid concentrations, the possible acceleration distances decrease dramatically—the particle velocity upon impact is thus reduced. Throughout the process, the particle size x and sphericity ψ change as breakage occurs. As a result, the fluid mechanics is influenced, which then

leads to a higher acceleration a of the particles in the jets.

$$a \sim \frac{F_W}{m_{particle}} \sim \frac{c_w}{x} \tag{14}$$

Equation 14 shows the dependency of the acceleration on the mass-specific drag force $F_W/m_{particle}$, which depends on the drag coefficient c_w and the inverse particle size. From Haider and Levenspiel [55] a relation between the drag coefficient and the sphericity is known:

$$c_w = 69.44 \cdot e^{-5.16\psi} \tag{15}$$

Both during the grinding process and the single particle experiments, the particle size and sphericity decrease. Based on Eq. 15, the drag coefficient will increase with decreasing sphericity. With a continuous increase in the drag coefficient and reduction of the particle size during comminution, the acceleration of the individual particles will increase significantly according to Eq. 14. Thus, the fragmentation process is self-enhancing, at least until intermediate fineness. Since smaller and smaller fragments are produced throughout the process—many of them close to the single-digit micrometre cut size—the impact behaviour of these particles should not be neglected. However, with their increased drag coefficient, the testing should be performed in a reduced pressure environment. These two prerequisites are met by the custom-build low-pressure impact device depicted in Fig. 22. Figure 22a shows the measured velocities for three different fractions of the glass beads ($x_{1,2}$ of 4.7, 17.3, and 60.8 µm). The chamber pressure was set to 100 mbar for all fractions.

The solids mass flow provided by the brush disperser was set to $2.75 \cdot 10^{-5}$ kg s^{-1}. Together with a gas flow rate of $1.6 \cdot 10^{-3}$ m^3 s^{-1}, which enters the acceleration tube through the brush disperser, a solid-to-air flow ratio of $6.8 \cdot 10^{-6}$ was achieved.

Fig. 22 **a** Box plot of particle velocities for glass bead fractions with different Sauter diameters. **b** Jet inside the impact chamber, visualized by high load of glass beads ($x_{1,2} = 4.7$ µm)
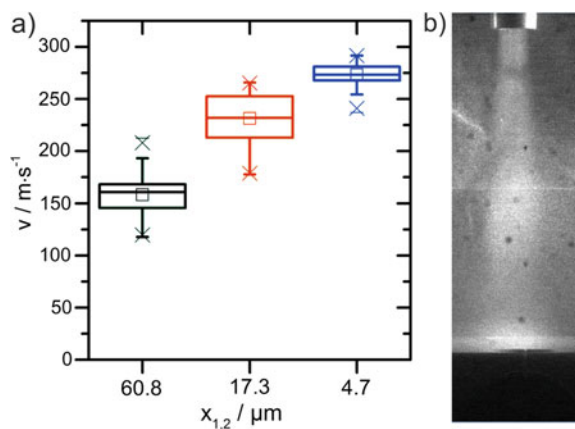
For solid-to-air flow ratios below 0.1 particle-particle interactions are minimized and single impact conditions prevail [56].

Mean velocities of 231 and 274 m s^{-1} were measured for particles with $x_{1,2}$ of 17.3 and 4.7 μm, respectively. The distributions are desirably narrow as indicate by the small boxes. To visualize the behaviour of the particles entering the impact chamber, the solid load was drastically increased. Obviously, turbulences do not interfere with particle impacts on the plate which occur with an angle between 85.8° and 90°. Taking into account the previously determined relative low particle impact velocities (Sect. 3.3.2), product PSDs and morphologies (Sect. 3.1.1), the device provides a sufficient way do determine breakage probabilities for a wide range of materials down to lower micron-size range.

3.7   Modelling Product Mass Flow

Combining all the previously made observations, a simplified model for the product mass flow on the basis of the data for constant mass flow in the jets was introduced by Köninger, based on several assumptions for the boundary conditions: All solids that are added at a particular time step are comminuted. A shift of the particle sizes in the intermediate range is neglected since almost no more changes in the Sauter diameter are observed for process times greater than 40 min. For a constant holdup and PSD in the mill, the product mass flow equals the breakage rate of the added solid material. The breakage rate S is calculated using the breakage probability P_B and the mass flow in the jet area:

$$S = \sum P_{B,i} \cdot \dot{m}_{jet,i} \sim P_B \cdot \dot{m}_{jet} \qquad (16)$$

The individual particle classes i and their respective breakage probability $P_{B,i}$ and mass flow in the jet $\dot{m}_{jet,i}$ are neglected. The breakage rate is therefore written as P_B and the solids mass flow in a single jet as $\dot{m}_{jet}$.

For the calculation of the breakage probability (Eq. 13), an averaged value for the impact number k and the particle impact velocity (necessary for $W_{m,kin}$) are used. These averaged values were determined with the particle probe method introduced in Sect. 3.3.1 and applied in Sect. 3.3.2. For a grinding pressure of 5 bar average values of 6.6 m s^{-1} (impact velocity) and 1 s^{-1} (impact rate) were interpolated. Thus, for a residence time of 30 min 1800 impacts are assigned to each particle.

For these stressing conditions, a simplifying assumption for the breakage probability was made: As the average impact velocities from particle probe measurements are far below the minimum impact velocity of approximately 40 m s^{-1}, the minimum mass-specific energy input $W_{m,min}$ is set to 0. If this would be not the case, P_B would vanish and no comminution would happen. We see the assumption $W_{m,min}$ close to 0 indeed as justified based on the observations reported earlier: Image analysis of the broken material and the detected high contact numbers prompted the role of abrasive

effects as one of the primary causes for size reduction. Thus, despite the relatively low impact velocities, comminution can take place. For $k \gg 1$ comminution at any given velocity will take place, and $W_{m,min} \sim 0$ holds true. The energy from these impacts with rather low energy adds up to an overall energy input, which, in consequence, is sufficient to induce breakage of the particle.

The breakage probability P_B of Vogel and Peukert (Eq. 13) can be expanded through a Taylor series (Eq. 17).

$$e^y = 1 + y + \frac{y^2}{2} + \ldots \tag{17}$$

Hence, we assume that the breakage probability is rather low, which is valid for the low impact velocities. A low breakage probability corresponds to low abscissas. Thus, the series expansion is terminated after the second term.

$$e^y = 1 + y \tag{18}$$

In consequence the breakage probability can be expressed as:

$$P_B = \frac{\Delta m_i}{m_{i,0}} = 1 - 1 - y = f_{mat} \cdot x \cdot k \cdot \left(W_{m,kin} - W_{m,min} \right) \tag{19}$$

With $y = f_{mat} \cdot x \cdot k \cdot \left(W_{m,kin} - W_{m,min} \right)$.

Taking the solids mass flow in the jet and the discharged product mass flow into account, Eq. (20) evolves:

$$P_B = \frac{\dot{m}_p}{\dot{m}_{jet}} = f_{mat} \cdot x \cdot k \cdot \left(W_{m,kin} - W_{m,min} \right) \tag{20}$$

Equation 20 can be rearranged for the product mass flow for the jet, which is proportional to the breakage rate S:

$$S \sim \dot{m}_p = f_{mat} \cdot x \cdot k \cdot \left(W_{m,kin} - W_{m,min} \right) \cdot \dot{m}_{jet} \tag{21}$$

The necessary mass-specific kinetic energy input is calculated using the relative particle impact velocity Δv.

$$W_{m,kin} = \frac{1}{2} \cdot v^2 \tag{22}$$

The solids mass flow in a single jet can be calculated using Eq. 23:

$$\dot{m}_{jet} = \rho_p \cdot (1 - \varepsilon)_{jet} \cdot d_0^2 \cdot \frac{\pi}{2} \cdot u_{p,jet} \tag{23}$$

Fig. 23 Stationary product mass flow determined from experiments and approximated according to Eq. 25 for different solid concentrations in the jets (5 bar grinding pressure, 12,500 rpm classifier speed, with kind permission of B. Köninger)
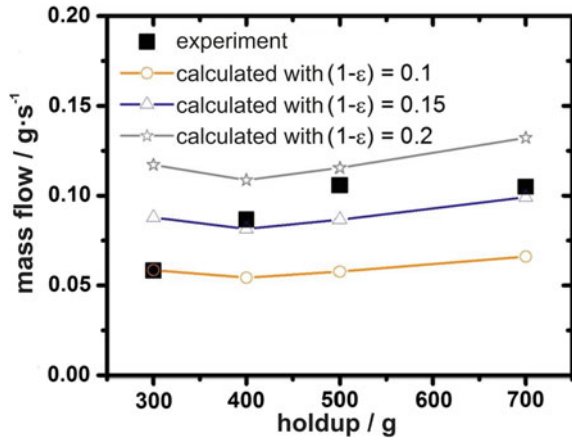
At this point we assume, that the average particle velocity $u_{p,jet}$ in the jet equals the relative particle impact velocity Δv. Inserting Eqs. 22 and 23 into Eq. 21 the following equation results for the breakage rate, respectively the product mass flow.

$$S \sim \dot{m}_p = f_{mat} \cdot x \cdot k \cdot \frac{\pi}{8} \cdot \Delta v^3 \cdot \rho_p \cdot (1 - \varepsilon)_{jet} \cdot d_0^2 \qquad (24)$$

For n nozzles in the considered jet mill are used, Eq. 25 results for the overall product mass flow.

$$\dot{m}_p \sim n_{nozzles} \cdot f_{mat} \cdot x \cdot k \cdot \Delta v^3 \cdot \rho_p \cdot (1 - \varepsilon)_{jet} \cdot d_0^2 \qquad (25)$$

To calculate the product mass flow according to Eq. 25 a mean solid concentration in the jets is needed. Values between 0.1 and 0.3 are inserted for $(1 - \varepsilon)_{jet}$. As particle diameter $x_{50,3}$ is used, the model gives a trend for different holdups in the fluidized bed opposed jet mill (Fig. 23).

Since the relative particle impact velocity is taken into consideration with a power of 3, a closer look at the impact conditions within the mill is required for further refinements, i.e. by considering both, the whole particle size and impact velocity distribution. The assumptions made for the solid mass flow in the jets together with the breakage model of Vogel and Peukert led to a satisfying first approximation of the product mass flow in fluidized bed opposed jet mills. Moreover, the given equation offers interesting possibilities for the scale-up of these mills, since the diameter d_0 of the used nozzles is taken into account. However, scaling effects concerning the fluid mechanics within the jets need to be examined in greater detail. Köninger varied the nozzle diameter between 1 and 4 mm providing first hints on prevailing correlations.

4   Conclusion

In this chapter, the grinding process in a lab-scale fluidized bed opposed jet mill was investigated. The process and its three different unit operations—namely the comminution in the lower part, the pneumatic transport in the middle section, and the classification step at the top of the mill—were thoroughly discussed. Besides tracking the evolution of the particle sizes in quasi-batch grinding experiments, the morphology of the received fines was discussed. Four different breakage modes could be assigned to the particles from image analysis. The frequency of the cases provides hints on the stressing conditions in the jet mill: In the first minute, most particles exhibit small cracks, small chips and debris are identified, or the particles are unharmed. Larger fragments from high energy impacts were rarely observed.

From grinding kinetics, a medium holdup in the range of 400 g was identified as optimum for the investigated mill size. For larger particles, faster comminution took place. Strong influences of the particle feed size on the final product size could not be observed. Since the holdup influences the grinding kinetics, fed-batch experiments were performed with a constant holdup along the whole process time. In contrast to the quasi-batch experiments, faster comminution was observed for higher holdups in fed-batch mode. However, the accumulation of product particles in the milling chamber strikingly increased towards higher processing times, which led to a more detailed investigation of the classification and transport process.

The presented separation curves showed a fish-hook effect. Product-sized particles accumulated inside the mill for all investigated conditions. For increasing solid holdups and classifier speeds, the amount of accumulated fines increases together with the solid concentration in the transport zone. Additionally, it takes significantly longer for higher holdups to reach a steady state. High-speed images showed the formation of clusters and strands around the classifier: these clusters scavenge fine particles. The fine particles trapped in the cluster are rejected and driven periodically to the outer periphery of the classifier. The formation of clusters at the classifier blades and in the periphery of the classifier wheel is strongly influenced by the classifier speed and solid holdup. Further, the breakage behaviour of the used glass beads was examined by impact testing. The obtained data were in excellent agreement with the breakage model of Vogel and Peukert. For the impact testing of particles below 20 μm, a custom-build low-pressure single particle impact device was designed and operated.

The experimental evaluation of the solid distribution was only addressed for the transport area in the middle section of the mill. However, in addition to the capacitance measurements, the solid distribution in the jet and the surrounding bed was targeted with X-ray tomography. For further information on this method and conducted experiments within this priority program we recommend further works of the authors that are not targeted in this contribution [34, 52].

To gain better insight into the stressing conditions, aluminium particles were used to assess the relative particle impact velocity and stress frequency. The ratio of the formed contact diameter and the particle diameter correlates with the relative particle

impact velocity before the impact. Thus, distributions of the relative particle impact velocity, i.e. of the acting stress energies and stress frequencies in the process were obtained. These experiments clearly confirmed the impression of the breakage modes from SEM images of the glass spheres: A high number of impacts occurs during the process in the mill, while at the same time, the mean relative particle impact velocity is surprisingly low.

Finally, a product mass flow model of Köninger was presented. Based on an adaption of the breakage model of Vogel and Peukert, and using the mean relative particle impact velocity determined by the particle probes, this model provides a reasonable approximation of the experimental data.

References

1. Skorych, V., Dosta, M., Hartge, E.-U., Heinrich, S.: Novel system for dynamic flowsheet simulation of solids processes. Powder Technol. **314**, 665–679 (2017)
2. Brosh, T., Kalman, H., Levy, A., Peyron, I., Ricard, F.: DEM–CFD simulation of particle comminution in jet-mill. Powder Technol. **257**, 104–112 (2014)
3. Wheeldon, M., Galk, J., Wirth, K.-E.: Investigation of the comminution process in pendular roller mills. Int. J. Miner. Process. **136**, 26–31 (2015)
4. Ataş, S., Tekir, U., Paksoy, M.A., Çelik, A., Çam, M., Sevgel, T.: Numerical and experimental analysis of pulverized coal mill classifier performance in the Soma B power plant. Fuel Process. Technol. **126**, 441–452 (2014)
5. Rajeswari, M.S.R., Azizli, K.A.M., Hashim, S.F.S., Abdullah, M.K., Mujeebu, M.A., Abdullah, M.Z.: CFD simulation and experimental analysis of flow dynamics and grinding performance of opposed fluidized bed air jet mill. Int. J. Miner. Process. **98**, 94–105 (2011)
6. Toneva, P., Epple, P., Breuer, M., Peukert, W., Wirth, K.-E.: Grinding in an air classifier mill—part I: characterisation of the one-phase flow. Powder Technol. **211**, 19–27 (2011)
7. Weerasekara, N.S., Powell, M.S., Cleary, P.W., Tavares, L.M., Evertsson, M., Morrison, R.D., Quist, J., Carvalho, R.M.: The contribution of DEM to the science of comminution. Powder Technol. **248**, 3–24 (2013)
8. Toneva, P., Peukert, W.: A general approach for the characterization of fragmentation problems. Adv. Powder Technol. **18**, 39–51 (2007)
9. Berthiaux, H., Chiron, C., Dodds, J.: Modelling fine grinding in a fluidized bed opposed jet mill. Powder Technol. **106**, 88–97 (1999)
10. Gommeren, H.J.C., Heitzmann, D.A., Moolenaar, J.A.C., Scarlett, B.: Modelling and control of a jet mill plant. Powder Technol. **108**, 147–154 (2000)
11. Vogel, L., Peukert, W.: Modelling of grinding in an air classifier mill based on a fundamental material function. KONA **21**, 109–120 (2003)
12. Fuerstenau, D.W., Kapur, P.C., De, A.: Modeling breakage kinetics in various dry comminution systems. KONA **21**, 121–132 (2003)
13. Vogel, A.: The Alpine fluidised bed opposed jet mill: a case history. Powder Handling Process. **3**, 129–132 (1991)

14. Lu, X., Liu, C.-C., Zhu, L.-P., Qu, X.-H.: Influence of process parameters on the characteristics of TiAl alloyed powders by fluidized bed jet milling. Powder Technol. **254**, 235–240 (2014)
15. Palaniandy, S., Azizi Mohd Azizli, K., Hussin, H., Fuad Saiyid Hashim, S.: Mechanochemistry of silica on jet milling. J. Mater. Process. Technol. **205**, 119–127 (2008)
16. Schwarzwälder, S., Nied, R., Sickel, H.: Dry fine grinding with jet mills: potentials of energy optimization. Chem. Eng. Technol. **37**, 806–812 (2014)
17. Tasirin, S.M., Geldart, D.: Experimental investigation on fluidized bed jet grinding. Powder Technol. **105**, 337–341 (1999)
18. Wang, Y., Peng, F.: Parameter effects on dry fine pulverization of alumina particles in a fluidized bed opposed jet mill. Powder Technol. **214**, 269–277 (2011)
19. Berthiaux, H., Dodds, J.: Modelling fine grinding in a fluidized bed opposed jet mill. Powder Technol. **106**, 78–87 (1999)
20. Fukunaka, T., Golman, B., Shinohara, K.: Batch grinding kinetics of ethenzamide particles by fluidized-bed jet-milling. Int. J. Pharm. **311**, 89–96 (2006)
21. Xu, X., Li, X., Liu, F., Wei, W., Wang, X., Liu, K., Liu, Z.: Batch grinding kinetics of scrap tire rubber particles in a fluidized-bed jet mill. Powder Technol. **305**, 389–395 (2017)
22. Toneva, P., Wirth, K.-E., Peukert, W.: Grinding in an air classifier mill—part II: characterisation of the two-phase flow. Powder Technol. **211**, 28–37 (2011)
23. Galk, J., Peukert, W., Krahnen, J.: Industrial classification in a new impeller wheel classifier. Powder Technol. **105**, 186–189 (1999)
24. Guo, L., Liu, J., Liu, S., Wang, J.: Velocity measurements and flow field characteristic analyses in a turbo air classifier. Powder Technol. **178**, 10–16 (2007)
25. Liu, R., Zhu, F., Steinberger, Y.: Effectiveness of afforested shrub plantation on ground-active arthropod communities and trophic structure in desertified regions. CATENA **125**, 1–9 (2015)
26. Stender, M., Legenhausen, K., Weber, A.P.: Visualisierung der Partikelbewegung in einem Abweiseradsichter. Chem. Ing. Tec. **87**, 1392–1401 (2015)
27. Sun, Z., Sun, G., Liu, J., Yang, X.: CFD simulation and optimization of the flow field in horizontal turbo air classifiers. Adv. Powder Technol. **28**, 1474–1485 (2017)
28. Xing, W., Wang, Y., Zhang, Y., Yamane, Y., Saga, M., Lu, J., Zhang, H., Jin, Y.: Experimental study on velocity field between two adjacent blades and gas–solid separation of a turbo air classifier. Powder Technol. **286**, 240–245 (2015)
29. Köninger, B., Hensler, T., Romeis, S., Peukert, W., Wirth, K.-E.: Dynamics of fine grinding in a fluidized bed opposed jet mill. Powder Technol. **327**, 346–357 (2018)
30. Richtberg, M., Richter, R., Wirth, K.-E.: Characterization of the flow patterns in a pressurized circulating fluidized bed. Powder Technol. **155**, 145–152 (2005)
31. Köninger, B., Spötter, C., Romeis, S., Weber, A.P., Wirth, K.-E.: Classifier performance during dynamic fine grinding in fluidized bed opposed jet mills. Adv. Powder Technol. **30**, 1678–1686 (2019)
32. Spötter, C., Legenhausen, K., Weber, A.P.: Separation characteristics of a deflector wheel classifier in stationary conditions and at high loadings: new insights by flow visualization. KONA **35**, 172–185 (2018)
33. Strobel, A., Köninger, B., Romeis, S., Schott, F., Wirth, K.-E., Peukert, W.: Assessing stress conditions and impact velocities in fluidized bed opposed jet mills. Particuology, accepted
34. Köninger, B., Hensler, T., Schug, S., Arlt, Wirth, K.-E.: Horizontal secondary gas injection in fluidized beds: solid concentration and velocity in multiphase jets. Powder Technol. **316**, 49–58 (2017)
35. Godet-Morand, L., Chamayou, A., Dodds, J.: Talc grinding in an opposed air jet mill: start-up, product quality and production rate optimization. Powder Technol. **128**, 306–313 (2002)
36. Fukunaka, T., Golman, B., Shinohara, K.: Continuous grinding kinetics of ethenzamide particles by fluidized-bed jet-milling. Drug Dev. Ind. Pharm. **32**, 347–355 (2006)
37. Sigmund Lindner GmbH, Data Sheet. www.sigmund-lindner.com. Accessed 26 June 2017 (2017)
38. Meier, M., John, E., Wieckhusen, D., Wirth, W., Peukert, W.: Influence of mechanical properties on impact fracture: prediction of the milling behaviour of pharmaceutical powders by nanoindentation. Powder Technol. **188**, 301–313 (2009)

39. Vogel, L., Peukert, W.: From single particle impact behaviour to modelling of impact mills. Chem. Eng. Sci. **60**, 5164–5176 (2005)
40. Merkel, M., Thomas, K.-H.: Taschenbuch der Werkstoffe, 7th edn. Fachbuchverlag Leipzig im Carl Hanser Verlag, München (2008)
41. Schittich, C.: Glasbau Atlas, 2nd edn. Birkhäuser, Basel, s.l. (2006)
42. Schönert, K.: Breakage of spheres and circular discs. Powder Technol. **143–144**, 2–18 (2004)
43. Salman, A.D., Gorham, D.A.: The fracture of glass spheres. Powder Technol. **107**, 179–185 (2000)
44. Romeis, S., Schmidt, J., Peukert, W.: Mechanochemical aspects in wet stirred media milling. Int. J. Miner. Process. **156**, 24–31 (2016)
45. Strobel, A., Romeis, S., Wittpahl, S., Herre, P., Schmidt, J., Peukert, W.: Characterization of stressing conditions in mills—a comprehensive research strategy based on well-characterized model particles. Powder Technol. **305**, 652–661 (2017)
46. Strobel, A., Schwenger, J., Wittpahl, S., Schmidt, J., Romeis, S., Peukert, W.: Assessing the influence of viscosity and milling bead size on the stressing conditions in a stirred media mill by single particle probes. Chem. Eng. Res. Des. **136**, 859–869 (2018)
47. Kapur, P.C.: Kinetics of batch grinding: part B. An approximate solution to the grinding equation. Trans. Soc. Min. Eng. AIME **247**, 309–313 (1970)
48. Bilgili, E., Scarlett, B.: Population balance modeling of non-linear effects in milling processes. Powder Technol. **153**, 59–71 (2005)
49. Toneva, P.: Experimentelle und numerische Untersuchungen zur Mehrphasenströmung in Sichtermühlen, 1st edn. Cuvillier Verlag, Göttingen (2010)
50. Altun, O., Benzer, H.: Selection and mathematical modelling of high efficiency air classifiers. Powder Technol. **264**, 1–8 (2014)
51. Paul, J., Romeis, S., Tomas, J., Peukert, W.: A review of models for single particle compression and their application to silica microspheres. Adv. Powder Technol. **25**, 136–153 (2014)
52. Köninger, B., Kögl, T., Hensler, T., Arlt, Wirth, K.-E.: Solid distribution in fluidized and fixed beds with horizontal high speed gas jets. Powder Technol. **336**, 57–69 (2018)
53. Nied, R.: Fine classification with vaned rotors: at the outer edge of the vanes or in the interior vane free area. Int. J. Miner. Process. **74**, S137–S145 (2004)
54. Leschonski, K.: Classification of particles in the submicron range in an impeller wheel air classifier. KONA **14**, 52–60 (1996)
55. Haider, A., Levenspiel, O.: Drag coefficient and terminal velocity of spherical and nonspherical particles. Powder Technol. **58**, 63–70 (1989)
56. Lecoq, O., Chouteau, N., Mebtoul, M., Large, J.-F., Guigon, P.: Fragmentation by high velocity impact on a target: a material grindability test. Powder Technol. **133**, 113–124 (2003)

Chapter 10
Dynamics of Separation Characteristics of Sieving and Flow Classification Processes

Martin Weers, Annett Wollmann, Ulrich Teipel, and Alfred P. Weber

Abstract In spite of the broad range of applications of flow and sieve classification, the physical phenomena for higher particle loadings are not completely understood. As a starting point, common models such as the one of Molerus may be used and optimized to include particle-particle and particle-wall collisions. In this contribution, it is investigated to which extent single particle models may be employed to describe the performance of a deflector wheel classifier and a circular vibratory screening machine at higher loadings. For the sieving process, the Molerus model was modified with a selectivity parameter, while for the deflector wheel, a differentiation of particles with low and high Stokes numbers was made. For high Stokes numbers, in a first approximation, the particularities of the airflow can be neglected, but the impaction behavior on the wheel blades needs to be taken into account. With the detailed knowledge of the mean airflow, a much better prediction of the separation curve can be obtained. In particular, the dynamic aspects of flow and sieving classification have been studied.

Nomenclature

$T_{(x)}$	Separation efficiency (–)
x	Particle size (m)
x'	Dimensionless particle size (–)

M. Weers (✉) · A. Wollmann · A. P. Weber
Institute of Particle Technology, Technical University of Clausthal, Clausthal-Zellerfeld, Germany
e-mail: martin.weers@tu-clausthal.de

A. Wollmann
e-mail: annett.wollmann@tu-clausthal.de

A. P. Weber
e-mail: weber@mvt.tu-clausthal.de

U. Teipel
Institute of Particle Technology and Raw Material Innovation, TH Nürnberg, Nuremberg, Germany
e-mail: ulrich.teipel@th-nuernberg.de

k	Coefficient for the sharpness of cut (–)
COR	Coefficient of restitution (–)
v	Velocity (m s^{-1})
η	Viscosity (Pa s)
ρ	Density (kg m^{-3})
H	Particle layer height (cm)
τ	Characteristic particle relaxation time (s)
τ*	Particle cloud relaxation time (s)
$\dot{V}$	Carrier gas volume flow rate (m^3 s^{-1})
R	Wheel radius (m)
h	Height of the openings in the deflector wheel (m)
U	Circumference (m)
Ψ_{2D}	2D Sphericity (–)
SEM	Scanning electron microscope
σ	Standard deviation (depends on related variable)
E	Kinetic energy (J)
JKR	Johnson-Kendall-Roberts
p	Pressure (Pa)
E*	Average Young's modulus (Pa)
υ	Poisson ratio (–)
Θ	Angle related to the deflector wheel blade (°)
L	Impaction length (m)
f	Revolution rate (s^{-1}), fine material fraction (–)
c_D	Drag coefficient (–)
Re	Particle Reynolds number (–)
κ	Sharpness of cut (–)
F	Force (N)
c	Coarse material fraction (–)
Q	Distribution sum function (–)
a	"Dead flow" parameter (–)
α, β	Measure of selectivity (–)
Γ	Dimensionless acceleration number (–)
A	Amplitude (m)
ω	Angular velocity (° s^{-1})
g	Gravitational constant (m s^{-2})
q	Density distribution (m^{-1})
$\dot{m}$	Massflow rate (kg s^{-1})
K_V	Throwing coefficient (–)

Indices

| p | Particle |

air	Air
eff	Effective
f	Fines
G	Coarse
A	Feed
25	Particle size related to $T(x) = 0.25$
50	Mean particle size
75	Particle size related to $T(x) = 0.75$
3	Mass-weighted
t	Cut particle size related to $T(x) = 0.50$
v	Volume equivalent
area-equivalent	Projection area equivalent
perimeter-equivalent	Projection perimeter equivalent
r	Rebound
i	Approach
0	Initial
imp	Absolute normal impaction
rad	Radial
tan	Tangential
rel	Relative
w	Wall
kin.	Kinetic

1   Introduction

Dry classification processes are employed in powder technology for the separation of outsize particles (e.g. following milling) as well as for the production of narrow fractions. They can be divided into flow and sieving classification processes. In this chapter, the classification processes of deflector wheel separation for fine particles and sieving for coarser particles are treated. In spite of their broad use, the physical principles, which need to be taken into account for an optimized layout of the processes, are still not completely understood.

In sieve classification, the collision processes take place between the sieve wires and the particles of the collective. With the successful transport of the particles across the meshes a fractionation in two or more specific size classes is obtained. The passing probability depends in particular on the particle properties (e.g. size, form, orientation), sieve geometry (mesh size and form, sieve inclination) and operational parameters (loading, frequency, amplitude), respectively [1]. For the steady state sieve classification process models have been presented by Plitt [2], Rogers [3], Molerus [4] and Trawinski [5] while for the instationary process additional models were provided by Soldinger [6], Deghani [7], Nakajima and Whiten [8, 9] and Hatch

and Mular [10]. In this context, the formation of particle layers, the so called stratification, where finer particles move downwards across the openings between larger particles, has to be considered. In this way, fine particles may pass the meshes or may be reflected by collisions with the sieve wires. According to the model by Molerus [4] the fractional separation efficiency T(x) can be described by:

$$T(x) = 1/[1 + (x_t/x)^2 \exp(k[1 - (x_t/x)^2])] \tag{1}$$

where x is the particle size, x_t the cut size and k represents a coefficient for the sharpness of cut.

Also for the deflector wheel separators, the model by Molerus [4] was applied. It was later improved by Rumpf [11], Senden [12, 13], Schubert [14] and finally by Husemann [15]. As a simplification, all these models assume a steady state process, for which the classification corresponds to a counter flow separation of single particles. The forces at work are on the one side the drag force of the gas flow radially passing the wheel blades inwards and on the other hand, the centrifugal force directed outwards deflecting coarser particles.

In his theoretically based model, Husemann considered the geometry and operational parameters where, however, also four fitting parameters were used. In this way, a calibration is necessary to find the appropriate parameter values for the separation characteristics of a classification process. In addition, particle-particle interactions and particle-wall collisions with the blades of the deflector wheel were neglected. However, since deflector wheel separators are usually operated at high loadings [16] other approaches need to be developed to capture the underlying physical principles in a sound manner.

The objectives of this chapter are to give deeper insights into the characteristics and the analogy of flow and sieve classification and to develop optimized models for steady state and instationary operations of the classification processes. For flow and sieve classification the model by Molerus (Eq. 1) will serve as starting point, but it will experience some modifications.

2 Deflector Wheel Classifier

2.1 Model Considerations

The deflector wheel separator used here is an ATP 50 (Hosokawa Alpine) which is schematically shown in Fig. 2 (left). The powder, which is added by a conveying screw, approaches the rotating wheel carried by an air stream. Between the blades, the particles experience a drag force inwards by the carrier air which is counteracted by the centrifugal force originating from the vortex induced by the rotating wheel (Fig. 1, left). Therefore, it is tempting to calculate the cut size from a force balance on individual particles as done by Molerus leading to the Eq. (1). However, for the ATP 50 used here, previous investigations have shown that, especially for particles with
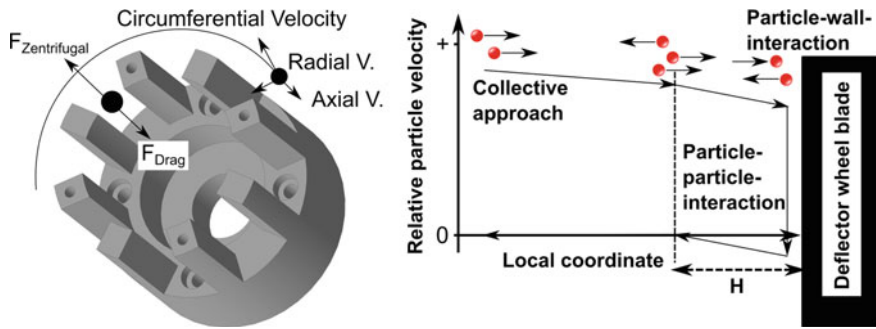
Fig. 1 (Left) Schematic diagram of the deflector wheel; (right) model for the particle-blade collisions including particle-particle collisions

significant Stokes numbers, particle-blade collisions have a major influence on the particle motion [17]. In addition, particle-particle collisions need to be included in an appropriate model for the deflector wheel classifier. The concept of such a model is schematically shown in Fig. 1 (right). Initially, a cloud of particles with similar trajectories and velocities approach the deflector blade. At a certain distance H from the blade, the incoming particles start to collide with the particles reflected from the blade. Due to the mutual collisions, the reflected particles, as well as the incoming particles, are decelerated where the velocity of the reflected particles relative to the blade vanishes at a distance H away from the blade. Knowing the initial particle velocity relative to the blade and the distance H the particle motion can be approximated by assuming an effective viscosity similar to the Richardson–Zaki approach [18]. From this consideration also the coefficient of restitution (COR), which is the ratio of rebound velocity v_r to the approach velocity v_i, can be deduced. This model gives a good representation of the particle motion within the blades.

From the model presented in Fig. 1 (right) Spötter derived a simple relation between effective viscosity η_{eff} and distance H [17]:

$$\eta_{eff} = \rho_p x^2 v_0/(18\,H) \tag{2}$$

where ρ_p is the particle density and v_0 is the velocity of the particles when they arrive at the distance H from the blade. In this way, the influence of particle-particle collisions, which influence both H and η_{eff}, is taken into account, i.e. the solid loading. In addition, if the COR is known also the rebound velocity v_r immediately after the particle reflection from the blade can be calculated:

$$v_r = COR\,v_0(1 - H/(v_0\,\tau)) \tag{3}$$

where $\tau = \rho_p\,x^2\,v_0/(18\,\eta_{eff})$ is the characteristic particle relaxation time (in the particle cloud).

Applying the balance between drag force and centrifugal force the cut size x_t can be related to operational parameters such as the radial inward velocity between the

blades v_{rad}, where $v_{rad} = \dot{V}/(h\,U_{eff})$ where $\dot{V}$ is the carrier gas volume flow rate, U_{eff} is the open circumferential length and h is the height of the openings:

$$x_t = 18\,\eta_{eff}\,\tau^*/\rho_p \tag{4}$$

where τ^* is obtained by solving the quadratic equation:

$$\tau^{*2}((COR\,v_0)^2/R) + \tau^*(v_r + 2\,H(COR\,v_0)^2/v_0) - (H^2(COR\,v_0)^2/v_0^2) = 0 \tag{5}$$

Finally, the distance H could be measured in an idealized experiment where particles are shot against an immobile target wall and observed with a high speed camera (cf. [17]) or derived from DEM simulations together with values for the COR [17, 19]. However, for dense particle clouds within the rapidly rotating blades of the deflector wheel, it is very challenging to observe the distance H. Therefore, direct measurements of the particle velocities before and after impact on the blades were performed using high speed camera at low concentrations (cf. Sect. 2.4). Also, the particle trajectories were recorded and the particle impaction area on the blades was derived.

Since the airflow has a significant influence on the cut size (cf. Eqs. (4) and (5)) and on the sharpness of cut, the mean airflow between the deflector wheel blades and in the wheel center was determined using a 2D LDV system. However, the geometry of the addition of the classifying air (cf. Fig. 2, left) results in an asymmetrical flow towards the deflector wheel. Therefore, the measurements were performed on two perpendicular positions, i.e. on the top ("North") and on the right side ("East") of the wheel.
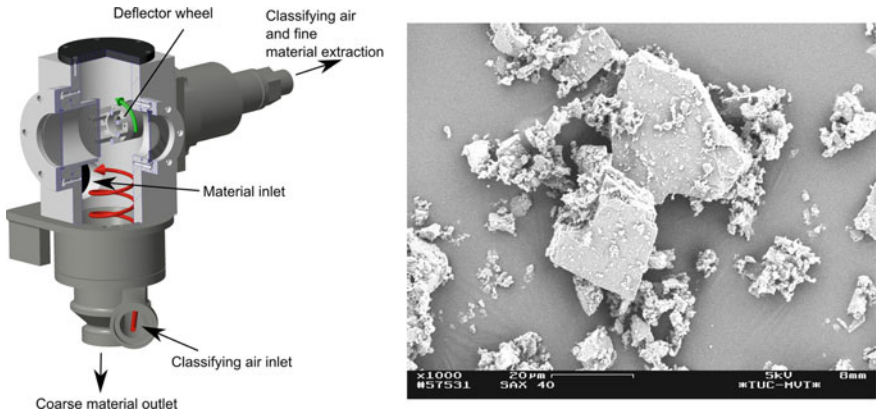

Fig. 2 (Left) 3D design of the modified ATP 50 deflector wheel classifier with the airflow marked as red helix and the direction of rotation of the classifier wheel as green arrow. (Right) Scanning electron microscope (SEM) micrograph of the used limestone particles

2.2   Deflector Wheel Classifier

The used deflector wheel classifier is a modified ATP50 from Hosokawa-Alpine (Fig. 2, left). The optical access to the wheel was achieved by changing the two-sides bearing to a one-sided bearing while the flow and classifying conditions remained unchanged [20]. To keep the front side particle-free, a special sheath air system was installed. The illumination was kept versatile by installing windows on the top and the two sides of the impeller chamber. In addition, the cover plate could be replaced by an insert sleeve.

The following section comprises a short description of the powder system, followed by investigations of the particle collision behavior and the characterization of the airflow within the deflector wheel. From these results, separation curves are derived and compared with experimental ones. Then, a sensitivity analysis is performed and the instationary separation process is commented. Finally, the gained insights are summarized and implemented into a new model.

2.3   Material Characteristics

As powder mainly limestone of different fractions (SH Minerals) was used. Saxolith 40 exhibits a mass-weighted mean particle size $x_{50,3}$ of 44 µm and Saxolith 70 an $x_{50,3}$ of 77 µm, respectively. The Particle Size Distributions (PSD) were measured with a laser diffraction instrument (HELOS, Sympatec) while the powders were dispersed with a dry disperser (RODOS, Sympatec). A SEM micrograph of Saxolith 40 particles is shown in Fig. 2 (right).

Since the particle sphericity is expected to have a significant influence on the classification, the powders were analyzed with a high speed particle imaging system (QICPIC, Sympatec). From the data, the 2D sphericity Ψ_{2D} was determined according to Eq. (6):

$$\Psi_{2D} = \frac{x_{area-equivalent}}{x_{perimeter-equivalent}} \tag{6}$$

The results for the sphericity Ψ_{2D} as a function of the projection equivalent diameter are presented in Fig. 3 for Saxolith 40 and Saxolith 70. The non-spherical shape of the particles is due to the production process using comminution. Regarding the size-dependent sphericity, the powders exhibit hardly any difference. The 2D sphericity varies mostly within the limits of squares and equilateral triangles.
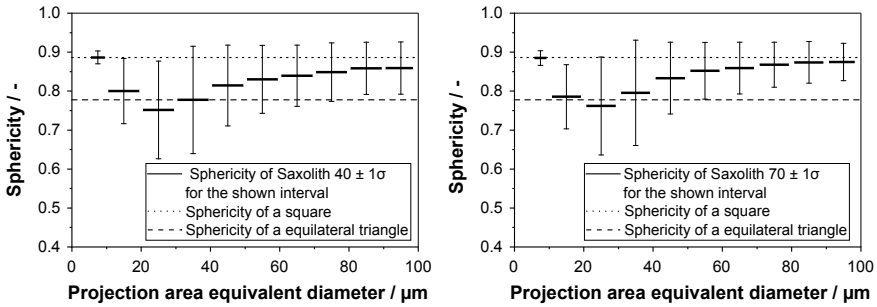
Fig. 3 2D sphericity versus particle diameter for the used limestone particles. Shown are mean values for the indicated range and 1σ: (left) for Saxolith 40 and (right) for Saxolith 70

2.4 Particle Impaction Behavior

As shown in Fig. 1 (right), the particle trajectory can be divided into an approach phase, the impaction, the bouncing on the blade and the retraction phase. In order to study the impaction behavior in detail, single particle experiments on a fixed plate were performed and the particle trajectory was recorded with a high speed camera. Figure 4 shows a series of 3 pictures which are 1.5 ms apart from each other. Three particles (indicated by arrows) approach the impaction plate (red line). In the second and the third picture the previous particle positions are indicated by circles and the trajectories by dashed lines. For the evaluation, particles with curved trajectories (green arrow) and particles staying attached to the plate due to high rotational moments (yellow arrow) have not been considered. However, the fraction of these particles was negligible. For all the other particles (magenta arrow) the velocities and angles of impaction and rebound were recorded and the normal COR was calculated from the perpendicular velocity components according to Eq. (7). With a stationary impaction plate, the relative velocity is only the particle velocity.

$$\text{COR} = \frac{v_{rel,r}}{v_{rel,i}} = \frac{v_{p,r}}{v_{p,i}} = \frac{v_{p,r} - v_w}{v_{p,i} + v_w} = \sqrt{\frac{E_{kin.,r}}{E_{kin.,i}}} \tag{7}$$
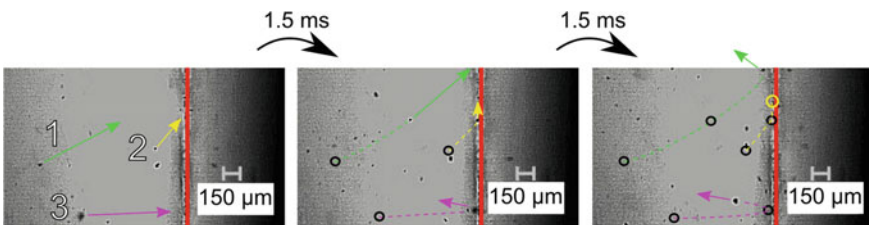

Fig. 4 Impact behavior of limestone particles hitting a steel plate in the model setup

2.4.1   Estimation of the COR with the Model of Thornton and Ning

To compare the measured values to each other and the ones expected for perfect spheres having the same bulk material properties, Eq. (8) was used [21]. This model is derived from the JKR theory by Thornton et al. and valid for a wide range [21–23]. The absolute normal impact velocity is represented by v_{imp}, whereas v_y is the yield velocity indicating the end of the fully elastic impaction regime. The yield velocity can be calculated by Eq. (9) with the limiting contact pressure p_y being approximately 2.5 times the yield stress of the material [21]. Additionally, the density ρ and E*, the average Young's modulus, of the materials is calculated from the sum of their yield abilities [21, 24].

As particle material limestone was used and the plate consisted either from marble, steel or from aluminum. For the evaluation of Eqs. (8) and (9) the bulk material properties from literature were applied: $E_{limestone} = 27.1$ GPa, $\upsilon_{limestone} = 0.47$ [25], $E_{marble} = 50.5$ GPa, $\upsilon_{marble} = 0.27$ [26], $E_{steel} = 210$ GPa and $\upsilon_{steel} = 0.3$ [27] and $E_{aluminum} = 72.2$ GPa and $\upsilon_{aluminum} = 0.34$ [27]. The yield stress of the limestone was the lowest of the aforementioned materials with 130 MPa [25].

$$\text{COR} = \left(\frac{6\sqrt{3}}{5}\right)^{1/2} \cdot \left[1 - \frac{1}{6}\left(\frac{v_y}{v_{imp}}\right)^2\right]^{1/2} \cdot \left[\frac{\left(\frac{v_y}{v_{imp}}\right)}{\left(\frac{v_y}{v_{imp}}\right) + 2\sqrt{\frac{6}{5} - \frac{1}{5}\left(\frac{v_y}{v_{imp}}\right)^2}}\right]^{1/4} \tag{8}$$

$$v_y = 1.56\left(\frac{p_y^5}{\rho_p \cdot E^{*4}}\right)^{1/2} \tag{9}$$

The estimated yield velocity for limestone particles on a steel or aluminum plate and for limestone particles impacting on a marble plate was therefore 0.016 m s^{-1}, 0.024 m s^{-1} and 0.032 m s^{-1}, respectively.

2.4.2   Rebound Behavior in the Model Set up

In order to validate the COR measured in the classifier, the normal COR was also determined in a model setup. This offers several advantages such as an easier comparison with available literature data and a more precise investigation of the impaction behavior due to the improved magnification.

To acquire reliable data, the particles in the model set-up were accelerated in a horizontal direction in a steel pipe, 100 mm long and 12 mm in diameter so that the airflow did not slow down too much but the flow had a horizontal alignment (cf. Fig. 5). The irregularly shaped particles of limestone with a diameter between 20 and 100 μm are first placed in the rubber storage box and then accelerated. A slot geometry of 1 mm in diameter focused the particle flow in the focus area of the high speed camera onto a 10 mm thick steel or marble plate.
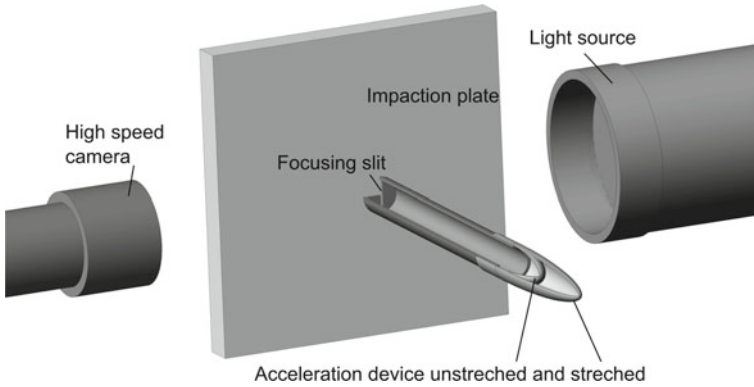
Fig. 5 Model setup to measure particle impaction properties using a microscopic lens with a high speed camera in a bright field. The particles are accelerated by the linear acceleration device

The high speed camera (Keyence Corporation, VW-600M) with a microscopic lens (VH-Z50L) was operated in bright field microscopy with a high-energy light source and a $50\times$ magnification. The frame rate was set to 230,000 fps and the shutter-speed therefore down to $1/230{,}000$ s^{-1}. In this way, the time steps between two pictures were 4.3 μs, enabling the observation of 30 μm particles with a velocity up to 60 m s^{-1}.

The measured normal COR are presented in Fig. 6 where (a) refers to limestone particles hitting a steel plate and (b) to limestone particles impacting on a marble plate. The case (a) is intended to reflect the situation in the deflector wheel which is made of aluminum with a naturally occurring thin oxide layer on the surface. In the case (b), due to similar material properties, the system resembles the particle-particle collisions between limestone particles. While in the case (a) high impact velocities were applied, in case (b) low velocities were realized. Using the above mentioned
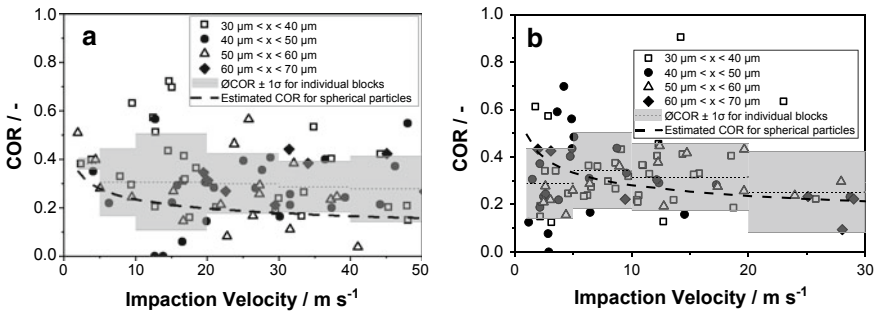
Fig. 6 Measured COR in the model set up. (Left) for limestone particles impacting on a steel surface, while (right) shows the measurements for limestone particles impacting on a marble plate with very similar material properties as the impacting particles

model of Thornton et al. the expected behavior of spherical limestone particles was included using literature material values.

The measured values refer to the projection area equivalent diameter where within the investigated size range between 30 and 70 µm no velocity dependence was observed. However, for a broader size range, this dependence should be taken into account. In general, the measured COR follows the expectation values where the scattering due to the non-spherical particle shape is superimposed. In addition, in the low velocity range, the average value does not follow the model trend. In the model, spherical particles hardly experience plastic deformation in this regime, but the impaction energy is nearly completely transferred into elastic deformation which is recovered with some dissipation in the rebound process. In contrast, for the real non-spherical particles a higher number of multiple collisions due to excentric impaction and a higher fraction of plastic deformation is expected, in particular, when the particles are impacting on their edges or corners (cf. Fig. 2, right).

2.4.3 Particle Impaction Behavior in the Classifier

The impaction behavior in the modified ATP50 was measured as shown in Fig. 7. In position a the recording direction is perpendicular to the rotation axis. The recordings
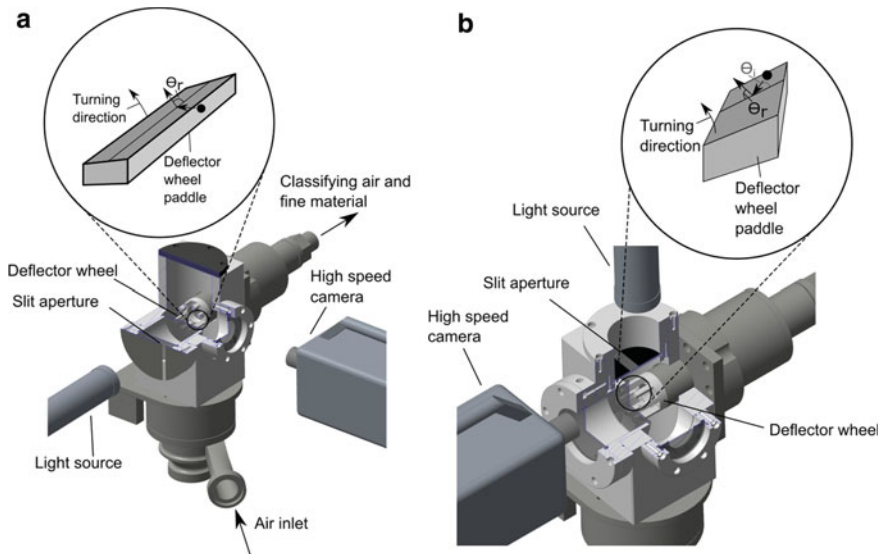

Fig. 7 Set-up of the deflector wheel classifier with the high speed camera and light source. **a** Set-up with the high speed camera aligned perpendicular to the deflector wheel axis and a schematic camera view in the circle with the long side of the paddle as angle reference side. **b** Set-up with the high speed camera aligned coaxially to the deflector wheel axis and the schematic camera view in the circle with the short side of the deflector wheel paddle as angle reference side

were performed with a Fastcam SA-X2 type 1080K-M2 high speed camera (Photron) equipped with a Nikon AF Nikkor 50 mm with an aperture opening of f# = 1.8. The used light system was a dedocool D2 (Dedotec Inc.). The frame rate was 20,000 fps and the shutter speed $1/20,670 \text{ s}^{-1}$.

In position b the camera was oriented in the direction of the rotation axis. Here a Keyence VW-600 M high speed camera with a Keyence VW-Z2 Macroobjective was employed. The recording rate was 230,000 fps with a shutter speed of $1/230,000 \text{ s}^{-1}$. The illumination system was again the dedocool D2.

The results are shown in Figs. 8, 9 and 10 where in position a the long side of the blades serve as reference system and in position b the short sides. Since in position a the particles move radially inwards (away from the observer) and exhibit little lateral motion, they appear to be nearly at rest before they are hit by the blades.
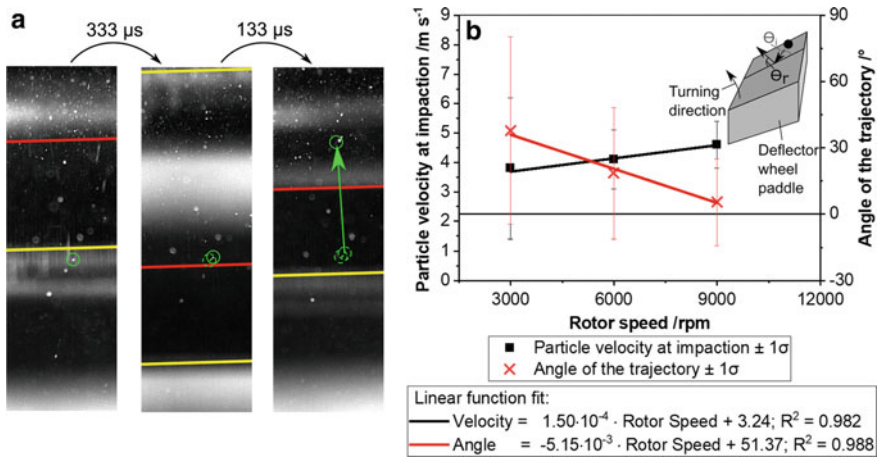
Fig. 8 Inbound behavior of particles on the deflector wheel paddle. In **a** the perpendicular view in which a particle seems to be standing still before the impaction and **b** the particle velocity is shown with its angle related to the deflector wheel blade for different rotor speeds
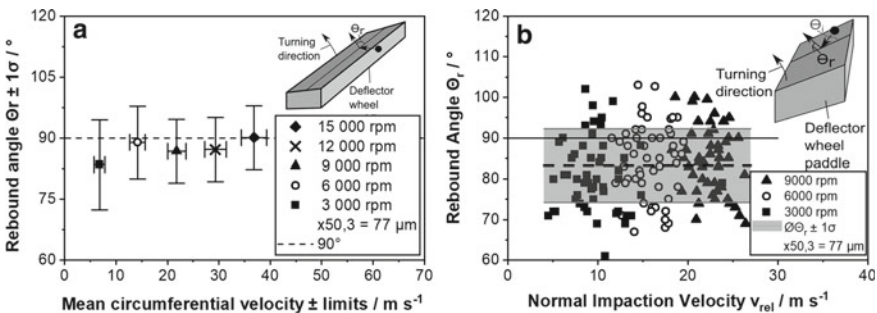

Fig. 9 Rebound angle after the particle-deflector wheel impact. In **a** the camera is aligned perpendicular to the deflector wheel axis of rotation and in **b** coaxial
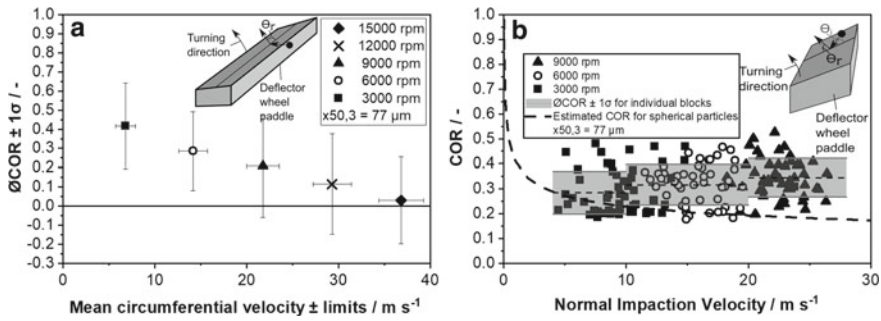
Fig. 10 COR measured in the deflector wheel classifier. In **a** the camera is aligned perpendicular to the deflector wheel axis of rotation and in **b** coaxial

This effect is demonstrated on a single particle in Fig. 8 (left). The blades move upwards (preceding side in red and persuing side in yellow). The particle trajectory is indicated by a green line while the momentary position is given by a full green circle and the previous position by a dashed green circle. Although the particle is moving radially inwards the depth of focus of the macro lens is sufficiently large to supply useful data. Therefore, the results are presented versus the mean radius-dependent circumferential speed (each point represents an average over 80 data points). The limits of the circumferential speed have been taken from the work by Spötter [17] and are indicated in Figs. 8 and 9 (left) by minimal and maximal values.

In position b a significant particle motion before the impaction is observed. The results are shown in Fig. 8. It is observed that the absolute particle velocity principally increases with the rotor speed, but is mainly dominated by a large data scattering. The modified rotor speed seems to influence the characteristics of the airflow near the deflector wheel implying to affect the particle motion in spite of their high Stokes number.

Figure 9 shows the bouncing angle of the particles after impaction on the blades. In Fig. 9 (left) the bouncing angle amounts to about 90° where at higher rotor speeds a slight focusing effect towards 90° is discerned. That the enclosed area is rather situated below 90° can be explained with the vortex (Fig. 2) and the flow through the hollow shaft for the fine powder exhaust. The approach to the 90° angle can be interpreted along the lines that the particle has less time to adapt to the air stream. The already high Stokes number increases further with increasing rotor speed.

Figure 9 (right) shows the results for the bouncing angle related to the short blade side (position b). The particles move mainly perpendicularly and are not affected by the airflow inwards between the blades. The measured bouncing angle exhibits an average value of 83°. For low rotor speeds the particle momentum before the impaction is comparable with the one transferred from the blade in the collision, while for higher rotor speeds the transferred momentum of the blade is dominating.

In Fig. 10 the normal COR is shown as a function of the impaction velocity. The COR decreases from 0.4 at 3000 rpm to 0 at 15,000 rpm where the large scattering also includes negative values. This may be due to the motion into the depth of the

wheel (parallel to the axis of rotation) is not taken into account here. With the setup shown in Fig. 6b an average contact time of 20 µs was determined. During this time the particle may undergo a deviation into the depth of the wheel which could be reflected in the results.

The results in Fig. 10b have been obtained with the coaxial setup (position b in Fig. 6). The COR were ordered according to their revolution rate and the corresponding mean velocity over each range is indicated with a dashed line and a gray area reflecting one standard deviation. The thick dashed line over the entire velocity range indicates the expected value for spherical particles based on the literature values for limestone particles and an aluminum impaction plate. The behavior of the measured data deviates substantially from the expectation for spherical particles. This observation can be explained based on the results presented in Fig. 9a. At low revolution rates, the velocity directed into the depth of the blades is larger since also the bouncing angle scatters more. At higher revolution rates, the particles rebound more often under 90°, thereby reducing the fraction of the non-detected velocity component.

2.4.4 Particle Trajectory in the Classifier at Low and High Particle Loadings

From the particle velocities shown in Fig. 8b and their angles in relation to the deflector wheel blades the particle trajectories can be derived. In the beginning, particles with high Stokes numbers are considered where the influence of the airflow is estimated to be negligible for the approach phase. In an absolute coordinate system, the particle trajectory is rectilinear (in radial inward direction), which will be transformed into a coordinate system, which rotates with the deflector wheel. In this rotating system, the trajectories shown in Fig. 11 (left) are obtained for low particle loadings where the particles can be treated individually.

In Fig. 11 the model predictions (left) are compared with the measurements of Stender [20] are shown which have been recorded with a high speed camera at a loading of $1\%_w$. The blades are discernible on the left and the right side in the pictures and the particle motion is indicated by arrows. For the calculation, particles with a size of 60 µm were assumed, while the pictures with the high speed camera were taken for limestone particles with a median diameter $x_{50,3}$ of 59.86 µm. On the left, for each revolution rate three different particle trajectories are labeled which all start on the circumference but at different positions. The red trajectory starts in the middle between the blades, while the green trajectory starts at a quarter to the persuing blade and the blue trajectory begins immediately behind the preceding blade (experiencing the longest residence time before being hit by the pursuing blade). For the blue trajectory, the spread of the flight path due to the scattering in velocity and in approach angle is indicated by the gray area. The fastest particles are indicated by the dashed line and the slowest particles by the dotted line corresponding to one standard deviation from the average velocity (blue line).
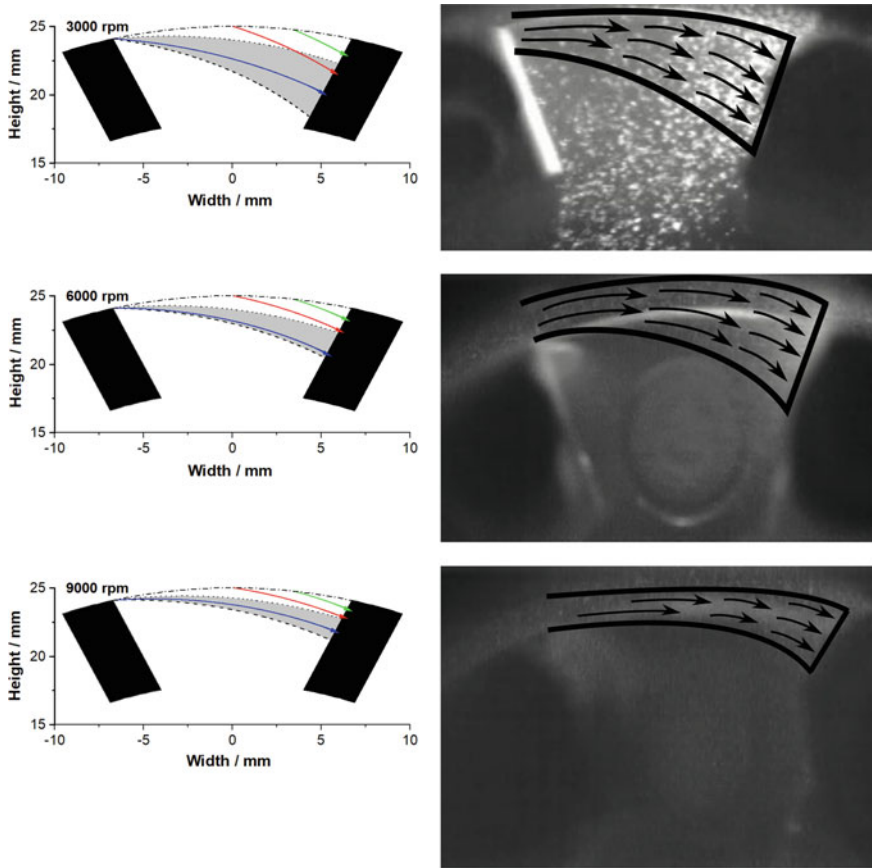
Fig. 11 Comparison between particle trajectories recalculated for low concentrations from their impaction behavior on the left side and measured at $1\%_w$ mass loading [20] on the right side. On the left side are particles with different starting positions marked in blue, red and green, while the grey area indicates a trajectory range, derived from absolute particle plus-minus standard deviation and its trajectory angle plus-minus one standard deviation

It is obvious that with increasing revolution rate the particles are more and more focused as a consequence of the reduced residence time before impaction. The calculated (single particle) and the measured approaching pattern (cloud of particles) show a strong resemblance so that in the following the expected distribution of impactions events on the persuing blade will be calculated based on single particle trajectories.

In Fig. 12 (left), the impaction probability distribution of a particle on the blue trajectory is indicated as a function of the radial position on the persuing blade. Vertical and horizontal velocity components have been varied in steps of 0.1 m s^{-1} ranging from the mean velocity minus one standard deviation until the mean velocity plus one standard deviation. The impaction probability is given as density distribution
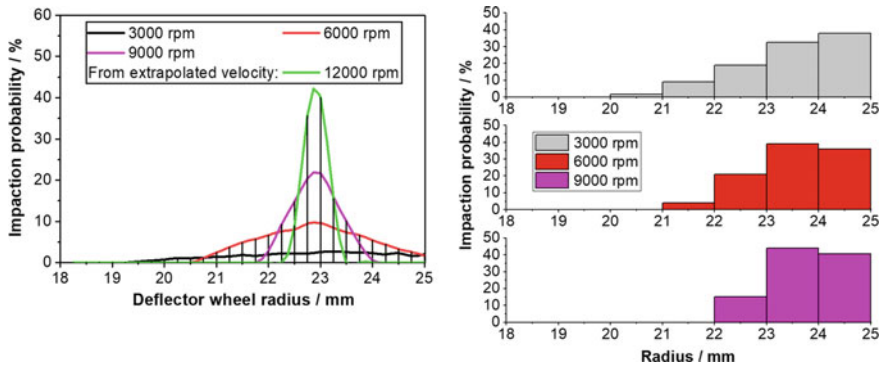
Fig. 12 (Left) Impaction probability calculated for a particle trajectory starting right after the preceding blade (blue trajectories). (Right) Impaction probability versus deflector wheel radius for a distributed addition of the particle (all along the circumference)

with an interval length of 0.25 mm. The focusing effect with increasing revolution rate is clearly visible where also the position of the maximum value varies.

Figure 12 (right) shows the cumulative impaction probability for various revolution rates when assuming that the incoming particles are evenly distributed over the circumference. The curves underline the focusing towards the outer area of the blade, but also that with increasing revolution rate the distribution becomes more homogeneous over the impaction range. At a lower revolution rate, only a few early entering particles with high radial velocity reach deep into the inter-blade volume so that the cumulative distribution is fading away towards smaller radii.

The length L of the impaction zone (Fig. 12) is shown in Fig. 13 as a function of the revolution rate. Again these results for single particles are compared to the observations of Spötter made for higher loadings [17]. The absolute values differ only by 0.5 mm from each other. The higher values of L for higher loadings may reflect the broadening effect of the particle beam due to particle-particle collisions which have been neglected in the low concentration model. This concentration-dependent effect may contribute to the lower sharpness of cut observed throughout the literature [4, 28–31]. While other phenomena such as the dispersion quality and the homogeneous particle feeding at the outer circumference of the deflector wheel may be mitigated to a certain extent by geometric and operational variations, the particle-particle collisions will always limit the achievable sharpness of cut.

Basically, it is sound to assume that with increasing revolution rate the impaction length is reduced proportionally since the particles have a shorter residence time before impaction. Applying this model strictly would result in an inverse behavior as indicated with the green curve in Fig. 13. However, this behavior is not even reached for low concentrations since the impaction length does not only depend on the revolution rate, but also on the particle entry which itself depends on the revolution rate. Therefore, an empirical power law approach between impaction length L and revolution rate f was postulated in the form of:
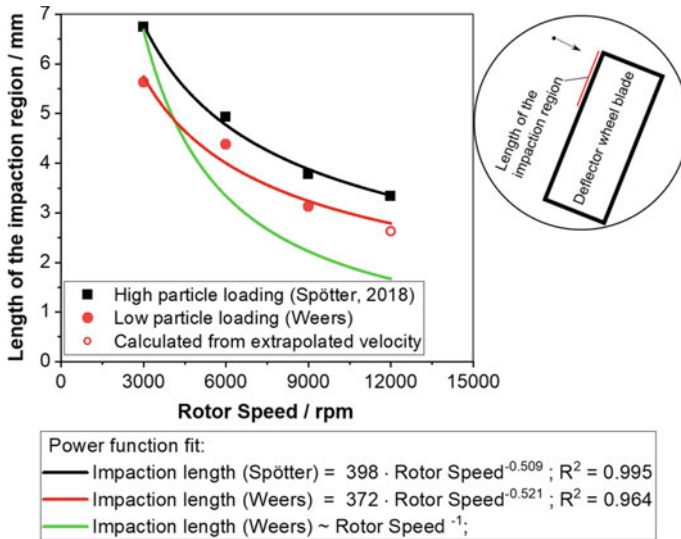
Fig. 13 Comparison between the impact length determined by [32] at a mass loading of $1\%_w$ and recalculated from the single particle impaction behavior

$$L = \text{const} \cdot f^m \tag{10}$$

It was found that values of m are close to -0.5 as indicated in Fig. 13. The good agreement of the reproduced values of L for measurements at low and high loadings with Eq. (10) indicates a more general scaling law which may apply over a broad concentration range. As will be outlined below, the value of L can be used as input parameter for a very simple model for the separation curve.

2.4.5 From Particle Impaction Derived Deflection Probability

By equating centrifugal force and drag force a cut size was determined for each radial position on the blade. For the considered particles with high Stokes numbers, it was assumed that the particle trajectory is only influenced by the radial motion inwards but otherwise remains unaffected by the flow field between the blades. The force balance was evaluated right after the particle impact on the blade. Since the airflow around the particle is close to the transition regime, the cut size was calculated iteratively taking the velocity-dependent drag coefficient into account. The cut size was calculated considering the volume V and the surface A of the particle:

$$\frac{V}{A} = \frac{1}{2} \frac{\rho_{air}}{\rho_p} \frac{v_{rad}^2}{v_{tan^2}} \cdot c_D \cdot R \tag{11}$$

where ρ_{air} and ρ_p are the densities of air and the particle, respectively, v_{rad} is the radial velocity and v_{tan} the circumferential velocity, R the radial distance to the rotation axis and c_D the drag coefficient [33]:

$$c_D = \frac{24}{Re}(1 + 0.15\,Re^{0.687}) \qquad (12)$$

where Re is the particle Reynolds number.

For non-spherical particles, the usual definition of the particle diameter is not constructive, so that the volume equivalent diameter will be used in the following. In Table 1 the volume-to-surface ratio is listed as a function of the particle geometry. It is obvious that with increasing deviation from the spherical geometry this ratio decreases influencing the cut size due to a different drag force.

To obtain a separation curve for the outlined model the cut sizes need to be weighted with the radially dependent impaction probability (Fig. 12, right). In Fig. 14 the separation curves are shown for revolution rates of 3000, 6000 and 9000 rpm. Basically, the calculated single particle separation curves reflect the experimental results over a certain range. The largest deviations were found for large and small particles, while the x_t values are well recovered at high revolution rates and even for 3000 rpm the values of x_t differ only by 20%. In these calculations, an idealized flow was assumed which seems to be audacious when looking at Fig. 2 (left). The vertically moving-up vortex is expected to also affect the flow pattern around the horizontally revolving deflector wheel and, therefore, the particle separation. With increasing revolution rate it is expected that the influence of the vertical vortex diminishes which is supported by the better agreement of calculated and measured separation curves in Fig. 14.

In summary, it was shown that for particles with high Stokes numbers the separation curves at high loadings can reasonably be approximated from the trajectories measured at low concentrations and from the particle shape factor. However, for particles with lower Stokes numbers, this approach has to be extended to include the flow field between the blades as outlined in the following.

Table 1 Comparison of the volume-to-surface ratio for different regular particle geometries

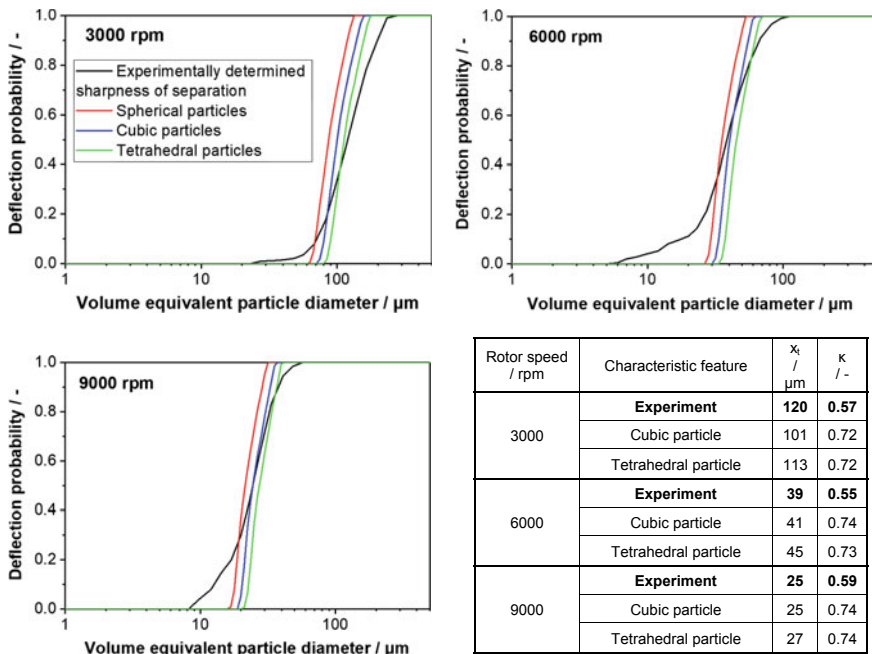| Shape	Volume/Surface
Sphere	$\frac{1}{6}x \approx 0.167\,x$
Cube	$\frac{1}{6}\sqrt[3]{\frac{\pi}{6}}x_V \approx 0.134\,x_V$
Regular tetrahedron	$\sqrt[3]{\frac{\pi}{2}}\frac{1}{6\sqrt{3}}x_V \approx 0.112\,x_V$

Rotor speed / rpm	Characteristic feature	x_t / µm	κ / -
3000	**Experiment**	**120**	**0.57**
	Cubic particle	101	0.72
	Tetrahedral particle	113	0.72
6000	**Experiment**	**39**	**0.55**
	Cubic particle	41	0.74
	Tetrahedral particle	45	0.73
9000	**Experiment**	**25**	**0.59**
	Cubic particle	25	0.74
	Tetrahedral particle	27	0.74

Fig. 14 Curve of separation derived from the particle impaction behavior compared to experimentally determined ones

2.5 Airflow

In literature, numerical simulations and experimental characterizations of deflector wheel classifiers with different designs have been performed by several groups [28, 34–37]. Usually, the momentary flow pattern was investigated. For instance, Sun et al. simulated the flow field within the complete apparatus with CFD [38], while Toneva et al. reproduced the gas flow in the channel between the blades using the PIV technique and simulations [39]. Also, Stender imaged the channel vortex with a high speed camera and tracer particles having a Stokes number of approximately 1 [20]. The vortices occurring at fast revolving parts can hardly be suppressed [40] so that they have a significant influence on the separation behavior. In spite of the highly turbulent flow behavior in the interior of the deflector wheel classifier and between the blades, so far no average flow pattern has been provided in the literature. Here this task was tackled through 2D-LDV measurements where the average flow velocities were obtained by averaging over 100,000 tracer particles per measuring point.
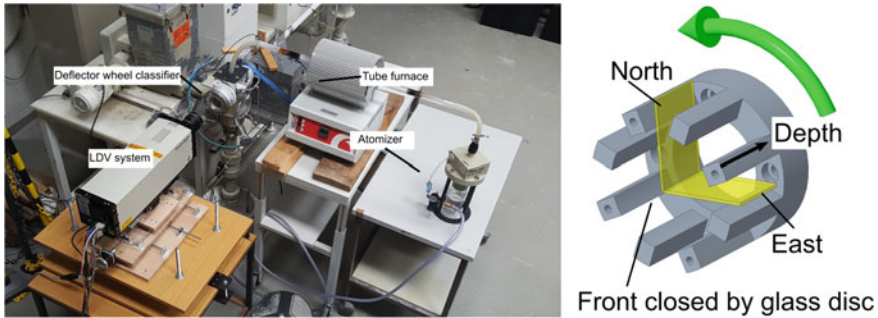
Fig. 15 (Left) Measurement setup with the tracer particle generation (right part) and the LDV system aligned with the deflector wheel classifier. (Right) shows the area of interest ("North" and "East") in the deflector wheel for the conducted measurements along with the deflector wheels direction of rotation

2.5.1 Experimental Setup

For the determination of the average flow velocity, a 2D-LDV system of the TSI Inc. (TR-SS-2D) with a Bragg cell and a focal length of 350 mm was used. The metering modes were optimized for each measuring position with respect to the burst efficiency. The rotation of the deflector wheel was directly recorded by the LDV system using an optical revolution sensor (Avibia, AV-ROS-W) with a measuring range of 1–250,000 rpm. The LDV was mounted on a horizontal traverse which could be moved in steps of 40 μm. The height was adjusted manually using threaded rods where the outer edge of the deflector wheel served as reference.

The tracer particles were produced by nebulization (Pallas, Type AKG2000, 4 bar pressure) of a $10\%_w$ NaCl solution with subsequent drying by passing a tube furnace (Carbolite Gero, Type MTF 12/38/250) at 400 °C. The tracer particles were added on the top close to the observation area (cf. Fig. 15). The observed area is shown in Fig. 15 (right) including the revolution sense of the deflector wheel. For the following results, the origin of the coordinate system is always the center of the deflector wheel immediately behind the glass disc. Due to its refraction behavior, the rotating glass disc represents a challenge for the measurements. The setup was verified with velocity measurements at the rear area of the deflector wheel.

2.5.2 Measurement Results

In Sect. 2.4.5 the hypothesis was put forward that the perpendicular vortex has a negative impact on the particle separation between the blades of the deflector wheel. In this chapter, first the angular-dependent flow fields measured at 9000 rpm at depths of 6, 9, 12 and 15 mm will be shown and discussed (cf. Fig. 15, right). The chapter is focused on the average flow velocities.
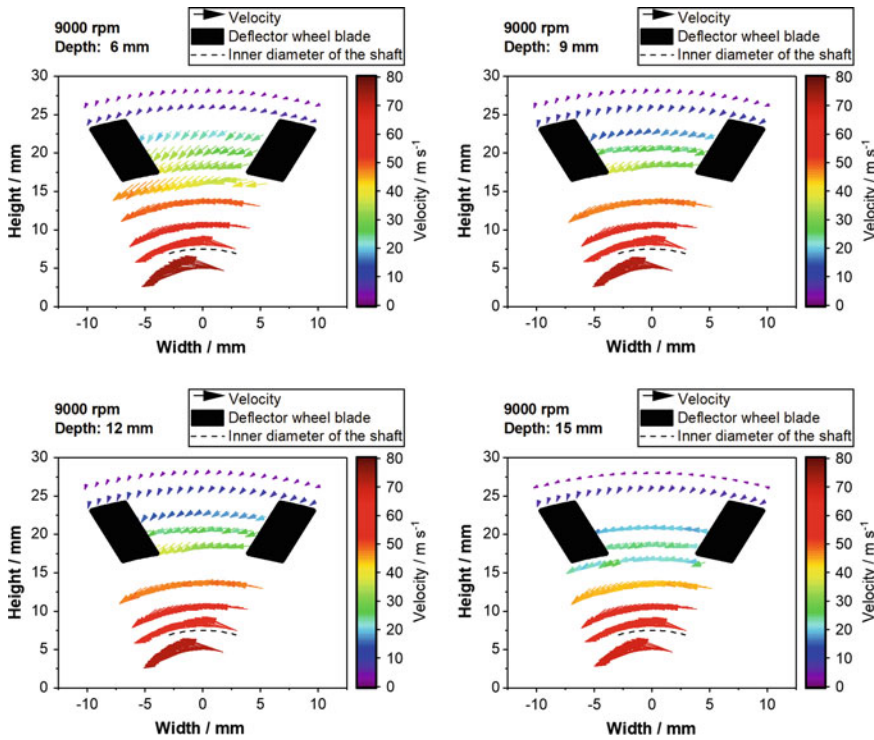
Fig. 16 Angular resolved presentation of the LDV measurement at 9000 rpm for the depths of 6, 9, 12 and 15 mm

In Fig. 16 the angularly resolved flow profiles are shown. The deflector wheel blades are indicated as black areas on the left and on the right. The velocities measured in one plane (cf. Fig. 15, right) have been split over the rotation angle and the direction was corrected for the rotation. It can be seen that the air outside of the deflector wheel is accelerated by the wheel. Due to the suction in the center, the airflow is slightly directed inwards. In between the blades the average velocity is stronger directed inwards closer to the glass disc compared to the rear area. This phenomenon may be explained by a secondary vortex in the outside domain which creates a low pressure area like it was found by Sun et al. in simulations of a similar classifier [38]. In the center of the wheel, the airflow is significantly more rectified and, due to the conservation of angular momentum and continuity, the velocity increases strongly with decreasing radius. At a radius of 6 mm, however, the airflow is directed outwards. Here the tracer particles cannot follow the gas flow sufficiently which is a consequence of the high circumferential velocity in combination with the decreasing radial velocity which is induced by the suction at the center.

Figure 17 shows the spatial distribution of the average air velocity at revolution rates of 3000 rpm, 9000 rpm and 15000 rpm, respectively. Each black point indicates a measuring position. On the left side the tangential velocities are shown and on
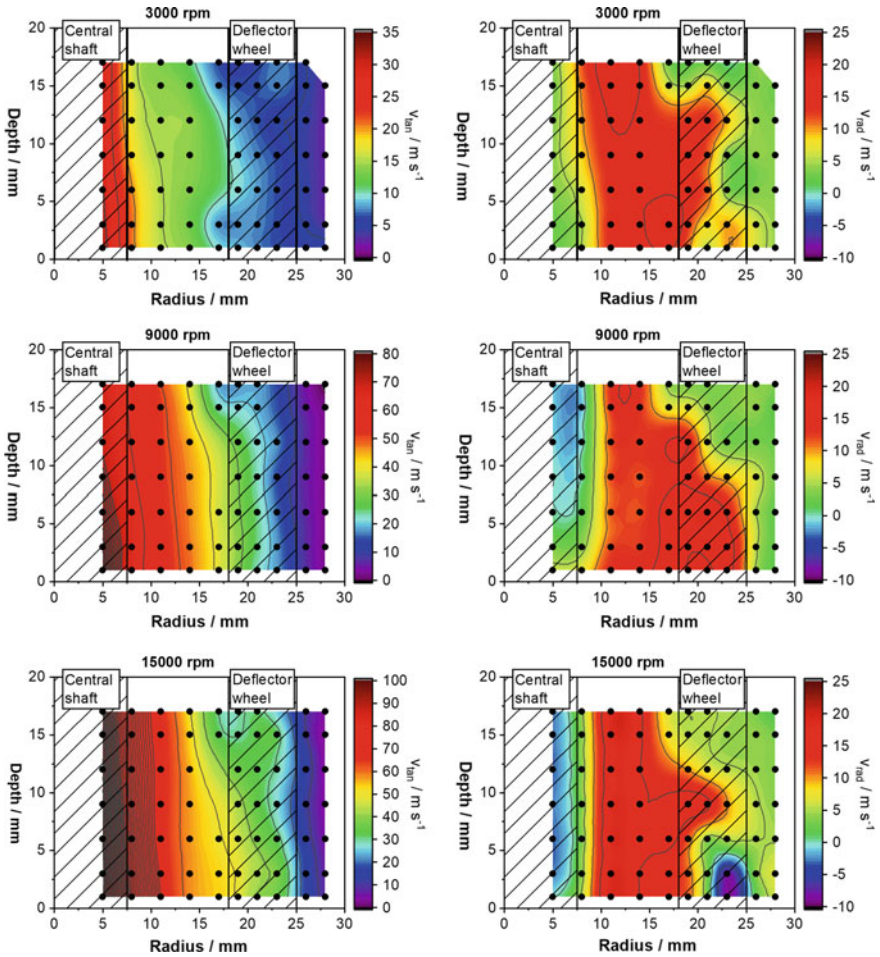
Fig. 17 Mean tangential (left) and radial (right) air velocities in the "North" region of the deflector wheel

the right side the radial velocities. The behavior of the tangential velocities is very similar for all three revolution rates. Initially, there is a certain acceleration from the outside area inwards before the deflector wheel imposes its angular speed. At the outer edge, the measured air velocity is slightly lower than expected from revolution rate and wheel radius. At 3000 rpm the expected value at the edge is 8 m s^{-1}, at 9000 rpm 24 m s^{-1} and at 15,000 rpm 39 m s^{-1}, respectively. At the inner edge of the wheel, the measured tangential air velocity is slightly higher than the wheel speed which is due to the conservation of the angular momentum and the acceleration of the air by the wheel. Subsequently, the classifying airflow follows an eddy motion. Towards the center, the velocity is reduced due to viscous friction which, however,

could not be proven with LDV since the tracer particles were rarely carried into this area.

For the radial velocities, the same color code was used. For all three revolution rates, the radial velocity was negative in the central shaft area as a consequence of the centrifugal force affecting the tracer particles. Between suction and the inner edge of the wheel, the airflow is very rectified due to the continuity condition. Between the blades, the radial velocity varies significantly. Based on a mass balance, the radial velocity at the outer edge of the wheel is about 7 m s^{-1} and increases up to ca. 12 m s^{-1}.

While at 3000 rpm a relatively uniform velocity profile is established, which follows the above constructed picture, at 9000 and 15,000 rpm the profiles are much less homogeneous The formation of the profile is due to the secondary vortex discussed above.

The deflector wheel considered here exhibits an experimental sharpness of cut of 0.57 at 3000 rpm, 0.59 at 9000 rpm and 0.50 at 15,000 rpm. Comparing these observations with the flow fields shown before, the reduction of the sharpness of cut at high revolution rates is not surprising.

This effect will be included in the calculated separation curves shown in the following.

A parameter which affects the sharpness of cut is the rotational symmetry of the airflow. At low revolution rates, radial and tangential velocities at the outer edge of the wheel are very similar and rather low. It is expected that the airflow is more symmetrical at higher revolution rates where the circumferential velocity of the wheel dominates. In Fig. 18 the average tangential velocities are shown on the left and the radial velocities on the right for different revolution rates. The measurements on the "North" side are indicated in black (cf. vertical plane at radii of 23 and 26 mm shown in Fig. 15, right) and the "East" side in red (horizontal plane mostly at a radius of 25 mm in Fig. 15, right).

Generally, it is observed that the tangential velocity is more homogeneous than the radial velocity which was already found for the North side in Fig. 17. At the different revolution rates, local minima appear which are not at the same positions for North and East measurements. This indicates that the vortices in the apparatus affect the flow around the wheel in different ways. The radial velocity, on the other hand, exhibits a more pronounced and rather systematic divergence. While on the North side a mostly inwards oriented flow is encountered, the radial velocity on the East side is nearly zero up to moderate revolution rates. Only at higher revolution rates, the radial velocity is slightly oriented outwards. This missing rotational symmetry needs to be taken into account in the following considerations about the particle separation.
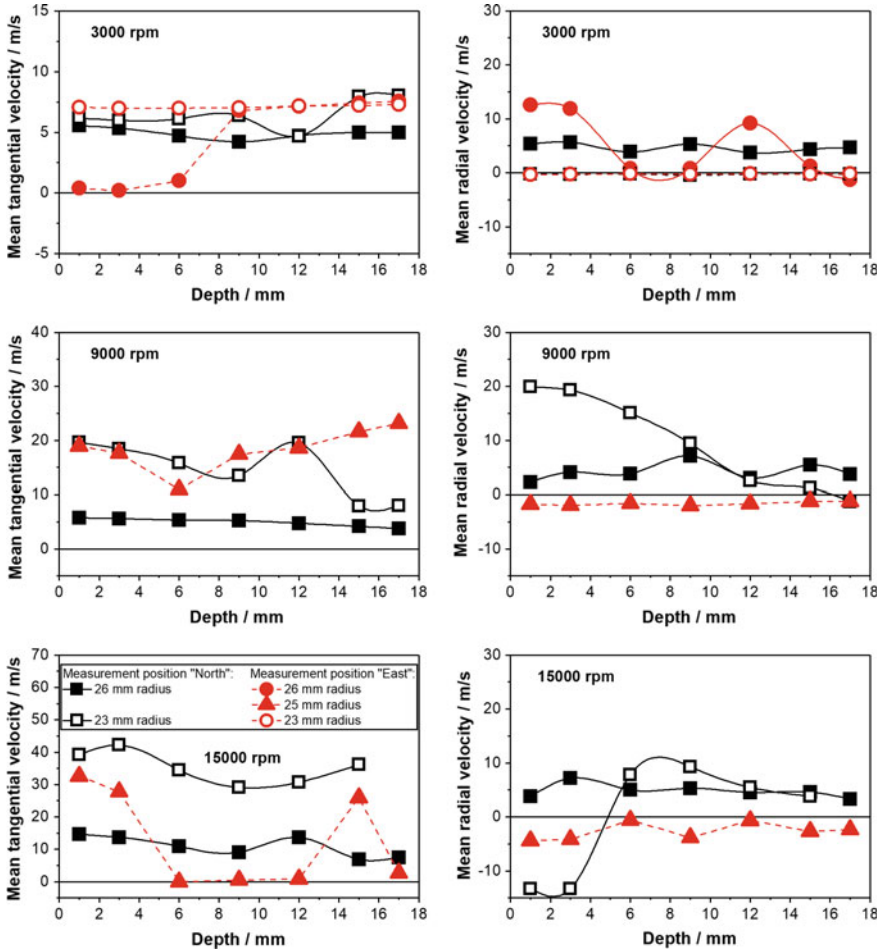
Fig. 18 Estimation of the rotational symmetry of the airflow between the deflector wheel blades for different rotor speeds. Measurement position "North" is related to the upper area, shown in Fig. 15, right, while "East" is related to the right side horizontal area

2.5.3 Deflection Probability Derived from Particle Impaction and Measured Airflow

From the measured flow profiles and the impaction behavior shown in Fig. 12 a deflection probability, i.e. a separation curve for the deflector wheel classifier can be determined. As outlined in Sect. 2.4.5, the grade efficiency curve is calculated. Figure 19 shows deflection probability curves calculated for tetrahedral particles at 9000 rpm. The curves have been calculated based on the measured radial and tangential velocities for different planes along the depth between the blades. In addition, the measured separation curve is indicated by the bold black line in Fig. 19. Since for

Fig. 19 Deflection probability for different depths at 9000 rpm for tetrahedral particles calculated with measured circumferential and radial air velocity
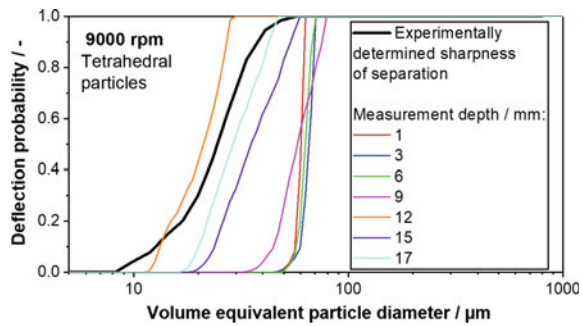
the used deflector wheel classifier the particles are added into the apparatus without previous dry dispersion, it is possible that very fine particles (ca. 10 μm) are attached to coarser particles and are separated with them. This may explain why the measured separation curve is not enclosed by the calculated curves in the range below 10 μm.

If it is assumed that the particles enter the wheel at each depth with the same frequency, an overall separation curve can be constructed by adding all the individual curves shown in Fig. 19. The results of this procedure are shown in Figs. 20 and 21 including the calculated standard deviation. Besides tetrahedral particles also the results for cubic and spherical particles are presented. Particles with a low Stokes number are more prone to reach positions of high radial velocities between the blades. An analogous phenomenon is known in the flow measuring technology regarding the LDA method where tracer particles of a higher velocity exhibit a higher probability to be detected [41]. Therefore, it may be assumed that the reality lies in between the averaged separation curves and the ones weighted with the radial velocity. Figure 20 shows separation curves derived from the airflow measurements which can be compared with the ones based on the impaction probability shown in Fig. 14. In Fig. 14 the deviations between predicted and measured separation curves were the highest für 3000 rpm, while at higher revolution rates a good agreement of calculated and measured cut sizes was observed.

In comparison with the results in Fig. 14, the findings in Fig. 20 indicate that not only the cut size but also the sharpness of cut can well be predicted by using the real flow field. At low revolution rates, the experimental separation curve runs close to the calculated one based on the weighted radial velocity. This is due to the low revolution rate and the corresponding low influence of the airflow. With increasing revolution rate, the circumferential velocity raises from 8 m s^{-1} at 3000 rpm to 39 m s^{-1} at 15,000 rpm. Hence the Stokes number increases and the particles enter the apparatus with less preclassification (cf. Fig. 20). At 9000 rpm, it is expected that the separation curve lies in between the lower and the upper limit. However, the experimental separation curve is shifted to smaller sizes and is situated on the left of the weighted and unweighted curves. A possible explanation may be related to the missing rotational symmetry and/or a secondary vortex which focuses the particles preferentially into one plane along the depth.
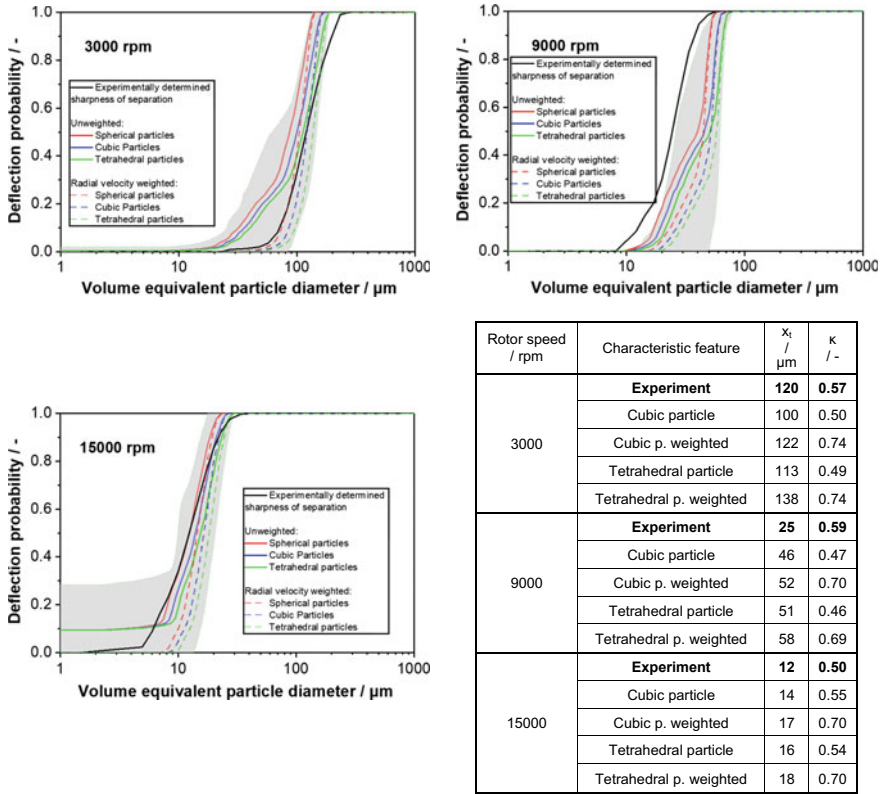
Fig. 20 From measured mean airflow and particle impaction behavior derived deflection probability

In this work, the model concept presented in Fig. 1 will be followed. Particles enter the space between the blades as collective and they are decelerated by the particles, which had already been reflected by the blade before they impact on the blade themselves. Based on the high loading, it is assumed that particle-particle collisions ensure that at the outer edge of the particle cloud the particles have the same velocity as the circumferential speed of the wheel. Therefore, in Fig. 21 it is checked how far the prediction of the separation properties remains correct when instead of the measured tangential velocity the calculated one, i.e. circumferential velocity, is used. As radial velocity, the measured one is used.

In general, Figs. 20 and 21 show hardly any deviations. The separation curves for 3000 and 15,000 rpm exhibit nearly identical parameters, but the experimental separation curve at 9000 rpm is much better reflected by the unweighted prediction.

This result supports the validity of the model outlined in Fig. 1. This means that the Molerus model can be applied for particles with high Stokes numbers when cut size and sharpness of cut are deduced from the measured radius-dependent impaction probability of the particles and the distribution of the radial air velocity. As a first
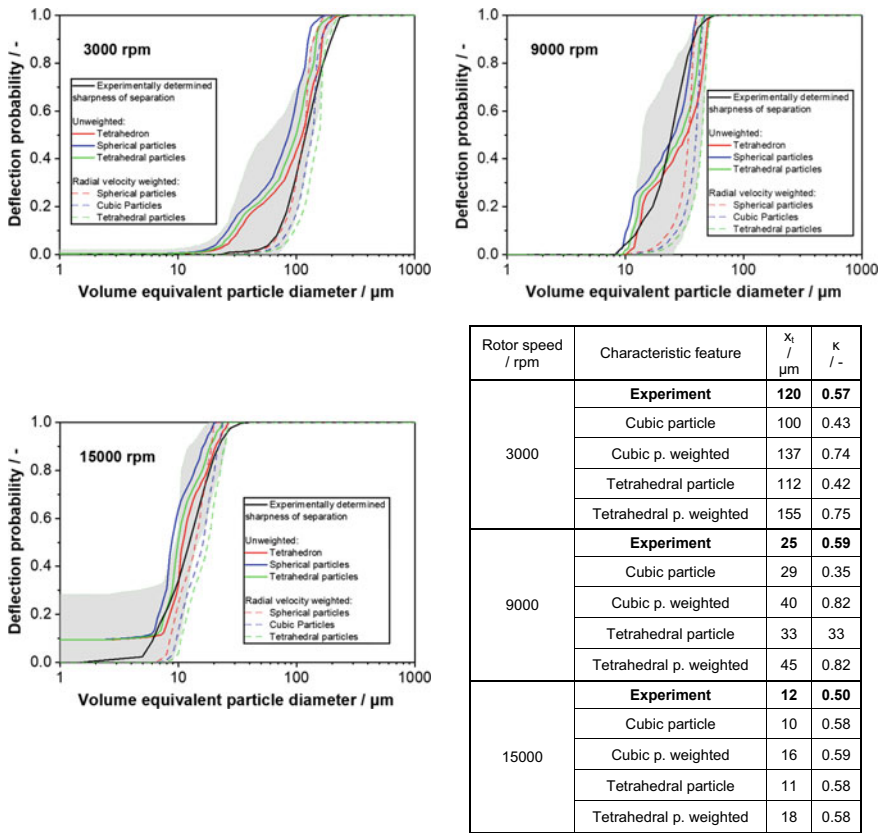
Rotor speed / rpm	Characteristic feature	x_t / µm	κ / -
	Experiment	**120**	**0.57**
	Cubic particle	100	0.43
3000	Cubic p. weighted	137	0.74
	Tetrahedral particle	112	0.42
	Tetrahedral p. weighted	155	0.75
	Experiment	**25**	**0.59**
	Cubic particle	29	0.35
9000	Cubic p. weighted	40	0.82
	Tetrahedral particle	33	33
	Tetrahedral p. weighted	45	0.82
	Experiment	**12**	**0.50**
	Cubic particle	10	0.58
15000	Cubic p. weighted	16	0.59
	Tetrahedral particle	11	0.58
	Tetrahedral p. weighted	18	0.58

Fig. 21 From measured mean air radial velocity with calculated tangential velocity and particle impaction behavior derived deflection probability

approximation, the entry trajectories of the particles allow calculating the cut size (cf. Fig. 14). For particles with low Stokes numbers, however, the rotational symmetry of the airflow gains on importance while the characteristics of the particle entrance into the space between the blades become less significant. In turn, this means that for another deflector wheel classifier particle entrance conditions and flow fields are needed for the prediction of the separation performance.

2.6 Transient Aspects

Although the microprocesses on the deflector wheel are very rapid (typically the residence time of an air volume within classifier is 80 ms), the classification process exhibits an instationary behavior over many minutes up to an hour. This behavior

is due to the partition of the apparatus in two different zones. In Fig. 22 (left) a cross sectional view of the classifier is presented. The separation of the particles on the deflector wheel has been elaborated exhaustively above. However, the fate of the coarse, deflected particles was not further discussed so far. In the cone between the deflector wheel and the coarse powder outlet, an upward airflow encounters the settling coarse particles. While for an airflow of $75\,\mathrm{m^3\,h^{-1}}$ a cut size of ca. $10\text{--}100\,\mu\mathrm{m}$ is observed on the deflector wheel for limestone (depending on the revolution rate), the cut size obtained from the balance of gravity and drag force in the coarse material cone is expected to be in the range of $400\,\mu\mathrm{m}$. Thus, the coarse particles cannot leave the classifying chamber as individual grains, but due to the rotational airflow of the incoming air, they will be concentrated near the walls forming streaks. These streaks will finally end up in the coarse material container similar to a cyclone separator.

The accumulation of powder in the classifier chamber by the mechanisms discussed above, which is called hold-up, may affect the effective loading and thereby the classification performance. Therefore, the effective loading was determined with the setup shown in Fig. 23, where a 3-way valve (V03) was introduced into the fine powder line. In order to determine the amount of powder in the hold-up, the classifier was running until a steady state was reached (cf. below). Then, the feeding was stopped (X01) and the fine powder line was blocked with the 3-way valve (V03) where the aspirator at the end was fed with environmental air. Since the original airflow ceased the particles in the hold-up settled onto the closed valve (V01) of the coarse material container which was then cleaned. By opening the V01 valve the hold-up material could be collected. The effective loading was found to be much higher than the nominal value based on the feed as shown in Fig. 22. The effective loading lies in the range between medium and high pressure pneumatic conveying [42].

It was found that in the steady state the effective loading was not influenced by the operational parameters. However, the time to reach the steady state may very well depend on the operation conditions. Spötter et al. investigated the starting-up phase for a revolution rate of 9000 rpm and mass loadings of $1\text{--}5\%_\mathrm{w}$ of limestone particles. The results in Fig. 24 (left) show that with decreasing loading the time
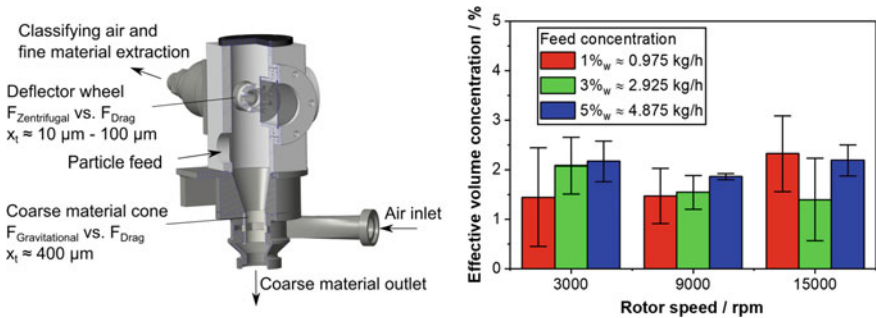

Fig. 22 (Left) The two cut sizes in the operation of the deflector wheel classifier. (Right) Effective mass concentration
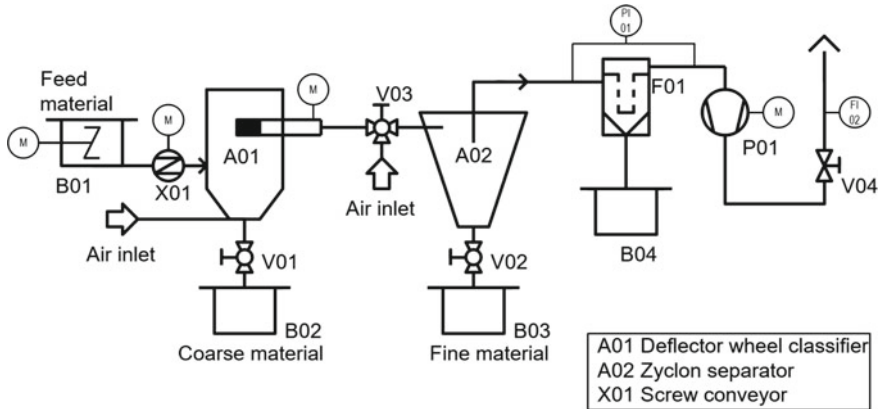
Fig. 23 P&ID of the deflector wheel classifier with the set up for the hold-up determination
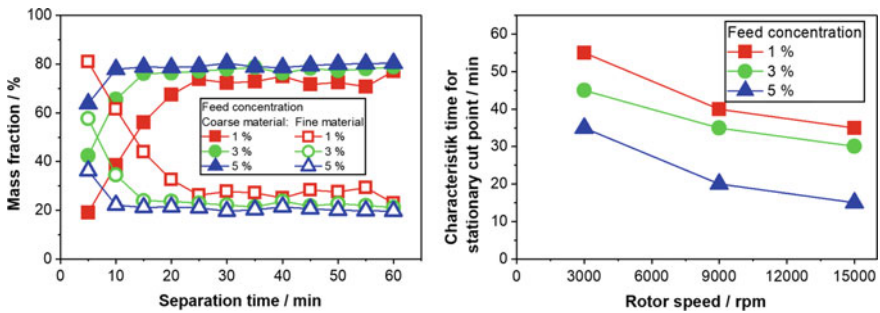

Fig. 24 (Left) Coarse and fine fraction in relation to the process time for 9000 rpm and a feed concentration from 1 to 5%$_w$, (right) characteristic time to reach the stationary cut size in relation to the rotor speed and feed concentration [32]

to reach steady state increases and may be as long as 30 min for 1%$_w$. Also the revolution rate influences this time where the steady state is reached earlier at higher revolution rates (cf. Fig. 24, right).

This characteristic time is needed to achieve a steady state between incoming feed rate and removal rate for fine and coarse material. Within this conception, the hold-up represents a storage volume which has to be filled before inflow and outflow are balanced. The speed of filling this storage volume can be influenced either by the feed rate (i.e. loading and flow rate) or by deflection rate (i.e. revolution rate). It would be interesting to see if this conception applies also for the variation of other parameters which influence the cut size such as the wheel radius.

3 Screening Technology

3.1 Introduction

Screening is a process for the separation of particulate solids. In this process, a disperse particle collective is transported over a moving surface and separated by a screen. During this process, the particle size x of the feed material is constantly geometrically compared with the mesh size w of the screen bottom. When the particles are successfully transported through the screen mesh, the feed material is separated into a coarse material fraction (c) and a fine material fraction (f). Whether and with what probability a particle passes through a sieve opening depends on the ratio particle size to mesh size (x/w), the particle shape and mesh shape, the orientation of the particle at the point of contact and the angle of impact in respect to the sieve plane. Figure 25 shows the relationships between the correspondence of a particle and the sieve mesh. The near size particle (x ~ w) present in the feed material is of particular importance for the screening success. They influence the degree of selectivity and screening quality.

In the case of a continuous screening process, the transport velocity and the size of the screen determine the dwell time of the screenings on the screen. The dwell time is mainly responsible for the success of the separation. Furthermore, the possibility of how the particles can arrange above a screen opening is important. This depends decisively on the layer thickness of the material on the sieve. If there is a multiparticle layer, this is referred to as thick film screening, in which the required relative movement of the particle must be ensured by loosening or circulating the screening
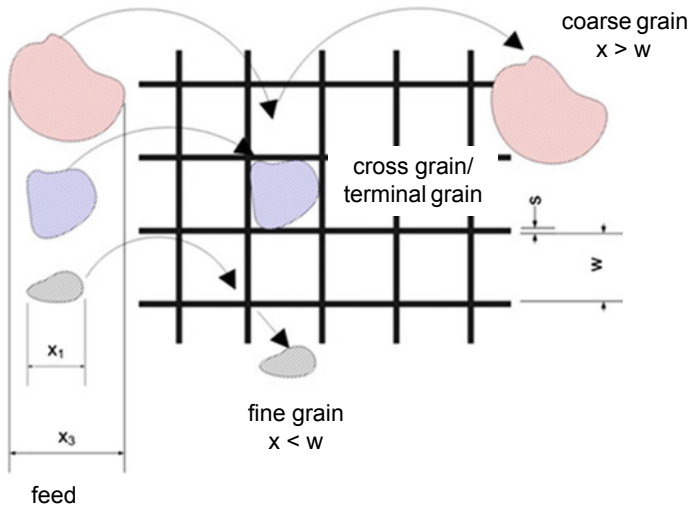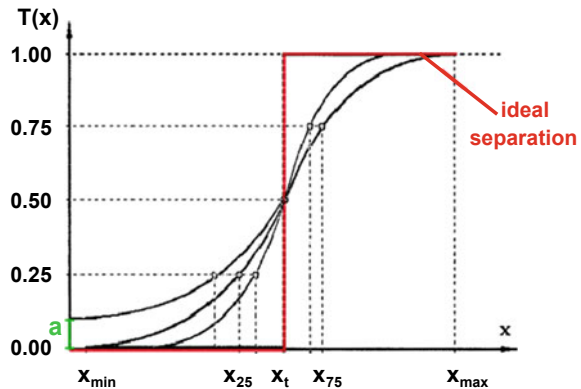

Fig. 25 Screening as a comparison between particles with size x and mesh with aperture w

Fig. 26 Typical functions of classification (grade efficiency curves)

material. On the other hand, with thin film screening, the kinetics of the screening process depends only on the conditions that the particles find for passing through the screen openings [1].

The screening machines are divided into flat screens with a movement of the sieve bottom in the plane, throw screens (movement perpendicular to the sieve bottom plane) and tumbling screens in which a circular oscillation in the plane is superimposed by a tumbling stroke component. The quality of the screen classification is determined not only by the parameters of the feed material (particle size distribution, shape, density and interaction potential) but also by the feed material mass, the design of the screens used (mesh size, mesh shape, wire thickness and open screen area) and in particular by the influencing variables of the screening machines such as amplitude, frequency and angle of inclination. In practice, there is usually no ideal separation of the particle fill, but a part of the particles with $x < w$ remains on the sieve and thus remains in the coarse material and a part of larger particles is found in the fine material as misplaced particles. Figure 26 shows typical separation functions $T(x)$. The ideal separation is characterized by the jump function. The "dead flow a" describes the proportion of particles that have not been classified. The closer the separation function is to the ideal separation, the sharper the separation process is.

To characterize a separation, the passages or the distribution sum functions for the feed material $Q_{3A}(x)$, the coarse material $Q_{3G}(x)$ or the fines $Q_{3F}(x)$, as well as the mass flows, must be determined.

3.2 Separation Function for a Steady State Screening Process

Knowledge of the separation function $T(x)$ is the most important information for describing the sieve classification process. Various approaches are known from the literature. All models are dependent on three model parameters:

a   "dead flow", function value for $T(x \to 0)$; applies: $0 \leq a \leq 1$

x_t corresponds to the median separation limit of the grade efficiency curve, if a $= 0$

α measure of selectivity; applies: $0 < \alpha < \infty$.

A model to describe a separation function was described by Plitt [2]. Here the classification is postulated as a reversal of an ideal mixture.

$$T(x)_{Plitt} = (1 - a) \cdot \left(1 - \exp\left(-\ln(2) \cdot \left(\frac{x}{x_t}\right)^{\alpha}\right)\right) + a \tag{13}$$

Molerus and Hoffmann [4] presented a separation function for air classifiers.

$$T(x)_{Molerus} = \frac{1 - a}{1 + \left(\frac{x_t}{x}\right)^2 \cdot \exp\left(\alpha \cdot \left(1 - \left(\frac{x}{x_t}\right)^2\right)\right)} + a \tag{14}$$

For all the models above, the model parameter α is directly related to the sharpness of cut or selectivity $\kappa_{25/75}$ according to Eder [1]:

$$\kappa = \frac{x_{25}}{x_{75}} \tag{15}$$

Within the scope of this project, a new improved separation function for the stationary screening process was developed [4, 10, 43]. This function contains a new selectivity parameter β.

$$T(x) = \cdot (1 - a)\left[1 - \left(1 + 3 \cdot x'^{(((x')+\alpha)\cdot\beta)}\right)^{-\frac{1}{2}}\right] + a \tag{16}$$

In this, a is the dead flow for T(x $\rightarrow$ 0), α and the newly introduced parameter β as a measure of the selectivity of the sieve classification. For β the following applies: $0 < \beta < \infty$. Furthermore, in Eq. (4) the dimensionless particle size x' is defined as the quotient of the particle size x to the median value of the grade efficiency curve x_t (for a $= 0$):

$$x' = x/x_t \tag{17}$$

3.3   Transportation of Particles on Vibrating Surfaces

Particles carry out specific movements on a vibrating surface, which depend on the frequency, amplitude, inclination of the sieve bottom and the dispersity properties of the particles as well as the concentration or number of the particles (thin or thick film sieving). For the analysis of the movements of the particles on vibrating surfaces an electrodynamic vibration exciter was used, which simulates the sieve

movement. It performs a linear, frequency- and amplitude-dependent movement in vertical direction. A function generator from Hameg Instruments GmbH transmits a sinusoidal standard signal to the power amplifier TGA 251 from RMS GmbH, which transmits the amplified standard signal to the shaker. Depending on the amplification factor, the amplitude of the design of the base plate or sieve bottom is varied. Figure 27 shows the experimental setup of the shaker system. The high-speed camera VW-9000 from Keyence is used to track the particle movement.

Initially, investigations were carried out to describe the movement of individual particles on the vibrating support. Spherical glass particles with a particle size of x = 3.3 mm were used. Figures 28 and 29 show the motion profile of this particle at a frequency of f = 60 Hz and f = 45 Hz and corresponding amplitudes of 1.6 and 2.1 mm.

It clearly shows the dependence of the movement pattern of the particles on frequency and amplitude at low number densities (thin film). Completely different conditions are observed when the particle concentration or the number density increases significantly. These conditions are present in a real screening process. This is a superposition of convective transport and segregation. The experiments described below
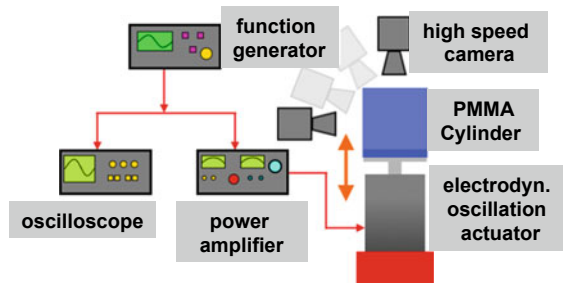

Fig. 27 Experimental set, electrodynamic vibration exciter

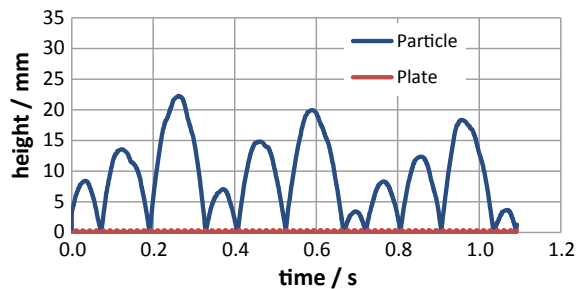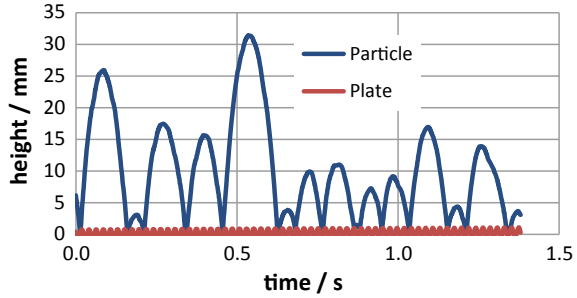**Fig. 28** Single particle movement, f = 60 Hz, A = 1.6 mm

Fig. 29 Single particle movement, f = 45 Hz, A = 2.1 mm

were carried out with quartz particle fills with a mean diameter of $x_{50,3} = 1$ mm and a quantity of m = 250 g. The dimensionless acceleration number Γ was determined for each experiment:

$$\Gamma = \frac{A\,\omega^2}{g} = \frac{4A\,\pi^2 f^2}{g} \tag{18}$$

Figure 30 shows that for the upward movement of the particles a clear influence of the amplitude is to be recognized but the influence of the frequency is not so significant.

The following Figs. 31, 32 and 33 show the movements of the particles on moving surfaces with different amplitudes and frequencies.

At low amplitudes, there is a harmonious movement of the particles on the vibrating surface. With an increase in amplitude, a significant polarisation of concentration takes place at certain locations. This results in the sieving of a thin layer at some points on the sieve surface and thus a correspondence of the particles and the mesh is possible. At other points, no unhindered passage through the meshes is possible due to the polarization.
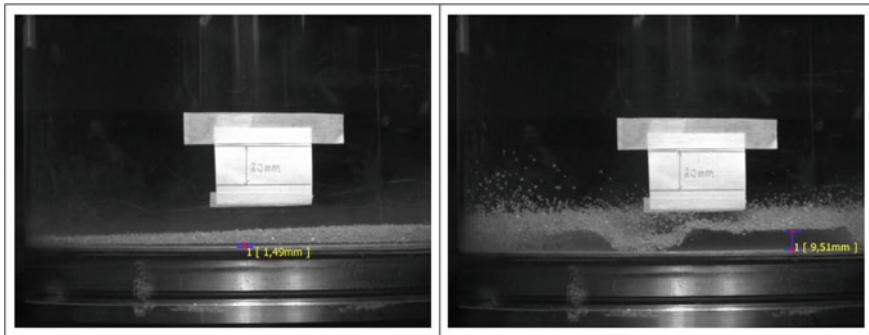

Fig. 30 Movement of the particle layer: (left) f = 60 Hz, A = 0.62 mm, Γ = 8.98 and (right) f = 20 Hz, A = 3.86 mm, Γ = 6.21
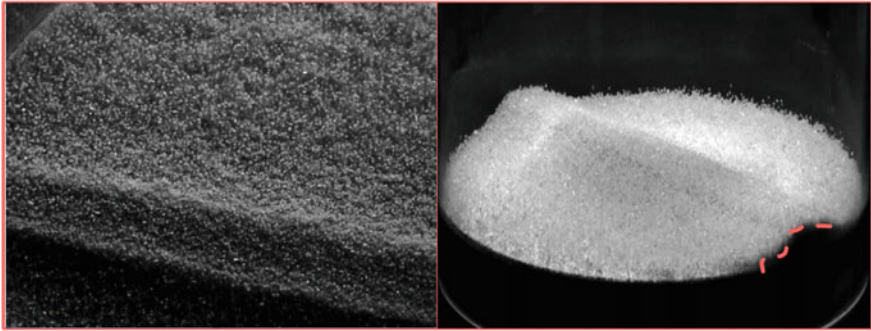
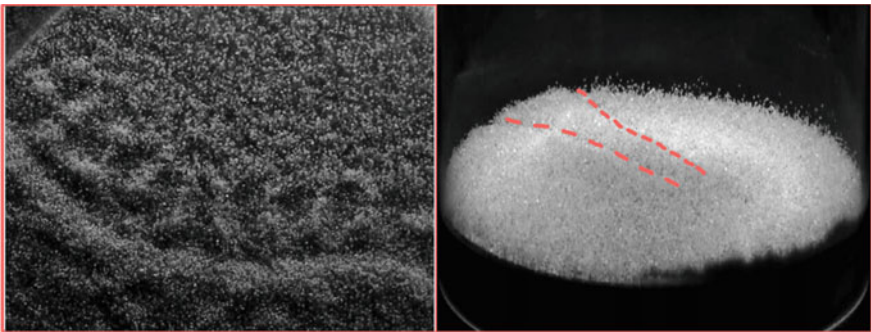**Fig. 31** Particles on moving surfaces: f = 45 Hz, A = 0.78 mm, Γ = 6.32

Fig. 32 Particles on moving surfaces: f = 40 Hz, A = 1.28 mm, Γ = 8.24

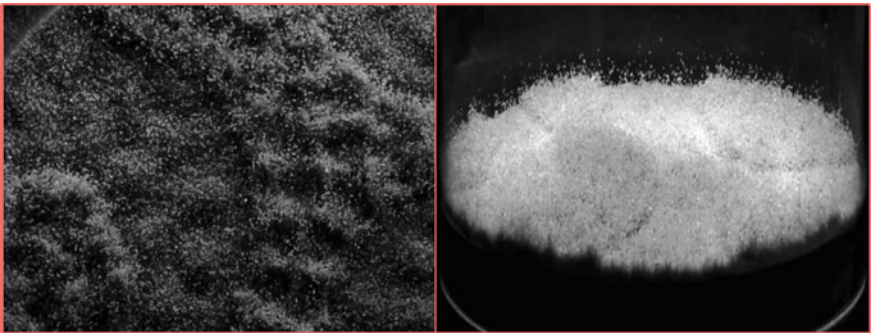**Fig. 33** Particles on moving surfaces f = 25 Hz, A = 2.76 mm, Γ = 6.94

Fig. 34 Circular vibratory screening machine (Rekord V 3/10/I L of Siebtechnik GmbH)

3.4 Sieving in Transient Mode of Operation

The circular vibratory screening machine Rekord V 3/10/I L of Siebtechnik GmbH (Fig. 34) was used to investigate the transient mode of operation of screening machines. The length of the sieve of the sieving machine is 1000 mm and thus has a usable screen area of 0.3 m^2. The vibration is generated by an exciter shaft through two unbalances. The screen inclination can be varied between 0° and 40° to the horizontal. Screens with mesh widths w = 0.125 mm, 0.25 mm, 0.5 mm and 1.0 mm are available.

For these investigations, the screening machine is designed in such a way that a temporal and spatial resolution of the product can be detected. For this purpose, various collection containers were fitted under the sieve (see Fig. 35).

In these containers, the fines can now be detected along the sieve surface in a time-resolved manner. The grade efficiency curves T(x, t) can be determined from the analysis of the feed, the fines and the coarse. Figure 36 shows an example of how the fines are changing over the length of the sieve.

The following parameters were varied in the following investigations of the transient mode of operation: duration of sieving, sampling position and angular velocity ω. Quartz particles at a mass flow rate of 250 kg/h were used as material. The separation functions were calculated according to Eqs. (19) and (20).

$$T(x) = \frac{m_G}{m_A} \cdot \frac{q_G(x)}{q_A(x)} \tag{19}$$

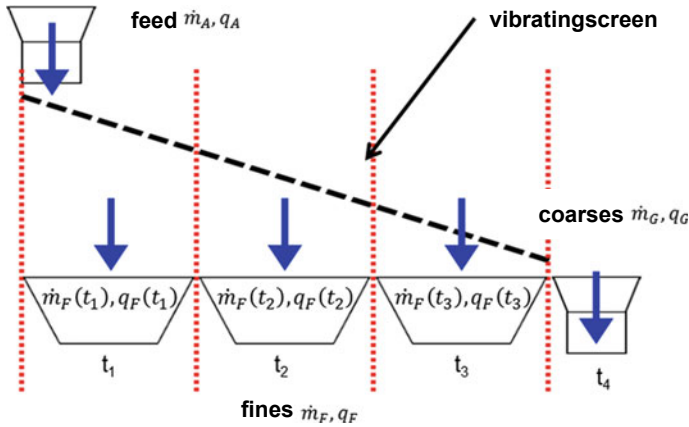$$T(x) = 1 - \frac{m_F}{m_A} \cdot \frac{q_F(x)}{q_A(x)} \tag{20}$$

Fig. 35 Vibrating Screen with different collecting containers which can be operated for different durations
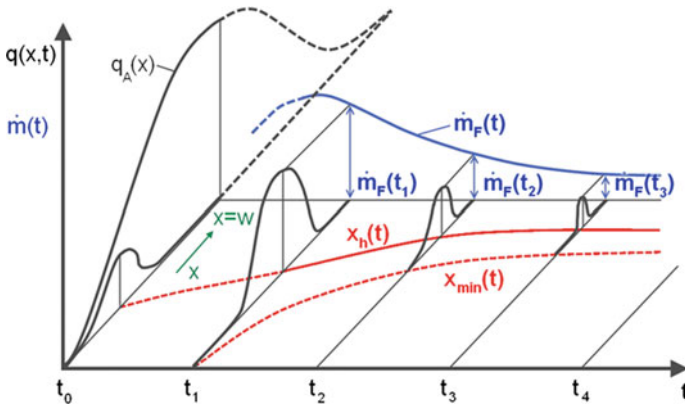

Fig. 36 Time-dependent change of fine material

In a first series of experiments, the revolution rate was varied between 900 and 1550 min^{-1}. Figure 37 shows the different separation functions depending on the different revolution rates for a feed mass flow of $\dot{m} = 250$ kg/h. It appears that with increasing the revolution rate the separation function shifts into the fine material range, but the gradient remains almost identical. Also the selectivity according to Eder (see Eq. (16)) drops continuously with increasing revolution rate but within a rather small range of κ (cf. Fig. 38).

The decrease of x_t with the revolution rate can be explained by the throwing coefficient K_V.

$$K_V = \frac{r \cdot \omega^2 \cdot \sin(\alpha + \beta)}{g \cdot \cos \beta} \tag{21}$$
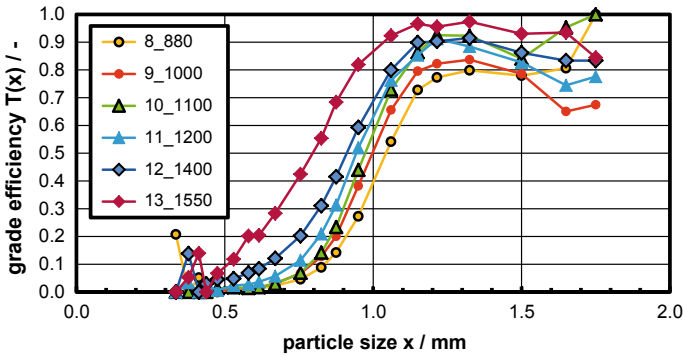
Fig. 37 Grade efficiency function of different number of revolution of circular vibrating screen

Fig. 38 Sharpness of cut κ and cut size x_t as a function of revolution rate
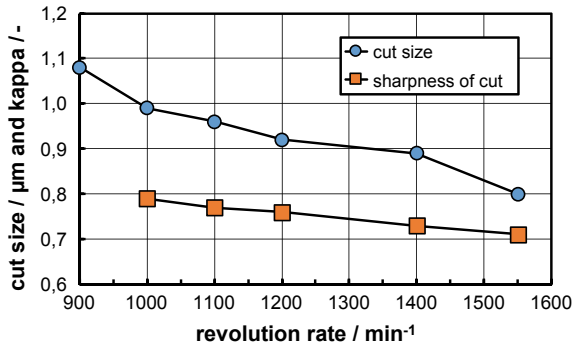
Here the accelerations, which also affect the particles, are characterized. Due to the higher revolution rate, the particles are accelerated stronger, thus being moved further and transported faster through the sieve. As a result, there is a less frequent comparison between mesh size and particle size.

In a further step, the local distribution of the particles in the collection containers (cf. Fig. 39) was investigated at different times ($t_1 = 1$ min, $t_2 = 2$ min and $t_3 = 10$ min) at a revolution rate of 1200 min^{-1}.

Fig. 39 Collecting container under the screening machine

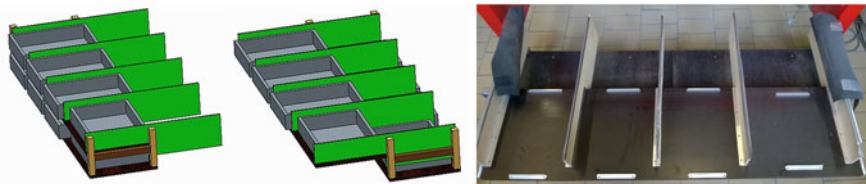In Fig. 40 it is shown that for a given container the size distribution of the fines does not change with the duration of the screening. For 1 and 10 min screening nearly indistinguishable size distributions are obtained. However, when comparing the first and the second container for collection of the fine fraction, a clear shift towards larger particles is observed. This may be explained by the conception that the finer particles pass first the screen leaving behind larger particles which pass later.

The experimental results of the separation curves for the first and the third container are shown in Fig. 41. Within the experimental uncertainties, the grade efficiency curves are close to each other. Using the different models outlined in Eqs. (13), (14) and (16) the calculated separation curves are compared with the measured ones. It can be seen that for the model of Plitt no parameter could be found so that a reasonable agreement with experimental data was obtained. For the model of Molerus, a much better agreement was observed. Finally, with the own model (T_beta) a very good approximation of the measurement results is achieved.
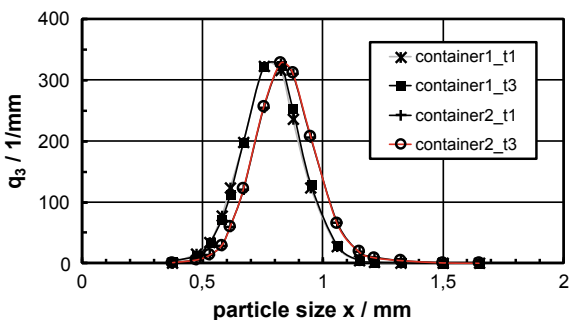

Fig. 40 Density distribution of the fines in the first and the second container for different durations ($t_1 = 1$ min and $t_3 = 10$ min)
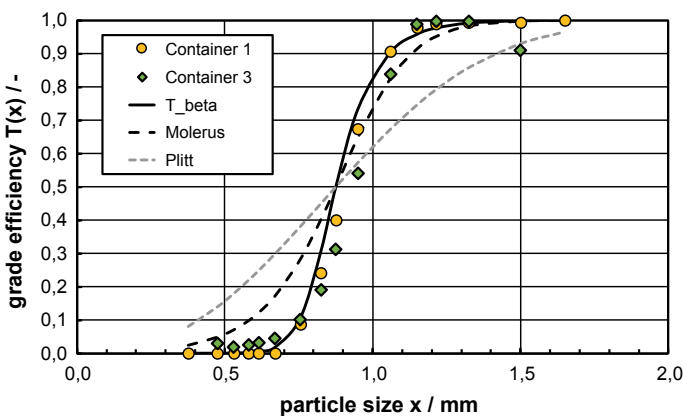

Fig. 41 Grade efficiency curves for the first and the last sieve parts and comparison of the measured values with the models of Plitt, Molerus and the own model

4   Conclusion

In spite of the broad range of applications of flow and sieve classification the physical phenomena of higher particle loadings are not completely understood. As common departure point, the single particle model of Molerus was used here. For the sieving, the single particle motion and acceleration was studied and the Molerus model was modified with a selectivity factor, which accounts for particle-particle interactions as well as the formation of particle layers on the sieve bottom. Particle accumulation effects, which occur in steady state and in instationary operation, may hinder the particle mobility at higher loadings. However, it was observed that along the vibrating screen the separation curve did not change significantly.

In flow classification, the commonly used models cannot account for instationary effects. Therefore, a new system to measure the time to reach steady state was employed. It turned out that a hold-up volume needs to be filled before steady state is reached which may take several tens of minutes for low loadings. However, the hold-up volume seems to be rather constant. For steady state operation, the Molerus model was used by refining tangential and radial velocities. For particles with high Stokes numbers, the flow field can be neglected in a first approximation and the cut size is dependent on the particle impaction probability on the blades. With the detailed knowledge of the mean radial airflow, a much better prediction of the separation curve can be obtained. In contrast to the radial velocity, the tangential air velocity is of less significance for the cut size and sharpness of separation. This is due to the formation of a particle cloud, whose tangential velocity is to a large extent dominated by the circumferential velocity of the deflector wheel.

For particles with low Stokes numbers, the rotary symmetry of the airflow entering the deflector wheel will gain in importance, while the particle entrance trajectories will be less significant. Ironically, the model of Molerus gives a good prediction of the cut size even its conception of the particle motion is not correct for particles with high Stokes numbers.

References

1. Teipel, U.: Energetic Materials: Particles Processing and Characterization. Wiley-VCH Verlag, Weinheim (2006). ISBN 3-527-30240-9
2. Plitt, L.R.: The analysis of solid-solid separations in classifiers. CIM Bull. **64** (1971)
3. Rogers, R.S.C.: A classification function for vibrating screens. Powder Technol. **31**, 135 (1982)
4. Molerus, O., Hoffmann, H.: Darstellung von Windsichtertrennkurven durch ein stochastisches Modell. Chem. Ing. Tech. **41**(5+6), 340–344 (1969)
5. Trawinski, H.: Die mathematische Formulierung der Tromp-Kurve. Aufbereitungstechnik **17**, 248–254, 449–459 (1976)
6. Soldinger, M.: Influence of particle size and bed thickness on the screening process. Miner. Eng. **13**, 297–312 (2000)
7. Deghani, A., Monhemius, A.J., Gochin, R.J.: Evaluating the Nakajim et al. model for rectangular-aperture screens. Miner. Eng. **15**, 1089–1094 (2002)

8. Nakajima, Y., Whiten, W.J.: Method for measurement of particle-shape distribution by sieves. Trans. Inst. Min. Metall. **87**, C194–C203 (1978)
9. Nakajima, Y., Whiten, W.J.: Behaviour of non-spherical particles in screening. Trans. Inst. Min. Metall. **88**, C88–C92 (1979)
10. Hatch, C.C., Mular, A.L.: Simulation of the Brenda Mines Ltd. secondary crusher. In: SME-AIME Annual Meeting, pp. 54–79 (1979)
11. Rumpf, H., Leschonski, K.: Prinzipien und neuere Verfahren der Windsichtung. Chem. Ing. Tech. **21**, 1231–1241 (1967)
12. Senden, M.M.G., Tels, M.: Trennschärfe und mittlere Teilchenverweilzeit im Gleichgewichts-sichter. Chem. Ing. Tech. 530 (1977)
13. Senden, M.M.G.: Stochastic models for individual particle behavior in straight and zig zag air classifier. Eindhoven University of Technology (1979)
14. Schubert, H., Al, E.: Mechanische Verfahrenstechnik. Deutscher Verlag für Grundstoffindustrie (1977)
15. Husemann, K.: Modellierung des Sichtprozesses am Abweiserrad/Modelling of a classifying process using a deflecting wheel. Aufbereitungstechnik **31**, 359–366 (1990)
16. Furchner, B., Zampini, S.: Air classifying. Ullmann's Encycl. Ind. Chem. **2**, 215–234 (2012)
17. Spötter, C.: Dynamik der Trenncharakteristik eines Abweiseradsichters. TU-Clausthal (2018)
18. Richardson, J.F., Zaki, W.N.: The sedimentation of a suspension of uniform spheres under conditions of viscous flow. Chem. Eng. Sci. **3**, 65–73 (1954)
19. Spötter, C., et al.: Separation curves of screening and air classifying processes at low material loadings. Chem. Ing. Tech. **89**, 1726–1738 (2017)
20. Stender, M., Legenhausen, K., Weber, A.P.: Visualisierung der Partikelbewegung in einem Abweiseradsichter. Chem. Ing. Tech. **87**, 1392–1401 (2015)
21. Thornton, C., Cummins, S.J., Cleary, P.W.: On elastic-plastic normal contact force models, with and without adhesion. Powder Technol. **315**, 339–346 (2017)
22. Thornton, C., Ning, Z.: A theoretical model for the sick/bounce behaviour of adhesive, elastic-plastic spheres. Powder Technol. **99**, 154–162 (1998)
23. Kleinhans, U., Wieland, C., Frandsen, F.J., Spliethoff, H.: Ash formation and deposition in coal and biomass fired combustion systems: progress and challenges in the field of ash particle sticking and rebound behavior. Prog. Energy Combust. Sci. **68**, 65–168 (2018)
24. Antonyuk, S.: Deformations- und Bruchverhalten von kugelförmigen Granulaten bei Druck- und Stoßbeanspruchung (2006)
25. Zou, F., Fang, Z., Xia, M.: Study on dynamic mechanical properties of limestone under uniaxial impact compressive loads. Math. Probl. Eng. **2016**, 1–11 (2016)
26. Chang, S.H., Yun, K.J., Lee, C.I.: Modeling of fracture and damage in rock by the bonded-particle model. Geosyst. Eng. **5**, 113–120 (2002)
27. Meerkamm, H.: Technisches Taschenbuch. Schaeffler Technologies GmbH & Co. KG (2013)
28. Bauder, A., Müller, F., Polke, R.: Investigations concerning the separation mechanism in deflector wheel classifiers. Int. J. Miner. Process. **74**, 147–154 (2004)
29. Smigerski, H.-J.: GVC-Dezembertagung 1993 'Feinmahl- und Kiassiertechnik'. In: VDI-Gesellschaft Verfahrenstechnik (1993)
30. Bauer, U.: Zur trennscharfen Feinstsichtung in Fliehkraft-Abweiseradsichtern. Technische Universität Clausthal (2002)
31. Galk, J.: Feinsttrennung in Abweiseradsichtern. Technische Universität Clausthal (1995)
32. Spötter, C., Legenhausen, K., Weber, A.P.: Separation characteristics of a deflection wheel classifier in stationary conditions and at high loadings: new insights by flow visualization. KONA Powder Part. **34**, 1–14 (2017)
33. Hinds, W.C.: Aerosol Technology. Wiley, Hoboken (1999). ISBN 0-471-19410-7
34. Ren, W., Liu, J., Yu, Y.: Design of a rotor cage with non-radial arc blades for turbo air classifiers. Powder Technol. **292**, 46–53 (2016)
35. Xing, W., et al.: Experimental study on velocity field between two adjacent blades and gas-solid separation of a turbo air classifier. Powder Technol. **286**, 240–245 (2015)

36. Leschonski, K.: Windsichter, verfahrenstechnische Maschinen zur Herstellung definierter pul-verförmiger Produkte. Jahrb. 1988 der Braunschw. Wissenschaftlichen Gesellschaft, 175–196 (1988)

37. Barimani, M., Green, S., Rogak, S.: Particulate concentration distribution in centrifugal air classifiers. Miner. Eng. **126**, 44–51 (2018)

38. Sun, Z., Sun, G., Liu, J., Yang, X.: CFD simulation and optimization of the flow field in horizontal turbo air classifiers. Adv. Powder Technol. **28**, 1474–1485 (2017)

39. Toneva, P., Epple, P., Breuer, M., Peukert, W., Wirth, K.E.: Grinding in an air classifier mill. Part I: characterisation of the one-phase flow. Powder Technol. **211**, 19–27 (2011)

40. Schulz, H.: Die Pumpen. Springer, Berlin (1967)

41. Tropea, C., Yarin, A.L., Foss, J.F.: Springer Handbook of Experimental Fluid Mechanics. Springer, Berlin (2007). ISBN 9783540251415

42. Stieß, M.: Mechanische Verfahrenstechnik 2. Springer, Berlin (1997). ISBN 978-3-540-55852-1

43. Hennig, M., Teipel, U.: Modellierung der Trenncharakteristik für den Siebklassierprozess. In: Produktgestaltung in der Partikeltechnologie, pp. 517–534. Fraunhofer Verlag (2011)

Chapter 11
Experimental Study and Modelling of Particle Behaviour in a Multi-stage Zigzag Air Classifier

Eduard Lukas, Christoph Roloff, Hannes Mann, Kristin Kerst, Thomas Hagemeier, Berend van Wachem, Dominique Thévenin, and Jürgen Tomas

Abstract In most industrial solid processing operations, the classification of particles is important and designed based on the terminal settling velocity as the main control parameter. This settling velocity is dependent on characteristic particle properties like size, density, and shape. Turbulent particle diffusion is the other key property controlling the efficiency of the separation. In this project, multi-stage separation experiments of a variety of materials have been performed using different flow velocities, mass loadings of the air, number of stages. Separation has been investigated separately concerning particle size, particle density, and particle shape. Continuous operation in terms of solid material and airflow has been mostly considered. However, variations in mass loading and pulsating operation of the fan have been investigated as well. The performance has been analyzed and discussed with respect to the separation functions, for instance regarding separation sharpness. Several modelling approaches have been checked and/or developed to describe theoretically the corresponding observations. After fitting the free model parameters, a very good agreement has been obtained compared to experimental measurements. Finally, the reduced model has been implemented into the central software DYSSOL.

E. Lukas · H. Mann · B. van Wachem · J. Tomas (Deceased)
Laboratory of Mechanical Process Engineering, Otto von Guericke University Magdeburg, Magdeburg, Germany
e-mail: eduard.lukas@ovgu.de

B. van Wachem
e-mail: berend.vanwachem@ovgu.de

C. Roloff · K. Kerst · T. Hagemeier · D. Thévenin (✉)
Laboratory of Fluid Dynamics and Technical Flows, Otto von Guericke University Magdeburg, Magdeburg, Germany
e-mail: thevenin@ovgu.de

C. Roloff
e-mail: christoph.roloff@ovgu.de

K. Kerst
e-mail: kristin.kerst@ovgu.de

T. Hagemeier
e-mail: thomas.hagemeier@ovgu.de

1 Introduction

The treatment of raw materials, intermediates, products, and waste is one of the most important processes for many industrial applications. Usually, the final process outcome depends strongly on the quality of separation. Separation by particle size is mostly done by sieving. For lower cut points (for a particle diameter in the order of mm), air classifying performs better because fine particles often adhere to and block the openings of the sieves. One apparatus for air classifying is the zigzag air classifier. This system has been known for a long time [1–3]. It is widely used for a variety of industrial applications, e.g. for classifying shredded PET bottles [4], municipal solid waste [5], scrap cables, or stalks and leaves for the tea and tobacco industry [6].

The main advantage of multi-stage air classifying is the wide range of possible cut sizes, in the range of micrometers to several millimeters. Sorting (separation by density) can be done within a wide density range as well. Separation is done based on the differences in settling velocity, which is the main characteristic parameter and is determined by particle properties as size, density, and shape [6].

Obviously, the air velocity in any separation chamber impacts the particle dynamics, in particular with respect to the flow direction. Due to this fact, the zigzag air classifier has a wide field of possible applications. The mass flux of one stage in practical applications is typically between 5 and 15 t/(m h); an even higher throughput can be reached by using several channels in parallel. The number of stages affects the separation performance since, at every stage, separation of fine and coarse (or light and heavy) particles occurs as the particles flow across the air stream. Therefore, every particle that leaves the channel has been separated repeatedly, which leads to a high operational efficiency. Additionally, the process can be linked to pneumatic conveying without the requirements for any additional device [6].

However, problems are also encountered when using a zigzag air classifier (ZAC). In particular, variations in properties of the feed (in size, density, or shape) e.g. due to segregation in the silo, eventually lead to local and temporal fluctuations of the mass loading of air. This affects the efficiency of the separation in a negative way. Due to these fluctuations, pulsations of the air stream may also be observed. All in all, the unknown dynamics of the process lead to insufficient reliability of the ZAC operation, reducing separation efficiency. Though the efficiency might be increased again by employing a larger number of stages, those cause additional pressure loss, increasing energy consumption. As a consequence of this trade-off, it is expected that an optimal number of separation stages exists for a given process.

Since ZACs have been used for many decades, they have been the topic of several investigations. Selected publications are discussed in what follows. For instance, Worrell and Vesilind [7] investigated the separation performance of different air classifiers based on various throat configurations. They used municipal solid waste to separate light (paper and plastics) and heavy (aluminum and steel) materials and introduced a new concept to evaluate the operational efficiency. The total efficiency was defined as the product of the fractional recoveries of light and heavy material in the overflow and underflow. Therefore, the highest efficiency of 100% can only be

reached if 100% of the lightweight material is discharged as light product and 100% of the heavyweight material is delivered as heavy product.

The operational efficiency of ZACs at low particle concentrations has been investigated by Senden [5] who used square pieces of paper and porous polystyrene spheres as test materials during the experiments. He analyzed the influence of different channel depths and bending angles (90°, 120°, 150°) and found the 150° case showing the highest separation efficiency associated with an enormous increase of particle residence time. Furthermore, he developed a stochastic model to describe the separation behavior based on observations of every single stage. Rosenbrand [8] extended Senden's model [5] for high particle concentrations using a dimensionless correlation.

Vesilind and Henrikson [9] studied the influence of feed rate on the separation performance in a zigzag channel with a bending angle of 120° using square-shaped plastic and aluminum pieces. It was shown that particle residence times decrease with increasing feed rate; the same applies to separation efficiency. Both effects were ascribed to an increased particle-particle collision frequency.

For performance comparison of different air classifiers, Biddulph and Connor [10] developed a simple test based on the estimation of effective diffusivity; good separation efficiencies were assumed to be connected with low diffusivities.

The research group around Tomas [11, 12] developed a model to describe the separation performance in a ZAC. This model agreed well with experimental data measured by separation experiments of glass beads, sand, split, and gravel at low mass loadings of the air. One important advantage of their model is a flexible application concerning separation by size, density, or shape. The zigzag air classifier was found to deliver satisfactory to good separations, and this at low energy consumption.

The separation of PET flakes by particle shape in a zigzag separator has been studied in several studies [4, 13, 14]. Using a low mass loading of the air, the process showed good separation efficiency.

Several investigations can also be found in the literature (e.g., [13, 15]) concerning the simulation of one- and multi-phase flows in zigzag-shaped channels using Computational Fluid Dynamics (CFD). However, only few of these publications attempted to quantify separation performance.

The aim of the present investigation was to investigate in a systematic manner the processes leading to particle separation in a ZAC, by combining in a suitable manner theoretical, experimental and numerical investigations.

The installation used for all studies is shown in Fig. 1. The pilot-scale air separator used in this research consists of the zigzag channel featuring four exchangeable channel modules aligned vertically and housing two segments each, which are connected under a prescribed inclination angle. A controllable blower drives the air in a closed circuit through the apparatus. Air flows through the inflow pipe and then from bottom to top through the zigzag channel, through an aero-cyclone and a filter before it re-enters the blower. Particles are fed to the system through a small square duct at mid-height of the zigzag channel by means of a controllable vibration conveyer connected to a hopper. The separated material is collected in two containers, one for
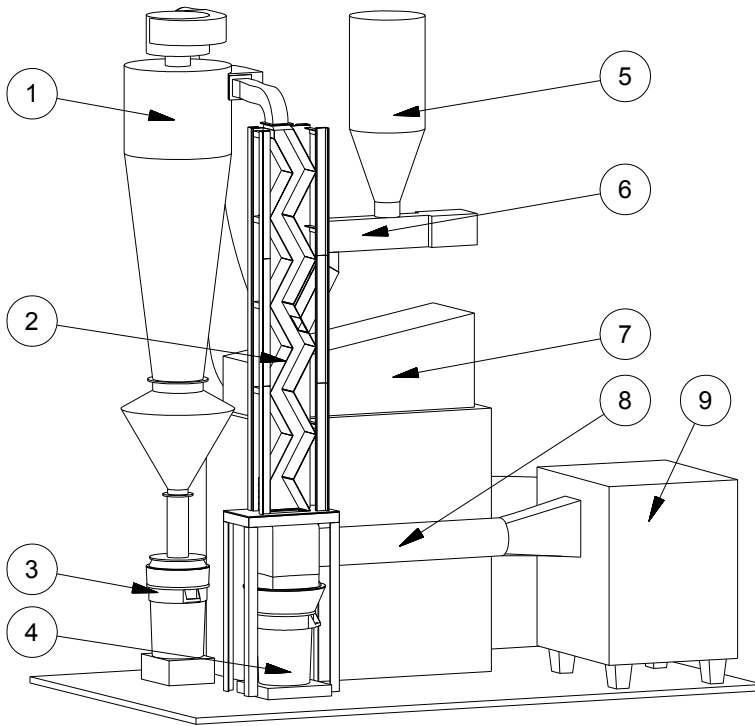
Fig. 1 Principle sketch of the investigated pilot-scale zigzag air classifier with (1) aero-cyclone, (2) zigzag channel, (3) container for fine fraction, (4) container for coarse fraction, (5) hopper, (6) screw feeder, (7) filter, (8) inflow pipe, (9) fan

the coarse fraction falling down into the underflow bin, and one for the fine fraction lifted with and separated from the airstream by a cyclone into the fine fraction bin.

Many different process conditions have been considered and analyzed in a systematic manner using this system. Thanks to such extensive studies, it should become ultimately possible to derive best-practice recommendations for designing and using a ZAC in an optimal manner for a given process. Since all the results of this project have been already extensively published, the rest of this chapter consists mainly in summarizing the most important findings regarding each aspect of this combined study.

2 Research Strategy

Considering the complexity of the process, a combination of theoretical, numerical and experimental studies was considered best to get a deep insight regarding the controlling physical mechanisms, with a view toward optimal design and operating

conditions. The corresponding subprojects are described in Fig. 2 and correspond to following steps:

- Theoretical description of a single spherical particle settling in a gas flow under laminar or turbulent conditions;
- Experimental investigation of fluid velocities, turbulent properties and vortex structures in the ZAC;
- Numerical simulations of fluid velocities, turbulent properties and vortex structures in the ZAC;
- Experimental investigation of particle trajectories in the ZAC;
- Numerical simulation of particle trajectories in the ZAC (coupling Computational Fluid Dynamics with either Discrete Particle Model—DPM—or Discrete Element Model—DEM);
- Experimental investigations of separation based on particle size, particle density, particle shape;
- Derivation of a simplified model of particle separation in the ZAC and integration of this model into the central simulation platform DYSSOL developed in the group of S. Heinrich at the Technical University Hamburg.
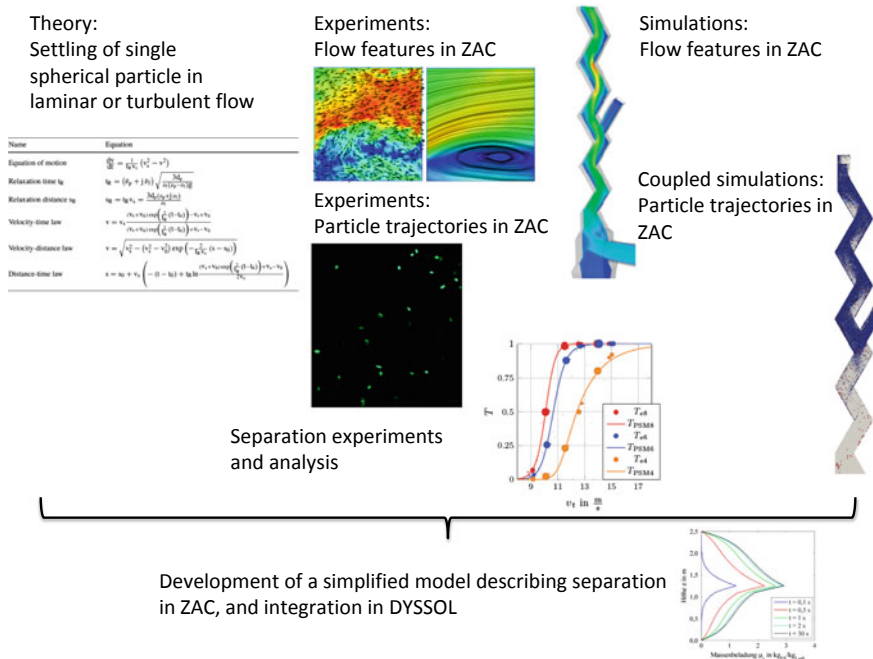

Fig. 2 Research strategy used for this project

Table 1 Analytical solution for a turbulent flow around a settling particle in the Newton regime

| Name	Equation
Equation of motion	$\frac{dv}{dt} = \frac{1}{t_R v_s}\left(v_s^2 - v^2\right)$
Relaxation time t_R	$t_R = \left(\rho_p + j\,\rho_f\right)\sqrt{\frac{3 d_p}{\rho_f(\rho_p - \rho_f) g}}$
Relaxation distance s_R	$s_R = t_R v_s = \frac{3 d_p (\rho_p + j\,\rho_f)}{\rho_f}$
Velocity-time law	$v = v_s \dfrac{(v_s + v_0)\exp\left(\frac{2}{t_R}(t - t_0)\right) - v_s + v_0}{(v_s + v_0)\exp\left(\frac{2}{t_R}(t - t_0)\right) + v_s - v_0}$
Velocity-distance law	$v = \sqrt{v_s^2 - (v_s^2 - v_0^2)\exp\left(-\frac{2}{t_R v_s}(s - s_0)\right)}$
Distance-time law	$s = s_0 + v_s\left(-(t - t_0) + t_R \ln \dfrac{(v_s + v_0)\exp\left(\frac{2}{t_R}(t - t_0)\right) + v_s - v_0}{2 v_s}\right)$

3 Main Results

3.1 Theoretical Study

The settling process of particles in the Stokes and the Newton regimes are of central importance for understanding separation in the ZAC. Considering only spherical and isolated particles, it is possible to obtain full analytic solutions for this configuration, in particular regarding terminal settling velocity and corresponding relaxation times. The main results of the theoretical investigations carried out during this project have been documented in [16]. Additional details and information can be found (in German) in [17]. For instance, the main resulting equations regarding the behavior when a turbulent flow is found around the particle are given in Table 1, in which the notations of [16] have been kept.

Using these relations, it is now easily possible to derive corresponding results for relevant materials considered in the rest of this study. For instance, the behavior of gravel settling in air is shown in Fig. 3.

3.2 Experimental Investigations Regarding the Turbulent Air Flow

Apart from systematic separation experiments described later in this chapter, the physical processes controlling the coupled behavior of turbulent flow and particles have been investigated in detail. For this purpose, a variety of measurement methods have been used. The simplest ones relied on probes placed within the set-up. In this

Fig. 3 Particle velocity of a gravel particle (10 mm diameter) in air at ambient conditions (reprinted with permission from [16])
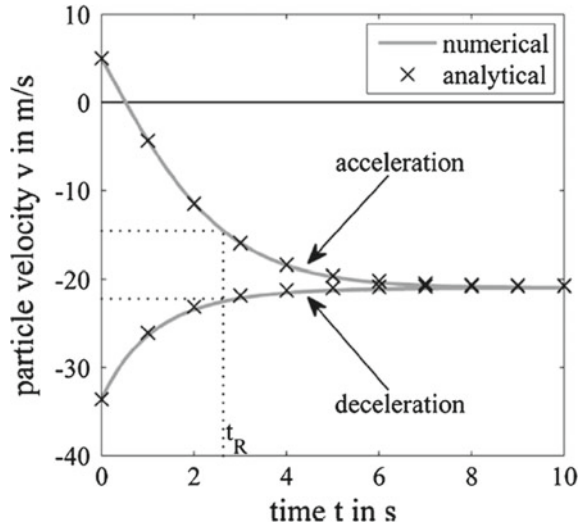
manner, it was for instance possible to investigate the pressure drop induced by the channel (Fig. 4).

The results of the measurement campaigns have been used for two different purposes:

- Foster our understanding of the processes controlling particle separation;
- Support accompanying numerical simulations, by delivering boundary conditions and reference data for validation.

Regarding the latter point, laser-based measurement techniques have been used. Being purely optical and thus non-intrusive, they have the advantage of not perturbing the observed process in any manner. In a first step, Laser-Doppler Velocimetry (LDV) has been employed in the entry section of the zigzag channel (Fig. 5). In this manner, proper inflow boundary conditions have been obtained for mean velocity and

Fig. 4 Dependency of average vertical velocity component in the channel (U_z, blue-filled circles) and pressure loss through the channel (Δp, red plus signs and green circles, obtained to check the repeatability of the measurements) on temperature T
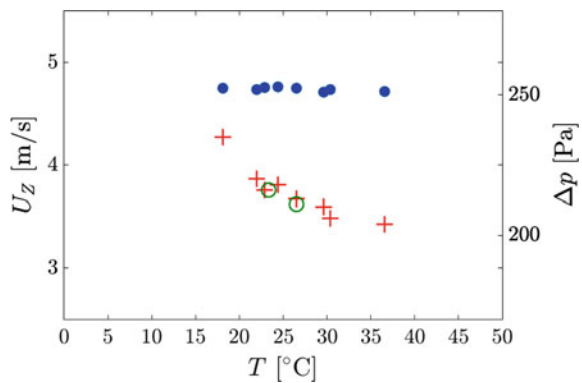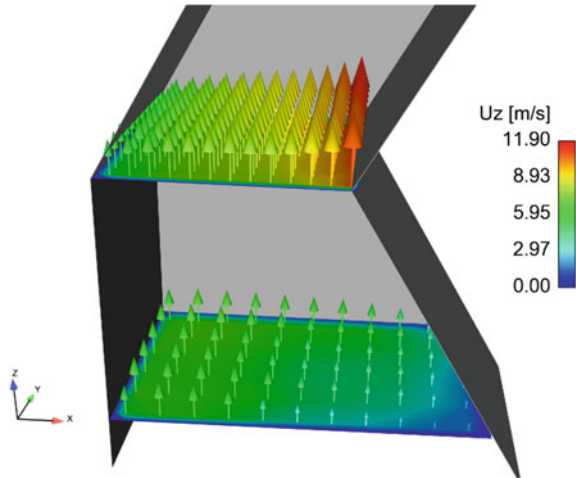
Fig. 5 LDV measurement
planes with vectors
indicating the measured,
time-averaged magnitude of
the z-velocity (vertical, or
axial) component U_z at the
sampling points, for a fan
speed of 0.35 V_{max}. The
corresponding magnitude is
also shown as colour field in
the corresponding plane

turbulence intensity. Those form the basis for all simulations relying on the Unsteady
Navier-Stokes Reynolds-Averaged (URANS) equations, discussed in the next sub-
section. Using this experimental information as boundary conditions, it becomes
possible to compute only the zigzag channel itself, excluding the fan section and
the coarse fraction (i.e., bottom) container from all further simulations. Since the
employed installation is large, this is important to limit the volume of the simulation
domain and, therefore, the necessary number of discretisation cells, allowing a better
resolution and/or shorter computational times.

In a second step, the focus has been mainly set on Particle Image Velocimetry
(PIV). Note that such PIV measurements are very challenging in our pilot-scale
apparatus, since many difficulties must be met: large-scale system, leading to mea-
surements several meters above ground level; related safety issues (laser protection);
very complex geometry; limited optical access (a large part of the channel had to
be reconstructed out of high-quality acrylic glass to enable laser-based measure-
ments); very dusty environment; strong vibrations. Most PIV studies documented
in the scientific literature investigate academic configurations under well-controlled
conditions, very often in a dedicated optical laboratory. In the present case, PIV
measurements must take place in a very large experimental hall hosting more than
10 different experiments—sometimes running simultaneously.

The employed PIV setup is shown in Fig. 6. The acquisition of images at 5 Hz
was carried out for a variety of process conditions.

By analyzing the obtained PIV images, a variety of information can be obtained.
Both instantaneous and average velocity fields have been derived, as shown in Fig. 7.
Additionally, the dominating features of the vortical structures found in the channel
have been identified. Finally, information is also obtained regarding turbulence inten-
sity and the main frequencies of the fluctuations observed in the channel. This first
investigation is helpful to identify key features of the complex and highly unsteady
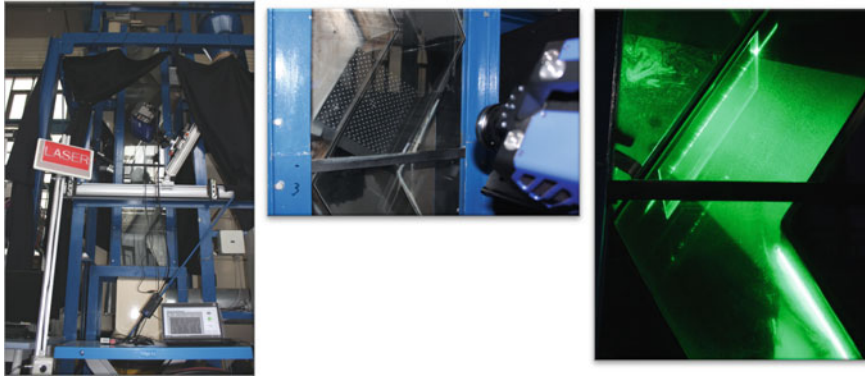turbulent air flow within the zigzag channel.

Fig. 6 View of the PIV hardware around the zigzag channel (left). Zoom on the PIV camera imaging the calibration target within the channel (centre). Laser light-sheet used for PIV (right)
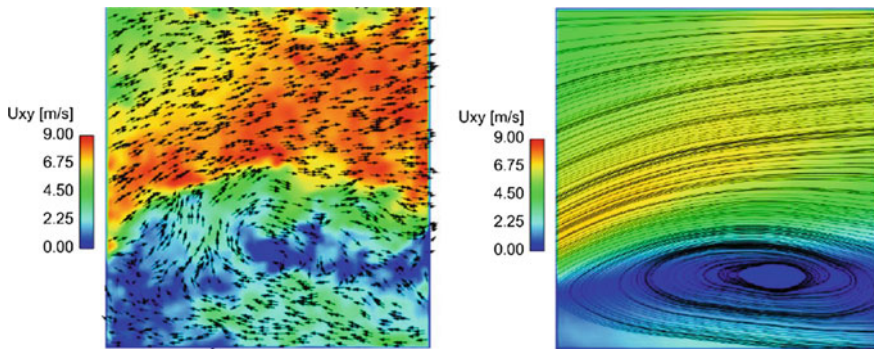
Fig. 7 Exemplary PIV images within the zigzag channel: instantaneous (left) and average flow field with recirculation zone (right) at the same location

3.3 Numerical Investigations Regarding the Turbulent Air Flow

In parallel to these first experimental investigations, a large number of numerical simulations based on Computational Fluid Dynamics (CFD) have been carried out, first considering only the gas flow. For all these simulations, the exact geometry of the installation has been taken into account and used as a basis for discretisation. First simulations considered the whole system starting at fan outlet. This leads unfortunately to a very large gas volume; for this reason, a satisfactory resolution could not be achieved with reasonable computing times. In order to solve this issue, the LDV measurements described previously have then been used systematically as boundary conditions. In this manner, only the zigzag channel itself needs to be taken into account in the numerical simulation, reducing drastically computational times.

Fig. 8 Instantaneous velocity field obtained by URANS simulations in one segment of the ZAC under identical conditions and resolution for different turbulence models: standard k-ε (left), k-ω-SST (center), and SAS (right)
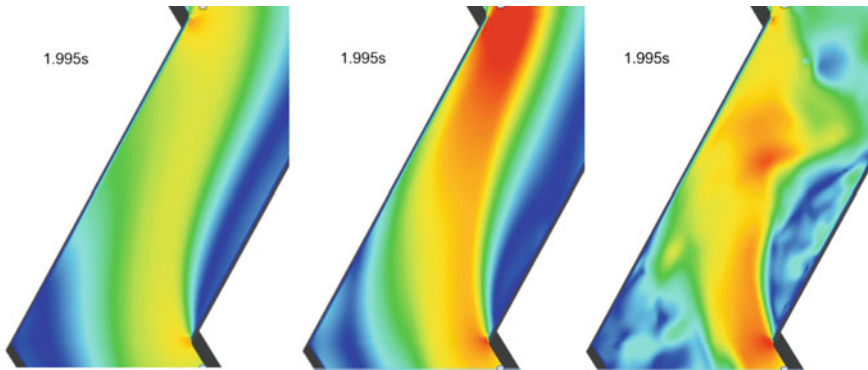
The flow in the zigzag channel is highly turbulent. Considering the complexity of the geometry and of the resulting flow features, high-fidelity simulations like direct numerical simulation (DNS) or large-eddy simulation (LES) would be recommended. However, DNS is simply impossible for this configuration; a single LES simulation would be acceptable, but systematic studies involving additionally particles are again beyond reach. The only approach allowing many different simulations relies on the unsteady RANS equations. As a consequence, in a second step, the impact of the turbulence model used in all further URANS simulations has been assessed. During the course of this 6-year research project, URANS simulations have been carried out using different versions of the industrial software ANSYS-Fluent, STAR-CCM+, or OpenFOAM, depending on license availability and on the proposed models. As a matter of fact, no relevant difference has been obtained among these different software solutions when using similar resolution and models. On the other hand, the impact of the employed turbulence model was found to be extremely high. As an illustration, Fig. 8 shows instantaneous results obtained in the same segment of the channel with the same grid resolution and at the same time with three different, well established turbulence models: standard k-ε, k-ω-SST (Shear Stress Transport), and SAS (Scale-Adaptive Simulation).

These turbulent flow simulations revealed that the standard k-ε model does not lead to sustained unsteady features; after computing about 1 s of physical time, a steady solution without any fluctuation is established within the channel, which is in contradiction to the experimental observations. Using now the k-ω-SST model, only very weak periodic fluctuations involving a single large-scale vortex pair are observed in the corner of the channel; again, this behavior does not coincide with experimental measurements. Only the SAS model is able to deliver a highly unsteady velocity field involving a number of small-scale vortices, in qualitative agreement with experimental observations. Unfortunately, the SAS model (or equivalent formulations) are not available in all simulation platforms yet; additionally, these models come in general

with a noticeably higher computing time, since finer grids and smaller timesteps are required to get properly resolved features. Further studies will be necessary before getting final statements regarding the recommended URANS turbulence model for the ZAC.

3.4 Experimental Investigations Regarding the Particles

After having properly characterized the turbulent air flow, further experimental investigations elucidated the behavior of the particles during the separation process in the ZAC. In order to avoid any perturbation of the system, optical measurements have been again preferred, this time relying on shadowgraphy. This means that a background illumination is employed, and the shadows of the particles on the camera image are post-processed to get a variety of information, like particle number density, particle movement, particle velocity (using consecutive images), and possibly particle shape and orientation. The main findings of these measurements have been documented extensively in [18]. Apart from delivering useful information regarding the local particle velocity at different levels within the zigzag channel, this investigation also revealed the main characteristic particle movements, as shown in Fig. 9.

In particular, the following conclusions can be drawn from these measurements: the dominating motion for particles flowing downward is a sliding motion along the bottom wall of the channel; the flow separation found behind each channel bend is of central importance to explain particle trajectories, increasingly so for higher flow-rates; collisions of particles with other particles or with the channel walls play a prominent role to understand the non-homogeneous distribution of particle number density; the upward movement of the particles is dominated mainly by the features of the air flow and is more complex than the downward movement. These observations are essential to develop proper theoretical models able to describe particle separation with sufficient accuracy.

Fig. 9 Dominating particle trajectories identified by shadowgraphy along each bend of the zigzag channel

3.5 Coupled Simulations of the Particulate Flow Within the Zigzag Channel

Again, in parallel to the experimental study discussed previously, a variety of numerical simulations have been carried out in an effort to describe the behavior of the particles within the turbulent air flow found within the zigzag channel. Keeping in mind, as discussed previously in Sect. 3.3, that it was already extremely challenging to solve for the turbulent air flow *without* any particles, it is clear that this objective is extremely ambitious, both regarding the needed computational resources (computing time and memory) as well as model accuracy (availability of sufficiently accurate numerical models).

The first attempt in the project was to couple the URANS simulation with a very simple particle model (Discrete Particle Model, or DPM) using a one-way approach, considering all particles as points, neglecting any influence of the particles on the flow, and disregarding all collisions. These very strong simplifying hypotheses are helpful to reduce computational times; however, it is clear from the start that getting suitable predictions with such simplifications would be a good surprise. Indeed, and independently from the employed turbulence model, it has been fully impossible to get any acceptable agreement regarding process outcome using such simplifications, as exemplified in Fig. 10. At best, some qualitative trends can perhaps be derived from such simple simulations; but quantitative predictions appear to be impossible. More details regarding such comparisons with separation experiments discussed in the next subsection can be found in [14].

In an effort to improve the accuracy of the numerical predictions, it was decided to switch from the simple DPM model to the more advanced DEM approach (Discrete Element Model). In principle, URANS-DEM simulations come at a considerably higher numerical cost but open the door for truly coupled simulations between turbulent flow and particles, and are able to directly take particle collisions into

Fig. 10 Exemplary comparison of measured separation sharpness (denoted "Exp") and prediction obtained by URANS-DPM simulations using as turbulence model k-ε, k-ω-SST, or Reynolds-Stress Model (RSM) for sand particles
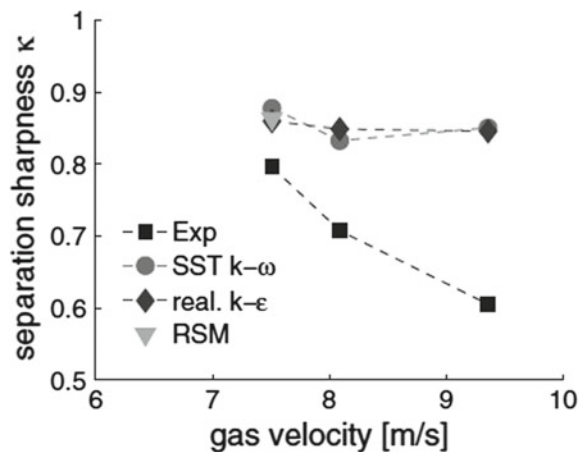
account. Therefore, it is expected that such numerical predictions should be closer to the experimental observations. However, depending on the employed software, such simulations do show also some limitations. Since open-source solutions are of course advantageous for fundamental research projects, it was decided to perform these URANS-DEM simulations using the coupled open-source software CFDEM-coupling [19]. CFDEMcoupling combines the C++-based open-source software environments OpenFOAM (for CFD) and LIGGGHTS (for DEM). Hence, CFD and DEM calculations rely on two separate codes. The interaction between the two calculations is realized by exchanging relevant information with a predefined timestep. Unfortunately, advanced turbulence models like SAS are not available in CFDEMcoupling. Looking back at the results of Sect. 3.3, the "best" model currently implemented there is the *k*-ω-SST model. Even if our previous study has demonstrated that this model leads only to weak flow fluctuations involving few large-scale vortices (at the difference of experimental observations), it had to be kept for the present simulations. In Fig. 11, the numerical prediction for classification based on particle density is shown, in comparison with experimental data.

In particular, this study revealed an unexpectedly strong influence of the employed drag model. For Fig. 11, the model of Di Felice [20] has been retained. Switching to another model, or modifying the poorly-known coefficients appearing in the drag law, the results become very noticeably different. Using model fitting, it is then possible to reach in principle a good agreement by comparison with the separation experiments discussed in the next subsection. However, this is obviously not a satisfactory solution. This highlights the need for further research regarding CFD-DEM simulations and all underlying models in the future.
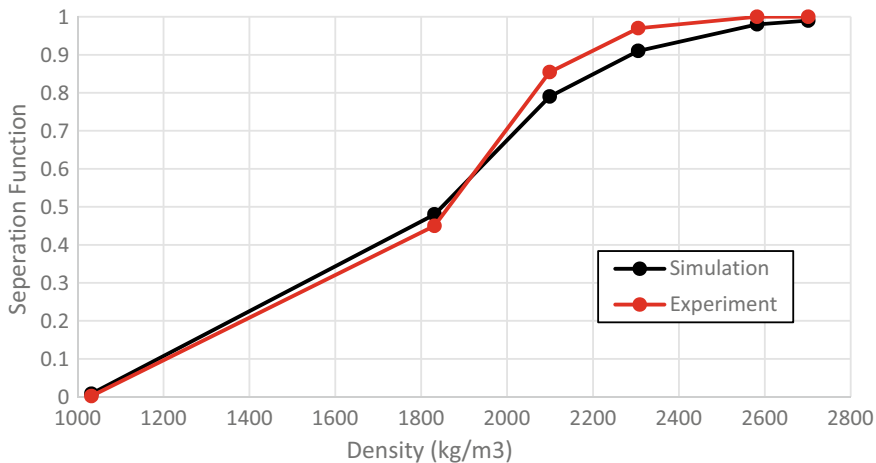

Fig. 11 Separation function predicted by URANS-DEM using the drag model of Di Felice in comparison with own experimental results when separating particles based on their density

3.6 Separation Experiments

During the course of this project, uncountable separation experiments have been
carried out. It is not the purpose of this section to discuss all corresponding results.
Interested readers can find more information in the references listed at the end of
this work, in particular in [21]. Further publications on this topic are currently under
review or being written.

In order to get insight of practical relevance, different kinds of separation
experiments have been documented, in chronological order:

- Separation based on particle size, for a variety of materials (constant air flow);
- Separation based on particle density (constant air flow);
- Separation using a pulsating air flow;
- Separation based on particle shape (constant air flow).

The experiments corresponding to the two last steps are currently being post-
processed, and are thus left for future publications. Separation of sand and gravel
based on particle diameters has been documented in [21]. The results are exemplified
in Fig. 12 for gravel, with particle diameters between 0.1 and 9 mm and a high
sphericity of 0.85, all particles having the same density.

Concerning now density-based separation, the central objective was to investigate
this effect on its own. As a consequence, the diameter and shape of the particles should
be kept identical. Additionally, since optical measurement techniques should be used,
it was desirable to directly encode the particle density in the acquired images. After
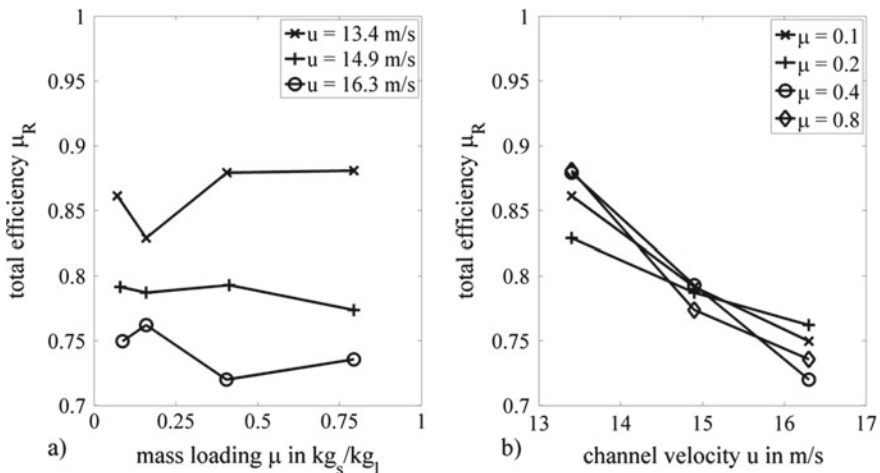a long search, it was finally possible to find suitable particles of different color (see

Fig. 12 Measured total efficiency for the separation of gravel as a function of mass loading (left)
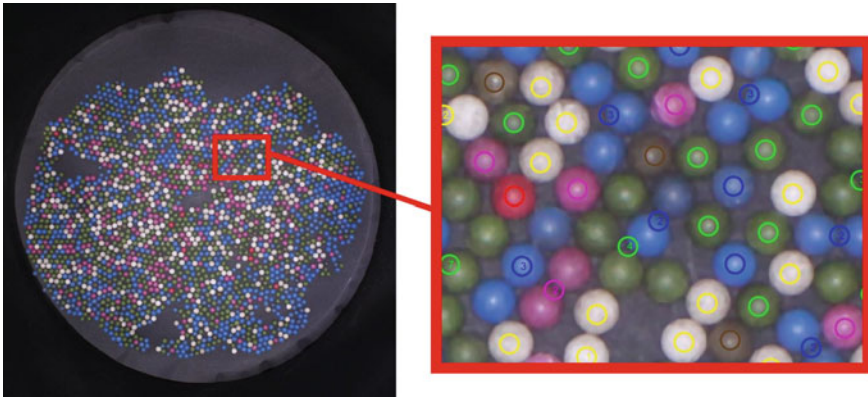or channel flow velocity (right)

Fig. 13 Spherical particles used for density-based separation experiments. Each color corresponds to a different density, with identical diameter. In this picture, the image post-processing software developed for an automatic recognition of the particles in the coarse-fraction container has been validated by comparison with a manual treatment. Circles correspond to individual particle detections, circled numbers to particle groups

also Fig. 13), all spherical, with the same diameter and density, at a still acceptable price, and hence perfectly suitable for corresponding experiments.

4 Development of Reduced Models

All these results have been used to check, validate, and improve models able to describe particle separation in the ZAC. Of particular importance for this purpose are:

- The reference data for comparison provided by the separation experiments (for instance Fig. 12);
- The identification and quantification of typical flow features, necessary to drive model development (for instance Fig. 7);
- The identification of relevant particle movements (for instance Fig. 9), shown again in an exemplary manner in Fig. 14;
- The theoretical investigations given for a single particle at the beginning of this chapter, together with our knowledge regarding the importance of turbulent particle diffusion.

Combining all these features, and based on the existing literature regarding ZAC modelling, different approaches can be developed, either building directly on top of existing models [11, 22], or by proposing new directions.
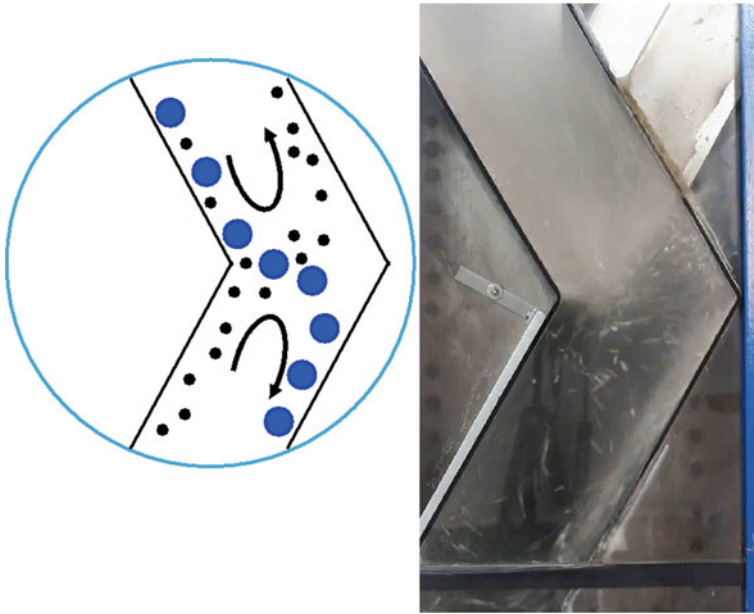
Fig. 14 Typical particle movement controlling the classification process

4.1 One-Dimensional Discretized Approach

One original approach regarding the modelling of the process is the one-dimensional discretisation of the separation process in axial direction, as described schematically in Fig. 15. This approach has been presented in detail in the PhD Thesis of Hannes
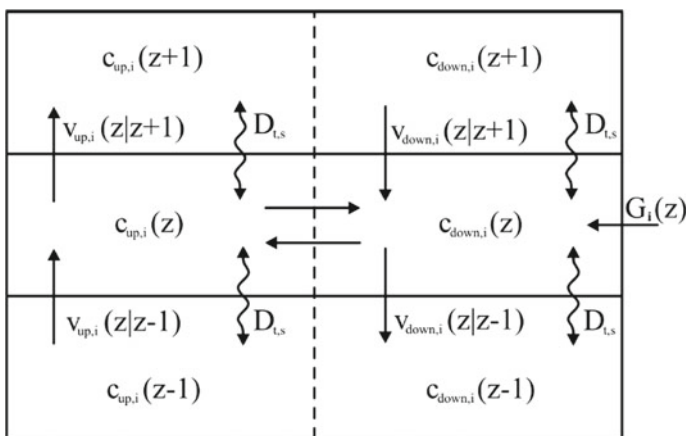
Fig. 15 Balance of particle fluxes around a discretized portion of the zigzag channel at position z

Mann, "Experimentelle Untersuchung, Modellierung und dynamische Simulation der mehrstufigen turbulenten Partikel-Querstromklassierung" (Otto-von-Guericke-Univ. Magdeburg, 2016). In principle, it amounts to a discretisation of the zigzag channel in a (possibly large) number of compartments exchanging mass fluxes of particles with specific properties through their boundaries. Using an iterative approach, steady-state conditions can be reached.

Unsteady predictions are in principle possible as well. Though this model is attractive and could deliver a high accuracy, it requires a good knowledge of many parameters and is not well suited for an integration into the central simulation software DYSSOL. For this reason, alternatives are needed.

4.2 Improving Classical Models

During the course of this investigation, two established models have been revisited. Of particular importance is the turbulent particle diffusion, being a central control parameter regarding separation efficiency. Using the model of [11] while properly fitting the unknown model parameters, a very good agreement can be obtained for density-based separation, as illustrated in Fig. 16. However, one issue encountered in this modelling approach, is that the proposed range for turbulent particle diffusion is in complete disagreement with the experimental observations gained during this project. It was thus decided to revisit the original model of [22] in the light of the new experimental findings. This important part of the project is the subject of a publication currently under review, and will not be described further here in the interest of space.

Fig. 16 Comparison of model predictions using the approach of [11] (lines) with measurement data (symbols) regarding separation of gravel particles for different mass loadings, after fitting of model parameters
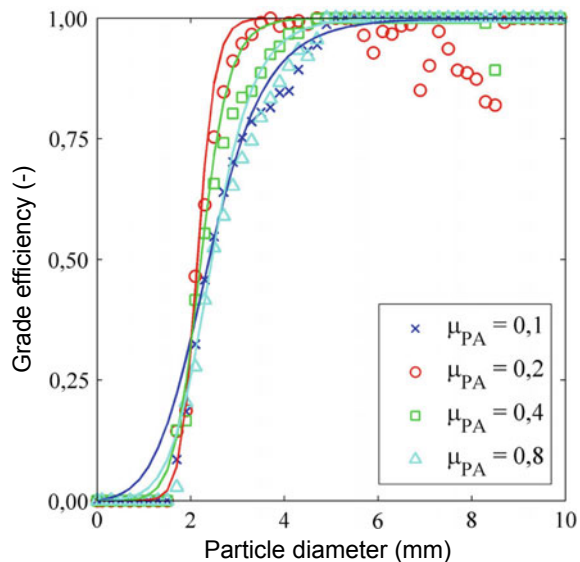
Fig. 17 Comparison of model predictions regarding grade efficiency versus terminal particle velocity using a model derived from [22] (lines) with measurement data (symbols) regarding separation of glass beads, after fitting of model parameters
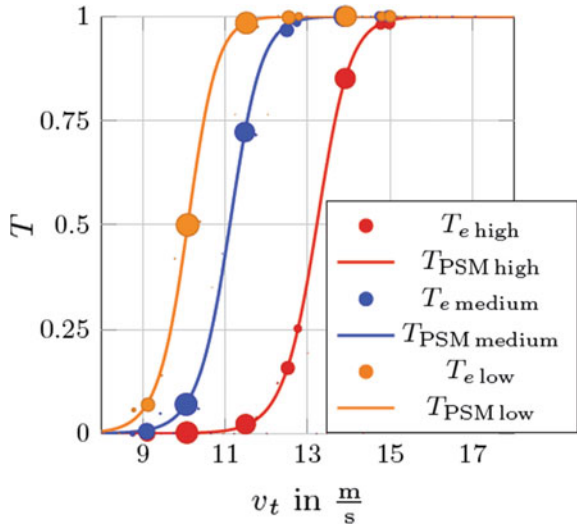
As exemplified in Fig. 17, it leads to an excellent agreement with the measurement data.

4.3   Implementation in DYSSOL

The final step of this project is an implementation of the reduced models into the central software DYSSOL, derived at the Technical University Hamburg in the group of S. Heinrich. This has already been carried out for the model derived from [11], as illustrated in Fig. 18. In this manner, coupled simulations involving zigzag classifiers can readily be carried out in this context.
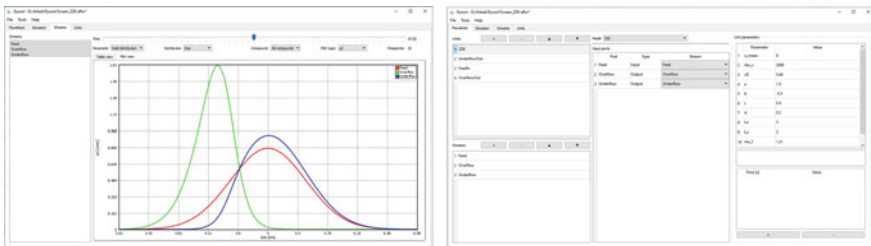
Fig. 18 Screenshot from DYSSOL (left: computation results; right: employed setting) showing the implementation of the ZAC model derived from the model of Tomas and Gröger [11]

5 Conclusion and Perspectives

The zigzag air classifier is a device of high practical importance for a variety of industrial applications. Additionally, the processes controlling separation in the zigzag channel are extremely interesting from a fundamental point of view, since they highlight the importance of coupled aspects (modification of the turbulent flow induced by the particles; particle-particle and particle-wall collisions; particle swarm effects…). In this combined study, theoretical developments, systematic experiments, and numerical simulations relying on different approaches have been combined to elucidate the controlling parameters and to develop reduced models, suitable for integration into simulation platforms like DYSSOL. It appears that, after proper model fitting, a good agreement can be obtained between measurement data and model predictions. Nevertheless, the large differences still found between experiments and simulations reveal the need for further studies before fully predictive numerical studies of practical systems become possible with standard computational resources.

References

1. Stebbins, A.H.: Air classifier. US-Patent 1861248 (1930)
2. Kaiser, F.: Der Zickzack-Sichter – ein Windsichter nach neuem Prinzip. Chem. Ing. Tech. **35**(4), 273–282 (1963)
3. Fastov, B.N., Valuskii, P.F., Lebedev, V.N., Oskalenko, G.N.: Testing of the zigzag classifier for granulated materials. Chem. Pet. Eng. **11**(5), 477–479 (1975)
4. Friedländer, T., Kuyumcu, H.Z., Rolf, L.: Untersuchung zur Sortierung von PET-Flakes nach der Teilchenform. Aufbereitungs Tech. **47**(8), 24–38 (2006)
5. Senden, M.M.G.: Stochastic models for individual particle behavior in straight and zig zag air classifiers. PhD, Technical University Eindhoven (1979)
6. Furchner, B. Zampini, S.: Air classifying. In: Ullmann's Encyclopedia of Industrial Chemistry, vol. 2, pp. 215–234. Wiley-VCH, Weinheim (2012)
7. Worrell, W.A., Vesilind, P.A.: Testing and evaluation of air classifier performance. Resour. Recovery Conserv. **4**, 247–259 (1979)
8. Rosenbrand, G.G.: The separation performance and capacity of zigzag air classifiers at high particle feed rates. PhD, Technical University Eindhoven (1986)
9. Vesilind, P.A., Henrikson, R.A.: Effect of feed rate on air classifier performance. Resour. Conserv. **6**, 211–221 (1981)
10. Biddulph, M.W., Connor, M.A.: A method of comparing the performance of air classifiers. Resour. Conserv. Recycl. **2**, 275–286 (1989)
11. Tomas, J., Gröger, T.: Mehrstufige turbulente Aerosortierung von Bauschutt. Aufbereitungs Tech. **40**(8), 379–386 (1999)
12. Tomas, J.: Gravity separation of particulate solids in turbulent fluid flow. Part. Sci. Technol. **22**, 169–188 (2004)

13. He, Y., Wang, H., Duan, C., Song, S.: Airflow fields simulation on passive pulsing air classifiers. J. S. Afr. Inst. Min. Metall. **105**, 525–532 (2005)
14. Hagemeier, T., Glöckner, H., Roloff, C., Thévenin, D., Tomas, J.: Simulation of multi-stage particle classification in zigzag apparatus. Chem. Eng. Technol. **37**(5), 879–887 (2014)
15. Gillandt, I., Fritsching, U., Riehle, C.: Zur mehrphasigen Strömung in einem Zick-Zack-Sichter. Forsch. Ingenieurwes. **62**(11), 315–321 (1996)
16. Mann, H., Mueller, P., Hagemeier, T., Roloff, C., Thévenin, D., Tomas, J.: Analytical description of the unsteady settling of spherical particles in Stokes and Newton regimes. Granular Matter **17**, 629–644 (2015)
17. Glöckner, H., Hagemeier, T., Müller, P., Roloff, C., Thévenin, D., Tomas, J.: Beschleunigter Sinkprozess fester Partikel bei laminarer und turbulenter Umströmung. Chem. Eng. Tech. **87**(5), 644–655 (2015)
18. Roloff, C., Lukas, E., van Wachem, B., Thévenin, D.: Particle dynamics investigation by means of shadow imaging inside an air separator. Chem. Eng. Sci. **195**, 312–324 (2019)
19. Goniva, C., Closs, C.: CFDEM coupling. Accessible under http://www.cfdem.com (2016)
20. Di Felice, R.: The voidage function for fluid-particle interaction systems. Int. J. Multiph. Flow **20**(1), 153–159 (1994)
21. Mann, H., Roloff, C., Hagemeier, T., Thévenin, D., Tomas, J.: Model-based experimental data evaluation of separation efficiency of multistage coarse particle classification in a zigzag apparatus. Powder Tech. **313**, 145–160 (2017)
22. Schubert, H., Böhme, S., Neeße, T., Espig, D.: Classification in turbulent two-phase flows. In: 1st World Congress on Particle Technology, Nuremberg, pp. 419–442 (1986)

Part II
Material Parameters in Solids Process Engineering

Chapter 12
Property Function to Compute the Dustiness of Powders

Kai Vaupel, Tim Londershausen, and Eberhard Schmidt

Abstract The dustiness of a disperse solid can be understood as a property, which when handled in a gaseous environment, behaves similar to an aerosol, releasing the respective particle fraction of given quantity and size distribution. In general, this release of dust is undesirable because it might result in material loss and often is associated with an exposure of personnel involved or represents a risk of environmental pollution. The dustiness is therefore a product property, which might change along the process path, for example through comminution, agglomeration, classification or mixing of solids involved. Property functions which describe time variable dustiness integrated in dynamic processes as a function of the distribution of particle size, particle shape, and particle interaction during a certain handling, were determined as part of this project. For this purpose, experiments with laboratory equipment such as "free fall in still air", "moving in a rotating drum", "dispersion, pressure surges method", or "airflow dispersion" were performed at very well defined boundary conditions and physically based models were established. The prediction functions were successfully implemented in the flow sheet simulation DYSSOL. These models will be further used through the introduction of the so called "Fractionated grade of release". Together with the description of time-dependent changes of the related strain-functions (apparatus properties) and rigidity-functions (material properties) this approach will help to better predict transient processes of dustiness in future.

Nomenclature

c Particle mass concentration [g/m^3]
d_{32} Sauter diameter [m]
E_{30} Light attenuation after 30 s [1]
E_{max} Light attenuation maximum [1]
ε Bulk porosity [1]

K. Vaupel · T. Londershausen · E. Schmidt (✉)
Institute of Particle Technology, Bergische Universität Wuppertal, Wuppertal, Germany
e-mail: eberhard@uni-wuppertal.de

H	Channel height [m]
K	Apparatus specific factor [1]
L	Channel length [m]
m_0	Mass of the powder sample [g]
m_1	Mass of the unused filter [g]
m_2	Mass of the used filter [g]
$q_r(x)$	Particle size distribution density [m^{-1}]
$Q_r(x)$	Particle size cumulative distribution [1]
S	Dust release number [1]
t	Time [s]
W	Channel width [m]
x	Particle equivalent diameter, particle size [m]
$x_{i,r}$	Percentile of particle size distribution [m]
$X_{0.8}$	Moisture content of a sample at 80% relative humidity
$X_{0.9}$	Moisture content of a sample at 90% relative humidity
X_A	Moisture content of a sample

Indices

0	Quantity by number
2	Quantity by area
3	Quantity by volume/mass
10	10% percentile
50	50% percentile, median
90	90% percentile
E	Experimental
GP	Greater particles
i	Percentile
mod	Modal
P	Prognosed
r	Type of quantity
R	Respirable dust
RD	Rotating drum (Heubach)
SD	Single drop (Palas)
T	Total dust
UNC	University of North Carolina

1   Introduction

The dust formation tendency (dustiness) of bulk materials can be understood as release of particle fractions of a special quantity and size distribution into a gaseous environment given certain handling. Dustiness of bulk materials may change along the process path, for example, through comminution, agglomeration, classification or mixing of the solids involved. In general, such release of particles is undesirable because it might result in material loss, is often associated with personnel being exposed to it and may cause environmental pollution.

Within the scope of DFG-focus program 1679 "Dynamic simulation of inter-linked solid matter processes", empirical formulas describing these processes were developed by the project group B1 "Property functions for calculating dust formation tendency of powders". Dustiness forecast functions were derived from the three testing methods "single drop", "UNC dustiness tester", and "rotating drum", taking into account material density, particle mass and size distribution, particle shape and moisture. By implementing these functions into the DYSSOL flowsheet simulation framework, dust formation tendencies of simulated products can be predicted within the flowsheet. Additionally dustiness quantification of powders based on fractional release rate and established laboratory testing methods was experimentally investigated. These findings were meant to support the work of cooperation partners and may improve the fractional release model developed recently [1].

2   Experimental Investigations

2.1   Cooperation with Project A1: Influence of Deposit Thickness on Powder Layer Dustiness

In cooperation with project A1 "Process modeling for dynamic disperse separation and deposition processes", maintained by University of Bremen, dynamic layer growth and layer stability in separation processes of particulate material from fluid streams was investigated.

For this purpose powder layers of varying thicknesses were generated within an electrostatic precipitator at the University of Bremen. Filter test materials Pural NF (bohemite, density 2.47 g/cm^3, bulk density 0.51 g/cm^3) and Ulmer Weiß XMF (limestone, density 2.68 g/cm^3, bulk density 0.66 g/cm^3) were utilized in these tests. Particle size distrubutions were determined with a Retsch made Horiba LA-950 laser light diffraction measurement unit. Particle size of Pural NF ranges from $x_{10,0}$ = 1.34 µm to $x_{90,0}$ = 4.29 µm with the number median $x_{50,0}$ = 1.98 µm and a standard deviation of 1.77 µm. Particle size of Ulmer Weiß XMF ranges from $x_{10,0}$ = 0.57 µm to $x_{90,0}$ = 2.28 µm with the number median $x_{50,0}$ = 1.16 µm and a standard deviation of 0.81 µm. Both materials have a white color.

Fig. 1 Schematics of the electrostatic precipitator, with three wire electrodes and copperplate anode
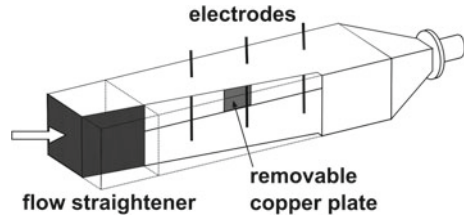
The schematics of the electrostatic precipitator are shown in Fig. 1. Dimensions of the precipitation chamber are length L = 1.2 m, width W = 0.5 m and height H = 0.3 m.

Particulate test material was dispersed by a K-Tron screw feeder combined with an air pressure nozzle and homogenized before entering the precipitation chamber. Inside the chamber three high voltage precipitation wire electrodes are placed along the center axis, at a distance to the chamber inlet. The distance between the equally spaced wires was 0.3 m. By using a high voltage supply (70 kV) corona discharge was created. These charges precipitate particles from the aerosol on the conducting copperplate. For optical analysis of the deposited particles, three stubs with a diameter of 20 mm were mounted into the conducting copperplate. They were positioned lengthwise with respect to the second electrode at a height of 0.15 m. Precipitated particle layers were examined by means of a Keyence digital microscope as shown in Fig. 2. Examination criteria were thickness and surface morphology of the deposit. Results of precipitation tests with duration 10 min, 20 min and 30 min are shown in Table 1. The standard deviation within the deposit thicknesses may be the result of aerodynamic ripple building, as reported in [2, 3].
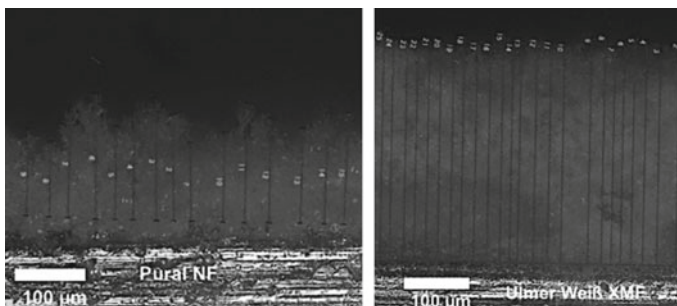
Fig. 2 Layer formation after 20 min test duration at 400× magnification for two test dusts

Table 1 Deposit thicknesses at different test durations

Test duration	10 min	20 min	30 min
Pural NF	125.2 μm ± 29.0 μm	169.0 μm ± 47.3 μm	225.3 μm ± 61.8 μm
Ulmer Weiß XMF	93.6 μm ± 17.3 μm	351.8 μm ± 55.7 μm	553.9 μm ± 47.9 μm
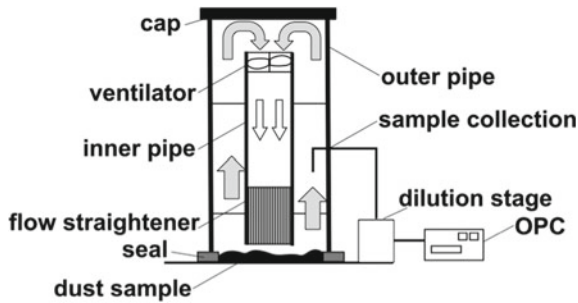
Fig. 3 Schematics of the redispersion dust in a double pipe-system (RDDS)

Resuspension experiments were carried out by means of a redispersion dust in a double pipe-system (RDDS), connected to a dilution stage and a Grimm 1.108 optical aerosol spectrometer (OPC). Schematics of the RDDS are shown in Fig. 3.

The implementation of a dilution stage between sample collection and the OPC ensures not to exceed the maximum permissible particle load of the aerosol spectrometer. Results of the resuspension experiments are shown in Figs. 4 and 5 for three particle size fractions. In time zone B the ventilator was running and thus resuspending the particles. In A and C the ventilator was switched off. As for Pural NF the influence of the deposit thickness on dust formation tendency for different particle fractions is clearly recognizable while the resuspension experiments with Ulmer Weiß XMF where inconclusive.

Similar experiments were made with fly ash to support modeling processes of project A1.
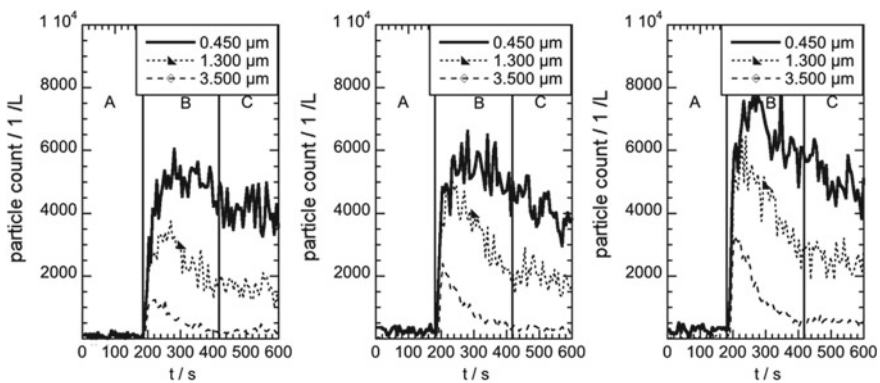
Fig. 4 Resuspension of Pural NF (10, 20, 30 min deposition time from left to right)
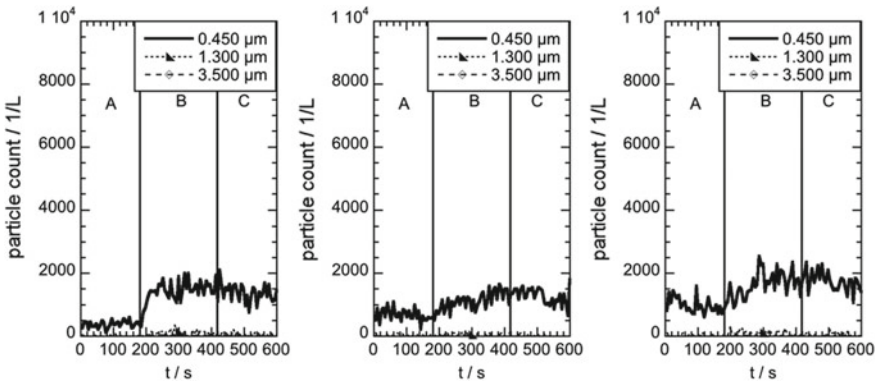
Fig. 5 Resuspension of Ulmer Weiß XMF (10, 20, 30 min deposition time from left to right)

2.2　Cooperation with Project A3: Agglomeration in a Fluidized Bed Reactor

In cooperation with project A3 "Spray granulation in a fluidized bed reactor" maintained by the Technische Universität Hamburg-Harburg formation of fine particles due to overspraying were investigated in a Glatt G25 fluidized bed reactor, with a Grimm 1.108 aerosol spectrometer. The aim of this cooperation was the identification and characterization of the dust content within the granulation process. In particular the occurrence of thermal overspray could be detected. In addition, an influence of process temperature, layer height of the particle bed in combination with the use of bottom spray nozzles and dust reduction through the filter cleaning could be determined.

On the basis of the obtained results it can be confirmed that overspray has occurred in the processes carried out under the process conditions used. Based on these results, it was possible to identify the direct formation of fine particles from the solution within the particle size range 0.3–4 µm. These findings contradict the assumption of the formation of particles within the size range from 6.5–110 µm, which is based on previous investigations to characterize the spraying process of the nozzles. However, it should also be mentioned that the Grimm 1.108 can only be used up to a measuring range of 20 µm. Due to the coarse resolution of the Parsum probe, which is regularly used for online measurements within the G25, the range of fines between 20 µm and below 500 µm could not be resolved. The formation of germ particles by spraying cannot be confirmed or refuted accordingly for this size range.

2.3   Cooperation with Project A5: Separation by Sieving

In cooperation with project A5 "Development of a dynamic physical based model for the sieving process" maintained by the Technische Universität Berlin (TUB) emissions of the sieving process of reference test bulk material (RTBM) were investigated, to generate reference scenarios for computational simulations.

In contrast to conventional laboratory sieving towers, where material is strained in the ground-parallel X-Y-plane, the in-house development of TUB will strain the material in vertical Z-direction. The test materials RTBM 1A and 1B were developed by Bergische Universität Wuppertal (BUW) to minimize the difference between numerical and experimental input data in computational dust release simulations [4]. One component of the binary powder mixtures consists of 1500 µm diameter steel balls made of AlSi 420. The second component consists of calcium carbonate, which was obtained from KSL Staubtechnik GmbH under the trade name Eskal 15. The particle sizes of the Eskal 15 used range from $x_{10.3} = 13.5$ µm to $x_{90.3} = 27.0$ µm, the mass median $x_{50.3}$ being 19.5 µm. RTBM 1A is composed of 95 g steel balls and 5 g Eskal 15. RTBM 1B is formed from 98 g steel balls and 2 g Eskal 15.

Particle immission in the range from 0.3 µm up to 20 µm was recorded at 6 s sampling rate for 300 s by a Grimm 1.108 optical particle counter. The sampling inlet was positioned 50 mm above the strained particle reservoir. After preliminary investigations on a steel wire screen with a mesh width of 0.8 mm, an aluminium plate was used instead as base in all of the experiments. Vertical straining was carried out at sieving frequencies 3.3 s^{-1}, 6.6 s^{-1} and 10.0 s^{-1}. Results are shown in Figs. 6, 7, 8.

Fig. 6 Immission 50 mm above the reservoir at 3.3 s^{-1} sieving frequency
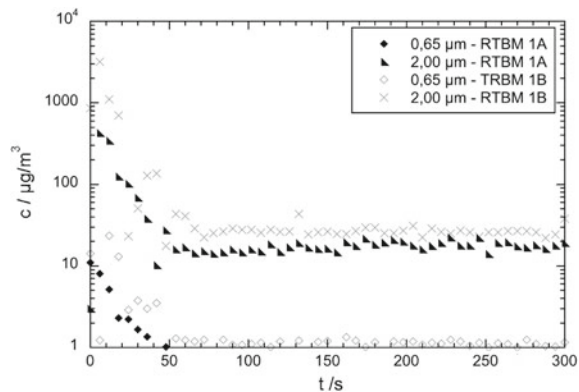
Fig. 7 Immission 50 mm above the reservoir at 6.6 s^{-1} sieving frequency
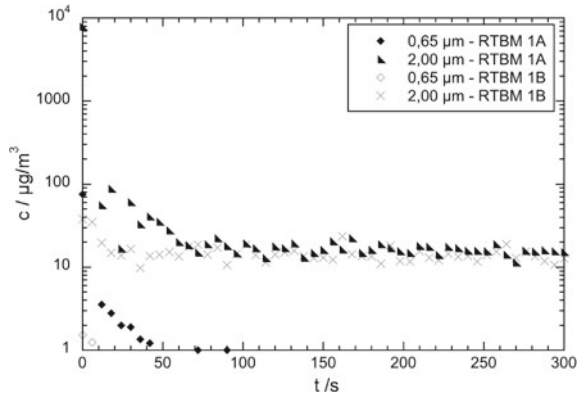
Fig. 8 Immission 50 mm above the reservoir at 10.0 s^{-1} sieving frequency
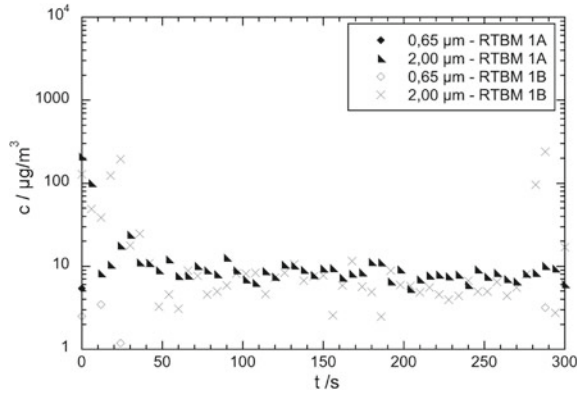
2.4 Cooperation with Project A6: Grinding Aids

In cooperation with project A6 maintained by the Technische Universität Braunschweig influences of grinding aids on product dustiness were investigated. Durcal40 limestone supplied by Omya AG, Switzerland was milled for 80 min in a GSM 06 (Siebtechnik GmbH, Germany) vibrating mill, with the addition of 0.1 mass percent of grinding aid. Purpose of the grinding was to produce limestone paticles with particle sizes in the lower micrometer range, since they have a wide industrial application. As grinding aids pure substances Triethanolamin (TEA) ($C_6H_{15}NO_3$), Diethylenglycol (DEG) ($C_4H_{10}O_3$) and heptanonic acid ($C_7H_{14}O_2$) with purities >96% were added.

The milling process took place in a hermetically sealed steel container with a volume of 1 L, which was filled to 30% with 6 mm diameter steel balls as grinding body. Sample size of Durcal40 was 198.1 g [5]. As a reference Durcal40 was milled without addition of a grinding aid, too. In preparation of the experiments, the limestone was dried for 20 h at 80 °C. In this way, four limestone powders were milled

from Durcal40. Particle size distribution of the ground powders was investigated by means of a HELOS laser light diffraction spectrometer made by Sympatec GmbH, Germany, and a Horiba LA 950 laser light diffraction particle size analyzer made by Retsch Technology, Germany. Dustiness of the ground powders was investigated with a single drop apparatus (Sect. 3.2.1) and the UNC dustiness tester (Sect. 3.2.3).

Since dry powders were characterized in dustiness investigation, the measurement with the HELOS system was carried out as dry measurement. Therefore the HELOS diffraction spectrometer was coupled with a RODOS dry dispersion unit made by Sympatec, and a dispersion pressure of 2 bar was set. For comparison wet dispersion measurements were made with the Horiba LA 950. Results of both measurements are shown in Figs. 9 and 10.

It should be noted, that in dry particle size analysis, tightly bound agglomerate structures are actual depicted as primary particles, since dry dispersion in the air stream is usually insufficient for complete digestion of the agglomerates in this particle size range. However, the particle sizes obtained with the HELOS system will more realistically represent the conditions in the single drop apparatus as well

Fig. 9 Particle distribution density by mass of dry dispersion measurement with HELOS/RODOS combination for reference grinding and grinding with different grinding aids
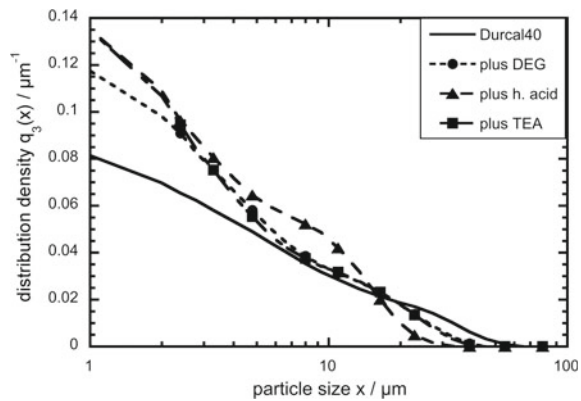
Fig. 10 Particle distribution density by mass of wet dispersion measurement with Horiba LA 950 for reference grinding and grinding with different grinding aids
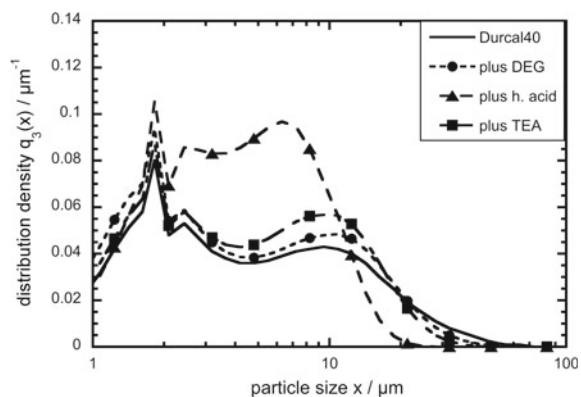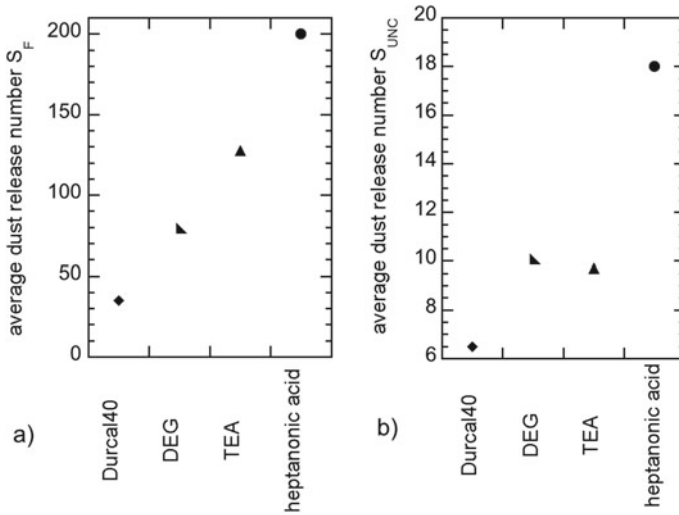
Fig. 11 Results of experimental dustiness assessment. **a** with single drop apparatus and **b** with UNC dustiness tester for total suspended particles

as in the UNC dustiness tester than those obtained with the wet dispersion analysis of the Horiba LA 950.

The average dust release numbers of the experimental dustiness assessments are shown in Fig. 11. When comparing against Durcal40, which was milled without the use of grinding aids, it can be seen that the use of grinding aids results in a significant increase of material dustiness. Particularly noteworthy in this context is the use of heptanonic acid, which led to the highest dust measurement in both test methods.

2.5 Cooperation with Project A10: Jet Mill

In cooperation with project A10 "grinding with a jet mill" maintained by the University of Erlangen dustiness of jet mill grind material was investigated. Soda-lime-silica glass beads (SiLibeads Solid Micro Glass Beads) and Nabalox® calcinated alumina for grinding (>99.6% Al_2O_3) were milled in the jet mill at different process conditions. The obtained particle size distributions of the ground substances shown in Figs. 12 and 13 were measured in water at the University of Erlangen with a Mastersizer 2000 made by Malvern Panalytical.

Based on the material-specific parameters density, porosity and particle size distribution of the SiLiBeads and Nabalox®, a dustiness potential prognosis was carried out according to [6] for the rotating drum apparatus. The results of the prognosis are shown in Table 2 together with supplementary laboratory dustiness analysis with the rotating drum method.

Fig. 12 Cumulative particle size distribution by mass of the investigated Soda-lime-silica glass beads
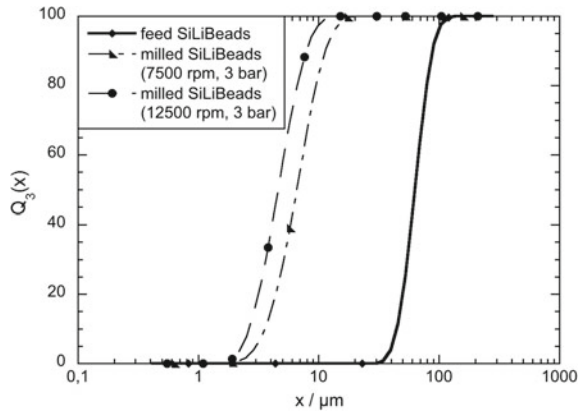
Fig. 13 Cumulative particle size distribution by mass of the investigated calcinated Alumina
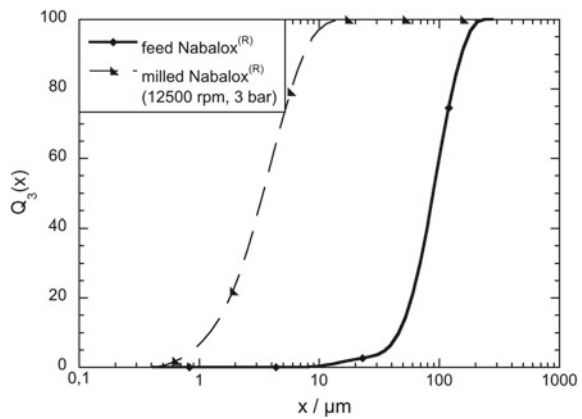
Table 2 Comparison between prognosed and measured dust release

Material	Bulk density/ g cm^{-3}	Porosity	Milling parameter	Prognosed dust release number $S_{RD,P}$	Experimental dust release number $S_{RD,E}$
SiLiBeads	282.4	0.89	feed	109	39
SiLiBeads	205.6	0.85	7500 rpm, 3 bar	232	996
SiLiBeads	188.9	0.86	12500 rpm, 3 bar	202	505
Nabalox®	245.3	0.93	feed	325	658
Nabalox^b	179.9	0.93	12500 rpm, 3 bar	112	79

Referring to Table 2, it can be seen that the predicted dustiness tendencies deviate significantly from the measured dust releases. This indicates, that the test materials, that underlie the prediction formula used, do not adequately represent the dusting properties of the investigated materials.

3 Development of Dustiness Forecast Functions

3.1 Introduction

At Bergische Universität Wuppertal dustiness forecast functions based on experiments with single drop method, rotating drum method and the UNC dustiness tester were developed [6]. These prognosis functions will allow estimations of dust formation tendency by means of distribution and material specific parameters for dry and moist materials and are implemented into the newly developed DYSSOL flow sheet simulation [7].

3.2 Testing Methods

3.2.1 Single Drop Method

To simulate filling processes of bulk material a laboratory scale single drop testing method is used (see also Fig. 14). After opening a trapdoor, a 30 g powder sample falls through a 0.5 m long pipe into the measurement chamber. Here collision with and sedimentation on the chamber bottom occurs. By logging the extinction of two laser light sources the time dependent development of dust emission can be monitored.

Fig. 14 Schematics of the single drop testing method
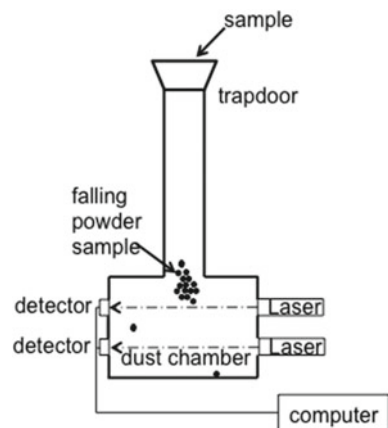
The dustiness number S_{SD} is derived from the maximum attenuation of light E_{MAX} and the light attenuation E_{30}, which is recorded 30 s after the drop of the sample (Eq. 1).

$$S_{SD} = E_{MAX} + E_{30} \tag{1}$$

3.2.2   Rotating Drum Method

To simulate mixing and filling of powders, the rotating drum testing method according to DIN 55992-1 is used. Schematics of the method are shown in Fig. 15. A powder sample (100 g) is placed in the rotating drum of the apparatus. By rotation with a fixed rate of 30 rpm the sample is simultaneously mixed, dropped and dispersed as shown in Fig. 16. An axially induced air flow, generated by the service modul will transport the released particles out of the rotating drum, beyond a separator for coarse
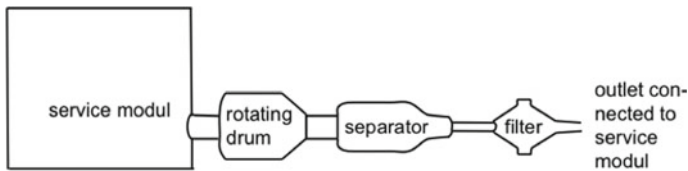
Fig. 15   Schematics of the rotating drum testing method according to DIN 55992-1

Fig. 16   Demonstration of the rotating drum method sample straining (counterclockwise rotation)
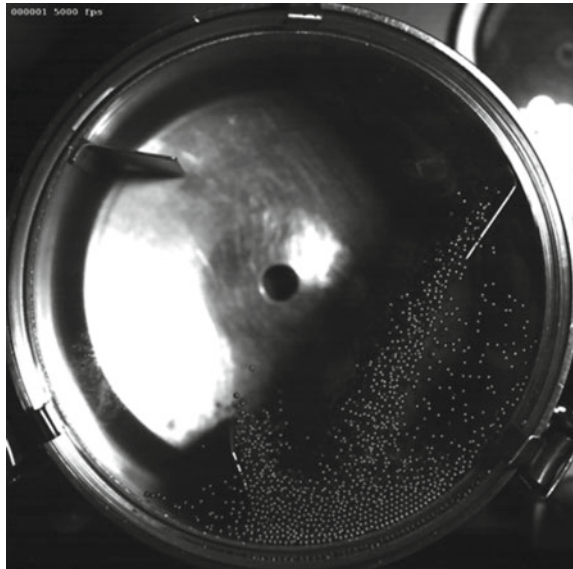
Fig. 17 UNC dustiness tester

particles onto a filter. The amount of released and transported particles is determined gravimetrically after a sampling time of 5 min and an overall air flow of 100 L. Calculation of the dust release number S_{RD} is based on Eq. (2); m_0 is mass of the powder sample, m_1 is mass of the unused filter, m_2 is mass of the used filter.

$$S_{RD} = 10^5 \cdot (m_2 - m_1)/m_0 \tag{2}$$

3.2.3 UNC Dustiness Tester

The UNC Dustiness tester shown in Fig. 17 was developed at the University of North Carolina to simulate the dust dispersion by a single blast of compressed air. This batch device has been specifically designed for the testing of potential hazardous or costly powders. Therefore the sample mass is limited to 10 mg per test. The dispersed powder will be collected by two samplers, to quantify gravimetrically the respirable and total dust that was generated with a given energy input.

The calculation of the dust release number S_{UNC} for respirable (index R) and total dust (index T) is based on Eqs. (3) and (4); m_0 is mass of the powder sample, m_1 is mass of the unused filter, m_2 is mass of the used filter.

$$S_{UNC,T} = 100 \cdot (6.2/2.0) \cdot \left(m_{2,T} - m_{1,T}\right)/m_{0,T} \tag{3}$$

$$S_{UNC,R} = 100 \cdot (6.2/4.2) \cdot (m_{2,R} - m_{1,R})/m_{0,R} \tag{4}$$

3.3   Materials

Nine different test materials as listed in Tables 3 and 4 and depicted in Fig. 18 were used to develop empiric dustiness forecast functions for the methods described in Sect. 3.2. Care was taken in the selection process to ensure, that the selected test materials will cover a wide range of material- and distribution-specific properties. For each material sorption isotherms were derived from experiments with a climate test chamber [6].

Table 3   Test materials [6]

Material		Main components	Density, g/cm^3	Bulk density, g/cm^3	Porosity
Arizona test dust	A1	>98% SiO_2	2.54	0.53	0.79
Arizona test dust	A2	>98% SiO_2	2.62	0.74	0.72
Arizona test dust	A3	>98% SiO_2	2.61	0.84	0.68
Arizona test dust	A4	>98% SiO_2	2.63	1.10	0.58
Pural NF	F1	77% Al_2O_3, 22.998% H_2O	2.35	0.50	0.79
Ulmer Weiß XMF	F2	99.2% $CaCO_3$, 0.4% $MgCO_3$, 0.25% SiO_2, 0.1% Al_2O_3 0.035% Fe_2O_3	2.68	0.69	0.74
KSL 14027 construction site test dust	Bau	ca. 25% SiO_2, ca. 25% $Ca(SO_4)$ ½ H_2O ca. 25% brick dust ca. 25% Portland cement	2.80	0.85	0.70
ECE R-45	P1	ca. 88% SiO_2, ca. 10% charcoal-dust ca. 2% NaCMC	2.30	0.80	0.65
KSL 11047	P2	37 … 72% SiO_2, 7 … 14% Al_2O_3, 3 … 6% $CaMg(CO_3)_2$ 2.5 … 40% viscose rayon 2 … 4% Fe_2O_3 1.35 … 10% cotton fiber	2.08	0.27	0.87

Table 4 Material specific parameters [6]

Parameter	A1	A2	A3	A4	F1	F2	BAU	P1	P2
$x_{10,2}$, μm	0.57	0.44	0.38	0.96	1.41	1.35	1.12	1.00	0.49
$x_{10,3}$, μm	1.06	1.44	2.25	4.57	2.76	1.73	8.48	4.92	14.25
$x_{50,2}$, μm	1.68	1.64	1.56	4.16	4.28	2.59	3.18	5.02	5.71
$x_{50,3}$, μm	2.74	6.75	19.98	32.84	9.06	3.55	350.25	26.95	43.52
$x_{90,2}$, μm	3.73	5.73	12.51	31.34	12.02	5.33	24.70	29.99	40.23
$x_{90,3}$, μm	9.78	52.09	68.20	106.22	40.72	6.54	637.77	87.64	251.34
$x_{mod,3}$, μm	2.77	3.18	36.65	63.17	9.42	4.18	479.91	42.00	28.12
d_{32}, μm	2.14	3.35	5.01	12.01	6.25	3.02	21.39	12.00	18.75
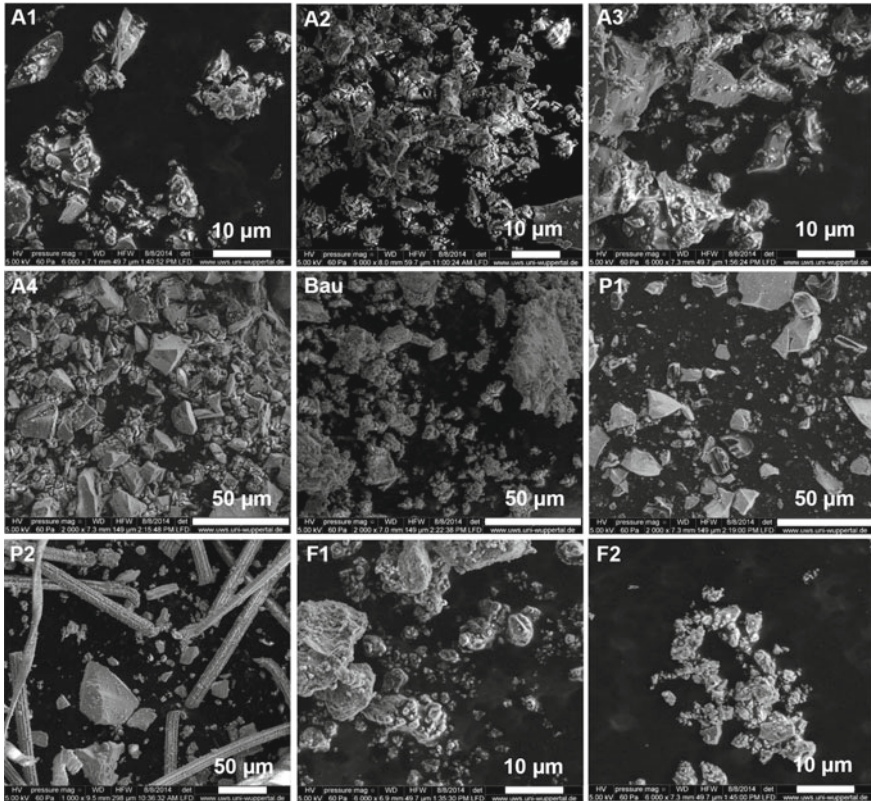
Fig. 18 Scanning electron micrographs of nine test material (cf. Tables 3 and 4)

3.4   Forecast Functions

For each testing apparatus several forecast functions were developed, taking into account relative humidity, particle distribution parameters as mass median $x_{50,3}$ and Sauter diameter d_{32}. In case of the single drop method prognosis functions the two attenuations of light E_{max} and E_{30} are predicted by the equations given in Table 5, using the apparatus specific calculation factor K_{SD} as shown in Eq. (5).

$$K_{SD} = (2/3) \cdot (d_{32}/\mu m) \cdot (\varepsilon/(1-\varepsilon)) \cdot \left(x_{50,2} - x_{10,2}\right)/x_{50,2} \tag{5}$$

ε is bulk porosity; d_{32} is Sauter diameter; $x_{i,2}$ is a percentile of the particle size distribution by area.

Table 5 Prediction functions for single drop method under different environmental conditions [6]

Environmental conditions	Forecasting functions
20% relative humidity	$E_{max} = -14.32 + 30.98 \log K_{SD}$ $E_{30} = -11.80 + 21.49 \log K_{SD}$
50% relative humidity	$E_{max} = -19.19 + 29.14 \log K_{SD}$ $E_{30} = -14.10 + 17.79 \log K_{SD}$
80% relative humidity	$E_{max} = -20.00 + 29.30 \log K_{SD}$ $E_{30} = -14.04 + 17.33 \log K_{SD}$
Low vacuum	$E_{max} = -14.76 + 24.71 \log K_{SD}$ $E_{30} = 8.88 + 14.91 \log K_{SD}$

Table 6 Prediction functions for rotating method, X_A = moisture content of material sample, $X_{0.9}$ = moisture content of a material at 90% relative humidity [6]

Dry bulk material	$\log S_{RD,dry} = 3.11 - 0.67 \, K_{RD}$
Wet bulk material	$\log (S_{RD,wet}/X_{0.9}) = 2.21 \, (X_A \, K_{RD})^{-0.14}$

In case of rotating drum method, the apparatus specific calculation factor K_{RD} is based on Eq. (6). Mean prediction functions for dry and wet bulk materials are given in Table 6.

$$K_{RD} = (d_{32,GP} / d_{32}) \cdot (1/\varepsilon) \cdot x_{50,3}/(x_{90,3} - x_{10,3}) \tag{6}$$

ε is bulk porosity; d_{32} is Sauter diameter; $d_{32,GP}$ is Sauter diameter taking into account all particles larger than 2.9 µm for dry bulk material and 3.9 µm for wet bulk material; $x_{i,3}$ is a percentile of the particle size distribution by mass.

In case of the UNC dustiness tester only the amount of total dust is predicted (see Eq. (7) and Table 7).

$$K_{UNC} = (3/2) \cdot (\mu m / d_{32}) \cdot ((1 - \varepsilon)/\varepsilon) \cdot (d_{32,GP} / d_{32}) \cdot x_{50,3}/(x_{90,3} - x_{10,3}) \tag{7}$$

ε is bulk porosity; d_{32} is Sauter diameter; $d_{32,GP}$ is Sauter diameter taking into account all particles larger than 8.8 µm (for dry bulk material); $x_{i,3}$ is a percentile of the particle size distribution by mass.

Table 7 Total dust prediction functions for UNC dustiness tester, X_A = moisture content of material sample, $X_{0.8}$ = moisture content of a material at 80% relative humidity [6]

Dry bulk material	$\log S_{UNC,dry} = 0.93 \exp (-0.15 \, K_{UNC})$
Wet bulk material	$\log (S_{UNC,wet} \, X_A) = 0.50 + 0.44 \, (\varepsilon \, X_A \, X_{0.8} \, (x_{90,3} - x_{10,3})/(x_{90,2} - x_{10,2}))$
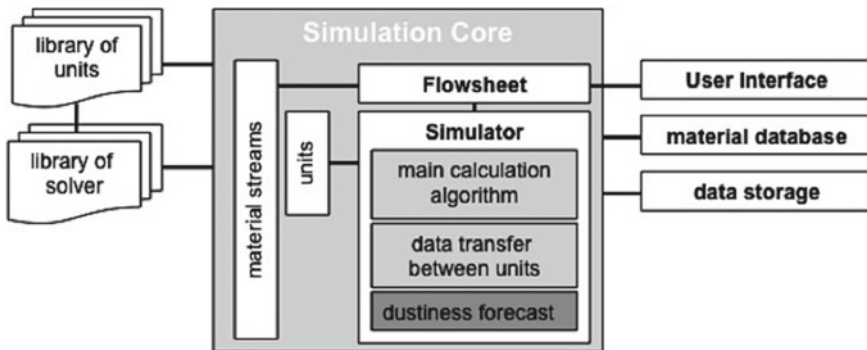
Fig. 19 DYSSOL flowsheet simulation schematics [7]

3.5 *Implementation in DYSSOL*

Releasing particles does not only represent loss of material and thus a cost factor but also a potential threat to human health as well as to the environment. Because of this it may be relevant to know the dust formation tendency of a simulated substance for classification issues according to the European Chemicals Regulation REACH (Registration, Evaluation, Authorization and Restrictions of Chemicals). In DYSSOL dynamic flow sheet [7], dust formation tendency prognosis based on single drop, rotating drum and UNC dustiness tester are part of simulation results. The dustiness forecast module is an integral part of the simulation core (cf. Fig. 19), connected to relevant simulation results obtained from the product stream leaving the simulated units.

4 Further Research

The prediction functions offer development potential beyond their use in DYSSOL, for instance in the development of a more efficient particle reservoir model using Exner equation based sediment mass balance approach. Such a reservoir model may improve the performance of the recently published fractionate release model [1] and other geoscientific dust release models.

Another application of such a reservoir model may be in further development of the adhesion-based assessment of the dustiness of powders and binary powder mixtures, as reported by Parey [8]. Irrespective of such development options further experimental research is needed in case of fractionate release of particles from strained reservoirs as for instance powders grinded with grinding aids.

References

1. Schmidt, E.: Fraktionsfreisetzungsgrad-Ein neuer Ansatz zur Quantifizierung der Staubungsneigung von Pulvern. Chem.-Ing.-Tech. **87**(5), 638–643 (2015)
2. Parsons, A.J., Abrahams, A.D. (eds.): In: Geomorphology of Desert Environments, Springer Science + Business Media B.V., 2. Auflage (2009)
3. Londershausen, T., et al.: Characterization of powder layer dustiness – influence of the deposit thickness. Chem. Eng. & Technol. **40**(9), 1720–1725 (2017)
4. Schwindt, N., et al.: Development of dust release functions to describe the particle emissions of bulk materials. In: 9th International Conference for Conveying and Handling of Particulate Solids, 10th–14th September, London, UK
5. Londershausen, T. Vaupel, K., Prizwara, P., Schmidt, E.: Einfluss von Mahlhilfsmitteln auf die Staubungsneigung. Chemie Ingenieur Technik Chem.-Ing.-Tech., 91 (2019). https://doi.org/10.1002/cite.201800084
6. Londershausen, T.: Entwicklung von Prognosefunktionen zur Abschätzung der Staubungsneigung von trockenen und feuchten Schüttgütern. Shaker Verlag, Aachen (2018)
7. Skorych, V., et al.: Novel system for dynamic flowsheet simulation of solid processes. Powder Technol. **314**, 665–679 (2017)
8. Parey, M.: Ein Modell zur haftkraftbasierten Bewertung der Staubungsneigung von Pulvern und binären Mischungen. Shaker Verlag, Aachen (2017)

Part III
Algorithms and Process Simulation

Chapter 13
Morphological Modelling and Simulation of Crystallization Processes

Simon Schiele, Tijana Kovačević, and Heiko Briesen

Abstract The shape of crystals is an important property that has a great impact on their physical behavior. Examples are flowability, dissolution, and growth kinetics. Still, crystals are often described by a single size parameter. One reason is, that today shape information is still hard to measure. Additionally, only few modeling techniques exist that are able to describe the shape of crystals. In this chapter, these issues are addressed by accurately describing crystals with mathematical models, making the full morphological structure of crystals and their agglomerates accessible by stereoscopic and three-dimensional (3D) imaging techniques and using these methods to model crystallization while considering the complex shape of the crystals. In addition, artificial neural networks (ANN) are used to classify whether projections of crystals show single crystals or agglomerates. As a final step, a case study of a model of a mixed suspension mixed product removal (MSMPR) crystallizer and a hydrocyclone are integrated into the software platform Dyssol and used to dynamically simulate a crystallization process with recycling stream.

1 Introduction

Crystallization is an important process step in many pharmaceutical, chemical and food processes. It is used to purify and formulate solid products. After crystallization the products are initially suspended in the crystallization mother liquor. Subsequent process steps then deal with the separation of the valuable solids from the rest of the suspension. Such processes are typically centrifugation, filtration, and/or drying. All of the mentioned downstream processes and crystallization itself are highly dependent on the morphology of the particles. The morphology also affects physical properties such as dissolution rates that are particularly interesting for pharmaceutical substances.

S. Schiele · T. Kovačević · H. Briesen (✉)
Chair for Process Systems Engineering, Technische Universität München, 85350 Freising, Munich, Germany
e-mail: heiko.briesen@tum.de

Commonly, crystals are still described with only few size parameters (such as a diameter or other characteristic lengths). Such descriptions neglect the complex shape that crystals may express. It is not uncommon that crystals have e.g. needle-like shapes or form even more complex structures through agglomeration that are impossible to describe with only one or even a few size parameters.

Today, morphology of crystals is gaining increasing attention not only as a quality criterion, but also as process parameter. Therefore, it is of great interest to describe the morphology of crystals correctly in order to be able to model crystallization with correct consideration of crystal morphology.

The aim of this article is to summarize the efforts that was made in context of a collaborative research project (DFG SPP 1679) towards correct description of crystals and crystallization modeling [1–9]. Such models could then be used in future to optimize and control crystallization processes with respect to downstream process performance and product quality.

2 Mathematical Description of Crystals

This section summarizes the basic mathematical crystal representation used in Reinhold et al. [9] and Kovačević et al. [1, 2, 4], which all used potash alum as an exemplary substance. The crystal structure of potash alum is shown in Fig. 1 along with the corresponding miller indices of their faces.

A common way to describe the form of facetted crystals is by Miller indices of their specific faces. This description however, brings two major drawbacks for morphological modeling. First of all, the Miller indices describe each face of a crystal independently and they do not contain any size information. The second drawback
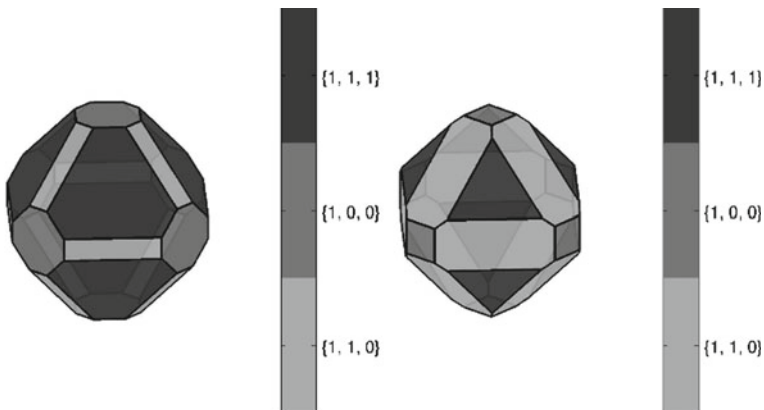
Fig. 1 Crystalline structure of potash alum crystals according to Ma et al. [10]. The crystals have different morphologies depending on which faces are most expressed. (Reprinted with permission from [8], Copyright (2015) Elsevier)

is that only ideal crystals can be described. More complex crystal shapes that may result from abrasion or agglomeration cannot be described. Therefore, alternative descriptions are explained here.

In mathematical terms, facetted convex shapes consisting of points x in space can be described by $\mathcal{H}$-representations [11]:

$$C(\boldsymbol{h}) = \{\boldsymbol{x} | \boldsymbol{A}\boldsymbol{x} \leq \boldsymbol{h}\} \tag{1}$$

where $\mathbf{A}$ is a matrix with normal vectors of facets in space $\boldsymbol{a_i}$, and $\boldsymbol{h}$ is a vector with the length of these vectors. The $\mathcal{H}$-representation describes all points that are within the facets defined by $\boldsymbol{A}$ and $\boldsymbol{h}$. For crystals, rows of $\boldsymbol{A}$ can be interpreted as normal vectors of the faces of such a crystal. $\boldsymbol{A}$ is therefore specific for each crystal morphology. The vector $\boldsymbol{h}$ then describes the exact shape and size of an ideal crystal of form $\boldsymbol{A}$. Herein, the dimension of $\boldsymbol{x}$ is either two or three dimensional (2D/3D).

For crystals it is common that symmetry conditions apply. To reduce the dimension of $\boldsymbol{h}$, one can, therefore, introduce a crystal model-specific group mapping matrix $\mathbf{M_{h_C \to h}}$ [11]

$$\boldsymbol{h} = \boldsymbol{M_{h_C \to h}} \cdot \boldsymbol{h_C} \tag{2}$$

This operation can also be formulated in a reverse way with the pseudo inverse matrix $\mathbf{M_{h_C \to h}^+}$ [11]

$$\boldsymbol{h_C} = \boldsymbol{M_{h_C \to h}^+} \cdot \boldsymbol{h} \tag{3}$$

These constrained crystal models are called constrained $\mathcal{H}_C$-representations [11–13].

Because $\mathcal{H}$-representations only allow the description of ideal single crystals, the representation is extended so that also more complex shapes can be described. Abraded crystals, for instance, may not have sharp edges that would be described by an $\mathcal{H}$-representation, but may appear with round edges and corners. Agglomerates on the other hand may be concave and can therefore also not be represented by simple $\mathcal{H}$-representations.

For the description of rounded particles, an ideal kernel crystal (index k) was combined with a sphere. The combination of sets in general can be performed by the so-called Minkowski addition [14]. The combination of i sets $S_{1\ldots i}$ can be written as

$$S = \sum S_i = \left\{ \sum \boldsymbol{x_i} | \boldsymbol{x_i} \in S_i \forall i \right\}. \tag{4}$$

The addition of an ideal kernel crystal $C(\mathbf{h}_k)$ and a sphere B that has the radius λ_r [11] is accordingly written as

$$C(\boldsymbol{h}_k, \lambda_r) = C(\boldsymbol{h}_k) + \lambda_r B. \tag{5}$$
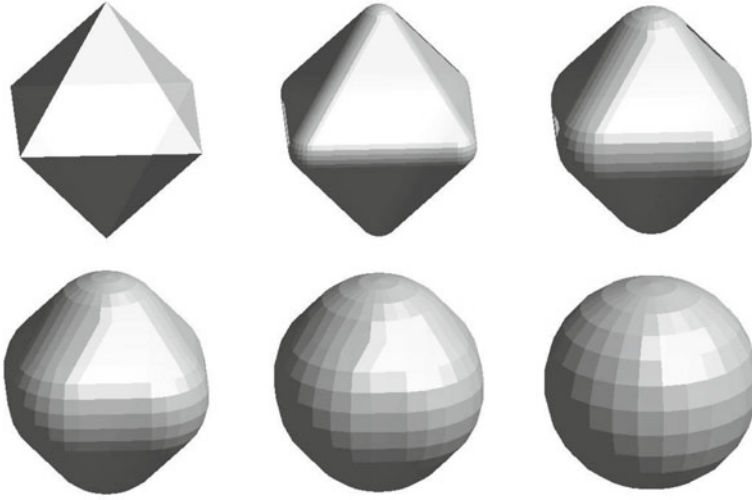
Fig. 2 3D models with increasing roundness obtained by the addition of octahedral potash alum kernel crystals with spheres. (Reprinted with permission from [9], Copyright (2015) Elsevier)

A graphical representation of Eq. (5) for six different radii and an octahedral potash alum kernel crystal can be seen in Fig. 2.

The representation as a 3D body allows the calculation of the volume μ^{vol}, surface area μ^{sur}, and mean width μ^{mw} from the corresponding measures μ_k^{vol}, μ_k^{sur}, and μ_k^{mw} of the kernel crystal and the radius of the sphere λ_r [14]:

$$\mu^{vol} = \mu_k^{vol} + \mu^{sur}\lambda_r + 2\pi\mu_k^{mw}\lambda_r^2 + \frac{4}{3}\pi\lambda_r^3 \tag{6}$$

$$\mu^{sur} = \mu_k^{sur} + 4\pi\mu^{mw}\lambda_r + 4\pi\lambda_r^2 \tag{7}$$

$$\mu^{mw} = \mu_k^{mw} + 2\lambda_r \tag{8}$$

For 2D bodies only μ_k^{sur}, and μ_k^{mw} can be calculated.

Agglomerates can be described by an $\mathcal{H}$-representation for each primary crystal. Additionally, information on orientation and location of the center of mass of the primary crystals is needed. Details are described in Sect. 2.3.

Another way to describe crystals is by a matrix $\boldsymbol{V}$ that contains vectors that point to the vertices of a crystal.

$$\boldsymbol{V} = \begin{bmatrix} \boldsymbol{v}_1, & \ldots, & \boldsymbol{v}_{n_v} \end{bmatrix}^T \tag{9}$$

Kovačević et al. call this a V-representation [1].

2.1 Description of Crystal Projections and Roundness Measurement

A fundamental question in crystal or particle representation is, how to deal with roundness instead of sharp edges and corners. A framework in this respect was introduced by Reinhold et al. [9]. The roundness of a crystal can be used as a parameter that describes how much attrition occurs in a process. To achieve this, first 3D crystals were modeled and then projections of these models were generated. They were used to validate the experimental procedures that are described in the end of this section. The comparison of the exact roundness obtained from 3D models and the roundness obtained from 2D projections of the model crystals allowed an evaluation of how well the roundness can be measured when only 2D information is available and how non-ideal images affect the roundness measurement. This is particularly interesting because it is currently not possible to obtain 3D images of crystals in real time and on-line analysis of particulate systems is often done by 2D image analysis.

To define the roundness of a particle, several definitions exist in the literature [15–18]. Here, a new descriptor for roundness μ^B was defined so that it can be calculated from the geometric properties of the Minkowski addition [9]. A spherical crystal which is by definition perfectly round, can be described by Eq. (5) with $\boldsymbol{h}_k = 0$ and hence $\mu^{\mathrm{mw}} = 2\lambda_r$ results from Eq. (8). A crystal that has sharp edges and is therefore as little round as possible for a given kernel crystal, is described by Eq. (5) with $\lambda_r = 0$ and hence $\mu^{\mathrm{mw}} = \mu_k^{\mathrm{mw}}$ results from Eq. (8). To reflect this concept of roundness the roundness parameter μ^B is written as

$$\mu^B = 1 - \frac{\mu_k^{mw}}{\mu^{mw}} = \frac{2\lambda_r}{\mu_k^{mw} + 2\lambda_r} \tag{10}$$

Note that it can be calculated for a body of any dimension, in this case for 2D and 3D bodies equivalently.

3D crystals with roundness between 0 and 1 and defined mean width were simulated using Eq. (5). A potash alum model with 26 faces was used for the kernel crystal model (see Fig. 3 left-hand side). This gained numerous crystal models with

Fig. 3 Rendered 3D model of a potash alum crystal model with 26 faces (left), a 2D projection of this crystal (middle) and the same 2D projection to which blur was added (right). (Reprinted with permission from [9], Copyright (2015) Elsevier)

known, exact measure of their roundness and mean width (grey line in Fig. 2). From each body, multiple 2D projections Π_p were generated and blur was added to the images, as described in [9] (see Fig. 3 middle and right-hand side). Finally, two additive roundness parameters were calculated for each particle from its 2D projections with the sharp and blurred 2D images (black lines in Fig. 2). The additive roundness estimates the roundness parameter of the real 3D particle from its n_{proj} projections:

$$\mu^B \approx 1 - \frac{\mu^{mw} - \sum_p \frac{1}{n_{proj}} \lambda_{r,\Pi_p}}{\mu^{mw}} \tag{11}$$

In the following, it is described how μ^{mw} and λ_{r,Π_p} were obtained from n_{proj} projections of a particle in order to be able to calculate the roundness μ^B according to Eq. (11). The first step was to find a 2D $\mathcal{H}$-representation of each individual projection. It was found by Hough transform [19] performed as follows. First, the center of mass of a projection was determined and considered as the center of a Cartesian coordinate system. Lines on the border of a projection can be described by an angle $\overline{\varphi}$ and distance from the center of mass $\overline{\rho}$. The vector $(\cos\overline{\varphi}, \sin\overline{\varphi})^T$ describes a normal vector of such a line. Then any point on the line x is described by the scalar product

$$\overline{\rho} = \left\langle x, \begin{pmatrix} \cos\overline{\varphi} \\ \sin\overline{\varphi} \end{pmatrix} \right\rangle \tag{12}$$

The pixels on the outline of a projection Π_p were considered as data points. $\overline{\varphi}$ and $\overline{\rho}$ were discretized in pieces $\overline{\varphi}_j$ and $\overline{\rho}_l$. Each point x could be described by several lines defined by Eq. (12) and a combination of $\overline{\rho}_l$ and $\overline{\varphi}_j$. A bin value was introduced for each combination of $\overline{\rho}_l$ and $\overline{\varphi}_j$ that represented how many data points x were described by such a line. This yielded a grey scaled image with the coordinates $0 \leq \varphi_i \leq 2\pi$ and $\overline{\rho}_{min} \leq \overline{\rho}_l \leq \overline{\rho}_{max}$ (see Fig. 4). High bin values (represented as dark points in Fig. 4) indicate coordinates which describe many points of the outline

Fig. 4 Bin values of a Hough transform. (Reprinted with permission from [9], Copyright (2015) Elsevier)
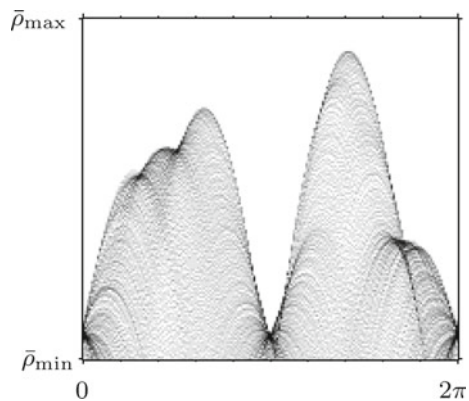
of a projection. In other words, these lines represent long sections of the outline. The corresponding distance $\overline{\rho}_l$ and normal vector $(\cos \overline{\varphi}_j, \sin \overline{\varphi}_j)^T$ were hence potential values for an $\mathcal{H}$-representation.

To reduce the number of outlines, only local maximum bin values (index m) were considered as detected lines. They were described by the vectors

$$\boldsymbol{a}_{c,\Pi_p,m} = (\cos \overline{\varphi}_m, \sin \overline{\varphi}_m)^T \tag{13}$$

that make up the matrix A of a 2D $\mathcal{H}$–representation. The face distances $\boldsymbol{h}$ were given by all $\overline{\rho}_m$. Like this, a 2D $\mathcal{H}$–representation of a projection was found.

To describe not only the kernel crystal but also the roundness, a disc with radius λ_r was added to the $\mathcal{H}$-representation using the Minkowski addition. The size of this disc was determined by solving a minimization problem: The experimental data contained the outline of a projection. This outline was also described by the Minkowski addition of the previously found $\mathcal{H}$–representation and a disk of unknown radius λ_r (Eq. 5). An appropriate disc radius was then found by minimizing the distance between these two lines. A detailed description is given by Reinhold and Briesen [9].

From the Minkowski additions of each projection Π_p, a mean width $\mu_{\Pi_p}^{\mathrm{mw}}$ was obtained according to Eq. (8) and used to calculate the additive roundness defined in Eq. (11).

It can be seen in Fig. 5, that even for crystals that had perfect edges (set $\mu^B = 0$) a roundness of 0.17 was measured. This was caused by the discretization of the boundary points during image analysis. This error was even more pronounced for blurred images. As it can be seen in Fig. 3 that corners of the projections were not as expressed as in the sharp images. For very round particles, 2D analysis yielded lower roundness than one should expect (c.f. Fig. 5). This was caused by the fact that small line segments fitted well to a hand-full of boundary points, hence faces

Fig. 5 Simulated roundness (solid gray line) and the roundness obtained based on ideal (dashed black line) and blurred (solid black line) 2D images. (Reprinted with permission from [9], Copyright (2015) Elsevier)
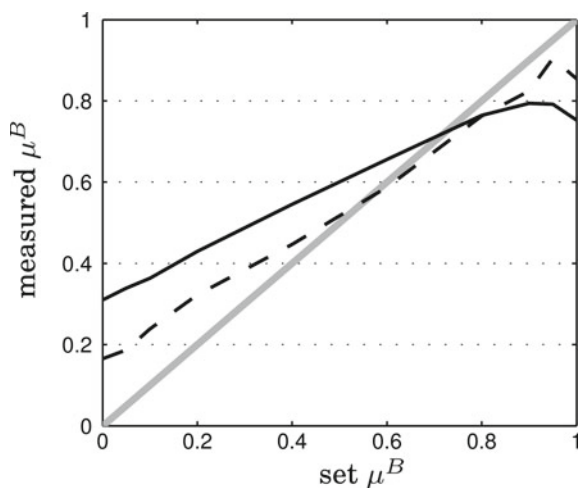
were found and the kernel crystal never fully disappeared. Overall, the roundness of particles can be measured well for roundness values below 0.85.

Going one step further, stereoscopic 2D images of real abraded potash alum crystals were obtained on-line from suspension with the stereoscopic imaging method described by Schorsch et al. and Reinhold et al. [9, 20]. Stereoscopic images were taken of potash alum crystals in a saturated, agitated solution at three points in time (start of the experiment, two hours and five hours after the start). Both the mean width and the additive roundness of the particles were calculated with Eqs. (14) and (11). A high stirring rate (1800 rpm) was used so that excessive abrasion occurred. Because the crystals were suspended in a saturated solution, neither growth nor dissolution was expected. Stereoscopic imaging as performed here yielded two orthogonal projections of a particle. For each of these projections a Minkowski addition was found by appropriate image analysis as described above.

The mean width of the real 3D particle was estimated by the weighted addition of the mean widths of the two obtained stereoscopic projections Π_p.

$$\mu^{mw} \approx \sum_p \frac{1}{n_{proj}} \mu_{\Pi_p}^{mw} \tag{14}$$

Figure 6 shows that at the beginning of the abrasion experiment the crystals were large (mean width between 450 and 850 µm) and have sharp edges (roundness around 0.3). With increasing experiment time, roundness increased (up to 0.7) and the mean width decreased (250 µm). Following the theory of Gahn and Mersmann
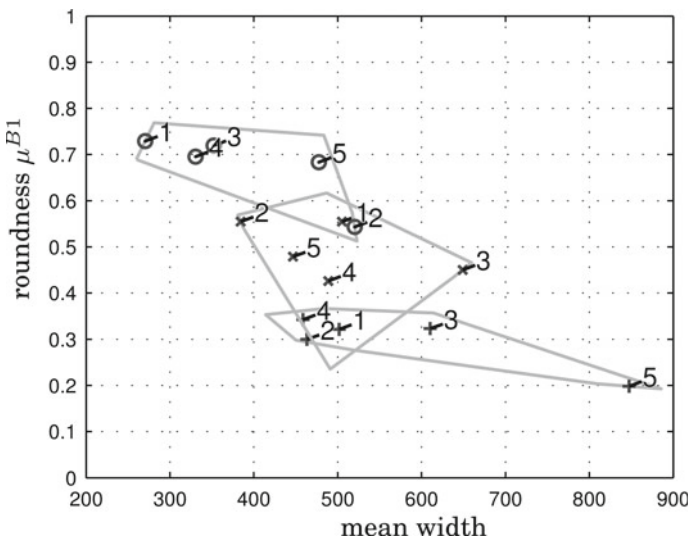

Fig. 6 Measured roundness of real crystals over their measured mean width at different time of the crystallization experiment. + indicate samples obtained at the start of the experiment, x after two hours and o after 5 h. (Reprinted with permission from [9], Copyright (2015) Elsevier)

[21], abrasion occurs through impact of crystals on the stirrer. This impact causes breakage predominantly at corners and edges of the particles [22, 23]. This explains that roundness increased and the mean width of the particles decreased through intensive agitation.

In conclusion, limitations of the measurement of roundness from 2D projections of particles were revealed and quantified. Further, a new method was demonstrated that is able—under the previously mentioned limitations—to quantify the particle roundness and mean width during crystallization by using stereoscopic imaging in combination with appropriate image analysis.

2.2   Shape Identification of 3D Single Crystals

Similar image analysis concepts as described in the previous subsection can be applied to 3D images of crystals. 3D images can be obtained by micro-computed tomography (μCT) as described by Kovačević et al. [1]. This imaging technique allows capturing the full shape information of particles. However, images are much harder to obtain.

The goal here was to find faces of measured crystals and fit them to a predefined crystal model. Here again, the image analysis involved face identification using Hough transform. Subsequently face normals of the predefined crystal models—given by a crystal specific matrix A—were matched to the faces found in a 3D image. The main difference to the problem in Sect. 2.1—except for the higher dimensionality—is that a crystal model was predefined and then fitted to the 3D images. The goal was to find faces that appear in a measured crystal.

In a first step, it was assumed that a 3D image of a crystal is given as a set of regularly distributed surface points. This data set was extracted from μCT measurements. A 3D polar coordinate system was chosen so that it originated from the arithmetic mean of these surface points. In this coordinate system face normal vectors were described by an azimuthal angle θ and a polar angle ϕ. Distances from the origin were described by ρ. Both angles θ and ϕ were then discretized using the HEALPix algorithm [24].

Figure 7 visualizes the HEALPix discretization of a unit sphere with 12 principal elements (solid outline), with $N_{\text{side}}^2 = 16$ subelements of equal area (dashed outline). For calculations in this work N_{side} was chosen as 20. Each of these $12 \cdot N_{\text{side}}^2$ subelements were represented by a potential face normal vector and face distance. The face distance was also discretized. To apply the Hough transform, each grid point that was defined by θ_i, ϕ_j and ρ_l was assigned a bin value $b(\theta_i, \phi_j, \rho_l)$ that represented the number of surface points within it. To obtain the directions of the face normals it was sufficient to define one bin value $\tilde{b}(\theta_i, \phi_j)$ per subelement:

$$\tilde{b}(\theta_i, \phi_j) = \max_{\rho} b(\theta_i, \phi_j, \rho_l) \tag{15}$$

Local maxima of this function represent orientations of face normals. A typical
function with its local maxima is shown in Fig. 8. Such local maxima were found by
a non-maximum suppression search [19, 26]. This algorithm was slightly adapted to
be used for points on a sphere as described by Kovačević et al. [1].

The points of the local maxima led to measured face normals that can be written
as

$$\boldsymbol{n}_F(\theta_i, \phi_j) = \left[\cos(\theta_i)\sin(\phi_j), \sin(\theta_i)\sin(\phi_j), cos(\theta_i)\right] \tag{16}$$

in a Cartesian coordinate system. All the measured face normals were summarized
in the matrix A_F.

The next challenge was to match the face normals of a crystal model A to these
measured face normals. This task was subdivided into three individual problems.
First, the measured vectors may had different order in A_F than their corresponding
model vectors in A, and A may contained faces that were not measured in a real
crystal because faces had disappeared e.g. due to fast growth. Second, the measured
matrix A_F may contained faces that were not included in the crystal model. This may
had happened due to agglomeration of breakage of the real crystals. Third, measured
face normal vectors needed to be rotated to point in the directions of the model.

The first problem was solved by defining a mapping matrix S_M that permuted the
vectors in A and excluded normal vectors which had no corresponding face in A_F.
For the second problem, a filter matrix S_D that excluded all faces in A_F that had no
corresponding face in A was defined. For the rotation of the measured into the model
vectors a rotation matrix R was defined. With these definitions, a real crystal was
approximated by a crystal model with
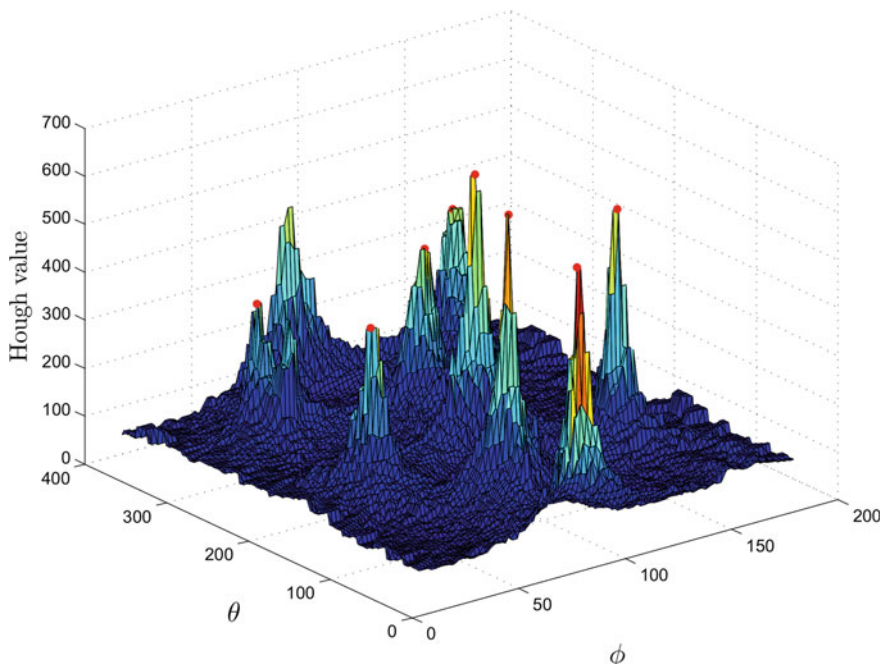
Fig. 8 Bin values of the Hough transform. Red dots mark local maxima. (Reprinted with permission from [1], Copyright (2014) American Chemical Society)

$$S_D \cdot A_F \approx (S_M \cdot A) \cdot R^T \tag{17}$$

The problem to rotate a set of vectors r_i into the vectors b_i was formulated by Wahba [27] and solved by Markley [28] by minimizing the least-square cost function

$$L(R) = \frac{1}{2} \sum_i \omega_i \|b_i - Rr_i\|^2 \tag{18}$$

We chose to use equal weights ω_i that satisfy $\sum_i \omega_i = 1$. The rotation matrix R was calculated from

$$R = UMW^T \tag{19}$$

Therein, U and W resulted from the singular value decomposition of the matrix B

$$B = \sum_i b_i r_i^T \tag{20}$$

into

$$B = UDW^T \tag{21}$$

and

$$M = diag(1, 1, \det(U), \det(W)) \tag{22}$$

Provided S_M and S_D were known, one could solve Wahba's problem given in Eq. (18). However, S_M and S_D were unknown and one could have found a solution to the problem by testing all possible combinations of S_M, S_D and R:

$$L(R, S_D, S_M) = \frac{1}{2} \sum_i \omega_i \left\| (S_D \cdot A_F)_i - \left[(S_M \cdot A) R^T \right]_i \right\| \tag{23}$$

This had involved the optimization over a huge parameter space, which is computationally inefficient. Kovačević et al. [1] developed an algorithm to efficiently solve this problem and described it in detail. Within the scope of this contribution it is sufficient to understand that a numerically efficient solution exists that yields R, S_D and S_M.

To obtain a description of a measured crystal by a crystal model so far a rotation matrix, a mapping, and a filtering matrix has been found. The face distances remained to be determined. This could have been done quite easily by finding the ρ_l that maximize Eq. (15) for faces that have been measured. However, for faces that have grown out of the crystal, and are hence not found in the measurement data, this does not work. For these cases, the measured data was cut into planar slices that are orthogonal on a face normal vector, and are therefore defined by $\rho n(\theta_i, \phi_j)$. The triangles in Fig. 9 show, that slices inside the measured data contain an outline of the crystal at distance ρ from the center. The ratio between the number of pixels on the outline and the area of the convex hull of the outline was then maximized by finding an appropriate face distance ρ. This principle is illustrated in Fig. 9. Therein the arrow indicates a normal vector of a face of a potash alum crystal that is not expressed in the measured data. The triangles represent the outline for a face distance that is too small, and squares indicate a slice where the mentioned ratio reaches its maximum.

In the last two steps towards a successful fit, it needed to be assured that all identified faces lied within the crystal model and fulfilled the symmetry conditions defined by the crystal model. The first issue is illustrated in Fig. 10: If a face distance was identified to be too long, a face lied outside of the model.

To assure that all identified crystal faces lied within the fitted model, invalid entries in the vector h were identified according to Reinhold and Briesen [11], and Borchert and Sundmacher [12] and then modified according to

$$h_i = \max_{1 \le i \le n_H, 1 \le j \le n_V} \langle a_i, v_j \rangle \tag{24}$$
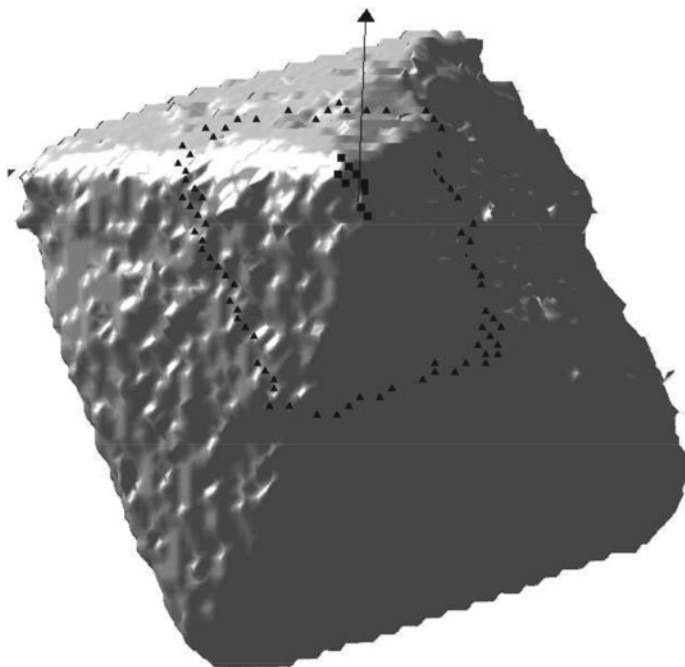
Fig. 9 Measured hull of a potash alum crystal with a model normal vector of a face that is not expressed in the measurement (arrow). Triangles indicate points in a slice that is orthogonal to the vector and that has a distance that is too small to appropriately describe the face distance. Squares indicate the length of the normal vector that describes a disappearing face of the crystal. (Reprinted with permission from [1], Copyright (2014) American Chemical Society)
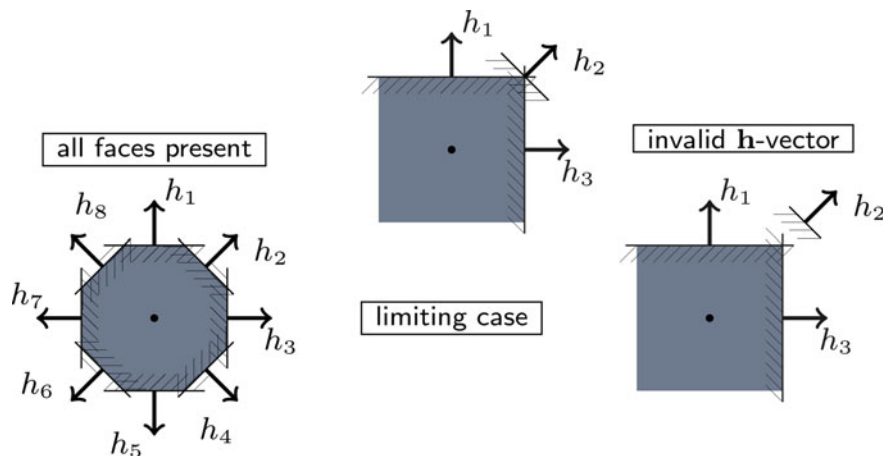
Fig. 10 Illustration of the problem of faces lying outside of a crystal model as discussed by Reinhold and Briesen [11]. An invalid face vector is shown on the right-hand side of the figure. (Reprinted with permission from [1], Copyright (2014) American Chemical Society)

where the vector $\boldsymbol{v}_\mathrm{j}$ represents vertices in the crystal's V-representation as defined in Eq. (9).

Finally, symmetry conditions were applied to ensure that all faces belonging to the same facet group had the same distance to the crystal center. The procedure is described by Kovačević et al. [1].

As measures how well investigated crystals were fitted, the mean quadratic deviation, d_quad, a volume ratio, r_vol, and the volume deviation, d_vol were introduced. d_quad is a measure to determine how much measured points differ from their fit. Therein long distances between model and measurement are weighted stronger. The volume ratio is a measure how well the volume is conserved and the volume deviation is a scaled measure of how much the fitted shape mismatches the measured shape. Details on how these measures were calculated can be retrieved from Kovačević et al. [1].

The method described in this section enables to fit crystal models to 3D μCT images obtained from regular potash alum crystals. Results of the fits are shown in Fig. 11. Irregular particles that resulted from e.g. breakage or agglomeration were identified by high volume deviations and high quadratic deviations.

In conclusion, the methods that were developed enable face identification in 3D images. It was described how these faces can be matched to predefined particle models. The method was applied to the model substance potash alum and it was shown that single particles can be described with only few parameters by appropriate crystal models.

2.3   Shape Identification of Crystal Agglomerates

Even more challenging than identifying single crystals is the identification of several primary crystals constituting a crystal agglomerate. Kovačević et al. [2] presents an approach how concepts of identification of single crystals can be transferred to the identification of agglomerates.

Generally, one needs to find all primary particles in an agglomerate and then use the methods described by Kovačević et al. [1] and in the previous section to model their structure with individual $\mathcal{H}$-representations. Thus, each agglomerate would be described by a hand full of $\mathcal{H}$–representations of its primary particles.

To separate agglomerates into their primary particles an algorithm based on the seeded watershed segmentation and region recombination was developed (see Fig. 12). The steps defined in Fig. 12 are illustrated with an example agglomerate in Fig. 13. The first step of the agglomerate segmentation algorithm is to find concavity points that are an indicator for contact points of primary particles. The 2D approach of Fernandez et al. [29] and Indhumathi et al. [30] was used and transferred to the presented 3D problem: A cubic mask was centered at each surface point of the measurement and a concavity value $c_\mathbf{p}$ was calculated. It was defined as the quotient of the number of voxels that contain material $N_\mathrm{foreground\ mask}$ and the number of voxels inside the mask N_mask.

(a) Error measures: $d_{\text{quad}} = 0.049, r_{\text{vol}} = 1.038, d_{\text{vol}} = 0.083$

(b) Error measures: $d_{\text{quad}} = 0.062, r_{\text{vol}} = 1.031, d_{\text{vol}} = 0.144$

(c) Error measures: $d_{\text{quad}} = 0.066, r_{\text{vol}} = 1.02, d_{\text{vol}} = 0.146$
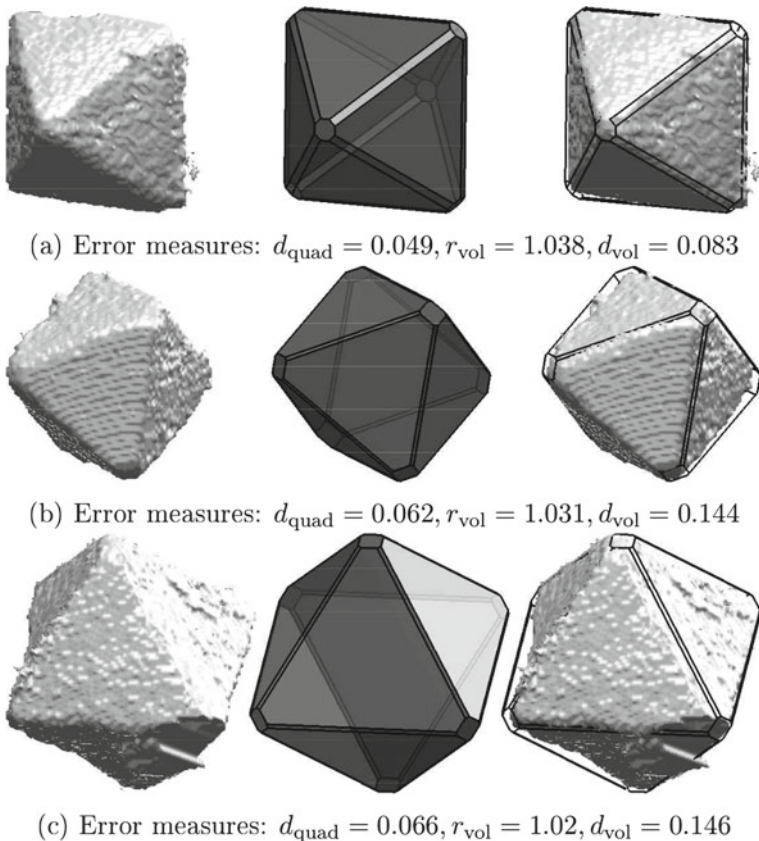
Fig. 11 Successful fits of regular potash alum crystals. (Reprinted with permission from [1], Copyright (2014) American Chemical Society)

In measurements with infinite resolution a concave region is identified by a concavity value higher than 0.5, meaning that more than half of the mask is filled. However, this is not a reasonable threshold for real measurement data. Due to the discretization of an image into voxels, surfaces appear rough even if they may be flat in reality. The concavity value also depends on the orientation and size of the mask. Therefore, the mask edge length was set to $2a + 1$ where $a = \sqrt[3]{0.0013 N_{\text{voxels}}}$. N_{voxels} is the total number of voxels inside a measured agglomerate. The concavity threshold was then calculated using

$$c_t = 1.2 \frac{(2a + 1)^2(a + 1)}{(2a + 1)} \tag{25}$$

The factor 1.2 was used to compensate for boundary roughness, different orientations of the masks, and measurement inaccuracies. Finally, concavity points were
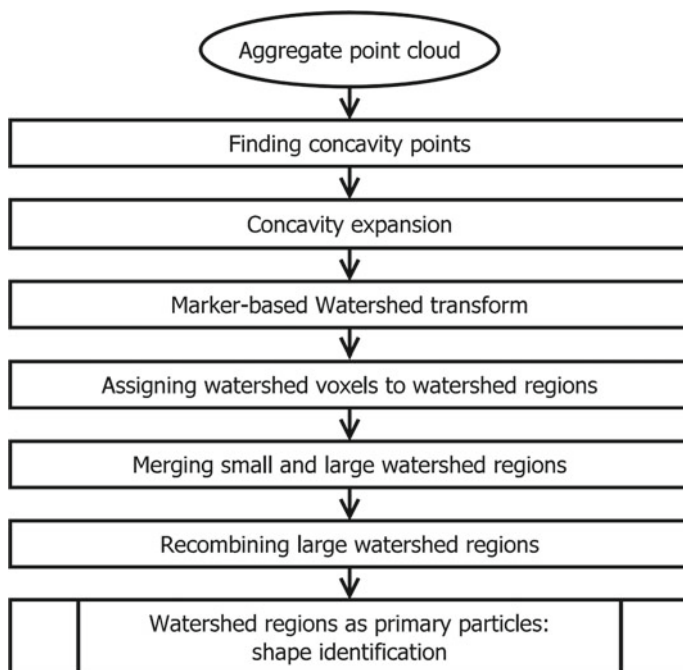
Fig. 12 Algorithm to separate agglomerates into their primary particles. (Reprinted with permission from [2], Copyright (2016) American Chemical Society)

identified by the local maxima of all points on the surface that satisfied $c_{\mathbf{p}} > c_t$. This was done by a non-maximum suppression peak search in cube shaped windows with an edge length of $a + 1$ [19, 26]. These concavity points were then expanded to prevent under-segmentation of the following distance transform-based watershed segmentation. The expansion was done in a way that a hole was drilled into the measured structure at every concavity point perpendicular to the surface (c.f. Fig. 13b). For details on the concavity expansion refer to Kovačević et al. [2]. Finally, watershed transform was applied to segment the agglomerate into primary particles. A description of the watershed transform algorithm can be found in the work of Vincent and Soille [31] and Gonzales et al. [32].

Although the concavity point expansion prevented under-segmentation by the watershed algorithm (under-segmentation shown in Fig. 13a), it often led to over-segmentation (Fig. 13c). Therefore, segments that belonged to the same primary particle needed to be identified and subsequently merged. To achieve this, first neighboring regions were identified. Then small regions that each made up less than 3% of the total number of voxels were merged with an adjacent region so that the concavity of the resulting larger region was minimized (Fig. 13e). The concavity of the merged region was calculated from Eq. (26):
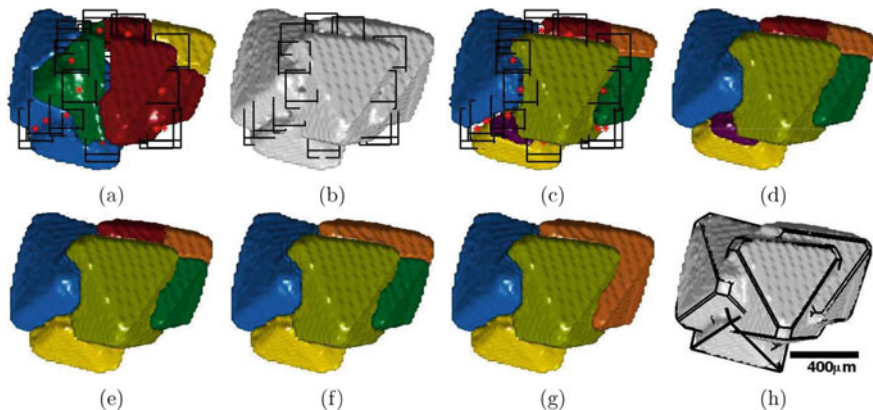
Fig. 13 Segmentation of an exemplary potash alum agglomerate with the algorithm summarized in Fig. 12. The images **a** and **c** show the difference of the result of the watershed transform when concavities are (**c**) or are not (**a**) expanded. Concavities are marked as red stars with their corresponding masks as black cubes. **b** shows the agglomerate with expanded concavity points. Image **c** shows the result of the watershed transform. In **d** the boundary voxels that have been identified by the water shed transform are merged into adjacent regions. In **e** the small, purple region in **d** is merged with the yellow region, **f**, **g** show the first and second iteration of the large region merging, so that (**g**) is the result of the segmentation algorithm. **h** shows the rendered measured crystal together with a successful fit obtained with the methods described in Sect. 2.2. (Reprinted with permission from [2], Copyright (2016) American Chemical Society)

$$c_r = \left| 1 - \frac{N_i + N_j}{V} \right| \tag{26}$$

N_i and N_j are the number of voxels of the two regions to be merged and V is the volume of their convex hull. For details on the exact procedure refer to Kovačević et al. [2].

After the small regions were merged, it was checked whether merging of large regions also led to a smaller average concavity of a merged region. Examples are the combination of the red and orange regions in Fig. 13e and the green and orange regions in Fig. 13f. While this was done, concavity points were considered. If the mask of a concavity point included exactly two regions, the merging of these two regions was forbidden. Another case where merging was forbidden is when merging would have been allowed according to the first condition, but the concavity value of a concavity point was increased through merging over some threshold. This could have been the case if a concavity point contained e.g. three regions. For details on this procedure again refer to Kovačević et al. [2].

Once an agglomerate was divided into its primary particles, the methods described in Sect. 2.2 could be adopted and applied to find $\mathcal{H}$-representations for each primary particle, as shown in Fig. 14h.

(a) Simulated polytopes   (b) Identified polytopes
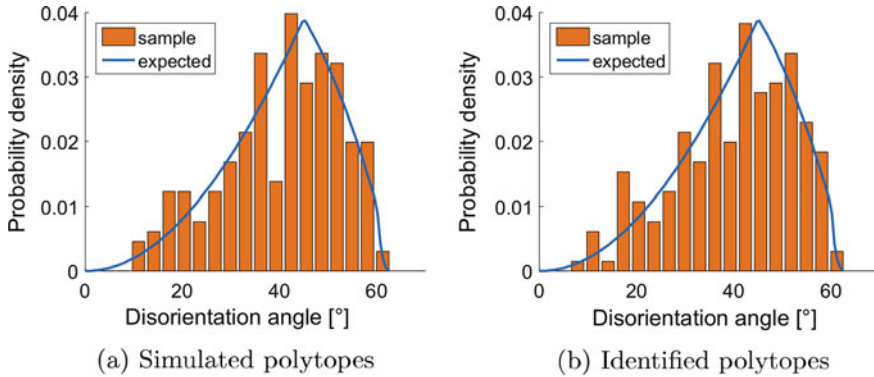
Fig. 14 In both panels the theoretical probability density of disorientation angles according to Mackenzie and Thomson [31] is shown as a blue line. Panel **a** shows the disorientation angles obtained with exact rotation matrices of a simulated sample population. **b** shows the angles obtained with rotation matrices that were identified with the algorithm summarized in [4] of the same population as used for panel (**a**). (Reprinted with permission from [4], Copyright (2017) Elsevier)

Kovačević et al. [2] also describe how non-ideal cases in which the segmentation algorithm produced regions that could not be fitted with the algorithm described in Sect. 2.2 were treated.

In conclusion, this section describes how agglomerates can be represented in their full geometric complexity. A seeded watershed algorithm was applied to separate a measured particle into several segments. The segments were then merged under consideration of certain criteria to yield primary particles inside an agglomerate. Finally, the methods described in Sect. 2.2 were applied to describe each primary particle separately.

2.4 Disorientation Angles in Potash Alum Agglomerates

The procedures described in Sects. 2.2 and 2.3 enable the mathematical description of measured 3D crystal images. The mathematical description allows detailed analysis of the complex structures. One particular feature of crystal agglomerates which is accessible with the presented tools is the angle between the primary particles. To check whether there is a preferred orientation Kovačević et al. [4] used their techniques to measure disorientation angles between primary crystals in potash alum agglomerates comprising two primary particles. They compared the distribution of measured disorientations with simulated agglomerates that have randomly oriented primary particles. Agglomerates were represented using $\mathcal{H}$-representations as shown in Eq. (1). The simulated agglomerates also provided the opportunity to validate the algorithms described in Sects. 2.2 and 2.3.

Two primary crystals A and B were considered and it was assumed that B could be rotated into A by an arbitrary rotation matrix $\tilde{\mathbf{R}}$. If the crystal model of A and B has n_S symmetry operations, then the rotation of B into A can also be performed by additionally applying the n_s rotation matrices $\tilde{\mathbf{R}_i}$ that perform a symmetry operation. This was possible because the symmetry operations do not change the appearance of the shape and thus give n_s identically-looking crystals. According to Mackenzie and Thomson [33], a disorientation angle Θ is the smallest of angles Θ_i which can be calculated for each rotation with

$$\Theta_i = \arccos\left(\frac{tr\left(\tilde{\mathbf{R}}_i\tilde{\mathbf{R}}\right) - 1}{2}\right) \tag{27}$$

In this work, potash alum crystals were considered to be octahedral. For an octahedron, there are 24 symmetry operations. Thus, to compute the disorientation angle between two primary particles, one must first find the rotation matrix $\tilde{\mathbf{R}}$ between these two primary crystals. This could be easily computed provided a shape fit for each primary particle. Then, 24 symmetry operations were applied and the 24 angles Θ_i were computed according to Eq. (27). The disorientation angle is the smallest of these angles. A disorientation angle of 0° means that particles are oriented the same way.

In order to validate the algorithm, agglomerates were first simulated. For the simulated agglomerates, it was possible to compute the distribution of the disorientation angles because the rotation matrices of the simulated primary crystals were known exactly. Figure 14a shows the probability density of the resulting angles together with the theoretical distribution that would be expected to result from an infinite number of samples. This theoretical distribution is given in the literature for cubes and also holds for octahedra [33]. In the next step, simulated 3D images of these agglomerates were created and the disorientation angle was computed based on the shapes identified in the images. The result is shown in Fig. 14b. The comparison of Fig. 14a, b shows that the proposed algorithms work well for simulated ideal agglomerates and yield meaningful disorientation angles.

In a next step, a potash alum crystal population was grown in a lab scale reactor and sampled at the end of the crystallization. The agglomerates of these samples were visualized using μCT measurements. The 3D images were then processed with the algorithms described in Sects. 2.2 and 2.3. The segmentation procedure was adapted to include user-interaction steps which made the segmentation more accurate. The shape identification procedure was also adapted to work with asymmetrical crystals observed in the measurement. Then the disorientation angle of the agglomerates was calculated. Details on the experimental procedures are provided by Kovačević et al. [4]. Exemplary results are shown in Fig. 15. It was observed, that agglomeration of potash alum crystals tends to show lower disorientation angles than it was expected if randomly oriented particles form agglomerates. This expectation is shown by the blue line in Fig. 15, obtained from theoretical considerations in the literature. Kovačević

Fig. 15 Disorientation angles of a population of 74 experimentally obtained potash alum agglomerates. (Reprinted with permission from [4], Copyright (2017) Elsevier)
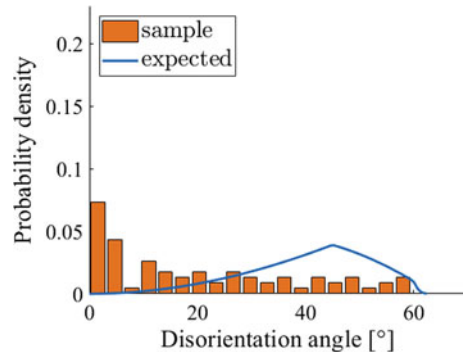
et al. [4] further discriminate between two different types primary particle contact: *slightly touching* and *growth together*.

In conclusion, the methods described in Sects. 2.2 and 2.3 were applied to potash alum crystals to yield geometric representations of crystals. The main contribution of this work was to use these models to analyze the particles. By measuring the disorientation angle of primary particles in agglomerates—a measure that is inaccessible by traditional 2D imaging methods—it was demonstrated that 3D image analysis is a powerful tool for particle characterization.

3 Classifiers for Agglomerates

The previous sections deal with the exact characterization of crystal populations. This section follows a more basic approach where particles are only classified whether they are agglomerates or not. It is common that particle populations are characterized by a size distribution. A common way to measure particles size distributions is by dynamic image analysis. Therein size information is retrieved from image analysis of projections of a sample of particles from a bulk.

A bulk property that can be used to characterize the quality is the degree of agglomeration which represents the ratio of the number of particles that are agglomerates to total number of particles. The aim here was to additionally retrieve the degree of agglomeration from the same images used for particle size measurements.

The identification of the degree of agglomeration has been studied in Heisel et al. [5] by comparing artificial neural networks (ANN) and discriminant factorial analysis (DFA) with respect to their accuracy. Further a procedure to set up appropriate training sets and to select appropriate discriminant variables was proposed. The experimental work and the parts regarding DFA are conducted by the work group of Prof. Schembecker whereas the work concerning ANN has been conducted in the group of Prof. Briesen.

Projections of L-alanine and adipic acid crystals in suspension were obtained by dynamic image analysis. Example images can be seen in Fig. 16. For the scope of
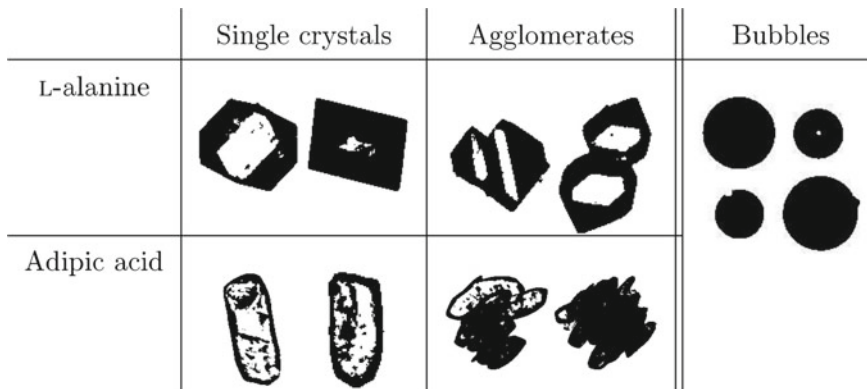
Fig. 16 Example images of the three categories single crystals, agglomerates, and bubbles of both material systems L-alanine and adipic acid. (Reprinted with permission from [5], Copyright (2017) Elsevier)

this section it is important that the obtained images may contain images of crystals that either were (1) agglomerates or (2) single crystals. The images also contained (3) artefacts of measurements, specifically, gas bubbles (c.f. Fig. 16). For classification 19 image descriptors were studied. The image descriptors provided information about particle size and shape such as the area, equivalent diameter, or number of concavity points. A full list and description of how they can be calculated is provided by Heisel et al. [5].

The quality of the descriptors in respect to their potential to distinguish between the three classes was ranked using proportional similarity [34, 35]. This statistical tool yields the PS value that is one for two identical distributions and zero for two completely different distributions. One PS value that evaluates the potential to distinguish between single crystals and agglomerates was calculated (PS_{sa}). Another PS value that evaluates the potential to distinguish between crystals and bubbles (PS_{cb}) was calculated for each descriptor. These two values were used to rank the descriptors in respect to their potential in distinguishing between the classes. PS_{mn}—the mean of PS_{sa} and PS_{cb}—was also used to rank the image descriptors. Only the latter is considered in the present summary. For more results regarding the other two PS values see Heisel et al. [5].

To obtain three training data sets per material system, six crystallization experiments were conducted. From each experiment thousands of images were acquired of which the first 600 images of single crystals and 600 images of agglomerates were selected manually. These experiments produced only few images of gas bubbles. This is why 600 images of gas bubbles were created by a separate experiment with only water and extensive stirring. Using these 1800 images per experiment various training (TR), test (TE) sets were created. The training sets were *combined* training sets (C) if images of different experiments of one material system and gas bubbles were used, or *separate* training sets (S) if images of only one experiment and gas

bubbles were used. The training sets were also varied in total number of images between 27 and 1800.

The training sets were then used to train DFA and ANN classifiers. For evaluation of the performance of the classifiers, two quality criteria were introduced. The first one was the performance index PI_{All} which represents the fraction of correctly classified objects. The aim was to reach values above 0.9. The second value was the error made in the degree of agglomeration Ag. Since the test sets were made of the same number of agglomerated crystals and single crystals, the value for each test set was known to be $Ag = 0.5$. The error in degree of agglomeration δAg made by the classifier was therefore defined as:

$$\delta Ag = \frac{\left|Ag_{classifier} - 0.5\right|}{0.5} \tag{28}$$

This value should be below 0.1 for a well-trained classifier. Some exemplary results for the material system adipic acid/water and the ANN classifier are summarized in Fig. 17.

Both ANN and DFA are able to accurately distinguish between the three classes. Figure 17 shows that there are only three descriptors necessary to classify images with ANN. For DFA 7 descriptors are necessary.

Heisel et al. [5] discuss that training a DFA classifier is easier than that of an ANN classifier. However, DFA needs more descriptors. Which leads to the conclusion that ANN is an attractive alternative if much effort needs to be put in the development of calculation procedures of the image descriptors. It was further shown that PS is a powerful tool to select appropriate image descriptors even for the classification into three classes. It was also discussed that the classifiers could be used for different
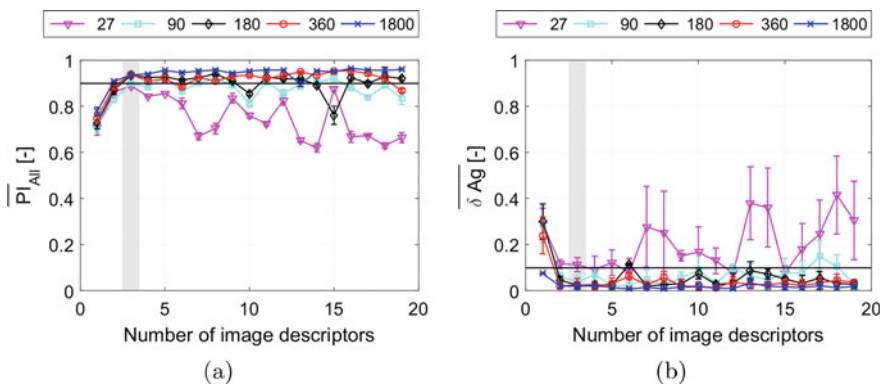
Fig. 17 Results for a ANN classifier for different numbers of image descriptors (in order of their PS rank) and number of samples in the training data sets (27, 90, 180, 360 or 1800). Gray areas indicate the number of image descriptors necessary to reach the predefined classification quality (horizontal black lines). Error bars indicate standard deviations compared between different test sets. (Reprinted with permission from [5], Copyright (2017) Elsevier)

experimental conditions. That is, provided the size of the particles remains similar to the particles in the training set. It was proposed to optimize the developed procedure so that it works for differently sized particles, too.

4   Modelling of Crystallization with Consideration of Morphology

The previous sections explain how crystal morphology can be mathematically described or classified into categories. This section focuses on the effects of complex morphology on growth of single crystals and agglomerates.

For simulations of crystallization processes it is common to assume populations of crystals that can be described with only one size parameter (e.g. diameter for spherical particles) [36]. However, Fig. 11 shows that this a bad assumption for complex crystalline structures and complex single crystals (Fig. 3 left-hand side). The problem with this assumption is that one can often not correctly describe both the volume and the surface area of crystals at the same time with only one size parameter. Authors then often chose volume-equivalent diameters to model e.g. growth of the crystals because so at least the mass is conserved. However, growth depends on the surface area that is available for growth. Therefore, significant inaccuracies are introduced by simplifying the morphology of crystals.

4.1   Modelling of the Growth of Faceted Crystals

Reinhold and Briesen [8] addressed the growth of potash alum crystals under consideration of their morphology. The behavior of populations—such as crystals in suspensions—is frequently modeled with population balance models [37]. A simplified version that considers only growth of a constant number of particles can be written as [8]:

$$\frac{\partial n}{\partial t} + \nabla(gn) = 0 \tag{29}$$

where n is the number density distribution of a population of, in this case, crystals and g is the growth rate of crystal surfaces. Equation (29) describes the problem studied by Reinhold and Briesen [8]: 26-faced potash alum crystals (as shown in Fig. 1) were considered to grow in an ideally mixed batch crystallizer. A constrained $\mathcal{H}_{\mathrm{C}}$-representation was employed to reduce the dimension of the face distances to seven entries in $\boldsymbol{h}_{\mathrm{C}}$. This means that the growth rate g in Eq. (29) was actually a vector with seven entries that each described the growth rate of one crystal face group. Therefore, the number density distribution also features seven internal coordinates.

Even though only growth was considered in this model equation, its solution is not trivial.

Because growth rates depend on the supersaturation which is again dependent on the volume of the crystals, a solution of the problem involved the evaluation of the integral for the total volume of the population. The integral for the volume can be generalized for any geometric property of the crystals μ and can be written as

$$I_\mu(t) = \int \mu(\boldsymbol{h}_C) n(\boldsymbol{h}_C, t) d\boldsymbol{h}_C \tag{30}$$

Because of the high dimension of the problem the solution becomes numerically challenging. It was solved using a Monte Carlo method that calculated solutions at n_{sample} random points $\boldsymbol{h}_{C,i}$. The probability functions $w(\boldsymbol{h}_{C,i}, t)$ of these points were assumed to be known. Then the integral in Eq. (30) was estimated by [38, 39]

$$I_\mu(t) \approx \frac{1}{n_{sample}} \sum_i \mu(\boldsymbol{h}_{C,i}) \frac{n(\boldsymbol{h}_{C,i}, t)}{w(\boldsymbol{h}_{C,i}, t)} \tag{31}$$

Based on a simplified model with only three faces, for which an analytical solution is available, Reinhold and Briesen [8] describe which effect the choice of the initial probability function $w(\boldsymbol{h}_{C,i}, 0)$ and n_{sample} has on the accuracy of the numerical integration. They finally conclude that

$$w(\boldsymbol{h}_C, 0) = \frac{1}{2} \left(\frac{\mu_{volume}(\boldsymbol{h}_C)}{I_{volume}(0)} + \frac{1}{I_1(0)} \right) n_0(\boldsymbol{h}_C) \tag{32}$$

was a reasonable choice that balances between the relative errors for the volume and surface area integration. $n_{sample} = 2 \times 10^4$ was determined to be a sufficient number of samples for the Monte Carlo integration to achieve relative errors below 10^{-3} at reasonable computational cost.

To be able to numerically solve the partial differential Eq. (29) it needed to be transferred to a system of ordinary differential equations. This was done employing the method of characteristics. For details refer to Reinhold and Briesen [8].

With these parameters the growth of a batch of 7.66×10^7 26-faced potash alum crystals was simulated over a time span of 1 h. The initial distribution of the constrained face distances $\boldsymbol{h}_C$ was chosen as a multivariate Gaussian normal distribution with mean face distances of 10 µm and 1 µm standard deviation. The growth rates were taken from the literature [40] and vary between 0.2 mm/s for the (100) and (010) faces and 6 mm/s for the (111) faces. These different growth rates led to the disappearance of the fast-growing crystal faces during growth (Fig. 18); which has an influence on the growth of the particles—and, therefore, also on the course of supersaturation—that could not be modeled with growth models that do not consider each face separately.

To determine which faces were disappearing during simulation it was important to detect face distances that would result in faces that were outside of a crystal. The
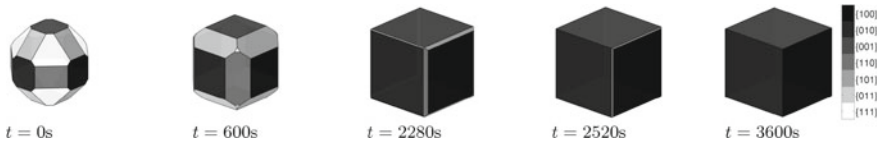
Fig. 18 Visualization of the evolution of one $\mathbf{h}_{C,i}$ vector over the course of the simulation. (Reprinted with permission from [8], Copyright (2015) Elsevier)

concept is illustrated for a 2D case in Fig. 10 and is discussed by Reinhold and Briesen [11]. In context of this work Reinhold and Briesen [8] described how they detected that face distances became too large and limited their growth accordingly.

The evolution of the constrained face distances of a single crystal of the simulated population is displayed in Fig. 19. The corresponding surface areas of the same crystal are displayed in Fig. 20. It can be observed that the fast growing (111) face was initially able to grow with its maximum growth rate until its surface area became very small. Then its growth rate was limited by the growth of the (110), (101), and

Fig. 19 Evolution of the face distances of a single crystal over the course of the simulation. (Reprinted with permission from [8], Copyright (2015) Elsevier)
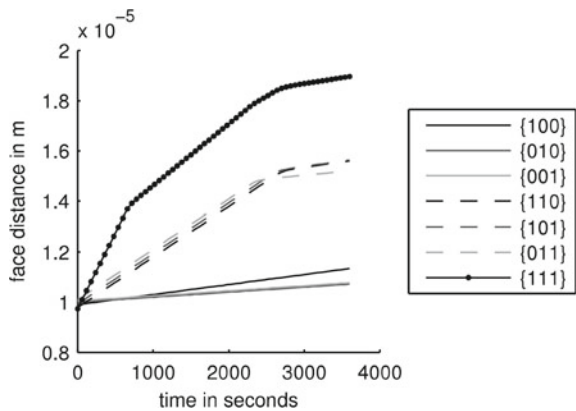
Fig. 20 Evolution of the surface areas of specific crystal faces over the course of the simulation. (Reprinted with permission from [8], Copyright (2015) Elsevier)
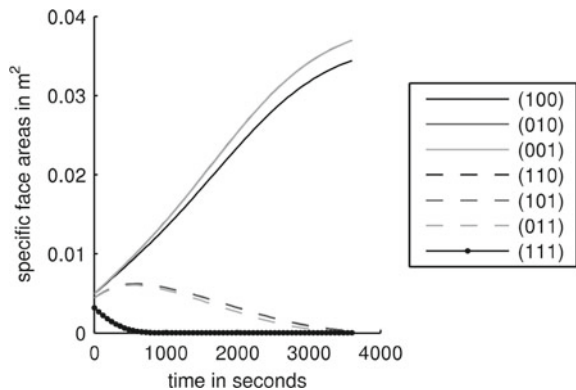
Fig. 21 Evolution of the total number, surface area and volume relative to their corresponding initial values. (Reprinted with permission from [8], Copyright (2015) Elsevier)
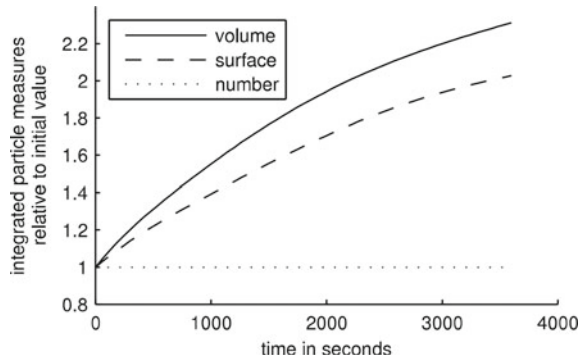
(011) faces. Once also these areas became small due to the slow growth of the (100), (010), and (001) faces the growth of all faces was limited through the growth rates of these faces.

The population balance model also yielded the evolution of the total area and volume of all crystals of the population. The evolution of the volume and area of all crystals relative to the initial condition is displayed in Fig. 21. Note that the number of crystals remained constant because neither agglomeration nor breakage were modeled.

In conclusion, it was demonstrated how a population balance model for face-specific growth of single crystals can be solved. For the solution it was necessary to estimate integrals in a high dimensional space. This was achieved with a Monte Carlo based scheme, that allows to determine the error of the integral estimate. To solve the differential equations, the method of characteristics was applied. The accuracy of the method was evaluated based on a lower dimensional problem for which an analytical solution is available. It was further applied to solve a high dimensional population balance model for the growth of single potash alum crystals under consideration of their full morphology. It was thereby demonstrated that disappearing faces have an impact on the growth of the crystals that could not be modeled by conventional crystal models.

4.2 Modelling of the Growth of Crystal Agglomerates

While Reinhold an Briesen [8] focused on the growth of single crystals, Kovačević and Briesen [3, 6] studied agglomeration and growth of crystals. The challenge was that upon agglomeration of two primary particles the agglomerate should be described in a way that preserves both the surface area and the volume of the primary particles. In conventional models it is often assumed that upon agglomeration a new particle is generated that has a single size parameter (e.g. a diameter or a face distance as shown in Fig. 22) that preserves the volume of the two primary particles. The area
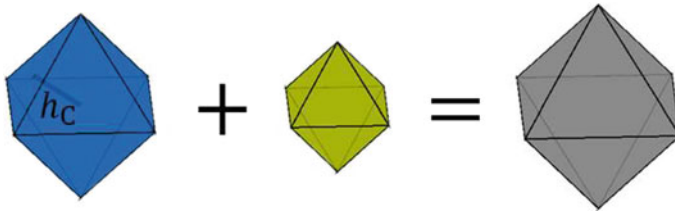
Fig. 22 Agglomeration following the simple approach: When the blue and green crystal agglomerate the volume equivalent grey crystal is generated. The surface area is way too smaller than the sum of the surface areas of the constituting primary particles. (Reprinted with permission from [6], Copyright (2019) American Institute of Chemical Engineers)

is then calculated for the larger particle. This introduces a high error for the surface area and therefore for subsequent growth of the agglomerate.

Kovačević and Briesen [6] studied three different modeling approaches: The first one, the *simple approach,* represents the state of the art in which only the volume of particles is conserved after agglomeration (Fig. 22). The second approach is called the *2D approach* where a 2D population balance equation that considers particle volume and area as internal coordinates was set up. Therein both particle volume and surface area are conserved upon agglomeration. However, modeling the growth rate of the surface was not as straightforward as the increase of volume by additive agglomeration. The third method they studied was a Monte Carlo based, highly accurate, but also very computationally expensive method that was previously published by Briesen [41] and adapted for the agglomeration of octahedral potash alum crystals in Kovačević and Briesen [3]. It describes agglomerates with their full morphological complexity and was therefore able to accurately describe both the volume and surface area of agglomerates (Fig. 23). This was made possible by using the appropriate functionality of the MATLAB framework of Reinhold [42] and the cdd library [43]. This *complex method* was also used to parametrize the 2D approach.

The complex approach considers a sample number of crystals that was assumed to be representative for the whole population that was to be simulated. It was computationally expensive to calculate the volume of the agglomerates, which makes the method infeasible for simulations of long process times [3].
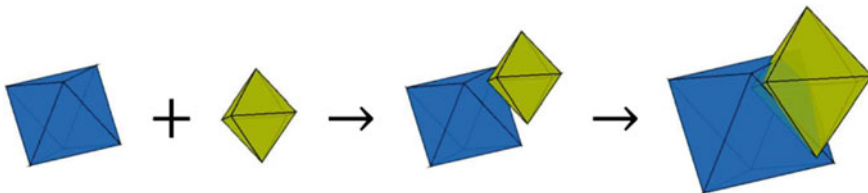
Fig. 23 Aggregation following the complex approach: The agglomerate is described with its full geometric complexity. (Reprinted with permission from [6], Copyright (2019) American Institute of Chemical Engineers)

With the 2D approach a compromise was made between the complex and simple approach. A 2D population balance is more complex to solve than a 1D one, but still leads to a manageable computational effort. The corresponding 2D population balance equation that describes growth and agglomeration can be written as [44–46]

$$\frac{\partial f(V, A)}{\partial t} + \frac{\partial (G_V f(V, A))}{\partial V} + \frac{\partial (G_A f(V, A))}{\partial A}$$

$$= \frac{1}{2} \int\limits_{V'=0}^{V} \int\limits_{A'=0}^{A} \beta f(V - V', A - A') f(V', A') dA' dV'$$

$$- f(V, A) \int\limits_{V'=0}^{V} \int\limits_{A'=0}^{A} \beta f(V', A') dA' dV' \tag{33}$$

$f(V, A)$ is the 2D crystal size distribution with the volume V and surface area A as internal coordinates. The growth terms G_V and G_A describe the increase of particle volume and area through growth respectively. β is the agglomeration rate kernel. Upon agglomeration it is easy to add the volume and surface area of the two primary crystals to yield their respective values for the agglomerate. The increase of the volume can easily be derived from face displacement rates. However, it was not as straightforward to model the growth of the surface area.

All of the three approaches were solved with the same numerical scheme to ensure that no numerical differences of the results could occur. The solver was an event-driven Monte Carlo approach that determines time steps according to agglomeration events. Between the time steps constant supersaturation was assumed and used to calculate growth. The procedure is summarized in Fig. 24.

In the initialization step an initial crystal population that was assumed to be representative for the population in the process was generated. Octahedral potash alum crystals were described with one size parameter, the constrained face distance h_C (displayed in Fig. 22). A number of N_{part} crystals with normally distributed face distances and uniformly distributed orientations was generated to be further simulated. The respective orientations were held constant throughout the simulation. The particles existed in a small control volume V_{MC} that was chosen so that the number density concentration in the control volume was the same as in the total suspension volume.

Following the initialization, the main simulation loop was entered by evaluating mass balances. This yielded the present supersaturation that is the driving force for growth. Based on the supersaturation the face displacement rates were calculated according to literature [47]. It was assumed to be constant in each time step.

The length of such a time step was determined based on agglomeration events. It was assumed that all particles have the same probability to agglomerate (constant $\beta = \beta_0$) for some calculations. For others a shear rate and particle size dependent agglomeration rate kernel was introduced according to Briesen [48]. For the constant
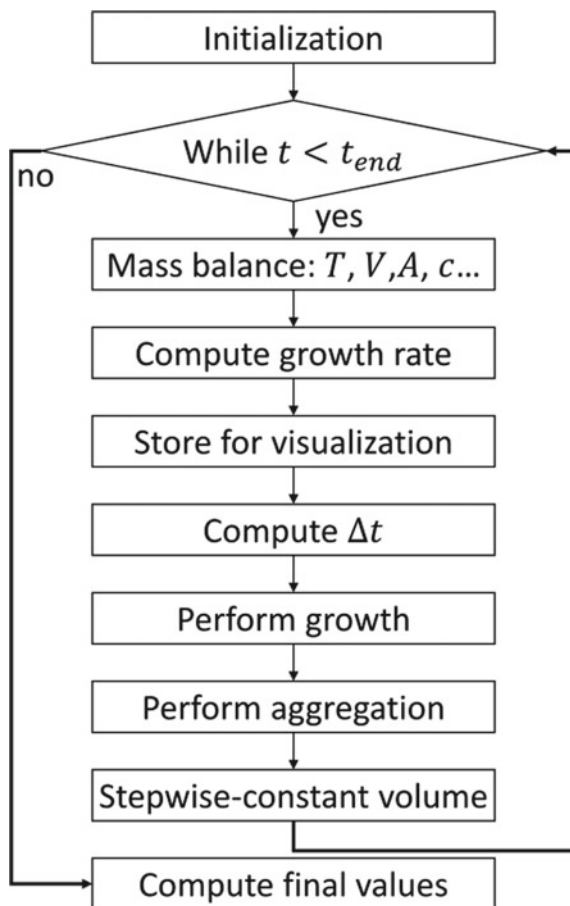
agglomeration kernel, the agglomeration rate was calculated from the agglomeration kernel and was also dependent on the size of the control volume and the number of crystals in it:

$$r = \beta_0 \left(\frac{N_{part}}{V_{MC}} \right)^2 \tag{34}$$

This means that, on average, in 1 s rV_{MC} particles will agglomerate, which again means that the average time step size is $\overline{\Delta t} = (rV_{MC})^{-1}$. For the Monte Carlo solver, the time step size was sampled from an exponential distribution according to [49]

$$\Delta t = -\overline{\Delta t} \cdot ln(x) \tag{35}$$

where x is a uniformly distributed random number between 0 and 1. The calculation of the time steps for the shear rate dependent agglomeration kernel was more complex and explained in detail by Briesen [48] and Kovačević and Briesen [6].

With the time step size at hand, growth of the particle population was calculated. For the simple and complex approach this was done in a straightforward way with $h_{C,new} = h_C + \Delta t G_h$ for each particle in the simple approach or with $h_{C,part\,new,i} = h_{C,part,i} + \Delta t G_h$ for each face distance i of each primary particle for the complex approach.

The population balance of the 2D approach did not directly contain the face distances. The growth was modeled based on the growth of the volume and surface area directly: $V_{new} = V + \Delta t G_V$ and $A_{new} = A + \Delta t G_A$. The growth rate of the volume is given as $G_V = A G_h$. Until this point G_A remained unknown. An empirical relation with the parameters p_1 and p_2 was proposed:

$$G_A = p_1 A^{p_2} V^{\frac{1-2p_2}{3}} G_h \qquad (36)$$

Kovačević and Briesen [6] derived that for single crystals p_1 is in fact a function of p_2. For octahedral particles the following function was found:

$$p_1 = \frac{24\sqrt{3}}{\left(12\sqrt{3}\right)^{p_2}\left(4\sqrt{3}\right)^{\frac{1-2p_2}{3}}} \qquad (37)$$

p_1 and p_2 can be interpreted as geometric factors that are specific for certain geometries and do not only differ depending on whether a particle is an agglomerate or not, but also on the geometry of each individual agglomerate. Kovačević and Briesen [6] studied various values for p_1 and p_2 and find that—even though the values slightly vary for different simulation cases—reasonable average values can be found to describe particles in a process. To study different parameters, they used the complex method to generate 1000 *isolated agglomerates*. The term *isolated* stems from the fact that they are not simulated within a reaction environment. p_1 and p_2 are only dependent on the geometry. How a certain geometry is reached is not important for their calculation. To produce a set of agglomerates, two particles were brought to contact. Subsequently their face distances were displaced in several steps without consideration of a supersaturation. Therefore, the time-consuming calculation of the mass balances was not necessary. After each face displacement step, both volume and area were calculated and then allowed a correlation between growth rate by means of face displacement, and the change of the surface area. The procedure is illustrated in Fig. 25.

With $p_2 = 1.135$ a hypothetical crystallization process was simulated with the scheme displayed in Fig. 24. The results are shown in Fig. 26. The agglomeration kernel was chosen relatively high compared to a real crystallization problem to make the effect of agglomeration clearer.
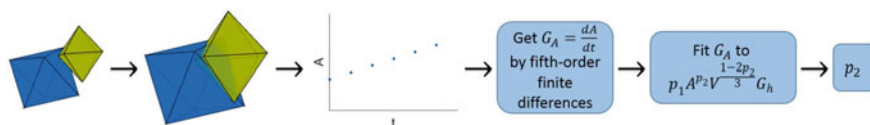
Fig. 25 Illustration of the procedure to determine p_2: First particles are brought to contact, then their faces are displaced in several steps t which produces an increase in the surface area A of their agglomerate. The growth rate of the surface area is determined and used to calculate p_2 from Eq. (37). (Reprinted with permission from [6], Copyright (2019) American Institute of Chemical Engineers)
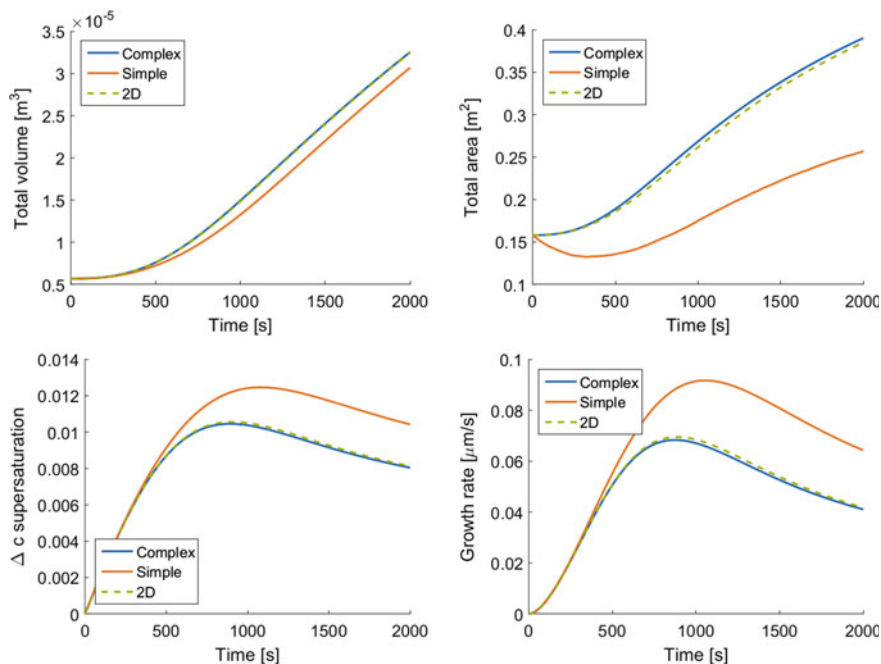
Fig. 26 Simulation results for the complex (blue line), simple (orange line), and 2D (green dashed line) approaches with a constant agglomeration kernel. (Reprinted with permission from [6], Copyright (2019) American Institute of Chemical Engineers)

Figure 26 shows the evolution of the volume of the crystals (top left), the total surface area (top right), the supersaturation (bottom left) and the growth rate (bottom right). It can be seen that the 2D approach is able to reproduce the results of the complex approach, while it used much less computational recourses. It further strikes that even though the simple approach makes a relative error of up to two compared to the complex approach when calculating the surface area, the supersaturation, and the growth rate, the total volume was calculated quite accurately. The reason for this is that due to the underestimation of the surface area, less material was built into

the crystals. This led to a higher supersaturation, which again led to higher growth rates. These higher growth rates were therefore able to compensate for the error that is made for the surface area.

In conclusion, a procedure to accurately model agglomeration and growth of crystals with a 2D population balance was proposed. The population balance equation considers the volume and surface area of the particles as internal coordinates and was therefore able to conserve both of these values upon agglomeration. The growth is also expressed with respect to growth of volume and area. The second subsection summarizes how both of these rates can be determined. While the growth rate of the volume was determined on a straightforward way, the growth rate of the surface area needed to be estimated with a Monte Carlo based scheme. The scheme proposed here was applied for potash alum crystals but is formulated in a way that it can be applied to other material systems.

5   Integrated Crystallization Modelling in Dyssol

The crystallization models proposed in the previous sections are able to describe the crystallization phenomena growth and agglomeration in an accurate way; however, they are computationally expensive. They are, therefore, with currently available hardware hardly suitable for process simulations that span long process times and include complex flowsheets. There are, however, simpler crystallization models available in the literature, that are able to describe several crystallization phenomena simultaneously, and have less computational cost. A case study on the implementation of such a crystallization process within Dyssol was presented by Kulozik et al. [7].

Kulikov et al. [50] study the performance of the dynamic flow sheet integration platform CHEOPS [51]—that is in some ways similar to Dyssol—based on an integrated crystallization flowsheet. Therefore, a similar process was implemented for Dyssol and compared to the results of Kulikov et al. [50]. The main difference between CHEOPS and Dyssol is that CHEOPS is used to couple models that are generated in different simulation environments. Dyssol now allows simulations in one combined software package that can be used to model each unit operation and couple different unit operations to form a flowsheet.

The flowsheet of Kulikov et al. [50] contains four units: (1) a mixed suspension mixed product removal (MSMPR) crystallizer, (2) a hydrocyclone, (3) an evaporator and (4) an ideal mixer. For all of the units a model was implemented in Dyssol. They were then combined to an integrated flowsheet and Dyssol was used to simulate the behavior of this exemplary process over a process time of 72 h. The first two of the mentioned units will be briefly explained in the following sections. The mixer is considered trivial and is not explained. It accepts two feed streams that are ideally mixed to a product stream of the mixer. The evaporator is implemented in a way that a constant ratio of pure solvent is withdrawn to concentrate its feed. It has a vapor stream and a concentrate stream as outputs.

5.1   MSMPR Crystallizer

The central equation of the mixed suspension mixed product removal (MSMPR) crystallizer model is again a population balance equation. In this case growth of spherical particles (diameter d) with a growth rate G, and nucleation with a birth rate B were considered. In addition, the crystallizer accepts a feed stream and has a vapor and a product stream as output.

$$\frac{\partial n(d)}{\partial t} + \frac{\partial (G(d)n(d))}{\partial d} + \frac{1}{V} \sum_{j}^{n_{streams}} \left(n_j(d)\dot{V}_j \right) + n(d)\frac{d\, ln\, V}{dt} = \frac{\partial B(d,n)}{\partial d} \tag{38}$$

Growth and nucleation kinetics were as proposed by Jones and Mydlarz [52]. The discretization as done with the method of classes and a flux limiter was used as proposed by Qamar [53]. Additionally, mass balances were introduced. The resulting set of differential algebraic equations is then solved using Dyssol [54].

5.2   Hydrocyclone

The implementation of the hydrocyclone is based on the work of Braun [55] and the descriptions of Kulikov et al. [50]. The static model proposed by Braun divides a hydrocyclone into four zones (c.f. Fig. 27): Zone A is a tube-like inlet zone to which a suspension is fed and forced onto a circular downward movement. The suspension then enters an outer tube-like zone B where the fluid continues to move downward on

Fig. 27 Abstraction of the hydrocyclone as proposed by Braun [55]
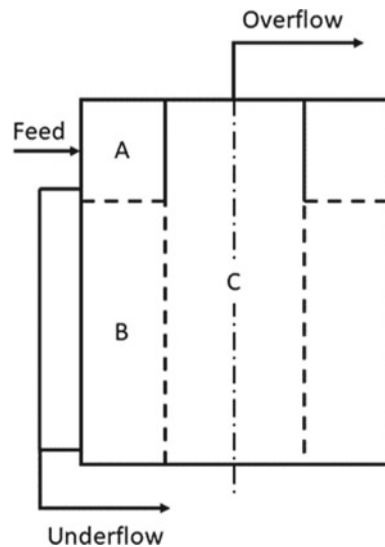
its circular path. Inside the outer zone B Braun considers a cylindrical inner zone C where the fluid moves upwards towards the outlet where the overflow is withdrawn.

The model assumes material transport between the zones that is dependent on particle sizes. Larger particles are drawn to the outer wall by centrifugal force and are added to the underflow if they are large enough to touch the outer wall of the zones A and B. Particles that reach the top of zone C are added to the overflow. The reflux parameter $R_f = \frac{\dot{V}_{\text{overflow}}}{\dot{V}_{\text{feed}}}$ is used to define which proportion of a feed suspension is leaving the cyclone through the overflow.

5.3 Flowsheet and Simulation Results

The units were combined to a flowsheet as shown in Fig. 28: Feed material is mixed with a recycle stream and then concentrated in an evaporator. The concentrate is fed to the crystallizer where vapor is withdrawn at a constant rate to induce crystallization. The product suspension is then classified in the hydrocyclone. The fine fraction is recycled and the coarse product leaves the process. For this study the material system water/potash alum was used.

For a simulation scenario, a sieve or filter unit at the end of the process was assumed but not included in the model. It is further assumed, that this unit should not be fed with a product that is too fine to prevent blocking. This scenario is also studied by Kulikov et al. [50]. The goal of the simulation is, therefore, to reduce the mass stream of fine particles ($d < 50\ \mu$m). Here, the effects of the reflux ratio R_f (as also studied by Kulikov et al. [50]) and the feed stream were studied.

Figure 29 shows that after the start of the process, the mass stream of fines rapidly raised, reached a maximum and finally approaches an equilibrium state. For higher
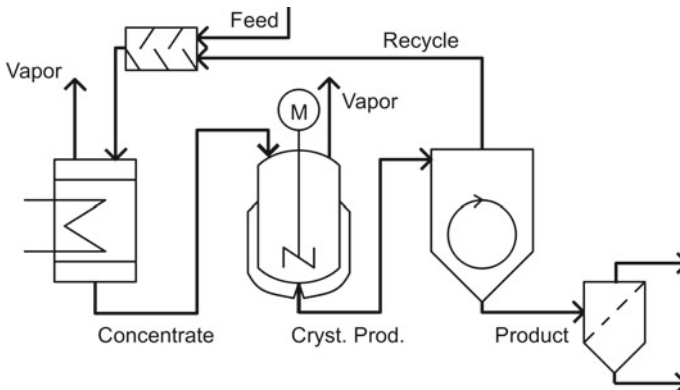
Fig. 28 Crystallization flowsheet with reflux. The sieve is not considered in the model but used in the optimization discussion

Fig. 29 Mass stream of fine particles dependent on reflux ratio. The feed mass stream was 0.5 kg/s
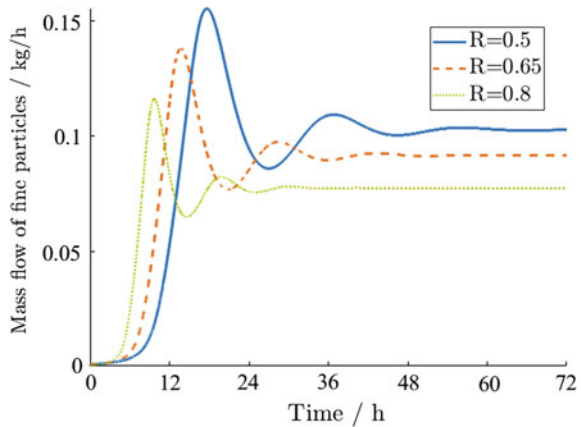
reflux ratios less fine particles were contained in the product. This is also observed by Kulikov et al. [50] for a different material system.

Figure 29 suggests that for all cases the highest mass flows of fine crystals can be observed within one day after startup of the process. A further simulation goal was to reduce the maximum mass flow by appropriate adaption of the feed stream. For this case the reflux ratio was fixed to 0.5. The simulation result for this reflux ratio and a feed mass stream of 1 kg/s was used as a benchmark (blue solid lines in Figs. 29, 30, and 31). In a first attempt, the feed rate was kept at only 0.5 kg/s for the first 18 h and was then rapidly increased to 1 kg/s.

Figure 30 shows that this procedure led to a slower increase of the mass stream of fine particles. Once the feed rate was increased a sharp increase in the mass stream of fine particles was observed. The peak was higher than in the benchmark simulation. It rapidly decreased and converged towards the expected equilibrium. A second simulation was done where the feed stream was gradually increased from 0.5 to 1 kg/s within 18 h (c.f. Fig. 31). In this case it was observed that the peak of

Fig. 30 Simulation result for a rapidly increased feed rate (orange dashed line) and comparison to the benchmark result (blue solid line)
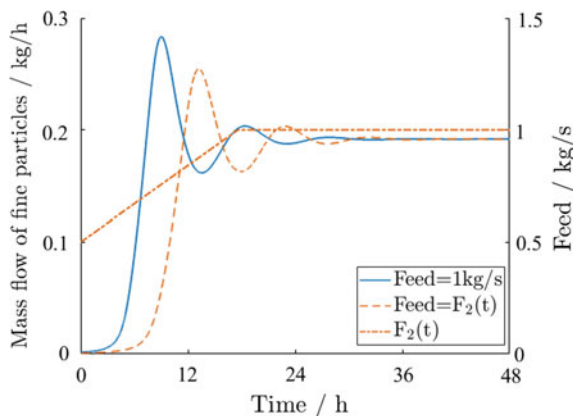
the mass flow of fine particles was delayed and was not as pronounced as for the benchmark. The equilibrium was still reached at a similar time.

In conclusion, it was demonstrated that Dyssol can be used to dynamically simulate crystallization flowsheets. Even complex cases such as reflux streams can be handled and Dyssol can be used for long process time calculations.

6   Conclusion

Sections 2 and 3 deal with the analysis of crystal morphology. Section 4 focuses on the modelling of crystallization under consideration of morphology and discusses errors that are made by the classical assumptions that neglect morphology. Finally, in Sect. 5 a crystallization process was modeled using the dynamic flowsheet simulator Dyssol and it was shown that it can be efficiently used to dynamically simulate integrated flowsheets.

The analysis of crystal morphology is often done by 2D on-line image analysis in both industry and science. It was demonstrated that certain errors with respect to morphology have to be accepted when only 2D information is available. This concept has been demonstrated for the measurement of a roundness parameter of abraded crystals. It was further demonstrated that morphological bulk properties such as the degree of agglomeration can be extracted from particle projections. Procedures for the calibration of artificial neural networks were proposed.

To overcome the limitations of measurements where only 2D information is available, 3D particle images were acquired and analyzed. It was demonstrated that the full morphological information that was provided by 3D particle description can be used to measure properties that are inaccessible from 2D images—such as disorientation angles in agglomerates. Even though 3D image acquisition and analysis are much

more sophisticated than of 2D images, the proposed methods help to understand morphological influences on important phenomena like crystal growth, agglomeration and breakage.

Another aspect of the work was the modeling of crystallization under consideration of the influence of morphology. Using a high dimensional population balance model the important influence of multiple surfaces with different growth rates on crystal growth was demonstrated. For the effective solution of such a model, novel numerical methods have been developed. It is common practice to neglect the combined influence of agglomeration and growth on the surface area of crystal populations. It was herein demonstrated that this introduces high errors in such models. A method was proposed to parametrize a population balance model that considers both the evolution of crystal volume and area correctly. Because such models are still numerically challenging and computationally expensive even if not included in a flowsheet, they are currently not suitable for simulation of integrated flowsheets. Therefore, a simpler model was included in the simulation platform Dyssol. It is demonstrated that Dyssol can be used to efficiently calculate integrated crystallization processes.

References

1. Kovačević, T., Reinhold, A., Briesen, H.: Identifying faceted crystal shape from three-dimensional tomography data. Cryst. Growth Des. **14**(4), 1666–1675 (2014)
2. Kovačević, T., Schock, J., Pfeiffer, F., Briesen, H.: Shape identification of primary particles in potash alum aggregates using three-dimensional tomography data. Cryst. Growth Des. **16**(5), 2685–2699 (2016)
3. Kovačević, T., Briesen, H.: Determining the full geometric complexity of crystal aggregates via Monte Carlo Simulation. In: PARTEC: International Congress of Particle Technology, Nuremberg, pp. 19–21 (2016)
4. Kovačević, T., et al.: Disorientation angle distribution of primary particles in potash alum aggregates. J. Cryst. Growth **467**, 93–106 (2017)
5. Heisel, S., Kovačević, T., Briesen, H., Schembecker, G., Wohlgemuth, K.: Variable selection and training set design for particle classification using a linear and a non-linear classifier. Chem. Eng. Sci. **173**, 131–144 (2017)
6. Kovačević, T., Briesen, H.: Simulations of crystal aggregation and growth: towards correct crystal area. AIChE J. **65**(5) (2019)
7. Kulozik, S., Buchholz, M., Kovačević, T., Haus, J., Heinrich, S., Briesen, H.: Dynamic flowsheet simulation of a crystallization reactor with material recovery via a hydrocyclone. In: PARTEC 2019, Nuremberg, VDI Verlag (2019)
8. Reinhold, A., Briesen, H.: High dimensional population balances for the growth of faceted crystals: combining Monte Carlo integral estimates and the method of characteristics. Chem. Eng. Sci. **127**, 220–229 (2015)
9. Reinhold, A., Schorsch, S., Mazzotti, M., Briesen, H.: Modeling and measurement of abraded particles. Powder Technol. **271**, 134–140 (2015)
10. Ma, C.Y., Wang, X.Z., Roberts, K.J.: Morphological population balance for modeling crystal growth in face directions. AIChE J. **54**(1), 209–222 (2008)
11. Reinhold, A., Briesen, H.: Convex geometry for the morphological modeling and characterization of crystal shapes. Part. Part. Syst. Charact. **28**(3–4), 37–56 (2012)
12. Borchert, C., Sundmacher, K.: Morphology evolution of crystal populations: modeling and observation analysis. Chem. Eng. Sci. **70**, 87–98 (2012)

13. Singh, M.R., Verma, P., Tung, H.-H., Bordawekar, S., Ramkrishna, D.: Screening crystal morphologies from crystal structure. Cryst. Growth Des. **13**(4), 1390–1396 (2013)
14. Schneider, R.: Convex Bodies: The Brunn-Minkowski Theory. Cambridge University Press, Cambridge (2008)
15. Al-Rousan, T., Masad, E., Tutumluer, E., Pan, T.: Evaluation of image analysis techniques for quantifying aggregate shape characteristics. Constr. Build. Mater. **21**(5), 978–990 (2007)
16. Hentschel, M.L., Page, N.W.: Selection of descriptors for particle shape characterization. Part. Part. Syst. Charact. **20**(1), 25–38 (2003)
17. Masad, E., Button, J.W.: Unified imaging approach for measuring aggregate angularity and texture. Comput.-Aided Civil Infrastruct. Eng. **15**(4), 273–280 (2000)
18. Pons, M.N., et al.: Particle morphology: from visualisation to measurement. Powder Technol. **103**(1), 44–57 (1999)
19. Burger, W., Burge, M.J.: Principles of Digital Image Processing, Undergraduate Topics in Computer Science (2009)
20. Schorsch, S., Ochsenbein, D.R., Vetter, T., Morari, M., Mazzotti, M.: High accuracy online measurement of multidimensional particle size distributions during crystallization. Chem. Eng. Sci. **105**, 155–168 (2014)
21. Gahn, C., Mersmann, A.: Brittle fracture in crystallization processes Part A. Attrition and abrasion of brittle solids. Chem. Eng. Sci. **54**(9), 1273–1282 (1999)
22. Briesen, H.: Model-based analysis of the effect of particle and impact geometry on attrition of brittle material. Powder Technol. **178**(2), 87–98 (2007)
23. Briesen, H.: Two-dimensional population balance modeling for shape dependent crystal attrition. Chem. Eng. Sci. **64**(4), 661–672 (2009)
24. Gorski, K.M., et al.: HEALPix: a framework for high-resolution discretization and fast analysis of data distributed on the sphere. Astrophys J **622**(2), 759–771 (2005)
25. Naruse, Y.: HEALPix Library for Matlab. 1.0 ed (2011)
26. Neubeck, A., Van Gool, L.: Efficient non-maximum suppression. In: Presented at the 18th International Conference on Pattern Recognition (ICPR'06) (2006)
27. WAHBA, G.: A least-squares estimate of satellite attitude, Problem 65–1. SIAM Rev. **7** (1965)
28. Markley, F.L.: Attitude determination using vector observations and the singular value decomposition. J. Astronaut. Sci. **36**(3), 245–258 (1988)
29. Fernàndez, G., Kunt, M., Zrÿd, J.P.: A new plant cell image segmentation algorithm. In: Image Analysis and Processing (Lecture Notes in Computer Science), pp. 229–234 (1995)
30. Indhumathi, C., Cai, Y.Y., Guan, Y.Q., Opas, M.: An automatic segmentation algorithm for 3D cell cluster splitting using volumetric confocal images. J. Microsc. **243**(1), 60–76 (2011)
31. Vincent, L., Soille, P.: Watersheds in digital spaces: an efficient algorithm based on immersion simulations. IEEE Trans. Pattern Anal. Mach. Intell. **13**(6), 583–598 (1991)
32. Gonzales, R.C., Woods, R.E., Eddis, S.L.: Digital Image Processing Using Matlab, 2nd ed. McGraw Hill Education, India (2010)
33. Mackenzie, J.K., Thomson, M.J.: Some statistics associated with the random disorientation of cubes. Biometrika **44**(1–2), 205–210 (1957)
34. Vegelius, J., Janson, S., Johansson, F.: Measures of similarity between distributions. Qual. Quant. **20**(4) (1986)
35. Renkonen, O.: Statistisch-ökologische Untersuchungen über die terrestrische Käferwelt der finnischen Bruchmoore. Dissertation, Societas zoologica-botanica Fennica Vanamo (1938)
36. Omar, H.M., Rohani, S.: Crystal population balance formulation and solution methods: a review. Cryst. Growth Des. **17**(7), 4028–4041 (2017)
37. Ramkrishna, D.: Population Balances. Academic Press, San Diego (2000)
38. Kroese, D.P., Taimre, T., Botev, Z.I.: Handbook of Monte Carlo Methods. Wiley, Hoboken (2011)
39. Press, W.H., Teukolsky, S.A., Vetterling, W.T., Flannery, B.P.: Numerical Recipies in C++, 2 ed. Cambridge University Press, Cambridge (2007)
40. Snyder, R.C., Doherty, M.F.: Faceted crystal shape evolution during dissolution or growth. AIChE J. **53**(5), 1337–1348 (2007)

41. Briesen, H.: Hierarchical characterization of aggregates for Monte Carlo simulations. AIChE J. **52**(7), 2436–2446 (2006)
42. Reinhold, A.: Crystal Shape Modeling and Convex Geometry—Analysis of Geometric State Spaces. Dissertation, Fakultät Wissenschaftszentrum Weihenstephan, Technische Universität München (2015)
43. Fukuda, K.: cdd library, 094 g ed (2012)
44. Wright, D.L., McGraw, R., Rosner, D.E.: Bivariate extension of the quadrature method of moments for modeling simultaneous coagulation and sintering of particle populations. J. Colloid Interface Sci. **236**(2), 242–251 (2001)
45. Kraft, M.: Modelling particulate processes. KONA Powder Part J. **23**, 18–25 (2005)
46. Zucca, A., Marchisio, D.L., Vanni, M., Barresi, A.A.: Validation of bivariate DQMOM for nanoparticle processes simulation. AIChE J. **53**(4), 918–931 (2007)
47. Kim, D.Y., Yang, D.R.: A novel method for measurement of crystal growth rate. J. Cryst. Growth **373**, 54–58 (2013)
48. Briesen, H.: Aggregate structure evolution for size-dependent aggregation by means of Monte Carlo simulations. KONA Powder Particle J. **25**, 180–189 (2007)
49. Fichthorn, K.A., Weinberg, W.H.: Theoretical foundations of dynamical Monte Carlo simulations. J. Chem. Phys. **95**(2), 1090–1096 (1991)
50. Kulikov, V., Briesen, H., Grosch, R., Yang, A., von Wedel, L., Marquardt, W.: Modular dynamic simulation for integrated particulate processes by means of tool integration. Chem. Eng. Sci. **60**(7), 2069–2083 (2005)
51. Schopfer, G., Yang, A., von Wedel, L., Marquardt, W.: CHEOPS: A tool-integration platform for chemical process modelling and simulation. Int. J. Softw. Tools Technol. Transfer **6**(3), 186–202 (2004)
52. Jones, A.G., Mydlarz, J.: Continuous crystallization of potash alum: MSMPR kinetics. Canadian J. Chem. Eng. **68**(2), 250–259 (1990)
53. Qamar, S., Elsner, M.P., Angelov, I.A., Warnecke, G., Seidel-Morgenstern, A.: A comparative study of high resolution schemes for solving population balances in crystallization. Comput. Chem. Eng. **30**(6–7), 1119–1131 (2006)
54. Skorych, V., Dosta, M., Hartge, E.-U., Heinrich, S.: Novel system for dynamic flowsheet simulation of solids processes. Powder Technol. **314**, 665–679 (2017)
55. Braun, B.: Theoretische und experimentelle Untersuchungen des Einflusses der Feststoffkonzentration und der Partikelgrössenverteilung auf das Trennverhalten von Hydrozyklonen, Dissertation, Universität Braunschweig (1989)

Chapter 14
Numerical Methods for Coupled Population Balance Systems Applied to the Dynamical Simulation of Crystallization Processes

Robin Ahrens, Zahra Lakdawala, Andreas Voigt, Viktoria Wiedmeyer, Volker John, Sabine Le Borne, and Kai Sundmacher

Abstract Uni- and bi-variate crystallization processes are considered that are modeled with population balance systems (PBSs). Experimental results for uni-variate processes in a helically coiled flow tube crystallizer are presented. A survey on numerical methods for the simulation of uni-variate PBSs is provided with the emphasis on a coupled stochastic-deterministic method. In this method, the equations of the PBS from computational fluid dynamics are solved deterministically and the population balance equation is solved with a stochastic algorithm. With this method, simulations of a crystallization process in a fluidized bed crystallizer are performed that identify appropriate values for two parameters of the model such that considerably improved results are obtained than reported so far in the literature. For bi-variate processes, the identification of agglomeration kernels from experimental data is briefly discussed. Even for multi-variate processes, an efficient algorithm for evaluating the

R. Ahrens · S. Le Borne
Faculty of Electrical Engineering, Informatics and Mathematics,
Institute of Mathematics, Hamburg University of Technology,
Am Schwarzenberg-Campus 3, 21073 Hamburg, Germany
e-mail: robin.ahrens@tuhh.de

S. Le Borne
e-mail: leborne@tuhh.de

Z. Lakdawala · V. John (✉)
Weierstrass Institute for Applied Analysis and Stochastics (WIAS),
Mohrenstr. 39, 10117 Berlin, Germany
e-mail: john@wias-berlin.de

Z. Lakdawala
e-mail: lakdawala@wias-berlin.de

A. Voigt · K. Sundmacher
Department Process Systems Engineering, Otto-von-Guericke-University Magdeburg,
Universitätsplatz 2, 39106 Magdeburg, Germany
e-mail: andreas.voigt@ovgu.de

K. Sundmacher
e-mail: sundmacher@mpi-magdeburg.mpg.de

475

agglomeration term is presented that is based on the fast Fourier transform (FFT). The complexity of this algorithm is discussed as well as the number of moments that can be conserved.

1 Introduction: Modeling of Crystallization Processes with Population Balance Systems

Solid state processing is an important part of the industrially relevant production as about 70% of products of the chemical and pharmaceutical industry are sold as solids. An important part of this processing is crystallization of solid materials from liquid solutions. Fundamental and applied research in this area of crystallization will lead to improved process performance with less energy consumption as well as more efficient material utilization. Also the product quality and specifications like size and its distribution, shape, and agglomeration degree have to be considered in more detail, as many process steps are dependent on such characteristics [44]. The DFG priority programme 1679 "Dynamic simulation of interconnected solids processes" addressed many of the current issues and our particular contribution has been the investigation of different important aspects of continuous crystallization processes. As solid-liquid systems are complex and challenging in many ways and fluid flow and particles interact in a variety of fashions, the numerical methods had to be extended and new tools had to be developed to simulate crystallization in a better way. We focus here on relevant phenomena of crystal growth of multi-faceted crystals as well as on crystal agglomeration with two specifically developed model experiments working with selected well-understood model substances.

Crystallization processes are often modeled in terms of a crystal population instead of considering the behavior of each individual crystal. Utilizing macroscopic conservation laws, one derives a system of coupled equations for the population, a so-called population balance system (PBS), that describes an averaged behavior of the crystals.

We consider crystallization processes within a moving incompressible fluid, which occur, e.g., in pipes or batch crystallizers. It is assumed that the suspension of the crystals is dilute such that the impact of the crystals on the fluid flow is negligible. Then, the first two conservation laws are the balance of the linear momentum and

V. Wiedmeyer
ETH Zurich, Institute of Energy and Process Engineering, Sonneggstrasse 3, 8092 Zurich, Switzerland
e-mail: wiedmeyv@ipe.mavt.ethz.ch

V. John
Freie Universität Berlin, Department of Mathematics and Computer Science,
Arnimallee 6, 14195 Berlin, Germany

K. Sundmacher
Process Systems Engineering, Max Planck Institute for Dynamics of Complex Technical Systems, Sandtorstr. 1, 39106 Magdeburg, Germany

the conservation of mass for the fluid flow, which are modeled by the incompressible Navier–Stokes equations

$$\partial_t \boldsymbol{u} - \nabla \cdot \left(\frac{\rho}{\eta} \nabla \boldsymbol{u} \right) + (\boldsymbol{u} \cdot \nabla) \boldsymbol{u} + \nabla p = \boldsymbol{f} \text{ in } (0, t_{\text{end}}) \times \Omega,$$
$$\nabla \cdot \boldsymbol{u} = 0 \text{ in } (0, t_{\text{end}}) \times \Omega. \tag{1.1}$$

In (1.1), t_{end} (s) is a final time, $\Omega \subset \mathbb{R}^3$ is a bounded domain, which is assumed to be constant in the whole time interval, $\boldsymbol{u}$ (m/s) is the velocity field, p (Pa) is the pressure, $\boldsymbol{f}$ (m/s²) represents forces acting on the fluid, ρ (kg/m³) is the density of the fluid, and μ (kg/s m) is the dynamic viscosity of the fluid. Often, the body forces possess the form $\boldsymbol{f} = (0, 0, g)^T$ with g (m/s²) being the gravitational acceleration.

The other equations of a PBS are usually coupled. These are equations for the energy balance, where the unknown quantity is the temperature T (K), for the balance of the molar concentration c (mol/m³) of dissolved species, and for the balance of the particle population density f (1/kg m³) (the unit is for a particle population density with the only internal coordinate mass, it is different in other situations).

The energy balance of the PBS has the form

$$\partial_t T - D_T \Delta T + \boldsymbol{u} \cdot \nabla T = F_{\text{ener,growth}}(c, T, f) \text{ in } (0, t_{\text{end}}) \times \Omega, \tag{1.2}$$

where D_T (m²/s) is a diffusion coefficient, $\boldsymbol{u}$ is the velocity from (1.1), and the right-hand side $F_{\text{ener,growth}}(c, T, f)$ (K/s) models the energy consumption or production in the growth process of the crystals. Since the velocity is divergence-free, it holds that $\boldsymbol{u} \cdot \nabla T = \nabla \cdot (T\boldsymbol{u})$.

In a crystallization process, the dissolved material in the fluid is used in the growth process of the crystals. The corresponding balance equation has the form

$$\partial_t c - D_c \Delta c + \boldsymbol{u} \cdot \nabla c = F_{\text{conc,growth}}(c, T, f) \text{ in } (0, t_{\text{end}}) \times \Omega. \tag{1.3}$$

Here, D_c (m²/s) is again a diffusion coefficient and $F_{\text{conc,growth}}(c, T, f)$ (mol/s m³) represents the consumption or production of dissolved material. We like to mention that there are PBSs with a coupled system of equations of type (1.3) for several concentrations, like in the modeling of precipitation processes, e.g., see [36].

The final part of a PBS is an equation for the particle population density. Assuming that the number of internal or property coordinates is $d_{\text{int}} \geq 1$, then this equation might read as follows

$$\partial_t f + (\boldsymbol{u} + \boldsymbol{u}_{\text{sed}}) \cdot \nabla f + \nabla_{\text{int}} \cdot (G(c, T)f)$$
$$= F_{\text{agg}}(\boldsymbol{u}, c, T, f) + F_{\text{break}}(\boldsymbol{u}, c, T, f) \text{ in } (0, t_{\text{end}}) \times \Omega \times \Omega_{\text{int}}. \tag{1.4}$$

Here, Ω_{int} is the d_{int}-dimensional domain for the internal coordinates and $\boldsymbol{u}_{\text{sed}}$ (m/s) is the sedimentation velocity, which is assumed to be divergence-free. The growth term is assumed to be linear with the growth rate $G(c, T)$ (kg/s), and ∇_{int} is the

nabla operator with respect to the internal coordinates. Nucleation is included via appropriate boundary conditions with respect to the internal coordinates. The right-hand side of (1.4) describes the agglomeration (aggregation, coalescence) of crystals and their breakage (fragmentation).

To simplify the presentation below, the case $d_{\text{int}} = 1$ will be considered in the remainder of this section, i.e., a so-called uni-variate population. Then, Ω_{int} is just an interval, e.g., an interval with respect to the mass of the crystals $\Omega_{\text{int}} = [m_{\text{min}}, m_{\text{max}}]$ in kg and it is $\nabla_{\text{int}} = \partial_m$. In this case, the agglomeration term for every time-space point $(t, \boldsymbol{x})$ has the form

$$F_{\text{agg}}(\boldsymbol{u}, T, f) = \frac{1}{2} \int_{m_{\text{min}}}^{m_{\text{max}}} \kappa_{\text{agg}}(\boldsymbol{u}, T, m - m', m') f(m - m') f(m') \, dm'$$

$$- \int_{m_{\text{min}}}^{m_{\text{max}}} \kappa_{\text{agg}}(\boldsymbol{u}, T, m - m', m') f(m) f(m') \, dm', \qquad (1.5)$$

where κ_{agg} ($\mathrm{m^3/s}$) is the agglomeration kernel. The first term, which is the source term, models the amount of crystals of mass m that are created by the agglomeration of two crystals with masses m' and $m - m'$, where $m' \in (m_{\text{min}}, m_{\text{max}})$. The corresponding sink term accounts for the crystals of mass m that vanish because they are consumed by agglomeration with other crystals of mass m'. The breakage term might be of the form

$$F_{\text{break}}(\boldsymbol{u}, c, T, f) = \int_{m_{\text{min}}}^{m_{\text{max}} - m} \kappa_{\text{break}}(\boldsymbol{u}, T, m, m') f(m + m') \, dm'$$

$$- \frac{1}{2} \int_{m_{\text{min}}}^{m} \kappa_{\text{break}}(\boldsymbol{u}, T, m - m', m') f(m') \, dm', \qquad (1.6)$$

where κ_{break} ($\mathrm{1/kg \ s}$) is the breakage kernel. The first term on the right-hand side describes the appearance of crystals of mass m and the second term describes the disappearance of such crystals due to breakage events.

2   Uni-variate Processes

2.1   Benchmark Problem

Different phenomena such as nucleation, growth, breakage, and agglomeration occur during crystallization. It depends on the particular crystallization process, which

phenomena are dominant. They have to be identified and integrated in the PBS as shown in (1.4), while other terms may be neglected. The resulting coupled PBS needs to be parameterized. For that, benchmark problems are required. Here, a growth dominated crystallizer is selected.

As mentioned in the previous section, the crystal mass can be used as internal property coordinate of the PBS. The goal of the presented benchmark problem is to intensify a process to grow faceted crystals shape-selectively. Hence, a measure of crystal size is applied as internal coordinate. To determine the crystal size distribution (CSD), 3d-crystal shapes are estimated from 2d-projections of the observed crystals following the methods by [9–11]. The shape is described by the perpendicular distances of the crystal faces to the crystal center. It is sufficient to consider one perpendicular distance x (m) for each face type to describe the full symmetry of an ideal crystal. Potassium aluminum sulfate dodecahydrate, also called potash alum, crystallizes predominantly as octahedron in aqueous solution. Hence, its shape can be characterized by one face type. The resulting crystal distribution is uni-variate.

The benchmark problem is of high dimension. There are four dimensions in time and space and one internal coordinate. Further, the solid and liquid phases are coupled.

2.2 Helically Coiled Flow Tube Crystallizer

2.2.1 Setup and Process

Growth-dominated experiments are realized in a helically coiled flow tube (HCT) crystallizer. The crystallization is temperature controlled. For the experiments, solution is pumped from a reservoir to the HCT, as depicted in Fig. 1. The solution passes a degasifier before crystal seeds are added, where the seeds are of a defined size fraction. The suspension is cooled in the HCT to grow. At the outlet of the HCT, the crystal population is imaged by a flow-through microscope. Finally, the crystals are dissolved in a reservoir.

Seeds are sieved in different size fractions. The seed fractions are applied for residence time experiments without growth and for growth experiments. In the experiments, several process parameters can be varied systematically: helix orientation, average fluid flow rate, crystal seed fraction, feed concentration, and temperature [66, 67]. Selected results are shown for an HCT crystallizer with a coil diameter of 0.11 m and an inner tube diameter of 0.006 m at laminar flow rates.

2.2.2 Residence Time Distribution

In residence time experiments for the dispersed phase, a sieved crystal size fraction was added within 10 s at the inlet. The solution was saturated and isothermal conditions were applied to avoid crystal growth. The residence time was estimated from

the crystal projections, which were recorded at the tube outlet by the flow-through
microscope. Further, the crystal shape and a size descriptor were estimated from the
projections. Crystal velocities were calculated from the measured residence times
and known geometry of the HCT and are depicted in Fig. 2. They were measured
in an HCT crystallizer made of glass (length of 35 m, upward flow). Mean crystal
velocities were calculated for several size classes. It was observed that large crystals
of about 200 µm size are faster than smaller crystals of a size of about 100 µm. This
observation holds for crystals of a density which deviates from the fluid density at
laminar flow rates in HCTs [66, 67]. In the PBS, the residence time can be empir-
ically described in dependence on the crystal size by a polynomial function or by
interpolation from measurements. To apply the model in a size range that exceeds
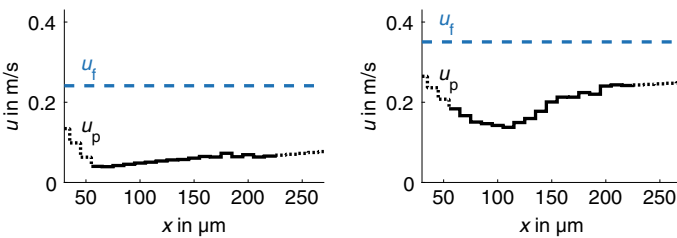
Fig. 2 Crystal-size dependent crystal velocities at two different laminar average fluid velocities
(blue, dashed) for the uni-variate potash alum. Measured in experiments (black, solid) and extrap-
olated (black, dotted)

the measured sizes, it can be assumed that very small crystals follow the fluid flow, as shown in Fig. 2.

The crystal residence time depends on the process parameters. Crystallization experiments in HCTs show that crystals of different size have different velocities in HCTs. Large crystals are faster than small crystals. Size-dependent residence times can be used to separate crystals of certain sizes in batch or periodic operation.

2.2.3   Crystal Growth

Crystals can be grown in HCTs by cooling crystallization. The longer the tubes and the lower the fluid velocities, the more time crystals have to grow and the larger the attainable final crystal sizes. This is illustrated for the case of varying fluid velocity in Fig. 3.

Crystal growth can be realized continuously in HCTs to change the CSD (Fig. 4).
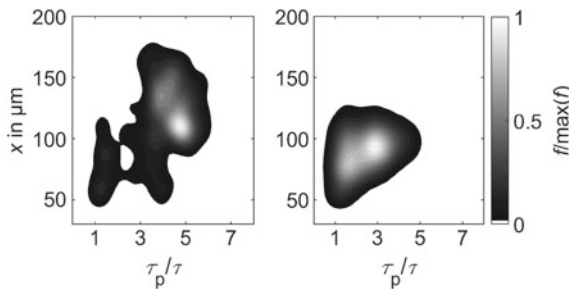
Fig. 3 Product crystal number density distributions after crystal growth experiments for varying average fluid flow rate: left: $u = 0.24$ m/s; right: $u = 0.35$ m/s. Potash alum seed fraction of a size x of $(95\pm11)\,\mu$m at a feed saturation temperature of $40\,^\circ$C and an initial outlet supersaturation of $\sigma = 4\%$

Fig. 4 Crystal growth experiments (blue bars) and simulation (green solid curve) of a potash alum seed fraction at a feed saturation temperature of 40° and an initial supersaturation of $\sigma = 17\%$ at the outlet for an average fluid flow rate $u = 0.24$ m/s. Crystal number density distributions: top: seed crystals; bottom: product
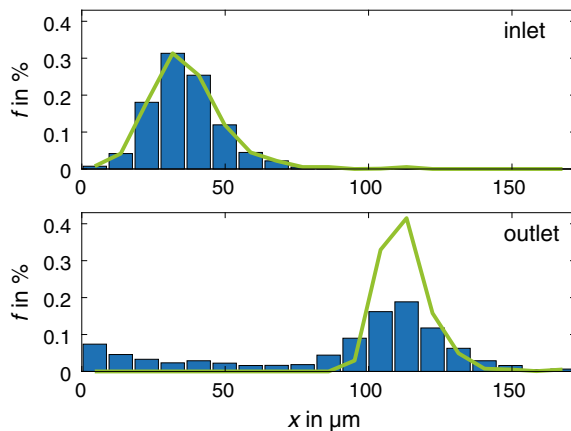
Numerically, the solution of the full model of the form (1.1)–(1.6) is expensive due to the mutual coupling of the equations. Hence, the model is reduced and assumptions are made for a dynamic simulation with reasonable computation times:

(a) It is assumed that the energy balance (1.2) can be neglected when a temperature profile is given.
(b) The momentum balance (1.1) is neglected.
(c) Only one spatial coordinate is considered, which is the z-coordinate along the tube axis.
(d) A low suspension density and moderate cooling are applied experimentally to suppress nucleation, breakage, and agglomeration.
(e) Crystal growth is size-independent.

The reduced population balance equation (PBE) is

$$\partial_t f + u \cdot \nabla f + G(c, T) \nabla_{\text{int}} \cdot f = 0 \quad \text{in } (0, t_{\text{end}}) \times \Omega \times \Omega_{\text{int}}. \tag{2.1}$$

For the continuous phase, there are two balance equations, since potash alum crystallizes as dodecahydrate under consumption of water from the solution. The diffusion term in (1.3) is replaced by a dispersion term of the same structure, but of a different value for the coefficient D_c. The crystal growth rate depends on the supersaturation of the continuous phase and thereby on the local temperature $T(t, z)$. The local temperature can be set by external cooling and it can vary dynamically.

The reduced PBS consisting of (1.3) and (2.1) was discretized in space z and in the internal size coordinate x via a finite volume method. The derived differential algebraic equation system was solved with the MATLAB-ODE23 solver, which is based on a Runge-Kutta approach. Product CSDs resulting after crystal growth are depicted in Fig. 5. As expected, the final crystal size increases with tube length during
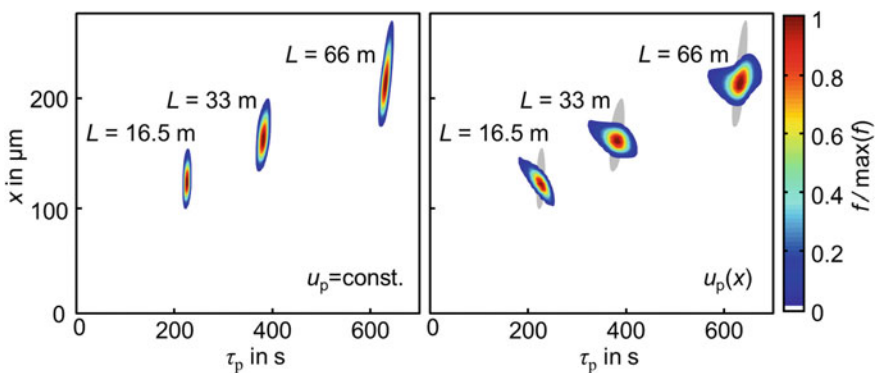
Fig. 5 Simulated product number density distribution based on a reduced model for the crystal growth of a normally distributed potash alum seed fraction ($\mu = 106\,\mu\text{m}$, $\sigma = 41\,\mu\text{m}$) for different tube lengths. Left: a constant crystal velocity; right: a size-dependent crystal velocity based on the measurement data

cooling crystallization. In batch simulations, the size-dependent residence time leads to narrow crystal size distributions compared to a uniform crystal residence time.

2.3   Brief Survey on Numerical Methods for Solving a PBS

Let the time interval be decomposed into subintervals $[t_{n-1}, t_n]$, $n = 1, \ldots N$, with $0 = t_0 < t_1 < \cdots < t_N = t_{\text{end}}$ and let the (numerical) solution $\boldsymbol{u}_{n-1}, T_{n-1}, c_{n-1}, f_{n-1}$ at the time instance t_{n-1} be given. Then, one has to apply some time stepping scheme to compute the (numerical) solution at t_n. This section provides a brief survey on methods that are proposed in the literature for computing a numerical solution at t_n.

Since a monolithic approach for solving the PBS, which computes all unknown functions together from (1.1) to (1.4), is computationally too demanding, the PBS is split into several parts and these parts are solved consecutively.

2.3.1   The Navier–Stokes Equations

Because the velocity appears in all equations and there is no back coupling of the other unknowns to the flow field, it is a straightforward idea to solve first the Navier–Stokes equations (1.1). These equations can be solved monolithically or decoupled by a so-called projection scheme. As temporal discretization, often first or second order time stepping schemes are used, like the Euler schemes, the Crank–Nicolson scheme, or the backward difference formula of order 2 (BDF2). The nonlinear term in the momentum balance can be treated implicitly, semi-implicitly, or explicitly. The semi-implicit approach is called implicit-explicit (IMEX) scheme. Usual spatial discretizations include finite element methods (FEM), finite volume methods (FVM), or, for simple domains, finite difference methods (FDM). A detailed description of all these approaches is far beyond the scope of this paper. Many of them are described, within the framework of FEMs, in [35, Chap. 7].

The situation becomes more complicated if the flow is turbulent. There is no mathematical definition of turbulence, but a good physical description is that a turbulent flow contains a wide range of physically important scales. In particular, there are many small scales that cannot be resolved on affordable grids and, consequently, that cannot be simulated. Standard discretizations cannot cope with this situation since they try to simulate all important scales. Simulations with such discretizations usually blow up in finite time. Since neglecting the small scales leads to physically incorrect numerical simulations, an approach is needed to model the impact of the unresolvable scales onto the resolvable scales. This approach is called turbulence modeling. In the literature, many turbulence models are proposed, e.g., see [54, 58], and turbulence modeling is still an active field of research. There is no turbulence model that can be considered to be the best one.

At the end of this step, $\boldsymbol{u}_n$ is known and it can be used in the other equations of the PBS.

2.3.2   The Energy and Concentration Equations

As a next, natural step, the Eq. (1.2) for the energy balance and (1.3) for the concentration balance can be solved. Again, due to the numerical complexity, a monolithic solution of this system of equations does not seem to be attractive. Instead, the equations are solved individually, by using the currently available data, e.g.,

1. $\partial_t T_n - D_T \Delta T_n + \boldsymbol{u}_n \cdot \nabla T_n = F_{\text{ener,growth}}(c_{n-1}, T_{n-1}, f_{n-1})$,
2. $\partial_t c_n - D_c \Delta c_n + \boldsymbol{u}_n \cdot \nabla c_n = F_{\text{conc,growth}}(c_{n-1}, T_n, f_{n-1})$,

where still the temporal derivatives have to be discretized. In this approach, one has to solve two linear equations. The individual solution of these equations can be iterated by using in the second iteration the temperature and concentration solution computed in the first iteration and so on.

In many applications, in particular in crystallization processes, the diffusion parameters in (1.2) and (1.3) are smaller by several orders of magnitude compared with the size of the velocity field. This situation is called convection-dominated and there is a similar difficulty as for turbulent flows: there are important features of the solution, so-called layers, that cannot be resolved on affordable grids. As for turbulent flows, standard numerical discretizations fail in this situation and the use of a so-called stabilized discretization is necessary, e.g., see [55]. There are many proposals for stabilized discretizations in the literature. In the context of the coupled system (1.2) and (1.3), it is essential that the numerical solution computed with the stabilized method must not possess unphysical values, so-called spurious oscillations, or it is allowed to exhibit only negligible spurious oscillations. This property is important because the computed solutions serve as data in other equations, for certain coefficients, and if the numerical solutions have spurious oscillations, then non-physical coefficients in other equations might be computed. At any rate, it was noted in [36] for a precipitation process that using a stabilized discretization that does not sufficiently suppress spurious oscillations usually leads to a blow-up of the simulations of the coupled system in finite time.

As a matter of fact, many of the proposed stabilized schemes lead to numerical solutions with non-negligible spurious oscillations, e.g., see the numerical assessment in [39]. Some schemes that satisfy the requirement with respect to the spurious oscillations are the followings:

- finite difference methods
  - upwind; very diffusive and very inaccurate,
  - FCT (flux-corrected transport) schemes [14];
  - ENO (essentially non-oscillatory) [32], WENO (weighted ENO) [45]; much more accurate, small spurious oscillations possible,
- finite element methods
  - linear FEM-FCT [42]; often good compromise between accuracy and efficiency,
  - FEM-FCT [43, 46]; nonlinear method, often quite accurate,

- finite volume methods

  - Scharfetter–Gummel method [59]; improved upwind but still quite diffusive,
  - FCT [70].

The assessments provided above are based mostly on our experience from [37].

2.3.3 The Population Balance Equation

After having discretized the temporal derivative in (1.4), one obtains an equation for f_n in a four- or even higher-dimensional domain. But this difficulty is not the only one for solving the population balance equation. There is a transport operator on the left-hand side of (1.4) whose discretization requires special techniques, and on the right-hand side there are integral operators whose efficient evaluation is complicated, in particular for the first term of the agglomeration (1.5).

First of all, there are several principal ways for designing a scheme for computing a numerical approximation of f_n:

- solve an equation in the high-dimensional domain $\Omega \times \Omega_{\text{int}}$, where the left-hand side is discretized with some appropriate discretization based on FDM, FEM, or FVM, the so-called direct discretization,
- apply an operator-splitting scheme that deals first with an equation in Ω and after this with an equation in Ω_{int},
- utilize a momentum-based method to transform the population balance equation to a system of equations in a three-dimensional domain,
- apply a stochastic method for solving (1.4).

The first approaches will be discussed briefly in the following whereas the last approach is presented in detail in Sect. 2.4.

Utilizing the first approach, the direct discretization, is computationally demanding. One issue is that usual CFD codes do not support four- or higher-dimensional domains. Using an implicit approach, then the system matrix becomes comparatively dense, compared with 3d, and the question of an appropriate solver for the linear systems of equations arises. The left-hand side of (1.4) is a transport operator, which can be considered as a limit case with vanishing diffusion of the convection-dominated operators from the energy and concentration balances. The discretizations mentioned for the convection-dominated operators in Sect. 2.3.2 can be applied also for the transport operator of the population balance equation. In addition, one needs a numerical method for evaluating the integral terms on the right-hand side of (1.4), see Sect. 3.2 for a discussion of this topic. Direct discretizations of 4d population balance equations can be found, e.g., in [12, 13, 60], and of a 5d population balance equation in [40].

Operator-splitting schemes for population balance equations in the form mentioned above were proposed in [25], see also [26]. Motivations for this proposal are efficiency, the possibility to use software that is designed for domains in usual dimensions, and the possibility to apply different discretizations for the different equations.

The principal form of the equations to be solved is as follows. Let $\hat{f}_n = f_{n-1}$, solve in the first step

$$\partial_t \hat{f} + \left(\boldsymbol{u}_n + \boldsymbol{u}_{\text{sed},n-1}\right) \cdot \nabla \hat{f} = 0 \quad \text{in } (t_{n-1}, t_n) \times \Omega \tag{2.2}$$

for all $y \in \Omega_{\text{int}}$. Then, set $\tilde{f}_{n-1} = \hat{f}_n$, solve

$$\partial_t \tilde{f} + \partial_m \left(G(c_n, T_n)\tilde{f}\right)$$
$$= F_{\text{agg}}(\boldsymbol{u}_n, c_n, T_n, \hat{f}_n) + F_{\text{break}}(\boldsymbol{u}_n, c_n, T_n, \hat{f}_n) \quad \text{in } (t_{n-1}, t_n) \times \Omega_{\text{int}} \tag{2.3}$$

for all $\boldsymbol{x} \in \Omega$, and set $f_n = \tilde{f}_n$. There are several modifications of this basic operator-splitting scheme for population balance equations, in particular to perform the steps in a different order, e.g., see [3, 25, 27]. Equation (2.2) is usually a transport equation with dominating convection, such that one has to utilize a stabilized discretization, see Sect. 2.3.2. Also (2.3) is a transport equation, but the growth of the crystals might be sufficiently slow such that one can apply some standard discretization. The operator splitting introduces an additional splitting error which does not spoil the optimal order of convergence for low order finite element methods [25].

As already mentioned at the beginning of this section, the definition of the population balance equation (1.4) for the crystal size distribution in a higher-dimensional domain is a major challenge for the simulation of population balance systems. A popular way to avoid this issue is the consideration of the first moments of the crystal size distribution, as proposed the first time in [33], where the so-called Method of Moments (MOM) was derived. The kth moment of the crystal size distribution is given by

$$M_k = \int_0^\infty m^k f \, dm, \quad k = 0, 1, 2, \ldots. \tag{2.4}$$

It will be assumed, that f is zero for $m \leq m_{\text{min}}$ and $m \geq m_{\text{max}}$, i.e., that there are a minimal and a maximal mass for the crystals. Hence, the domain of integration in (2.4) can be restricted to this interval. On the one hand, the first moments are often important in practice because they correspond to physical quantities, like the number of crystals (0th moment) or the mass of crystals (3rd moment). But on the other hand, the reconstruction of the crystal size distribution from its moments is a severely ill-posed problem and it is hard to design stable algorithms [34].

Multiplying (1.4) with m^k, integrating with respect to the internal coordinate, commuting this integration with differentiation in time and with respect to the external variable yields an equation for the kth moment

$$\partial_t M_k + (\boldsymbol{u} + \boldsymbol{u}_{\text{sed}}) \cdot \nabla M_k = \int_{m_{\text{min}}}^{m_{\text{max}}} m^k S \, dm, \quad k = 0, 1, 2, \ldots, \tag{2.5}$$

with

$$S = F_{\text{agg}}(\boldsymbol{u}, c, T, f) + F_{\text{break}}(\boldsymbol{u}, c, T, f) - \partial_m (G(c, T)f).$$

System (2.5) is a closed system for a finite number of moments only in special cases, e.g., if there are no agglomeration, no breakage, and special growth functions.

For the case that a closure of (2.5) cannot be found, we consider for simplicity only the growth term on the right-hand side of (2.5). Applying integration by parts and using that f vanishes at m_{min} and m_{max}, this term can be reformulated as follows

$$-\int_{m_{\text{min}}}^{m_{\text{max}}} m^k \partial_m (G(c, T)f) \ dm = \int_{m_{\text{min}}}^{m_{\text{max}}} k m^{k-1} G(c, T) f \ dm$$

$$= \int_{m_{\text{min}}}^{m_{\text{max}}} \tilde{G}(c, T) f \ dm, \quad k \geq 1,$$

with the new growth function $\tilde{G}(c, T) = k m^{k-1} G(c, T)$. Note that this integral still contains the unknown crystal size distribution f. The principal idea of the Quadrature Method of Moments (QMOM) proposed in [49] consists in approximating this integral by some quadrature formula

$$\int_{m_{\text{min}}}^{m_{\text{max}}} \tilde{G}(c, T) f \ dm \approx \sum_{i=1}^{N} \omega_i \tilde{G}(m_i), \tag{2.6}$$

where N is the number of quadrature points, which is prescribed by the user, ω_i are the weights of the quadrature rule and m_i are the nodes (quadrature points, abscissas). Then, at time instance t_n, one considers the system of equations for the moments

$$\partial_t M_k + (\boldsymbol{u} + \boldsymbol{u}_{\text{sed}}) \cdot \nabla M_k = \int_{m_{\text{min}}}^{m_{\text{max}}} \tilde{G}(c_n, T_n) f_{n-1} \ dm, \quad k = 0, \ldots, 2N - 1, \tag{2.7}$$

where the left-hand side has still to be discretized appropriately and the right-hand side is approximated with (2.6).

To keep the quadrature error in (2.6) as small as possible, the weights and abscissas should be chosen such that the optimal order $(2N - 1)$ of the numerical quadrature is obtained. Several algorithms are available for this purpose. In [41], it is shown that the long quotient-modified difference algorithm (LQMDA) behaves better than two other algorithms concerning stability and efficiency. For computing the optimal weights and abscissas, the knowledge of f is not necessary, but only of the first $2N$ moments of f. Thus, for the first time step $n = 1$, one can use the known initial condition of f for computing the right-hand side in (2.7) such that the first $2N$ moments at time

t_1 can be computed. Then, these moments can be used for computing the right-hand side for the next time instance and so on.

Agglomeration and breakage processes can be also incorporated into the framework of QMOM, e.g., see [48]. An extension of the QMOM, which does not compute the moments, but directly the weights and abscissas, is the Direct Quadrature Method of Moments (DQMOM), as proposed in [47]. It is also possible to simulate multivariate populations with QMOM, e.g., see [18].

2.3.4 On Our Experience with Some of the Methods

As already mentioned above, it was noted in [36] that the use of a stabilized scheme for convection-diffusion equations, which does not suppress spurious oscillations sufficiently, often leads to a blow up of the simulations. Only cutting off such oscillations appropriately led to stable simulations. However, such cut-off techniques lead inevitably to violations of conservation properties. Moreover, in the same paper, it was concluded that the use of upwind techniques led to completely smeared and practically useless results. A clear improvement of the quality of the numerical solutions was observed in [38] by using a linear FEM-FCT scheme for the convection-diffusion and transport equations in the PBS. Based on this experience, we have employed the linear FEM-FCT scheme for solving the energy equation (1.2) and concentration equation (1.3) in PBSs. Different numerical methods for the 4d population balance equation were studied in [13]. The problem of interest was a turbulent air-droplet flow in a segment of a wind tunnel, where $\Omega \times \Omega_{\text{int}}$ was a tensor product domain in 4d. In this situation, FDM approaches can be applied easily. Two kinds of linear FEM-FCT schemes and an FDM ENO scheme were compared. It turned out that the FDM ENO scheme was by far the most efficient approach, such that it was recommended for population balance equations on tensor product domains. This scheme was also applied successfully for the simulation of a bi-variate population balance in [40]. In [3], a direct discretization using the FDM ENO approach for the population balance equation (1.4) and an operator-splitting scheme were compared for an axisymmetric problem. While the operator-splitting scheme converged faster to a steady-state, the evolution of the transition was predicted more accurately by the direct discretization.

In summary, up to the publication of [3], we could, on the one hand, identify accurate and efficient approaches for simulating PBSs that are given on tensor product domains. Here, efficiency refers only to the differential operators in the population balance equation (1.4). Efficient methods for the integral operators are a different topic, which will be discussed in Sect. 3.2. But on the other hand, it is very complicated to extend our favorite approach, the direct discretization, to problems defined in more general domains, which occur usually in applications. In this respect, we could make decisive progress in the preceding years by employing and further developing a stochastic method, which will be discussed in detail in Sect. 2.4.

2.4 A Stochastic Method for Simulating the Crystal Size Distribution

This section describes a stochastic particle simulation (SPS) method for computing a numerical approximation of the crystal size distribution f whose behavior is modeled by the population balance equation (1.4). This method can be applied successfully for the simulation of problems given in complex spatial domains.

The basis of the SPS method that is utilized in our simulations is the method proposed in [52, 53]. This method had to be extended by all features that are caused from the movement of the crystals in the spatial domain: convective transport in three dimensions, sedimentation, crystal-wall collisions, and the coupling with the deterministic methods for solving the other equations (1.1)–(1.3) of the PBS. The algorithms from [52, 53] include convective transport in one dimension, growth, and coagulation (collision growth). With respect to the first and third feature, the method is based on two classical algorithms. The first one is Bird's direct simulation Monte-Carlo algorithm for the Boltzmann equation [8] that proposes an approach to handle the convective transport part with a splitting method. The second algorithm is the Gillespie algorithm [28, 29] that models the coagulation via stochastic jump processes. One of the original contributions from [53] is a stochastic algorithm for simulating crystal growth via a surface reaction model.

Altogether, the splitting scheme applied in the SPS method consists of two parts: the convective transport of crystals, discussed in Sect. 2.4.1, and Markov jump processes for simulating growth, agglomeration, and insertion of crystals, described in Sect. 2.4.2. Section 2.4.3 presents the complete algorithm that simulates the PBSs (1.1)–(1.4).

2.4.1 Convective Transport of Stochastic Computational Crystals

The spatial domain Ω is triangulated by a triangulation consisting of mesh cells $K_j, j \in \{1, \ldots, N\}$. Each mesh cell contains a crystal ensemble $\mathcal{E}_j$. In the stochastic method, computational crystals (particles) are considered that represent an ensemble of physical crystals (particles). For simplifying the notion, the computational crystals will be called just 'crystals' in the following.

Consider a spatial mesh cell K and a crystal ensemble $(K, \mathcal{E})$, where each crystal e_i in $\mathcal{E}$ possesses a spatial and an internal coordinate $e_i = (\mathbf{x}_i, m_i)$, with $\mathbf{x}_i \in K$ and $m_i \in \Omega_{\text{int}}$. The complete ensemble $\mathcal{E}$ with $N_{\mathcal{E}}$ crystals is given by $\mathcal{E} = (e_1, \ldots, e_{N_{\mathcal{E}}})$.

Let Δt be a constant splitting time. First of all, the flow field $\mathbf{u}$ from the Navier–Stokes equations (1.1) is responsible for the transport of crystals. Second, crystals are also moved by sedimentation with the sedimentation velocity $\mathbf{u}_{\text{sed}}$. In the convection step, each crystal e_i is transported along the trajectories of $\mathbf{u} + \mathbf{u}_{\text{sed}}$

$$\mathbf{x}_i \longrightarrow \mathbf{x}_i + \Delta t \left(\mathbf{u}(\mathbf{x}_i) + \mathbf{u}_{\text{sed}}(\mathbf{x}_i) \right). \tag{2.8}$$

There are two topics that will be discussed in this section. From the modeling point of view, a model for the sedimentation velocity $\boldsymbol{u}_{\text{sed}}$ is needed. From the algorithmic point of view, one has to detect whether the crystal left its mesh cell after the transport step or even would hit the boundary of the domain if the transport step is performed and appropriate numerical procedures have to be performed in these situations.

For the considered application, a crystallization process in a fluidized bed crystallizer, the sedimentation of crystals has to be taken into account. Sedimentation depends on various aspects, like the form of the crystals and the actual local velocity field. In our application, the crystals can attain quite different forms. Since we could not find an appropriate sedimentation model in the literature, we decided to use as basis a sedimentation model for spherical particles, see [7, pp. 58] for its derivation. However, numerical studies in [6] showed that we had to modify this model for our purposes. Concretely, a scaling factor was introduced. Finally, the sedimentation velocity in our numerical simulations has the form

$$\boldsymbol{u}_{\text{sed}} = (0, 0, u_z)^T \quad \text{with} \quad u_z = \sigma \frac{\left(\frac{6}{\rho\pi}\right)^{\frac{2}{3}} (\rho_{\text{cryst}} - \rho) g}{18\mu} m^{\frac{2}{3}}. \tag{2.9}$$

In this model, ρ (kg/m³) is the density of the fluid, ρ_{cryst} (kg/m³) the density of the crystals, μ (kg/m s) the dynamical viscosity of the fluid, $g = 9.81$ m/s² the gravity, and σ the numerically determined scaling factor. It can be observed that the sedimentation model (2.9) depends on the mass of the crystals. In [6], a brief numerical study led to the choice $\sigma = 0.1$ in (2.9). Section 2.5 will present results that are obtained also with a different scaling factor.

After having performed the transport step (2.8), it must be checked whether each moved crystal still belongs to the same mesh cell. If not, then it must be removed from its current ensemble. If the final point of the relocation is within Ω, it is inserted in the ensemble of the new cell. However, it might happen that this point is outside Ω such that the crystal hits the boundary of the flow domain. The treatment of this situation required a notable extension of the algorithm for the crystal transport.

First of all, for the considered application, we distinguished the boundary part through which the crystal would leave the domain. Crystals that would leave through the inflow boundary, which is located at the bottom of the fluidized bed crystallizer, are measured and removed from the simulations. This situation happens because of the sedimentation of crystals. Crystals that would leave through other boundaries are reflected and repositioned in the domain. Two reflection algorithms were implemented, which both model elastic wall collisions where no kinetic energy is absorbed in the collision. A perfect reflection is utilized if the starting point of the crystal's movement is sufficiently away from the boundary of the domain, i.e., its distance is larger than a prescribed tolerance. Otherwise, a random reflection is applied. This random reflection is also used in the case of double reflections at two boundary parts. For details describing the reflection algorithms, it is referred to [4, 6].

2.4.2   Modeling of Growth, Coagulation, and Crystal Insertion by Markov Jump Processes

The crystals are allowed to interact with each other only within their current ensemble. In particular, crystals do not have to meet in the same point in space in order to agglomerate, it is enough for them to be contained in a common mesh cell.

Growth, agglomeration, and insertion of crystals are modeled with Markov jump processes. These processes are described in this section, following [52, 53], in terms of the so-called 'stochastic weighted algorithm'. For further technical details, it is referred to [52, 53].

Starting at some time $t \in [0, t_{\text{end}})$, the system stays in the state $\mathcal{E}(t)$ for an exponentially distributed waiting time τ, $P(\tau \geq s) = \exp(-\lambda(\mathcal{E})s)$. Here, $\lambda(\mathcal{E})$ is the waiting time parameter that is the sum of the individual rates of all jumps that are possible in $\mathcal{E}(t)$. This parameter is the sum of the growth jump rate $\lambda_{\text{grow}}(\mathcal{E})$ and the agglomeration jump rate $\lambda_{\text{aggl}}(\mathcal{E})$:

$$\lambda(\mathcal{E}) = \lambda_{\text{grow}}(\mathcal{E}) + \lambda_{\text{aggl}}(\mathcal{E}).$$

First, the simulation of crystal growth will be described. The growth term as it stands in the population balance equation (1.4) is a transport term along the internal coordinate. The rationale behind a stochastic simulation of this term by Markov jump processes is the interpretation of crystal growth as crystal surface growth via a chemical reaction. One can derive a relation between the growth rate $G(c, T)$ and the corresponding reaction rate, e.g., see [5]. A crystal growth jump has an impact on just one crystal e_i. Given a growth height Δm_i, the state of e_i is changed by

$$e_i = (\boldsymbol{x}_i, m_i) \longrightarrow (\boldsymbol{x}_i, m_i + \Delta m_i) =: \tilde{e}_i.$$

The crystal e_j for which the next growth jump occurs is chosen with the probability

$$\frac{G(c, T, m_j)}{\Delta m_i} \left(\lambda_{\text{grow}}(\mathcal{E})\right)^{-1}. \tag{2.10}$$

In our implementation of the SPS method, c and T are assumed to be constant in K in expression (2.10). The total rate for the growth jumps in $\mathcal{E}$ is given by

$$\lambda_{\text{grow}}(\mathcal{E}) = \sum_{i=1}^{N_{\mathcal{E}}} \frac{G(c, T, m_i)}{\Delta m_i}.$$

In agglomeration jumps, two crystals e_i and e_j, with $i < j$, are involved. Such a jump has the form

$$e_i, e_j \longrightarrow (\xi(\boldsymbol{x}_i, \boldsymbol{x}_j), m_i + m_j) =: \tilde{e}_i.$$

After having performed this jump, the crystal e_j is removed from the ensemble and the crystal $\tilde{e}_i$ has to be placed in an appropriate way in the ensemble, i.e., one has to assign an appropriate position to $\tilde{e}_i$. For designing a stable method, it is proposed in [52] to choose the new position $\mathbf{y}$ of a crystal that emerged from coagulation of the crystals $(m_i, \mathbf{x}_i)$ and $(m_j, \mathbf{x}_j)$ stochastically, distributed according to the probabilities

$$P(\mathbf{y} = \mathbf{x}_i) = \frac{m_i}{m_i + m_j}, \quad P(\mathbf{y} = \mathbf{x}_j) = \frac{m_j}{m_i + m_j},$$

i.e., to use the center of mass in the probabilities. Similarly as for the growth, the total rate of agglomeration jumps is the sum of all individual agglomeration jump rates of pairs of crystals

$$\lambda_{\mathrm{aggl}}(\mathcal{E}) = \frac{1}{2N_{\mathcal{E}}} \sum_{i,j=1}^{N_{\mathcal{E}}} \kappa_{\mathrm{agg}}(m_i, m_j).$$

The involvement of two crystals in an agglomeration jump is random with the probabilities

$$P(e_i \text{ and } e_j \text{ chosen for agglomeration}) = \frac{\kappa_{\mathrm{agg}}(m_i, m_j)}{2N_{\mathcal{E}}}.$$

Ensembles of crystals might be changed also by insertion of crystals in the flow domain. This process affects usually only a few mesh cells. Crystal insertion is modeled by so-called inception jumps, i.e., each ensemble in mesh cells, where crystals are injected, is equipped with an additional jump rate $\lambda_{\mathrm{in}}(\mathcal{E})$ and a corresponding jump, which adds a new crystal to the ensemble.

2.4.3   Coupled Simulation with a Splitting Scheme

Our basic approach for developing a code for solving the PBS (1.1)–(1.4) numerically consisted in coupling two separate codes: one designed for simulating the Computational Fluid Dynamic (CFD) equations (1.1)–(1.3) with deterministic methods, and the other one designed for simulating crystal interactions with stochastic methods. For this purpose, we used the in-house codes PARMOON [24, 68] for the CFD part and BRUSH [53] for the SPS part.

The complete simulation procedure is sketched in Fig. 6. In each time instance, first the CFD equations are solved and then the population balance equation (1.4) with the SPS method. In order to couple the two codes, an interface was developed and implemented that is responsible for the data transfer between the codes. Other major extensions of BRUSH that were necessary include the simulation of the transport of the crystals in three dimensions, the implementation of the sedimentation model, the implementation of crystal-wall interactions, and the implementation of routines for assigning the crystals to mesh cells. For more details, it is referred to [4].
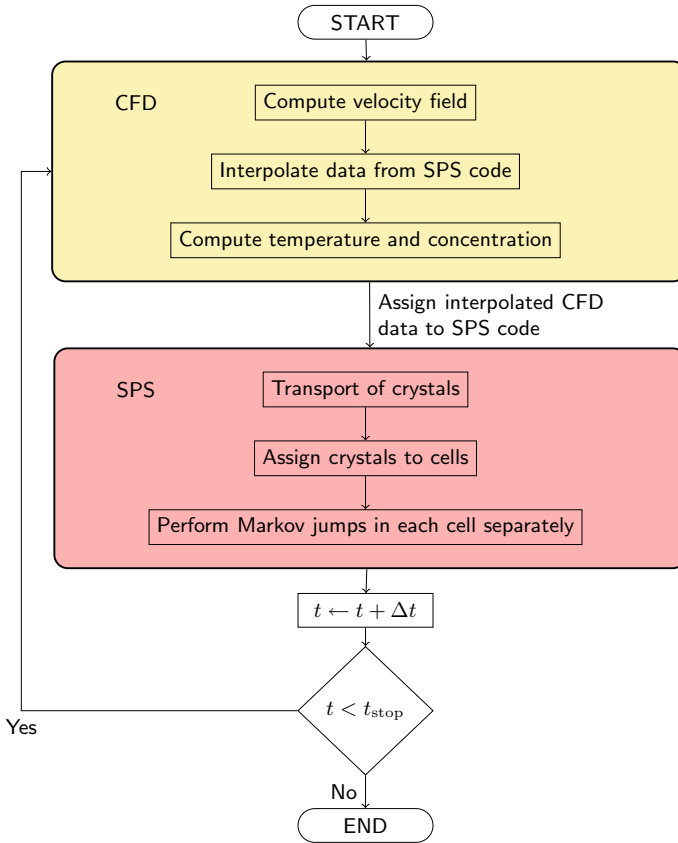
Fig. 6 Schematic sketch of the coupled simulation via a splitting scheme

2.5   Numerical Simulations of a Fluidized Bed Crystallizer

The deterministic-stochastic approach described in Sect. 2.4 was utilized for the simulation of the behavior of the crystallization process for another benchmark problem. The second benchmark was a crystallization process in a fluidized bed crystallizer.

In a fluidized bed crystallizer, crystal growth and agglomeration can be combined, where the main control variables are temperature profiles and flow rates. Crystals can be separated by size and withdrawn at a varying crystallizer height. The size separation is again controlled by the flow rates.

The experimental implementation of such a crystallizer is depicted in Fig. 7. Solution is removed from the top of the fluidized bed crystallizer through a filter. It is pumped back into the device from the bottom to fluidize the crystals. The crystallizer is cooled by a double jacket to increase the supersaturation over time. Crystals can be sampled from a variable height in the fluidized bed crystallizer during an exper-

Fig. 7 Schematic of the
benchmark experiment in the
fluidized bed crystallizer
with exemplary crystals in
different withdrawal heights

500 µm
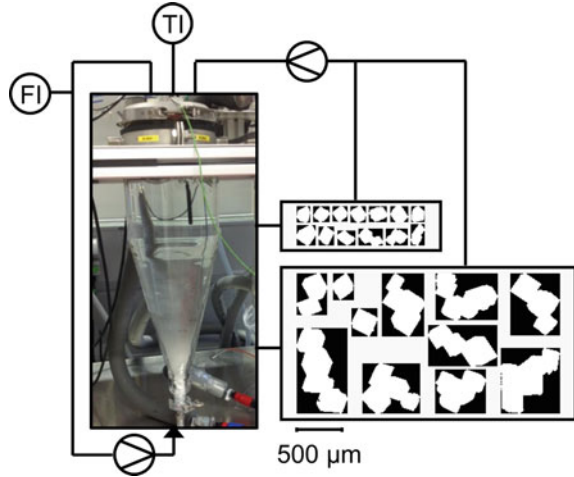
iment. As in the first benchmark problem, the crystal shape can be analyzed by a
flow-through microscope.

A PBS of the form (1.1)–(1.4) was used for modeling this process. Figure 8
presents the computational domain and its decomposition in tetrahedra. The compu-
tational domain neglects the small inlet extension at the bottom, compared with the
fluidized bed crystallizer used in the experiment. This modification is caused from
an algorithmic issue, since the routine that locates the mesh cell where a crystal is
situated after a transport step requires a convex domain. A routine implemented in
the research code TETGEN [63] was used for this purpose. The grid shown in Fig. 8
consists of 10,752 tetrahedra.

Preliminary numerical studies showed that the used grids were too coarse for sim-
ulating all scales of the flow field. This situation is the typical one that is encountered
in the simulation of turbulent flows and it is well known that one has to utilize a
turbulence model. There are many proposals for such models, e.g., see [54, 58]. In
our simulations, we applied the Smagorinsky Large Eddy Simulation (LES) model,
which adds to the momentum equation of the Navier–Stokes equations (1.1) the
nonlinear viscous term

$$\nu_{\mathrm{Smago}}\|\nabla\boldsymbol{u}\|_F \nabla\boldsymbol{u} = C_{\mathrm{Smago}}\delta^2\|\nabla\boldsymbol{u}\|_F \nabla\boldsymbol{u}, \tag{2.11}$$

where δ is the local filter width, which was chosen to be piecewise constant, namely
twice the length of the shortest edge of a tetrahedron, C_{Smago} is a user-chosen param-
eter, and $\|\cdot\|_F$ is the Frobenius norm of a tensor. Numerical studies showed that
the value $C_{\mathrm{Smago}} = 5 \times 10^{-4}$ was sufficient, which is a comparably small value and
which indicates that the flow is only slightly turbulent. In the experiments, a typical
average inflow velocity was $U \approx 0.08$ m/s. Together with the choice of a characteristic
length $L = 0.1$ m as a typical inner diameter and the density and dynamic viscosity
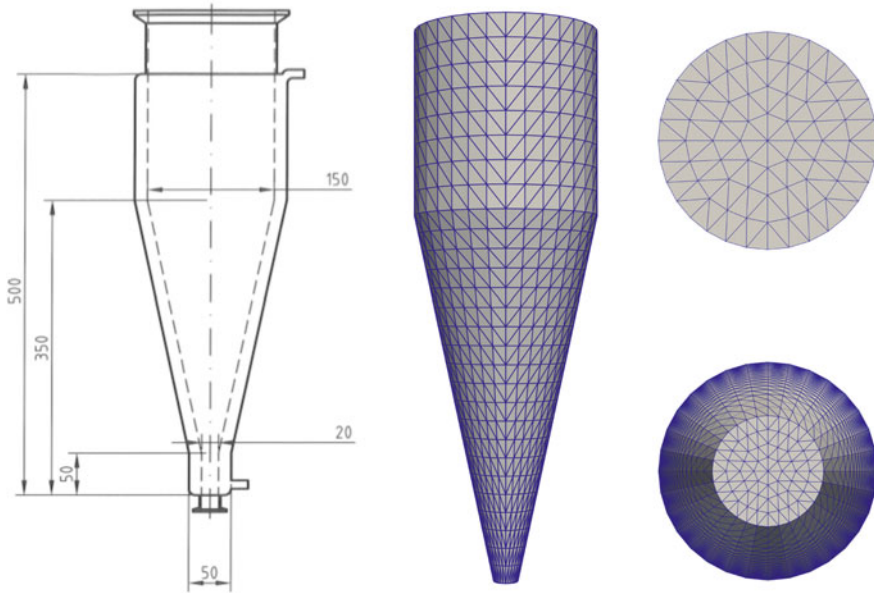
Fig. 8 Geometry (in mm) and mesh used in the simulations, left: front view; right: top and bottom views

of purified water, the Reynolds number is $\text{Re} = \mu U L/\rho \approx 6000$, see Table 1 for the values of the physical coefficients. These coefficients were kept constant during the simulation since there were only small variations of the temperature (± 1 K) and the amount of crystals was negligible.

The Navier–Stokes equations (1.1) were discretized in time with the Crank–Nicolson scheme, which is of second order, and the equidistant time step $\Delta t = 0.05$ s. They were linearized with a standard Picard iteration and the arising linear saddle point problems were discretized in space with the popular inf-sup stable pair P_2/P_1, a so-called Taylor–Hood pair of finite element spaces. That means, the velocity was approximated with continuous and piecewise quadratic functions and the pressure with continuous piecewise linear functions. Hence, the resolution of the velocity field is in fact twice as fine as suggested by the grid from Fig. 8. A snapshot of the flow field is displayed in Fig. 9. For the temporal discretization of the temperature equation (1.2) and the concentration equation (1.3) also the Crank–Nicolson scheme was used, with the same time step as for the Navier–Stokes equations. The spatial discretization was performed with the linear FEM-FCT scheme from [37, 42] with P_1 finite elements, see Sect. 2.3.2. Finally, the population balance equation (1.4) was simulated with the SPS method described in Sect. 2.4. The breakage of crystals was neglected in the numerical simulations. The coupled PBS was simulated with the splitting scheme presented in Sect. 2.4.3. There were 49,419 degrees of freedom for the velocity and 2349 for the pressure, temperature, and concentration.

Table 1 Coefficients for the PBSs modeling the fluidized bed crystallizer process

Name	Notation	Unit	Value/Function
Density of purified water	ρ	kg/m^3	1050
Dynamic viscosity of purified water	μ	kg/m s	0.0014
Diffusion coefficient in (1.2)	D_T	m^2/s	$\frac{\lambda_{susp}}{\rho_{susp} C_{susp}}$
Thermal conductivity	λ_{susp}	W/m K	0.6
Suspension density	ρ_{susp}	kg/m^3	1050
Suspension specific heat capacity	C_{susp}	J/kg K	3841
Scaling parameter in (1.2)	g_T	K·m^3/kg	$\frac{\Delta h_{cryst}}{\rho_{susp} C_{susp}}$
Crystallization enthalpy	Δh_{cryst}	J/kg	89,100
Diffusion coefficient (c)	D_c	m^2/s	5.4×10^{-10}
Scaling parameter (1.2)	g_c	mol/kg	$-\frac{1}{M_{hydrate}}$
Molar mass of hydrate	$M_{hydrate}$	kg/mol	0.4744
Density of crystals	ρ_{cryst}	kg/m^3	1760
Boltzmann constant	k_B	J/K	$1.3806504 \times 10^{-23}$
Universal gas constant	R	J/K mol	8.314

Fig. 9 Snapshot of the flow field with velocities in m/s inflow rate 56 kg/h
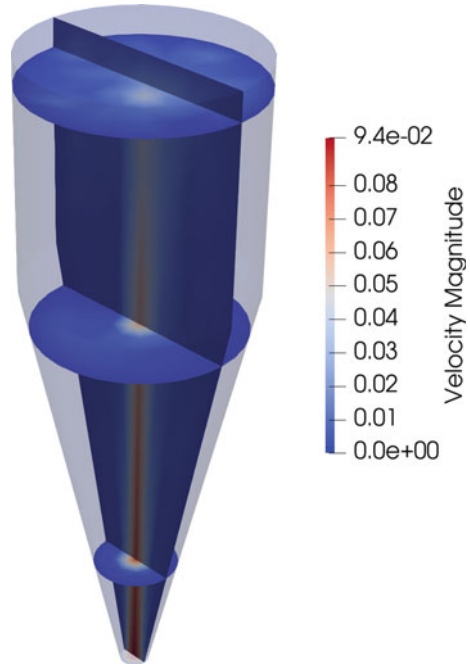
As final simulation time, $t_{\text{end}} = 1800\,\text{s} = 30\,\text{min}$ was set, such that 36,000 time steps had to be performed. For the flow, the mass flow rate at the inlet was 56 kg/h in the whole time interval. The flow field was allowed to develop in the first 30 s. Then, the crystals were inserted in the flow during the time interval [30 s, 40 s]. In contrast to the experiment, where all crystals are inserted into the crystallizer basically at the same time, the crystals enter in the simulations during a short time interval. There is an algorithmic reason, since the SPS method works better if there is a rather uniform distribution of crystals. The seed mass of the crystals was 10^{-4} kg. It was divided equally into two parts, one with crystals of diameter 75 µm and one of crystals with diameter 125 µm. Both parts were represented via a log-normal distribution with 25 µm standard deviation.

Storage for 256 computational crystals was assigned to each mesh cell of the flow domain Ω. As already mentioned in Sect. 2.4.1, each computational crystal represents a number of physical crystals. In preliminary simulations, 5.0×10^8 # physical crystals/m³ was found to be an upper bound for the concentration of physical crystals away from the bottom of the device. In this region, a linear conversion to computational crystals was used such that this upper bound corresponds to 256 computational crystals. Close to the bottom, the concentration of physical crystals was often higher, due to sedimentation. In this region, still a linear conversion was applied, but the conversion factors were increased by 10 below 0.1 m and by 100 below 0.05 m. The choice of the conversion factor is a purely numerical issue. It influences the computational cost and the numerical precision, but otherwise it has no effect on the results for the physical quantities. This setup led to roughly 150,000 computational crystals in Ω after having completed the insertion at 40 s. This number is typically reduced by around 50% at the end of a simulation because of agglomeration and in addition since, as explained in Sect. 2.4.1, crystals that would leave through the inlet due to sedimentation were removed from the simulations.

The coupling term for the temperature equation (1.2) is given by

$$F_{\text{ener,growth}}(c, T, f) = g_T \int_{\Omega_{\text{m}}} Gf(t, \boldsymbol{x}, m)\,dm,$$

where the model for the growth term will be discussed below. Table 1 presents all other coefficients for this equation. The Dirichlet boundary data for the temperature were linearly interpolated in the time interval $[0, t_{\text{end}}]$, where the initial temperature was $T(0\,\text{s}) = 288.95\,\text{K}$, i.e. $15.8\,°\text{C}$, and the final temperature was $T(3600\,\text{s}) = 288.35\,\text{K}$, which is $15.2\,°\text{C}$. The right-hand side of the concentration equation (1.3) is given by

$$F_{\text{conc,growth}}(c, T, f) = g_c \int_{\Omega_{\text{m}}} Gf(t, \boldsymbol{x}, m)\,dm.$$

Also the coefficients for this equation are provided in Table 1. As initial condition $c(0\,\text{s}) = 207$ mol/m³ was chosen, which corresponds to the saturation concentration at $17\,°\text{C}$.

For the sedimentation, the model (2.9) was utilized. A brief numerical study in [6] showed that one has to choose the scaling factor in this model rather small. Otherwise, too many crystals would leave through the inlet of the domain due to sedimentation, compare Sect. 2.4.1. In [6], $\sigma = 0.1$ was used. In this section, also results obtained with $\sigma = 0.05$ are presented to continue the study with respect to the scaling factor.

For the growth term in the population balance equation (1.4), a model from [64] is utilized

$$
G = \begin{cases} \frac{\sqrt{2}}{\pi^{\frac{1}{3}}} k_{G_1} \exp\left(-\frac{k_{G_2}}{RT}\right) \left(S_{\text{hyd,H}_2\text{O+}} - 1\right)^{k_{G_3}} \ (\text{m/s}), & \text{if } S_{\text{hyd,H}_2\text{O+}} > 1, \\ 0 & \text{else}, \end{cases}
$$

where the model parameters are given by $k_{G_1} = 5 \times 10^7$ m/s, $k_{G_2} = 75 \times 10^3$ J/mol, $k_{G_3} = 1.4$. The factor $\sqrt{2}/\pi^{\frac{1}{3}}$ comes from converting an octahedral to a spherical crystal shape. The quantity

$$
S_{\text{hyd,H}_2\text{O+}} = \frac{w_{\text{hyd,H}_2\text{O+}}}{w_{\text{hyd,H}_2\text{O+}}^{\text{eq}}(T)} \ (\text{kg/kg})
$$

is the relative supersaturation of the solution. Here, $w_{\text{hyd,H}_2\text{O+}}$ (kg/kg) is the current mass loading and $w_{hyd,H_2O+}^{eq}(T)$ (kg/kg) is the mass loading in equilibrium given by

$$
w_{hyd,H_2O+}^{eq}(T) = a_1 + a_2 T + a_3 T^2 + a_4 T^3 + a_5 T^4 \quad \left(\frac{\text{kg hydrate}}{\text{kg added water}}\right),
$$

with coefficients $a_1 = 0.0506$, $a_2 = 0.0023$, $a_3 = 7.76 \times 10^{-5}$, $a_4 = -2.43 \times 10^{-6}$, and $a_5 = 4.86 \times 10^{-8}$. This solubility model is known to be valid in a temperature range from 10 to 60 °C. To apply this growth model in our simulations, a number of conversions had to be made, see [4, 6] for details.

For the agglomeration kernel in (1.5), the Brownian kernel

$$
\kappa_{\text{agg}}(T, m_1, m_2) = \kappa \frac{2Tk_B}{3\mu} \left(\frac{1}{d(m_1)} + \frac{1}{d(m_2)}\right) (d(m_1) + d(m_2)) \quad (\text{m}^3/\text{s}) \quad (2.12)
$$

was utilized, where κ is a scaling parameter and $d(m) = \sqrt[3]{6m/\rho_{\text{cryst}}\pi}$ (m) is the sphere equivalent diameter. The same kernel was applied in the simulations presented in [6], where different values of $\kappa \le 5000$ were tested. In fact, most results from [6] were computed with $\kappa = 5000$. However, in other applications, where we used the Brownian kernel, we found higher values of the scaling factor, e.g., $\kappa = 7000$ in [3] and even $\kappa \in [200{,}000, 300{,}000]$ for a strongly agglomeration-dominated problem studied in [31]. For this reason, we continued the numerical studies with respect to the scaling factor of the Brownian kernel to higher values of κ and the results will be presented in this section.

The internal coordinate in the PBS is crystal mass. However, for the evaluation of the numerical simulations, the sphere equivalent diameter in μ will be used, since
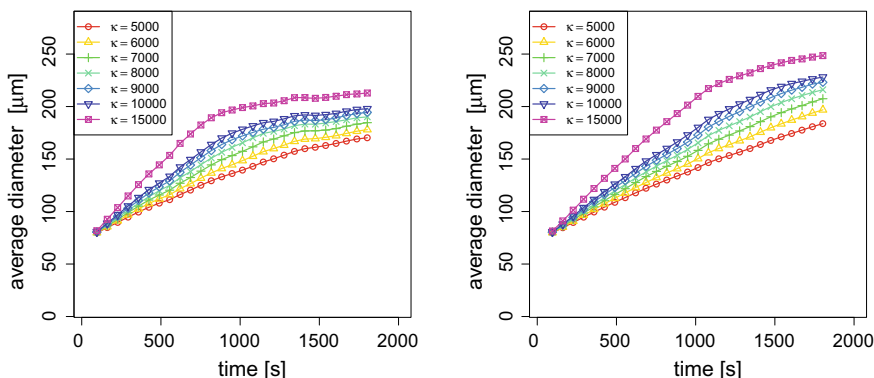
Fig. 10 Dependency of the average crystal diameter on the parameter κ of the Brownian agglomeration kernel: left $\sigma = 0.05$, right $\sigma = 0.1$. Averaging was performed for all crystals with diameter larger than or equal to $5\,\mu m$

this facilitates the interpretation of the computational results and the comparison with the experimental data.

In the simulations, the nuclei were of $5\,\mu m$ diameter. Figure 10 presents the temporal development of the average crystal diameter in the whole fluidized bed crystallizer for the two considered parameters $\sigma \in \{0.05, 0.1\}$ in the sedimentation model (2.9) and for different values of the parameter κ in the Brownian agglomeration kernel (2.12). For both values of σ there is the same tendency: the larger κ, the larger is the average diameter. For smaller values of κ, the temporal growth of the average diameter is approximately linear in the considered time interval. There is also a linear growth in the first part of the time interval for larger values. But then, a flattening of the curves can be observed. At the final time, one obtains in average larger crystals with $\sigma = 0.1$. With this higher value of the sedimentation parameter, there is a higher concentration of crystals close to the inlet, which increases the probability for agglomeration events in this region. These crystals are comparably large since the sedimentation velocity depends also on the mass of the crystals, such that the agglomeration events lead to even larger crystals.

In the experiment, the smallest measurable crystals were of diameter $50\,\mu m$. In order to compare numerical results and experimental data, the same value was used as lower threshold for computing the average diameter of the simulation results. Experimental data are displayed in Fig. 11. One can see that in the considered time interval, the averaged diameter increased approximately linearly by around $80\,\mu m$. At the final time, the average diameter is between 234 and $261\,\mu m$. There is no separation of different sizes of crystals in different heights of the fluidized bed crystallizer. In the results for the simulations, Figs. 12 and 13, the value of the coordinate z comprises all computational crystals in the interval $[z - 0.025, z + 0.025]$ of 5 cm width.

Figure 12 presents the results obtained with the parameter $\sigma = 0.1$ in the sedimentation model (2.9), which is the same parameter as used in [6]. One can observe

Fig. 11 Development of the average diameter in different heights (m) of the fluidized bed crystallizer, experimental results. Crystals with diameter larger than or equal to $50\,\mu$m were measured. The average diameter is between 234 and $261\,\mu$m at the final time
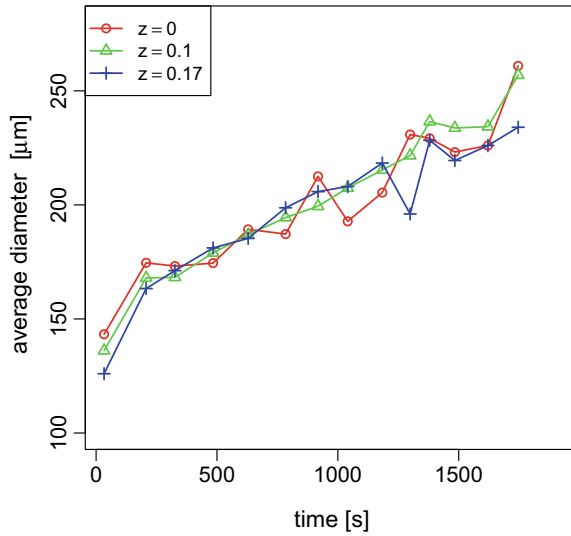
that for all parameters κ of the Brownian kernel (2.12) there is more or less a linear increase of the crystal diameter only at the beginning of the process. In the last part of the time interval, the average diameter is nearly constant. There is a slight increase of the average diameter with an increase of κ. For $\kappa = 5000$, the average diameter at the final time is in the interval $[187, 205]\,\mu$m and for $\kappa = 10,000$, it is in the interval $[196, 215]\,\mu$m. There is a clear separation of the average diameter with respect to the regions of the fluidized bed crystallizer. The largest crystals are close to the inlet and the smallest crystals in the upper region. Comparing the curves of Figs. 10 and 12, one can observe that there are only comparatively small differences of the average diameter at the final time. Hence, there are not many small crystals with diameter lower than $50\,\mu$m left in the fluidized bed crystallizer.

The results for the newly considered segmentation parameter $\sigma = 0.05$ are shown in Fig. 13. For this parameter, there is in a long part of the time interval an almost linear increase of the average diameter. Like for $\sigma = 0.1$, the average diameter increases if the parameter κ of the Brownian kernel increases and there is layering of the crystals with the largest crystals close to the inlet and the smallest crystals in the upper part of the device. The average crystal parameter at the final time is between 211 and $236\,\mu$m for $\kappa = 5000$ and for $\kappa = 10,000$, it is in the interval $[241, 272]\,\mu$m. From comparing Figs. 10 and 13, one can see that the average diameter at the final time is considerably larger if the small crystals with diameter smaller than $50\,\mu$m are neglected. Hence, it seems that there are still many small crystals in the fluidized bed crystallizer.

Altogether, the results show the enormous impact of the choice of the sedimentation parameter σ in model (2.9) on the obtained computational results. The results for $\sigma = 0.05$ are considerably closer to the experimental data, both with respect to the nearly linear increase of the average diameter and with respect to the average

Fig. 12 Development of the average diameter in different heights of the fluidized bed crystallizer, $\sigma = 0.1$ and $\kappa \in \{5000, 6000, 7000, 8000, 9000, 10{,}000\}$, top left to bottom right. Averaging was performed for all crystals with diameter larger than or equal to $50\,\mu\text{m}$
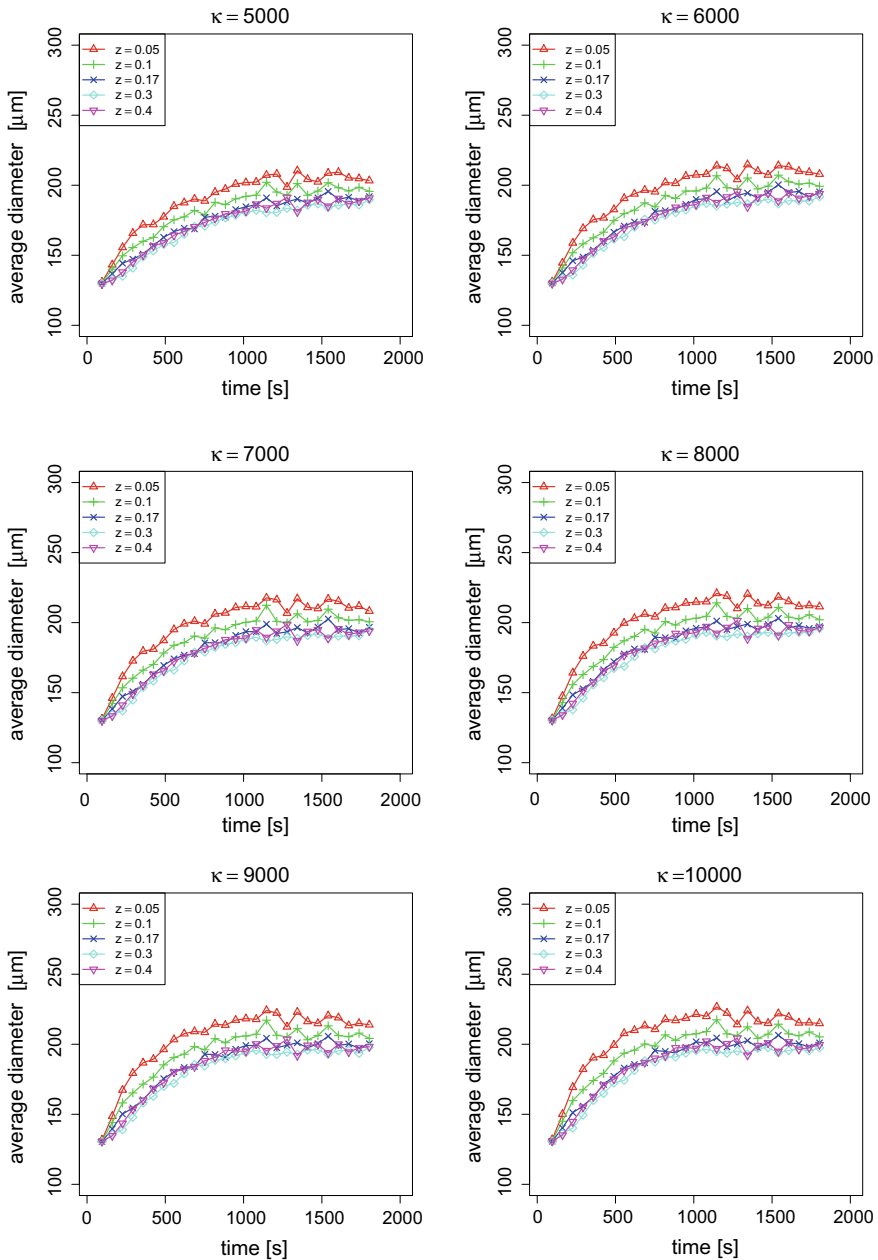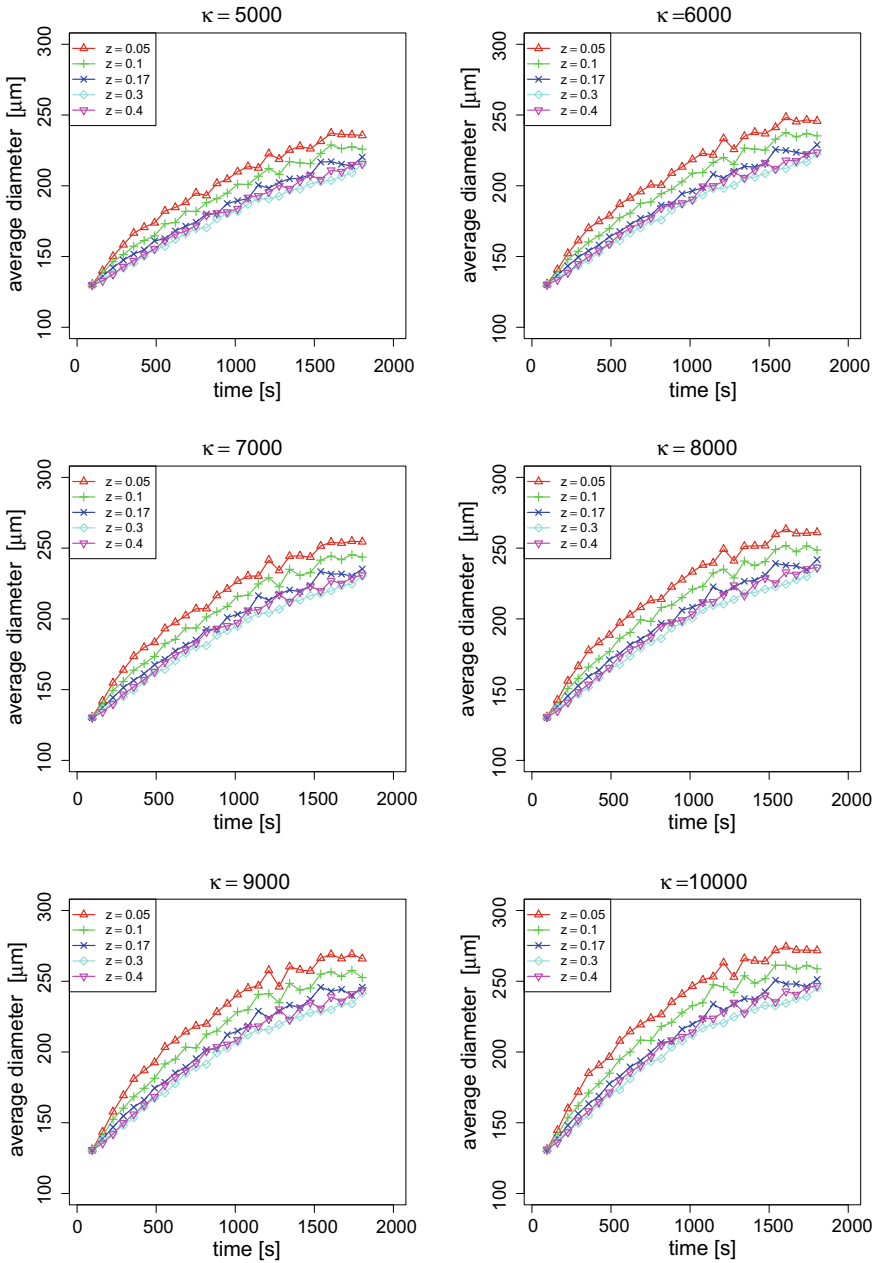
Fig. 13 Development of the average diameter in different heights of the fluidized bed crystallizer, $\sigma = 0.05$ and $\kappa \in \{5000, 6000, 7000, 8000, 9000, 10,000\}$, top left to bottom right. Averaging was performed for all crystals with diameter larger than or equal to $50\,\mu m$

diameter at the final time, than the results for $\sigma = 0.1$. There is a particularly good agreement with respect to the second issue for $\kappa = 8000$, where the average diameter is in the interval $[232, 260]\,\mu$m.

3   Bi- and Multi-variate Processes

The evolution of the crystal population is defined in (1.4) for a d_{int}-dimensional internal property coordinate. The internal coordinates are estimates for the crystal size and shape. In Sect. 2.1, the description of a uni-variate substance was introduced. An example of a bi-variate substance is potassium dihydrogen phosphate. Also for the bi-variate system, the 3d-crystal shape of single crystals can be determined with high accuracy [15]. For agglomerated particles, further descriptors can be selected to describe the size and shape of a particle that is composed of several primary particles. Primary and agglomerated potash alum crystals are depicted in Fig. 7. The descriptors for agglomerates may again be based on a shape estimation, e.g., the projections may be fitted to geometrical polytopes [61]. There is a large number of further shape descriptors, such as the Feret diameter [23], the length of the boundary curve of a projected particle, the projection area, the area of the convex hull of the projection, the diameter, perimeter, and volume of a circle of the same projected area, the widths of the major and minor axes of an ellipse, the convexity [23], the eccentricity [71], the sphericity, and the fractal dimension [65]. Here, the volume of a sphere of equivalent diameter is chosen since the agglomerates in the considered benchmark process are compact. The volume is used to calculate the mass of a crystal. The mass is assumed to be an additive property.

3.1   Agglomeration Kernel Identification from Experiments

In Sect. 2.5, an agglomeration dominated crystallizer was presented. Agglomeration depends on the local distribution of crystals in the fluidized bed crystallizer (FBC), which is determined by the fluid dynamics in the FBC [6]. The particle movement was therefore simulated as described in Sect. 2.5. In the agglomeration term (1.5) of the PBE, the agglomeration kernel κ_{agg} determines the rate of agglomeration. Required agglomeration kernels can be identified from measurement data and numerical simulations by solving inverse problems. An example of such measurement data is shown schematically in Fig. 14.

The agglomeration kernel is usually an unknown functional relation of the volumes of agglomerating particles. Thus, the identification of the kernel is an ill-conditioned problem. To solve the problem, two approaches can be applied. A set of unknown parameters can be identified using measurement data. For this approach, the structure of the kernel has to be known, which can be estimated from modeling the agglomeration process [51] or from known approaches [17]. A second approach

Fig. 14 Exemplary agglomeration kernel for stronger agglomeration of small crystals for the internal size coordinates x and y of two agglomerating particles
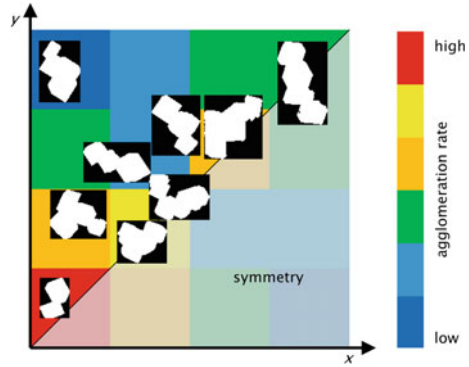
is the solution of inverse problems [19, 69]. This approach is based on the measurement data and the dynamic agglomeration model whereas a priori knowledge on the kernel is not required. Solving the inverse problem, the kernel can be approximated with Laurent polynomials [22]. Like this, the kernel can be described with a small set of parameters and it is separable. An efficient calculation of a separable source term is possible via the fast Fourier transform [16, 30].

3.2 Efficient Evaluation of Agglomeration Terms

This section is concerned with the efficient evaluation of the agglomeration terms (1.5) in the uni-variate case ($d_{\text{int}} = 1$) as well as the extension to multi-variate distributions ($d_{\text{int}} \geq 2$). The foundation for an efficient method for the uni-variate case has been laid in [30] and numerically realized, tested and extended in [16, 21, 56, 57, 62]. In a multi-variate case, the particle properties are denoted by $\mathbf{m} = (m_1, \ldots, m_{d_{\text{int}}}) \in \mathbb{R}_{\geq 0}^{d_{\text{int}}}$ with a maximum value of m_{max}, i.e., $m_j \in [0, m_{\text{max}}]$. In this section, the internal properties are not associated with physical units (e.g. length or mass) but treated as dimensionless quantities. For simplicity of notation, the kernel is assumed to be only dependent on the particle properties $\mathbf{m}$ and $\mathbf{m}'$ but neither on time nor location. Under these assumptions, the agglomeration term is given by

$$
\begin{aligned}
F_{\text{agg}}(f, \mathbf{m}) &= F_{\text{agg}}^+(f, \mathbf{m}) - F_{\text{agg}}^-(f, \mathbf{m}) \\
&= \frac{1}{2} \int_0^{m_1} \cdots \int_0^{m_{d_{\text{int}}}} \kappa_{\text{agg}}(\mathbf{m} - \mathbf{m}', \mathbf{m}') f(\mathbf{m} - \mathbf{m}') f(\mathbf{m}') \, d\mathbf{m}' \\
&\quad - \int_0^{m_{\text{max}}} \cdots \int_0^{m_{\text{max}}} \kappa_{\text{agg}}(\mathbf{m}, \mathbf{m}') f(\mathbf{m}) f(\mathbf{m}') \, d\mathbf{m}',
\end{aligned}
\tag{3.1}
$$

where $F_{\mathrm{agg}}^{+}(f, \mathbf{m})$ denotes the source term and $F_{\mathrm{agg}}^{-}(f, \mathbf{m})$ denotes the sink term of the agglomeration process. This definition of the source term does not account for any particles forming with a property larger than the maximum $m_{\max}$. The sink term, however, allows a particle to disappear, when it agglomerates with another particle to one with property larger than $m_{\max}$. Hence, technically particles may be lost over time if $m_{\max}$ is too small. The choice of $m_{\max}$ should reflect this consideration. The two key ingredients toward the proposed efficient evaluation of these integrals are a discretization of the property space Ω_{int} on a uniform grid and a separable approximation of the agglomeration kernel,

$$\kappa_{\mathrm{agg}}(\mathbf{m}, \mathbf{m}') \approx \sum_{\nu=1}^{M} \alpha^{\nu}(\mathbf{m}) \cdot \beta^{\nu}(\mathbf{m}') \tag{3.2}$$

for a moderate *separation-rank* $M \in \mathbb{N}$ of the kernel κ_{agg}. This allows to simplify the convolution-type integral of $F_{\mathrm{agg}}^{+}(f, \mathbf{m})$ to a sum of M multi-dimensional convolution integrals,

$$
\begin{aligned}
F_{\mathrm{agg}}^{+}(f, \mathbf{m}) &= \frac{1}{2} \int_{0}^{m_1} \cdots \int_{0}^{m_{d_{\mathrm{int}}}} \sum_{\nu=1}^{M} \alpha^{\nu}(\mathbf{m} - \mathbf{m}') \beta^{\nu}(\mathbf{m}') f(\mathbf{m} - \mathbf{m}') f(\mathbf{m}') \, d\mathbf{m}' \\
&= \frac{1}{2} \sum_{\nu=1}^{M} \int_{0}^{m_1} \cdots \int_{0}^{m_{d_{\mathrm{int}}}} \phi^{\nu}(\mathbf{m} - \mathbf{m}') \psi^{\nu}(\mathbf{m}') \, d\mathbf{m}'
\end{aligned}
\tag{3.3}
$$

with $\phi^{\nu}(\mathbf{m}) := \alpha^{\nu}(\mathbf{m}) f(\mathbf{m})$ and $\psi^{\nu}(\mathbf{m}) := \beta^{\nu}(\mathbf{m}) f(\mathbf{m})$.

Analogously, the sink term results in

$$
\begin{aligned}
F_{\mathrm{agg}}^{-}(f, \mathbf{m}) &= \int_{0}^{m_{\max}} \cdots \int_{0}^{m_{\max}} \sum_{\nu=1}^{M} \alpha^{\nu}(\mathbf{m}) f(\mathbf{m}) \beta^{\nu}(\mathbf{m}') f(\mathbf{m}') \, d\mathbf{m}' \\
&= \sum_{\nu=1}^{M} \phi^{\nu}(\mathbf{m}) \cdot \int_{0}^{m_{\max}} \cdots \int_{0}^{m_{\max}} \psi^{\nu}(\mathbf{m}') \, d\mathbf{m}'.
\end{aligned}
\tag{3.4}
$$

In particular, $\mathbf{m}$-dependent terms have been factored out of the integral which reduces the complexity to evaluate $F_{\mathrm{agg}}^{-}(f, \mathbf{m})$.

3.2.1   Discretization of the Property Space

In order to evaluate the integrals in (3.3) and (3.4) numerically, a suitable discretization of the property space Ω_{int} to discretize $f(\mathbf{m})$ is introduced. One first defines a uniform tensor grid $\mathcal{G}$ by choosing the number of degrees of freedom per property,

Fig. 15 A uniform tensor grid with $d_{\text{int}} = 2$ and $n = 4$
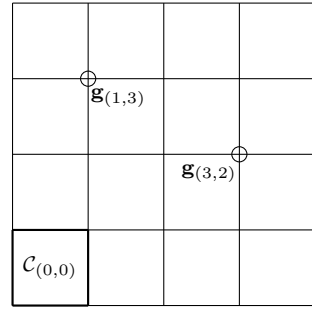
n, and divides the interval $(0, m_{\max})$ into n sub-intervals of width $h := \frac{m_{\max}}{n}$ which is used to define grid points $\mathbf{g_j} = (j_1 h, \ldots, j_{d_{\text{int}}} h)$ and cells

$$\mathcal{C_j} := (j_1 h, j_1 h + h) \times \cdots \times (j_{d_{\text{int}}}, j_{d_{\text{int}}} h + h), \text{ for } \mathbf{j} \in \{0, \ldots, n-1\}^{d_{\text{int}}}.$$

An example of this grid with $d_{\text{int}} = 2$ and $n = 4$ is given in Fig. 15. Each of the $N := n^{d_{\text{int}}}$ cells has volume of $V := h^{d_{\text{int}}}$.

In the following derivations, the density distribution $f(\mathbf{m})$ (and the kernel factors $\alpha^\nu(\mathbf{m})$ and $\beta^\nu(\mathbf{m}')$) are discretized to be piecewise constant with respect to this grid $\mathcal{G}$, i. e.,

$$f(\mathbf{m}) = f(\mathbf{m}') =: f_\mathbf{j} \quad \text{if } \mathbf{m}, \mathbf{m}' \in \mathcal{C_j}, \tag{3.5}$$

hence the function $f(\mathbf{m})$ is approximated by a tensor $f \in \mathbb{R}^{n \times \cdots \times n}$ with N entries $f_\mathbf{j}$.

For piecewise constant integrands, the agglomeration integrals (3.3) and (3.4) can be evaluated exactly at all grid points through evaluation of the nested sums

$$F_{\text{agg}}^+(\mathbf{g_{j+1}}) = \frac{V}{2} \sum_{\nu=1}^M \sum_{k_1=0}^{j_1} \cdots \sum_{k_{d_{\text{int}}}=0}^{j_{d_{\text{int}}}} \phi_{\mathbf{j-k}}^\nu \cdot \psi_\mathbf{k}^\nu =: \frac{V}{2} \sum_{\nu=1}^M Q_{\text{agg}}^{+,\nu}(\mathbf{j}), \tag{3.6}$$

using $Q_{\text{agg}}^{+,\nu} \in \mathbb{R}^{n \times \cdots \times n}$ in (3.6) to denote the unscaled and unshifted result of the discrete convolution. The efficient evaluation of $Q_{\text{agg}}^{+,\nu}$ will be the focus of Sect. 3.2.2 to reduce the complexity of the straightforward evaluation $\mathcal{O}(N^2)$ to a log-linear complexity of $\mathcal{O}(N \log N)$. The resulting F_{agg}^+ is piecewise linear and needs to be projected to a piecewise constant function. This issue is addressed in Sect. 3.2.3.

The sink-term (3.4) within a cell $C_\mathbf{j}$ is computed as

$$F_{\text{agg}}^-(\mathbf{m})|_{\mathcal{C_j}} = V \cdot \sum_{\nu=1}^M \phi_\mathbf{j}^\nu \cdot \sum_{k_1=0}^n \cdots \sum_{k_{d_{\text{int}}}=0}^n \psi_\mathbf{k}^\nu =: V \cdot \sum_{\nu=1}^M \phi_\mathbf{j}^\nu \cdot S_{\text{agg}}^{-,\nu} \tag{3.7}$$

with a scalar $S_{\text{agg}}^{-,\nu}$ as the result of the summation. The computation of (3.7) is of complexity $\mathcal{O}(kN)$ and results in a piecewise constant function (in the form of a tensor with N entries) corresponding to the number of disappearing particles in each cell.

3.2.2 Efficient Evaluation of a Discrete Convolution via Fourier Transform

This section deals with the efficient evaluation of

$$Q_{\text{agg}}^+(\mathbf{j}) = \sum_{k_1=0}^{j_1} \cdots \sum_{k_{d_{\text{int}}}=0}^{j_{d_{\text{int}}}} \phi_{\mathbf{j}-\mathbf{k}} \cdot \psi_{\mathbf{k}}, \tag{3.8}$$

which is required in order to compute the source term $F_{\text{agg}}^+(f, \mathbf{m})$ in (3.6). Since the computation is analogous for all kernel factors, the index ν has been dropped.

It is well known that a discrete convolution (3.8) can be evaluated simultaneously for all $\mathbf{j}$ using the multi-dimensional convolution theorem [50],

$$Q_{\text{agg}}^+ = \mathcal{F}^{-1}(\mathcal{F}(\phi) \odot \mathcal{F}(\psi)), \tag{3.9}$$

where $\mathcal{F}$ and $\mathcal{F}^{-1}$ denote the Fourier transform and its inverse and $\odot$ denotes the elementwise (or Hadamard) product.

The result of a convolution of a tensor of size $n \times \cdots \times n$ is a tensor of size $2n \times \cdots \times 2n$ with an index $\mathbf{j} \in \{0, \ldots, 2n - 1\}^{d_{\text{int}}}$. However, one is only interested in the $n \times \cdots \times n$ subtensor since all other entries go beyond the computational domain (properties larger than m_{max}). In order to calculate the full convolution result via a sequence of uni-variate Fourier transforms, the input tensors ϕ and ψ need to be enlarged to this size by adding zeros. One then obtains tensors $\widetilde{\phi}, \widetilde{\psi} \in \mathbb{R}^{2n \times \cdots \times 2n}$ with entries

$$\widetilde{\phi}_{\mathbf{j}}, \widetilde{\psi}_{\mathbf{j}} = \begin{cases} \phi_{\mathbf{j}}, \psi_{\mathbf{j}} & \text{if } \mathbf{j} \in \{0, \ldots, n-1\}^{d_{\text{int}}}, \\ 0 & \text{else}, \end{cases} \tag{3.10}$$

in a process called *zero-padding*.

The multi-variate Fourier transform (3.9) is defined by

$$\mathcal{F} : \mathbb{R}^{2n \times \cdots \times 2n} \to \mathbb{C}^{2n \times \cdots \times 2n}, \quad \widetilde{\phi} \mapsto \mathcal{F}(\widetilde{\phi}) \quad \text{with} \tag{3.11}$$

$$(\mathcal{F}(\widetilde{\phi}))_{\mathbf{j}} := \sum_{\mathbf{s}=\mathbf{0}}^{2\mathbf{n}-1} \widetilde{\phi}_{\mathbf{s}} \cdot \prod_{q=1}^{d_{\text{int}}} e^{\mathrm{i}\pi s_q j_q / n}.$$

The function $\mathcal{F}$ is rewritten in the form

$$
\begin{aligned}
\mathcal{F}(\widetilde{\phi}) &= \sum_{\mathbf{s}=\mathbf{0}}^{2\mathbf{n}-1} \widetilde{\phi}_{\mathbf{s}} \cdot \prod_{q=1}^{d_{\text{int}}} e^{i\pi s_q j_q/n} \\
&= \sum_{s_{d_{\text{int}}}=0}^{2n-1} \cdots \left(\sum_{s_1=0}^{2n-1} \widetilde{\phi} \cdot e^{i\pi s_1 j_1/n} \right) \cdots e^{i\pi s_{d_{\text{int}}} j_{d_{\text{int}}}/n} \\
&= \mathcal{F}^{d_{\text{int}}} \circ \mathcal{F}^{d_{\text{int}}-1} \circ \cdots \circ \mathcal{F}^1(\widetilde{\phi}),
\end{aligned}
\tag{3.12}
$$

reducing it to a composition of uni-variate Fourier transforms in the qth dimension,

$$
\mathcal{F}^q : \mathbb{C}^{2n\times\cdots\times 2n} \to \mathbb{C}^{2n\times\cdots\times 2n}, \quad \widetilde{\phi} \mapsto \mathcal{F}^q(\widetilde{\phi}) \quad \text{with} \tag{3.13}
$$

$$
(\mathcal{F}(\widetilde{\phi}))_{\mathbf{j}}^q := \sum_{s=0}^{2n-1} \widetilde{\phi}_{j_1,\cdots,j_{m-1},s,j_{m+1},\ldots,j_{d_{\text{int}}}} \cdot e^{i\pi s j_q/n}.
$$

The implication is that the complete Fourier transform of $\widetilde{\phi}$ can be computed via a sequence of one-dimensional Fourier transforms. Every $\mathcal{F}^q$ can be calculated via multiple applications of the FFT-algorithm [20]. This reduces the complexity of each one-dimensional Fourier transform to $\mathcal{O}(n \log n)$ and hence reduces the complexity of $\mathcal{F}$ down to $\mathcal{O}(d_{\text{int}} n^{d_{\text{int}}} \log n) = \mathcal{O}(N \log N)$. The same techniques are employed for the inverse Fourier transform to calculate the complete convolution in $\mathcal{O}(N \log N)$ instead of $\mathcal{O}(N^2)$ without using FFT.

An additional acceleration of the calculation is achieved by exploiting the zero-padding, which is necessary to obtain the full convolution result. When computing $\mathcal{F}^1(\widetilde{\phi})$, one needs to calculate $(2n)^{d_{\text{int}}-1}$ fast Fourier transforms of length $2n$, each one over $d_{\text{int}} - 1$ fixed indices j_2 through $j_{d_{\text{int}}}$ from 0 to $2n - 1$. By taking the zero-pattern of $\widetilde{\phi}$ into account, many one-dimensional Fourier transforms are applied to zero-vectors which can be skipped to save computational time. These superfluous Fourier transforms are characterized by a multi-index $\mathbf{j}$ with at least one $j_q > n$ for $q > 1$. This reduces the number of one-dimensional FFTs during the computation of $\mathcal{F}^1$ from $(2n)^{d_{\text{int}}-1}$ to $n^{d_{\text{int}}-1}$, a factor of $2^{d_{\text{int}}-1}$ compared to the straightforward implementation. The same argument can be used to reduce the number of one-dimensional Fourier transforms in the subsequent calculations of $\mathcal{F}^2$ to $\mathcal{F}^{d_{\text{int}}-1}$ as part of the zero-pattern is preserved. An illustration of this zero-pattern for $d_{\text{int}} = 3$ is shown in Fig. 16. The number of one-dimensional Fourier transforms for the computation of $\mathcal{F}^q$ is reduced to $2^q \cdot n^{d_{\text{int}}-1}$, reducing the total number of one-dimensional Fourier transforms from $d \cdot (2n)^{d_{\text{int}}-1}$ to $(2^{d_{\text{int}}} - 1)n^{d_{\text{int}}-1}$. The total complexity is thereby reduced to $\mathcal{O}(N \log n)$. Further details can be found in [1].
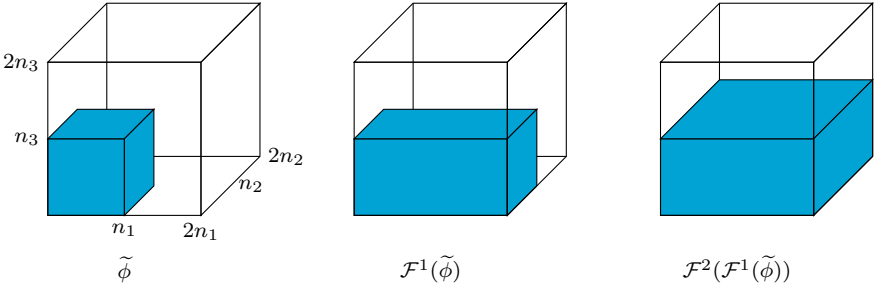
3.2.3 Conservation of Multi-variate Moments

So far, the source term (3.6) has been calculated at the grid-points $\mathbf{g_j}$ that can efficiently be calculated via the procedure outlined in Sect. 3.2.2. The function $F^+_{\text{agg}}(f, \mathbf{m})$ is piecewise linear with respect to all internal variables since it is the result of an integration of a piecewise constant function. The values $F_{\mathbf{j}} = F(\mathbf{g_j})$ of the function at every grid point $\mathbf{g_j}$ are given, $F^+_{\text{agg}}(f, \mathbf{m})$ is represented with the standard basis of piecewise linear "hat" functions

$$\Lambda_{\mathbf{j}}(\mathbf{m}) = \prod_{q=1}^{d_{\text{int}}} T_{j_q}(m_q) \quad \text{with} \tag{3.14}$$

$$T_{j_q}(m_q) = \begin{cases} m_q/h - j_q + 1, & \text{if } (j_q - 1) \cdot h \le m_q \le j_q \cdot h, \\ -m_q/h + j_q + 1, & \text{if } j_q \cdot h \le m_q \le (j_q + 1) \cdot h, \\ 0, & \text{else,} \end{cases} \tag{3.15}$$

with standard hat functions $T_{j_q}(\cdot)$. The function $\Lambda_{\mathbf{j}}(\mathbf{m})$ satisfies $\Lambda_{\mathbf{j}}(\mathbf{g_j}) = 1$ and $\Lambda_{\mathbf{j}}(\mathbf{g_{\widetilde{j}}}) = 0$ if $\widetilde{\mathbf{j}} \ne \mathbf{j}$ which allows to write

$$F^+_{\text{agg}}(f, \mathbf{m}) = \sum_{\mathbf{j}=0}^{\mathbf{n}-1} F_{\mathbf{j}} \cdot \Lambda_{\mathbf{j}}(\mathbf{m}).$$

Since the result is piecewise linear, it does not satisfy (3.5) and requires a projection. It is possible to construct a projection that preserves all square-free moments.

A multi-variate moment $M_{\mathbf{e}}(f)(t)$ (for a vector $\mathbf{e} = (e_1, \ldots, e_{d_{\text{int}}}) \in \mathbb{N}_0^{d_{\text{int}}}$) of a particle density distribution $f(\mathbf{m})$ at time t is defined by

$$M_{\mathbf{e}}(f)(t) := \iint\limits_{\Omega_{\text{int}}} f(\mathbf{m}) \prod_{q=1}^{d_{\text{int}}} m_q^{e_q} \, d\mathbf{m}, \tag{3.16}$$

and a moment $M_{\mathbf{e}}(f)(t)$ with all $e_q < 2$ is called *square-free*, i.e., if $\mathbf{e} \in \{0, 1\}^{d_{\text{int}}}$.

It is a natural choice to distribute all particles associated with a single basis function $\Lambda_{\mathbf{j}}(\mathbf{m})$ onto its $2^{d_{\text{int}}}$ cells of support denoted by $C_{\mathbf{j}+\mathbf{k}}$ with $\mathbf{k} = \{-1, 0\}^{d_{\text{int}}}$ to preserve all $2^{d_{\text{int}}}$ square-free moments. This can be done for each basis function individually since local preservation implies global preservation of moments.

One calculates

$$M_{\mathbf{e}}(\Lambda_{\mathbf{j}}) = \iint\limits_{\Omega_{\text{int}}} \Lambda_{\mathbf{j}}(\mathbf{m}) \prod_{q=1}^{d_{\text{int}}} m_q^{e_q} \, d\mathbf{m}$$

$$= F_{\mathbf{j}} \prod_{q=1}^{d_{\text{int}}} \int_{j_q h - h}^{j_q h + h} m_q^{e_q} T_{j_q}(m_q) \, dm_q = F_{\mathbf{j}} \prod_{q=1}^{d_{\text{int}}} \mathcal{I}_{e_q}^{j_q},$$

with

$$\mathcal{I}_{e_q}^{j_q} := \int_{(j_q-1)h}^{(j_q+1)h} m^{e_q} T_{j_q}(m) \, dm = \begin{cases} h, & \text{if } e_q = 0, \\ h^2 j_q, & \text{if } e_q = 1, \end{cases} \tag{3.17}$$

to simplify notation. A cell $C_{\mathbf{j}+\mathbf{k}}$ with an associated piecewise constant value $w_{\mathbf{j}+\mathbf{k}}$ carries moments determined by

$$M_{\mathbf{e}}(C_{\mathbf{j}}) = \iint\limits_{\Omega_{\text{int}}} w_{\mathbf{j}} \prod_{q=1}^{d_{\text{int}}} m_q^{e_q} \, d\mathbf{m}$$

$$= w_{\mathbf{j}+\mathbf{k}} \prod_{q=1}^{d_{\text{int}}} \int_{(j_q+k_q)h}^{(j_q+k_q+1)h} m_q^{e_q} \, dm_q = w_{\mathbf{j}+\mathbf{k}} \prod_{q=1}^{d_{\text{int}}} \mathcal{J}_{e_q}^{j_q+k_q},$$

with

$$\mathcal{J}_{e_q}^{j_q} := \int_{j_q h}^{(j_q+1)h} m^{e_q} \, dm = \begin{cases} h, & \text{if } e_q = 0, \\ h^2 \cdot (j_q + 0.5), & \text{if } e_q = 1, \end{cases} \tag{3.18}$$

to again simplify the integral.

Moment equality can be preserved by choosing values $w_{\mathbf{j}+\mathbf{k}}$ that satisfy

$$M_{\mathbf{e}}(\Lambda_{\mathbf{j}}) = \sum_{\mathbf{k}=\{-1,0\}^{d_{\text{int}}}} M_{\mathbf{e}}(\mathcal{C}_{\mathbf{j}+\mathbf{k}})$$

$$\Longleftrightarrow \quad F_{\mathbf{j}} \prod_{q=1}^{d_{\text{int}}} \mathcal{I}_{e_q}^{j_q} = \sum_{\mathbf{k}=\{-1,0\}^{d_{\text{int}}}} w_{\mathbf{j}+\mathbf{k}} \prod_{q=1}^{d_{\text{int}}} \mathcal{J}_{e_q}^{j_q+k_q}. \tag{3.19}$$

By using

$$\mathcal{J}_e^{j-1} + \mathcal{J}_e^j = \left\{ \begin{array}{l} 2h, \ \text{if } e = 0, \\ 2h^2 j, \ \text{if } e = 1 \end{array} \right\} = 2\mathcal{I}_e^j,$$

which follows directly from the definitions of (3.17) and (3.18), one pairs the $2^{d_{\text{int}}}$ summands in (3.19) and obtains

$$w_{\mathbf{j}+\mathbf{k}} = \frac{F_{\mathbf{j}}}{2^{d_{\text{int}}}},$$

implying a uniform distribution of particles associated with a single grid-point $\mathbf{g_j}$ to its surrounding $2^{d_{\text{int}}}$ cells.

This result is somewhat surprising as it does neither rely on the size of the grid (the cell-width h) nor the index $\mathbf{j}$ of the cell in question. Further details can also be found in [2].

3.2.4 Multi-variate Moments for the Pure Agglomeration Settings

This section is devoted to the analysis of moments $M_{\mathbf{e}}(f)(t)$ of a multi-variate particle distribution $f(\mathbf{m})$ over time. For this, one obtains expressions to track any multi-variate moment in the absence of breakage and growth and compares those values to numerical moments obtained over the course of a simulation using the discretization presented here.

Let $d_{\text{int}} = 2$ and denote the internal particle properties with $\mathbf{m} = (m_1, m_2)$. The change of a moment $M_{\mathbf{e}}(f)$ of a two-dimensional distribution $f(\mathbf{m})$ over time is given by

$$\frac{dM_{\mathbf{e}}(f)(t)}{dt} = \iint_{\Omega_{\text{int}}} m_1^{e_1} m_2^{e_2} F_{\text{agg}}(f, \mathbf{m}) \, d\mathbf{m}$$

$$= \frac{1}{2} \iint_{\Omega_{\text{int}}} m_1^{e_1} m_2^{e_2} \int_0^{m_1} \int_0^{m_2} \kappa_{\text{agg}}(\mathbf{m} - \mathbf{m}', \mathbf{m}') f(\mathbf{m} - \mathbf{m}') f(\mathbf{m}') \, d\mathbf{m}' \, d\mathbf{m}$$

$$- \iint_{\Omega_{\text{int}}} m_1^{e_1} m_2^{e_2} \iint_{\Omega_{\text{int}}} \kappa_{\text{agg}}(\mathbf{m}, \mathbf{m}') f(\mathbf{m}) f(\mathbf{m}') \, d\mathbf{m}' \, d\mathbf{m}.$$

Setting $\kappa_{agg}(\mathbf{m}, \mathbf{m}') = 1$ eliminates the kernel from the equation. The domain of integration of the inner integral in the source term can be expanded to $[0, m_{max}]^2$ by setting $f(\mathbf{m} - \mathbf{m}') := 0$ if any component of $\mathbf{m} - \mathbf{m}'$ is negative. A further change in the integration variable gives

$$\frac{dM_{\mathbf{e}}(f)(t)}{dt} = \frac{1}{2} \iint\limits_{\Omega_{int}} \iint\limits_{\Omega_{int}} f(\mathbf{m}) f(\mathbf{m}') \cdot (m_1 + m_1')^{e_1} \cdot (m_2 + m_2')^{e_2} \, d\mathbf{m}' \, d\mathbf{m}$$
$$- \iint\limits_{\Omega_{int}} \iint\limits_{\Omega_{int}} m_1^{e_1} m_2^{e_2} f(\mathbf{m}) f(\mathbf{m}') \, d\mathbf{m}' \, d\mathbf{m}.$$

The binomials in the first line are expanded in order to separate the integrations with respect to $\mathbf{m}$ and $\mathbf{m}'$ and then the order of summations and integrations is changed. A similar separation in the second line leads to

$$\frac{dM_{\mathbf{e}}(f)(t)}{dt}$$
$$= \frac{1}{2} \sum_{k_1=0}^{e_1} \sum_{k_2=0}^{e_2} \binom{e_1}{k_1} \binom{e_2}{k_2} \iint\limits_{\Omega_{int}} \mathbf{m}^{\mathbf{k}} f(\mathbf{m}) \, d\mathbf{m} \cdot \iint\limits_{\Omega_{int}} (\mathbf{m}')^{\mathbf{e}-\mathbf{k}} f(\mathbf{m}') \, d\mathbf{m}'$$
$$- \iint\limits_{\Omega_{int}} m_1^{e_1} m_2^{e_2} f(\mathbf{m}) \, d\mathbf{m} \cdot \iint\limits_{\Omega_{int}} f(\mathbf{m}') \, d\mathbf{m}'.$$

Every integral is in the form of (3.16) and is replaced accordingly. The rate of change of one moment then reads

$$\frac{dM_{\mathbf{e}}(f)(t)}{dt} = \frac{1}{2} \sum_{k_1=0}^{e_1} \sum_{k_2=0}^{e_2} \binom{e_1}{k_1} \binom{e_2}{k_2} \cdot M_{(k_1,k_2)}(f)(t) \cdot M_{(e_1-k_1,e_2-k_2)}(f)(t)$$
$$- M_{\mathbf{e}}(f)(t) \cdot M_{(0,0)}(f)(t), \tag{3.20}$$

which is an ordinary differential equation in the moments, independent of the detailed particle distribution $f(\mathbf{m})$. With this, one can calculate the evolution of all moments given the moments of an initial distribution.

By using the moments of a discrete distribution $f(\mathbf{m})$ (as opposed to a continuous distribution) as initial values for (3.20), the only error present is due to the projection presented in Sect. 3.2.3.

For the numerical simulation with $d_{int} = 2$, the initial distribution is discretized by

$$f(\mathbf{m}, 0) = N_0 e^{-200(m_1-0.1)^2} \cdot e^{-200(m_2-0.1)^2} \tag{3.21}$$
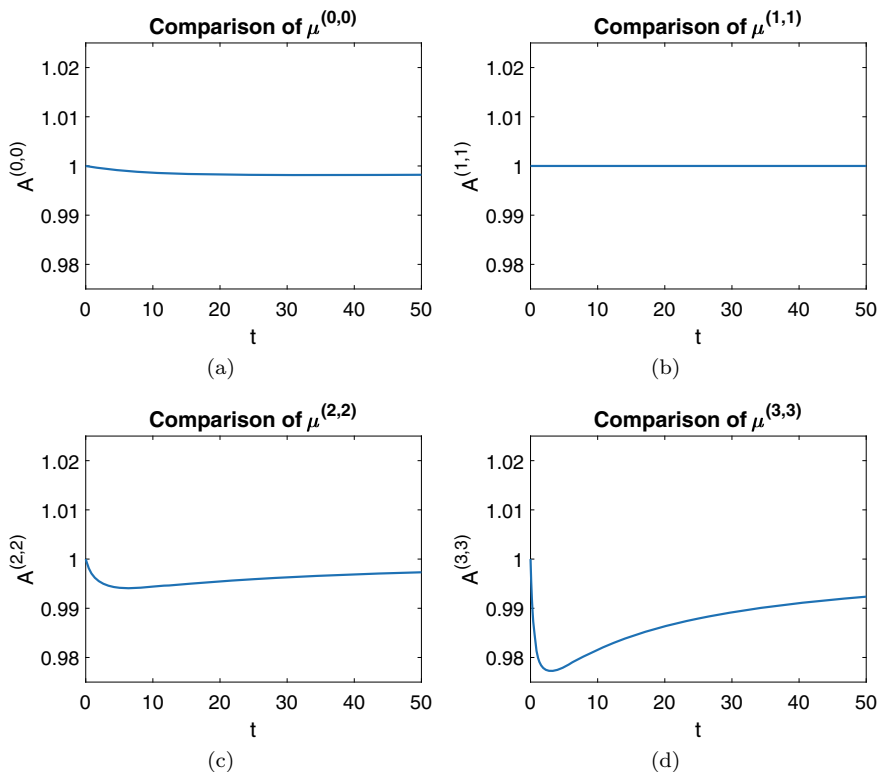
Fig. 17 $A^{\mathbf{e}}$ (3.22) over the course of a simulation for moments $M^{\mathbf{e}}$ with $\mathbf{e} = (0, 0)$ (top left), $\mathbf{e} = (1, 1)$ (top right), $\mathbf{e} = (2, 2)$ (bottom left) and $\mathbf{e} = (3, 3)$ (bottom right)

with $n = 512$ for both internal coordinates with $m_{\max} = 10$. This results in $N = 512^2$ degrees of freedom and a width of $h = \frac{10}{512}$. The constant N_0 will be chosen such that $M_{(0,0)}(f) = 0.1$ at $t = 0$.

Numerical simulation up to $t = 50$ will result in $M_{(0,0)}(f)(50) = 0.0286$ at the end. In order to keep track of the numerical moments $\widetilde{M}^{\mathbf{e}}(f)(t)$ in the simulation, the ratio between numerical and theoretical moments,

$$A^{\mathbf{e}} = \widetilde{M}^{\mathbf{e}}(f)/M_{\mathbf{e}}(f), \tag{3.22}$$

is computed.

The ratio $A^{(0,0)}$ is shown in the top left of Fig. 17 which displays a small loss of 0.18% (minimal ratio is $A^{(0,0)}(50) = 0.9982$) over time that is most likely caused by coarse time steps. There is no loss in the first cross moment as one finds $M_{(1,1)}(f) = 1$ for all t (shown in the top right of Fig. 17). A smaller ratio occurs for higher order moments that are not square-free. It is not expected that $A^{\mathbf{e}}(t) = 1$ for all t since the moments are not preserved analytically. The ratio $A^{(2,2)}$ is shown in the bottom left of

Fig. 17 and indicates an under-prediction over the entire time period, similar to $A^{(3,3)}$ in the bottom right. The error does not exceed 0.6% and 2.3%, respectively. Even though there is an error in the prediction of higher order moments, they are predicted with a very good accuracy given the grid with $N = 512^2$ degrees of freedom.

4 Summary and Outlook

The model experiment in the HCT crystallizer led to interesting and new results concerning the particle fluid interaction. Crystal size distributions change from the inlet to the outlet, already without growth, as crystals of varying size have a different residence time in the HCT. This newly found effect can be used to change the width of the CSD; or can be used under growth conditions to keep the typically observed broadening of the CSD very low. Some first insights on the shape dependence of this effect are encouraging to investigate this topic in more detail in our future work.

For the numerical simulation of PBSs, a deterministic-stochastic algorithm was developed that enables the simulation of PBSs in rather complex spatial domains. Here, it was utilized for the simulation of a crystallization process in a fluidized bed crystallizer. To this end, two codes, one with deterministic finite element methods for the CFD equations and one with stochastic methods for the crystals, were coupled. Furthermore, the stochastic code was extended by all features that are due to the transport of the crystals in the three-dimensional domain.

Future work concerning the numerical simulations comprises algorithmic and modeling issues. From the algorithmic point of view, the code with the SPS methods should be MPI parallelized (the finite element CFD code is already) such that simulations of PBSs can be performed on clusters of computers to enhance the efficiency. From the point of view of the model, different agglomeration kernels and sedimentation models should be implemented and the breakage of crystals should be included. In addition, the SPS method should be extended to multi-variate crystals. This method provides a natural framework for the simulation of crystals that are modeled in a more complex way than with one internal coordinate.

The computational bottleneck of the expensive computation of agglomeration terms has been overcome by the exploitation of fast Fourier transformation (FFT) for the evaluation of convolution sums and tensor trains (TT) for the representation and arithmetic of multi-variate density distributions. In a sense, numerical simulations have become feasible for a much higher resolution than experimental results are available. Future work might include the identification of models that include multi-variate agglomeration, e.g., the determination of physically relevant agglomeration kernels. Another point of interest would be the extension of tensor trains to the entire population balance model, for example their adaptation to the breakage term. Future work could also focus on a parallelization of the introduced algorithms.

The agglomeration phenomenon in the fluidized bed crystallizer clearly shows the potential of such a device for a selective product removal, which is an important aspect for the post-processing of solids under industrial settings. As agglomeration

can be modeled appropriately only with very specific parameters and kernels sets, the developed opportunity of big data acquisition within such a model experiment can be of great interest to the community of crystallization process engineers. In combination with the presented fast simulation methods for agglomeration and the corresponding fluid flow calculations, one may even start to optimize flow geometries in order to control the agglomeration in such crystallizers in the future.

References

1. Ahrens, R., Le Borne, S.: FFT-based evaluation of multivariate aggregation integrals in population balance equations on uniform tensor grids. J. Comput. Appl. Math. **338**, 280–297 (2018)
2. Ahrens, R., Le Borne, S.: Tensor trains and moment conservation for multivariate aggregation in population balance modeling. Appl. Numer. Math. **153**, 473–491 (2020)
3. Anker, F., Ganesan, S., John, V., Schmeyer, E.: A comparative study of a direct discretization and an operator-splitting solver for population balance systems. Comput. Chem. Eng. **75**, 95–104 (2015)
4. Bartsch, C.: A coupled stochastic-deterministic method for the numerical solution of population balance systems. Ph.D. Thesis, Freie Universität Berlin, Department of Mathematics and Computer Science (2018)
5. Bartsch, C., John, V., Patterson, R.I.A.: Simulations of an ASA flow crystallizer with a coupled stochastic-deterministic approach. Comput. Chem. Eng. **124**, 350–363 (2019)
6. Bartsch, C., Wiedmeyer, V., Lakdawala, Z., Patterson, R.I.A., Voigt, A., Sundmacher, K., John, V.: Stochastic-deterministic population balance modeling and simulation of a fluidized bed crystallizer experiment. Chem. Eng. Sci. **208**, 115102 (2019)
7. Berg, H.C.: Random Walks in Biology. Princeton University Press, Princeton, NJ (1983)
8. Bird, G.A.: Direct simulation and the Boltzmann equation. Phys. Fluids **13**(11), 2676–2681 (1970)
9. Borchert, C., Sundmacher, K.: Efficient formulation of crystal shape evolution equations. Chem. Eng. Sci. **84**, 85–99 (2012)
10. Borchert, C., Sundmacher, K.: Morphology evolution of crystal populations: modeling and observation analysis. Chem. Eng. Sci. **70**, 87–98 (2012)
11. Borchert, C., Temmel, E., Eisenschmidt, H., Lorenz, H., Seidel-Morgenstern, A., Sundmacher, K.: Image-based in situ identification of face specific crystal growth rates from crystal populations. Cryst. Growth Des. **14**(3), 952–971 (2014)
12. Bordás, R., John, V., Schmeyer, E., Thévenin, D.: Measurement and simulation of a droplet population in a turbulent flow field. Comput. Fluids **66**, 52–62 (2012)
13. Bordás, R., John, V., Schmeyer, E., Thévenin, D.: Numerical methods for the simulation of a coalescence-driven droplet size distribution. Theoret. Comput. Fluid Dyn. **27**(3–4), 253–271 (2013)
14. Boris, J.P., Book, D.L.: Flux-corrected transport. I: SHASTA, a fluid transport algorithm that works. J. Comput. Phys. **11**, 38–69 (1973)
15. Le Borne, S., Eisenschmidt, H., Sundmacher, K.: Image-based analytical crystal shape computation exemplified for potassium dihydrogen phosphate (KDP). Chem. Eng. Sci. **139**, 61–74 (2016)
16. Le Borne, S., Shahmuradyan, L., Sundmacher, K.: Fast evaluation of univariate aggregation integrals on equidistant grids. Comput. Chem. Eng. **74**, 115–127 (2015)

17. Bramley, A.S., Hounslow, M.J., Ryall, R.L.: Aggregation during precipitation from solution: a method for extracting rates from experimental data. J. Colloid Interf. Sci. **183**(1), 155–165 (1996)

18. Buffo, A., Vanni, M., Marchisio, D.L., Fox, R.O.: Multivariate quadrature-based moments methods for turbulent polydisperse gas-liquid systems. Int. J. Multiphase Flow **50**, 41–57 (2013)

19. Chakraborty, J., Kumar, J., Singh, M., Mahoney, A., Ramkrishna, D.: Inverse problems in population balances. Determination of aggregation kernel by weighted residuals. Ind. Eng. Chem. Res. **54**(42), 10530–10538 (2015)

20. Cooley, J.W., Tukey, J.W.: An algorithm for the machine calculation of complex Fourier series. Math. Comput. **19**(90), 297–297 (1965)

21. Dosta, M., Hartge, E.-U., Ahrens, R., Heinrich, S., Le Borne, S.: Investigation of an FFT-based solver applied to dynamic flowsheet simulation of agglomeration processes. Adv. Powder Technol. **30**, 555–564 (2019)

22. Eisenschmidt, H., Soumaya, M., Bajcinca, N., Le Borne, S., Sundmacher, K.: Estimation of aggregation kernels based on Laurent polynomial approximation. Comput. Chem. Eng. **103**, 210–217 (2017)

23. Ferreira, T., Rasband, Wayne: ImageJ User GuideIJ **1**, 46r (2012)

24. Ganesan, S., John, V., Matthies, G., Meesala, R., Abdus, S., Wilbrandt, U.: An object oriented parallel finite element scheme for computing PDEs: design and implementation. In: IEEE 23rd International Conference on High Performance Computing Workshops (HiPCW) Hyderabad, pp. 106–115. IEEE (2016)

25. Ganesan, S.: An operator-splitting Galerkin/SUPG finite element method for population balance equations: stability and convergence. ESAIM Math. Model. Numer. Anal. **46**(6), 1447–1465 (2012)

26. Ganesan, S., Tobiska, L.: An operator-splitting finite element method for the efficient parallel solution of multidimensional population balance systems. Chem. Eng. Sci. **69**(1), 59–68 (2012)

27. Ganesan, S., Tobiska, L.: Operator-splitting finite element algorithms for computations of high-dimensional parabolic problems. Appl. Math. Comput. **219**(11), 6182–6196 (2013)

28. Gillespie, D.T.: The stochastic coalescence model for cloud droplet growth. J. Atmos. Sci. **29**(8), 1496–1510 (1972)

29. Gillespie, D.T.: An exact method for numerically simulating the stochastic coalescence process in a cloud. J. Atmos. Sci. **32**(10), 1977–1989 (1975)

30. Hackbusch, W.: On the efficient evaluation of coalescence integrals in population balance models. Computing **78**(2), 145–159 (2006)

31. Hackbusch, W., John, V., Khachatryan, A., Suciu, C.: A numerical method for the simulation of an aggregation-driven population balance system. Int. J. Numer. Methods Fluids **69**(10), 1646–1660 (2012)

32. Harten, A., Engquist, B., Osher, S., Chakravarthy, Sukumar R.: Uniformly high-order accurate essentially nonoscillatory schemes. III. J. Comput. Phys. **71**(2), 231–303 (1987)

33. Hulburt, H.M., Katz, S.: Some problems in particle technology: a statistical mechanical formulation. Chem. Eng. Sci. **19**(8), 555–574 (1964)

34. John, V., Angelov, I., Öncül, A.A., Thévenin, D.: Techniques for the reconstruction of a distribution from a finite number of its moments. Chem. Eng. Sci. **62**(11), 2890–2904 (2007)

35. John, V.: Finite element methods for incompressible flow problems. In: Springer Series in Computational Mathematics, vol. 51. Springer, Cham (2016)

36. John, V., Mitkova, T., Roland, M., Sundmacher, K., Tobiska, L., Voigt, A.: Simulations of population balance systems with one internal coordinate using finite element methods. Chem. Eng. Sci. **64**(4), 733–741 (2009)

37. John, V., Novo, Julia: On (essentially) non-oscillatory discretizations of evolutionary convection-diffusion equations. J. Comput. Phys. **231**(4), 1570–1586 (2012)

38. John, V., Roland, M.: On the impact of the scheme for solving the higher dimensional equation in coupled population balance systems. Int. J. Numer. Methods Engrg. **82**(11), 1450–1474 (2010)

39. John, V., Schmeyer, E.: Finite element methods for time-dependent convection-diffusion-reaction equations with small diffusion. Comput. Methods Appl. Mech. Engrg. **198**(3–4), 475–494 (2008)
40. John, V., Suciu, C.: Direct discretizations of bi-variate population balance systems with finite difference schemes of different order. Chem. Eng. Sci. **106**, 39–52 (2014)
41. John, V., Thein, F.: On the efficiency and robustness of the core routine of the quadrature method of moments (QMOM). Chem. Eng. Sci. **75**, 327–333 (2012)
42. Kuzmin, D.: Explicit and implicit FEM-FCT algorithms with flux linearization. J. Comput. Phys. **228**(7), 2517–2534 (2009)
43. Kuzmin, D., Möller, M.: Algebraic flux correction. I. Scalar conservation laws. In: Flux-corrected transport, Sci. Comput., pp. 155–206. Springer, Berlin (2005)
44. Lewis, A., Seckler, M., Kramer, H., van Rosmalen, G.: Fundamentals and Applications. Cambridge University Press, Industrial Crystallization (2015)
45. Liu, X.-D., Osher, S., Chan, T.: Weighted essentially non-oscillatory schemes. J. Comput. Phys. **115**(1), 200–212 (1994)
46. Löhner, R., Morgan, K., Peraire, J., Vahdati, M.: Finite element flux-corrected transport (FEM-FCT) for the Euler and Navier-Stokes equations. Int. J. Numer. Methods Fluids **7**, 1093–1109 (1987)
47. Marchisio, D.L., Fox, R.O.: Solution of population balance equations using the direct quadrature method of moments. J. Aerosol Sci. **36**(1), 43–73 (2005)
48. Marchisio, D.L., Dennis Vigil, R., Fox, R.O.: Quadrature method of moments for aggregation-breakage processes. J. Colloid Interf. Sci. **258**(2), 322–334 (2003)
49. McGraw, R.: Description of aerosol dynamics by the quadrature method of moments. Aerosol Sci. Technol. **27**(2), 255–265 (1997)
50. Nussbaumer, H.J.: Fast Fourier Transform and Convolution Algorithms. Springer, Berlin (1982)
51. Ochsenbein, D.R., Vetter, T., Morari, M., Mazzotti, M.: Agglomeration of needle-like crystals in suspension. II. Modeling. Crystal Growth Des. **15**(9), 4296–4310 (2015)
52. Patterson, R.I.A., Wagner, W.: A stochastic weighted particle method for coagulation-advection problems. SIAM J. Sci. Comput. **34**(3), B290–B311 (2012)
53. Patterson, R.I.A., Wagner, W., Kraft, M.: Stochastic weighted particle methods for population balance equations. J. Comput. Phys. **230**(19), 7456–7472 (2011)
54. Pope, S.B.: Turbulent Flows. Cambridge University Press, Cambridge (2000)
55. Roos, H.-G., Stynes, M., Tobiska, L.: Robust numerical methods for singularly perturbed differential equations, volume 24 of Springer Series in Computational Mathematics. Convection-Diffusion-Reaction and Flow Problems, 2nd edn. Springer, Berlin (2008)
56. Shahmuradyan, L., Le Borne, S.: Algorithms for the Haar wavelet based fast evaluation of aggregation integrals in population balance equations. Appl. Numer. Math. **108**, 1–20 (2016)
57. Shahmuradyan, L., Le Borne, S.: Fast algorithms for hp-discretized univariate population balance aggregation integrals. Comput. Chem. Eng. **97**, 1–12 (2017)
58. Sagaut, P.: Large eddy simulation for incompressible flows. In: Scientific Computation, 3rd edn. Springer, Berlin. An introduction, Translated from the 1998 French original. With forewords by Lesieur, M., Germano, M. With a foreword by Meneveau, C. (2006)
59. Scharfetter, D.L., Gummel, H.K.: Large signal analysis of a silicon read diode. IEEE Trans. Elec. Dev. **16**, 64–77 (1969)
60. Schmeyer, E., Bordás, R., Thévenin, D., John, V.: Numerical simulations and measurements of a droplet size distribution in a turbulent vortex street. Meteorologische Zeitschrift **23**(4), 387–396 (2014)
61. Schorsch, S., Hours, J.-H., Vetter, T., Mazzotti, M., Jones, C.N.: An optimization-based approach to extract faceted crystal shapes from stereoscopic images. Comput. Chem. Eng. **75**, 171–183 (2015)
62. Shahmuradyan, L.: Efficient and accurate evaluation of aggregation integrals in population balance equations. Ph.D. Thesis, Hamburg University of Technology, Institute of Mathematics (2016)

63. Si, H.: TetGen, a Delaunay-based quality tetrahedral mesh generator. ACM Trans. Math. Softw. **41**(2), Art. 11, 36 (2015)

64. Temmel, E., Eisenschmidt, H., Lorenz, H., Sundmacher, K., Seidel-Morgenstern, A.: A short-cut method for the quantification of crystallization kinetics. 1. Method development. Cryst. Growth Des. **16**(12), 6743–6755 (2016)

65. Terdenge, L.M., Heisel, S., Schembecker, G., Wohlgemuth, K.: Agglomeration degree distribution as quality criterion to evaluate crystalline products. Chem. Eng. Sci. **133**, 157–169 (2015)

66. Wiedmeyer, V., Anker, F., Bartsch, C., Voigt, A., John, V., Sundmacher, K.: Continuous crystallization in a helically coiled flow tube: analysis of flow field, residence time behavior, and crystal growth. Ind. Eng. Chem. Res. **56**(13), 3699–3712 (2017)

67. Wiedmeyer, V., Voigt, A., Sundmacher, K.: Crystal population growth in a continuous helically coiled flow tube crystallizer. Chem. Eng. Technol. **40**(9), 1584–1590 (2017)

68. Wilbrandt, U., Bartsch, C., Ahmed, N., Alia, N., Anker, F., Blank, L., Caiazzo, A., Ganesan, S., Giere, S., Matthies, G., Meesala, R., Shamim, A., Venkatesan, J., John, V.: ParMooN—a modernized program package based on mapped finite elements. Comput. Math. Appl. **74**(1), 74–88 (2017)

69. Wright, H.A., Ramkrishna, D.: Solutions of inverse problems in population balances—I. Aggregation kinetics. Comput. Chem. Eng. **16**(12), 1019–1038 (1992)

70. Zalesak, Steven T.: Fully multidimensional flux-corrected transport algorithms for fluids. J. Comput. Phys. **31**(3), 335–362 (1979)

71. Zeidler, Eberhard: Springer-Handbuch der Mathematik I. Springer Spektrum, Wiesbaden (2013)

Chapter 15
Compartmental Population Balances by Means of Monte Carlo Methods

Gregor Kotalczyk and Frank Einar Kruis

Abstract Stochastic simulation techniques for the solution of a network of population balance equations (PBE) are discussed in this chapter. The application of weighted Monte Carlo (MC) particles for the solution of compartmental PBE systems is summarized and its computational efficacy in form of a parallel GPU implementation is pointed out. Solution strategies for coagulation, nucleation, breakage, growth and evaporation are thereby presented. An application example treats the simultaneous coagulation, nucleation, evaporation and growth encountered during particle production through the aerosol route. Furthermore, the simulation of a compartmental network is discussed and parallel simulation techniques for the transport of weighted MC particles are presented. The proposed methodology is benchmarked by comparison with a pivot method for a variety of test cases with an increasing degree of complexity. Simulation conditions are identified, for which conventional, non-weighted MC simulation techniques are not applicable. It is found, that the specific combination of a screen unit with tear-streams cannot be simulated by conventional methods, termed 'random removal', and make thus other techniques—like the here introduced merging techniques necessary.

Nomenclature

b	Breakage rate [s^{-1}]
d_g	Geometric mean diameter [m]
C_{dist}	Compare distance on GPU memory (integer) [–]
d^*	Kelvin diameter [m]
d	Diameter of particle [m]
$E_{i,j}$	Merging error of particles i and j [–]

G. Kotalczyk · F. E. Kruis (✉)
Institute of Technology for Nanostructures (NST),
University of Duisburg-Essen, Duisburg, Germany
e-mail: einar.kruis@uni-due.de

G. Kotalczyk
e-mail: gregor.kotalczyk@uni-due.de

$f_{A \to B}$	Relative particle exchange flow rate from compartment A to B [s^{-1}]
$F_{A \to B}$	Absolute particle exchange flow rate from compartment A to B [s^{-1}]
G	Growth rate [$m\ s^{-1}$]
k_B	Boltzmann constant [$J\ K^{-1}$]
m_1	Atomic (resp, molecule) mass [kg]
N_{MC}	Number of MC simulation particles [–]
N_G	Concentration of gas atoms (or molecules) [m^{-3}]
$n_C(v)$	PSD in compartment C [m^{-6}]
o_{idx}	Destination index on GPU memory (integer) [–]
i^*	Number of atoms (resp. molecules) in critical cluster [–]
$p_A^{(i)}$	i-th property of particle A [unit of i-th property]
p_s	Saturation pressure [Pa]
$Q_{A \to B}$	Volumetric flow rate of carrier gas/liquid from compartment A to B [$m^3\ s^{-1}$]
R	Mixing ratio for breakage scheme [–]
R_N	Nucleation rate [$m^{-3}\ s^{-1}$]
S	Supersaturation [–]
S_{sep}	Separation function for screen [–]
s_f	Reciprocal of stochastic resolution [m^{-3}]
T	Temperature [K]
t	(simulation) time [s]
t_{char}	Characteristic time [s]
v	Particle volume [m^3]
v^*	Kelvin volume [m^3]
v_M	Atomic (resp. molecular) volume [m^3]
V_C	Volume within compartment C filled with carrier liquid (or gas) [m^3]
W_i	Statistical weight of MC particle i [m^{-3}]
α_i	Merging weight for property i
β	Coagulation kernel [$m^3\ s^{-1}$]
γ	Breakage function [–]
ε	Maximal admittable merging error [–]
τ	Time step [s]
σ	Surface tension [$N\ m^{-2}$]

Indices

0	Initial values

1 Introduction

The solution of the population balance equation (PBE) [1] plays an important role in a wide area of applications ranging from natural sciences to many fields of engineering [2]. Especially the modelling of chemical engineering problems such as crystallization [3], milling [4], granulation [5] or particle production in aerosol reactors [6] resort to PBE based process modelling.

The modelling of single apparatuses can be seldomly done with the assumption of spatial uniformity (as in e.g. [7]) and the application of Computational Fluid Dynamics (CFD) simulations and/or compartmental modelling becomes necessary in order to describe different zones of single apparatuses correctly.

CFD modelling allows a very high spatial resolution of the investigated system: 30,000 [8]−1,000,000 [9] cells are sometimes applied. The drawback of a CFD-PBE modelling is its enormous computational cost, hence a PBE has to be solved for each of these cells. Due to the high computational cost, only a rough approximation of the particle size distribution (PSD) is encountered in such simulations which typically resort to sectional methods with a low resolution (of ca. 12–30 discrete points or sections [10, 11]) or to the method of moments [12, 13], limiting the particle modelling mostly to one property—the size.

To overcome this problem, compartmental modelling is often applied, simplifying the spatial complexity to a low number of compartments (examples are 3 compartments or 10 compartments [14]). This allows, on the other hand, a more complex particle modelling with a more detailed sectional grid (e.g. 1000 discrete sections for 3 compartments [15]) or even with a Monte Carlo (MC) simulation, where more than one particle property allow to model a more complex morphology of the particles [14].

The PBE for a network of compartments, like presented in Fig. 1. can be described by the following formula:

$$
\begin{aligned}
\frac{\mathrm{d}n_C(v,t)}{\mathrm{d}t} = &+ \underbrace{\frac{1}{2}\int_0^v \beta_C(v', v-v')n_C(v', t)n_C(v-v', t)\mathrm{d}v'}_{\text{coagulation birth term}} \\
&- \underbrace{n_C(v,t)\int_0^\infty \beta_C(v, v')n_C(v', t)\mathrm{d}v'}_{\text{coagulation death term}} \\
&+ \underbrace{R_{\mathrm{N},C}(t)\cdot\delta(v-v_C^*(t))}_{\text{nucleation}} \underbrace{-\nabla_v(G_C(v,t)n_C(v,t))}_{\text{growth}(G>0)/\text{evaporation}(G<0)} \\
&\underbrace{-b_C(v)\cdot n_C(v,t)}_{\text{breakage death term}} + \underbrace{\int_v^\infty b_C(v')\cdot n_C(v', t)\cdot\gamma_C(v|v')\mathrm{d}v}_{\text{breakage birth term}} \\
&+ \underbrace{\sum}_{\text{inflow from all compartments } i} f_{i\to C}\cdot n_i(v,t) \\
&- \underbrace{\sum}_{\text{outflow to all compartments } i} f_{C\to i}\cdot n_C(v,t)
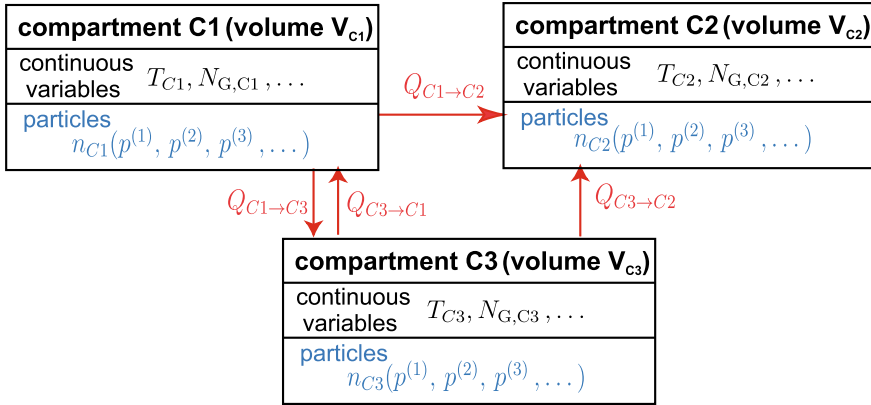\end{aligned}
\tag{1}
$$

Fig. 1 A network of compartments. Each compartment C_i models parts of a reactor (or equipment) volume, which is filled with the carrier gas (or liquid) with a volume V_C. The compartment contains a PSD, n_C, and is described by other continuous variables, like temperature T_C, a gas concentration $N_{G,C}$, etc

where the coagulation kernels β_C, growth rates G_C, nucleation rates $R_{N,C}$ and sizes of the nucleating particles v_C^*, breakage rates $b_C(v)$ and breakage functions $\gamma_C(v|v')$ can be defined differently for each compartment C. The shown particle exchange flowrates $f_{i \to C}$ and $f_{C \to i}$ may assume constant values, or reflect more complex—nonlinear—and particle size or time dependent forms. The given volumetric flow rates $Q_{A \to B}$ (shown in Fig. 1) of the carrier gas (or liquid) and the volumes of the carrier gas (or liquid) of the outflow compartments, V_A, are thereby used in order to determine the particle exchange flowrates via:

$$f_{A \to B} = Q_{A \to B}/V_A \tag{2}$$

In this way, a complex reactor structure can be modelled in more detail [16, 17] or the interconnection of single processing units in a flowsheet simulation can be analyzed [15, 18, 19].

Although Eq. (1) describes only one particle property, the volume v, one could interpret v as a vector describing multiple properties of the particle, such as volume ($p^{(1)}$), surface area ($p^{(2)}$), wet content ($p^{(3)}$), and so on, as suggested in Fig. 1. Only a stochastic modelling is able to solve Eq. (1) for a high number of properties and render the complete particle morphology.

In the following, stochastic solution strategies for Eq. (1) will be discussed in the frame-work of an operator splitting approach meaning that the single processes coagulation, nucleation, growth/evaporation, breakage and transport of particles are decoupled for short periods of time τ. The approximation error introduced by this decoupling can be minimized by a choice of a low enough separation time step τ. For this reason, the solution strategies for single processes, like coagulation, nucleation, growth/evaporation and breakage are discussed for one compartment first. The

implementation of the coagulation in the framework of a compartmental network, as well as the transport between single compartments is discussed in the section afterwards, where the modelling of multiple compartments is applied.

2   Weighted Monte Carlo Particles for the Solution of the Population Balance Equation

The use of weighted simulation particles (a particle with weight w represents w real particles within a given reactor volume) has several advantages: it allows to describe the interaction between simulation particles having different concentrations coming from different cells or compartments [14, 20, 21]. It can also be used as a tool to control the number of simulation particles (e.g. to gain numerical accuracy). In the following, some techniques will be introduced to solve the single mechanisms presented in Eq. (1) by the application of weighted MC particles.

2.1   *Coagulation*

The correct description of the coagulation rates for the weighted particles, especially for a complex coagulation scheme, like the one introduced Zhao et al. [22] shown in Fig. 2, poses a great difficulty.

The authors [22] presented the 'ficticious particle theory' which leads to the following modified coagulation kernel:

$$\beta^{(fp)} = \frac{2W_j \max\left(W_i, W_j\right)}{W_i + W_j}\beta \tag{3}$$

The weights of the particles are denoted by W_i and W_j. The coagulation kernel β describes the coagulation of the original (non-weighted) system—which might be the Brownian kernel for the free molecular regime, etc. The resulting coagulation rate is asymmetric, making a distinction necessary, whether particle i coagulates with j or vice versa. This definition is 1) difficult to understand conceptually and 2) difficult to extend on other process—like nucleation or transport of fictitious particles.

We developed in [23] the concept of the stochastic resolution which describes each coagulation in the frame-work of equally weighted MC-particles, where each MC-particle describes s_f real particles. The value for the parameter s_f can be set arbitrarily. Figure 2 shows that the setting $s_f = W_{\min} = \min\left(W_i, W_j\right)$ leads to the correct description of the coagulation-scheme. The scaling factor s_f depends on the chosen coagulation pair, so that different coagulation-events are described in different stochastic resolutions.

general rule W$_{min}$ ≠ W$_{max}$ (case 1)
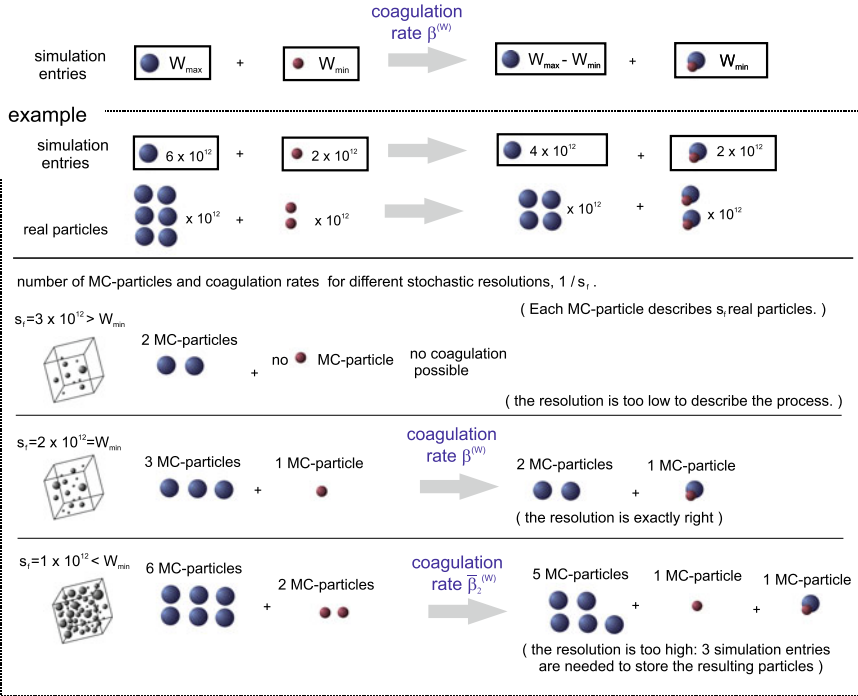
Fig. 2 The concept of 'stochastic resolution' can be used to describe the coagulation-scheme developed Zhao et al. [22]. Only the choice for $s_f = W_{min}$ leads to the correct description of the general rule presented in the 'simulation entries' line

The coagulation rate $\beta^{(w)}$ for this coagulation-scheme can be derived from the population balance equation:

$$\frac{dn(v)}{dt} = \frac{1}{2}\int_0^v \beta(v-v', v')n(v-v')n(v')dv' - n(v)\int_0^\infty \beta(v, v')n(v')dv' \qquad (4)$$

Instead of the 'original' concentrations $n(v)$, the concentrations of the MC-systems $n^{(MC)}(v) = \frac{n(v)}{s_f}$ are being considered. The multiplication of the PBE with the factor $\frac{1}{s_f} = \frac{1}{W_{min}}$ leads to the following modified coagulation rate of the MC-particles: $\beta^{(MC)} = W_{min} \cdot \beta$. Hence there is one MC-particle of the W_{min}-species and $\frac{W_{max}}{W_{min}}$ MC-particles of the W_{max}-species, the overall rate for the coagulation between one W_{min}-MC-particle and one of the W_{max}-MC-particles is:

$$\beta^{(w)} = \frac{W_{max}}{W_{min}} \cdot \beta^{(MC)} = W_{max} \cdot \beta \qquad (5)$$

The second case $W_{max} = W_{min}$, which is not shown in Fig. 2, is also described with the resolution $s_f = W_{min}$. Both particle species are described by only one MC-particle, so that only one MC-particle can be found after the coagulation. In order to apply the constant number scheme, the weight of the simulation entry representing this particle is divided by two and the particle properties are stored in both positions.

The thus derived coagulation kernel $\beta^{(w)}$ is easier to calculate than the originally introduced $\beta^{(fp)}$ —a speed up of the simulation up to 10% could be noticed. Due to its symmetric form, computational advantages for the implementation of the inverse method can be expected, as only half of the computations of the $\beta^{(w)}$ kernel are necessary. The simulation results of particle coagulation for the newly estimated coagulation kernel $\beta^{(w)}$ could be found to be as accurate as the $\beta^{(fp)}$-kernel results (which show excellent agreement with the solution produced by means of the Discrete-sectional-method in the first place) within the MC-stochastic noise [23].

2.2   Nucleation

Homogeneous nucleation is a mechanism that leads to the formation of new particles, which have to be included among the simulation entries. Constant number simulation-schemes sum up all possible algorithms, which update—somehow—the simulation properties, but keep the number of the used simulation entries constant. Keeping the number of simulation entries constant ensures a constant level of stochastic accuracy and makes a simple prediction of needed computational resources possible. Figure 3 shows possible constant-number nucleation algorithms. They can be used to model the inclusion of the nucleation particles or particles included by other processes: like breakage or transport.

The random removal algorithm has been introduced Lin et al. [24] in the framework of the concept of a 'constant number Monte Carlo simulation' which is based on the not-weighted particle scheme. The algorithms applying the merging step are based on the weighted-particles scheme and the concept of the merging error. They cannot be used for non-weighted MC simulations. The merge-List is created each 100 merge-steps and contains 100 simulation entries with low-weights.

2.2.1   Merging

The concept of 'merging' of simulation entries is proposed in [23]: if two simulation entries with exactly the same properties are merged, the resulting representation of the particle size distribution will not change and all the physical processes will be described in the same way. If the simulation entries differ slightly in their properties, a small error will be introduced.
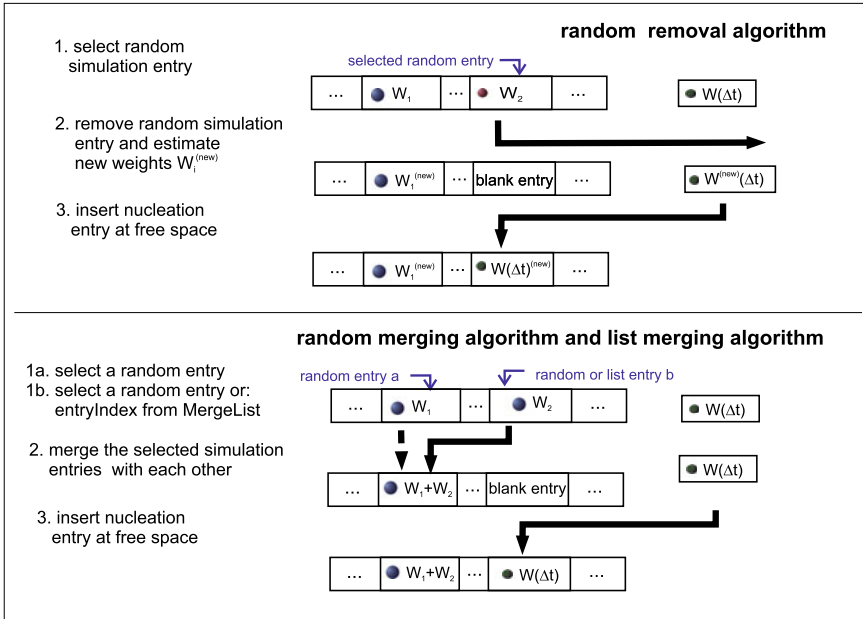
Fig. 3 Different simulation algorithms which combine the MC constant-number simulations based on weighted particles with the nucleation process

The merging scheme:

Each simulation entry contains the weight W, and other properties $p^{(1)}$, $p^{(2)}$, $p^{(3)}$, ... of the rendered part of the particle population (where $p^{(i)}$ could be the volume, porosity, electric charge, etc.). If the simulation entry A (weight W_A) and B (weight W_B) are merged into the new simulation entry C (weight W_C and several properties $p_C^{(i)}$), the following two rules should apply:

(i) The total weight of the simulation-entries before and after the merge-step should be preserved:

$$W_C = W_A + W_B \tag{6}$$

(ii) If the total amount of the particle-properties is preserved one can write:

$$W_C \cdot p_C^{(i)} = W_A \cdot p_A^{(i)} + W_B \cdot p_B^{(i)} \Leftrightarrow p_C^{(i)} = \frac{W_A \cdot p_A^{(i)} + W_B \cdot p_B^{(i)}}{W_A + W_B} \tag{7}$$

This is the most simple assumption which should hold true for most of the physical applications, but other definitions—which make a more complex calculation necessary can be used. E.g., if the described property is the diameter d but the volume v is preserved, one can write (assuming sphere-like particles):

$$W_C \cdot \frac{\pi}{6}(d_C)^3 = W_A \cdot \frac{\pi}{6}(d_A)^3 + W_B \cdot \frac{\pi}{6}(d_B)^3$$

$$\Leftrightarrow d_C = \left(\frac{W_A \cdot (d_A)^3 + W_B \cdot (d_B)^3}{W_A + W_B} \right)^{1/3} \tag{8}$$

The merging error:
The error introduced into the simulation by the merging of the simulation entries can be estimated by the following formula:

$$E_{(A,B)} = \sum_{\text{all roperties } i} \alpha_i \cdot \left(\frac{p_A^{(i)} - p_B^{(i)}}{\min\left(p_A^{(i)}, \cdot p_B^{(i)} \right)} \right)^2 \tag{9}$$

where α_i are merging-weights, which can be set arbitrarily—depending on the physical process—they can be interpreted as a measure of the severity, which the deviation of the property $p_A^{(i)}$ from $p_B^{(i)}$ would have—compared to the deviation of other properties $p_A^{(j)}$ from $p_B^{(j)}$.

2.2.2 Parallel Merging Algorithm

The merging-algorithms presented in Fig. 3. use the selection of random simulation entries, resulting therefore in a random merging error $E_{(A,B)}$—which may be excessively high. The smallest possible merging error can be estimated by the comparison of all simulation-entry-pairs—which would prove very costly: $N_{\text{MC}} \cdot (N_{\text{MC}} - 1)/2$ comparisons are necessary, if N_{MC} simulation-entries are used. A sound compromise between both scenarios is the sampling of a 'representation of the simulation entries' and the estimation of the minimum merging error of this representation. A parallel algorithm can be applied for this purpose, easily adaptable for GPU computing: the merging errors for $(N_{\text{MC}} - 1)$ pairs of simulation-entries can be computed in parallel and the comparison of the calculated merging errors is done within only $\log_2 N$ computational steps, like shown in Fig. 4.

2.2.3 Validation of Coupled Coagulation and Nucleation

The nucleation is combined with the simulation of coagulation in two steps: First, a classical event-driven MC coagulation step is performed, this includes the selection of the coagulation pair via the fast parallel A/R-method introduced Wei [25] with the
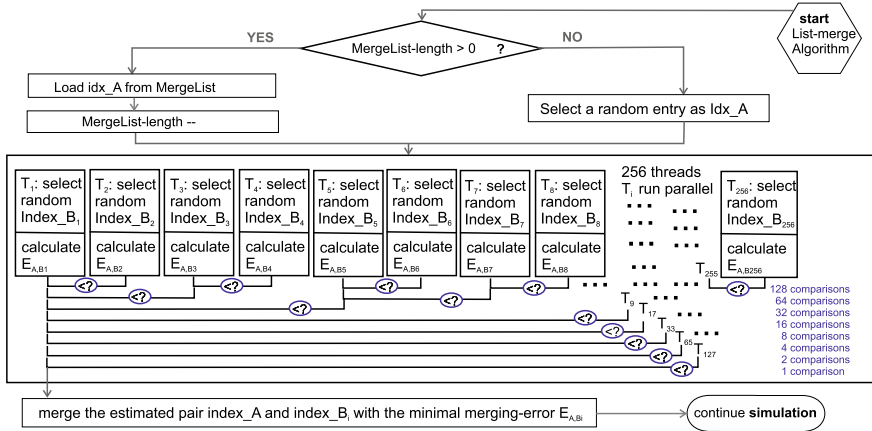
Fig. 4 The parallel low weight merging algorithm [23]: only 8 parallel thread-executions are necessary in order to estimate the pair (1 out of 256) of simulation-entries with the minimal merging error

weighting scheme based on the stochastic resolution—the actual time-step $\Delta\tau_{MC}$ is evaluated in this step, too. In a second step, the number of the nucleating particles is estimated, for this purpose the solution of the differential equation (which describes the nucleation) can be approximated by the Euler-method (more complicated Runge-Kutta methods or other ODE-solvers can be used for the modeling of the interaction with the continuous phase [26, 27]). The newly created simulation entry is then included by means of the merging algorithms from Fig. 4.

A typical benchmark test case[1] shows the advantage of the merging of particles compared to the random removal method, as sketched in Fig. 3. A part of the simulation results already discussed in [23] are summarized in Table 1, where the mean values d_g and standard deviations Δd_g of the geometric mean diameter are shown. Hence each MC simulation is executed with a different sequence of random numbers, the resulting geometric mean diameter $d_g^{(i)}$ is different for each simulation i. The arithmetic mean values (d_g) and standard deviations Δd_g of 100 $d_g^{(i)}$ values resulting from of 100 MC simulations are shown. (Similar findings could also be presented for the number concentration of the particles or the geometric standard deviations of the resulting PSDs.) It can be clearly seen that the application of merging techniques leads to significantly lower noise levels. For example, 10,000 simulation particles in combination with the random removal method cannot reach the same precision levels as the application of 1000 simulation particles in combination with the low

---

[1]A constant nucleation rate R_N is assumed, so that newly introduced simulation entries have the weight $W_0 = R_N \cdot \Delta\tau_{MC}$ and a predefined diameter d_0. For the simulation has been set: $R_N = 10^{14} \frac{1}{m^3 s}$, $d_0 = 3$ nm. A monodisperse population with an initial concentration of $10^{17} \frac{1}{m^3}$ has been used as start condition, the initial MC particles are equally weighted. The temperature was set to 300 K and the particle density to $1 \frac{g}{cm^3}$. The simulated time was ca. 25.8 s, which is 500 times the characteristic time needed to reach the self-preserving distribution [28] due to coagulation.

Table 1 Values of the geometric mean diameter and simulation times (CPU time) for the discrete sectional (DS) method and MC simulations using Random removal (RR) and Low weight Merging (LWM) with 1000 and 10,000 MC particles

Method	Mean value d_g [nm]	Standard deviation Δd_g (absolute) [nm]	$100\Delta d_g/d_g$ (percent) [−]	CPU time [s]
DS (20 100)	4.736	–	–	8.4
DS (250 380)	4.740	–	–	332.1
RR 1000	4.820	0.544	11.29	330.3
RR 10,000	4.736	0.180	3.79	3964.2
LWM 1000	4.733	0.100	2.11	300.4
LWM 10,000	4.742	0.033	0.70	3643.2

The number of used sections and discrete points for DS are indicated by the values in the brackets (discrete points, sections). The exact 1D grid specifications are described in [23]

weight merging. It should also be noted that the computation of 10,000 MC particles requires ca. 10 times larger computing times than of 1000 particles. The computing times shown in Table 1 refer to the simulation of 100 MC simulations run in parallel on the GPU and one discrete-sectional run sequentially on the CPU.

2.3 Coupled Condensational Growth and Evaporation, Coagulation and Nucleation

A varying nucleation rate, R_N, as well as a changing critical nucleus size, d^*, is often encountered when a metallic vapor is created and then cools down, leading to the nucleation rate increasing over tens of orders of magnitude and then going down when the free atoms have been largely consumed. The size of the critical nucleus, d^*, on the other hand, decreases from very large values to atomic sizes, and rises again when the nucleation rate is increasing. This presents a severe test for the numerical solution, as the source term is moving rapidly through the size spectrum, leading to a dramatic change of the growth and evaporation rates of the simulated particles, as well. Hence particles larger than the nucleating particle (i.e. with volumes $v_i > v^*$) will grow, while those which are smaller (i.e. with volumes $v_i < v^*$) will evaporate. This is described by the equation of the growth-rate $G(v_i, N_G)$ of particles with the volumes v_i in the free-molecule regime [29]:

$$G(v_i, N_G) = \frac{dv_i}{dt} = \frac{v_M \cdot \pi \cdot d_i^2}{\sqrt{2\pi \cdot m_1 \cdot k_B \cdot T}}$$
$$\cdot (k_B \cdot T \cdot N_G - p_s \cdot \exp\{4 \cdot \sigma \cdot v_M/(k_B \cdot T \cdot d_i)\}) \qquad (10)$$

The value of the critical diameter is given by:

$$d^* = 4 \cdot \sigma \cdot \upsilon_M/(k_B \cdot T \cdot \ln(S))$$
$$\text{with} \quad S = \frac{N_G k_B T}{P_s} \tag{11}$$

So that $G(v_i, N_G) = 0$ for $v_i = v^*$ and $G(v_i, N_G) > 0$ for $v_i > v^*$. The growth rate of the particles is also dependent on the number of atoms (or molecules) of the condensable material in the gaseous phase, N_G. The depletion (resp. increase) of the monomers due to condensation on (resp. evaporation of) the particles is described by a mass balance:

$$\frac{dN_G}{dt} = -\sum_i W_i \cdot G(v_i, N_G)/v_M - R_N \cdot i^* \tag{12}$$

Thereby, the nucleation of particles is also taken into account by the nucleation rate R_N and the number of atoms (resp. molecules) i^* in a particle of the critical size d^*.

We proposed an operator-splitting based approach for the parallel solution of this system [26, 27, 30], by decoupling the growth-evaporation and nucleation mechanism from the coagulation mechanisms for short periods of time, like in the presented coupled simulation of coagulation and nucleation in Sect. 2.2.3. The condensational growth (resp. evaporation) of the simulated particles is solved in parallel by application of time-step adaptive Runge-Kutta techniques (see e.g. [31]). A parallel addition algorithm, similar to the presented parallel comparison algorithm in Fig. 4, is used for the fast calculation of the term $\sum_i W_i \cdot G(v_i, N_G)$ in Eq. (12). A more detailed description of this approach can be found in [30]. This modelling of the continuous PSD with discrete MC particles avoids the effect of numerical diffusion [32, 33], encountered in models describing particle growth, in analogy to moving grid techniques for sectional methods [34].

It has be shown, that all of the mentioned mechanisms (i.e. evaporation, condensation, nucleation and coagulation) have to be considered and that the omission of one of these mechanisms leads to severe deviations from the 'complete' system [26].

The thus introduced methodology can be used to determine the influence of different formulations of nucleation rates and allows to identify experimental conditions for the experimental investigation of those. There exist several approaches for the description of nucleation theories [35]. We consider in the following these three expressions for the nucleation rate R_N, as discussed in [36]:

$$R_N^{(cou)}(N_G) = N_G \cdot \sqrt{\frac{2\sigma}{\pi \cdot m_1}} \frac{p_s}{k_B \cdot T} \cdot v_1$$
$$\cdot \exp\left(-\frac{16 \cdot \pi \cdot \sigma^3 \cdot v_M^2}{3 \cdot k_B^3 \cdot T^3 \cdot \ln(S)^2}\right),$$

Table 2 Material constants for Ag at a temperature of 1300 K

Symbol	Description	Value	Source
m_1	Atomic mass	1.792×10^{-25} kg	[37]
v_M	Atomic volume	1.922×10^{-29} m^3	[37]
p_s	Vapor pressure	1.324 pa	[37]
σ	Surface tension	0.9024 J/m^2	[38]

$$\text{with}\quad S = \frac{N_G k_B T}{p_s} \tag{13}$$

$$R_N^{(gir)}(N_G) = R_N^{(cou)} \cdot \exp\left((36 \cdot \pi)^{\frac{1}{3}} \cdot \frac{\sigma \cdot v_1^{\frac{2}{3}}}{k_B \cdot T} \right); \quad R_N^{(cls)}(N_G) = R_N^{(cou)} \cdot S \tag{14}$$

The influence of these different nucleation theories has been discussed for atmospheric simulation scenarios [27] and are briefly sketched for a metallic system describing the nucleation of Ag vapor in the following. The material parameters in Eqs. (10–14) assume values summarized in Table 2 at a temperature of $T = 1300$ K.

The simulation of a isothermal nucleation induced due to an initial supersaturation of $S_0 = 100$ of Ag vapor and the presence of an initial (background) PSD with a mean geometric diameter of 2 nm and a geometric standard deviation of 1.2 rendering a total number-concentration of 10^{16} m^{-3} is used as an initial condition. The temperature is kept constant to 1300 K during the course of the simulation.

The monomer concentration exhibits the fastest depletion rate for the Girshick-based nucleation rate, as is shown in Fig. 5a. This is due the highest nucleation rate which is plotted in comparison with other nucleation theories in Fig. 5b. This leads in turn to the highest particle concentrations for the Girshick-based nucleation theory (see figure Fig. 5c). The nucleation theories show the most striking differences at the early stages of the simulation, for longer simulation times, (i.e. t > 0.01 s), similar
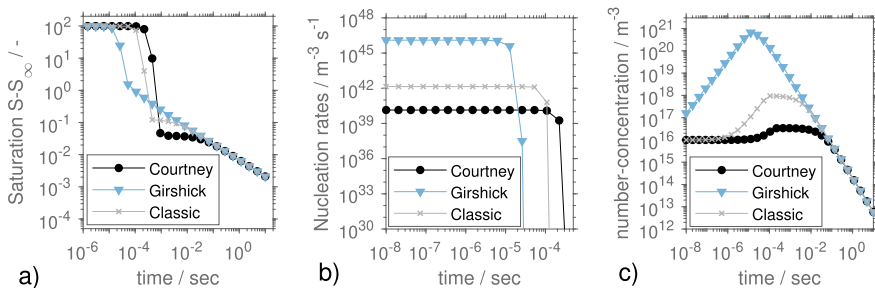

Fig. 5 Isothermal Ag particle synthesis with initial PSD and supersaturation $S_0 = 100$. The saturation surplus $S - 1$ (**a**), the corresponding nucleation rates (**b**) and the total particle number-concentrations (**c**) are shown. The nucleation rates $R_N^{(cou)}$ (Courtney) $R_N^{(gir)}$ (Girshick) and $R_N^{(cls)}$ (Classic) are defined in Eqs. (13) and (14)
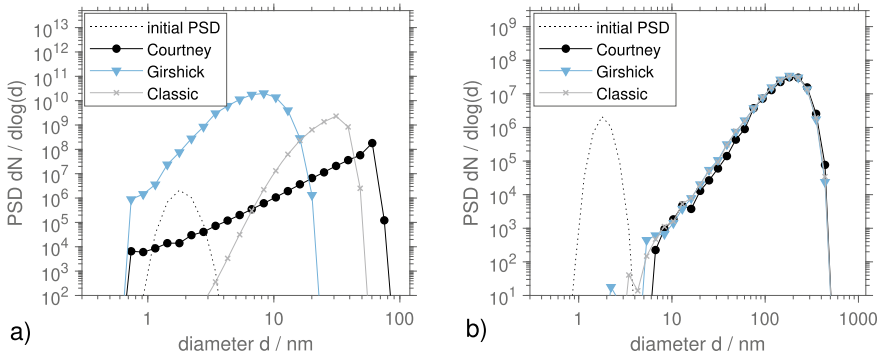
Fig. 6 Isothermal Ag particle synthesis with initial PSD and supersaturation $S_0 = 100$. Resulting PSDs after $2.2 \cdot 10^{-4}$ s (**a**) and $1.4 \cdot 10^{-1}$ s (**b**) for the nucleation rates $R_N^{(kin)}$ (Kinetic) $R_N^{(gir)}$ (Girshick) and $R_N^{(cou)}$ (Courtney) defined in Eqs. (13) and (14)

supersaturations and concentrations can be observed (in Fig. 5 a-c). This is a signature of the similar PSDs resulting from the simulation, as they are shown in Fig. 6.

The PSDs at the initial stages of the simulation (see Fig. 6a) show tremendous differences and allow to attribute each of the different shapes to a specific nucleation theory. For longer simulation times, on the other hand, a self-preserving PSD is reached and all of the presented nucleation theories can be attributed to the shown PSDs. The shown self-preserving PSD is the result of the complex coupling of the mechanisms of coagulation and evaporation. This PSD deviates from the self-preserving PSD for the coagulation only as reported Vemury and Pratsinis [28]. Similar self-preserving PSDs deviating from the self-preserving PSD for coagulation only have been already reported for similar metallic systems [26] and [30]. This approach allows thus to roughly approximate a time window, for which specific differences between the different nucleation rates can be expected. Allowing thus to give hints for measurements set-ups investigating the specific forms of the nucleation rate R_N.

2.4 Breakage

Breakage of particles is relevant for the modeling of particle mills, but also for granulation, emulsions, sprays and even for aerosols when agglomerates break up by collisions or turbulences. The rendering of the large number of particles which are produced during the continuous breakage process poses a major problem for MC simulations, because large computational resources have to be provided for this purpose. In a typical milling process, for example, reductions of the particle diameters from 500 to 0.5 μm are encountered, the same amount of volume, which is rendered by one simulation particle with a size of 500 μm has to be rendered by

10^9 simulation particles with a diameter of $0.5\,\mu$m, if all particles represent the same number concentration of real particles.

Traditional solutions of this problem encompass the discretization of the particle property into bins [39], which would render the combination with the developed growth/evaporation algorithm impossible, and constant-number approaches [40], which are known to produce a high level of statistical noise [41].The application of merging schemes [42] (i.e. the approximation of the properties of several simulation particles by one simulation particle) would pose an attractive alternative. However, the vast amount of newly resulting particles makes a lot of merging steps necessary, leading to large computing times. A recent constant-number method has been presented [41], which renders the breakage event of one particle into many fragments by a single particle. The size of the fragment is selected stochastically, the use of many simulation particles leads to the correct distribution of fragment sizes. This scheme is only able to render the parts of the particle size distribution which represent high number concentrations of the particles. Furthermore, only binary breakage can be described.

We developed an alternative approach [43] for the derivation of the breakage scheme by resorting to the argument that the breakage of many MC-particles with equal properties and weights has to lead to a particle size distribution (PSD) of fragments, which is described by the corresponding breakage kernel. It allows to formulate any probability distribution function (PDF) with which the new volume of the simulation particle is selected by adjusting the statistical weight of the resulting fragments depending on 1) the selected particle properties, 2) the used PDF and 3) the given breakage density function. This newly proposed scheme encompasses the already introduced SWA schemes, especially a number-based (NB, named SWA1 in [41]) and volume-based (VB, named SWA2 in [41]) breakage scheme, and it makes novel formulations possible: the low volume scheme (LV), which renders preferably fragment particle sizes at the lower end of the size spectrum, and the combination of LV with the NB (NB-LV) or VB (VB-LV). Exemplary simulation results are shown in Fig. 7. It can be seen that the SWA methods (NB and VB) are only able to render large particle sizes, and that LV, NB-LV and VB-LV are able to render the whole spectrum of particle sizes. Smaller noise levels are found for VB and specific VB-LV schemes, making both more suitable for prolonged simulations than the other presented methods. The LV based simulation method fails to predict the correct PSDs for longer simulation times. For this reason, the combinations of LV with VB or NB are needed, in order to ensure the correct shapes of the PSDs for longer simulation times. The combination ratio $R \in (0, 1)$ between the LV and NB leads to different schemes, while lower ratios R lead to a higher representation of low-volume MC particles, they also lead to higher noise levels: the setting $R = 0.6$ leads to more statistical noise than $R = 0.9$, as it can be seen in Fig. 7. The adaptive resetting of the factor R in order to avoid the systematical errors, as it is shown in Fig. 7 for the LV scheme is briefly discussed in [44].

The required simulation times are listed in Table 3, 10^5 simulation particles are required in order to ascertain a computational accuracy of less than 1%. (I.e. the
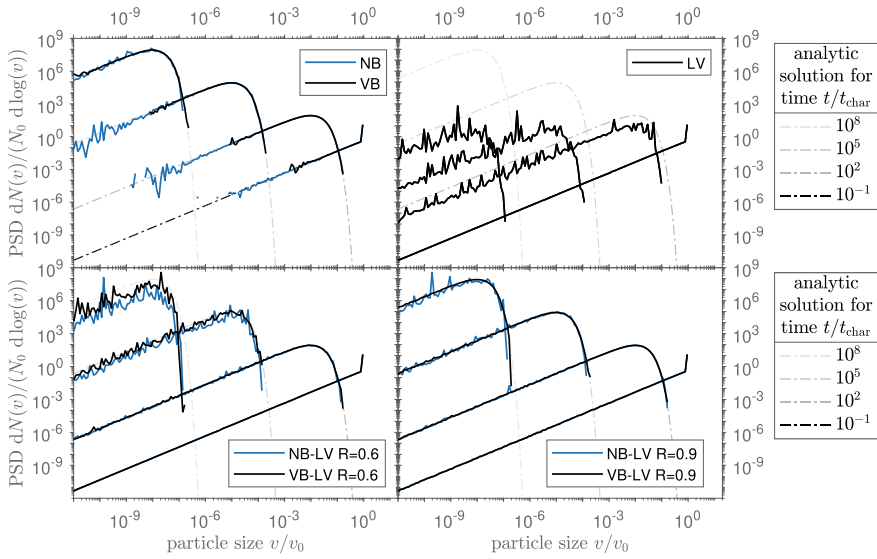
Fig. 7 Resulting PSDs from the simulation of a test cases describing a binary, homogeneous particle breakage function $\gamma(v_F, v_P) = 2/v_P$ and a breakage rate $b(v) = v$ (test case 1 in [43]) for a monodisperse initial condition v_0 and the thus defined characteristic time $t_{char} = b(v_0)^{-1}$. The MC-simulations are compared with analytic solutions found in [46]

Table 3 Computational times required for the simulation of $t = t_{char} \times 10^8$ in dependency on the used number of simulation particles

Simulation particles	NB	VB	VB-LV
1000	0.5 s	0.8 s	0.6 s
10,000	2.8 s	4.4 s	3.0 s
100,000	27.1 s	42.5 s	29.8 s

arithmetic standard deviation of the moments of the distributions performed for 100 different sets of random numbers is smaller than 1% of the mean value.)

3 Compartmental Population Balance Modelling

The modelling of flow-sheet simulations in the scope of an operator-splitting approach (see e.g. [47]) requires a specific time step management, so that ongoing simulations processes can be forced to stop at specific simulation time points. This issue is addressed first, in a second, longer paragraph, the implementation of particle transport between single compartments by means of weighted MC particles is introduced and some typical simulation scenarios are presented.

3.1   Time Step Control for Compartmental PBE Networks

The combination of simultaneous processes rendered by the PBE solver poses a challenging task, hence the characteristic time-scales for the corresponding processes may differ in several orders of magnitude and change vastly during the simulation. Although the developed algorithms for the breakage, coagulation and growth (resp. evaporation) already adapt to the optimal time-step for each single process (in the absence of other processes), the simulation of the combined coagulation, nucleation and growth is driven by the discrete coagulation processes providing an inherent MC time step τ_{MC}. This is a computationally advantageous setting, if the inherent growth step τ_G is smaller than the coagulation step τ_{MC}. The opposite case, in which τ_G is bigger than τ_{MC}, forces the simulation to use much smaller time steps τ_G' and thus to use much more computationally demanding growth steps. The incorporation of the breakage as a third process with an inherent time step τ_B may force the simulation to reset this step to a lower value τ_B' in a coagulation driven implementation, as well.

This situation becomes even more complicated, if the PBE is solved for different compartments and a particulate flow between the compartments is simulated. Consider, for example two compartments, in which coagulation takes place, so that compartment 1 has an intrinsic MC coagulation time step $\tau_{MC}^{(C1)}$, while the second compartment has the inherent coagulation time step $\tau_{MC}^{(C2)}$, the additional particulate flowrate between compartment 1 and compartment 2 might make the update of the particle populations due to the transport of particles each time interval τ_{Tr} necessary. It depends on the specific modelled application, whether the minimum of these three time steps has to be used, or some other minimal time step τ_{min} can be applied. In all cases, there exists the need, to perform, at least in one of the two compartments, a smaller time step than the one intrinsically provided ($\tau_{MC}^{(C1)}$ and/or $\tau_{MC}^{(C2)}$).

The application of time-driven MC methods [48] allows the setting of a variable time step, but this time step has to be set proportional to the intrinsic step in order to avoid systematical errors [49], although smaller values are allowed. The main disadvantage of this approach is, however, its computational costs, hence all possible coagulation pairs have to be checked for coagulation during the suggested time step— special book-keeping methods [50] might help to address this problem for the single simulation of coagulation but their usage is not possible[2] in the context of a PBE network modelling multiple simultaneous processes.

We have developed the concept of 'fractional MC time steps' [51], in order to address this problem. In the scope of this approach, we modified the fast GPU acceptance-rejection algorithm [25] in such a way, that an additional stochastic probability is formulated, whether the particles coagulate or not if a smaller time step than the intrinsic MC AR-time step is needed. We compared our methodology (marked

---

[2]Special modeling is necessary in order to capture the changes of the 'book kept' entries due to other non-coagulation processes—this might or might not be possible, depending on the specific process being modelled. Additionally, the tracking of the changes might prove more expensive than the application of the time-driven MC methods without book-keeping.

Fig. 8 PSDs resulting from simulation conditions as described in [51]
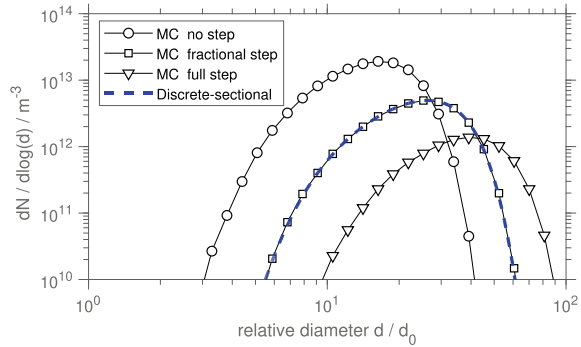
as 'MC full step') with (1) another approach from the literature [21], where no coagulation of the particles takes place in such an event (marked as 'no step') and (2) with the self-proposed approach, where the particles simply coagulate—even if the simulated time step is smaller than the intrinsic time step (marked as 'full step'). A typical isothermal coagulation scenario describing Brownian motion of particles in the free-molecule regime (full details can be found in [51]), leads to the following simulation results shown in Fig. 8, if the simulated system is forced to perform not the intrinsic MC time steps but an artificial time step of 1 ms. It can be clearly seen, that only the application of the fractional MC time steps leads to the correct description of the PSDs, which is in excellent agreement with the reference result gained by the application of the discrete-sectional method, as described in [52, 53].

3.2 Compartmental Monte Carlo Simulation

Modelling of MC particle transport as a stochastic process with discrete events is sometimes suggested [54]. Such a modelling, could—however— entail a large number of stochastic events for small simulation times and slow down the simulation considerably. The other disadvantage of such an approach is the potential increase of the stochastic noise of the simulation.

The description of weighted simulation particles makes novel simulation strategies for the transport possible, the adjustment of the statistical weight of each MC particle makes the exact description of the depletion of particles due to particle outflow possible—as is discussed in [20] (termed 'rescale outflow') and shown in the following. First, the description of a two-step (inflow and outflow) method is suggested and the merging and random removal techniques are briefly described, then the methodologies are validated and compared by simulations of exemplary flowsheets.

3.2.1 Transport of Weighted MC Particles

In the following, the transport of MC particles from one compartment to other compartments will be described. It consists of two steps: (1) the particle outflow and (2) the particle inflow. This is being realized by the computational implementation of 'streams' which are able to store a population of MC particles, as large as the population stored for each compartment.

In the first outflow step, particles are inserted into the streams. This can be easily done by copying all particles from the hold-up into the stream and adjusting the statistical weights accordingly, in the stream and in the hold-up. If, for example, the particles from compartment 1 stream into compartment 2 with the size v dependent relative rate $f_{1 \to 2}(v)$, then one can describe for each particle i the change of its statistical weight W_i for a small interval of time Δt as:

$$W_i(t + \Delta t) = W_i(t) - \Delta t \cdot f_{1 \to 2}(v_i) \cdot W_i(t) \tag{15}$$

This is shown as particle outflow step in Fig. 9. The new weights W_i^{s1} and $\overline{W}_i^{c1}$ are set to $W_i^{s1} = \Delta t \cdot f_{1 \to 2}(v_i) \cdot W_i^{c1}$ and $\overline{W}_i^{c1} = W_i^{c1} - W_i^{s1}$.

In the inflow step in Fig. 9, the particles from the streams are inserted into the compartments. Analogously to the already discussed nucleation of particles, one encounters at this step the problem of the limited CPU memory: each connecting stream contains as many particles as the destination compartment, so that only a fraction of all MC particles can be stored in the destination compartments. This problem has been solved in two ways in the here presented work: (1) randomly selected particles are removed from the simulation—adjusting the statistical weights in such a way, that the mass of the system remains constant as in the conventionally used constant number algorithms [55, 56] and (2) the particles are merged together using a parallel merge algorithm as it is briefly discussed in [57].
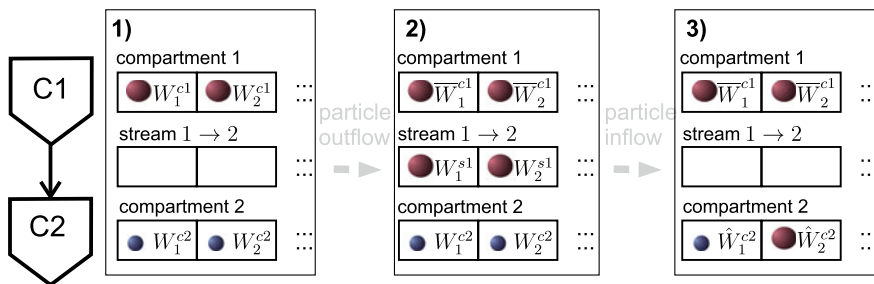

Fig. 9 MC particles stored in the memory assigned for compartment 1 and 2, as well as in the stream connecting both compartments. The stages (1) before the particle outflow (2) between outflow and inflow and (3) after the inflow during the simulation of a single time step are shown
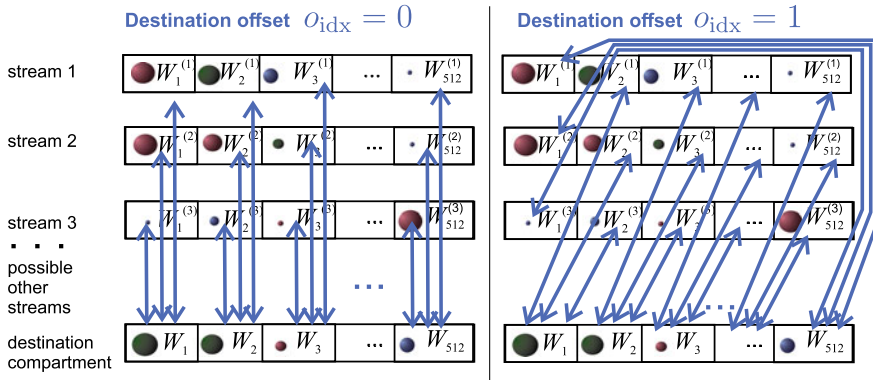
Fig. 10 Compartment-Stream merge pattern. Each double arrow represents one merge attempt. All merge attempts which are executed in parallel with the destination offset $o_{idx} = 0$ are shown in comparison with all parallel merge attempts made for the offset $o_{idx} = 1$

3.2.2 Parallel Merge Algorithm

The merging algorithm described in Fig. 4 could be used for the merging of MC particles within stream and the destination compartment. However, such an approach would be computationally not efficient due to the large number of MC particles ranging in typical applications between 1000 and 10000. This would imply 1000 or 10000 sequential or parallel invocations of the algorithm presented in Fig. 4. In order to accelerate the merging process, a novel parallel algorithm has been briefly sketched in [57] and is discussed here in more detail. The GPU's capability to process a large amount of data in parallel can be exploited in a more efficient way, if not only one (as in Fig. 4) but a large number of MC particles has to be merged together (as in Fig. 9).

The merging scheme described by Eq. (6) and (7) can be thereby used in combination with the merging error described by Eq. (9). A maximal admittable merging error ε can be formulated and all particle pairs (i, j) with a merging error $E_{i,j}$ (Eq. (9)) smaller than ε are merged together. A large number of parallel comparisons can thereby be performed, forming potential pairs for the merging by calculation of the merging errors of the pairs consisting of one particle in the destination compartment and one particle in one of the streams, as shown as 'Compartment-stream merge pattern' in Fig. 10. The destination offset, o_{idx}, is thereby increased by one after each comparison attempt, so that different pairs are formed for the calculation of the merging error. After 512 steps, all possible pairs between each of the compartment particle and another stream MC particle would have been checked in this way.[3] An internal check between particles stored in the compartment (resp. streams) is also

---

[3]In order to use the GPU efficiently, larger particle numbers (like e.g. 10000) have to be divided into data blocks consisting of e.g. 512 particle numbers. In the here presented implementation, particle numbers that are multiples of 512 are considered.

Fig. 11 Intern merge pattern. All merge attempts which are executed in parallel within one stream or compartment with different compare distances C_{dist}
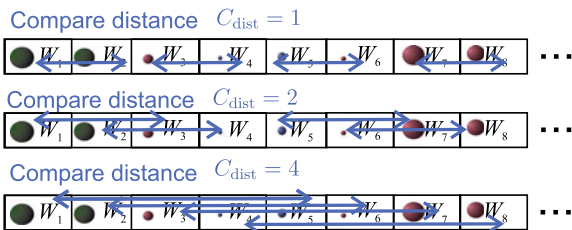
performed, in order to address situations, in which the populations in the streams are so different from the population in the compartment, that a merging is only possible with very high merging errors. These 'internal merges' are shown in Fig. 11. The multiplication of the compared distance C_{dist} with the factor of 2, ensures the treatment of different pairs after each invocation of the routine.

The complete algorithm for the parallel merging is shown in Fig. 12, the following settings are set arbitrarily:
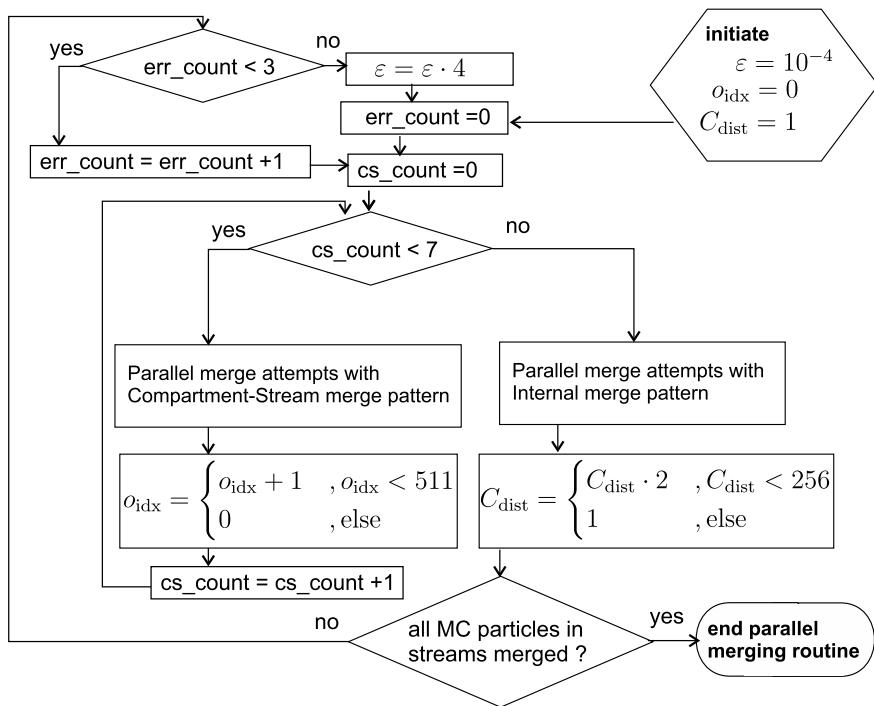

Fig. 12 Sketch of the merge algorithm for MC particle insertion. The Compartment-Stream merge pattern is shown in Fig. 10 and the internal merge pattern is shown in Fig. 11
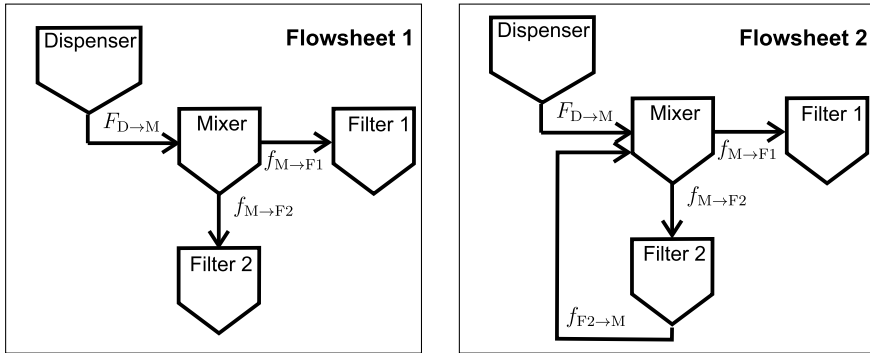
Fig. 13 Exemplary flow-sheets with and without a feedback stream

- 8 Compartment-Stream merge patterns are performed for each invoked intern merge-pattern ('cs_count < 7' in Fig. 12). This combination is invoked each time before the (rather costly) check if all particles have been merged is initiated.
- After each 4 unsuccessful checks if all particles have merged, the maximal admittable merging error is increased ('err_count < 3' in Fig. 12).
- The maximal admittable merging error is increased by a factor of 4 ('$\varepsilon = \varepsilon \cdot 4$').

These settings prove to work efficiently for the presented test cases in the validation section. Other settings might be more appropriate for other application scenarios and the dynamic adaptation of these values to given simulation conditions might pose an interesting research topic for future investigations.

3.2.3 Validation

The proposed simulation techniques are validated on several test-cases, which reflect simple engineering problems and are shown in the figures Figs. 13 and 14. The shown flowsheets increase in complexity, hence the implementation of a tear stream (Flowsheet 2, Fig. 13) or a sieve unit (Flowsheet 3, Fig. 14) or both in combination (Flowsheet 4, Fig. 14) poses a greater challenge for the numerical solution than the simple flowsheet 1 in Fig. 13. This methodology allows to identify the specific simulation scenario, for which conventional MC strategies are not suitable and the here presented methodology based on weighted MC particles has to be applied in order to obtain correct results.

For each of the presented units in Fig. 13, the evolution of the PSDs n_M (mixer), n_{F1} (filter 1) and n_{F2} (filter 2) can be modelled by the explicit set of differential equations:

$$\frac{dn_M(v, t)}{dt} = + f_{F2 \to M} \cdot n_{F2}(v, t) - f_{M \to F1} \cdot n_M(v, t) - f_{M \to F2} \cdot n_M(v, t)$$
$$+ F_{D \to M} \cdot n_D(v, t)$$

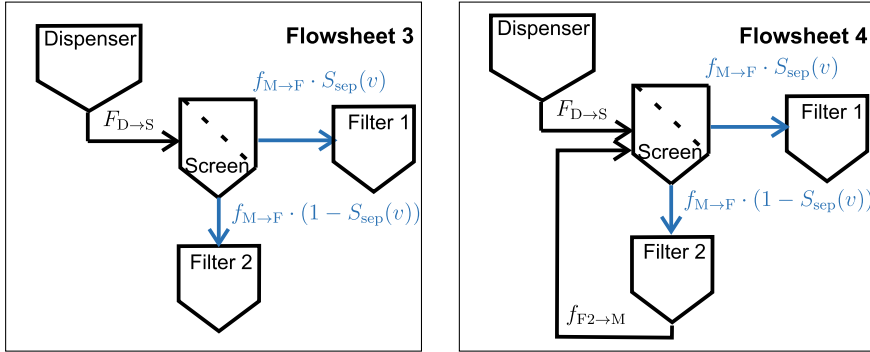**Fig. 14** Exemplary flow-sheets with and without feedback including a feedback stream

$$\frac{\mathrm{d}n_{\mathrm{F1}}(v,t)}{\mathrm{d}t} = + f_{\mathrm{M}\to\mathrm{F1}} \cdot n_{\mathrm{M}}(v,t)$$

$$\frac{\mathrm{d}n_{\mathrm{F2}}(v,t)}{\mathrm{d}t} = + f_{\mathrm{M}\to\mathrm{F2}} \cdot n_{\mathrm{M}}(v,t) - f_{\mathrm{F2}\to\mathrm{M}} \cdot n_{\mathrm{F2}}(v,t) \qquad (16)$$

The relative particle exchange rates $f_{\mathrm{A}\to\mathrm{B}}$ from unit A to unit B are multiplied with the particle PSDs in A, n_A, which change over time. The external particle exchange rate $F_{\mathrm{D}\to\mathrm{M}}$ is multiplied with a PSD, n_D, which does not change in time, realizing thus in a constant in-flow into the mixer unit. The explicit values for the exchange rates used for these benchmarking test cases are summarized in Table 4.

The system in Fig. 13 described by Eq. (16) does not take specific particle sizes v into account, so that the same particle exchange rates apply for all sizes v. The application of a screen unit changes this situation, so that the total particle exchange rate from the screen to both filters, $f_{\mathrm{S}\to\mathrm{F}}$, is multiplied with the separator function, $S_{\mathrm{sep}}(v)$. This leads to the following set of equations for the flowsheets shown in Fig. 14:

Table 4 Particle exchange rates for Eqs. (16) and (17)

	Flowsheet 1 in Fig. 13	Flowsheet 2 in Fig. 13	Flowsheet 3 in Fig. 14	Flowsheet 4 in Fig. 14
$F_{\mathrm{D}\to\mathrm{M}}$ or $F_{\mathrm{D}\to\mathrm{S}}$ [1/s]	3	3	3	3
$f_{\mathrm{M}\to\mathrm{F1}}$ [1/s]	1	1	–	–
$f_{\mathrm{M}\to\mathrm{F2}}$ [1/s]	2	2	–	–
$f_{\mathrm{M}\to\mathrm{F}}$ [1/s]	–	–	3	3
$f_{\mathrm{F2}\to\mathrm{M}}$ or $f_{\mathrm{F2}\to\mathrm{S}}$ [1/s]	0	2	0	2

$$\frac{dn_S(v, t)}{dt} = +f_{F2 \to S} \cdot n_{F2}(v, t) - f_{S \to F} \cdot n_M(v, t) + F_{D \to S} \cdot n_D(v, t)$$

$$\frac{dn_{F1}(v, t)}{dt} = +f_{S \to F} \cdot n_S(v, t) \cdot S_{sep}(v)$$

$$\frac{dn_{F2}(v, t)}{dt} = +f_{S \to F} \cdot n_S(v, t) \cdot (1 - S_{sep}(v)) - f_{F2 \to S} \cdot n_{F2}(v, t) \quad (17)$$

The explicit particle exchange rates for these equations are summarized in Table 4. The following form of the separation function $S_{sep}(v)$ has been used for the screen:

$$S_{sep}(v) = \begin{cases} 1, & v > v_{max}^{sep} \\ (v - v_{min}^{sep})/(v_{max}^{sep} - v_{min}^{sep}), & v_{max}^{sep} > v > v_{min}^{sep} \\ 0, & v_{min}^{sep} > v \end{cases} \quad (18)$$

The separation cut-off values $v_{max}^{sep} = \pi(d_{max}^{sep})^3/6$ and $v_{min}^{sep} = \pi(d_{max}^{sep})^3/6$ correspond to the diameters $d_{max}^{sep} = 57$ nm and $d_{min}^{sep} = 40$ nm.

As initial conditions for the PSDs in the mixer $n_M^0(v)$ (resp. screen $n_S^0(v)$), two identic log-normal distributions with a geometric mean diameter of 50 nm, a geometric standard deviation of 1.2 and a total number-concentration of $10^{10} \, \mathrm{m}^{-3}$ have been used. The same distribution has been used as feed PSD, i.e. $n_D(v)$. Both filters are empty at the beginning of the simulation ($n_{F1}^0(v) = n_{F2}^0(v) = 0$).

A fixed pivot method [58] has been used as benchmark. The continuous initial PSDs are thereby discretized with the help of a geometric grid of 1000 pivot points, covering a particle size range from 1 nm to 10 μm. In the scope of this approach, the set of Eqs. (16) or (17) is interpreted as the rate of change for each single pivot point with its respective volume v.

The resulting PSDs after a simulation time of 10 s are shown in Figs. 15, 16, 17, 18. It can be seen, that flowsheet 1 (without tear streams and a screen) is very well
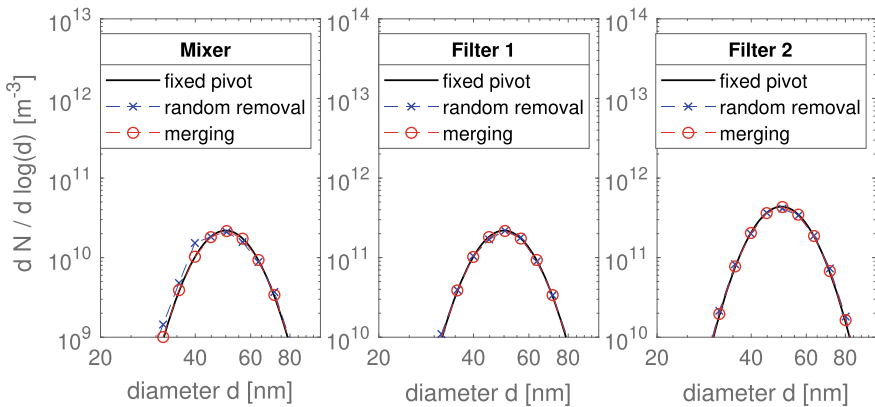

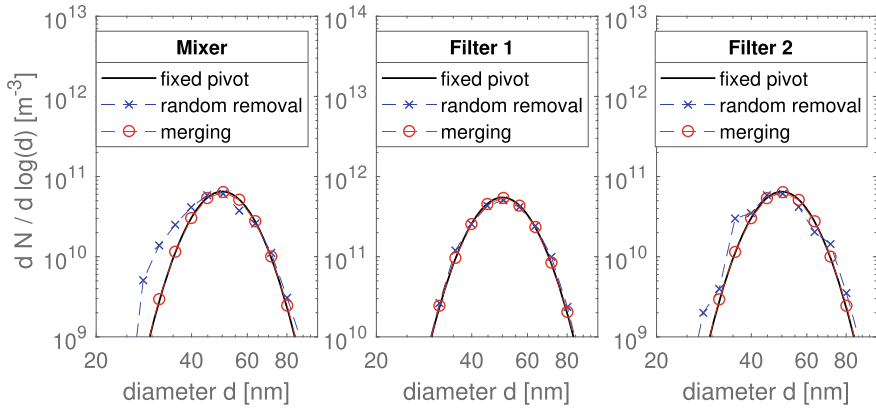Fig. 15 PSDs in compartments as described in Flowsheet 1 in Fig. 13 and Eq. (16)

Fig. 16 PSDs in compartments as described in Flowsheet 2 in Fig. 13 and Eq. (16)
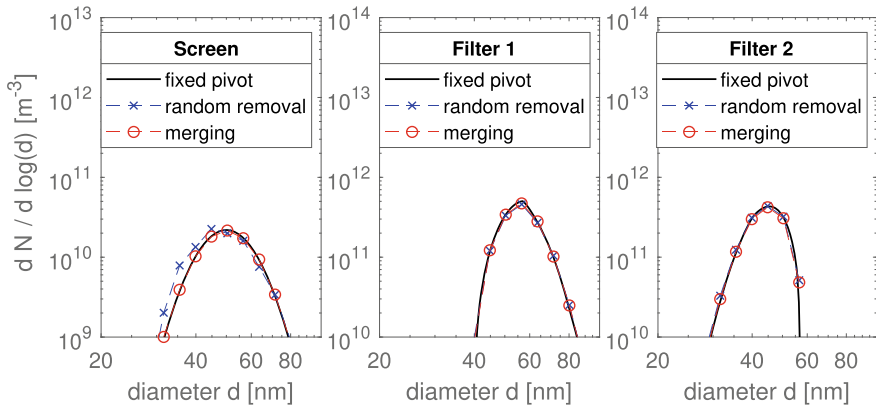

Fig. 17 PSDs in compartments as described in Flowsheet 3 in Fig. 14 and Eq. (17)
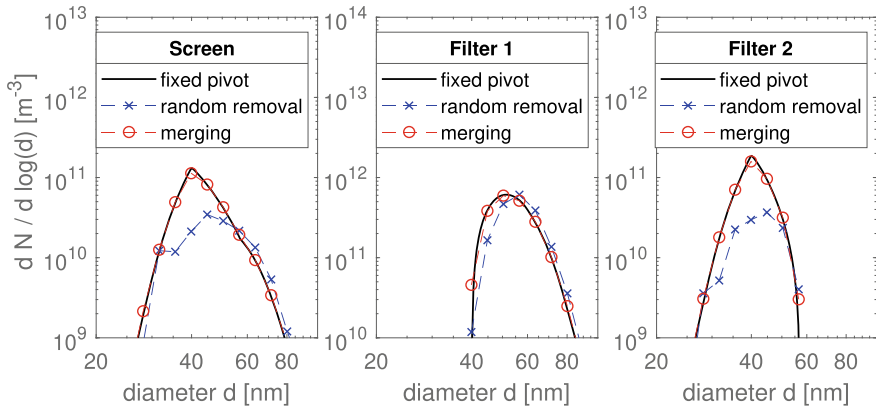

Fig. 18 PSDs in compartments as described in Flowsheet 4 in Fig. 14 and Eq. (17)

reproduced by the merging as well as the random removal approach. The random removal approach leads to larger noise levels, which can be seen in slight deviations of the PSD in the mixer unit in Fig. 15. The addition of a tear stream leads to an increase of these noise levels, as can be seen Fig. 16—the approximations based on the random removal technique become less accurate but can be still considered to be in accordance with the results obtained by the fixed pivot method.

The replacement of the mixer with a sieve unit (or replacing flowsheet 1 with flowsheet 3) leads also to a system, which can be well simulated by the random removal technique (see Fig. 17). The addition of a tear stream to flowsheet 3 (resulting in flowsheet 4) leads—however—to such a complex system, that the random removal method is not applicable. Figure 18 shows the striking deviations of the PSDs obtained with the random removal method—which predict a wrong particle-number concentration in the screen and filter 2 by a factor of nearly 10. The suggested merging techniques—on the other hand—are able to reproduce the benchmark results with a very high accuracy. This allows to say, that the specific combination of tear-stream and screen leads to a simulation scenario, which cannot be addressed with conventional MC simulation techniques—as the random removal technique. This finding also explains the failure of the random removal techniques to describe an even more complex simulation scenario, reported in [57].

4 Conclusions

The application of weighted MC particles for the solution of a compartmental network in the framework of an operator splitting approach (the single processes like coagulation and nucleation are separated for short periods of time) has been discussed.

First, the solution of a one-compartmental system has been discussed, it has been found that:

- the application of the stochastic resolution allows to describe the coagulation between weighted simulation particles (like already discussed in [23]).
- merging techniques allow to simulate the combined nucleation and coagulation with a lower amount of statistical noise than conventional MC simulation techniques (like already discussed in [23]).
- the parallel simulation of evaporation and condensational growth allows to simulate particles formation processes and investigate the role of different nucleation theories (this has been already discussed for metallic [26] and atmospheric systems [27], but the here presented case-study of Ag-particle synthesis has not been published prior to this work).
- novel selection and weighting techniques of the MC fragment population resulting from particle breakage lead to simulation techniques which are able to render the full particle size spectrum completely (these simulation techniques and findings have already been presented in [43]).

As a second step, the combination of the findings above in an operator splitting approach for the full simulation of a compartmental network has been sketched. It has been found that:

- the computationally advantageous event-driven simulation technique can be also used for the simulation of smaller time steps than the intrinsic MC time step—making this method applicable for a network of PBE compartments (like already discussed in [51]).
- the merging techniques introduced in [23] can be used for the simulation of particle transport between single compartments. (These findings have already been presented on a more complicated system in [57], the here presented description of the simulation algorithm is, however, far more detailed.)
- out of 4 case studies of a flow-sheet with increasing degree of complexity,[4] conventional MC methods can simulate the 3 simplest cases while merging techniques are needed for the simulation of the most complex case (this finding has not been published prior to this work).

References

1. Ramkrishna, D.: In: Population Balances: Theory and Applications to Particulate Systems in Engineering, 1st edn., Academic (2000). ISBN 978–0-12-576970-9
2. Ramkrishna, D., Singh, M.R.: Population balance modeling: current status and future prospects. Ann. Rev. Chem. Biomol. Eng. **5**, 123–146 (2014)
3. Schwarzer, H.-C., Peukert, W.: Combined experimental/numerical study on the precipitation of nanoparticles. AIChE J. **50**(12), 3234–3247 (2004)
4. Sommer, M., Stenger, F., Peukert, W., Wagner, N.J.: Agglomeration and breakage of nanoparticles in stirred media mills—a comparison of different methods and models. Chem. Eng. Sci. **61**(1), 135–148 (2006)
5. Peglow, M., Kumar, J., Heinrich, S., Warnecke, G., Tsotsas, E., Mörl, L., et al.: A generic population balance model for simultaneous agglomeration and drying in fluidized beds. Chem. Eng. Sci. **62**(1–2), 513–532 (2007)
6. Kraft, M.: Modelling of particulate processes. KONA Powder Particle J. **23**, 18–35 (2005)
7. Kiparissides, C.: Challenges in particulate polymerization reactor modeling and optimization: a population balance perspective. J. Process. Control. **16**(3), 205–224 (2006)
8. Bhole, M.R., Joshi, J.B., Ramkrishna, D.: CFD simulation of bubble columns incorporating population balance modeling. Chem. Eng. Sci. **63**(8), 2267–2282 (2008)
9. Schütz, S., Gorbach, G., Piesche, M.: Modeling fluid behavior and droplet interactions during liquid–liquid separation in hydrocyclones. Chem. Eng. Sci. **64**(18), 3935–3952 (2009)

---

[4]The four case studies comprise: (1) a flowsheet without recycle stream and screen units, (2) a flowsheet with one recycle stream and without sieve unit, (3) a flowsheet with one sieve unit and without recycle stream and (4) a flowsheet with a recycle stream and a sieve unit.

10. Sanyal, J., Marchisio, D.L., Fox, R.O., Dhanasekharan, K.: On the comparison between population balance models for CFD simulation of bubble columns. Ind. Eng. Chem. Res. **44**(14), 5063–5072 (2005)

11. Cheng, J., Yang, C., Jiang, M., Li, Q., Mao, Z.-S.: Simulation of antisolvent crystallization in impinging jets with coupled multiphase flow-micromixing-PBE. Chem. Eng. Sci. **171**, 500–512 (2017)

12. Marchisio, D.L., Fox, R.O.: Solution of population balance equations using the direct quadrature method of moments. J. Aerosol Sci. **36**(1), 43–73 (2005)

13. Gavi, E., Marchisio, D.L., Barresi, A.A.: CFD modelling and scale-up of Confined Impinging Jet Reactors. Chem. Eng. Sci. **62**(8), 2228–2241 (2007)

14. Boje, A., Akroyd, J., Sutcliffe, S., Edwards, J., Kraft, M.: Detailed population balance modelling of TiO_2 synthesis in an industrial reactor. Chem. Eng. Sci. **164**, 219–231 (2017)

15. Szilágyi, B., Nagy, Z.K.: Population balance modeling and optimization of an integrated batch crystallizer-wet mill system for crystal size distribution control. Cryst. Growth Des. **18**(3), 1415–1424 (2018)

16. Hao, X., Zhao, H., Xu, Z., Zheng, C.: Population balance-Monte Carlo simulation for gas-to-particle synthesis of nanoparticles. Aerosol Sci. Technol. **47**(10), 1125–1133 (2013)

17. Irizarry, R.: Stochastic simulation of population balance models with disparate time scales: hybrid strategies. Chem. Eng. Sci. **66**(18), 4059–4069 (2011)

18. Dosta, M., Heinrich, S., Werther, J.: Fluidized bed spray granulation: analysis of the system behaviour by means of dynamic flowsheet simulation. Powder Technol. **204**(1), 71–82 (2010)

19. Skorych, V., Dosta, M., Hartge, E.-U., Heinrich, S.: Novel system for dynamic flowsheet simulation of solids processes. Powder Technol. **314**, 665–679 (2017)

20. Menz, W.J., Akroyd, J., Kraft, M.: Stochastic solution of population balance equations for reactor networks. J. Comput. Phys. **256**, 615–629 (2014)

21. Kruis, F.E., Wei, J., van der Zwaag, T., Haep, S.: Computational fluid dynamics based stochastic aerosol modeling: combination of a cell-based weighted random walk method and a constant-number Monte-Carlo method for aerosol dynamics. Chem. Eng. Sci. **70**, 109–120 (2012)

22. Zhao, H., Kruis, F.E., Zheng, C.: Reducing statistical noise and extending the size spectrum by applying weighted simulation particles in Monte Carlo simulation of coagulation. Aerosol Sci. Technol. **43**(8), 781–793 (2009)

23. Kotalczyk, G., Kruis, F.E.: A Monte Carlo method for the simulation of coagulation and nucleation based on weighted particles and the concepts of stochastic resolution and merging. J. Comput. Phys. **340**, 276–296 (2017)

24. Lin, Y., Lee, K., Matsoukas, T.: Solution of the population balance equation using constant-number Monte Carlo. Chem. Eng. Sci. **57**(12), 2241–2252 (2002)

25. Wei, J.: A fast Monte Carlo method based on an acceptance-rejection scheme for particle coagulation. Aerosol Air Quality Research **13**(4), 1273–1281 (2013)

26. Kotalczyk, G., Skenderovic, I., Kruis, F.E.: Modeling of particle formation in arc discharges by Monte-Carlo based population balance modeling. MRS. Adv. **148**, 1–8 (2017)

27. Kotalczyk, G., Skenderovic, I., Kruis, F.E.: Monte Carlo simulations of homogeneous nucleation and particle growth in the presence of background particles. Tellus, Ser. B. Chem. Phys. Meteorol. **71**(1), 1–10 (2019)

28. Vemury, S., Pratsinis, S.E.: Self-preserving size distributions of agglomerates. J. Aerosol Sci. **26**(2), 175–185 (1995)

29. Kodas, T.T., Hampden-Smith, M.J.: Aerosol Processing of Materials, Wiley-VCH (1999). ISBN 0471246697

30. Kotalczyk, G., Skenderovic, I., Kruis, F.E.: A GPU-based Monte Carlo technique for the simulation of simultaneous nucleation, coagulation and growth based on weighted simulation particles. In: AIChE Annual Meeting, pp. 490–497 (2016)

31. Press, W.H.: In: Numerical recipes: The Art of Scientific Computing, 3rd edn. Cambridge University Press (2007). ISBN 978-0521880688

32. Tsang, T.H., Rao, A.: Comparison of different numerical schemes for condensational growth of aerosols. Aerosol Sci. Technol. **9**(3), 271–277 (1988)

33. Wu, C.-Y., Biswas, P.: Study of numerical diffusion in a discrete-sectional model and its application to aerosol dynamics simulation. Aerosol Sci. Technol. **29**(5), 359–378 (1998)
34. Kumar, S., Ramkrishna, D.: On the solution of population balance equations by discretization – III. Nucleation, growth and aggregation of particles. Chem. Eng. Sci. **52**(24), 4659–4679 (1997)
35. Wyslouzil, B.E., Wölk, J.: Overview: homogeneous nucleation from the vapor phase—the experimental science. J. Chem. Phys. **145**(21) (2016)
36. Girshick, S.L., Chiu, C.-P.: Kinetic nucleation theory: a new expression for the rate of homogeneous nucleation from an ideal supersaturated vapor. J. Chem. Phys. **93**(2), 1273–1277 (1990)
37. Lide, D.R. (ed.): CRC Handbook of Chemistry and Physics: A Ready-Reference Book of Chemical and Physical Data, 85th edn. CRC Press, Boca Raton (2004)
38. Egry, I., Ricci, E., Novakovic, R., Ozawa, S.: Surface tension of liquid metals and alloys-recent developments. Adv. Coll. Interface. Sci. **159**(2), 198–212 (2010)
39. Mishra, B.K.: Monte Carlo simulation of particle breakage process during grinding. Powder Technol. **110**(3), 246–252 (2000)
40. Lee, K., Matsoukas, T.: Simultaneous coagulation and break-up using constant-N Monte Carlo. Powder Technol. **110**(1–2), 82–89 (2000)
41. Lee, K.F., Patterson, R.I.A., Wagner, W., Kraft, M.: Stochastic weighted particle methods for population balance equations with coagulation, fragmentation and spatial inhomogeneity. J. Comput. Phys. **303**, 1–18 (2015)
42. Zhao, H., Zheng, C., Xu, M.: Multi-Monte Carlo approach for general dynamic equation considering simultaneous particle coagulation and breakage. Powder Technol. **154**(2–3), 164–178 (2005)
43. Kotalczyk, G., Devi, J., Kruis, F.E.: A time-driven constant-number Monte Carlo method for the GPU-simulation of particle breakage based on weighted simulation particles. Powder Technol. **317**, 417–429 (2017)
44. Devi, J., Kotalczyk, G., Kruis, F.E.: Accuracy control in Monte Carlo simulations of particle breakage. Int. J. Model. Ident. Control **31**(3), 278–291 (2019)
45. Muscato, O., Di Stefano, V., Wagner, W.: A variance-reduced electrothermal Monte Carlo method for semiconductor device simulation. Comput. Math Appl. **65**(3), 520–527 (2013)
46. Ziff, R.M., McGrady, E.D.: The kinetics of cluster fragmentation and depolymerisation. J. Phys. A: Math. Gen. **18**(15), 3027–3037 (1985)
47. Celnik, M., Patterson, R.I.A., Kraft, M., Wagner, W.: Coupling a stochastic soot population balance to gas-phase chemistry using operator splitting. Combust. Flame **148**(3), 158–176 (2007)
48. Liffman, K.: A direct simulation Monte-Carlo method for cluster coagulation. J. Comput. Phys. **100**(1), 116–127 (1992)
49. Zhao, H., Maisels, A., Matsoukas, T., Zheng, C.: Analysis of four Monte Carlo methods for the solution of population balances in dispersed systems. Powder Technol. **173**(1), 38–50 (2007)
50. Wei, J.: A parallel Monte Carlo method for population balance modeling of particulate processes using bookkeeping strategy. Physica A **402**, 186–197 (2014)
51. Kotalczyk, G., Kruis, F.E.: Fractional Monte Carlo time steps for the simulation of coagulation for parallelized flowsheet simulations. Chem. Eng. Res. Des. **136**, 71–82 (2018)
52. Gelbard, F., Tambour, Y., Seinfeld, J.H.: Sectional representations for simulating aerosol dynamics. J. Colloid Interface Sci. **76**(2), 541–556 (1980)
53. Landgrebe, J.D., Pratsinis, S.E.: A discrete-sectional model for particulate production by gas-phase chemical reaction and aerosol coagulation in the free-molecular regime. J. Colloid Interface Sci. **139**(1), 63–86 (1990)
54. Marshall, C.L., Rajniak, P., Matsoukas, T.: Multi-component population balance modeling of granulation with continuous addition of binder. Powder. Technol. **236**, 211–220 (2013)
55. Khalili, S., Lin, Y., Armaou, A., Matsoukas, T.: Constant number Monte Carlo simulation of population balances with multiple growth mechanisms. AIChE J. **56**(12), 3137–3145 (2010)

56. Smith, M., Matsoukas, T.: Constant-number Monte Carlo simulation of population balances. Chem. Eng. Sci. **53**(9), 1777–1786 (1998)
57. Kotalczyk, G., Lambach, K., Kruis, F.E.: Parallel GPU-based monte carlo techniques for the flow-sheet simulation of solid processes. In: 8th World Congress on Particle Technology (2018)−Applications of Solids Processing Unit Operations, pp. 64–71
58. Kumar, S., Ramkrishna, D.: On the solution of population balance equations by discretization –I. A fixed pivot technique. Chem. Eng. Sci. **51**(8), 1311–1332 (1996)

Chapter 16
Modeling, Simulation and Optimization of Process Chains

Michele Spinola, Alexander Keimer, Doris Segets, Lukas Pflug, and Günter Leugering

Abstract Processes in the field of chemical engineering do not consist of one single step, but typically a high number of strongly interconnected unit operations linked with recycling streams. This inherent complexity further exacerbates when distributed particle properties, i.e., dispersity, must be considered, noteworthy being the case whenever particulate products are in focus. Out of all five possible dimensions of dispersity (size, shape, composition, surface and structure) particle size most often determines the efficiency of particulate products. Thus, its optimization is key to reach tailored handling and end product properties. In this work, a model-based optimization tool for particle synthesis was elaborated which is often the first step

M. Spinola
Department of Mathematics, Applied Analysis (Alexander von Humboldt-Professorship), Friedrich-Alexander-Universität Erlangen-Nürnberg (FAU), Cauerstraße 11, 91058 Erlangen, Germany
e-mail: michele.spinola@fau.de

A. Keimer
UC Berkeley, Institute of Transportation Studies (ITS), 109 McLaughlin Hall, Berkeley, CA 94720, USA
e-mail: keimer@berkeley.edu

D. Segets
Process Technology for Electrochemical Functional Materials, Institute for Combustion and Gas Dynamics-Reactive Fluids (IVG-RF), and Center for Nanointegration Duisburg-Essen (CENIDE), Carl-Benz-Straße 199, 47057 Duisburg, Germany
e-mail: doris.segets@uni-due.de

L. Pflug
Central Institute for Scientific Computing, Friedrich-Alexander-Universität Erlangen-Nürnberg (FAU), Martensstraße 5a, 91058 Erlangen, Germany
e-mail: lukas.pflug@fau.de

Department of Mathematics, Chair of Applied Mathematics (Continuous Optimization), Friedrich-Alexander-Universität Erlangen-Nürnberg (FAU), Cauerstraße 11, 91058 Erlangen, Germany

G. Leugering (✉)
Department of Mathematics, Applied Mathematics 2, Friedrich-Alexander-Universität Erlangen-Nürnberg (FAU), Cauerstraße 11, 91058 Erlangen, Germany
e-mail: guenter.leugering@fau.de

549

of a process chain. It is described by population balance equations relying on the method of characteristics for the numerical simulation and on the usage of gradient information to enhance the performance of the optimization. The presented scheme to optimize time-dependent process conditions in a time efficient manner is applicable for a wide range of particle syntheses.

Keywords Ripening · Method of characteristics · Population balance equation · Gradient-based optimization · Sensitivity · Adjoint

1 Introduction

Process conditions of most nanoparticle syntheses can be adjusted over time. In order to achieve high quality particulate products, the question arises how to optimize synthesis processes by their process conditions. Model-based optimization of process conditions and an efficient, gradient based concept for this will be focused in this work.

For example, in the last decades, the class of quantum dots emerged. Due to their semiconductor properties, they play an important role in the field of nanoparticle technology. There, many issues regarding process design and the production on higher scales arised which are still not fully covered [1–3]. Several contributions such as [4–10] showed that the development of disperse properties during a chemical process can mathematically be described by population balance equations (PBEs). Due to their general formulation, PBEs are suitable to appropriately describe the evolution of disperse properties of the mentioned sub-10 nm particles due to ripening [11–16]. Originally, PBEs were used to model growth mechanisms operating outside of the nanoregime. For instance, fluidized bed spray granulation (FBSG), crystallization and aggregation [17–19], a.o., can be depicted by this modeling. PBEs also allow to track the dispersity in all five dimensions, i.e., size, shape, surface, composition and structure, during the process (cf. [20]). Even though growth dynamics of the particles can be described appropriately by means of PBEs, in general the modeling of process chains with interconnected reaction modules is a complex issue to solve (cf. [21]). This becomes especially challenging when process conditions are considered which are varied in course of time, such as feeding rates of new nuclei into reaction systems or process-temperature profiles (see Fig. 1). The corresponding mathematical model consists of systems of nonlinear, fully coupled differential equations. Thus, on the one hand, numerical methods are strongly required not only to simulate the development of the synthesis process and to predict its further development but also to enable the path towards a model-based optimization (cf. [22]).

In literature, essentially three categories of methods for the numerical approximation of balance laws are discussed [23]. The first and most widespread are finite volume type methods or in more generality, discontinuous Galerkin type approaches on a—with respect to process time—fixed discretization of the spatial as well as disperse coordinates [24–28]. The second category is a class of methods which rely
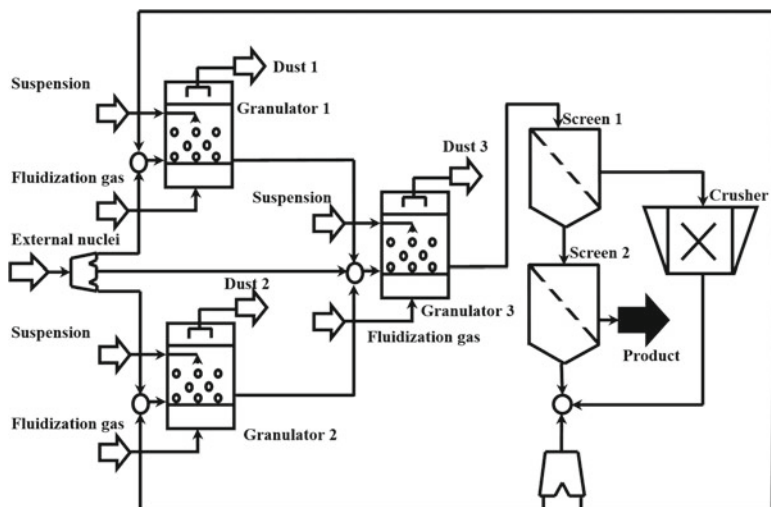
Fig. 1 Granulation as an example for an interconnected solid production process chain with recycling streams (adapted from [21, Fig. 1b])

on the method of characteristics. These methods are in terms of accuracy superior to finite volume methods as they are not prone to numerical diffusion [29–31]. The third category is a class based on the method of moments of the distribution [6]. In terms of computational efficiency, they are by far superior to the two aforementioned types of methods but, as they only compute moments of the mathematical solution, they do not provide access to the fully distributed information itself [32]. Depending on the dominating character of the PBE which can be parabolic or hyperbolic, among the first two alternatives, the finite volume method or the method of characteristics are preferable. As compared in [33, Fig. 3], in the absence of agglomeration and diffusion the method of characteristics is by far superior.

Despite the fact that optimization relying on gradient information is recommendable if differentiable numerical schemes are provided (e.g. optimization of single hyperbolic balance laws [34, 35] as well as networks of these [36]), in the context of particle synthesis they are applied only in specific cases. In the literature, optimization is exemplarily done by using collocation methods on finite elements (e.g. [37]), model-predictive techniques for a quadratic cost functional (in [38]), or based on moments of particle size distributions (PSDs), e.g. as in [39, 40]. In the last mentioned method it is possible to determine the therein considered PSDs by only a few moments, which unfortunately does not hold for every synthesis process.

For a majority of optimization problems, gradient-free schemes as in [41] or parameter studies are the commonly chosen approaches. Actually, when assuming that process conditions hardly change over time, these methods can be exploited successfully as described in [22]. However, the presence of time-dependent process conditions in established complex synthesis procedure increases the number of

degrees of freedom significantly such that gradient-free optimization methods lead to large computation times.

Thus, here, a numerical tool relying on the method of characteristics which provides a numerical approximation of the development of the synthesis process with high accuracy was combined with a sensitivity-based optimization ansatz in which a fast computation of gradient information is provided. By this method, optimal process conditions within interconnected process chains were determined. It further reduced the mentioned computational times, also in the case of time-dependent process parameters.

In the following, the proposed optimization method, which can be applied for a variety of optimization problems within chemical engineering, will be pointed out in detail. At first, the underlying mathematical model for processes in which seeded growth occurs, will be presented and the numerical scheme will be outlined. This is based on the method of characteristics which depicts the evolution of the PSD in a natural way due to the incorporated conservation property and the hyperbolic behavior of the corresponding PBE.

Relying on this scheme for the simulation of the state equation, i.e., the considered PBE, a so-called adjoint equation was provided to require gradient information for the here used optimization method instead of using the gradient by commonly-used finite differences methods. Compared to finite differences methods and to gradient-free approaches, applying this method to reaction plants, this enables the calculation of optimal time-varying process conditions by far faster since only two equations have to solved, the state equation and the adjoint equation. [42–44] also provided an optimization method relying on adjoint equations. However, no explicit applications are outlined in [42, 43]. In opposite to this contribution, no optimization of complex process chains was performed in [44].

To show the broad applicability of this approach, a range of synthesis processes with different growth dynamics, optimization goals and also containing process chains with recycling streams were considered. These examples justify the usage of the here presented model-based optimization technique in the context of particle synthesis, especially when only time-varying process conditions yield optimal PSDs.

2 Mathematical Model and Gradient-Based Optimization Framework

This work aims to determine several time-varying process conditions simultaneously which will yield optimal results for the corresponding synthesis processes. Before proposing a mathematical formulation of the optimization approach, first, the mathematical model for the development of PSDs will be stated, which is done in the following primal equation (1):

$$q_t(t, \boldsymbol{x}) + \nabla_{\boldsymbol{x}} \cdot \big(\mathbf{G}\big(u_{\mathbf{G}}(t), W_q(t), t, \boldsymbol{x}\big) q(t, \boldsymbol{x})\big) = u_{\mathrm{in}}(t) q_{\mathrm{in}}(\boldsymbol{x}) - u_{\mathrm{out}}(t) q(t, \boldsymbol{x})$$

$$q(0, \boldsymbol{x}) = u_0 q_0(\boldsymbol{x})$$

$$W_q(t) := \iint_{\Omega} \gamma(\boldsymbol{y}) q(t, \boldsymbol{y}) \, \mathrm{d}\boldsymbol{y}$$

$$(1)$$

For $(t, \boldsymbol{x}) \in (0, t_{\mathrm{f}}) \times \Omega$ with $\Omega := \{\boldsymbol{x} \in \mathbb{R}^n : \boldsymbol{x} \geq \boldsymbol{x}_{\min}\}$ and $\boldsymbol{x}_{\min} \in \mathbb{R}^n$. Throughout this contribution, bold symbols are used for vectors. The term $\mathbf{G}$ denotes the growth velocity which can be affected by the time-dependent process condition $u_{\mathbf{G}}$ over time, i.e., such as process temperature or mass fluxes. Also influx of new particles with PSD q_{in} with influx rate u_{in} and extraction of particles out of the system with extraction rate u_{out} are incorporated into this model. u_0 represents a scaling factor of q_0, i.e., of the initial PSD. The crucial dependence of the synthesis rate with respect to the amount of produced particles is given by the term W_q which e.g. describes the total surface ($\gamma(x) = 4\pi x^2$, see e.g. [45, Eq. 6]), or mass ($\gamma(x) = \frac{4}{3}\pi x^3$, see e.g. [22, Eq. 2]). As W_q depends in an integral way on the solution q, W_q will be called a nonlocal term. For this system of equations a solution theory was developed, which also shows mathematical well-posedness for very general settings (cf. [46, 47]).

By the following optimization problem, a mathematical formulation of the considered task relying on (1) will be introduced. The therein used general notation allows to provide a framework for optimization within particle synthesis with two main advantages: First, by (1), the evolution of PSDs is tracked, different growth dynamics and inflow and outflow terms are incorporated into the model. Thus, not only single reaction modules can be considered but also more complex process chains. Second, a high variety of optimization tasks can be treated such as, for instance:

1. Minimizing the difference between the resulting PSD and a target PSD.
2. Reaching a preferably monodisperse PSD with a given diameter.
3. Maximizing the yield of the total product.

Moreover, it is also possible to include monetary cost terms into the framework. This is crucial when it is desired to simultaneously reach multiple targets which can contradict each other: For instance, maximizing the quality of goods and minimizing the costs caused due to energy consumption or improving the CO_2 footprint. Together with the precise numerical discretization method for the state equation, the mathematical optimization framework demonstrated in this work can handle a high amount of different established optimization issues within the area of process engineering and (nano)particle technology.

As already mentioned, this contribution focuses on the subsequent optimization problem which requires information resulting from the PSD described by (1):

$$\left.\begin{array}{r} \min\limits_{(u_\mathbf{G}, u_{\mathrm{in}}, u_{\mathrm{out}}, u_0) \in U_{\mathrm{ad}}} J[q, q(t_{\mathrm{f}}, \cdot)] \quad \text{s.t.} \quad q \text{ solves (PRI)} \quad \text{with} \\[2mm] U_{\mathrm{ad}} := \Big\{ (u_\mathbf{G}, u_{\mathrm{in}}, u_{\mathrm{out}}, u_0) \ : \ u_\mathbf{G}(t) \in [\underline{u_\mathbf{G}}, \overline{u_\mathbf{G}}], u_{\mathrm{in}}(t) \in [\underline{u_{\mathrm{in}}}, \overline{u_{\mathrm{in}}}], \\[2mm] u_{\mathrm{out}}(t) \in [\underline{u_{\mathrm{out}}}, \overline{u_{\mathrm{out}}}] \ \forall t \in [0, t_{\mathrm{f}}], u_0 \in [\underline{u_0}, \overline{u_0}] \Big\}. \end{array}\right\} \quad (2)$$

Since in real-world applications process conditions cannot reach any arbitrary values, e.g. due to technical or chemical restrictions, in U_{ad} box constraints on the process conditions are imposed which have to be set in agreement to the considered process. By putting information of the resulting PSD, either over the whole time horizon or at final time, into the cost functional J, a quantification of the quality of the synthesized particles will be obtained which can now be optimized.

In the context of optimizing cost functionals which depend on the solution of a PBE, which is the case in this article, an established and promising ansatz is the derivation of adjoint equations [48, 49]. These equations require data given out of (1) and due to the therein incorporated nonlocal term, this leads to (3), a linear transport equation backwards in time with a nonlocal term contributing to the source terms of this partial differential equation. Together with the characteristic function of Ω, denoted by χ_Ω, it leads to the following formulation:

$$\left.\begin{array}{r} p_t(t, \boldsymbol{x}) + \mathbf{G}\big(u_\mathbf{G}(t), W_q(t), t, \boldsymbol{x}\big)\nabla_{\boldsymbol{x}} p(t, \boldsymbol{x}) = -J_q[q, q(t_{\mathrm{f}}, \cdot)](t, \boldsymbol{x}) \\[2mm] + u_{\mathrm{out}}(t) p(t, \boldsymbol{x}) \\[2mm] - \gamma(\boldsymbol{x})\chi_\Omega(\boldsymbol{x}) Y_p(t, \boldsymbol{x}) \\[2mm] p(t_{\mathrm{f}}, \boldsymbol{x}) = J_{q(t_{\mathrm{f}}, \cdot)}[q, q(t_{\mathrm{f}}, \cdot)](t_{\mathrm{f}}, \boldsymbol{x}). \\[2mm] Y_p(t, \boldsymbol{x}) := \iint\limits_\Omega \mathbf{G}_{W_q}\big(u_\mathbf{G}(t), W_q(t), t, \boldsymbol{y}\big)q(t, \boldsymbol{y}) \cdot \nabla_{\boldsymbol{x}} p(t, \boldsymbol{y}) \, \mathrm{d}\boldsymbol{y} \end{array}\right\}$$

$$(3)$$

For $(t, \boldsymbol{x}) \in (0, t_{\mathrm{f}}) \times \Omega$. By speaking in terms of flowsheets and modularization of process plants as in [21], the dynamics incorporated in the adjoint equations allow these to be interpreted as "reactors". This means that at least in a structural way, adjoint equations can be included in process chains. Thus, two key elements, namely (1) and (3), for the determination of gradient information of an optimization problem can be depicted within a single flowsheet. This is illustrated in Fig. 2.

For the optimization method executed in this contribution, the sensitivity of the cost functional J with respect to the process conditions $(u_\mathbf{G}, u_{\mathrm{in}}, u_{\mathrm{out}}, u_0) \in U_{\mathrm{ad}}$ is required to determine how to adapt these optimization parameters such that J decreases up to a minimal value. This gradient can be written by means of the adjoint state p of (3) in the subsequent way:
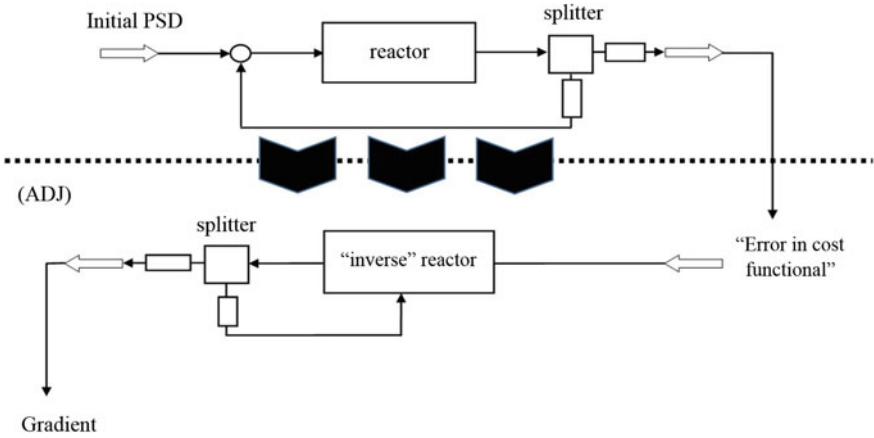
(PRI)

Fig. 2 Flowsheet representation of the calculation of the gradient of a cost functional with respect to process conditions. Above the dotted line, a reactor with splitter adjusting the proportion of recycling and generating information regarding the "error in cost functional" is shown. The latter together with the solution of (1) itself serve as input for the "inverse reactor", representing the dynamics in (3) backwards in time. The following splitter leads to a recycling of information into the system and generates the required data for the required gradient

$$\frac{d}{du_G} J[q, q(t_f, \cdot)](t) = \partial_{u_G} J[q, q(t_f, \cdot)](t)$$
$$+ \iint_\Omega \nabla_x p(t, x) \cdot \mathbf{G}_{u_G}\big(u_G(t), W_q(t), t, x\big) q(t, x) \, dx$$

$$\frac{d}{du_{in}} J[q, q(t_f, \cdot)](t) = \partial_{u_{in}} J[q, q(t_f, \cdot)](t) + \iint_\Omega p(t, x) q_{in}(x) \, dx$$

$$\frac{d}{du_{out}} J[q, q(t_f, \cdot)](t) = \partial_{u_{out}} J[q, q(t_f, \cdot)](t) - \iint_\Omega p(t, x) q(t, x) \, dx$$

$$\frac{d}{du_0} J[q, q(t_f, \cdot)] = \partial_{u_0} J[q, q(t_f, \cdot)] + \iint_\Omega p(0, x) q_0(x) \, dx$$

For $t \in (0, t_f)$. Due to the previous mathematical models, the first preliminaries are set to derive a numerical implementation of the optimization. Figure 3 shows the outline of the method. It consists of iteratively updating the process conditions such that the value of the cost functional will be diminished at every step up to the point where first-order optimality conditions are finally fulfilled. This means that the gradient of J with respect to an optimization parameter u has to vanish, i.e., $\frac{d}{du} J = 0$. If box constraints occur, then the projected gradient has to vanish (cf. [48, Chap. 5]).

Fig. 3 Scheme of gradient-based optimization framework
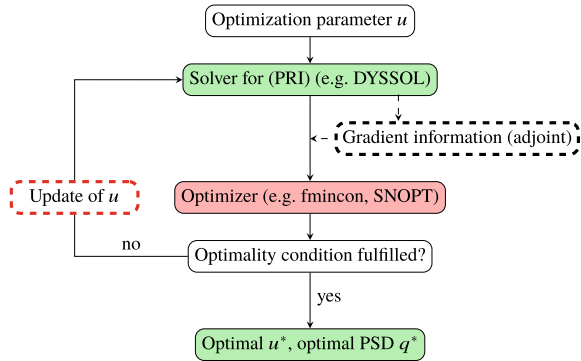
Gradient information are used to guarantee a sufficient descent of the cost functional. In this case, the computation of the gradients are done by using adjoint equations.

By speaking of efficiency, one major advantage of the adjoint method can be stated: The low computational costs for a high number of optimization parameters. The previous four derivatives state that for the computation of the gradient only two partial differential equations have to be solved, namely (1) and (3), once, respectively. The difference in computational effort between finite differences methods and the adjoint method becomes even more noticeable when process conditions can change over time. This is true for $(u_{\mathrm{G}}, u_{\mathrm{in}}, u_{\mathrm{out}})$ since, in contrast to finite differences methods, the adjoint approach is invariant with respect to the number of discretization points of the optimization parameters.

3 Numerical Scheme

Due to the extraordinary relevance of particle size for the quality of the final product, this and the following sections focus on the one-dimensional case of (1) with a positive, small $x_{\min}$ and $\Omega := \mathbb{R}_{>x_{\min}}$. A key element for this is the consideration of so-called characteristic curves ξ. Roughly speaking and as demonstrated in Fig. 4, these curves denote the trajectories on which particles are growing over time. These characteristics are from a mathematical standpoint a system of ordinary differential equations coupled by the growth dynamics G and thus by the nonlocal term W_q:

$$\dot{\xi}[t, x](\tau) = G(u_{\mathrm{G}}, W_q(t), t, \xi[t, x](\tau))$$
$$\xi[t, x](t) = x.$$

An important aspect of these characteristics is that between them the number of particles is conserved when no influx of new particles and extraction of produced particles occur, i.e., it holds for a set $S_1 \subset \mathbb{R}^n$:
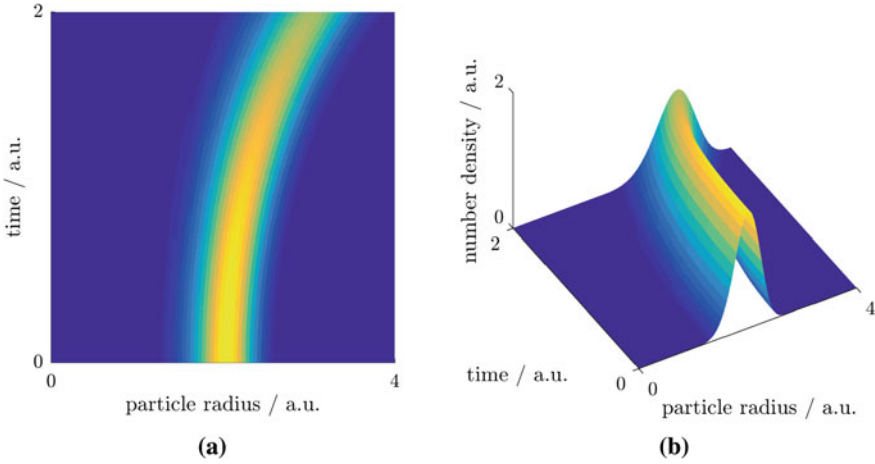
Fig. 4 Graphical illustration of the method of characteristics: characteristics (**a**) and resulting PSD (**b**)

$$\int\limits_{\xi[t,S_1](t)} q(t, y)\,\mathrm{d}y = \int\limits_{S_1} q_0(y)\,\mathrm{d}y.$$

More general, for a set $S_2 \subset \mathbb{R}^n$ the following is true:

$$\frac{\mathrm{d}}{\mathrm{d}t}\int\limits_{S_2} q(t, y)\,\mathrm{d}y = \int\limits_{S_2} q_t(t, y)\,\mathrm{d}y = \int\limits_{S_2} u_{\mathrm{in}}(t)q_{\mathrm{in}}(y) - u_{\mathrm{out}}(t)q(t, y)\,\mathrm{d}y.$$

Based on this conservation principle, the numerical scheme, also presented in [50], will be illustrated which encodes the evolution of the PSD in a precise way over time. At first, a semi-discretization of the required solutions and gradients will be considered, i.e., a discretization only in the disperse property whereas the time variable remains a continuous variable. After this, an arbitrary time-step method can be used to solve the system of ordinary differential equations in time. The convergence rate of the fully discretized optimization problem also depends on the chosen time-step method. However, for the here considered equations, the usage of the well-known explicit Euler method is reasonable. Starting with the semi-discretization of (1), $[x_{\min}, x_L] \subset \mathbb{R}$ where x_L is a sufficiently large number will be discretized by a K-point grid $\{x_1, \dots, x_K\}$ with $K \in \mathbb{N}_{\geq 2}$. With the approximations:

$$\xi \approx \hat{\xi}, \qquad W_q \approx \hat{W}_q, \qquad q \approx \hat{q}.$$

This yields the following numerical scheme for $t \in [0, t_f]$:

$$\dot{\hat{\xi}}_k(t) = \mathrm{G}(u_\mathrm{G}(t), \hat{W}_q(t), t, \hat{\xi}_k(\tau)) \qquad\qquad\qquad k \in \{1, \dots, K\}$$

$$\dot{q}_k(t) := u_\mathrm{in}(t) \int_{\hat{\xi}_k(t)}^{\hat{\xi}_{k+1}(t)} q_\mathrm{in}(y)\,\mathrm{d}y - u_\mathrm{out}(t)q_k(t) \qquad\qquad k \in \{1, \dots, K-1\}$$

$$\hat{W}_q(t) := \sum_{k=1}^{K-1} \frac{q_k(t)}{\hat{\xi}_{k+1}(t) - \hat{\xi}_k(t)} \int_{x_\mathrm{min}}^{\infty} \gamma(y)\chi_{(\hat{\xi}_k(t),\hat{\xi}_{k+1}(t))}(y)\,\mathrm{d}y$$

Such that the piecewise constant approximation of q is given by:

$$\hat{q}(t, x) := \sum_{k=1}^{K-1} \frac{q_k(t)}{\hat{\xi}_{k+1}(t) - \hat{\xi}_k(t)} \chi_{(\hat{\xi}_k(t),\hat{\xi}_{k+1}(t))}(x).$$

In the following, a semi-discretization of p solving (3) will be formulated. $\nabla_x p$ contributes to the gradient of J with respect to process conditions. Thus, a piecewise linear semi-discretization of p was chosen. p will be considered along the characteristic curves and this leads to the following approximation for every $t \in [0, t_\mathrm{f}]$, $k \in \{1, \dots, K\}$:

$$p(t, \xi[0, x_k](t)) \approx \hat{p}_k(t)$$

Which yields an approximation of p at final time:

$$\hat{p}_k(t_\mathrm{f}) = J_{q(t_\mathrm{f}, \cdot)}[\hat{q}, \hat{q}(t_\mathrm{f}, \cdot)](t_\mathrm{f}, \hat{\xi}_k(t_\mathrm{f})).$$

By the fundamental theorem of calculus, it holds for $t \in [0, t_\mathrm{f}]$:

$$\hat{p}_k(t) = \hat{p}_k(t_\mathrm{f}) - \int_t^{t_\mathrm{f}} \frac{\mathrm{d}}{\mathrm{d}t}\hat{p}_k(s)\,\mathrm{d}s.$$

Moreover, by computing the total derivative of $p(t, \xi[0, x_k](t))$ with respect to t, the partial differential equation in (3) yields:

$$\frac{\mathrm{d}}{\mathrm{d}t} p(t, \xi[0, x_k](t)) = -J_q[q, q(t_\mathrm{f}, \cdot)](t, \xi[0, x_k](t)) + u_\mathrm{out}(t)p(t, \xi[0, x_k](t))$$
$$- \gamma(\xi[0, x_k](t))\chi_\Omega(\xi[0, x_k](t))Y_p(t, \xi[0, x_k](t)).$$

Combining both, gives an approach to approximate p also for $t \in [0, t_\mathrm{f}]$:

$$\hat{\boldsymbol{p}}_k(t) = \hat{\boldsymbol{p}}_k(t_{\mathrm{f}}) + \int_t^{t_{\mathrm{f}}} J_q[\hat{q}, \hat{q}(t_{\mathrm{f}}, \cdot)](s, \hat{\boldsymbol{\xi}}_k(s)) + \gamma(\hat{\boldsymbol{\xi}}_k(s))\chi_\Omega(\hat{\boldsymbol{\xi}}_k(s))\hat{Y}_p(s)\,\mathrm{d}s$$

$$- \int_t^{t_{\mathrm{f}}} u_{\mathrm{out}}(s)\,\hat{\boldsymbol{p}}_k(s)\,\mathrm{d}s$$

$$\hat{Y}_p(t) = \sum_{k=1}^{K-1} \frac{1}{2}\left(\frac{q_{k-1}(t)(\hat{\boldsymbol{p}}_{k-1}(t)+\hat{\boldsymbol{p}}_k(t))}{\hat{\boldsymbol{\xi}}_k(t)-\hat{\boldsymbol{\xi}}_{k-1}(t)} + \frac{q_k(t)(\hat{\boldsymbol{p}}_k(t)+\hat{\boldsymbol{p}}_{k+1}(t))}{\hat{\boldsymbol{\xi}}_{k+1}(t)-\hat{\boldsymbol{\xi}}_k(t)} \right)\mathrm{G}_{W_q}\left(u_{\mathrm{G}}(t), \hat{W}_q(t), t, \hat{\boldsymbol{\xi}}_k(t) \right)$$

Where additionally it has to be set:

$$\hat{\boldsymbol{p}}_0 := \hat{\boldsymbol{p}}_1, \qquad \hat{\boldsymbol{p}}_{K+1} := \hat{\boldsymbol{p}}_K, \qquad \hat{q}_0 := 0, \qquad \hat{\boldsymbol{\xi}}_0 < \hat{\boldsymbol{\xi}}_1.$$

The approximated solution of the adjoint equation $\hat{p}$ can now be obtained as piecewise linear interpolation of $\hat{\boldsymbol{p}}_k(t)$ on the points $\hat{\boldsymbol{\xi}}_k(t)$. Denote the semi-discretization of the gradient of the cost functional for a process condition u by $\frac{\mathrm{d}}{\mathrm{d}u}\hat{J}$. Together with $\hat{q}$ and $\hat{p}$, the semi-discretized gradients can be formulated as follows:

$$\frac{\mathrm{d}}{\mathrm{d}u_{\mathrm{G}}}\hat{J}(t) = \partial_{u_{\mathrm{G}}} J[\hat{q}, \hat{q}(t_{\mathrm{f}}, \cdot)](t)$$
$$+ \sum_{k=1}^{K-1} \frac{1}{2}\left(\frac{q_{k-1}(t)(\hat{\boldsymbol{p}}_{k-1}(t)+\hat{\boldsymbol{p}}_k(t))}{\hat{\boldsymbol{\xi}}_k(t)-\hat{\boldsymbol{\xi}}_{k-1}(t)} + \frac{q_k(t)(\hat{\boldsymbol{p}}_k(t)+\hat{\boldsymbol{p}}_{k+1}(t))}{\hat{\boldsymbol{\xi}}_{k+1}(t)-\hat{\boldsymbol{\xi}}_k(t)} \right)\mathrm{G}_{u_{\mathrm{G}}}\left(u_{\mathrm{G}}(t), \hat{W}_q(t), t, \hat{\boldsymbol{\xi}}_k(t) \right)$$

$$\frac{\mathrm{d}}{\mathrm{d}u_{\mathrm{in}}}\hat{J}(t) = \partial_{u_{\mathrm{in}}} J[\hat{q}, \hat{q}(t_{\mathrm{f}}, \cdot)](t) + \sum_{k=1}^{K-1} \frac{1}{2}(\hat{\boldsymbol{p}}_k(t) + \hat{\boldsymbol{p}}_{k+1}(t)) \int_{\hat{\boldsymbol{\xi}}_k(t)}^{\hat{\boldsymbol{\xi}}_{k+1}(t)} q_{\mathrm{in}}(y)\,\mathrm{d}y$$

$$\frac{\mathrm{d}}{\mathrm{d}u_{\mathrm{out}}}\hat{J}(t) = \partial_{u_{\mathrm{out}}} J[\hat{q}, \hat{q}(t_{\mathrm{f}}, \cdot)](t) - \sum_{k=1}^{K-1} \frac{1}{2}(\hat{\boldsymbol{p}}_k(t) + \hat{\boldsymbol{p}}_{k+1}(t))\hat{q}_k(t)$$

$$\frac{\mathrm{d}}{\mathrm{d}u_0}\hat{J}(t) = \partial_{u_0} J[\hat{q}, \hat{q}(t_{\mathrm{f}}, \cdot)] + \sum_{k=1}^{K-1} \frac{1}{2}(\hat{\boldsymbol{p}}_k(0) + \hat{\boldsymbol{p}}_{k+1}(0)) \int_{\hat{\boldsymbol{\xi}}_k(0)}^{\hat{\boldsymbol{\xi}}_{k+1}(0)} q_0(y)\,\mathrm{d}y.$$

Finally, in order to compare optimization results for time-dependent process conditions u for constant and nonconstant instantiations, the number of discretization points is defined by $d(u) \in \mathbb{N}$. By this, the time interval $[0, t_{\mathrm{f}}]$ will be discretized into $d(u)$ points t_i, $i \in \{1, \ldots, d(u)\}$, and the discretization of u is defined as the piecewise linear interpolation of $u(t_i)$. For a better readability and whenever it is clear which process condition u will be considered, the argument in $d(u)$ will be neglected.

4 Numerical Study

In this section, the outlined scheme for gradient approximation will be applied on four examples. There synthesis processes and optimization goals are altered and corresponding numerical results are shown. The first two deal with reaching desired monomodal and bimodal PSDs, respectively, in a FBSG-like system. The third one aims to obtain a monodisperse PSD in an Ostwald ripening like module. Eventually, the last example considers a cycled process chain containing a FBSG-like module and milling module. Furthermore, it has to be mentioned that even though the processes in Sects. 4.3 and 4.4 cannot directly be represented by (1), the model can also be extended to include these cases. For sake of a clearer illustration of the concepts, the already stated (1) was chosen as the model depicting seeded growth processes. At specific points, it is necessary to distinguish between the development of a PSD on a whole time horizon and the corresponding PSD at a certain point in time. Thus, for sake of a more precise notation, the "dot notation" will be introduced: If q denotes the evolution of a PSD over $[0, t_f]$, the underlying PSD at time t of q is denoted by $q(t, \cdot)$.

4.1 Fluidized Bed Spray Granulation: Reaching Desired Monomodal PSDs

In this example, the underlying growth dynamics is chosen as it is typical for FBSG (cf. [19]). Here, u_G denotes the effective solid mass flux for the granulation process that can be continuously adjusted. It is assumed that external nuclei with PSD q_{in} flow into the system over time by the rate u_{in}. In the following, the relative standard deviation (RSD) of a PSD is needed. The RSD is defined as $\frac{\sigma}{\mu}$ with the standard deviation σ and mean particle size μ of a given PSD. Here, q_{in} has a mean radius of 2 mm and a RSD of 10 %. Considering the process on the time interval $[0, t_f]$ with $t_f = 1$ h, the goal is to reach a desired monomodal PSD q_d at final time t_f. This can be modeled by the subsequent framework:

$$\min_{(u_G, u_{in}) \in U_{ad}} \int_{x_{min}}^{\infty} |q(t_f, x) - q_d(x)|^2 \, dx + 10^{-3} \left(\|u_G\|_{H^1((0,t_f))}^2 + \|u_{in}\|_{H^1((0,t_f))}^2 \right) \quad \text{s.t.}$$

$$q_t(t, x) + \partial_x \left(\frac{100 u_G(t)}{100 + W_q(t)} q(t, x) \right) = u_{in}(t) q_{in}(x)$$

$$q(0, x) = q_0(x)$$

$$W_q(t) := \int_{x_{min}}^{\infty} 4\pi y^2 q(t, y) \, dy$$

$$U_{ad} := \left\{ (u_G, u_{in}) \ : \ u_G(t) \in [0, 50], u_{in}(t) \in [0, 6] \ \forall t \in [0, t_f] \right\}.$$

After having formulated the mathematical setting, the numerical results for this will be focused in the following. In order to obtain a convenient graphical illustration of the methods, the constant process conditions $(u_G, u_{in}) = (40, 4)$ will be used in Fig. 5. Figure 5a shows that a sufficiently precise approximation of the analytical solution was obtained. This advantage is due to the choice of the method of characteristics as discretization scheme.

Moreover, not only a suitable numerical approximation of the solution q of the state equation but also of the gradient are required. In Fig. 5b, c the gradient for the process conditions (u_G, u_{in}) will be compared. As illustrated there, also for a
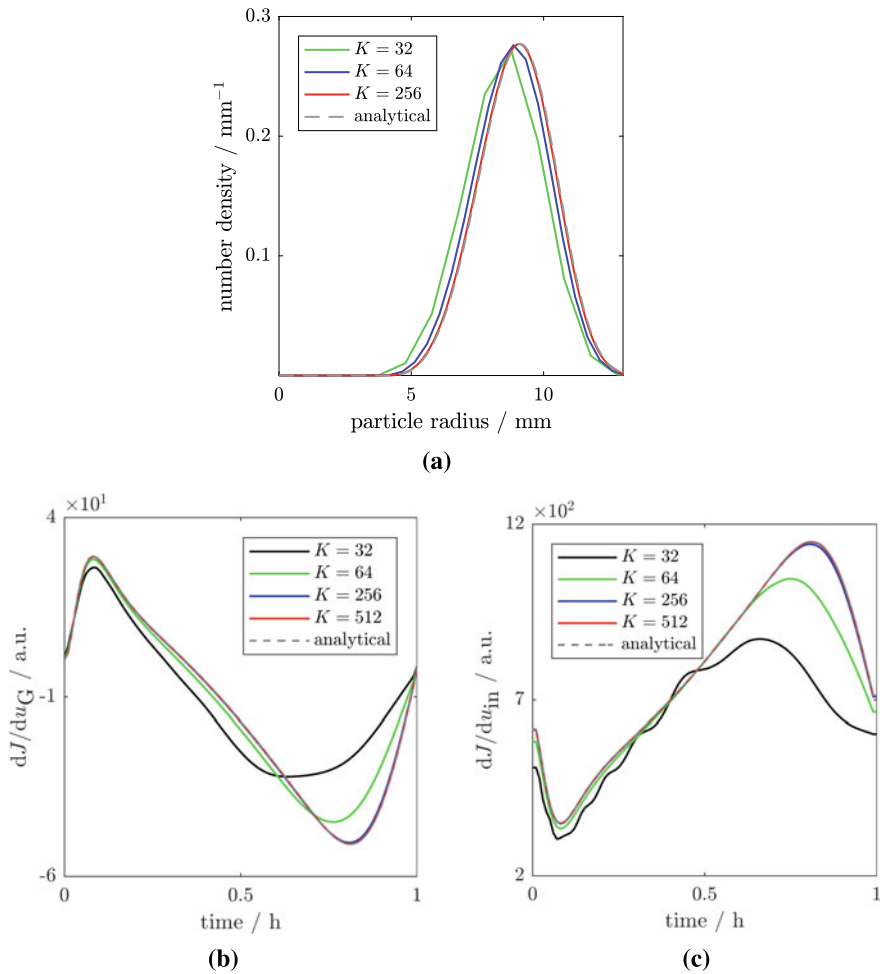

Fig. 5 Solution for different numbers K of grid points (**a**) and the gradients of the cost functional J with respect to process parameters u_G (**b**) and u_{in} (**c**) derived with different number K of grid points
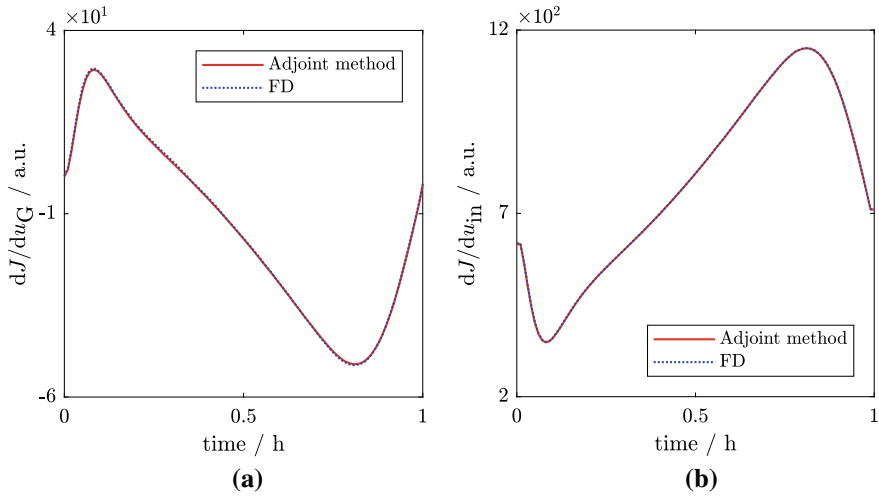
Fig. 6 Gradients of the cost functional J with respect to process parameters u_G (**a**) and u_{in} (**b**) derived both by finite differences and adjoint method

small number K of grid points a good agreement with the analytical gradient can be observed for both process conditions. Thus, the numerical scheme based on the method of characteristics yields an efficient discretization of the considered optimization problem.

Now it will be demonstrated that, as stated before, the representation of the gradient by the adjoint equation is indeed true, i.e., that actually the same results were obtained when using finite differences instead. 100 is chosen as number of discretization points for u_G and u_{in}, respectively, and the gradient is calculated on the one hand by (3) and on the other hand by commonly used finite differences. Figure 6 shows that the the resulting functions obtained by the two approaches highly coincide. Furthermore, for every gradient only (1) and (3) had to be calculated once in contrast to finite differences where 101 times (1) had to be solved. Thus, the adjoint method is the by far more efficient ansatz for gradient-based optimization when focusing on computational time which will be pointed out in the following more precisely.

After having demonstrated the applicability of the discretization schemes, the results obtained by different numbers of discretization points of the process conditions are illustrated and discussed. For both u_G, u_{in} the same number of discretization points were chosen, so $(d(u_G) = d(u_{in}))$. Figure 7 shows for different d the development of the relative cost functional with respect to the number of function evaluations. This number directly corresponds to computational time. In Fig. 7, finite differences (dotted lines) and adjoint equations (straight lines) are respectively used. There, the relative cost functional value is with respect to the value obtained by the constant optimization, so where only constant u_G, u_{in} are considered (i.e., $(d(u_G), d(u_{in})) = (1, 1)$). The log-log-plot shows multiple statements. First, the larger d is, the more the relative cost functional decreases with respect to the
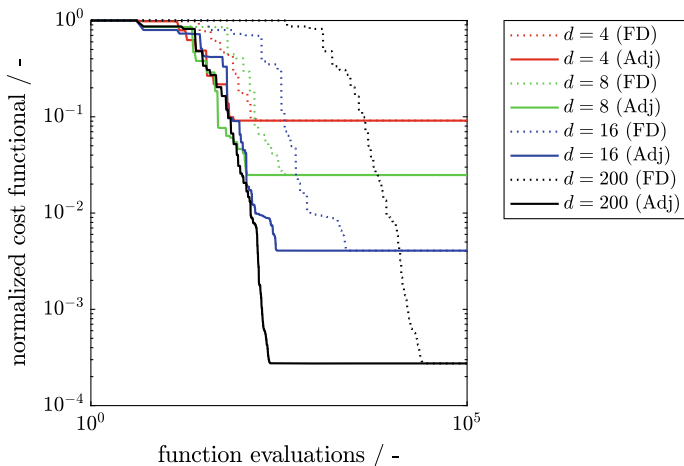
Fig. 7 Reduction of the cost functional value during the optimization using finite differences and the adjoint by increasing the number $(d(u_G), d(u_{in}))$ of discretization points of u_G and u_{in}. The normalization is with respect to the value in the constant optimization. The number of function evaluations corresponds to computational time

constant optimization. This is due to the fact that enlarging $d(u)$ increases the range of realizable process conditions. Second, both methods reach the same value since they differ only in the approximation of the same gradient. In every case a reasonable error tolerance in the optimality condition was chosen as stopping criterion.

And the last but most important aspect is, again, that each of the obtained optimal values is reached in the adjoint method with less function evaluations than with finite differences. The gap in the different computational costs increases with a larger d and becomes significant as can be seen at the logarithmically scaled abscissa. Figure 8a and b illustrate for different d the corresponding process conditions together with the optimal ones (red lines). Both graphics show that in this example small numbers of discretization points yield a visible difference to the optimized process condition. Figure 8c illustrates that this results in a significant deviation of the target PSD q_d which is only reached by the optimized PSD represented by the red curve. This PSD is generated by the optimal time-varying process conditions (u_G, u_{in}). The surface plot of the final optimized PSD is presented in Fig. 8d. In conclusion, these results show that for solving this optimization task, the adjoint method is the preferable one.

4.2   Fluidized Bed Spray Granulation: Reaching Desired Bimodal PSDs

This example yields an extension of the results obtained in Sect. 4.1. The same setup as in there will be considered but the desired PSD q_d is bimodal. As discussed
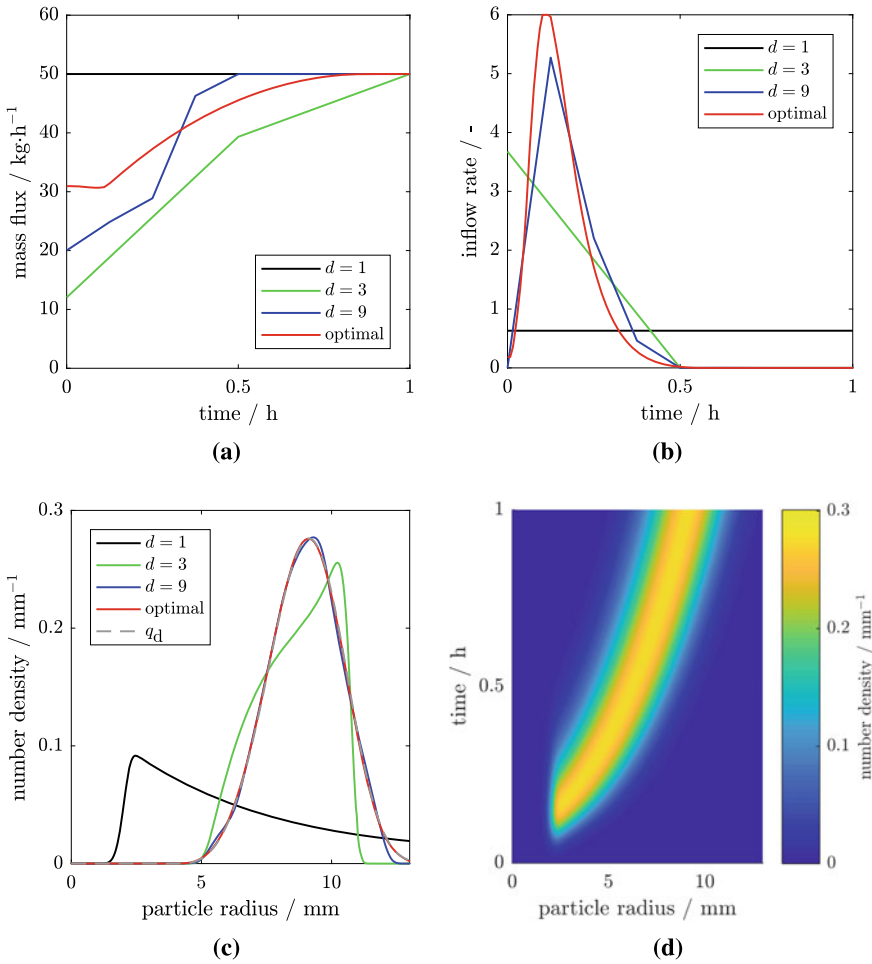
Fig. 8 Obtained process parameters u_G (**a**) and u_{in} (**b**) during optimization with $d(u_G) = d(u_{in})$ of discretization points together with the optimal ones illustrated in red, respectively. Generated PSDs $q(t_f, \cdot)$ at the final time for $d(u_G) = d(u_{in})$ together with the monomodal target q_d (**c**) and the surface plot of the resulting optimal solution (**d**)

in [51–55], the transformation of monomodal PSDs into bimodal distributions is a technically relevant issue. Since only the target PSD changes whereas the rest of the setting remains untouched, the here presented gradient-based optimization scheme can be used to obtain optimal process conditions despite the fact that there is a distinct difference in the shape of the inflow PSD q_{in} and the target PSD q_d.

Figure 9 shows, analogously to Fig. 8, the optimal process conditions, the final PSDs together with the target PSD q_d for different $(d(u_G), d(u_{in}))$ and the surface plot of optimal PSD q. Also here time-varying optimization parameters and thus
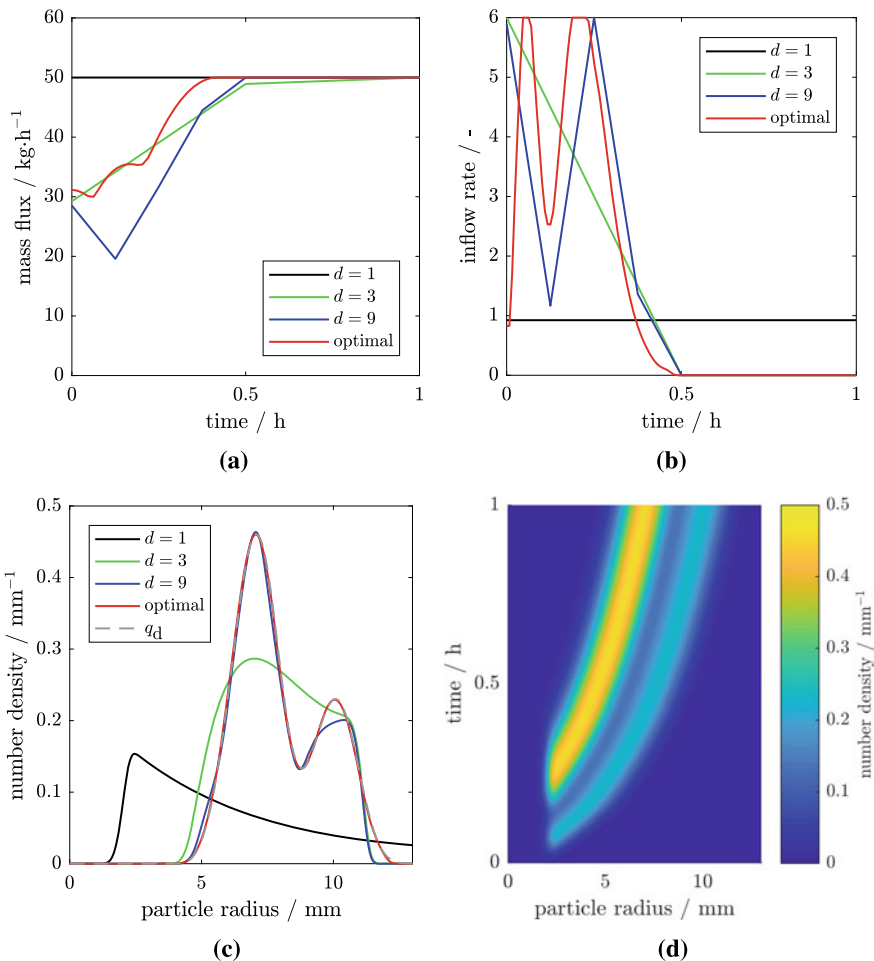
Fig. 9 Obtained process parameters u_G (**a**) and u_{in} (**b**) during optimization with $d(u_G) = d(u_{in})$ of discretization points together with the optimal ones illustrated in red, respectively. Generated PSDs $q(t_f, \cdot)$ at the final time for $d(u_G) = d(u_{in})$ together with the bimodal target q_d (**c**) and the surface plot of the resulting optimal solution (**d**)

higher numbers of discretization points are required to reach the desired goal. In order to reduce computational costs, the adjoint method is suitable. Furthermore, these examples indicate that the algorithm does not depend on the number of modi of given PSDs even though it is not always possible to reach targets exactly.

4.3   Ostwald Ripening: Minimization of Standard Deviation

In this example a different synthesis process will be considered where not only growth
dynamics were altered but also another optimization goal compared to Sects. 4.1 and
4.2 was aimed to reach. Even though a simplified Ostwald ripening mechanism of
particles is taken into account, it describes more complex growth of particles than in
the two previous examples. This is due to the fast ripening dynamics. The process
was started with a given monomodal PSD q_0 with mean particle size of 2 nm. During
the process, the rate u_{in} of particles with a PSD q_{in} is added which corresponds to
the initial PSD q_0.

   Here, the goal is to find an optimal inflow rate leading to a desired mean particle
size $\mu_d = 6$ nm and minimal standard deviation at final time $t_f = 100$ s. Again, a
penalty term for the process condition u_{in} will be added to the cost functional to
avoid an unnecessary inflow of new particles and an undesired oscillation in the
mentioned feeding over time. Together with the subscript 3 denoting a mass-related
PSD, the corresponding optimization problem exhibits the following structure:

$$\min_{u_{in}} (\sigma[q_3(t_f, \cdot)])^2 + 10^{-2}\|u_{in}\|^2_{L^2((0,t_f))} + 10\|\dot{u}_{in}\|^2_{L^2((0,t_f))} \quad \text{s.t.}$$

$$q_t(t, x) + \partial_x(G(W_q(t), t, x)q(t, x)) = u_{in}(t)q_{in}(x)$$

$$q(0, x) = 0.1q_0(x) = 0.1q_{in}(x)$$

$$W_q(t) = \int_{x_{min}}^{\infty} \tfrac{4}{3}\pi y^3 q(t, y)\, dy$$

$$\mu = E[q_3(t_f, \cdot)] := E^1[q_3(t_f, \cdot)] = \mu_d = 6$$

$$u_{in}(t) \in [0, 0.02]$$

With the regularized Ostwald ripening function G:

$$G(W_q(t), t, x) = \text{smax}\left\{\frac{M_{tot}(W_q(t), t) - \exp(\frac{1}{\text{smax}\{x, 0.1\}})}{\text{smax}(x, 0.1)}, -1\right\}$$

$$M_{tot}(W_q(t), t) := 2 + \int_0^t \int_{\Omega} u_{in}(s)q_{in,3}(y)\, dy\, ds - 0.2W_q(t)$$

Where a smoothed version smax of max was used. The n-th moment E^n, $n \in \mathbb{N}_{\geq 0}$,
and the standard devitation σ of $q_3(t_f, \cdot)$ are defined as follows:

Fig. 10 Plot of the usual and of the smoothly extended Ostwald ripening function together with the PSD $q_{in,3}$
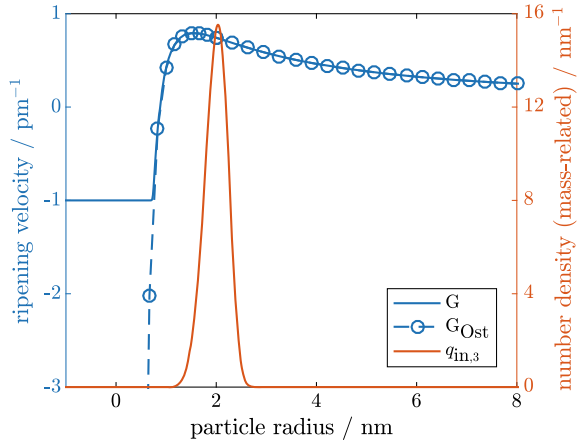
$$E^n[q_3(t_f, \cdot)] := \frac{\int_\Omega x^n q_3(t_f, x)\, dx}{\int_\Omega q_3(t_f, x)\, dx} \qquad \text{if } \int_\Omega q_3(t_f, x)\, dx > 0$$

$$\sigma \equiv \sigma[q_3(t_f, \cdot)] := \sqrt{E^2[q_3(t_f, \cdot)] - (E[q_3(t_f, \cdot)])^2}.$$

The choice of the smoothly extended Ostwald ripening function G and not of the actual G_{Ost} is only due to technical reasons since in the chosen numerical approach the growth function must be defined for every $x \in \mathbb{R}$. Comparing both ripening functions in Fig. 10, in the area where the PSD is positive, both functions coincide and thus result in the same process dynamics. Thus, G is suitable to properly depict Ostwald ripening dynamics. In the following, the results given by the numerical optimization of this application are described. Figure 11a illustrates the development of σ with respect to different $d(u_{in})$. By increasing d, σ decreases. And since the optimal influx rate, illustrated in Fig. 11b, shows a highly nonlinear behavior, again the gradient-based optimization approach using (3) can be used to obtain optimal solutions with by far less computational time compared to deriving the gradient by finite differences. In Fig. 11c, the optimal final PSD is depicted and it can be observed that the desired mean particle size is reached. Finally, Fig. 11d illustrates the temporal evolution of the optimal PSD.

4.4   Cycled Process Chain with FBSG and Mill: Maximization of Output

This final example focuses on an interconnected process chain with recycling streams as depicted in Fig. 12. It starts with a FBSG module from which particles with a given constant rate $u_{out} \equiv 0.1$ are extracted. These particles are separated into three
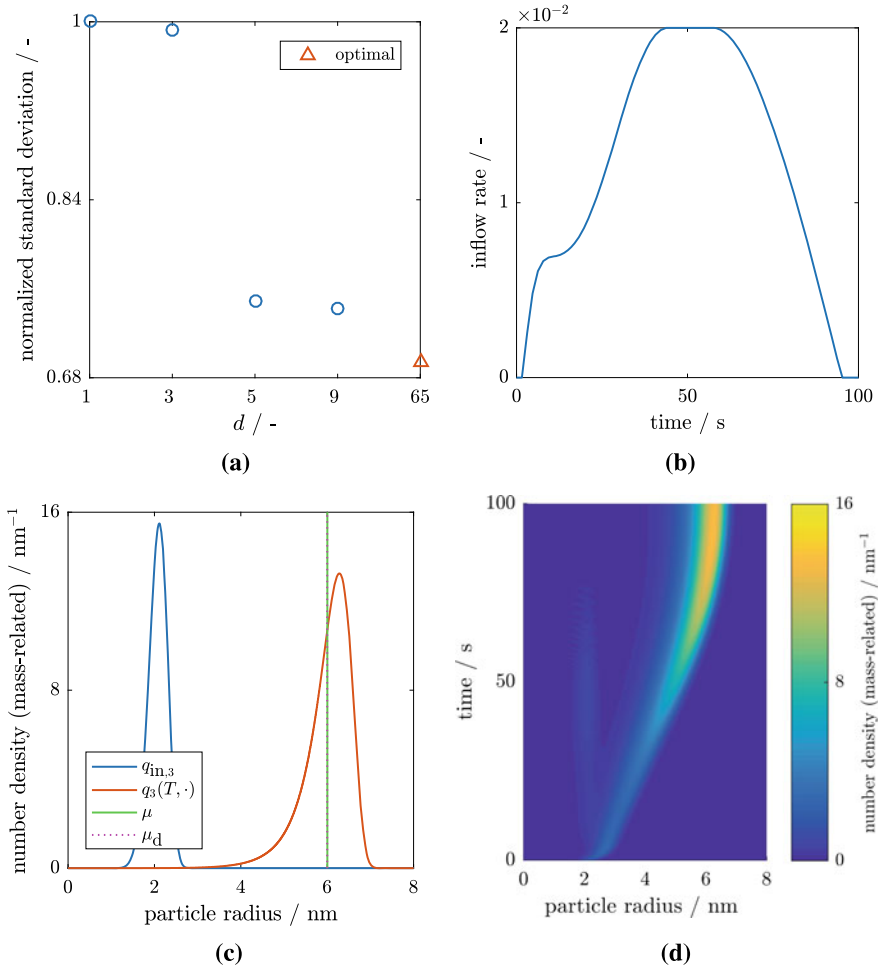
Fig. 11 Development of σ with respect to different $d(u_{in})$ and normalization respective to σ in the constant optimal case (**a**), optimal time-varying influx rate u_{in} (**b**), optimal solution at final time together with the PSD of external nuclei $q_{in,3}$ (**c**) and surface plot of the optimal solution (**d**)

fractions by two screens: The large fraction which is milled and fed back to the FBSG module, the product which is collected and the fine fraction which is also fed back to the FBSG module. An initial PSD q_0 with a mean particle size of 2 mm and with an RSD of approximately 20 % is considered. At final time $t_f = 70$ min, the goal is is to find a proper time-dependent milling power P such that simultaneously the mass of the total product with PSD q_{tot} cumulated over time is maximized and the energy consumption of the mill is minimized.

For screen 1 and screen 2, respectively, grade efficiency functions Φ_1, Φ_2 according to the model of Molerus and Hoffmann (cf. [56]) with cut size $x_{cut,1} = 7$ mm and
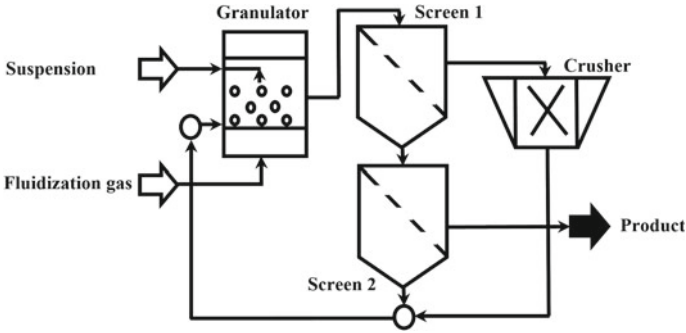
Fig. 12 Granulation process chain considered (adapted from [21, Fig. 13])

$x_{\text{cut},2} = 6$ mm with a separation sharpness of 10 for both were chosen:

$$\Phi_i(x) := \left(1 + \left(\tfrac{x_{\text{cut},i}}{x}\right) \exp\left(10\left(1 - \left(\tfrac{x}{x_{\text{cut},i}}\right)^2\right)\right)\right)^{-1} \qquad i \in \{1, 2\}.$$

The grade efficiency functions are illustrated in Fig. 13. By Φ_1, Φ_2, q_{tot} can be denoted as follows:

$$q_{\text{tot}}(x) = 0.1 \int_0^{t_{\text{f}}} (1 - \Phi_1(x))\Phi_2(x)q(t, x)\, \mathrm{d}t.$$

At first $0.1q(t, \cdot)$ is extracted from the system. Only the fine fraction of particles and the crushed ones reenter the FBSG module. The former particles have the PSD $0.1(1 - \Phi_1)(1 - \Phi_2)q(t, \cdot)$ and the latter have the PSD q_{crush}. Thus, the source and sink terms of the resulting PBE are:

$$0.1\big[(1 - \Phi_1(x))(1 - \Phi_2(x)) - 1\big]q(t, x) + q_{\text{crush}}(P(t), t, x)$$

Where q_{crush} depends on the mass flow entering the crusher and on the milling power. To derive q_{crush} more precisely, the milling dynamics will be formulated and for this, Bond's model is used (cf. [57]):

$$\mu_{\text{in}}(t) = \mathrm{E}[\Phi_1(\cdot)q_3(t, \cdot)]$$

$$\dot{m}(t) = 0.1 \int_{x_{\text{min}}}^{\infty} \Phi_1(y)q_3(t, y)\, \mathrm{d}y$$

$$\mu_{\text{out}}(t) = \max\left\{\left(\tfrac{P(t)}{100\dot{m}(t)} + \tfrac{1}{\sqrt{\mu_{\text{in}}(t)}}\right)^{-2}, 1\right\}$$

Fig. 13 Graphical
illustration of the grade
efficiency function of screen
1 and screen 2
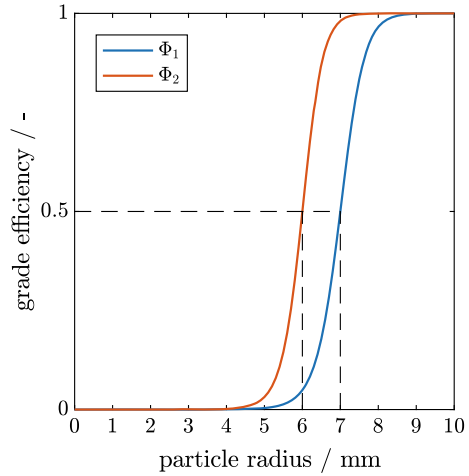
Where μ_{in} and μ_{out}, respectively, denote the mean particle size of the input and output
stream of the crusher and $\dot{m}$ is the incoming mass flow. In the definition of μ_{out} it
is ensured that it cannot reach arbitrary small values which is equivalent to set an
appropriate upper bound on the milling power depending on the incoming mass flow
and incoming mean particle size. By assuming a uniform crushing of the particles
and considering the conservation of mass, $q_{\text{crush},3}$ can be obtained as follows:

$$\int_{x_{\text{min}}}^{\infty} q_{\text{crush},3}(P(t), t, x)\,\mathrm{d}x = 0.1 \int_{x_{\text{min}}}^{\infty} \Phi_1(x) q_3(t, x)\,\mathrm{d}x$$

Such that it leads to the subsequent representation of q_{crush}:

$$q_{\text{crush}}(P(t), t, x) = 0.1 \frac{\mu_{\text{in}}(t)}{\mu_{\text{out}}(t)} \Phi_1\left(x \frac{\mu_{\text{in}}(t)}{\mu_{\text{out}}(t)}\right) q\left(t, x \frac{\mu_{\text{in}}(t)}{\mu_{\text{out}}(t)}\right).$$

Eventually, together with the introduced terms this leads to the following represen-
tation of the optimization problem considered in this example:

$$\min_{P} \quad -\mathrm{E}[q_{\mathrm{tot}}] + 10^{-2}\|P\|_{L^1((0,t_f))} + 10^{-2}\|\dot{P}\|^2_{L^2((0,t_f))} \quad \text{s.t.}$$

$$q_t(t,x) + \partial_x\left(\frac{100}{100+W_q(t)}q(t,x)\right) = 0.1\big[(1-\Phi_1(x))(1-\Phi_2(x)) - 1\big]q(t,x)$$

$$+ q_{\mathrm{crush}}(P(t),t,x)$$

$$q(0,x) = q_0(x)$$

$$W_q(t) = \int_{x_{\min}}^{\infty} 4\pi y^2 q(t,y)\,\mathrm{d}y$$

$$P(t) \in [0, 100]$$

Where it was used that a term maximizing a property also minimizes the sign changed property, and vice versa. After having stated the mathematical model of the here considered issue, the corresponding numerical results out of the optimization will be addressed. In Fig. 14, the development of the total mass and of the energy consumption of the mill, i.e., $\mathrm{E}[q_{\mathrm{tot}}]$, $\|P\|_{L^1((0,t_f))}$, respectively, and of the cost functional are recorded for different numbers $d(P)$. In every case the results are normalized with respect to the case $d(P) = 1$. As can be seen in the mentioned figure, in comparison to the constant optimization, the total mass could be increased by approximately 7 %. As illustrated in Fig. 14b, in the optimal case the energy consumption for the milling power was reduced by about 3.5 %. Here, for small d the energy consumption was higher than in the constant case. However, this highly depends on the choice of the weights in the cost functional.

Finally, Fig. 14c shows that overall the cost functional was improved by ca. 6.5 %. Here it has to be mentioned that actually a decreasing cost functional was obtained.
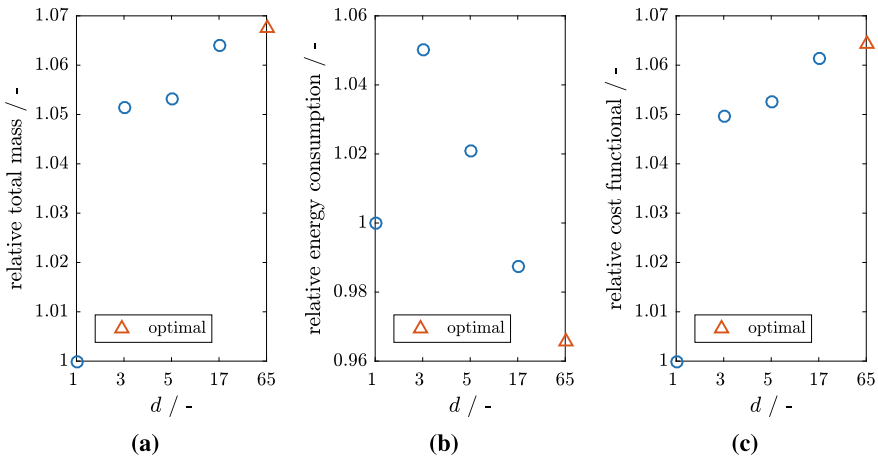

Fig. 14 Development of the relative mass (**a**), of the relative energy consumption (**b**) and of the relative cost functional (**c**) with respect to $d(P)$. The normalization is always respective to the value in the constant optimization
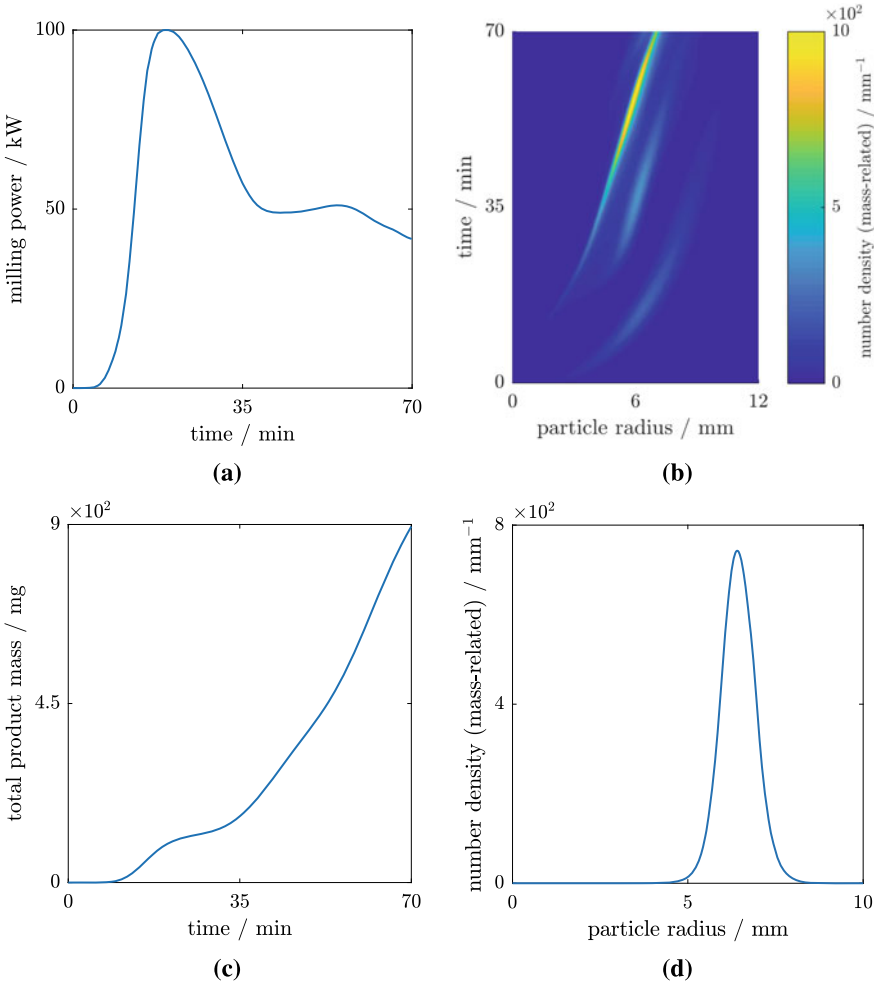
Fig. 15 Optimal milling power (**a**), surface plot of the resulting PSD within the reactor (**b**), the development of the mass of the cumulated product over time q_{tot} (**c**) and its plot (**d**)

This was due to the fact that the mass of the total product led to a higher contribution than $\|P\|_{L^1((0,t_f))}$ such that the cost functional is negative.

Figure 15 shows further corresponding optimization results. The optimal nonlinear milling power P is illustrated in Fig. 15a. In Fig. 15b a surface plot of the PSD q in the FBSG module is depicted. Here, the milling effect is observable since the number of larger particles decreases over time and new, smaller particles are produced. Furthermore, the large fraction of particles diminishes over time and this can be seen due to the fading shown there. Finally, Figs. 15c, d illustrate the evolution of $E[q_{tot}]$ over time and the PSD of the cumulated product, respectively.

It has to be mentioned that the choice of the weights in the cost functional determine the preferences between different optimization goals. For instance, a by far higher weight of the costs of P can lead to an (almost) vanishing milling power whereas the maximization of the total mass will be taken less into account. Thus, in actual applications these weights have to be selected problem-specifically. Finally, these results, especially Fig. 14, show that a larger number of discretization points of the process conditions are required to obtain significantly better outcomes compared to constant optimization which again leads to the advantage of adjoint equations when computing gradients.

5   Conclusions

The mathematical framework illustrated in this publication consists out of two major aspects. On the one hand, an on the method of characteristics relying numerical discretization scheme was used to obtain a sufficiently precise approximation of PSDs even for a rather coarse discretization grid. On the other hand, based on these simulations, an optimization tool was presented which can calculate optimal process conditions for a variety of applications within mechanical process engineering and powder technology. The numerical simulation consists of applying the method of characteristics on the here considered nonlocal PBEs and due to the conservation of number of particles incorporated in the scheme, the evolution of the PSD can be tracked with high accuracy.

To demonstrate its broad usability, it was shown that it is capable to handle PSDs with different numbers of modes, growth rates and even process chains with recycling streams. Due to the fact that process conditions can be adjusted in a time-varying manner, a sensitivity-based optimization scheme was chosen. This ensures that also these complex, interconnected reaction modules can be improved in small time in contrast to gradient-free approaches due to their high computational costs. Here, an adjoint equation was derived and with its solution a representation of the gradient of the cost functional with respect to the process conditions was obtained. By this adjoint method, only two partial differential equations, namely the state and the adjoint equation, have to be solved. This decreases the number of function evaluations and thus the computational effort by far compared to commonly used finite differences methods.

In this contribution four cases demonstrating the applicability of the presented methodology were considered. For the following real-world examples within chemical engineering, numerical optimization results were derived and discussed also concerning computational times:

1. In Sects. 4.1 and 4.2, the resulting PSD in the considered FBSG module was exactly driven to desired mono- and bimodal PSDs, respectively.
2. In Sect. 4.3 the standard deviation for a PSD with a desired mean diameter and obtained by Ostwald ripening was minimized.
3. In Sect. 4.4, within a cycled process chain with a FBSG module, two screens and one crusher simultaneously, the yield of the total product was maximized and the energy consumption due to milling was minimized.

In every example, it was elaborated that time-varying process conditions led to particulate products with a quality superior to the outcome generated by constant process conditions or, more general, with a low number of discretization points such that they justify the usage of the here used adjoint equations. Summarized, comparing to optimization schemes applied in the literature, gradient-based optimization methods relying on adjoint equations are suitable approaches to compute sensitivities fast also for a wide range of optimization tasks for particle synthesis processes.

To conclude this contribution, some possible topics for future research associated to the optimization approach described in this work are mentioned. Since the focus lies on the applicability to real-world processes and optimization within chemical engineering, it is required to validate numerical results obtained by the here used scheme to experimental data such that in case of deviations refinements of the models can be performed. Especially then when not single reaction modules but rather process chains occur, a high degree of interconnectivity of different reactors could lead to the case that the ansatz within this work is not fully applicable and thus it has to be adapted properly. Moreover, due to wall effects, different types of flow velocity profiles emerge and thus residence time distributions occur. Residence time reactors play a significant role within chemical engineering such that the mathematical model should be extended to include these. There, one can also include the residence time distribution itself as a process condition one aims to adjust to enhance the quality of the final particulate products. Finally, due to the fact that the shape of reactors influences their residence time distribution, this shape can thus be subject for optimization. By shape optimization techniques, desired residence time distributions can be achieved and thus also the field of reactor optimization (cf. [58]) can be connected to this work.

Symbols Used

Abbreviations

ADJ	Adjoint equation	FBSG	Fluidized bed spray granulation
PBE	Population balance equation	PRI	Primal equation
PSD	Particle size distribution	RSD	Relative standard deviation

Greek Letters

γ	[a.u.]	Weight function in nonlocal term	μ	[m]	Mean particle size
ξ	[a.u.]	Solution of characteristic equation	π	[–]	$3.1415\ldots$
σ	[m]	Standard deviation	Φ	[–]	Grade efficiency function
χ	[–]	Characteristic function	Ω	[–]	Domain of interest

Symbols

∂	[–]	Partial derivative	$\frac{d}{dz}$	[–]	Total derivative (to z)
∇	[–]	Gradient	t	[s]	Time
t_f	[s]	Fnal time	n	[–]	Dimension of disperse properties
x	[m]	Particle radius	$\boldsymbol{x}$	[a.u.]	Vector of disperse properties
G	[a.u.]	One-dimensional growth function	$\mathbf{G}$	[a.u.]	Multi-dimensional growth function
G_{Ost}	[–]	Ostwald ripening function	u_G	[a.u.]	Time-dependent parameter in G
$u_{\mathbf{G}}$	[a.u.]	Time-dependent parameter in $\mathbf{G}$	u_{in}	[–]	Time-dependent influx rate
u_{out}	[–]	Time-dependent extraction rate	u_0	[–]	Scaling factor of initial PSD
$\underline{u}$	[a.u.]	Lower bound on process condition u	$\bar{u}$	[a.u.]	Upper bound on process condition u
q	[a.u.]	PSD	q_3	[a.u.]	Mass-related PSD
q_{in}	[a.u.]	PSD of external nuclei	$q_{in,3}$	[a.u.]	Mass-related PSD of external nuclei
q_0	[a.u.]	Initial PSD	q_d	[a.u.]	Desired PSD
W_q	[a.u.]	Nonlocal term in (1)	$\boldsymbol{x}_{min}$	[a.u.]	Vector of minimal disperse properties
x_{min}	[m]	Minimal radius	p	[a.u.]	Solution of (3)
Y_p	[a.u.]	Nonlocal term in (3)	J	[a.u.]	Cost functional
U_{ad}	[–]	Set of admissible process conditions	$\hat{\boldsymbol{\xi}}$	[m]	Semi-discr. of ξ
$\boldsymbol{q}$	[a.u.]	Semi-discr. of q	$\boldsymbol{p}$	[a.u.]	Semi-discr. of p
$\hat{W}_q$	[a.u.]	Approx. of W_q	$\hat{q}$	[a.u.]	Approximation of q
$\hat{Y}_p$	[a.u.]	Approx. of Y_p	$\hat{p}$	[a.u.]	Approximation of p
$d(u)$	[–]	Number of discretization points of u	d	[–]	Number of discretization points
K	[–]	number of grid points	x_k	[a.u.]	Grid point
x_L	[a.u.]	Largest grid point	E^n	[a.u.]	n-th moment
E	[a.u.]	First moment	μ_d	[m]	Desired mean particle size
μ_{in}	[m]	Mean particle size of entering PSD	μ_{out}	[m]	Mean particle size of outgoing PSD
P	[W]	Milling power	q_{tot}	[m^{-1}]	PSD of total product
q_{crush}	[m^{-1}]	PSD of crushed particles	$q_{crush,3}$	[m^{-1}]	Mass-related PSD of crushed particles
x_{cut}	[m]	Cut size	$\dot{m}$	[kg·s^{-1}]	Mass flow

Norms

$\|\cdot\|_{L^p((0,t_f))}$	Norm on Lebesgue space of p-integrable functions on $(0, t_f)$
$\|\cdot\|_{H^1((0,t_f))}$	Norm on Sobolev space of functions $f \in L^2((0, t_f))$ with $\dot{f} \in L^2((0, t_f))$

References

1. Awschalom, D.D., Bassett, L.C., Dzurak, A.S., Hu, E.L., Petta, J.R.: Quantum spintronics: engineering and manipulating atom-like spins in semiconductors. Science **339**(6124), 1174–1179 (2013)
2. Lim, S.Y., Shen, W., Gao, Z.: Carbon quantum dots and their applications. Chem. Soc. Rev. **44**(1), 362–381 (2015)
3. Talapin, D.V., Rogach, A.L., Shevchenko, E.V., Kornowski, A., Haase, M., Weller, H.: Dynamic distribution of growth rates within the ensembles of colloidal II—VI and III–V semiconductor nanocrystals as a factor governing their photoluminescence efficiency. J. Am. Chem. Soc. **124**(20), 5782–5790 (2002)
4. Haderlein, M., Güldenpfennig, A., Segets, D., Peukert, W.: A widely applicable tool for modeling precipitation processes. Comput. Chem. Eng. **98**, 197–208 (2017)
5. Iggland, M., Mazzotti, M.: Population balance modeling with size-dependent solubility: Ostwald ripening. Crystal Growth Des. **12**(3), 1489–1500 (2012)
6. Marchisio, D.L., Fox, R.O.: Solution of population balance equations using the direct quadrature method of moments. J. Aerosol Sci. **36**(1), 43–73 (2005)
7. Ramkrishna, D.: Population balances: theory and applications to particulate systems in engineering. Elsevier (2000)
8. Ramkrishna, D., Singh, M.R.: Population balance modeling: current status and future prospects. Ann. Rev. Chem. Biomol. Eng. **5**, 123–146 (2014)
9. Segets, D., Hartig, M.A.J., Gradl, J., Peukert, W.: A population balance model of quantum dot formation: oriented growth and ripening of ZnO. Chem. Eng. Sci. **70**, 4–13 (2012)
10. Verkoeijen, D., Pouw, G.A., Meesters, G.M.H., Scarlett, B.: Population balances for particulate processes-a volume approach. Chem. Eng. Sci. **57**(12), 2287–2303 (2002)
11. Van Embden, J., Sader, J.E., Davidson, M., Mulvaney, P.: Evolution of colloidal nanocrystals: theory and modeling of their nucleation and growth. J. Phys. Chem. C **113**(37), 16342–16355 (2009)
12. Lifshitz, I.M., Slyozov, V.V.: The kinetics of precipitation from supersaturated solid solutions. J. Phys. Chem. Solids **19**(1–2), 35–50 (1961)
13. Madras, G., McCoy, B.J.: Continuous distribution theory for Ostwald ripening: comparison with the LSW approach. Chem. Eng. Sci. **58**(13), 2903–2909 (2003)
14. Thanh, N.T.K., Maclean, N., Mahiddine, S.: Mechanisms of nucleation and growth of nanoparticles in solution. Chem. Rev. **114**(15), 7610–7630 (2014)
15. Wagner, C.: Theorie der Alterung von Niederschlägen durch Umlösen (Ostwald-Reifung). Zeitschrift für Elektrochemie, Berichte der Bunsengesellschaft für physikalische Chemie **65**(7-8), 581–591 (1961)
16. Yec, C.C., Zeng, H.C.: Synthesis of complex nanomaterials via Ostwald ripening. J. Mater. Chem. A **2**(14), 4843–4851 (2014)
17. Borchert, C., Sundmacher, K.: Morphology evolution of crystal populations: modeling and observation analysis. Chem. Eng. Sci. **70**, 87–98 (2012)
18. Hussain, M., Kumar, J., Tsotsas, E.: A new framework for population balance modeling of spray fluidized bed agglomeration. Particuology **19**, 141–154 (2015)
19. Heinrich, S., Peglow, M., Ihlow, M., Henneberg, M., Mörl, L.: Analysis of the start-up process in continuous fluidized bed spray granulation by population balance modelling. Chem. Eng. Sci. **57**(20), 4369–4390 (2002)
20. Gröschel, M.: Optimization of particle synthesis-new mathematical concepts for a controlled production of functional nanoparticles. Dissertation, FAU University Press (2013)
21. Skorych, V., Dosta, M., Hartge, E.-U., and Heinrich, S.: Novel system for dynamic flowsheet simulation of solids processes. In: Powder Technology (2017)
22. Haderlein, M., Segets, D., Gröschel, M., Pflug, L., Leugering, G., Peukert, W.: FIMOR: an efficient simulation for ZnO quantum dot ripening applied to the optimization of nanoparticle synthesis. Chem. Eng. J. (2015)

23. Gunawan, R., Fusman, I., Braatz, R.D.: High resolution algorithms for multidimensional population balance equations. AIChE J. **50**(11), 2738–2749 (2004)
24. Chalons, C., Goatin, P., Villada, L.M.: High-order numerical schemes for onedimensional nonlocal conservation laws. SIAM J. Sci. Comput. **40**(1), A288–A305 (2018)
25. Friedrich, J., Kolb, O., Göttlich, S.: A Godunov type scheme for a class of LWR traffic flow models with non-local flux. Netw. Heterog. Media NHM **13**(4), 531–547 (2018)
26. Kumar, R., Kumar, J., Warnecke, G.: Moment preserving finite volume schemes for solving population balance equations incorporating aggregation, breakage, growth and source terms. Math. Models Methods Appl. Sci. **23**(07), 1235–1273 (2013)
27. Eymard, R., Gallouët, T., Herbin, R.: Finite volume methods. In: Handbook of Numerical Analysis, vol. 7, pp. 713–1018 (2000)
28. Qamar, S., Ashfaq, A., Warnecke, G., Angelov, I., Elsner, M.P., Seidel-Morgenstern, A.: Adaptive high-resolution schemes for multidimensional population balances in crystallization processes. Comput. Chem. Eng. **31**(10), 1296–1311 (2007)
29. Pilon, L., Viskanta, R.: Modified method of characteristics for solving population balance equations. Int. J. Numer. Methods Fluids **42**(11), 1211–1236 (2003)
30. Févotte, F., Févotte, G.: A method of characteristics for solving population balance equations (PBE) describing the adsorption of impurities during crystallization processes. Chem. Eng. Sci. **65**(10), 3191–3198 (2010)
31. Rehman, S.M., Qamar, S.: Application of the method of characteristics to population balance models considering growth and nucleation phenomena. Appl. Math. **5**(13), 1853 (2014)
32. De Souza, L.G.M., Janiga, G., John, V., Thévenin, D.: Reconstruction of a distribution from a finite number of moments with an adaptive spline-based algorithm. Chem. Eng. Sci. **65**(9), 2741–2750 (2010)
33. Qamar, S., Warnecke, G.: Numerical solution of population balance equations for nucleation, growth and aggregation processes. Comput. Chem. Eng. **31**(12), 1576–1589 (2007)
34. Ulbrich, S.: Adjoint-based derivative computations for the optimal control of discontinuous solutions of hyperbolic conservation laws. Syst. Control Lett. **48**(3–4), 313–328 (2003)
35. Ulbrich, M.: Optimization methods in Banach spaces. In: Optimization with PDE Constraints, pp. 97–156. Springer (2009)
36. Gugat, M., Herty, M., Klar, A., Leugering, G.: Optimal control for traffic flownetworks. J. Opt. Theory Appl. **126**(3), 589–616 (2005). issn: 0022-3239. http://dx.doi.org/10.1007/s10957-005-5499-z
37. Lang, Y.-D., Biegler, L.T.: A software environment for simultaneous dynamic optimization. Comput. Chem. Eng. **31**(8), 931–942 (2007)
38. Bück, A., Palis, S., Tsotsas, E.: Model-based control of particle properties in fluidised bed spray granulation. Powder Technol. **270**, 575–583 (2015)
39. Mantzaris, N.V., Daoutidis, P.: Cell population balance modeling and control in continuous bioreactors. J. Process Control **14**(7), 775–784 (2004)
40. Shi, D., El-Farra, N.H., Li, M., Mhaskar, P., Christofides, P.D.: Predictive control of particle size distribution in particulate processes. Chem. Eng. Sci. **61**(1), 268–281 (2006)
41. Madras, G., McCoy, B.J.: Temperature effects during Ostwald ripening. J. Chem. Phys. **119**(3), 1683–1693 (2003)
42. Gröschel, M., Keimer, A., Leugering, G., Wang, Z.: Regularity theory and adjoint based optimality conditions for a nonlinear transport equation with nonlocal velocity. SIAM J. Control Opt. **52**(4), 2141–2163 (2014)
43. Peukert, W., Segets, D., Pflug, L., Leugering, G.: Unified design strategies for particulate products. Adv. Chem. Eng. (2015)
44. Spinola, M., Keimer, A., Segets, D., Leugering, G., Pflug, L.: Model-based optimization of ripening processes with feedback modules. Chem. Eng. Technol. **43**, 896–903 (2020)
45. Dosta, M., Heinrich, S., Werther, J.: Fluidized bed spray granulation: analysis of the system behaviour by means of dynamic flowsheet simulation. Powder Technol. (2010)
46. Keimer, A., Pflug, L., Spinola, M.: Existence, uniqueness and regularity of multidimensional nonlocal balance laws with damping. J. Math. Anal. Appl. **466**(1), 18–55 (2018)

47. Keimer, A., Pflug, L., Spinola, M.: Nonlocal scalar conservation laws on bounded domains and applications in traffic flow. SIAM J. Math. Anal. **50**(6), 6271–6306 (2018)
48. De los Reyes, J.C.: Numerical PDE-constrained optimization. Springer (2015)
49. Tröltzsch, F.: Optimal control of partial differential equations: theory, methods, and applications, vol. 112. Graduate Studies in Mathematics. American Mathematical Society (2010)
50. Pflug, L.: One-dimensional nonlocal balance laws-modeling and simulation. Dissertation. Friedrich-Alexander-Universität Erlangen-Nürnberg (2018)
51. Goldschmidt, M.J.V., Weijers, G.G.C., Boerefijn, R., Kuipers, J.A.M.: Discrete element modelling of fluidised bed spray granulation. Powder Technol. **138**(1), 39–45 (2003)
52. Koeninger, B., Hensler, T., Romeis, S., Peukert, W., Wirth, K.-E.: Dynamics of fine grinding in a fluidized bed opposed jet mill. Powder Technol. **327**, 346–357 (2018)
53. Peglow, M., Kumar, J., Warnecke, G., Heinrich, S., Mörl, L.: A new technique to determine rate constants for growth and agglomeration with size-and time-dependent nuclei formation. Chem. Eng. Sci. **61**(1), 282–292 (2006)
54. Schmidt, M., Hoffmann, T., Bück, A., Tsotsas, E.: Experimental investigation of continuous fluidized bed spray granulation with internal classification. Proc. Eng. **102**, 565–574 (2015)
55. German, R.M.: Prediction of sintered density for bimodal powder mixtures. Metall. Trans. A **23**(5), 1455–1465 (1992)
56. Molerus, O., Hoffmann, H.: Darstellung von Windsichtertrennkurven durch ein stochastisches Modell. Chemie Ingenieur Technik **41**(5-6), 340–344 (1969)
57. Bond, F.C.: Crushing and grinding calculations, Part I. Brit. Chem. Eng. **6**(6), 378–385 (1961)
58. Tonomura, O., Tanaka, S., Noda, M., Kano, M., Hasebe, S., Hashimoto, I.: CFD-based optimal design of manifold in plate-fin microdevices. Chem. Eng. J. **101**(1–3), 397–402 (2004)

Part IV
Development of a Dynamic Simulation System for Interconnected Solids Processes

Chapter 17
A Framework for Dynamic Simulation of Interconnected Solids Processes

Vasyl Skorych, Moritz Buchholz, Maksym Dosta, and Stefan Heinrich

Abstract The application of flowsheet models to dynamic solids processes pose significant challenges, especially regarding the handling of the inherent multidimensionality of granular material properties, like particle size, shape and porosity distributions. The novel open-source flowsheet simulation framework Dyssol deals with this by applying an approach based on transformation matrices, which allows for the tracking of temporal changes in the multi-dimensional distributed parameters of the granular materials. The modelling system utilizes the sequential-modular approach in combination with partitioning and tearing methods as well as the waveform relaxation method for increased modelling flexibility while offering high computational performance. Dyssol includes an extensive and expandable model library for various unit operations in process engineering, that in turn may be calculated by user-defined solver units from a distinct library. To enhance the computational performance, the user may choose from different convergence and extrapolation methods. Material properties are defined in an extendable material database. Various case studies show robust stability and high convergence rates. The application of a global optimization algorithm shows promising results for the operational parameter adjustment in case of transient system behaviour. A concept of applying artificial neural networks to extend the scope of dynamic flowsheet simulation systems is proposed.

Nomenclature

API	Active pharmaceutical ingredient
DAE	Differential algebraic equation
DFG	Deutsche Forschungsgemeinschaft (German), German Research Foundation
DLL	Dynamically linked library
FFT	Fast Fourier transform

V. Skorych · M. Buchholz · M. Dosta · S. Heinrich (✉)
Institute of Solids Process Engineering and Particle Technology,
Hamburg University of Technology, Denickestrasse 15, 21073 Hamburg, Germany
e-mail: stefan.heinrich@tuhh.de

HDF   Hierarchical data format
NN   Neuronal network
MLP   Multilayer perceptron
MDB   Materials database
OOP   Object-oriented programming
PBE   Population balance equation
RAM   Random access memory
RMSE   Root-mean-square error
SMA   Sequential-modular approach
SMD   Sauter mean diameter
SPP   Schwerpunktprogramm (German), Priority Programme
WRM   Waveform relaxation method

1   Introduction

The application of flowsheet simulation for process optimization and control purposes is state of the art, especially in the area of systems comprising only fluid materials. The flowsheet modelling allows for an investigation of complex processes consisting of several interconnected apparatuses and subprocesses on long time scales [15]. For the solids process engineering, the multidimensionality of the properties of granular materials significantly complicates the solution of various problems, such as design or optimization of production processes. As most solids processing systems include unit operations that have a strong impact on the transient behaviour of the whole process, like conveyors or bunkers, the ability to simulate the behaviour of dynamic systems is crucial for applying flowsheet models for optimization or control purposes in the area of solids processing technology.

Programs like Aspen Plus [4, 36], gPROMS Formulated Products [9, 18], Solid-Sim [45], SolidSim-Dynamics [16], or JKSimMet [27], deal with the challenge of solids process simulation. However, none of the aforementioned tools offer the option of dynamic process simulation of solids processes with the inherent description of the multidimensional distributed parameters of the granular material.

The aim of the Priority Program SPP 1679 "Dynamic simulation of interconnected solids processes (DYNSIM-FP)" [11] of the German Research Foundation (DFG) is to study the dynamics of different processes in the area of solids process engineering, as well as understanding the phenomena that arise when combining various such subprocesses into a single interconnected system. The research within SPP 1679 was classified into 3 working group consisting of 27 projects in total. On top of that, a separate Central Project (Z-Project) was established. Its goal is to develop a flowsheet modeling system, which should serve as a platform for combining the results of all these individual groups into a single framework. To allow for mostly independent model development and research, the flowsheet simulation framework must provide high flexibility, extensible libraries and stable interfaces. The resulting

open-source modelling system Dyssol—an acronym for "**Dy**namic **s**imulation of **sol**ids processes"—offers these features through its high degree of modularity, open and standardized interfaces, efficient algorithms and a clear user interface.

In the following sections, the modular architecture with its application programming interfaces and data formats are introduced. Following, the main simulation algorithm is presented, giving insights to the applied methods like waveform relaxation, partitioning and tearing, and transformation matrices that allow an efficient calculation of complex processes. Various case studies are presented to demonstrate the validity of the implemented algorithms, with a focus on handling multidimensional distributed parameters of the solid phase. Additional features like unit and solver libraries and the material database are discussed afterwards. The chapter closes with the introduction to a global optimization strategy for the adjustment of dynamic process parameters and a conceptual presentation of the coupling of flowsheet and data-driven models for improved modelling accuracy.

2 Architecture

The Dyssol modelling system was developed and implemented using the C++ programming language [55] due to the following reasons:

- It is widely used in scientific computing, so many design patterns are known and can be adjusted and reused for the current task.
- It supports the object-oriented programming (OOP) paradigm [56], allowing to create robust modular solutions.
- The language has very low overhead and, therefore, provides high productivity even for large complex problems.
- Allows flexible and efficient management of system resources.
- Has a large and active community and many affordable libraries and tools that can simplify development.
- Is supported by various free cross-platform compilers.

2.1 Modular Structure

Given the tasks that were posed to the developing modelling system, as well as taking into account the heterogeneity of projects in the entire SPP, it was necessary to ensure high flexibility, customizability and extensibility of the simulation framework. To provide this, the development was carried out considering the techniques of modular design [43]. Such design implies the organization of the program as a set of small independent blocks that communicate with each other using predefined interfaces. Since the object-oriented programming paradigm, widely supported in C++, is a convenient method for designing modular software products, it was intensively used
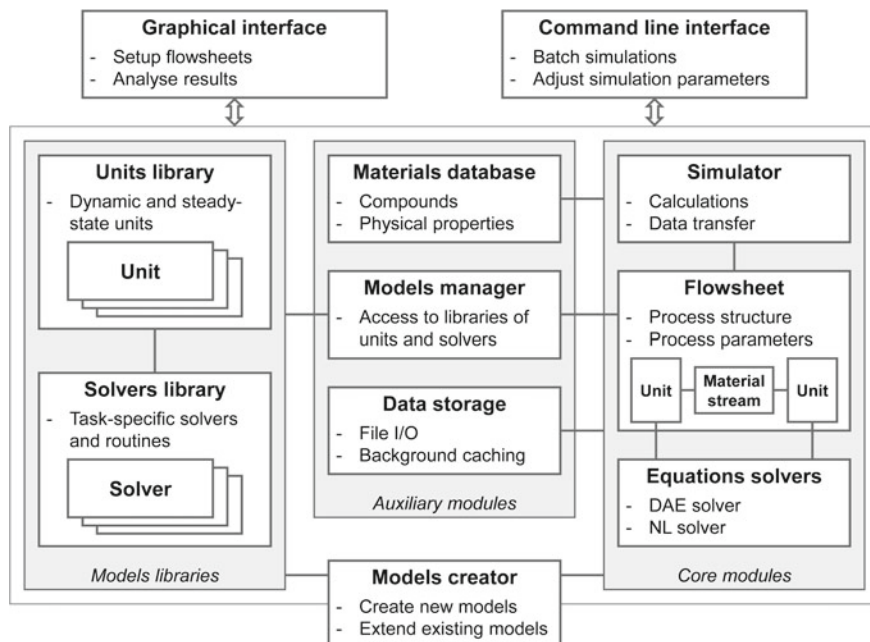
Fig. 1 General structure of the simulation framework Dyssol

during development, prototyping and implementation of the system. In the case of OOP, a module becomes a kind of logically interconnected set of functional elements and data designed as a program class or group of classes. At the most abstract level, several main blocks or modules can be distinguished in Dyssol (Fig. 1) [53].

Simulator, *Flowsheet* and a set of predefined *Equations solvers* form the core of the simulation system. *Flowsheet* is a central component, which serves as a repository of all information about the process parameters and the process structure for each individual simulation. The flowsheet is described by a set of *Units* and *Material streams* connecting them. *Material streams* (see Sect. 2.2) are used to store time-dependent information about the material parameters and to connect all the units on flowsheet. On the one hand, each *Unit* is described by a certain set of input parameters and state variables inherent in the unit itself. On the other hand, it describes and stores the state of the internal material at every moment in time. Thus, the structure of the *Unit* itself is quite complex (see Sect. 2.3). Each unit can be calculated either using one of the built-in *Equations solvers* (see Sect. 4), or using its own internal algorithms. The main task of *Simulator* is to perform the modelling itself by executing the main calculation algorithm (see Sect. 3). Additionally, it transfers data between different units following the flowsheet structure.

The auxiliary modules provide the interaction of core components with the environment. Among them can be distinguished: *Data storage* subsystem, *Materials database* and *Models manager*.

The *Data storage* module (see Sect. 6) implements all the functionality necessary for accessing the hard drive for writing, storing and reading data, such as the structure and settings of the flowsheet, material and process parameters, as well as simulation results. To organize data, the Hierarchical Data Format HDF5 and the HDF5 library [60] are used. During simulation, this subsystem also performs the functions of online data caching to reduce the need for working memory.

The *Materials database* (MDB) module (see Sect. 7) is used to store, organize and access information about materials and their properties. The database can be freely configured and modified by users, including adding new materials and new material properties. Constant, temperature- and pressure-dependent parameters are supported, as well as properties describing the interaction of two materials. The functionality of this module includes the access to properties of pure materials, phase specific mixture properties and properties for an entire material flow. Using the developed standardized software interfaces to access this module, one can further expand the modelling system by connecting to other materials databases.

In order not to limit the flexibility of the system, models of units and solvers were not directly incorporated into the simulation environment, but are delivered in the form of separate modules, which are collected in the corresponding libraries. To access both *Units library* and *Solves library*, *Models manager* is used. It provides communication interface between the system's core and libraries. The simulation system comes with a specific set of predefined models (see Sect. 8). However, it can be expanded by units and solvers in a form of dynamically linked libraries (DLL), implemented by third-party developers. To simplify this process, *Models creator* is provided with Dyssol. It can be used to develop new units and solvers using predefined program interfaces (see Sect. 2.4). Thus, each user can adjust the system in accordance with its tasks, implementing its own models of apparatuses, process sub-steps and task-specific solvers.

To manage the entire program, a simplified *Graphical user interface* was developed, which includes the ability to setup the structure of the flowsheet, model parameters and simulation settings, as well as to perform a basic analysis of the results. To provide portability and cross-platform capabilities, the graphical interface is based on the Qt software framework and Qt library [17, 46]. Additionally, there is a *Command line interface* that allows changing some parameters of pre-defined flowsheets and performing multiple simulations in batch mode.

2.2   Structure of Material Stream

Material stream is one of the main structural components of the flowsheet. It provides storage and transfer of information about the state and parameters of the material between units in the flowsheet. Thus, its structure determines the set of parameters that can be processed in the modelling system. The material stream object was designed to cover the following requirements:

- allow simultaneous description of solid, liquid and vapor phases;
- provide a correct and convenient description of multidimensional distributed properties of solid phase materials;
- enable modelling of solids processing units within a flowsheet simulation environment;
- provide the ability to describe and track time-dependent changes in material parameters to allow dynamic simulations.

Based on these requirements, the structure of the material stream object, which is schematically given in Fig. 2, was developed and implemented [53]. Each stream is described with a set of *overall* and *phase*-specific parameters. *Overall* ones are defined for the total mixture of materials and include *mass flow*, *temperature* and *pressure*. The *solid*, *liquid* and *vapor phases* can be defined separately and in any particular combination. Each phase is described by a set of *concentrated* and *distributed parameters*. In particular, *concentrated parameters* contain the *phase fraction* within the overall mass flow, whereas the *distributed parameters* describe the composition or *compounds content* of the material in each phase. Both phase fraction and composition are always present in each phase, whereas the solid phase can be additionally distributed over several other parameters, like particle size, form factor, or porosity, forming a set so called *multidimensional distributed parameters*. Their more detailed data structure and format is given in Sect. 5.

The specific structure of the material stream may be unique for any simulation, but it is always the same for all material streams of the respective flowsheet and stays unaltered during the whole simulation. The following structural components can be customized by the user depending on the process type and used models:
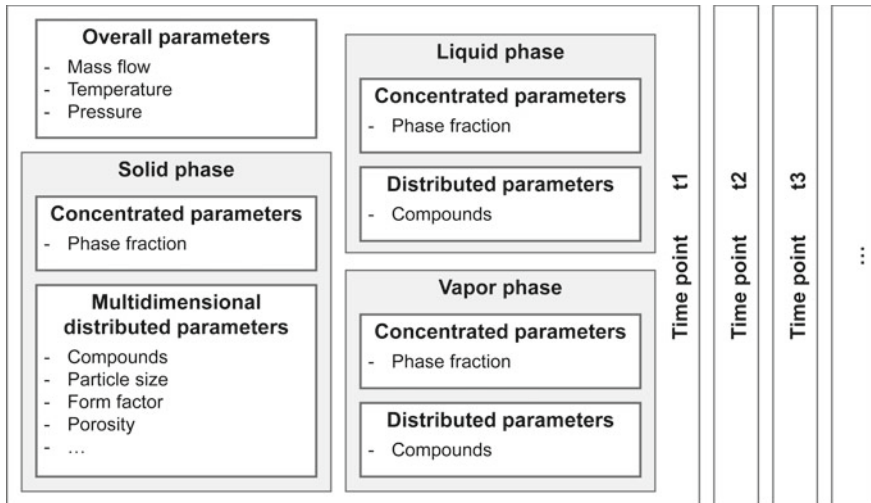

Fig. 2 General structure of *Material stream*

- number and composition of phases;
- total number and composition of compounds;
- set of distributed parameters.

Material stream interacts closely with the materials database (see Sect. 7). Thus, in addition to data, which is based on the general structure of the material stream, some additional MDB-related information is always available. In accordance with a given stream structure, various compound-related properties can be obtained for:

- Each individual material available in the database. The specific value is taken directly from the database (for constant properties) or calculated in accordance with the current stream temperature and pressure (for temperature- and pressure dependent properties).
- Each phase mixture indicated in the stream. The calculation method usually depends on the type of the phase (solid/liquid/vapor).
- Overall mixture of all available phases in the stream. Only possible for a limited set of properties.

The calculation of mixtures can be performed either on the basis of mass flow or on the basis of the molar amount of substance.

To describe continuous changes of material parameters through time, a discretized representation is used. All variations that occur in the material stream during the entire modelling interval $[t_{START}; t_{END}]$ are presented in the form of separate discrete states, which are called time points. Each time point describes the state of the material at that particular moment in time. Thus, in order to describe dynamic changes, the material stream is represented as a sequence of *time points* with the same structure given in Fig. 2. Wherein, access to data should be provided over the entire time interval, regardless of whether a particular time point was directly stored in the structure of the material stream. To do so, linear data interpolation is used to access data between points. At the same time, to represent the dynamic process with a given accuracy, the interval between neighbouring points should depend on the rate of change of material parameters and the user-specified tolerance. For more details on time integration, see Sect. 3.

In dynamic modelling, units can have an internal time-dependent state. In this case, in the simulation system Dyssol, the so-called holdup is used to describe the material inside the unit. Its structure is completely analogous to the structure of the material stream, except for the fact that the mass flow parameter in this case is replaced by the mass of the internal material.

2.3   Structure of Unit

The proposed structure of the unit (Fig. 3) was developed, on the one hand, to support the calculation algorithm for the dynamic simulation and, on the other hand, to provide interaction between the model, the simulation system and the user.
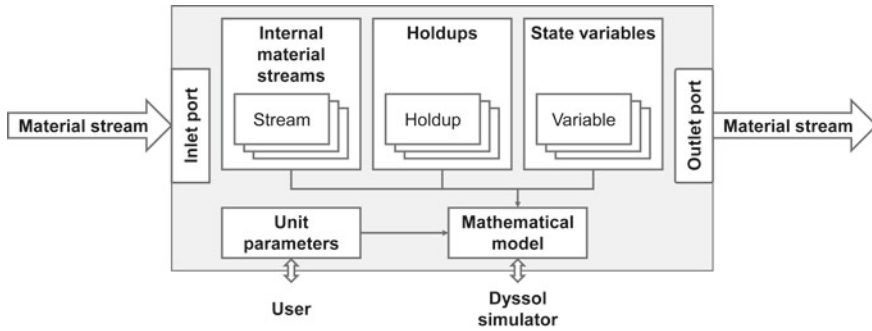
Fig. 3 General structure of *Unit*

Ports serve as interfaces for including a unit into the flowsheet structure and are access points to the parameters of the *material streams*, connected to them. The material streams themselves, connected to the input and output ports, ensure the interaction of units with each other by exchanging information about the state of the material.

Dynamic units are distinguished by the presence of an internal state, which must be stored and kept up to date during the entire simulation. If information about the internal state has the same structure as the material stream, it can be stored and maintained by *holdups*. If the variable that describes the internal state is not among the parameters of the material stream, it is supported by an additional data structure—*state variables*. *Streams* can be used to describe internal material flows within the unit. Internal material streams and holdups always have the same structure with respect to phase and material composition and a set of distributed parameters as "external" material streams.

Unit settings can be managed by the user of the simulation system through the block of *unit parameters*. Constant and time-dependent unit parameters are supported. Solvers from the solver's library can be also accessed through this block (see Sect. 2.4).

Despite the fact that Dyssol is a system for dynamic modelling, it is possible to work with both steady-state and dynamic models. Moreover, both types can be combined within one flowsheet. The structure of dynamic and steady-state units differs to some degree, as the latter do not have access to redundant holdups and state variables, but nevertheless can utilize time-dependent unit parameters.

2.4 Interfaces of Units and Solvers

One of the main requirements for the modelling framework is to provide users with the possibility to develop their own units and solvers with specific mathematical models and use them in simulations along with the already available modules. Therefore,

the units and solvers are not directly integrated into the modelling system, but are implemented as separate objects collected in the corresponding libraries. Herewith, the set of available units and solvers can be expanded by each user, to allow for modelling of specific problems.

New modules to be added to the modelling system can be developed using the C++ programming language utilizing predefined programming interfaces. Therefore, from a structural point of view, each unit is inherited from some basic object: *base unit* or *base solver* (Fig. 4). On the one hand, these base objects provide new modules with some primary functionality and give them access to other core and auxiliary components. It allows them to treat *material streams* and *holdups*, to access compounds properties through *materials database*, to use interfaces to internal *equation solvers*, to handle transformation matrices, etc. On the other hand, such basic modules define the interfaces via which the simulation system can interact with units and solvers. In particular, each base object defines a certain set of functions that must be extended by the developer of the model to implement the calculation algorithm of individual unit or solver. These functions are run by the simulation system during the execution of the main calculation algorithm. Both dynamic and steady-state units can be developed using the provided interfaces.

The difference between solvers and units is that solvers are most often used not directly by the simulation system, but by units to solve some sub-tasks within them. Moreover, it becomes possible to implement several different solvers for a single task of a certain type, and use them interchangeably within a unit. As an example, various approaches to solving the population balance equations (PBE) for the agglomeration process can be cited: using fixed pivot, cell average, or finite volume techniques—they all can be used within a single agglomeration unit to handle the same problem.

To simplify the development of new modules, the Dyssol installation package contains a *Models creator* kit with various templates of units and solvers, examples and comprehensive documentation.
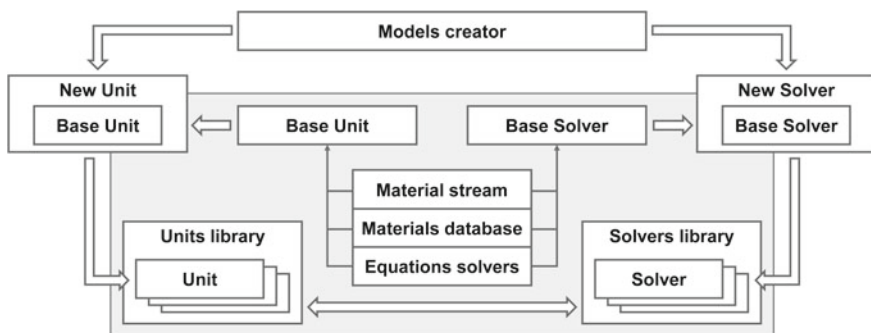

Fig. 4 Interfaces for development of new modes

3 Simulation Algorithm

Steady-state models do not have an internal state, so their output depends only on the input parameters. At the same time, dynamic models are characterized by the accumulation of material; therefore, their output streams additionally depend on their internal state at each moment of time. For the modelling algorithm, the main difference between them is that dynamic units are calculated at certain time intervals, while steady-state ones are processed at individual points in time. Thus, the use of steady-state units in a dynamic simulation system is straightforward and implies the consistent application of the model's algorithm to all input time points within the considered time interval.

The main simulation algorithm of Dyssol (Fig. 5) is based on the sequential-modular approach (Sect. 3.1) that implies individual calculation of all units on the flowsheet, using their own computational methods, equation solvers and time steps.
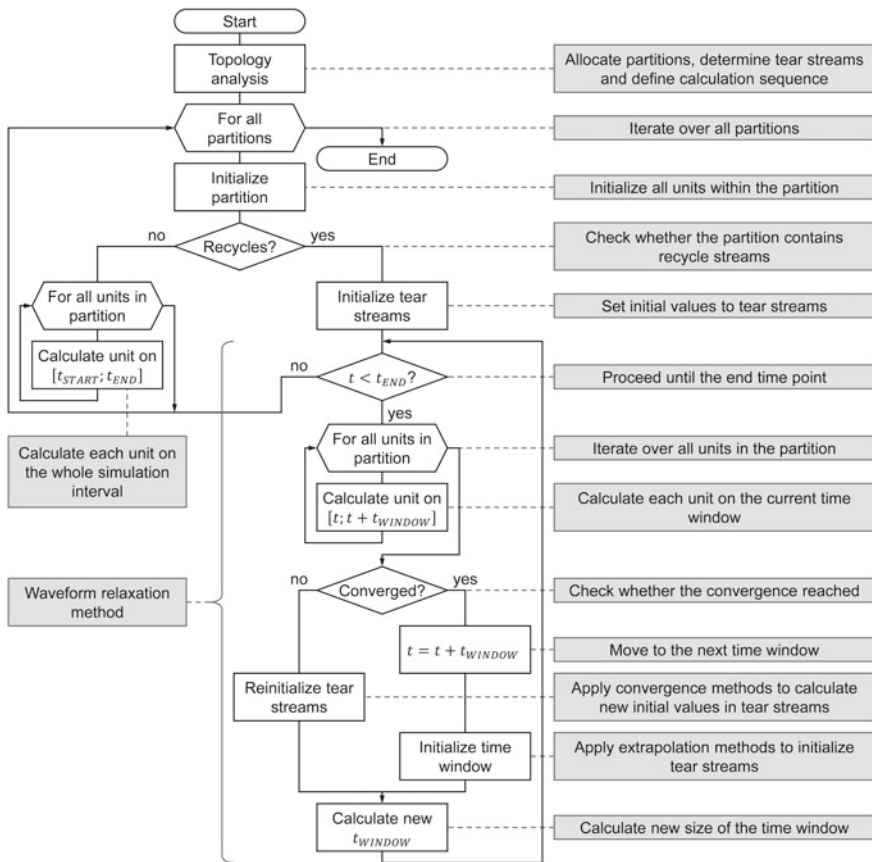
Fig. 5 Main calculation algorithm

To enable the calculation of complex process structures with recycle streams, partitioning and tearing algorithms are introduced at the stage of topological analysis (Sect. 3.2). The main goal of this step is to prepare the process structure for the sequential calculation of units. To do this, all present recycles must be initialized with some values, and units within the closed circuits must be associated with partitions. Partitions are such groups of units for which there are no recycle streams between them. Depending on the type of partition, one of the branches of the algorithm is executed (Fig. 5). In the simplest case, when all units within the partition are connected sequentially, the left part is chosen: units are calculated one by one on the whole simulation time interval $[t_{START}; t_{END}]$. For partitions with recycles, a more complex algorithm is applied: all units are calculated iteratively until the convergence in tear streams is reached. To improve the performance of the simulation system in this case, dynamic calculations are based on the waveform relaxation method (Sect. 3.3), supplemented by convergence (Sect. 3.4) and extrapolation (Sect. 3.5) methods.

3.1   *Sequential-Modular Approach*

There exist two commonly used calculation approaches applied to flowsheet simulation [38, 51, 14]: simultaneous (equation-oriented) [24] and sequential-modular [16]. The first one assumes combining all mathematical models of units, as well as the topological structure of the flowsheet into a single system of equations and its further simultaneous solution using a suitable integration method (Fig. 6, bottom). The homogenization of all equations and considering the information about the topology result in a good convergence rate, especially for flowsheets with complex structures and, therefore, in relatively fast computations [51]. This approach is usually applied in flowsheeting software developed for fluid processes.

However, the processes occurring in devices in the area of solid-phase process technology are usually described by a variety of heterogeneous mathematical models. Their numerical solution may require equation solvers of various types [38]. Therefore, it may be difficult or even impossible to formulate a single generalized system of equations for the entire flowsheet and there may be no suitable solver for it. To overcome this problem, the sequential-modular approach (SMA) can be applied. Here, each unit is treated as an individual entity, and can utilize its own equation solver, calculation algorithm and time step [16, 22, 24]. In this case, the main task of the modelling system is transferring data between units through material streams according to the flowsheet structure and ensuring the convergence of the entire solution [53]. This method leads to relative independence between units and provides high flexibility of the simulation system itself. The main advantages of this approach are conceptual simplicity, correspondence to the physical structure of processes, possibility to use different numerical methods to calculate models, greater flexibility during the development of units and simple initialization procedure. Moreover, this approach greatly simplifies the development of new models, which is one of the key
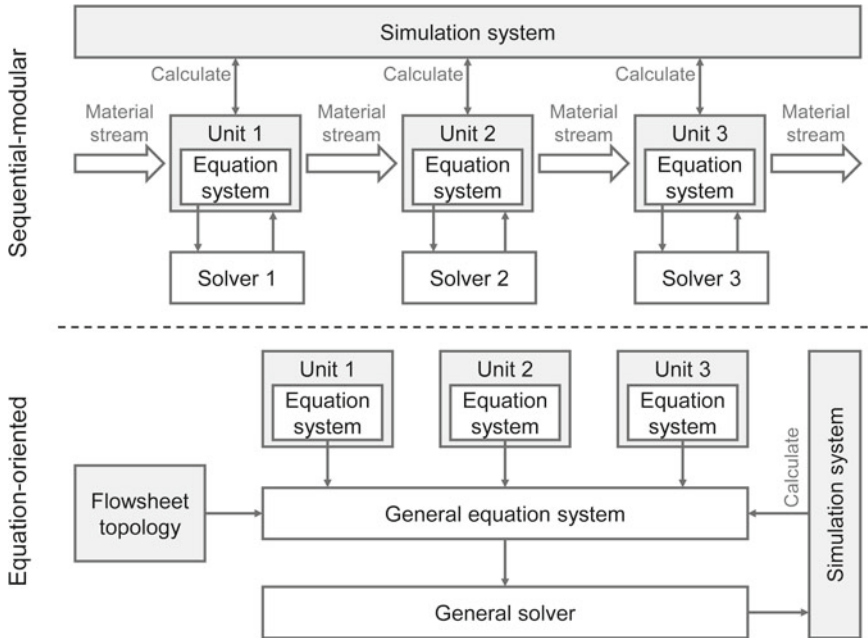
Fig. 6 Differences between sequential-modular (top) and equation-oriented (bottom) approaches

requirements for this simulation framework. Considering this, sequential-modular algorithms has been applied in Dyssol.

3.2 Topology Analysis

One of the most notable challenges applying the sequential-modular approach to the simulation of flowsheets with complex structures is related to the handling of recycle flows that are often present in production processes. A prerequisite for applying the SMA is the ability to calculate the parameters of the input flows of each unit at the time of its execution, which is not trivially achieved with recycle streams. Therefore, a topological analysis is required before the simulation can be started. In Dyssol, it includes [53]:

1. determination of tear streams;
2. decomposition of the flowsheet structure into partitions;
3. definition of the calculation order.

The general idea is to represent the flowsheet in the form of a directed graph, where units correspond to its nodes, and material streams correspond to its edges, and then apply graph algorithms to resolve these tasks [37].

The first step of topology analysis is aimed at solving the issue with recycle streams. The flowsheet has to be converted to a sequential form, which can be easily handled by the sequential-modular algorithm [13]. To do so, all available recycle streams must be found and some predefined initial values must be set to them [61]. This procedure is called tearing, and all found and initialized recycle flows are referred to as tear streams. Often the set of possible tear streams in the flowsheet is not unique, therefore, the algorithm for their selection can affect the rate of convergence, and, hence, the performance of the calculations. In Dyssol, the synthetic method of Roach [48] was implemented, which is able to find a near-to-optimal set of tear streams. This heuristic algorithm does not require preliminary decomposition of graph or detection of strongly coupled components, so it can be used already at the first step of topological analysis.

To come from the predefined initial values in the tear streams to the final solution, all units covered by a recycle loop must be calculated together iteratively until convergence. Such groups of units are known as partitions, and the process of their allocation is called partitioning. The main idea is to break the flowsheet into blocks that are connected exclusively sequentially. To search for partitions in Dyssol, the Tarjan algorithm for finding strongly connected components is used [58]. It takes a directed graph as input, distributes units into partitions in accordance with existing recycling flows, and organizes partitions in the order that corresponds to the calculation sequence. This method is a variation of the depth-first search algorithm and works in linear time. The original Tarjan algorithm allocates units that do not belong to any recirculation loop into partitions with one component. Therefore, it was supplemented by an additional step, which combines such sequentially arranged separate partitions into larger ones to simplify further calculations.

The last step in topological analysis is to determine the calculation sequence. The proper arrangement of partitions is already known from the previous step. To determine the order of units within them, the algorithm of simple topological sort based on the depth-first search [59] is applied in Dyssol simulation system. It takes a directed graph of a partition with preliminarily removed tear streams as input.

As a result, after partitioning, tearing and ordering, a flowsheet is obtained, which can be easily treated using the sequential-modular approach (Fig. 7).
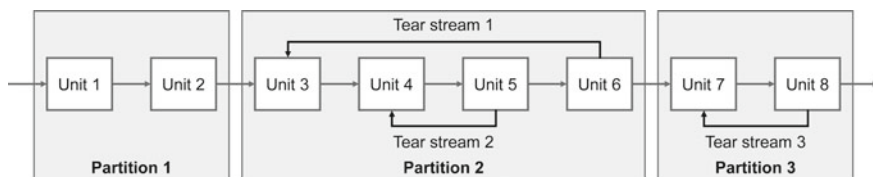

Fig. 7   Results of applying the topological analyser

3.3 Waveform Relaxation Method

To compute partitions with tear streams, an iterative procedure is applied in Dyssol. Dynamic modelling is usually performed for a large time interval, during which process parameters can vary significantly. Moreover, the number of parameters that participate in the convergence detection is not limited and depends on the complexity of the scheme. Consequently, the calculation of such partitions may be computationally intensive. To overcome this problem, the simulation framework Dyssol applies a calculation approach based on the waveform relaxation method (WRM). It was originally proposed to accelerate calculation of systems of differential algebraic equations by decomposing it into several subsystems, which can be then calculated separately [33].

To apply it to the solution of the convergence problem in dynamic flowsheet modelling, this method has been slightly modified [16, 53]. The entire simulation interval $[t_{START}; t_{END}]$ (Fig. 5) is sampled into smaller frames—so called time windows. The length of these windows (t_{WINDOW}) is selected such that the changes in the material parameters inside each of them are small, which ensures faster convergence. To calculate each partition, the first window $[t_{START}; t_{START} + t_{WINDOW}]$ is selected, all the parameters of tear streams inside the partition are initialized, and iterative calculation of all units is performed until convergence. In the simplest case, the difference between the parameters of tear streams at two consecutive iterations can serve as a convergence criterion. When the convergence is reached, the system initializes the next time window $[t_{START} + t_{WINDOW}; t_{START} + 2 \cdot t_{WINDOW}]$ and proceeds to its calculation according to the same procedure. Sequential calculation of all time windows from t_{START} to t_{END} for all partitions will lead to a rapid convergence of the entire solution.

The application of this approach imposes some restrictions on dynamic models: their internal simulation time step cannot be larger than the window size. Thus, t_{WINDOW} is an important parameter that affects the overall calculation performance. On the one hand, large time windows lead to an increase in deviations between successive iterations, which, in turn, can lead to poor convergence rates. On the other hand, too short time windows will lead to correspondingly small internal steps in the models, which can slow down the calculations. Therefore, the size of the time window in the Dyssol system is not a constant value, but may be changed dynamically, according to changes in the behaviour of the simulated processes. The faster convergence is achieved on a given time window, the larger the next one can be, and the other way around.

3.4 Convergence Methods

Iterative calculations of partitions on each time window are performed in the following order:

1. all parameters of tear streams in the partition are initialized;
2. units within the partition are calculated sequentially;
3. new values of tear streams' parameters are obtained;
4. the computed and initial values are compared to check convergence;
5. based on obtained values, new initials for tear streams are calculated;
6. calculations are repeated from step 2.

In this case, the convergence criterion can be defined as

$$\forall t \in [t_{START}; t_{STARTT} + t_{WINDOW}] : |x_{calc}(t) - x_{init}(t)| < |x_{calc}(t)| \cdot R_{tol} + A_{tol}, \quad (1)$$

where x_{init} is initial values; x_{calc} is new calculated values; R_{tol} and A_{tol} are relative and absolute tolerances, respectively.

Thus, calculating the initial values is an important step for the convergence rate. Dyssol applies special estimation algorithms, called convergence methods [13, 53], for proper calculation of initial values at each iteration. The main idea is to use the results of previous iterations to calculate improved initial values. Since Dyssol utilizes a modular approach, where only units in closed form are used, generally, there is no access to the models' internal equations. This imposes restrictions on the types of methods that can be applied in the framework and therefore, only the following convergence methods have been integrated into Dyssol [53]:

- *Direct substitution*, which is the simplest method that uses values calculated on the current iteration $F(x_k)$ as initial data for the next one (x_{k+1}):

$$x_{k+1} = F(x_k). \quad (2)$$

- *Direct substitution with relaxation* introduces the parameter λ, which determines the influence of the previous step $k - 1$ in addition to the results of the current iteration k:

$$x_{k+1} = (1 - \lambda)F(x_{k-1}) + \lambda F(x_k). \quad (3)$$

- *Wegstein's method* [64] performs a parabolic extrapolation using the results of two iterations. This method also provides the ability to control the rate of convergence using the acceleration parameter q [61]:

$$x_{k+1} = qx_k + (1 - q)F(x_k),$$
$$q = \frac{s}{s - 1},$$
$$s = \frac{F(x_k) - F(x_{k-1})}{x_k - x_{k-1}}, \quad (4)$$

- Steffenson's method that is an extension of Newton's method with Aitken's acceleration [39]. It uses the results of the current and previous two iterations. When

applying this method, for each three iterations, two steps of the direct substitution method and one step of the Aitkens acceleration formula are used:

$$x_{k+3} = x_k - \frac{(x_{k+1} - x_k)^2}{x_{k+2} - 2x_{k+1} + x_k}. \tag{5}$$

The choice of the convergence methods for a specific simulation depends entirely on the dynamics of the process under consideration.

3.5 Extrapolation Methods

After convergence has been achieved on the current time window, the simulation system proceeds to calculate the next one. To do so, the parameters of tear streams must be initialized again. The number of iterations and, hence, the convergence rate in this case will significantly depend on how close these initial values are to the final solution. The Dyssol system uses data extrapolation algorithms to calculate the initial assumption for each subsequent time window based on the results of the calculation of the current interval. One of the following methods can be applied for simulations in Dyssol [53]:

- *Nearest-neighbour* extrapolation that initializes the whole time window TW_{i+1} with values obtained at the last time point of TW_i.
- *Linear* extrapolation, which uses the first and the last time points of time window TW_i to extrapolate its values to TW_{i+1}.
- *Cubic spline* extrapolation [8] uses three points from TW_i to derive cubic polynomials describing its behaviour, and then extrapolates the resulting function to the next time interval TW_{i+1}.

The effectiveness of each method depends on the behaviour of a particular process: the nearest-neighbour is well suitable for nearly constant behaviour, the linear gives a good response if the data changes monotonously, and the cubic spline is the most advanced method that can well predict non-monotonic changes.

3.6 Validation of the Simulation Algorithm and Performance Analysis

To verify the developed calculation algorithms, several specially designed modelling experiments were performed. First, to test the basic calculation algorithm, flow-sheets consisting of purely mathematical functions were simulated, and the results were compared to the analytical solutions from Simulink (MATLAB). For instance, Eq. (6), which was represented by a scheme including three sine operations (marked

in (6) with {}-blocks), two separate operations of addition, and a multiplication block. The flowsheet also included a recycle stream to enable algorithms associated with waveform relaxation method.

$$y = 0.5 \cdot (\{0.5 \cdot \sin(\{\sin(t) + 2\} + \{\sin(2t) + 1\} + y) + 1\}). \qquad (6)$$

Figure 8 (left) shows the outcomes of modelling the given equation in Dyssol and MATLAB. It can be seen that the results obtained in both systems coincide.

To analyse the accuracy of calculations of the simulation system in dynamic mode, continuous fluidized bed spray granulation with external classification of product described in [47] was used as a reference process (Fig. 9). It includes one dynamic (granulator) and three steady-state (two screens and a mill) units enclosed into one recirculation loop. The granulation process in a fluidized bed apparatus is represented
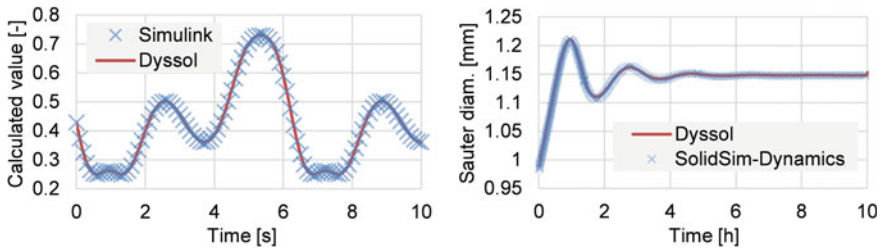
Fig. 8 Comparison of simulation results of purely mathematical functions obtained in Dyssol and Simulink (left) and comparison of simulation results of the granulation process obtained in Dyssol and SolidSim-Dynamics (right) [53]
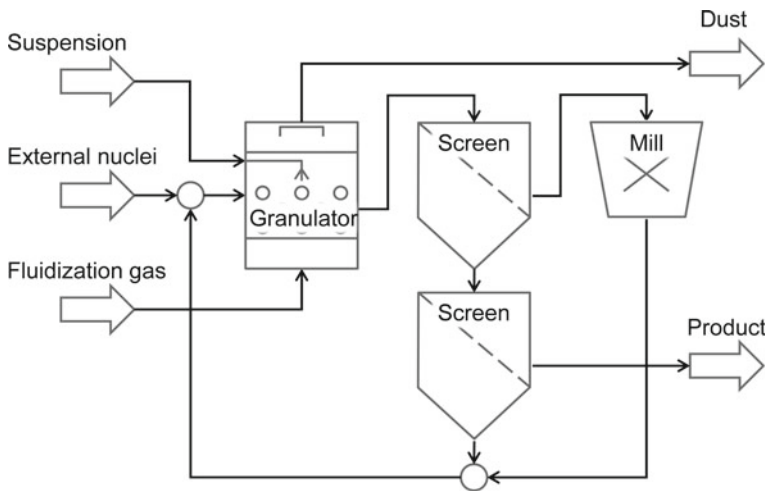
Fig. 9 Flowsheet of a continuous fluidized bed granulation process

by the one-dimensional population balance equation given in [47]. Verification of the simulation results from Dyssol showed very good agreement (Fig. 8, right) with the results obtained in SolidSim-Dynamics [16], which was used as the reference system.

Various test studies were performed to analyse the influence of the waveform relaxation method as applied to dynamic flowsheet simulation, as well as to estimate the contribution of different convergence and extrapolation methods. In one of them, the granulation process, whose flowsheet is shown in Fig. 9, was used as a reference. Its transient behaviour in an unstable operation mode, caused by fine milling [47], can be seen by the changes in the mass flow of the material leaving the granulator and by the changes in Sauter diameter of bed material inside the granulator as shown in Fig. 10a.

Figure 10b represents the sizes of the time windows, as well as the number of iterations required to achieve convergence at each moment of the process time. It can be seen that with monotonic changes in the process parameters the window size of the waveform relaxation method dynamically increases, while the number of iterations remains low. When significant changes in the process parameters occur at a certain time interval, the number of iterations increases, and the size of the time window decreases accordingly.

Convergence methods are involved in each iteration of the waveform relaxation method, so they significantly affect the performance of the calculations. For the granulation process, this effect can be seen in Fig. 10c. It shows the relationship between the model time and the cumulative number of iterations required to achieve convergence using different convergence methods and a fixed time window size (10 s). The methods of Wegstein and Steffensen require significantly less iterations to achieve convergence for the process under consideration compared to the basic direct substitution approach. Thus, it can be concluded that both advanced methods can provide higher convergence rates and potentially significantly shorter simulation times, despite their greater computational complexity.

To analyse the effectiveness of extrapolation methods that are used to initialize the first iteration at each time window, WRM-frames were also fixed at 10 s. Figure 10d shows the dependence of the cumulative number of necessary iterations at each moment of simulation time for three applied extrapolation algorithms. The most basic extrapolation using the nearest-neighbour method leads to a greater number of iterations compared to linear and cubic spline algorithms, which provide almost the same convergence rate in this case.

It should be noted, however, that the final choice of convergence and extrapolation methods in the general case should depend on the dynamics of the respective process.

4   Built-in Equation Solvers

In accordance with the applied sequential-modular approach, each model in the flowsheet can use its own equation solver. Therefore, models may have their own built-in mechanisms for calculation, depending on the type of algorithms used. However,
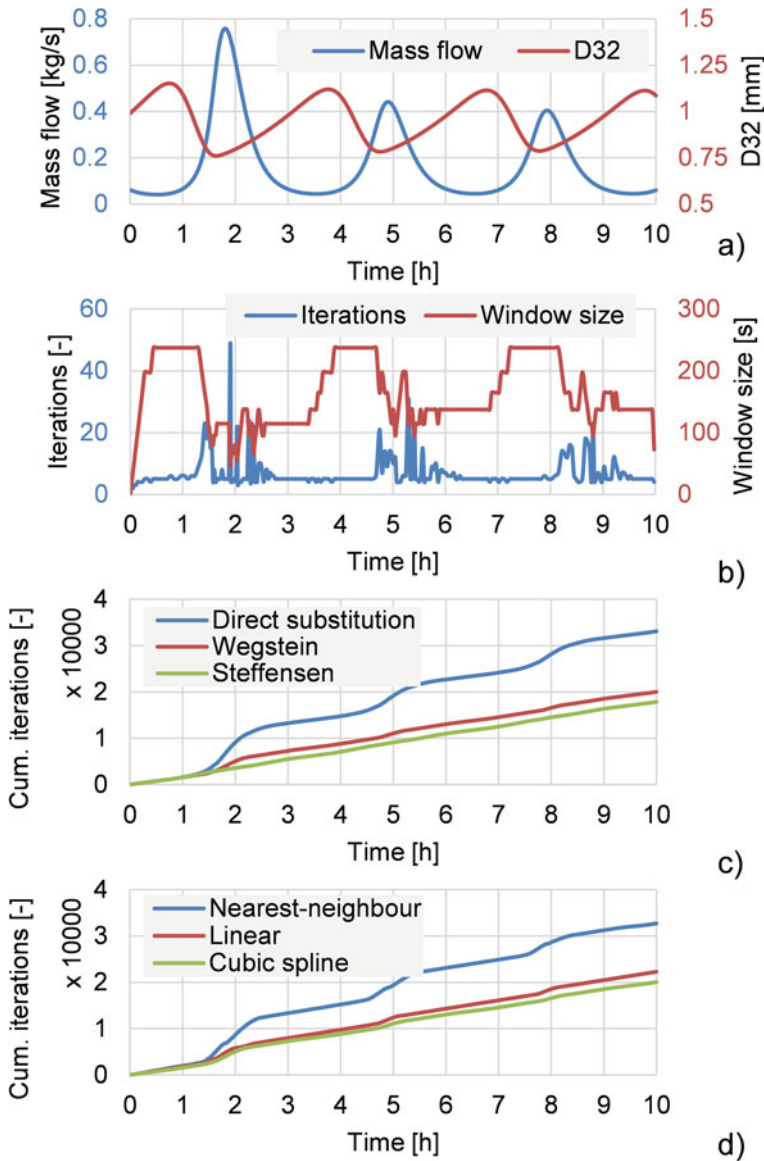
Fig. 10 Investigation of the influence of used simulation methods applied to the granulation process: mass flow of material leaving the granulator and Sauter diameter of bed material in the granulator (**a**); number of iterations required to reach convergence at each time window and the size of the WRM-window (**b**); influence of various convergence methods on the cumulative number of required iterations (**c**); influence of various extrapolation methods on the cumulative number of required iterations (**d**) [53]

since some types of equations are more common in models, several solvers were integrated into the modelling framework to facilitate the addition of new units to the system.

4.1 Solver of Differential-Algebraic Equations

To solve differential-algebraic equations (DAE) of form

$$F(t, y, \dot{y}) = 0, \quad y(t_0) = y_0, \quad \dot{y}(t_0) = \dot{y}_0, \tag{7}$$

the Dyssol simulation framework uses [54] the IDA (Implicit Differential-Algebraic) solver [25] from the SUNDIALS package [57]. It applies the variable-order, variable-coefficient backward differentiation formula in fixed-leading-coefficient form to solve the initial-value problem (7), transforming it into the following nonlinear algebraic system, which must be solved for each time step:

$$G(y_n) \equiv F\left(t_n, y_n, h_n^{-1} \sum_{i=0}^{q} \alpha_{n,i} y_{n-i}\right) = 0. \tag{8}$$

Here t is an independent variable denoting time; y and $\dot{y}$ are a dependent variable and its derivative, respectively; y_0 and $\dot{y}_0$ are initial values of the corresponding variables; y_n is the computed approximation of y at time point t_n; q is the order of the method in the range from 1 to 5; α is the coefficient, which is selected in accordance with the method order and the history of time steps in such a way as to maximize q; h is the time step size for each iteration, defined as

$$h_n = t_n - t_{n-1}. \tag{9}$$

Both h_n and q are varied dynamically to minimize local truncation error.

The system (8) is solved applying a modified Newton algorithm in which the calculation of the Jacobian can be skipped at some steps. The use of Newton's iteration leads to a linear system for Newton correction

$$J\left[y_{n(m+1)} - y_{n(m)}\right] = -G\left(y_{n(m)}\right),$$
$$J = \frac{\partial G}{\partial y} = \frac{\partial F}{\partial y} + \frac{\alpha_{n,0}}{h_n} \frac{\partial F}{\partial \dot{y}}, \tag{10}$$

where J is the approximation of the system's Jacobian; $y_{n(m)}$ is the m-th approximation of y_n. The linear system for the Newton's corrections is solved using a direct linear solver for dense matrices. If convergence is not possible with the current Jacobian, the time step is reduced by 4 times, and the integration step is repeated.

Since the proposed solver has internal variables that depend on the time and the current calculation step, there are issues associated with its application in a modelling system based on iterative calculations in conjunction with waveform relaxation method. To overcome these problems, the solver was expanded with additional functionality that allows saving and loading its internal state on demand when switching between different time windows of WRM.

From the point of view of unit developers, all the necessary functionality for describing the state variables and model equations of specific units is implemented as call-back functions.

4.2 Nonlinear Solver

The built-in solver for systems of nonlinear equations applies the KINSOL [10] solver from the SUNDIALS package [57]. KINSOL allows for the solution of systems of n nonlinear equations of the type

$$F(\vec{u}) = 0, F\colon \mathcal{R}^n \to \mathcal{R}^n \tag{11}$$

using Newton's method or Picard iteration [10]. Additionally, systems of type

$$G(\vec{u}) = \vec{u}, G\colon \mathcal{R}^n \to \mathcal{R}^n \tag{12}$$

can be solved by fixed-point iteration, which may be accelerated by Anderson acceleration method [3].

The Newton-type method computes the iteration step δ_n for iteration n using the Jacobian

$$J(u_n) = F'(u_n). \tag{13}$$

The updates are calculated by

$$u_{n+1} = u_n + \lambda \delta_n, \quad 0 < \lambda < 1 \tag{14}$$

before checking for convergence. For the fixed-point solver, the updated values of the variables

$$\vec{u}_{n+1} = G(\vec{u}_n) \tag{15}$$

are tested for convergence after each iteration. During Anderson acceleration, intermediate solution steps are performed and combined with computed weights to find the variable updates for the following iteration.

The solver class offers the user an interface for choosing the desired solving method and for setting different solver parameters, such as the maximum number of

iterations and the value for the Anderson acceleration. The model variables may be automatically scaled to accommodate possibly different ranges of their values. Once solved, the final values of the variables are stored into a system buffer for reutilization as initial values in following time steps.

4.3 Application Examples

The DAE solver has been utilized in several models from the Dyssol unit library. For example, in [54], it was used as part of the solution of the population balance equation of the agglomeration process. There an approach based on the separable approximation of the agglomeration kernel using the adaptive cross approximation method was proposed. Applying the fast Fourier transformation (FFT) to the obtained equations, it is possible to significantly speed up the calculation of agglomeration PBE. The IDA solver was consistently applied to solve the resulting equation in the form

$$\frac{\partial n(v, t)}{\partial t} = B_{agg}(n, v, t) - D_{agg}(n, v, t) + \dot{n}_{in}(t) - \dot{n}_{out}(t), \tag{16}$$

where v is the volume of particles; $n(v, t)$ is the number density function; B_{agg} and D_{agg} are the birth and death rates of particles calculated using the FFT solver; $\dot{n}_{in}(t)$ and $\dot{n}_{out}(t)$ are the number density distributions of inlet and outlet streams correspondingly.

Flowsheets of the processes studied, as well as some results of their modelling are shown in Fig. 11.
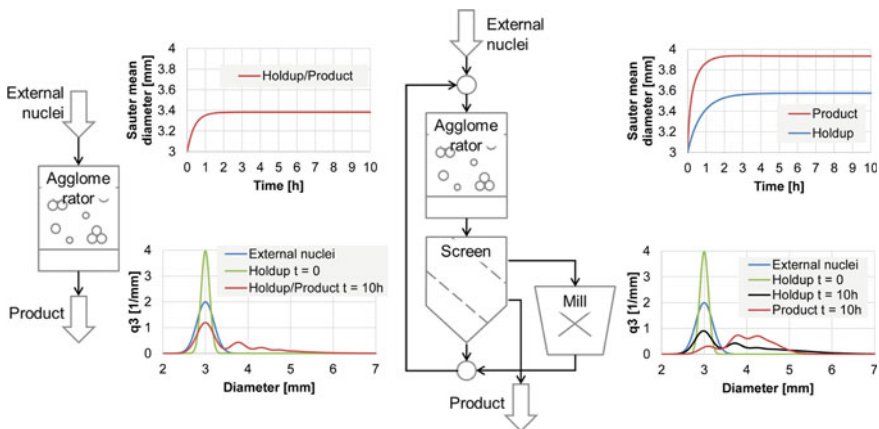
Fig. 11 Flowsheet structures of the investigated agglomeration processes and the results of their simulation [54]
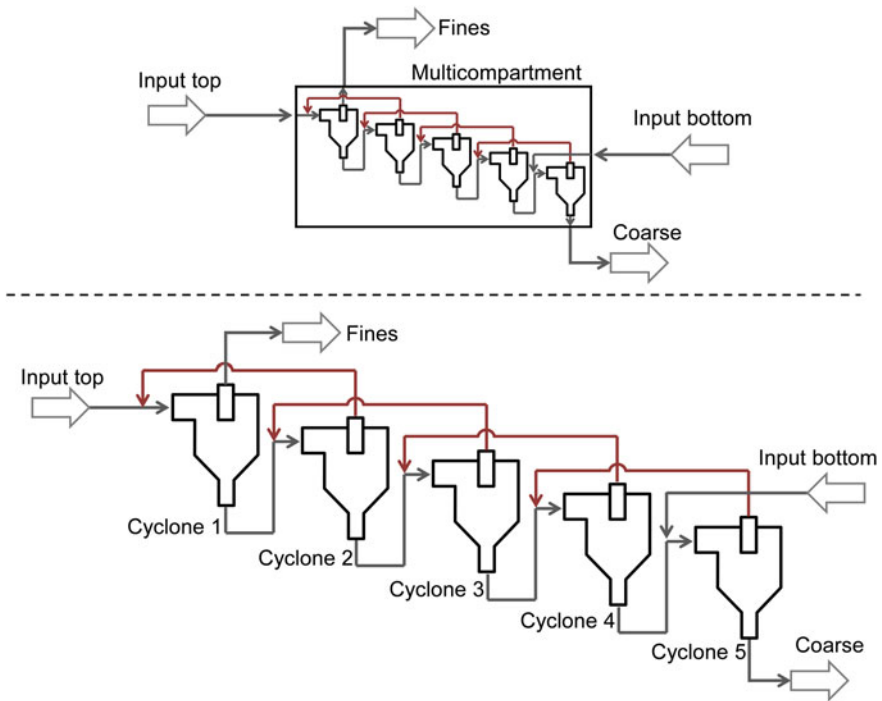
Fig. 12 Cyclone preheater process as a validation case for the KINSOL solver for systems of nonlinear equation, implemented as a multicompartment unit (top) and as a flowsheet of serially connected cyclone models (bottom)

A validation case for KINSOL solver has been set up using a flowsheet of a cyclone preheater which consists of five serially connected gas cyclones. The flowsheet was implemented in two different ways, shown in Fig. 12. The multicompartment unit (Fig. 12 (top)) uses the KINSOL solver for systems of nonlinear equations to compute the recycle streams in the unit, that are indicated in red. The validation flowsheet model of the cyclone preheater (Fig. 12 (bottom)) uses the calculation algorithms implemented in Dyssol (Sect. 3) to compute the recycle streams. The cyclone units apply the Muschelknautz approach [42] to calculate the particle separation and were taken from the Dyssol unit library (see Sect. 8).

The main model parameters for the validation case, i.e. the stream parameters for solid and gas inlets and the geometrical parameters of the cyclones, are given in Table 1. The materials for the gas and the solid phase are air and sand, respectively. The initial value of the mass flow in the recycle streams is set to zero. The initial particle size is normally distributed.

To compare the results of the simulations, the outlet stream *Coarse* is investigated. The results of both simulation cases are shown in Fig. 13, indicating the same results for the q3-distributions.

Table 1 Model parameters for cyclone preheating process

Input top		
Solid mass flow	$\dot{m}_{solid}$	0.18 kg/h
PSD: mean diameter/standard deviation	x_m/σ	1.2 mm/0.6 mm
Solids density	ρ_{solid}	1600 kg/m^3
Input bottom		
Gas mass flow	$\dot{m}_{gas}$	3.6 kg/h
Gas temperature	T_{gas}	300 K
Cyclone 1–5		
Cyclone outer diameter/total height/cylinder height	$d_{out}/h_{tot}/h_{cyl}$	2 m/1 m/0.1 m
Dip leg diameter/height	d_{dip}/h_{dip}	0.01 m/0.4 m
Entry width/height	b_e/h_e	0.4 m/0.3 m

Fig. 13 Comparison of simulation results of the cyclone preheating process, implemented as a multicompartment unit and as a flowsheet of serially connected cyclone models
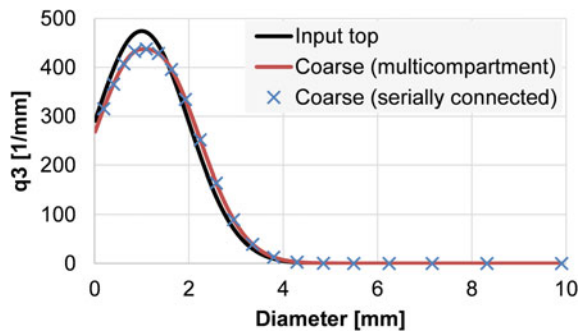
5 Multidimensional Distributed Parameters of Solids

For flowsheet modelling of the liquid and gaseous phases, it is sufficient to describe them with a finite number of concentrated parameters, such as mass flow, temperature or pressure. But things get more complicated if the solid phase is involved in the simulation. Typically, granular materials are composed of individual heterogeneous particles. The parameters of these particles (for example, their size, shape or porosity) vary in a certain range. From a mathematical point of view, with a sufficient number of particles, the entire bed of material can be quite accurately described using several continuous distribution functions that specify laws for all varying parameters. However, such a representation is not always convenient for modelling and numerical analysis. Therefore, in practice, the entire range over which a certain distributed parameter is defined is divided into several shorter discrete intervals, called classes. For each class, a representative value is selected, for example, the average value of this class. After that, all the material is distributed into these classes, assuming that all particles within each interval have the same parameters. Thus, instead of continuous functions, any distribution is represented as a finite set of discrete values that

Fig. 14 Matrix representation of multidimensional distributed parameters of solids
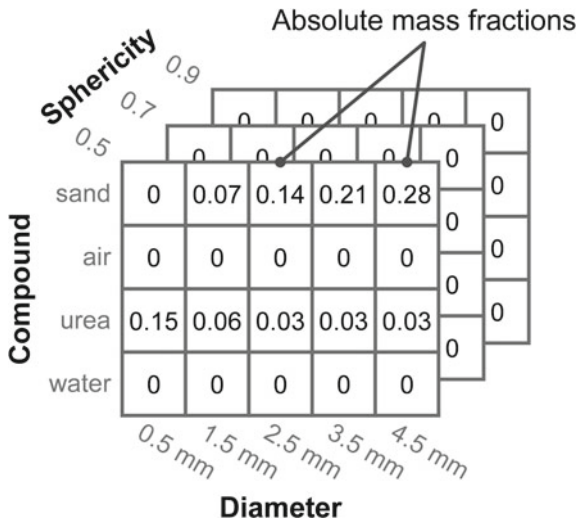
describe the amount of material (for example, mass, volume, or number of particles) in each class. By changing the number of classes, one can represent the entire initial distribution with the necessary accuracy.

For most models, one of the main parameters of the solid phase is the size distribution of particles. However, in addition to this, some other distributions can play an important role in individual devices, for example: yield strength in granulators [34], porosity and saturation in agglomerators [26], moisture content in dryers [1], shape and orientation of particles in crystallizers [29], chemical composition in many pharmaceutical subprocesses [40]. Thus, one model can utilize several interdependent parameters that form a multidimensional distributed set. It is usually mathematically described by multidimensional matrices, where the number of dimensions equals to the number of distributions (Fig. 14). Then each cell describes a fraction of material, which has the selected combination of parameters.

Thereby, in order not to limit the scope of the simulation system, the number and composition of the distributed properties may not be limited and must be flexibly configurable. Such an approach greatly complicates the modeling system. One of the major problems is that the number and composition of the distributed parameters used in each model on the flowsheet may not coincide. If these parameters are interconnected, maintaining their consistency becomes the task of the simulation framework.

5.1   Sparse Data Format and Tree Data Structures

One of the challenges that arises when dealing with multidimensional distributed parameters of solids, as applied to dynamic modelling, is the large amount of data

that must be easily and efficiently accessed, treated and stored. Therefore, a special sparse format was developed in Dyssol for multidimensional data structures (Fig. 15) [53, 52]. This format implements the following concepts to reduce the amount of data and to improve computing performance:

- tree topology;
- time-dependent distributions of fractions;
- relative mass fractions.

Parameters of solids are usually not distributed over the entire available grid, but are concentrated only on certain intervals. It means that matrices describing them may contain a lot of zero values (Fig. 14). To omit storing these unnecessary data, the sparse data structure implements the tree topology, where each level of the hierarchy describes the distribution of the material by a specific parameter (Fig. 15). This makes it possible to drop some branches of the tree if they are connected to empty values of the previous level, thereby reducing the amount of data that needs to be stored and processed. One of the frequently performed operations is the reduction of the entire set to only one or several dimensions. Such a tree structure greatly simplifies this procedure, since the distributions are stored in a partially precalculated form. So, in order to extract a distribution of the level L_N from the overall set, it is necessary to take into account only the current and higher hierarchical levels ($L_1 - L_N$). The higher the distribution in the structure, the fewer operations must be done to extract it. Thus, proper sorting of levels can significantly improve data access performance.

In dynamic processes, parameters of the material are changing in time. To represent this transient behavior, time as parameter must be introduced into the tree
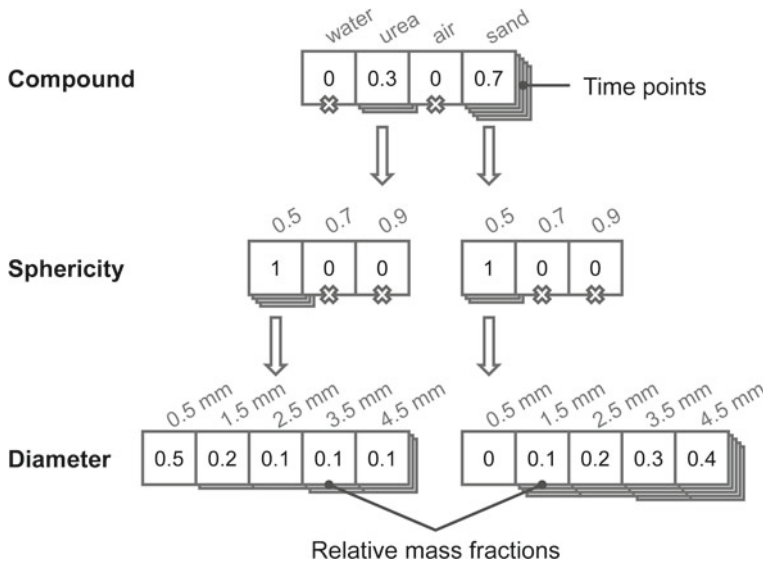

Fig. 15 Tree data structure for storing multidimensional distributed parameters of solids

structure. It can be done on two structural levels: (1) as the top parameter—the whole tree is defined for each time point; (2) as the bottom parameter—each value of the tree is distributed over time. For the Dyssol simulation system, the second approach was selected. Each record of the tree data structure is a time-dependent mass fraction of material, which has a selected combination of parameters. Since many parameters vary only slightly over time, some optimizations can be applied here. Values c of parameters at the certain time point t_i that can be obtained by linear interpolation between two adjacent time points t_{i-1} and t_{i+1} with sufficient accuracy via

$$\left| c(t_i) - \left(\frac{c(t_{i+1}) - c(t_{i-1})}{t_{i+1} - t_{i-1}} (t_i - t_{i-1}) + c(t_{i-1}) \right) \right| < |c(t_i)| \cdot R_{tol} + A_{tol} \qquad (17)$$

can be removed from the list. This approach assumes that the number of values in each array is not constant and depends on the behavior of the simulated process. Therefore, each stored value must be additionally labeled with a time. Data filtering at this level not only additionally decreases the amount of values being stored, but also further reduces the overhead of performing massive operations on time intervals, such as copying and mixing of streams.

Some initially empty classes can be populated during simulation, increasing the number of existing branches in the tree and, accordingly, reducing the efficiency of the method. To reduce this effect, the proposed approach can be expanded by dividing the entire structure into several time intervals, combining top-level and bottom-level approaches. However, to achieve the best result, this will require an online analysis of the data in order to coordinate the sizes of time intervals with the dynamics of the simulated process.

Instead of having fractions related to the entire amount of material, the proposed approach uses relative mass fractions. This becomes possible due to the fact that the information is stored separately at each level of the hierarchy. The use of relative mass fractions allows working with individual distributions without affecting information in the rest.

5.2   Calculation of Multidimensional Distributed Parameters

In the flowsheet modelling, two main approaches can be applied to calculate the parameters of holdups and outlets [16]:

- explicit: all distributed variables are calculated directly and set to output streams;
- implicit: inlet streams are transformed into outlet streams according to the laws of material transfer.

The explicit approach applied for a dynamic model, schematically shown in Fig. 16, can be described as [52]:
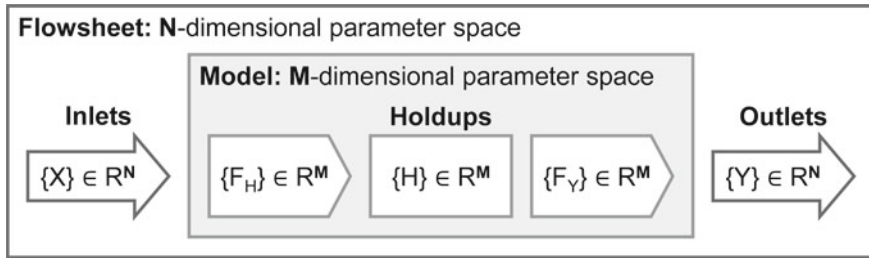
Fig. 16 Simplified scheme of embedding a model into a flowsheet

$$\begin{cases} H(t + \Delta t) = F_H(t + \Delta t, \{X(t + \Delta t)\}, \{H(t)\}, \{Y(t)\}) \\ Y(t + \Delta t) = F_Y(t + \Delta t, \{H(t + \Delta t)\}) \end{cases}, \tag{18}$$

where H, X, and Y are holdup, input, and output stream variables, correspondingly; F_H and F_Y are model functions, which describe changes in holdups and output streams, respectively.

The entire flowsheet can be defined for some set of distributed parameters N. At the same time, in a model developed in accordance with the explicit approach, function sets $\{F_H\}$ and $\{F_Y\}$ are usually defined for a limited set of distributed parameters M. And since the output distribution $\{Y\}$ is calculated directly from the internal state $\{H\}$ and the model functions $\{F_Y\}$, it will also be defined in M-dimensional parameter space:

$$\begin{aligned} &\{X\} \in R^N, \\ &\{F_H\}, \{F_Y\} \in R^M \rightarrow \{H\}, \{Y\} \in R^M, \end{aligned} \tag{19}$$

In general, if a change in the number and composition of distributed properties is allowed in the modelling system, M and N may not coincide. Then 3 cases can be distinguished [52]:

- $R^M = R^N$: the solution works well, since all distributed parameters can be calculated directly;
- $R^M \notin R^N$: the parameters cannot be calculated at all, because it requires more information than is available;
- $R^M \subset R^N$: the model in the M-dimensional parameter space will be calculated correctly, but the proper results cannot be obtained for the parameters R^N/R^M.

Thus, among the disadvantages of an explicit approach, it can be noted [52]:

- considering only the limited set of required distributed parameters leads to the loss of information about the others, despite the fact that there may be enough information to calculate them;
- all possible distributed parameters should be known and considered when developing the model;

- if the number or composition of the distributed parameters varies, the model itself must track these changes and correctly respond to them;
- the model should ensure the setting of all distributions defined at the input into the output flows, even those that are not explicitly considered in its equations.

It can be concluded that the commonly used explicit approach is not applicable for flowsheet simulation systems with flexible number of distributed parameters. Therefore, Dyssol implements an implicit approach based on the use of transformation matrices [16, 45, 52]. Here, model functions $\{F_H\}$ and $\{F_Y\}$ are not applied directly, but are used to derive the laws of the material transition θ between all classes in form of transformation matrices for holdups T_H and outlets T_Y:

$$\begin{cases} T_H(t) = \theta_H(F_H(t)) \\ T_Y(t) = \theta_Y(F_Y(t)) \end{cases}. \tag{20}$$

To describe transformation of N-dimensional space of distributed parameters, a $2N$-dimensional transformation matrix T is needed. Then each entry $T_{\{I^N\},\{J^N\}}$ of T describes the fraction of material that needs to be transferred from the $\{I^N\}$-th class of some input distribution to the $\{J^N\}$-th cell of the corresponding output distribution. Here $\{I^N\}$ and $\{J^N\}$ denote a set of indices for accessing any value of the N-dimensional parameter space, so that

$$\{I^N\} = i_1 i_2 \dots i_N, \, i_d \in [1 : L_d], \, d \in [1 : N], \tag{21}$$

where L_d is a number of discrete classes in the distributed property d.

The final values of the holdups and the output streams can be obtained by applying the transformation matrix to the corresponding input distribution as

$$\begin{cases} H(t + \Delta t) = T_H(t + \Delta t) \otimes H(t) \\ Y(t + \Delta t) = T_Y(t + \Delta t) \otimes H(t + \Delta t), \end{cases}$$
$$\{T_H\}, \{T_Y\} \in R^M \to \{H\}, \{Y\} \in R^N, \tag{22}$$

where $\otimes$ is the operation of applying the transformation matrix. Then for the case $R^M \subset R^N$, Eq. (18) for dynamic units takes the following form:

$$\forall\{J^N\} : \begin{cases} H_{\{J^N\}}(t + \Delta t) = \sum\limits_{\{I^N\}} H_{\{I^N\}}(t) \cdot T_{H_{\{I^M\},\{J^M\}}}(t + \Delta t) \\ Y_{\{J^N\}}(t + \Delta t) = \sum\limits_{\{I^N\}} H_{\{I^N\}}(t + \Delta t) \cdot T_{Y_{\{I^M\},\{J^M\}}}(t + \Delta t). \end{cases} \tag{23}$$

The same considerations can be applied to formulate Eqs. (18)–(23) for steady-state units.

5.3 Application of Transformation Matrices

From a mathematical point of view, the operation of applying the transformation matrix $\otimes$ on some distribution can be described as regular matrix multiplication. But since distributed sets are represented in Dyssol in a sparse format, special algorithms must be developed and applied. The use of a tree-like data structures with relative mass fractions simplifies this procedure, since it allows the use of transformation matrices for each level separately, without affecting all distributions located at higher hierarchical levels.

If the N-dimensional distribution is represented by N hierarchy levels, where L_d is the number of classes in the d-th dimension, and $X_q^p(t)$, $Y_q^p(t)$ and $H_q^p(t)$ are the relative mass fractions in the q-th class of the p-th level in the initial distribution, the transformed distribution, and the holdup, accordingly, the application of the transformation matrix T defined for the M-dimensional space of distributed parameters ($R^M \subset R^N$) will be performed in three stages [52]:

1. Apply T to the lowest M-th level of the tree structure according to (23) in the following form:

$$
\forall \{J^M\} :
$$
$$
\begin{cases}
H^M_{\{J^M\}}(t + \Delta t) = \sum_{\{I^M\}} \eta^M_I(t) \cdot T_{H_{\{I^M\},\{J^M\}}}(t + \Delta t) \\
Y^M_{\{J^M\}}(t + \Delta t) = \sum_{\{I^M\}} \eta^M_I(t + \Delta t) \cdot T_{Y_{\{I^M\},\{J^M\}}}(t + \Delta t), \\
\eta^M_I(t) = H^M_{\{I^M\}}(t) \cdot H^{M-1}_{\{I^{M-1}\}}(t) \cdot \ldots \cdot H^2_{\{I^2\}}(t) \cdot H^1_{\{I^1\}}(t)
\end{cases}
\tag{24}
$$

2. Reduce the transformation matrix T to obtain the transformation laws at the previous level $(M - 1)$ and apply them using (24). Repeat this for all hierarchy levels up to 1.
3. Apply T to calculate the remaining levels K according to:

$$
\forall K : M < K \leq N, \forall \{J^K\} :
$$
$$
\begin{cases}
H^K_{\{J^K\}}(t + \Delta t) = \dfrac{\sum_{i_1=1}^{L_1} \eta^K_J(t) \cdot T_{H_{\{I^1\},\{J^1\}}}(t+\Delta t)}{\eta^{K-1}_J(t+\Delta t)} \\
Y^K_{\{J^K\}}(t + \Delta t) = \dfrac{\sum_{i_1=1}^{L_1} \eta^K_J(t+\Delta t) \cdot T_{Y_{\{I^1\},\{J^1\}}}(t+\Delta t)}{\gamma^{K-1}_J(t+\Delta t)}
\end{cases}
\tag{25}
$$
$$
\eta^K_J(t) = H^K_{\{J^K\}}(t) \cdot H^{K-1}_{\{J^{K-1}\}}(t) \cdot \ldots \cdot H^2_{\{J^2\}}(t) \cdot H^1_{\{J^1\}}(t)
$$
$$
\gamma^K_J(t) = Y^K_{\{J^K\}}(t) \cdot Y^{K-1}_{\{J^{K-1}\}}(t) \cdot \ldots \cdot Y^2_{\{J^2\}}(t) \cdot Y^1_{\{J^1\}}(t)
$$

Applying this algorithm, using Eqs. (24) and (25), as well as sorting levels in the hierarchical data structure, it is possible to apply any valid transformation matrix to any input distribution.

The type of unit slightly affects the algorithm for applying transformation matrices:

- in steady-state units: the input distribution is copied to the output, then the transformation matrix is applied to the output;
- in dynamic units: the input distribution is mixed with the holdup, then the transformation matrix is applied to the holdup, after which the outputs are calculated.

5.4   Simulation Examples

In order to test and validate the developed algorithms for lossless calculation of the distributed parameters of the solid phase, several model experiments were performed. The flowsheet of one of the simulated processes [53] is presented in Fig. 17. It is a typical grinding process often used in the mineral processing industry [19, 50]. It consists of three successive crushing stages: pre-grinding of coarse material, separation and further grinding of large fractions, and the final crushing in a closed circuit.
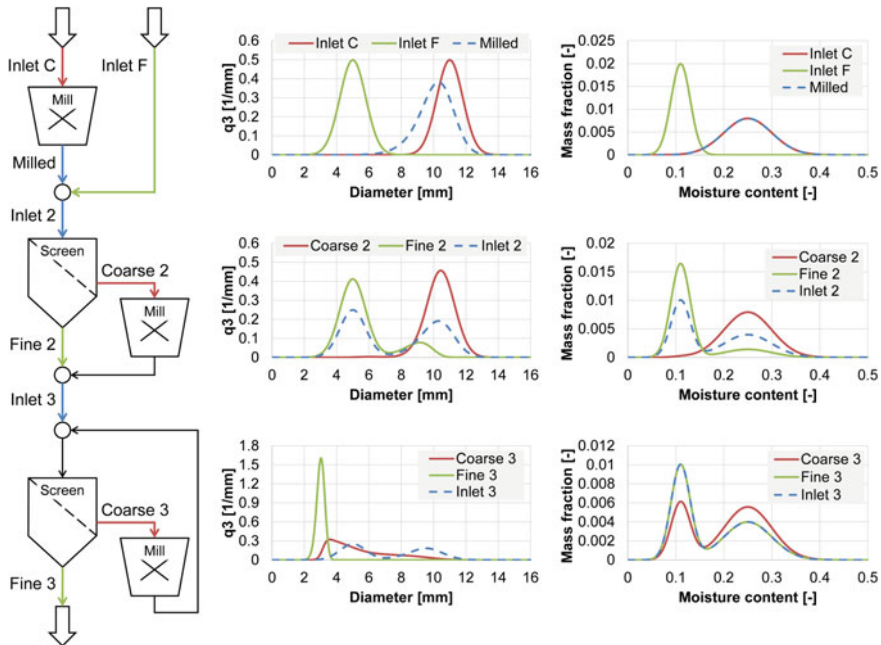
Fig. 17 Flowsheet of the three-stage crushing process and the results of its simulation in the Dyssol system [53]

Each unit on the flowsheet formulates and applies a two-dimensional transformation matrix for the particle size distribution.

The screen unit is defined in terms of grade efficiency, which determines a mass fraction of particles of a certain diameter that leaves the screen through the coarse outlet. The transformation matrices for coarse T^c and fine T^f output streams are calculated as:

$$\begin{cases} T^c_{i,i} = G(x_i) \\ T^f_{i,i} = 1 - G(x_i) \end{cases}, \tag{26}$$

where $G(x)$ is a grade efficiency for particles of size x, calculated according to Plitt's model [44].

Selection $S(x_k)$ and breakage $B(x_k, x_i)$ functions are used to describe the model of crusher. $S(x_k)$ determines the mass fraction of particles of size x_k, which will be crushed, while breakage function $B(x_k, x_i)$ defines the number of particles of size x_i that get the size of x_k after crushing. The transformation laws are calculated as

$$T_{i,k} = \begin{cases} B(x_k, x_i) \cdot S(x_k), & i <> k \\ 1 - S(x_k), & i == k \end{cases}. \tag{27}$$

As $B(x_k, x_i)$ Vogel's breakage function [62] was applied, whereas the selection function $S(x_k)$ was calculated according to King [28].

The source material was described using two interdependent distributed parameters:

- particle size: the main parameter that is calculated directly in all models;
- moisture content: a secondary parameter that is not considered in the models' equations, but is calculated indirectly by applying transformation matrices.

For simplification, it was assumed that no moisture transfer between particles and no drying occurs.

From the obtained simulation results (Fig. 17), it can be seen that, despite the fact that all models were defined to directly calculate only the particle size distribution, information about the secondary parameter was stored and properly considered in accordance with the formulated transformation laws. So, for example, at the first stage of the process (Fig. 17), one can observe a change in particle size (*Inlet C—Milled*) due to the operation of the mill. At the same time, the amount of moisture does not change. After that, the milled wet and small dry particles are mixed and fed to the next stage. Due to mixing, one can observe a bimodal distribution of both parameters in the *Inlet 2* stream. However, the application of the screen makes it possible to separate particles by size, while the moisture content is also mainly distributed between two streams *Coarse 2* and *Fine 2*. Since some initially large wet particles were crushed in the first mill, and also due to non-ideal separation in the screen, some mixing of different fractions is observed. At the last stage, the final

milling of the particles occurs. As a result, the proportion of wet material in the fine fraction increases.

In [52], new approaches for calculating transformation matrices from the population balance equations for agglomeration and milling have been developed. The finite volume method for spatial discretization and the second-order Runge-Kutta method for obtaining the complete discretized form of the PBE were applied to derive transformation laws.

Transformation matrices for agglomerator were calculated by introducing birth w^b and death w^d rates, which are responsible for conservation of number and mass of particles, in the form:

$$T_{i,j}(t) = \begin{cases} 1 + \left(\frac{1}{2} \sum_{(i,k) \in \mathbb{I}^i} g(x_i, x_k, t) \cdot w^b(x_i, x_k) - \sum_{j=1}^{L} g(x_i, x_j, t) \cdot w^d(x_i, x_j) \right) \Delta t, & i = j \\ \frac{1}{2} \sum_{(i,k) \in \mathbb{I}^i} g(x_i, x_k, t) \cdot w^b(x_i, x_k) \cdot \Delta t, & i < j \\ 0, & i > j \end{cases}$$

$$g(x_i, x_k, t) = \beta(x_i, x_k) \cdot \Delta x_k \cdot u(x_k, t).$$

(28)

Here x_i and x_k are sizes of agglomerating particles; $u(x_k, t)$ is the mass fraction of particles of size x_k at time t; Δx_k is the length of the size class k; $\beta(x_i, x_k)$ is the agglomeration rate for particles of sizes x_i and x_k; L is the number of size classes; $\mathbb{I}^i$ is a set of indices for accessing each object in a $L \times L$ matrix.

A similar approach was used to calculate the values of the transformation matrix for the mill unit:

$$T_{i,j}(t) = \begin{cases} 1 + \left(\varphi^b(x_i) \cdot \int_{x_{i-\frac{1}{2}}}^{x_i} B(x, x_i) dx - \varphi^d(x_i) \right) S(x_i) \Delta t, & i = j \\ S(x_i) \cdot \varphi^b(x_i) \cdot \int_{x_{j-\frac{1}{2}}}^{x_{j+\frac{1}{2}}} B(x, x_i) dx \cdot \Delta t, & i > j \\ 0, & i < j \end{cases}$$

(29)

where x_i is the size of the crushed particles; B and S are breakage and selection functions, respectively; φ^b and φ^d are birth and death rates, needed to conserve mass and particles number.

The proposed approach was implemented in form of dynamic units of a mill and an agglomerator and was then numerically investigated as applied to a part of a pharmaceutical process. Its flowsheet structure is given in Fig. 18. To calculate the screen unit, the same approach as it is described in Eq. (26) was used. The following dependencies were utilized in the applied models:

- screen: Plitt's model [44] for grade efficiency;
- mill: King's selection function [28] and Vogel's breakage function [62];
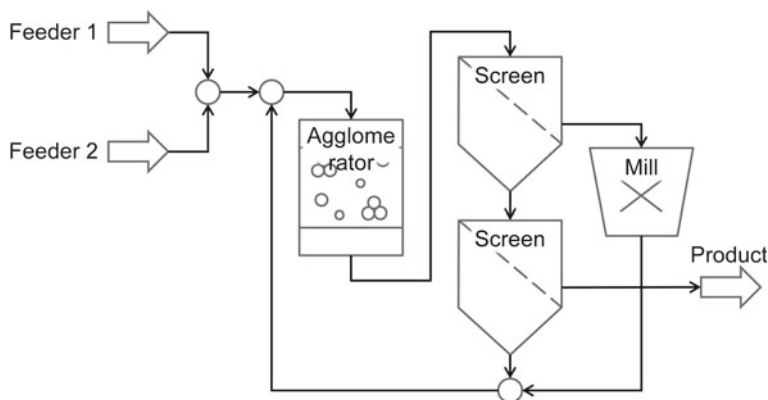- agglomerator: Brownian motion agglomeration kernel [2].

Fig. 18 Flowsheet structure of the agglomeration process

The simulated process (Fig. 18) is an agglomeration of a two-component blend. Two feeders supply materials with different particles sizes and different concentrations of an active pharmaceutical ingredient (API). Both materials mix and enter a closed circuit, where gradual particle growth occurs. After agglomeration, particles are classified by size. Too large particles are crushed in a mill, combined with small particles and sent back to the agglomerator. Medium sized agglomerates are considered as product.

The agglomerator model has been additionally enhanced by introducing averaging of secondary distributed parameter into transformation laws to treat the API concentration during agglomeration of particles [52].

The presented flowsheet was simulated until a steady state was reached [52]. The distribution of material in all apparatuses, as well as at the process outlet, is shown in Fig. 19. The obtained results show that the loss of information on the secondary distributed parameter is not observed, despite the fact that only the agglomerator model explicitly takes into account the concentration of API. For example, it can be seen that the distribution of particles with a higher concentration of API has two peaks: the first reflects the distribution of the initial material from feeder 2 mixed with new particles formed in the agglomerator and the mill; and the second is the result of agglomeration of particles with an equally high concentration of API with each other. Fractions with low API concentration are formed due to agglomeration of particles coming from feeder 1 with each other, as well as due to grinding of larger fractions by a mill unit. Since initially there were less particles with low API content, the distribution is more uniform. At the same time, a blend of two initial mixtures (from feeder 1 and feeder 2), formed as a result of agglomeration of materials with different API concentrations, is present in a significant amount, and can be clearly distinguished.

Thus, using transformation matrices to calculate the distributed parameters of the solid phase, it is possible to simulate complex processes involving materials described by a large number of interconnected parameters.
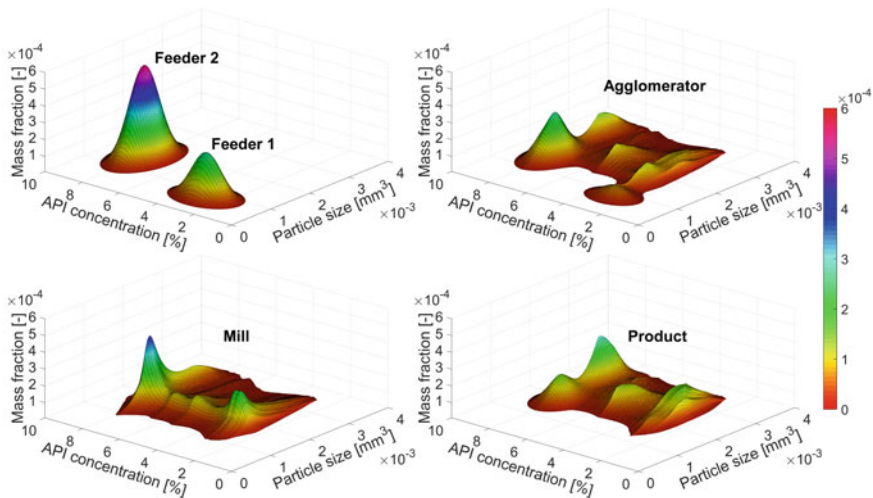
Fig. 19 Results of simulation of the agglomeration process in the Dyssol system

6 Data Storage Subsystem

6.1 Organisation of Data Storage

The data storage subsystem is responsible for writing, storing and reading all the data generated during the operation of Dyssol. Based on the requirements for the developed simulation framework, this subsystem should provide the following functionality:

- serialization/deserialization of complex data structures with various types of information;
- cross-platform access to the data regardless of operating system or file system;
- availability of data for third-party tools without using the Dyssol framework.

To ensure the fulfilment of all the requirements, the Hierarchical Data Format HDF5 and the HDF5 library [60] were utilized in the simulation system. HDF5 has been specifically designed to store and manage large and complex data sets. It is used in various applications where fast data processing and/or storage of a large amount of dynamically generated data is required. It allows developing easily extensible platform-independent solutions for organizing complex data structures and efficient work with large data sets. The use of the standardized data storage format and the availability of application programming interfaces for many tools and programming languages (for example, C/C++, Java, MATLAB, Python) allows organizing access to simulation results from external programs and utilities.

The provided programming interface for the C++ programming language [20] was used to integrate HDF5 into the Dyssol simulation environment. The HDF5

library was utilized as the lower layer of the data processing subsystem, where it is responsible for all direct work with the computer file system. The conversion between the Dyssol data format and the HDF5 data format is performed only during data serialization and deserialization, so the modelling system can use suitable and optimized data structures during its operation.

6.2 Dynamic Data Caching

One of the difficulties that arise when applying distributed parameters in dynamic simulations is the continuous generation of significant amounts of data. If the set of distributed parameters and the number of discretization classes for each dimension are not limited, the complexity of the flowsheets under study can be restricted by the free RAM of the computer.

To solve this problem, a subsystem for dynamic data caching was developed and implemented in Dyssol. Its work is based on the fact that at each moment the simulation framework works only with certain groups of units (partitions) in a certain time interval. The rest of the information is not used, so it can be temporarily unloaded from RAM. Therefore, at each moment of operation, the system stores only information about several time points from those material streams that are currently being involved in the calculations. For greater flexibility, the caching algorithm is applied for each material stream independently.

To minimize the impact of slow data backup and recovery, one must correctly select the time interval that will be available from the working memory. Since the Dyssol simulation system uses the waveform relaxation method, this interval should take into account the current size of the time window. On the one hand, if the boundary of the cached interval is inside the current time window, data backup and recovery will be performed at each iteration of the WRM, on the other hand, too large cache windows will increase the amount of unused information stored in RAM. Since for the correct operation of the waveform relaxation method, it is necessary to interpolate data from the previous time window, the minimum size of the uncached interval is $2 \cdot t_{WINDOW}$ (current and previous window) for each material stream in the partition.

7   Materials Database

The implemented materials database gives the option to choose from a set of predefined materials or to define new compounds. In addition to existing material properties, the user can define his own set. All of them are divided into constant properties and properties depending on temperature and/or pressure. While constant parameters, like molar mass, critical temperature and standard formation enthalpy, cannot change their value during the simulations, temperature or pressure (TP) depended parameters, like enthalpy or vapour pressure, have to be evaluated at runtime. The TP

dependencies may be either pre-defined correlations (e.g. polynomic functions), or lookup tables, that are directly visualized in the material database graphical interface. For each dependency a valid range has to be defined. If the function is evaluated outside of this range, a nearest neighbour value inside the valid range is selected instead. In addition, the user can define properties that describe the interaction between two compounds, like surface tension at a phase boundary.

8 Units and Solvers Library
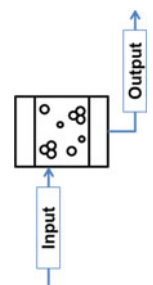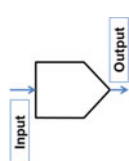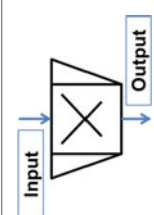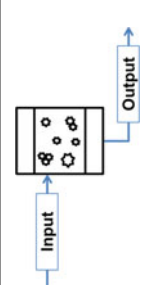
In Table 2, the units available in the Dyssol unit library are presented. The shown list is complemented by a set of service units, like basic inlet, mixer, or splitter, which are not described in detail. The available custom solvers from the Dyssol solver library are listed in Table 3. Additional modules, implemented in Dyssol, are described in Table 4.

9 Numerical Process Optimization and Parameter Adjustment

To allow for global optimization of unit and process parameters for dynamical processes, a genetic algorithm has been implemented according to Weicker [65]. Its flowchart is shown in Fig. 20.
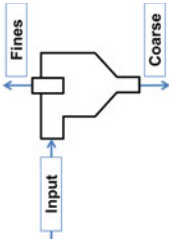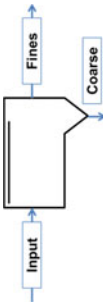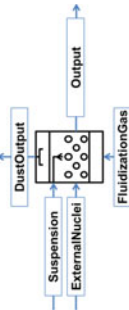
The main optimization parameters are the number of the so-called parent solutions n_{parent} and the number of child solutions per parent n_{child}. During initialization stage, a number of n_{parent} solutions are generated randomly within the defined bounds of the solution space. In the main loop, for each parent solution n_{child} solutions are generated by mutation of the respective parent solution. The mutation is achieved by addition of a random value from a gaussian function with zero mean and standard deviation σ. The standard deviation σ determines the size of the search space in which the child solutions may lie and influences the convergence of the optimizer. In one iteration of the main loop, a total of $n_{parent} \times n_{child}$ solutions are generated by mutation, for which the flowsheet model is simulated. The deviation of the variables, received from the flowsheet simulation, to the target values is evaluated using root-mean-square error (RMSE) function. Following, the n_{parent} best solutions are selected according to the lowest RMSE as start values for the next iteration. Additionally, if chosen via user input, the best parent solution may be taken to this list of selected solutions, if its RMSE is lower than the best child solutions. After a user-defined number of iterations, the standard deviation σ of the mutation function is adjusted. If the RMSE is not decreasing, the value of σ is reduced—and vice versa—to adjust the size of the solution space and therefore the convergence.

Table 2 List of units available in the Dyssol library

	Schematic	Type	Description
Agglomerator		Dynamic	The agglomerator unit [54] calculates the output particle size distribution based on simplified population balances that don't account for particle attrition. The unit parameters offer the option to select different agglomeration kernels as well as to choose from a list of available solvers from the solver library
Bunker		Dynamic	The bunker unit is modeled with an ideally mixed holdup. The target mass of the bunker is set via unit parameter. The output mass is controlled by an internal PID-controller to match the user-defined target holdup mass
Crusher		Steady state	There are multiple comminution laws for different applications available: • Bond's power law, originally developed for comminution in ball and rod mills [7] • Comminution for cone crusher, applying a selection function developed by King [28] and a breakage function presented by Vogel and Peukert [62] • A general population balance model including a solid holdup, applying a selection function presented by Austin and Luckie [6] and a breakage function shown by Austin [5]
Crystallizer		Dynamic	The crystallizer unit models simultaneous crystal growth and aggregation in a seeded batch crystallizer, presented by Kovacevic and Briesen [30]. To solve the population balances it uses a Monte-Carlo method

(continued)

Table 2 (continued)

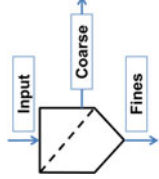|	Schematic	Type	Description
Cyclone		Steady state	The cyclone model is based on the model presented by Muschelknautz [42]. It is applicable for cyclones with tangential, axial and spiral inlet. There are two mechanisms of separation considered, namely the separation due to a surpassing threshold in solids loading and the separation in the inner cyclone vortex. Multiple geometric parameters of the cyclone can be defined in the user interface
Electrostatic precipitator		Dynamic	The model of the electrostatic precipitator [49] considers a preliminary separation of the particles according to Deutsch [12]. They reside in a layer of particles and may be resuspended to the gas stream depending on the layer thickness
Granulator		Dynamic	This unit represents a simplified model of a fluidized bed granulation reactor. The model is based on the work of Heinrich et al. [21]. It accounts for particle growth and for possible overspray, which may lead to additional dust formation in the system. The attrition of particles and the formation of nuclei is neglected
Heat exchanger		Steady state	The heat exchanger is based on a simplified approach calculating a heat flow for the ideal case, in which both output streams leave the system with the same temperature. A user-defined heat transfer efficiency parameter reduces the heat flow to account for output streams with different temperatures

(continued)

Table 2 (continued)

	Schematic	Type	Description
Screen		Steady state	There are multiple models for the calculation of the separation efficiency of the screen unit available, based on the research of the following authors: • Molerus and Hoffmann [41] • Plitt [44] • Probability model shown in Radichkov et al. [47] • Henning and Teipel [23]
Time delay		Dynamic	This unit adds a user-defined time delay to the incoming signal. To deal with numerical issues and to make it compatible with the sequential-modular approach, a first order time delay is additionally applied to the input variables, which acts as a smoother for step signals

Table 3 List of solvers available in the Dyssol library

	Method	Description
Agglomeration	Cell average	Based on the work of Kumar et al. [31]
	Fixed pivot	Based on the work of Kumar and Ramkrishna [32]
	FFT-based	Based on the work of Skorych et al. [54]

Table 4 List of additional modules available in Dyssol

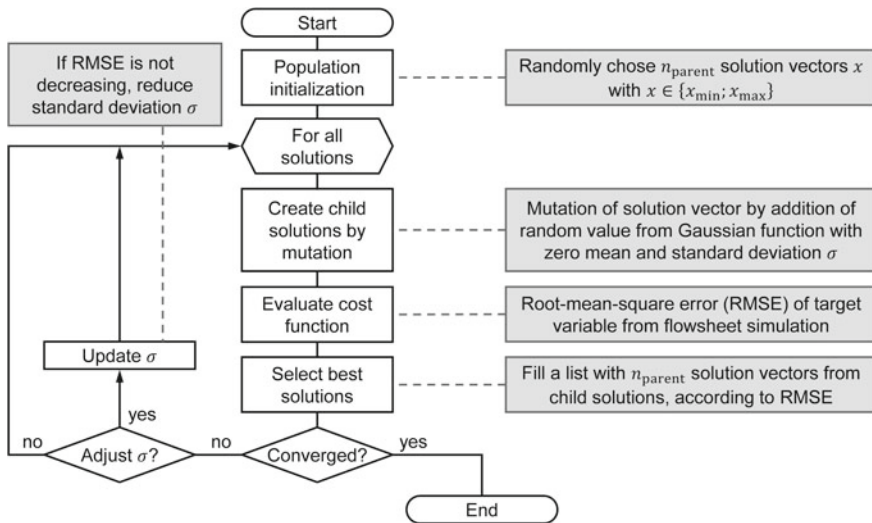|	Description
Dustiness tester	This module evaluates the dust tendency of each material stream in the flowsheet. It applies prognosis functions comparable to the testing methods such as single drop, rotating drum and UNC dustiness tester [35]

Fig. 20 Genetic optimization algorithm for parameter adjustment

To demonstrate the work of the developed optimization algorithm, it was applied to a simple generic flowsheet model of a grinding process, shown in Fig. 21. The units were taken from the general unit library (see Sect. 8). The model and optimization parameters are listed in Table 5. The model of the crusher unit uses Bond's law with the power input as a user parameter to adjust the degree of comminution. The splitter recycles 50% of the milled material independent of the particle size, which is fed back and mixed with the feed after applying a time delay of one second. The system response to a stepwise change of the inlet mass flow is shown in Fig. 22.

The goal of the optimization case is to reach a constant value of the Sauter mean diameter (SMD) at the outlet. The temporal progressions of the SMD and the power input for the best solution after 30 and 65 iterations are shown in Fig. 23, in which
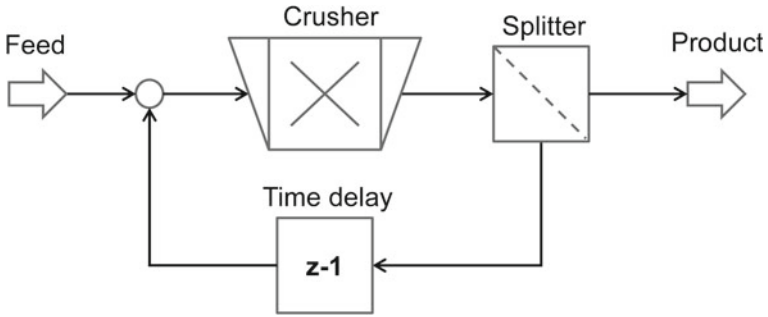
Fig. 21 Exemplary flowsheet model of the crushing process

Table 5 Model and optimization parameters for the test simulation

Feed	
$\dot{m}_{tot} = \dot{m}_{solid}$ (t = 0 s)	2 kg/s
$\dot{m}_{tot} = \dot{m}_{solid}$ (t = 50 s)	4 kg/s
x_m/σ	1.5 mm/0.1 mm
Crusher	
W_i	50 kWh/t
σ	0.15 mm
Splitter	
k_{split}	0.5
Time delay	
τ	1 s
Optimization parameters	
n_{parent}	50
n_{child}	50
σ_0	0.4

Fig. 22 Response to a stepwise change of the feed mass flow in the crushing process
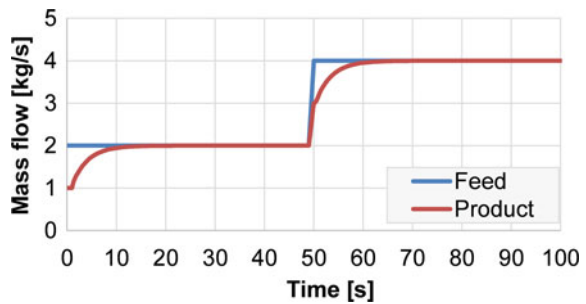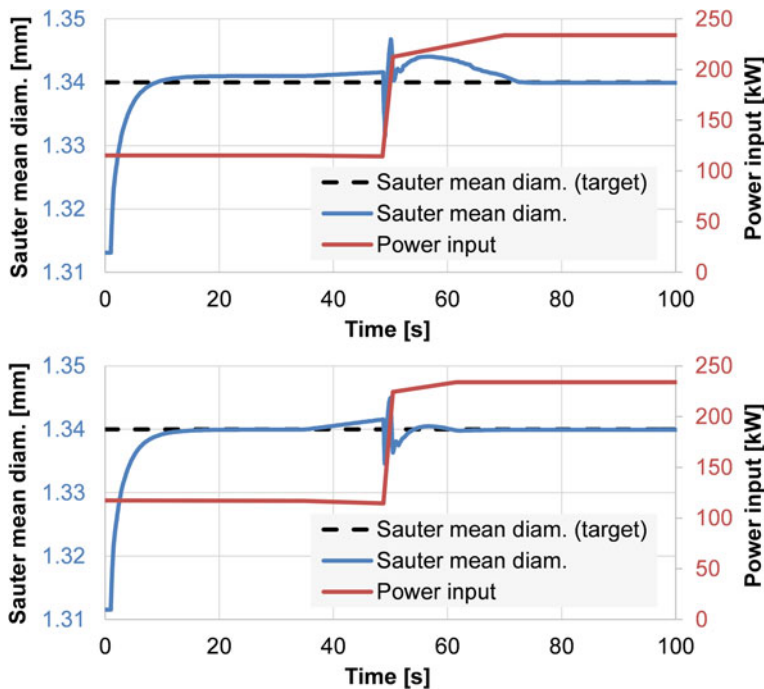
Fig. 23 Temporal progression of the SMD and power input for a solution of the genetic algorithm after 30 (top) and 65 (bottom) iterations

the dotted black line shows the target value of the SMD. In this case, the number of parent and child solutions is 50 and the starting value of σ is set to 0.4. The optimizer may vary the power input at 4 different time steps between 50 and 500 kW, which leads to a total of 8 independent variables. The power input may be changed in a time interval between 30 and 70 s.

In Fig. 23, it can be seen that the stepwise change of the input mass flow leads to a distortion in the SMD of the outlet. To mitigate the impact of the change in the feed, the power input of the crusher should be decreased in advance and after the change in the feed the power input should be gradually increased until the target value of the SMD is reached.

10   Approaches to Development of Data-Driven Flowsheet Models

The abundance of data and the increasing computational capacities have led to a wide use of data-driven models, like artificial neural networks (NNs), in different fields of both science and industry. The main advantage of NNs is the efficient
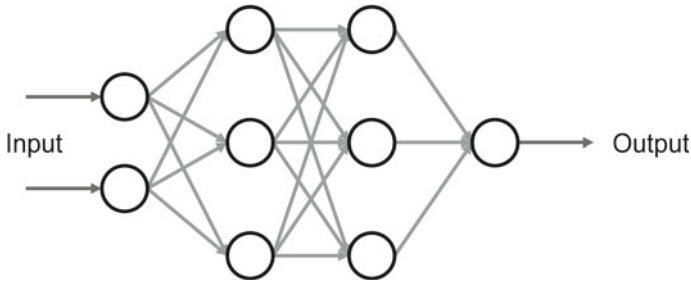
Fig. 24 Exemplary MLP neural network with two hidden layers and three neurons each

handling of large data sets for pattern recognition and information extraction. The most commonly used neural networks are the so-called multilayer perceptron (MLP) neural networks. An MLP consists of layers of nodes (neurons) and connecting edges. The first layer of neurons represents the input signals and the last layer the outputs of the network. The layers of neurons in between are called hidden layers, which apply a limiting transformation function, like tanh or sigmoid functions, on the respective input. An exemplary MLP with two inputs, one output, and two hidden layers, consisting of three neurons each, is shown in Fig. 24.

The main objective of an MLP is to find a suitable mapping of multiple input signals to one or more output signals. Therefore, the weights of the connecting edges are varied during the so-called training phase by error back-propagation, until the output data can be mapped to a certain degree. To achieve a satisfactorily trained MLP, either the network structure, the training parameters, or the training data set may be adjusted. After the training phase, the generalization capability of the NN is tested during the test phase by applying an unknown data set to the trained NN. In most cases, the training phase and testing phase is repeated multiple times to increase the generalization properties of the NN.

The main drawback of NNs is the tendency of overfitting the training data, i.e. the network may try to map the noise in the data set. In combination with the inaccessibility of the trained networks "knowledge", the use of NNs as black-box models for either control purposes or process optimization seems unadvisable, as the NN behavior regarding untrained system states is rather unpredictable. To tackle this issue, the use of hybrid models, i.e. NNs (black-box) combined with mechanistic (white-box) models seems especially promising. There are two main types of hybrid models, that have been presented by von Stosch et al. [63], namely by either parallel or serial combination, shown in Fig. 25.

In the parallel model configuration (Fig. 25a), the results of the black-box and the white-box model, are combined in a user-defined way. For a simple summation of the results, the neural network is trained on the residuals between the output data and the results of the white-box model. This configuration is especially suitable for systems with separable mechanisms or dynamics, such that each model will focus on distinct features of the system [63]. For the serial configuration, two model combinations are possible, while the structure in Fig. 25b (first black-box) has gained more attention
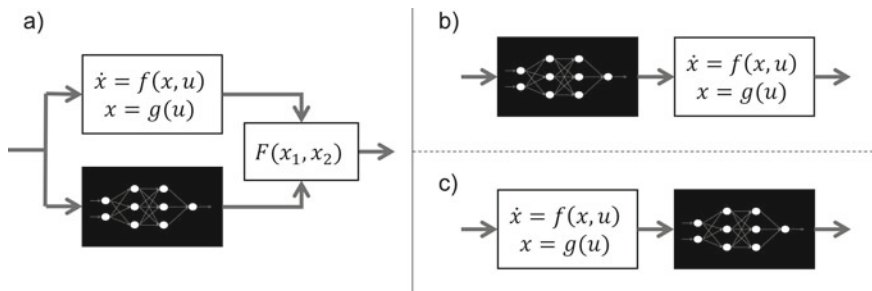
Fig. 25 Overview of hybrid model combinations, based on illustration of von Stosch et al. [63]

in research while hybrid models of structure Fig. 25c (second black-box) have not found much application in chemical engineering [63]. They are suited for systems with unknown underlying mechanism, with the black-box model acting as a state observer [63].

The white box model in the hybrid modeling approaches may be represented by a flowsheet model, which takes general mechanisms like mass and energy balances into account. In case of the parallel configuration, the flowsheet model may be used to roughly predict the corresponding outputs of the systems. E.g. for a milling process, as shown in Fig. 21, the flowsheet may predict the resulting particle size distribution based on mass balances and a simplified comminution model. The residuals between the computed values and the measured ones may be used as training data for a NN, to take possible mechanisms into account that are not considered in the flowsheet model, e.g. abrasion. After a successful training of the NN, the resulting PSD of the hybrid model is the combined value from flowsheet and NN.

The advantage of this procedure is, on the one hand, that the NN may take measurement data, like acoustic measurements, into account that can't be utilized by simple flowsheet models. On the other the flowsheet model assures, that basic physical principles are always considered.

11 Summary

The aim of the Z-Project in the Priority Program SPP 1679 of the German Research Foundation (DFG) was the development of a customizable, flexible and extensible platform for dynamic flowsheet simulations of interconnected solids processes. These requirements are met by the presented program Dyssol, offering a complete framework with an efficient architecture, interfaces and algorithms. Furthermore, Dyssol comprises a clear graphical user interface with the option of direct data visualization, extensible unit and solver libraries, as well as a material database to provide easy access to the program. The open structure of the flowsheet system also allows

for extensive customizability and integration of external programs to meet various requirements.

The main simulation paradigms and algorithms are presented in this chapter. Different case studies show a successful validation, good stability properties and a high performance of the implemented framework. An example of the application of the developed system for parameter optimization, as well as the outlook for possible coupling with data-driven models is given.

References

1. Alaathar, I., Hartge, E.-U., Heinrich, S., Werther, J.: Modeling and flowsheet simulation of continuous fluidized bed dryers. Powder Technol. **238**, 132–141 (2013)
2. Aldous, D.J.: Deterministic and stochastic models for coalescence (aggregation and coagulation): a review of the mean-field theory for probabilists. Bernoulli **5**, 3–48 (1999)
3. Anderson, D.G.: Iterative procedures for nonlinear integral equations. J. Assoc. Comput. Mach. **12**, 547–560 (1965)
4. Aspentech—Aspen Plus. [online]. [cit. 2019-12-10]. https://www.aspentech.com/en/products/engineering/aspen-plus
5. Austin, L.G.: A discussion of equations for the analysis of batch grinding data. Powder Technol. **106**, 71–77 (1999)
6. Austin, L.G., Luckie, P.T.: The estimation of non-normalized breakage distribution parameters from batch grinding tests. Powder Technol. **5**(72), 267–271 (1971)
7. Bond, F.C.: Crushing and grinding calculation Part I. Brit. Chem. Eng. **6**(6), 378–385 (1961)
8. Boor, DC.: A practical guide to splines. Appl. Math. Sci. **47**:39–50 (2001)
9. Boukouvala, F., Niotis, V., Ramachandran, R., Muzzio, F.: An integrated approach for dynamic flowsheet modeling and sensitivity analysis of a continuous tablet manufacturing process. Comput. Chem. Eng. **42**, 30–47 (2012)
10. Collier, A.M., Hindmarsh, A.C., Serban, R., Woodward, C.S.: User documentation for KINSOL v3.1.0 (SUNDIALS v3.1.0), Center for Applied Scientic Computing Lawrence Livermore National Laboratory (2017)
11. DFG-Priority Programme SPP 1679 [online]. [cit. 2019-09-09]. https://www.dynsim-fp.de/en/home
12. Deutsch, W.: Bewegung und Ladung der Electricitätsträger im Zylinderkondensator. Ann Phys **68**, 335–344 (1922)
13. Dimian, A.C., Bildea, C.S., Kiss, A.A.: Integrated Design and Simulation of Chemical Processes, 2nd edn, pp. 73–156. Elsevier, Amsterdam (2014)
14. Dosta, M., Heinrich, S., Werther, J.: Fluidized bed spray granulation: analysis of the system behaviour by means of dynamic flowsheet simulation. Powder Technol. **204**, 71–82 (2010)
15. Dosta, M., Litster, J.D., Heinrich, S.: Flowsheet simulation of solids processes: current status and future trends. Adv. Powder Technol. (in Press)
16. Dosta, M.: Dynamic Flowsheet Simulation of Solids Processes and Its Application to Fluidized Bed Spray Granulation. Cuvillier Verlag, Germany (2013)
17. Eng, L.Z.: Qt5 C++ GUI programming Cookbook. Packt Publishing, Birmingham (2016)
18. gPROMS Formulated Products—Solids Processing [online]. [cit. 2019-12-10]. https://www.psenterprise.com/products/gproms/formulatedproducts
19. Gupta, C.K.: Extractive Metallurgy of Molybdenum, p. 83. CRC Press, Boca Raton (1992)
20. HDF5 C++ Reference Manual [online]. [cit. 2019-12-06]. https://portal.hdfgroup.org/pages/viewpage.action?pageId=50073884
21. Heinrich, S., Peglow, M., Ihlow, M., Henneberg, M., Mörl, L.: Analysis of the start up process in continuous fluidized bed spray granulation by population balance modelling. Chem. Eng. Sci. **57**, 4369–4390 (2002)

22. Helget, A.: Modulare Simulation verfahrenstechnischer Anlagen. VDI Verlag GmbH, Fortschritt-Berichte (1997)
23. Hennig, M., Teipel, U.: Stationäre Siebklassierung. Chem. Ing. Tec. **88**, 911–918 (2016)
24. Hillestad, M., Hertzberg, T.: Dynamic simulation of chemical engineering systems by the sequential modular approach. Comput. Chem. Eng. **10**, 377–388 (1986)
25. Hindmarsh, A.C., Serban, R., Collier, A.: User Documentation for IDA v3.1.0 (SUNDIALS v3.1.0), Center for Applied Scientic Computing Lawrence Livermore National Laboratory (2017)
26. Iveson, S.M., Beathe, J.A., Page, N.W.: The dynamic strength of partially saturated powder compacts: the effect of liquid properties. Powder Technol. **127**(2), 149–161 (2002)
27. JKSimMet—JKTech Simulation of Comminution and Classification Circuits. [online]. [cit. 2019-12-10]. https://jktech.com.au/jksimmet
28. King, R. P.: Modeling and Simulation of Mineral Processing Systems. Butterworth & Heinemann, Oxford (2001)
29. Kovačević, T., Wiedmeyer, V., Schock, J., Voigt, A., Pfeiffer, F., Sundmacher, K., Briesen, H.: Disorientation angle distribution of primary particles in potash alum aggregates. J. Cryst. Growth **467**, 93–106 (2017)
30. Kovačević, T., Briesen, H.: Simulations of crystal aggregation and growth: Towards correct crystal area. AIChE **65**(5) (2019)
31. Kumar, J., Peglow, M., Warnecke, G., Heinrich, S.: An efficient numerical technique for solving population balance equation involving aggregation, breakage, growth and nucleation. Powder Technol. **182**(1), 81–104 (2008)
32. Kumar, S., Ramkrishna, D.: On the solution of population balance equations by discretization I. A fixed pivot technique. Chem. Eng. Sci. **51**(8), 1311–1332 (1996)
33. Lelarasmee, E., Ruehli, A.E., Sangiovanni-Vincintelli, A.L.: The Waveform Relaxation Method for Time-Domain Analysis of Large Scale Integrated Circuits: Theory and Applications. University of California (1982)
34. Liu, L.X., Litster, J.D., Iveson, S.M., Ennis, B.J.: Coalescence of deformable granules in wet granulation processes. AIChE J. **46**(3), 529–539 (2000)
35. Londershausen, T.T.: Entwicklung von Prognosefunktionen zur Abschätzung der Staubungsneigung von trockenen und feuchten Schüttgütern. Shaker Verlag, Aachen (2018)
36. Luyben, W.L.: Aspen dynamics simulation of a middle-vessel batch distillation process. J. Process Control **33**, 49–59 (2015)
37. Mah, R.: Chemical Process Structures and Information Flows, pp. 125–183. Butterworth Publishers, Oxford
38. Marquardt, W.: Dynamic Process Simulation—Recent Progress and Future Challenges, pp. 131–180. CACHE Publications, Chemical Process Control CPC-IV, London (1991)
39. Mathews, J.H., Fink, K.D.: Numerical Methods Using MATLAB, 3rd edn. Prentice Hall, Upper Saddle River (1999)
40. Metta, N., Ghijs, M., Schäfer, E., Kumar, A., Cappuyns, P., Van Assche, I., Singh, R., Ramachandran, R., De Beer, T., Ierapetritou, M., Nopens, I.: Dynamic flowsheet model development and sensitivity analysis of a continuous pharmaceutical tablet manufacturing process using the wet granulation route. Processes **7**, 234 (2019)
41. Molerus, O., Hoffmann, H.: Darstellung von Windsichtertrennkurven durch ein stochastisches Modell. Chemie Ingenieur Technik **41**(5 + 6), 340–344 (1969)
42. Muschelknautz, E.: Die Berechnung von Zyklonabscheidern für Gase. Chem. Ing. Tech. **44**(1/2), 63–71 (1972)
43. Parnas, D.L.: On the criteria to be used in decomposing systems into modules. Commun. ACM **15**(12), 1053–1058 (1972)
44. Plitt, L.R.: The analysis of solid-solid separations in classifiers. CIM Bull. **64**(708), 42–47 (1971)
45. Pogodda, M.: Development of an Advanced System for the Modeling and Simulation of Solids Processes. Shaker Verlag, Germany

46. Qt—Cross-platform software development for embedded & desktop [online]. [cit. 2019-12-06]. https://www.qt.io
47. Radichkov, R., Müller, T., Kienle, A., Heinrich, S., Peglow, M., Mörl, L.: A numerical bifurcation analysis of continuous fluidized bed spray granulation with external product classification. Chem. Eng. Process. **45**, 826–837 (2006)
48. Roach, J.R., O'Neill, B.K., Hocking, D.A.: A new synthetic method for stream tearing in process systems analysis. Chem. Eng. Commun. **161**, 1–14 (1997)
49. Sander, S., Gawor, S., Fritsching, U.: Separating polydisperse particles using electrostatic precipitators with wire and spiked-wire discharge electrode design. Particuology **38**, 10–17 (2018)
50. Sandgren, P.-E., Berglind, B., Modigh, S.: Basics in Minerals Processing, Handbook, 10th edn, p. 34 (2015)
51. Schopfer, G., Yang, A., von Wedel, L., Marquardt, W.: CHEOPS: a tool-integration platform for chemical process modelling and simulation. Int J. Softw. Tools Technol. Transfer **6**, 186–202 (2004)
52. Skorych, V., Das, N., Dosta, M., Kumar, J., Heinrich, S.: Application of transformation matrices to the solution of population balance equations. Processes **7**, 535 (2019)
53. Skorych, V., Dosta, M., Hartge, E.-U., Heinrich, S.: Novel system for dynamic flowsheet simulation of solids processes. Powder Technol. **314**, 665–679 (2017)
54. Skorych, V., Dosta, M., Hartge, E.-U., Heinrich, S., Ahrens, R., Le Borne, S.: Investigation of an FFT based solver applied to dynamic flowsheet simulation of agglomeration processes. Adv. Powder Technol. **30**(3), 555–564 (2019)
55. Stroustrup, B.: The C++ Programming Language, 4th edn. Addison-Wesley, New York (2013)
56. Stroustrup, B.: Tour of C++, 4th edn, pp. 23–57. Addison-Wesley, New York (2014)
57. SUNDIALS: SUite of Nonlinear and DIfferential/ALgebraic Equation Solvers [online]. [cit. 2019-12-06]. https://computation.llnl.gov/projects/sundials
58. Tarjan, R.: Depth first search and linear graph algorithms. SIAM J. Comput. **1**(2), 146–160 (1972)
59. Tarjan, R.: Edge-disjoint spanning trees and depth-first search. Acta Informatica **6**, 171–185 (1976)
60. The HDF5® Library & File Format [online]. [cit. 2019-12-06]. https://www.hdfgroup.org/solutions/hdf5
61. Towler, G., Sinnott, R.: Chemical engineering design. In: Principles, Practice and Economics of Plant and Process Design, 2nd edn, pp. 223–236. Butterworth-Heinemann, Oxford (2013)
62. Vogel, L., Peukert, W.: Modelling of grinding in an air classifier mill based on a fundamental material function. KONA **21**, 109–120 (2003)
63. von Stosch, M., Oliveira, R., Peresa, J., De Azevedoa, S.F.: A general hybrid semi-parametric process control framework. J. Process Control **22**, 1171–1181 (2012)
64. Wegstein, J.H.: Accelerating convergence of iterative processes. Commun. ACM **1**(6), 9–13 (1958)
65. Weicker, K.: Evolutionäre Algorithmen. Springer Fachmedien, Wiesbaden (2015)